A numerical tool for the frequency domain simulation of large clusters of wave energy converters

Francesc Fabregas Flavia

Thèse de Doctorat

Francesc FÀBREGAS FLAVIÀ

Mémoire présenté en vue de l'obtention
du grade de Docteur de l'École Centrale de Nantes
sous le sceau de l'Université Bretagne Loire

École doctorale : Sciences Pour l'Ingénieur, Géosciences, Architecture

Discipline : *Mécanique des Milieux Fluides*
Unité de recherche : *Laboratoire de recherche en Hydrodynamique, Énergétique et Environnement Atmosphérique*

Soutenue le 30 Mai 2017

A numerical tool for the frequency domain simulation of large clusters of wave energy converters

JURY

Président :	**M. Pierre FERRANT**	Professeur des Universités, Ecole Centrale de Nantes
Rapporteurs :	**M. Frédéric DIAS**	Professeur, University College Dublin (Irlande)
	M. Masashi KASHIWAGI	Professeur, Osaka University (Japon)
Examinateurs :	**M. Bernard MOLIN**	Docteur - HDR, Ecole Centrale de Marseille
	M. Julien SALOMON	Maître de conférences – HDR, Université Paris-Dauphine
Directeur de thèse :	**M. Alain CLÉMENT**	Ingénieur de Recherches - HDR, Ecole Centrale de Nantes

A Numerical Tool for the Frequency Domain Simulation of Large Clusters of Wave Energy Converters

Francesc Fàbregas Flavià

Laboratoire de recherche en Hydrodynamique, Énergétique et Environnement Atmosphérique

Ecole Centrale de Nantes

This dissertation is submitted for the degree of

Docteur de l'Ecole Centrale de Nantes

2017

This thesis is dedicated to my parents and to my brother.

Acknowledgements

I would like to express my gratitude to Prof. Masashi Kashiwagi, Prof. Bernard Molin, Prof. Frédéric Dias, Prof. Pierre Ferrant and Dr. Julien Salomon for having kindly accepted the role of PhD thesis examiner. It has been a great privilege to be able to present my research to internationally renowned figures in the domains of hydrodynamics and applied mathematics.

This thesis would not have been possible without the trust that my thesis director Dr. Alain H.Clément and both my co-supervisors Dr. Aurélien Babarit and Dr. François Rongère placed in me during the recruitment phase of the OceaNET multinational Initial Training Network, funded under the PEOPLE Programme (Marie Curie Actions), and throughout the whole duration of the project. I will always be indebted to them.

I would like to express my sincere gratitude to my Phd thesis director Dr. Alain H. Clément, with whom it has been a pleasure to work, for the numerous enjoyable and fruitful discussions that we had at the LHEEA laboratory. They undoubtedly sparked innovative hydrodynamic research paths and helped me steer my way through the research project. This would not have been possible without his availability and willingness to support me, and I deeply thank him for that. I have been impressed by the great effort he has devoted to providing thorough corrections and by his patience and pedagogical attitude when transferring both complex knowledge and unique experience gained after his long successful research career.

A special thanks goes to Dr. Aurélien Babarit for the trust he placed in me during the project. I will always be indebted to him for the unique and valuable career opportunities he has opened, notably the research collaborations in which I had the luxury to be involved. They would not have been a reality without his great ability to identify innovative and stimulating projects. I have really appreciated his effective communication and positive feedback which have greatly encouraged me to pursue my research.

I would like to thank Dr. François Rongère for his crucial programming support and advice at the beginning of the project. I really appreciated his positive attitude

and patience towards my poor explanations in French of the problems and bugs I encountered. I will always be indebted to him for his availability and for all the knowledge transferred which will undoubtedly be very useful in my future career.

I would like to extend my gratitude to Dr. Fabien Montiel for his warm welcome at the department of mathematics of the University of Otago, and for his support and knowledge transfer during all the research collaboration project which turned it into a thrilling and unforgettable experience.

Special thanks goes to Dr. Cameron McNatt for his warm welcome at the University of Edinburgh. I really appreciated his involvement in the research collaboration, especially at a very busy time coinciding with the end of his Phd thesis project. The interesting discussions that we had helped me to identify different paths to explore during my research, and I deeply thank him for that.

I would like to deeply thank Dr. Maxime Philippe for his guidance and supervision during the internship I carried out at INNOSEA, as well as to all the employees for their warm welcome to the company and for the enjoyable afterworks.

I will always be indebted to Prof. Pierre Ferrant, Philippe Baclet and Sandrine Jamet for their unconditional support to the INORE Symposium 2016 which I had the pleasure to co-organize with my colleagues Boris Teillant, François-Xavier Fäy and Loup Suja Thauvin. Thanks to their economic and logistical help, the event was an enormous success.

I would not have been able to attend international conferences, short courses, workshops, seminars, etc. without the assistance of Sonia Lambert, and I deeply thank her for being always so responsive, efficient and helpful.

I would like to express my sincere gratitude to the Phd student "family" of the LHEEA lab for the warm welcome and help at the beginning of the project, and for the enjoyable experiences spent together during these three years. I will always keep them as a truly valuable souvenir.

I feel very lucky to have been able to share plenty of fun experiences with the fellows of the OceaNET project, who have turned into very good friends after these years. This would not have been possible without the effort made by the OceaNET managing team composed of Mairead Atcheson, Soraya Hamawi, Erica Cruz and José Cândido.

Last but not least, I would like to deeply thank my parents and my brother for having supported me in this endeavour, in both the crests and troughs of the project.

Abstract

Compact arrays of small wave absorbers constitute an example of the multiple existing categories of wave energy converters (WECs) and have been identified as being an advantageous solution for the extraction of wave energy when compared to a big isolated point absorber.

Among the numerous challenges associated with the numerical modeling of such devices, one of the most relevant one is the evaluation of the hydrodynamic interactions amid the large number of floats O(100) they are composed of. Direct computations with standard Boundary Element Method (BEM) solvers, used extensively in wave/structure interaction problems, become prohibitive when the number of bodies increases. Thus, there is a need to employ an alternative approach more suitable for the study of the multiple-scattering in large arrays.

In this work, the Direct Matrix Method interaction theory has been implemented. Based on characterizing the way a WEC scatters and radiates waves, this methodology enables one to significantly reduce the number of unknowns of the classical boundary value problem dealt with by standard BEM solvers and, therefore, the computational time.

The acceleration provided by the numerical tool developed has allowed examining the power capture of a generic bottom-reference heave-buoy array WEC and optimizing its layout. We have shown that there exist an optimum number of floats for a given device footprint. Exceeding this number results in a "saturation" of the power increase which is undesirable for the economic viability of the device.

Contents

Contents **ix**

List of Figures **xv**

List of Tables **xxix**

1 Introduction **1**
1.1 Context 1
1.2 State-of-the-art 4
1.3 Aims and objectives 13
1.4 Thesis outline 14

2 Direct Matrix Method Interaction Theory in Finite-Depth **17**
2.1 Airy wave theory 17
2.2 Solution to the BVP for an isolated device 20
2.2.1 Outgoing waves 23
2.2.2 Incident waves 25
2.3 Solution of the array BVP: calculation of the scattering coefficients . . 27
2.3.1 Diffraction Problem 28
2.3.2 Radiation Problem 31
2.3.3 Calculation of the radiation hydrodynamic coefficients and the excitation forces 33
2.4 Numerical Implementation 34
2.4.1 Vectors and Matrices shapes 34
2.4.2 Bessel functions scaling 35
2.5 Summary 36

3 Hydrodynamic Operators of the Direct Matrix Method **39**
3.1 Method I 39

3.1.1 Diffraction Transfer Matrix . . . 39
3.1.2 Radiation Characteristics . . . 42
3.1.3 Force Transfer Matrix . . . 43
3.2 Method II . . . 44
3.2.1 Diffraction Transfer Matrix . . . 44
3.2.2 Radiation Characteristics . . . 46
3.2.3 Force Transfer Matrix . . . 46
3.3 Equivalence between Methods I and II . . . 47
3.4 Rotation of the body . . . 49
3.5 Numerical Implementation . . . 51
3.6 Results and Discussion . . . 52
3.6.1 Diffraction Transfer Matrix . . . 55
3.6.1.1 Cylinder . . . 55
3.6.1.2 Cube . . . 56
3.6.2 Radiation Characteristics . . . 56
3.6.2.1 Cylinder . . . 56
3.6.2.2 Cube . . . 59
3.6.3 Force Transfer Matrix . . . 59
3.6.3.1 Cylinder . . . 59
3.6.3.2 Cube . . . 60
3.7 Conclusions . . . 63

4 Validation of the Direct Matrix Method implementation 65
4.1 Isolated body . . . 66
4.1.1 Haskind's Relation . . . 66
4.1.2 Relationship between the Force Transfer Matrix and the Radiation Characteristics . . . 67
4.1.3 Radiation Damping Coefficients in terms of the far-field radiation potential . . . 73
4.1.4 Relationship between the Force Transfer Matrix and the Damping coefficients . . . 74
4.2 Array . . . 76
4.2.1 Generalisation of Haskind's relation for an array of bodies . . . 76
4.2.2 Relationship between the Excitation Force and the Radiation Characteristics . . . 77
4.2.3 Relationship between the Damping coefficients and the Radiation Potential . . . 79

4.3 Results and Discussion . . . 80
4.3.1 Progressive terms . . . 81
4.3.1.1 Isolated body . . . 81
4.3.1.2 Array . . . 81
4.3.2 Evanescent terms . . . 86
4.3.3 Condition Number . . . 95
4.3.4 Wall Clock Execution Time . . . 95
4.4 Conclusions . . . 103
4.4.1 Relationships for progressive terms . . . 103
4.4.2 Influence of the evanescent terms . . . 104
4.4.3 Condition number . . . 104
4.4.4 Wall clock time . . . 104

5 Numerical modeling and optimization of a bottom-referenced heave-buoy WEC array 105
5.1 Methodology . . . 107
5.1.1 Description of the System . . . 107
5.1.2 Equation of Motion . . . 107
5.1.3 Computation of the Hydrodynamic Coefficients . . . 110
5.1.4 Performance evaluation . . . 111
5.1.5 Wave Climate . . . 112
5.2 Results and Discussion . . . 113
5.2.1 Individual float response . . . 113
5.2.2 Three-float cluster . . . 115
5.2.3 60-float Configuration . . . 115
5.2.4 Power versus Number of Floats . . . 119
5.2.5 36-float Configuration . . . 122
5.2.6 Radius optimization . . . 123
5.3 Conclusions . . . 128

6 Impact of a large WEC farm on the ambient wave spectrum 131
6.1 Plane wave expansion of cylindrical harmonics . . . 133
6.2 Transmitted and reflected spectra . . . 138
6.2.1 Diffraction . . . 142
6.2.2 Radiation . . . 144
6.3 Numerical Implementation . . . 145
6.4 Results . . . 146

6.4.1 Reflection and transmission coefficients . . . 146
6.4.2 Free surface elevation . . . 149
6.5 Discussion and conclusions . . . 152

7 Conclusions **157**

References **161**

A Derivation of outgoing partial wave functions **173**
A.1 Separation of the z-coordinate . . . 173
A.2 Separation of the θ-coordinate . . . 174
A.3 Separation of the r-coordinate . . . 175
A.4 General solution . . . 176

B Transformation Matrix **179**

C Single truncated vertical cylinder at finite depth **183**
C.1 System of equations . . . 183
C.2 Numerical implementation . . . 185
C.3 Results . . . 186
C.4 Accuracy . . . 188
C.5 Parameters sensitivity analysis . . . 196

D Hydrodynamic interactions in an array of truncated circular cylinders **205**
D.1 Formulation . . . 205
D.1.1 Notation . . . 206
D.1.2 Radiation Characteristics . . . 207
D.1.3 Diffraction Transfer Matrix . . . 223
D.1.4 Hydrodynamic forces . . . 227
D.1.4.1 Force direction z . . . 229
D.1.4.2 Force direction x . . . 232
D.1.4.3 Force direction y . . . 234
D.1.4.4 Moment direction y . . . 236
D.1.4.5 Moment direction x . . . 241
D.1.4.6 Hydrodynamic coefficients . . . 245
D.1.4.7 Summary of Force Formulae . . . 245
D.2 Numerical results . . . 248

D.2.1 Isolated Cylinder . . . 248
D.2.2 Four cylinder array . . . 251
D.2.3 Sensitivity to evanescent modes truncation . . . 252

E Equivalence between Method I and II 265
E.1 Diffraction Transfer Matrix . . . 265
E.2 Radiation Characteristics . . . 267
E.3 Force Transfer Matrix . . . 268

F Reformulation of Green's function constant 271

G Numerical Integration 275

H Formulation of the Direct Matrix Method interaction theory for infinite depth 281
H.1 Array wave fields . . . 281
H.2 Diffraction Transfer Matrix and Radiation Characteristics . . . 284
H.3 Numerical implementation . . . 286
H.3.1 Array wave fields . . . 287
H.3.2 Diffraction Transfer Matrix and Radiation Characteristics . . . 288

I Hydrodynamic operators of a truncated vertical circular cylinder and a cube 291
I.1 Mesh Sensitivity . . . 291
I.1.1 Cylinder . . . 291
I.1.2 Cube . . . 293
I.2 Radiation Characteristics . . . 295
I.2.1 Cylinder . . . 295
I.2.2 Cube . . . 297
I.3 Force Transfer Matrix . . . 298
I.3.1 Cylinder . . . 298
I.3.2 Cube . . . 298

J Hydrodynamic coefficients of a small group of closely-spaced hemispheric floats 303

List of Figures

1.1 Three examples of multi-body WECs. *a*) FO^3 platform, *b*) Manchester Bobber, *c*) Wavestar SC-Concept 3

2.1 Schematic of the domain limited by the free surface (SL), the mean body's wetted surface (S_b), the seabed (F) and a control cylindrical surface at infinity (S_∞). 21

2.2 Partial waves modes. Progressive term $H_m^{(1)}(r)$ (a,b,c); evanescent term $K_m(r)$ (d,e,f). 25

2.3 Incident plane wave as a summation of partial cylindrical waves plotted as the surface elevation for increasing truncation values M. Source: McNatt et al. (2015). 26

2.4 Schematic of the plane view of two bodies of arbitrary geometry with the nomenclature and reference systems used herein. 28

3.1 Authorized a) and unauthorized b) relative position between bodies when using the Direct Matrix Method interaction theory. Source: adapted from Chakrabarti (2001). 48

3.2 Variation of the hyperbolic cosine depth dependence (a), the Bessel function of the first kind (b, e) and the modified Bessel function of the first kind (c, f) along the lateral side and the bottom of a cylinder respectively (3m radius, 6m draft in a 30m water depth). Results in (e) are calculated for $k_0a = 2.7523$ and in (f) for k_5a= 1.7279. Variation of the sinusoindal term $e^{-im\theta}$ along the perimeter of the cylinder (d). Red points represent the nodes of a given mesh 53

3.3 Truncated vertical cylinder mesh. Only half of the geometry is shown due to symmetry. (*a*) - coarse mesh, 361 panels; (*b*) - fine mesh 1521 panels. 54

3.4 Cube mesh. Only half of the geometry is shown due to symmetry. (a) - coarse mesh, 403 panels; (b) - fine mesh 2059 panels. 54

3.5 Real and imaginary parts of the Diffraction Transfer Matrix progressive terms for a truncated vertical cylinder of 3m radius (a), 6m draft in a 10m water depth. 55

3.6 Real and imaginary parts of the Diffraction Transfer Matrix progressive terms for a cube of 6m side (2a), 6m draft in a 10m water depth. . . . 56

3.7 Real and imaginary parts of the Radiation Characteristics progressive terms for a truncated vertical cylinder of 3m radius (a), 6m draft moving in surge in a 10m water depth. 57

3.8 Real and imaginary parts of the Radiation Characteristics progressive terms for a truncated vertical cylinder of 3m radius (a), 6m draft moving in heave in a 10m water depth. 58

3.9 Real and imaginary parts of the Radiation Characteristics progressive terms for a cube of 6m side (2a), 6m draft moving in surge in a 10m water depth. 59

3.10 Real and imaginary parts of the Radiation Characteristics progressive terms for a cube of 6m side (2a), 6m draft moving in heave in a 10m water depth. 60

3.11 Real and imaginary parts of the Force Transfer Matrix progressive F_x terms for a truncated vertical cylinder of 3m radius (a), 6m draft in a 10m water depth. 61

3.12 Real and imaginary parts of the Force Transfer Matrix progressive F_z terms for a truncated vertical cylinder of 3m radius (a), 6m draft in a 10m water depth. 61

3.13 Real and imaginary parts of the Force Transfer Matrix progressive F_x terms for a cube of 6m side (2a), 6m draft in a 10m water depth. . . . 62

3.14 Real and imaginary parts of the Force Transfer Matrix progressive F_z terms for a cube of 6m side (2a), 6m draft in a 10m water depth. . . . 62

3.15 Real and imaginary parts of the Force Transfer Matrix progressive M_z terms for a cube of 6m side (2a), 6m draft in a 10m water depth. . . . 63

4.1 Schematic of the domains used for the application of the Green's theorem. Free surface (SL); body's wetted surface (S_b); body's circumscribing cylinder radius (R_c); cylindrical surface infinitesimally larger than the body's circumscribing cylinder (S_c^ϵ), seabed (F); limit of the domain at infinity (S_∞); domain interior to the circumscribing cylinder (Ω_{int}); domain comprised between the circumscribing cylinder and the cylindrical surface at infinity (Ω_{out}). 68

4.2 Real (a) and Imaginary (b) parts of the FTM progressive terms in the surge (k=1) degree of freedom for an isolated cylinder of radius a, draft ($d - h = 2a$) in a water depth ($d = 4a$). The solid line (direct) corresponds to the direct calculation of the FTM using NEMOH. The dotted line (indirect) is obtained from the RC computed with NEMOH and by using the right-hand side of equation (4.1.39). 82

4.3 Real (a) and Imaginary (b) parts of the FTM progressive terms in the Roll (k=4) degree of freedom for an isolated cylinder of radius a, draft ($d - h = 2a$) in a water depth ($d = 4a$). The solid line (direct) corresponds to the direct calculation of the FTM using NEMOH. The dotted line (indirect) is calculated from the RC computed with NEMOH and by using the right-hand side of equation (4.1.39). 82

4.4 Diagonal radiation damping coefficients for the degrees of freedom Surge (a) and Roll (b) of a cylinder of radius a, draft ($d - h = 2a$) in a water depth ($d = 4a$). The solid line (direct) corresponds to the direct calculation of the damping coefficients using NEMOH. The dotted line (indirect) is calculated from the RC computed with NEMOH and by using the right-hand side of equation (4.1.58). 83

4.5 Schematic representation of an array composed of four truncated vertical cylinders of radius a and separated by a distance between centers d. $\beta = 0$ corresponds to the positive $x - axis$. 83

4.6 Non-dimensional excitation forces in Surge (a) and Heave (b) for the cylinders 1-2 in the array shown in Figure 4.5 from an incident plane wave with propagation direction ($\beta = 0$) and amplitude A . The solid line reproduces the results by Siddorn and Eatock Taylor (2008); the dotted green line has been computed with the IT by Kagemoto and Yue (1986) using NEMOH to compute the required hydrodynamic operators and the dotted blue line by means of the right-hand side of the extended cylindrical Haskind relation (4.2.12). The black dotted lines ($-\cdot-\cdot$) and ($\cdots$) correspond respectively to the contribution to the total excitation force from the isolated body and from the hydrodynamic interactions with the neighbours and have been computed from the first and second terms of equation (4.2.13) respectively. 84

4.7 Non-dimensional excitation forces in Surge (a) and Heave (b) for the cylinder 1 in the array shown in Figure 4.5 from an incident plane wave with propagation direction ($\beta = \pi/4$) and amplitude A . The legend follows as in Figure 4.6. 85

4.8 Non-dimensional Surge coupling radiation damping coefficients between two cylinders (1-3 in *a)*; 1-4 in *b)*) in the array shown in Figure 4.5. The first index indicates the cylinder on which the radiation force is evaluated due to the motion of the body indicated by the second index. The solid line reproduces the results by Siddorn and Eatock Taylor (2008); the dotted green line has been computed with the IT by Kagemoto and Yue (1986) using NEMOH to compute the required hydrodynamic operators and the dotted blue line by means of the right-hand side of equation (4.2.3). 86

4.9 Non-dimensional Heave coupling radiation damping coefficients between two cylinders (1-3 in *a)*; 1-4 in *b)*) in the array shown in Figure 4.5. The legend follows as in Figure 4.8. 87

4.10 Non-dimensional Heave-Surge coupling radiation damping coefficients between two cylinders (1-3 in *a)*; 1-4 in *b)*) in the array shown in Figure 4.5. The legend follows as in Figure 4.8. 87

4.11 Non-dimensional diagonal Surge (a) and Heave (b) radiation damping coefficients of cylinder 1 in the array shown in Figure 4.5. The solid line reproduces the results by Siddorn and Eatock Taylor (2008); the dotted green line has been computed with the IT by Kagemoto and Yue (1986) using NEMOH to compute the required hydrodynamic operators and the dotted blue line by means of the right-hand side of equation (4.2.3). The black dotted lines $(-\cdot-\cdot)$ and $(\cdots)$ correspond respectively to the contribution to the total radiation force from the isolated body and from the hydrodynamic interactions with the neighbours and have been computed from the first and second terms of equation (4.2.20) respectively. 88

4.12 Schematic of an array composed of two truncated vertical cylinders. $\beta = 0$ corresponds to the positive $x - axis$. 89

4.13 Added mass and damping coefficients for the first truncated vertical cylinder ($3m$ radius, $6m$ draft in a $50m$ water depth) in the two body array (Figure 4.12) for different separating distances ($d/a = 5000$ - (a), $d/a = 5$ - (b), $d/a = 5$ - (c)). First index corresponds to the direction of the force and the second to the degree of freedom. 90

4.14 Heave-heave coupling added mass coefficient as a function of the evanescent modes truncation L and for a small array of two truncated vertical circular cylinders of radius 3m, draft 6m in water depth of 50m. 91

4.15 Surge-surge coupling added mass coefficient as a function of the evanescent modes truncation L for two different wavelengths for a small array of two truncated vertical circular cylinders of radius 3m, draft 6m in water depth of 50m. 91

4.16 Magnitude of surface elevation for an array of 4 cylinders of $3m$ radius, $6m$ draft in a $50m$ water depth with a separation distance of 12m. Plots c, d, e, f show the percentage difference between the wave fields computed with the interaction theory (b) indicated by IT and the direct calculation using NEMOH (a) indicated by N as a function of the evanescent modes truncation L ((c) - $L = 0$, (d) - $L = 6$, (e) - $L = 12$, (f) - $L = 18$). Results are normalized by the amplitude of the incident wave (A). Propagation direction is defined from left to right. 93

4.17 Magnitude of surface elevation for an array of 4 cube boxes of $6m$ side, $6m$ draft in a $50m$ water depth with a separation distance of 12m. Plots c, d, e, f show the percentage difference between the wave fields computed with the interaction theory (b) indicated by IT and the direct calculation using NEMOH (a) indicated by N as a function of the evanescent modes truncation L ((c) - $L = 0$, (d) - $L = 6$, (e) - $L = 12$, (f) - $L = 18$). Results are normalized by the amplitude of the incident wave (A). Propagation direction is defined from left to right. 94

4.18 Condition number of the system scattering matrix of a 4 cylinder array (without Bessel functions normalization). 96

4.19 Condition number of the system scattering matrix of a 4 cylinder array (with Bessel functions normalization). 97

4.20 Schematic of an array of inline bodies separated by a distance d. 99

4.21 Discretization of a) a truncated vertical cylinder of $3m$ radius and $6m$ draft, b) a flap-type converter of $6m$ width by $2m$ side. 100

4.22 Comparison of wall clock computational times between the Direct Matrix Method interaction theory (IT) and direct NEMOH simulations for both a truncated vertical cylinder a) and a flap-type converter b), shown respectively in Figures 4.21a and 4.21b, as a function of the number of bodies positioned successively in line and separated by a distance of 60 meters. Calculations using the interaction theory require, first, the evaluation of the isolated body hydrodynamic characteristics and, then, the solution to the multiple scattering problem. The time associated with the former is indicated as “HC” and with the latter as “IT”. The evanescent modes truncation is referred to as “L”. Simulations were performed with 6 dofs per body, 30 frequencies (0.2 - 2.0 rad/s) and 5 propagation directions and both the diffraction and radiated problems were solved. 101

4.23 Curve fitting of the wall clock computational time of direct NEMOH simulations for both a truncated vertical cylinder a) and a flap-type converter b) shown in Figures 4.21a and 4.21b respectively. 102

5.1 Top (a) and Side (b) schematic views of the bottom-referenced heave-buoy array Wave Energy Converter. 108

5.2 Response Amplitude Operator (RAO) and power function of an individual isolated hemispherical float as a function of the Power Take-Off damping (B_{pto}) and for both a range of incoming wave frequencies and directions. 114

5.3 (a) Top view of a section of a three-float WEC; (b) Comparison of the Response Amplitude Operator (RAO) of float 2 computed using both a direct BEM calculation (both when isolated and in array) and with the Direct Matrix Method interaction theory (IT) using 4 evanescent modes (L) and a $\beta = 90°$ wave incidence; (c) relative difference between the (RAO) of float 2 computed using both a direct BEM calculation and with the Direct Matrix Method interaction theory (IT) for different values of the evanescent modes truncation (L) and a wave incidence of $\beta = 90°$. 116

5.4 Float interaction factors (q-factor) of the bottom-fixed heave-buoy array WEC and disturbance coefficient (H_s/H_s^I) of the wave field for a sea state with ($H_s = 0.75m$, $T_p = 4s$) and two mean propagation directions (0 and $\pi/3\,rad$) of the incident wave spectra. 118

5.5 Annual power (P_y) and separating distance between floats (dx) as a function of the number of units used in the bottom-referenced heave-buoy array WEC for two main propagation directions of the incident wave spectra. The annual power has been computed using the optimized separating distance ($dx\,opt$) between floats for each configuration comprised between the limits ($dx\,max$) and ($dx\,min$). 121

5.6 Float interaction factors (q-factor) of the 36-unit bottom-referenced heave-buoy array WEC and disturbance coefficient (H_s/H_s^I) of the wave field for a sea state with ($H_s = 0.75m$, $T_p = 4s$) and two mean propagation directions (0 and $\pi/3\,rad$) of the incident wave spectra. 124

5.7 Float significant motions (γ_s) of the 60 and 36-unit bottom-referenced heave-buoy array WEC for the sea state with ($H_s = 2.75m$, $T_p = 6.44s$) and two mean propagation directions (0 and $\pi/3\,rad$) of the incident wave spectra. 125

5.8 Annual power (P_y) produced by a 36-unit bottom-referenced heave-buoy array WEC as a function of both the radius of the hemispheric floats and the value of PTO damping (B_{pto}) used for two main propagation directions of the incident wave spectra (β). The values of PTO damping optimized for each float radius of the 36-unit configuration are indicated as ($B^{r}_{pto,36}$) whereas ($B^{r=3m}_{pto,60}$) refers to the PTO damping which optimizes the annual power produced by the 60-unit configuration with $3m$ radius floats. 127

5.9 Float significant motions (γ_s) of the 36-unit bottom-referenced heave-buoy array WEC with float radius $4.5m$ for the sea state with ($H_s = 2.75m$, $T_p = 6.44s$) and two mean propagation directions (0 and $\pi/3\,rad$) of the incident wave spectra. Results are presented for two different values of PTO damping ($B^{r=3m}_{pto,60}$) and ($B^{r=4.5m}_{pto,36}$). The former is optimized to maximize the energy capture of a 60-unit configuration with $3m$ radius floats and the latter of a 36-unit with $4.5m$ radius floats. 129

6.1 Schematic of the coupling between the IT and a Spectral wave model. Filled circles represent the array WECs whereas the empty ones the scattered and radiated wave fields given as a superposition of cylindrical harmonics by the IT (Kagemoto and Yue, 1986). S^{in} and S^{out} represent both the incident and transmitted spectra at the inlet and outlet of the wave farm respectively indicated as dotted lines. 132

6.2 Schematic of the integration contours in the complex χ plane. The arrows indicate direction. 135

6.3 Influence of the truncation parameter γ on the evaluation of the Hankel function of the first kind for the case $x \geq 0$ and with $r = x$ ($\theta = 0$). When only a single line is visible it means that a perfect match of results is obtained. 137

6.4 Schematic representation of the cylindrical harmonics transformation into plane waves in the horizontal plane. (x_j, y_j) represent the Cartesian reference system local to body j and OXY the global Cartesian reference system in which the jth body center O_j is expressed $O_j = (X_{0j}, Y_{0j})$. ξ_0 and ξ_1 are vertical planes parallel to the y axis and containing the centers of all the bodies in the array. 140

6.5 Schematic of three and two truncated vertical cylinder array configurations. 147

6.6 Transmission a) and reflection b) coefficient as a function of the angular variable sampling N_t for an array of 3 truncated vertical cylinders disposed parallel to the Y axis as in Figure 6.5a and with $d/a = 4$ . . . 148
6.7 Number of angular discretization samples N_t as a function of the separating distance between bodies d for both the transmission a) and reflection b) coefficients of an array of 3 truncated vertical cylinders as shown in Figure 6.5a. 148
6.8 Transmitted a) and reflected b) coefficients for an array of both 3 and 51 cylinders displayed parallel to axis Y as shown in Figure 6.5a. 149
6.9 Sensitivity of the angular variable discretization on the transmission a) and reflection b) coefficients as a function of the wave length to satisfy (6.2.6) with a precision of 10^{-5} 150
6.10 Reflected a) and transmitted b) energy spectra of the scattered wave field for a two cylinder array with separating distance $d = 6a$ between bodies with a the cylinder radius. The wave forcing is as in (6.4.1) with a wave length $\lambda/a = 10$. 151
6.11 Reflected a) and transmitted b) energy spectra of the radiated wave field for a two cylinder array with separating distance d between bodies with a the cylinder radius. The wave forcing is as in (6.4.1) with a wave length $\lambda/a = 10$. 151
6.12 Sensitivity study of the improper integral truncation parameter γ on the scattered free surface elevation (η). Plots on the left column (a, c, e) represent the absolute value of the scattered free surface elevation; right column (b, d, f) show the difference in percentage between the free surface elevation computed with the interaction theory (η^{IT}) and with the transformation of cylindrical harmonics to plane waves (η^{PC}). The incident wave forcing is as in (6.4.1) and the wave length $\lambda/a = 10$. . . 153
6.13 Sensitivity study of the improper integral truncation parameter γ on the radiated free surface elevation (η). Plots on the left column (a, c, e) represent the absolute value of the scattered free surface elevation; right column (b, d, f) show the difference in percentage between the free surface elevation computed with the interaction theory (η^{IT}) and with the transformation of cylindrical harmonics to plane waves (η^{PC}). The incident wave forcing is as in (6.4.1) and the wave length $\lambda/a = 10$. . . 154

B.1 Authorized a) and unauthorized b) relative position between bodies to comply with Graff's addition theorem restriction. 180

C.1 Coordinate system. Source: Sabuncu and Calisal (1981) 184
C.2 187
C.3 188
C.4 188
C.5 189
C.6 189
C.7 190
C.8 192
C.9 193
C.10 194
C.11 195
C.12 196
C.13 197
C.14 Bessel functions of the first kind and second kind (a); Modified Bessel functions of the first and second kind (b). Source: Abramowitz and Segun A. (1964) 199

D.1 Source: adapted from Zeng and Tang (2013) 207
D.2 249
D.3 250
D.4 250
D.5 251
D.6 252
D.7 253
D.8 254
D.9 255
D.10 256
D.11 257
D.12 Comparison between diagonal added mass and damping coefficients for two cylinders (Figure D.6b) of radius $3m$, draft $6m$ in a $10m$ water depth at several separation distances and for several truncation values (represented as L). First index corresponds to the direction of the force and the second to the degree of freedom. 259

D.13 Comparison between diagonal added mass and damping coefficients for two cylinders (Figure D.6b) of radius $3m$, draft $6m$ in a $10m$ water depth at several separation distances and for several truncation values (represented as L). First index corresponds to the direction of the force and the second to the degree of freedom. 260

D.14 Comparison between diagonal added mass coefficients computed with NEMOH, with the IT and a semi-analytical solution for two truncated vertical cylinders (Figure D.6b) of radius $3m$, draft $6m$ in a $10m$ water depth at several separation distances. First index corresponds to the direction of the force and the second to the degree of freedom. 261

D.15 Comparison between diagonal added mass coefficients computed with NEMOH, with the IT and a semi-analytical solution for two truncated vertical cylinders (Figure D.6b) at several separation distances. First index corresponds to the direction of the force and the second to the degree of freedom. 262

D.16 Diagonal and coupled added-mass and damping radiation coefficients in heave for two truncated vertical cylinders (Figure D.6b) as a function of the frequency. Two sets of results computed with a semi-analytical solution and with the IT are presented. The bodies have a radius of $5m$, a $10m$ draft in $50m$ water depth and are separated by $200m$. First index corresponds to the direction of the force and the second to the degree of freedom. 263

F.1 Real and imaginary parts of the Diffraction Transfer Matrix progressive terms for a truncated vertical cylinder of 3m radius (a), 6m draft in three different water depths. For $30m$ the Green's function constant used is in its original form. 272

F.2 Real and imaginary parts of the Diffraction Transfer Matrix progressive terms for a truncated vertical cylinder of 3m radius (a), 6m draft in three different water depths. For all water depths the Green's function constant has been reformulated. 273

G.1 Points of quadrature for a multidimensional integration. The square has limits $|x| \leq h$, $|y| \leq h$ whereas the triangle is inscribed in a circle of radius h. Source: Abramowitz and Segun A. (1964) 276

G.2 Four node bilinear quadrilateral and its image in parametric space. Source: adapted from Topper (2010). 277

G.3 Interpolation functions for node 1 of a quadrilateral element. Source: adapted from Felippa (2014) 277
G.4 Red numbers indicate node number and the limits of the domain are indicated in italic. Adapted from: Topper (2010) 278

I.1 Real and imaginary parts of the Diffraction Transfer Matrix progressive terms for a truncated vertical cylinder of 3m radius (a), 6m draft in a 10m water depth. 291
I.2 Real and imaginary parts of the Radiation Characteristics progressive terms for a truncated vertical cylinder of 3m radius (a), 6m draft moving in surge in a 10m water depth. 292
I.3 Real and imaginary parts of the Radiation Characteristics progressive terms for a truncated vertical cylinder of 3m radius (a), 6m draft moving in heave in a 10m water depth. 292
I.4 Real and imaginary parts of the Radiation Characteristics progressive terms for a truncated vertical cylinder of 3m radius (a), 6m draft moving in pitch in a 10m water depth. 293
I.5 Real and imaginary parts of the Diffraction Transfer Matrix progressive terms for a square box of 6m side (2a), 6m draft in a 10m water depth. 293
I.6 Real and imaginary parts of the Radiation Characteristics progressive terms for a square box of 6m side (2a), 6m draft moving in surge in a 10m water depth. 294
I.7 Real and imaginary parts of the Radiation Characteristics progressive terms for a square box of 6m side (2a), 6m draft moving in heave in a 10m water depth. 294
I.8 Real and imaginary parts of the Radiation Characteristics progressive terms for a square box of 6m side (2a), 6m draft moving in pitch in a 10m water depth. 295
I.9 Real and imaginary parts of the Radiation Characteristics progressive terms for a truncated vertical cylinder of 3m radius (a), 6m draft moving in sway in a 10m water depth. 295
I.10 Real and imaginary parts of the Radiation Characteristics progressive terms for a truncated vertical cylinder of 3m radius (a), 6m draft moving in roll in a 10m water depth. 296
I.11 Real and imaginary parts of the Radiation Characteristics progressive terms for a truncated vertical cylinder of 3m radius (a), 6m draft moving in pitch in a 10m water depth. 296

I.12 Real and imaginary parts of the Radiation Characteristics progressive terms for a square box of 6m side (2a), 6m draft moving in sway in a 10m water depth. 297
I.13 Real and imaginary parts of the Radiation Characteristics progressive terms for a square box of 6m side (2a), 6m draft moving in roll in a 10m water depth. 297
I.14 Real and imaginary parts of the Radiation Characteristics progressive terms for a square box of 6m side (2a), 6m draft moving in pitch in a 10m water depth. 298
I.15 Real and imaginary parts of the Force Transfer Matrix progressive F_y terms for a truncated vertical cylinder of 3m radius (a), 6m draft in a 10m water depth. 299
I.16 Real and imaginary parts of the Force Transfer Matrix progressive M_x terms for a truncated vertical cylinder of 3m radius (a), 6m draft in a 10m water depth. 299
I.17 Real and imaginary parts of the Force Transfer Matrix progressive M_y terms for a truncated vertical cylinder of 3m radius (a), 6m draft in a 10m water depth. 300
I.18 Real and imaginary parts of the Force Transfer Matrix progressive F_y terms for a square box of 6m side (2a), 6m draft in a 10m water depth. 300
I.19 Real and imaginary parts of the Force Transfer Matrix progressive M_x terms for a square box of 6m side (2a), 6m draft in a 10m water depth. 301
I.20 Real and imaginary parts of the Force Transfer Matrix progressive M_y terms for a square box of 6m side (2a), 6m draft in a 10m water depth. 301
I.21 Real and imaginary parts of the Force Transfer Matrix progressive M_z terms for a square box of 6m side (2a), 6m draft in a 10m water depth. 302

J.1 Diagonal and off-diagonal terms of the added-mass coefficient matrix **A**(equation 5.1.3) of the three-float system representing part of the generic bottom-fixed heave-buoy array WEC studied in Chapter 5. . . 305
J.2 Diagonal and off-diagonal terms of the hydrodynamic damping coefficient matrix **B** (equation 5.1.3) of the three-float system representing part of the generic bottom-fixed heave-buoy array WEC studied in Chapter 5. 306
J.3 Terms of the excitation moment vector $\mathbf{M^{ex}}$ (equation 5.1.3) of the three-float system representing part of the generic bottom-fixed heave-buoy array WEC studied in Chapter 5 for a wave incidence of $\beta = 90°$. 307

J.4 (a) Top view of a section of a three-float WEC with **no Power Take-Off (PTO)**; (b) Comparison of the Response Amplitude Operator (RAO) of float 2 computed using both a direct BEM calculation (both when isolated and in array) and with the Direct Matrix Method interaction theory (IT) using 4 evanescent modes (L) and a $\beta = 90°$ wave incidence; (c) relative difference between the (RAO) of float 2 computed using both a direct BEM calculation and with the Direct Matrix Method interaction theory (IT) for different values of the evanescent modes truncation (L) and a wave incidence of $\beta = 90°$. 308

List of Tables

4.1 Size of the Boundary Value Problem to be solved using both a direct NEMOH simulation and the interaction theory (IT) for different values of evanescent modes truncation (L). The highest and lowest truncation levels required for the IT in the frequency range of the case study are indicated as IT_{max} and IT_{min} respectively. The problem size is defined based on the discretizations of two different geometries, a truncated vertical circular cylinder and a flap-type converter shown in Figures 4.21a and 4.21b respectively. 100

5.1 Main parameters of the bottom-referenced heave-buoy array Wave Energy Converter. 109
5.2 Main parameters of an hemispheric float. 110
5.3 Wave climate series used in the simulations. 113
5.4 Influence of the evanescent modes truncation on the power generated. . 119
5.5 Comparison of wall clock execution time between the IT and direct NEMOH calculations for each of the optimized configurations in Figure 5.5. The execution time of the direct BEM simulations has been estimated following the procedure detailed in section 4.3.4. 122

C.1 Comparison between analytical and numerically calculated values ($\omega = 10^{-3}$) 191

Chapter 1

Introduction

1.1 Context

The reduction of greenhouse gas emissions, whose influence on global warming and climate change is clear (IPCC, 2014), has been set as a top priority for all the world countries. In December 2015, the first international climate agreement to limit temperature rise below 2°C was signed in the 21st annual session of the Conference of the Parties (COP) to the UN Framework convention on Climate Change (COP21, 2015). According to the Intergovernmental Panel on Climate Change (IPCC, 1988), global warming of more than 2°C would have important negative consequences for the planet, such as a global mean sea level rise and the increase in the number of extreme events like heat waves and strong precipitation (IPCC, 2014).

Although the use of renewable energy is rising, the process of transitioning away from fossil fuels has still a long way to go. Indeed, the estimated renewable energy share of global final energy consumption was of 19.2% in 2014, and of 23.7% when considering only the share of global electricity production (REN21, 2016). Of this latter total share, the highest contribution was from hydropower (16%) in contrast with the combination of geothermal, concentrated solar power and ocean energies which only accounted for 0.4%.

In spite of its small weight from a global scale perspective, ocean energy is expected to represent a significant part of the European Union's (EU) power mix. According to SI Ocean (2014), it is estimated that by 2050 wave and tidal energy alone could generate 10% of the EU's power demand through the deployment of 100GW of capacity. To reach this scenario, the cost of the electricity generated from these technologies ought to be significantly reduced. According to SI Ocean (2013), the lowest estimated cost of electricity produced by the first pilot 10MW arrays could orbit around the

0.35c€/kWh. However, to be competitive, the targeted cost should be 0.10c€/kWh or lower (TPOcean, 2016). This means that a reduction of the cost by at least a factor 3 is to be achieved.

In order to accomplish this ambitious target, the EU has identified a set of priority areas for R&I in what is referred to as the first ever European Strategic Research Agenda for ocean energy (TPOcean, 2016). The objective of the present work, whose main focus is exclusively on wave energy, is aligned with one of them which seeks the **creation of numerical models that optimise computational power** (priority area 1.2 part C).

To successfully develop wave energy converters (WECs) it is common practice (Cruz, 2008) to conduct numerical studies, at an early-stage and under simplified and rather idealized conditions, to assess the performance of the technology and to introduce, if required, modifications to the initial WEC design. Outputs from numerical models shall then be validated through experimental testing campaigns. The combination of both approaches enables one to check whether important physical phenomena have been omitted by the computational package and to feed back real experimental data to the numerical model to improve it further.

As opposed to other renewable energy technologies, such as wind turbines, convergence to a single or a reduced number of WEC designs has not yet been achieved. Indeed, Falcão (2010) states that more than a thousand patents had been registered by 1980 and that this number has significantly grown since then. In an attempt to organize the ensemble of WEC technologies, several classifications have been proposed. The subject is vast and the interested reader is encouraged to refer to dedicated reviews on the topic (Falcão, 2010; Pecher and Kofoed, 2017). Succinctly, based on the principle of operation one can distinguish amongst oscillating water columns, oscillating bodies and overtopping devices. With respect to their size, if they are small in comparison with the incident wave length they are referred to as point absorbers, in contrast with large absorbers. In addition, if their characteristic dimension is aligned with the main wave propagation direction they are categorized as attenuators and as terminators when they are oriented parallel to the wave crests.

As a consequence of the great variety of solutions proposed to extract power from ocean waves, dedicated numerical modeling tools adapted to each WEC need to be developed. The study by Babarit et al. (2012a) on the numerical modeling of an electro-active deformable wave energy converter or the review by Falcao and Henriques (2016) on oscillating water column technology are recent illustrative examples. For a more general review the reader should refer to the study by Babarit et al. (2012b) who

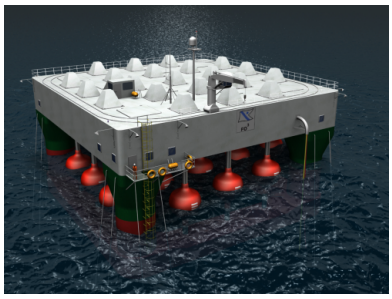

(a) Source: Fred Olsen Ltd (2009)

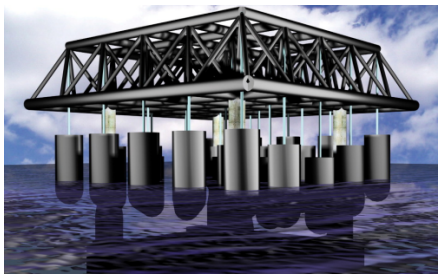

(b) Source: Manchester Bobber (2008)

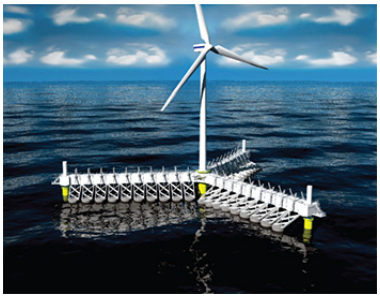

(c) Source: WAVESTAR (2015)

Figure 1.1: Three examples of multi-body WECs. *a*) FO^3 platform, *b*) Manchester Bobber, *c*) Wavestar SC-Concept

presented the numerical modeling of a selection of eight WECs with different working principles in an attempt to derive general trends of performance amongst the different converter categories.

The focus of this work is on the hydrodynamic numerical modeling of compact arrays of small wave absorbers, referred as well to as multi-body WECs, which constitutes one of the examples of the existing categories of WECs and have been identified as being an advantageous solution when compared to a big isolated point absorber (Garnaud and Mei, 2009). Examples of this type of converters include the FO^3 platform (Taghipour and Moan, 2008), the Manchester Bobber (Weller et al., 2010) and the Wavestar (Hansen and Kramer, 2011) which are depicted in Figure 1.1. Amid the numerous challenges associated with the numerical modeling of such devices, the most relevant one at the time of the present study is the computation of the hydrodynamic interactions amongst the large number of floats (> 20) they are composed of.

Certainly, numerical models conceived for the preliminary investigation of WEC power capture need to be accurate and have **as low computational cost as possible**. The latter is fundamental given that the predictions of power production on a site are to be computed over long periods of time, typically a year, and that the optimization of the device requires multiple evaluations of the annual energy absorption for each different geometrical parameter set.

Because of that, one of the most common approaches to study the wave-structure interactions in the context of wave energy conversion consists in linearizing the problem by assuming both a small wave steepness and small body motions and in adopting a perfect inviscid fluid model. These hypotheses enable one to use a relatively sim-

ple formulation, referred to as Boundary Element Method (BEM), associated with a remarkable calculation speed and with sufficiently accurate results for the targeted applications. Over the past decades, several BEM solvers have been developed for seakeeping computations (WAMIT (Lee and Newman, 1999), ANSYS Aqwa (ANSYS Aqwa, 2016), AQUAPLUS (Delhommeau, 1987), DIODORE (Principia, 2016), HYDROSTAR (Bureau Veritas, 2016), etc.) amongst which only one, developed at Ecole Centrale de Nantes and known as NEMOH (Babarit and Delhommeau, 2015), is available as open source since 2014.

In spite of its gain in computational speed with respect to other approaches, such as Computational Fluid Dynamics (CFD), the study of the hydrodynamic interactions with BEM solvers is hampered by an increase of the number of bodies considered. The fact that they solve the diffraction problem for all bodies simultaneously and given that all wetted parts need to be discretized leads to a very large system of equations. Indeed, for cases involving clusters of say O(100) floats, the increase in computational time precludes the direct simulation of such systems and their optimization.

Driven by this limitation, a set of alternative numerical modeling strategies have been proposed and are reviewed in the following section.

1.2 State-of-the-art

The challenges associated with the hydrodynamic modeling of a multi-body WEC composed of a large number of floats are analogous to those faced in the study of the park effect in large wave farms. The latter refers to the modification of the total power that a group of isolated WECs would absorb as a consequence of the wave interactions that deploying them in relatively close proximity gives rise to.

Numerous investigations on the park effect in WEC arrays have been conducted over the past years. In the following paragraphs, the numerical modeling techniques used to compute it will be reviewed. In addition, the approaches adopted to deal with the hydrodynamic interactions in other contexts, such as in the design of very large floating structures, will also be addressed.

In spite of the obvious similarities in the study of the multiple-scattering of waves in large clusters of bodies, such as a large WEC array and a multi-body WEC, there exist important differences between them as far as the magnitude of the wave interaction effects is concerned. The latter are clearly more important amongst closely spaced bodies. In fact, the review by Babarit (2013) on the park effect research conducted over the past 30 years concluded that, provided the separating distance between the devices

(typically of $10-20$m size) is on the order of $\sim 100-200$ meters, the interaction effects computed based on irregular waves cannot be considered to be significant. While this is true for small arrays of less than ~ 10 devices, the author adds that for larger arrays the number of rows (perpendicular to the main incident wave direction) should be kept as limited as possible to reduce destructive interaction effects.

The most common and generic approach to deal with WEC array interactions is to use BEM solvers which can account for the specificities of each WEC geometry and the bodies interdistances without restrictions. Not surprisingly, the majority of the studies conducted on multi-body WECs composed of O(20) floats such as the ones shown in Figures 1.1a and 1.1b (De Backer et al., 2010; Taghipour and Moan, 2008) and further analyzed in Chapter 5, have used a BEM to compute the hydrodynamic interactions. As of reminder, BEM solvers are built upon linear potential wave theory and, therefore, linearity of the governing equations and perfect fluid characteristics are assumed. The former implies a small wave steepness and a small amplitude of the body motions with respect to its characteristic dimensions. As stated in Folley et al. (2012), these hypotheses are usually satisfied in small to moderate sea states where good agreement between BEM output and results from more accurate models such as CFD is obtained. Significant discrepancies are obtained for larger sea states though.

Besides the inherent assumptions involved in the use of potential flow theory, the most limiting factor of BEM codes for the study of WEC interactions is the increase of the numerical complexity as a function of the square of the number of unknowns. In BEM solvers based on low-order methods, such as NEMOH , these are equal to the number of panels used to discretize the wetted surface of the bodies. In other solvers, such as WAMIT, computations can be performed using a higher-order method where the number of unknowns depends as well on the order of the basis functions.

In his attempt to derive initial guidelines for the design of wave farms, Babarit (2013) points out the contrast between the great amount of published works on the park effect of rather small arrays and the few studies available for larger wave farms. One of them was carried out recently by Borgarino et al. (2012b) who implemented a **Fast Multipole Method (FMM)** (Borgarino et al., 2012a) to accelerate the simulations of large WEC farms with the BEM solver AQUAPLUS (Delhommeau, 1993). This implied the extension of the infinite-depth free-surface Green's function multipole expansion to be used in a three-dimensional algorithm. The same development is expected to be applicable to the finite-depth formulation but was not attempted in Borgarino (2011). The author reported difficulties in the convergence of the multipole expansion for relatively small wave periods and therefore implemented a simplified

version of the FMM suited specifically to the modeling of wave farms. Other techniques, such as **pre-corrected Fast Fourier Transforms (FFT)**, have been used to accelerate BEM computations (Kring et al., 2000) but have some limitations when dealing with sparse arrays (Singh and Babarit, 2014).

While the use of BEM solvers provides an exact solution to the multiple-scattering problem of wave interactions in array, in certain circumstances approximations can be introduced to obtain significant computational savings through a reduction of the problem complexity. Analytical developments in the early works on the park effect in WEC arrays (Budal, 1977; Evans, 1980; Falnes, 1980) were based on such approximate techniques, in particular **the point absorber approximation** which assumes that the characteristic dimensions of the devices in array are much smaller than the wavelength of the incident waves. This implies that the diffraction by each device can be neglected. By means of this approximation, the aforementioned studies showed that significant constructive interactions could occur within an array provided that the layout of the converters was appropriately chosen.

While the early works on array interactions based on monochromatic unidirectional waves suggested exploiting the benefits of layout optimization, it was later found that the benefits of such constructive effects in irregular waves with directional spreading and with devices suboptimally controlled would be very limited. This conclusion was reached for instance in the study by Folley and Whittaker (2009) who investigated the maximum annual energy capture of a WEC array at the European Marine Energy Centre (EMEC) with a hydrodynamic model based on point absorber theory. Based on the same approximation, Fitzgerald and Thomas (2007) derived an important consistency condition for the array interaction factor, i.e. the ratio of the power produced by the WECs in array and the power they would produce in isolation. The relation obtained by the authors establishes that, provided the converters are optimally controlled, the sum of the array interaction factor for a fixed incident wave frequency over all the incident wave directions must equal unity. This means that constructive interactions occurring at specific incident wave propagation directions are balanced by destructive interactions at other wave directions.

A generalization of the identity derived by Fitzgerald and Thomas (2007) outside the zone of applicability of point absorber theory was obtained by Wolgamot et al. (2012) who showed that the sum of the maximum power absorbed by the array over all incident wave directions is proportional to the total number of degrees of freedom. As indicated by Babarit (2013), this result suggests that the multi-body WECs composed of a number of independent floats supported by a common platform, such as the ones

shown in Figure 1.1, might have a particularly high wave capture efficiency.

The point absorber approximation does not provide an accurate solution for the multiple-scattering problem of wave interaction in array for the whole frequency range as, by definition, it neglects the diffracted field by each device. As stated in preceding paragraphs, the solution to the full multiple-scattering problem computed by means of a direct diffraction calculation for the whole array becomes prohibitive when the number of bodies increases. Thus, alternative methods have been proposed which rely on the solution of the boundary value problem for a single isolated device. This solution is then combined with an interaction theory to account for the multiple-scattering in array. The latter involves satisfying the boundary conditions on the wetted surface of all the devices and for that two different approaches to achieve it can be distinguished.

On the one hand, if the boundary conditions are imposed simultaneously to all bodies, a system of equations to be solved for the unknowns which characterize the wave fields scattered by each device is obtained. This method is generally referred to as **Direct Matrix approach** and was first used by Spring and Monkmeyer (1974) in the context of ocean waves to extend the solution for a single bottom mounted surface piercing cylinder given by MacCamy and Fuchs (1954). On the other hand, the interactions can be taken sequentially as a succession of scattering events by imposing the boundary conditions at one body at a time in what is referred to as **Multiple-Scattering method**. In this case, the solution approaches the output from a Direct Matrix approach if enough orders of scattering are considered. Intuitively, the amplitude of the successively scattered waves is reduced until convergence is reached. In the context of ocean waves, the first use of such approach is attributed to Ohkusu (1974) who adapted the theory by Twersky (1952) in the context of acoustics.

Both the Direct Matrix approach and the Multiple-Scattering method are applicable if certain spacing limitations amongst devices are satisfied, i.e. no overlapping of vertical projections is allowed and the escribed cylinder to each body cannot overlap with neighbouring devices. Apart from these restrictions, both approaches are exact provided they are applied in combination with an exact representation of the array wave fields. In some cases though, approximations can be introduced to simplify the analysis. A clear example is the work by Simon (1982) who used the Direct Matrix approach in combination with a representation of the wave fields known as **plane-wave approximation** which relies on two main assumptions. First, the outgoing curved waves from each device generated by diffraction or radiation processes are modeled as being plane. Second, devices are assumed to be spaced wide enough so that the influence of the near wave field on the interactions can be neglected. The latter is

generally referred to as **wide-spacing approximation**.

As of reminder, the radiated or scattered wave field by a body can be decomposed into two separate contributions known generally as the far-field and the near-field. The former refers to progressive waves which carry energy to infinity as they propagate radially outward. In contrast, the latter are standing waves in the water column which have a fast decay away from the body (because of that they are usually referred to as evanescent waves) and are responsible for the transition between the fluid motion of propagating waves and that which satisfies the boundary conditions of the body geometry.

In the original work of Simon (1982) the model was restricted to axisymmetric bodies undergoing heave motions. McIver and Evans (1984) improved it further by adding a first correction to the plane wave expressions which relaxes the spacing requirements. More recently, Singh and Babarit (2014) coupled the BEM solver AQUAPLUS with the plane-wave approximation approach to estimate wave interaction effects in large sparse arrays of arbitrary shaped bodies.

Following the work of Ohkusu (1974), the Multiple-Scattering method was used by Mavrakos and Koumoutsakos (1987) and Mavrakos (1991) in combination with a matched eigenfunction expansion technique to solve for the Boundary Value Problem of each isolated axisymmetric body in array. In this case, and contrarily to the plane-wave approximation, evanescent modes were considered.

In spite of removing the need to store and treat simultaneously all the interactions at the same time, several authors (Kagemoto and Yue, 1986; Linton and McIver, 2001) have stated that, as the number of bodies increases, computations with the Multiple-Scattering method become impractical even for low orders of approximation and reduced number of bodies.

A comparison of the previous approximate methodologies, the point absorber and the plane-wave, and the exact multiple-scattering technique in the context of power absorption by an array of WECs was provided by Mavrakos and McIver (1997). The authors concluded that the plane-wave approximation can provide accurate results when the separating distance between devices is larger than 5 times their characteristic dimension.

In an attempt to combine the features of the Direct Matrix approach in Spring and Monkmeyer (1974) and Simon (1982), and the concept of Multiple-Scattering by Twersky (1952) and Ohkusu (1974), Kagemoto and Yue (1986) proposed an exact matrix method to solve the multiple-scattering problem. The initially unknown local wave fields at each body are characterized through a product of partial cylindrical wave

functions, which can account for both the near and far field contributions, and complex scattered wave coefficients which represent the amplitudes of the cylindrical wave functions. These are then transferred to the other devices by means of a transformation reminiscent of the Multiple-Scattering approach. In this case, however, the transferred wave fields represent the total converged wave fields around a body and not just one of the multiple successive scattering events. Finally, by applying this transformation which allows one to express the scattered wave field from a body as incident on the others, a system of equations is obtained and solved simultaneously as in a Direct Matrix approach.

For the use of the interaction theory by Kagemoto and Yue (1986), which solves the multiple-scattering problem by means of appropriate transformations of the isolated body solution, the latter needs to be computed in the basis of partial cylindrical wave functions. Indeed, the method makes use of a hydrodynamic operator known as diffraction transfer matrix (DTM) which mathematically characterizes the way an isolated body scatters waves by relating its incident and scattered partial complex cylindrical wave coefficients. Kagemoto and Yue (1986) only provided the way to compute it for axisymmetric geometries for which the single-diffraction solution was available on the basis of partial cylindrical wave functions.

The same approach was used by Yilmaz and Incecik (1998) who coupled the interaction theory by Kagemoto and Yue (1986) and the single body diffraction solution by Garrett (1971) to obtain analytical solutions for the diffraction problem of arrays of truncated cylinders. An extension to treat the radiation case of bodies moving as one was added in Yilmaz (1998). Using a similar strategy, Siddorn and Eatock Taylor (2008) provided extensive results for the hydrodynamic coefficients of a group of four truncated vertical cylinders set to oscillate independently and prone to near-trapped modes. Formulae for both the diffraction and radiation calculations were given within a unified framework.

In the context of the study of wave energy arrays, Child and Venugopal (2010) used an analogous approach to the one of Yilmaz to study optimal spatial configurations of heaving cylindrical wave energy converters using both a Parabolic Intersection method and a Genetic Algorithm as optimization strategies. More recently, and based on the same hydrodynamic model, Göteman et al. (2015) studied the power fluctuations of arrays of cylindrical WECs composed of O(100) bodies using a distance cut-off method, i.e. hydrodynamic interactions between two devices are only accounted for when they are separated by less than a specified distance. When using this approximation to solve the multiple-scattering diffraction problem the authors obtained a relative difference

of $\sim 3\%$ with respect to the exact solution but an increase in computational speed of $\sim 45\%$.

The generalization of the DTM calculation for arbitrary geometries in finite-depth was derived by Goo and Yoshida (1990) who used a cylindrical representation of the Green's function by Fenton (1978) to compute the elements of the DTM using a BEM. This approach has been used to study the forces on the fixed (Chakrabarti, 2000) and floating (Chakrabarti, 2001) modules of an interconnected multi-moduled floating offshore structure used by the US Navy. The extension to infinite-depth of both the interaction theory proposed by Kagemoto and Yue (1986) and the methodology of Goo and Yoshida (1990) was given by Peter and Meylan (2004a) who employed the former to study the interaction between ocean waves and large fields of ice floes in the marginal ice zone (MIZ).

As can be derived from the two preceding paragraphs, the application of the Direct Matrix method by Kagemoto and Yue (1986) to the study of the hydrodynamic interactions amongst bodies of arbitrary geometry is rather limited in contrast with the number of studies having focused on rather simple geometries such as a truncated vertical cylinder. This is fundamentally due to the difficulty in obtaining the solution for an isolated body of complex geometry in the form required by the Direct Matrix method. Indeed, the methodology by Goo and Yoshida (1990) requires the modification of the diffraction problem boundary conditions, as well as access to internal variables of the BEM code which are not part of its standard outputs.

Driven by this limitation, McNatt et al. (2015) derived an alternative strategy to compute the DTM for arbitrary geometries using the standard outputs of widely available standard BEM solvers. The method is based on a decomposition of the total velocity potential on the body's circumscribing cylinder into partial cylindrical waves by means of a Fourier Transform (McNatt et al., 2013) and has been applied to the study of the park effect in large arrays of wave farms. Recently, the method has been embedded in the open-source numerical tool produced by the European collaborative project DTOcean (DTOcean Project, 2017) aimed at the optimization of ocean energy arrays. In addition, Sharp and DuPont (2016) used it in combination with a real-coded Genetic Algorithm to study optimal WEC array layouts which maximize power production and minimize cost. While it eliminates the need to customize the BEM solver, the method proposed by McNatt et al. (2015) to compute the DTM cannot account for evanescent modes. Thus, the subsequent multiple-scattering analysis is restrained to the wide-spacing approximation.

The use of the interaction theory by Kagemoto and Yue (1986) for cases involving

more than several hundred bodies, such as in Very Large Floating structures (VLFs) or in large fields of ice floes, becomes impractical due to the size increase of the system to be solved.

On the one hand, to deal with VLFs, Kagemoto and Yue (1993) proposed a matching technique based on their original theory to circumvent its limitations. Similarly, Kashiwagi (2000) proposed another extension using a hierarchical scheme by which the array bodies are grouped and treated as a new fictitious body with its own diffraction characteristics. Results were presented for a column-supported structure composed of up to 5120 equally spaced circular cylinders. The author has been very prolific in this field and the interested reader is encouraged to refer to related publications (Kashiwagi, 1998, 2002; Kashiwagi and Kohjoh, 1995; Kashiwagi and Yoshida, 2001).

Furthermore, in the context of the study of wave attenuation in the MIZ modelled as an array of tens of thousands of circular thin-elastic plates of random sizes, Montiel et al. (2015a) proposed an approach known as slab-clustering method by which the whole array is decomposed into slabs. The multiple-scattering problem in each slab is solved using the interaction theory by Kagemoto and Yue (1986) and expressed in Cartesian coordinates. This allows one to represent the scattered wave fields within each slab as transmitted and reflected angular spectra. These are then used to define a scattering matrix for the slab relating incident with transmitted and reflected wave fields. The procedure is repeated for each slab and the extension of the interaction amongst all the bands is solved using a one dimension multiple scattering technique. A generalization of the method including evanescent modes in the interaction amongst slabs is given in Montiel et al. (2016).

Even if the focus of this review has been on the numerical techniques to evaluate the hydrodynamic interactions amongst a large number of bodies, and more specifically the park effect in large WEC arrays, it is as well of significant importance for planning consent purposes to evaluate the potential impact large clusters of bodies may have on the distal wave climate. Unfortunately, the tools dedicated to the study of the park effect are not suitable to model the impact of the array on the coast wave climate and vice versa (Folley et al., 2012). Because of that, special coupling methodologies between these tools have been proposed, a point which is further discussed in Chapter 6. For a detailed review of the available numerical approaches and their capabilities to model the interactions amongst WECs and with the environment the reader should refer to Folley et al. (2012).

To close this section, a summary of the main numerical modeling approaches reviewed based on linear potential wave theory is given as a series of bullet points:

- The study of hydrodynamic interactions with **BEM solvers** does not present limitations neither in terms of relative position between bodies nor with respect to their shape. However, the computational cost of BEM solvers increases significantly with the number of bodies and, therefore, they shall be used for cases involving<O(10) devices.

- Acceleration techniques, such as the **Fast Multipole Method (FMM)** or the **pre-corrected Fast Fourier Transform (FFT)**, enable one to circumvent the BEM excessive computational time for cases involving >O(10) bodies. However, they are associated with some limitations which may either restrict their application or make it sub-optimal with respect to other approaches in certain cases such as sparse wave farms.

- The **plane-wave** and the **point absorber** approximation only provide accurate results as long as their underlying assumptions are satisfied. Simplifying, this involves widely-spaced bodies and small enough with respect to the incident wavelength. Clearly, these hypothesis do not hold for multi-body WECs composed of closely-spaced floats such as the ones shown in Figure 1.1.

- The **Multiple-Scattering method** can account for the hydrodynamic interactions without approximations provided certain spacing requirements amongst devices are satisfied, i.e. no overlapping of vertical projections is allowed and the escribed cylinder to each body cannot overlap with neighbouring devices. The complexity of the approach makes its application impractical when the number of bodies increases.

- The **Direct Matrix Method interaction theory** by Kagemoto and Yue (1986) is exact and can be applied to the study of multiple-scattering amongst O(100) bodies provided the same spacing requirements of the Multiple-Scattering method are satisfied. For its use, the solution of the BVP for an isolated body needs to be available in the basis of partial cylindrical wave functions. For bodies of arbitrary shape it can be obtained using:

  - The methodology by Goo and Yoshida (1990) which implies introducing modifications to the source code of standard BEM solvers so that they can represent cylindrical waves as opposed to exclusively plane waves.
  - The alternative approach by McNatt et al. (2015) which makes use of the standard output from widely available BEM solvers. Contrarily to the

strategy by Goo and Yoshida (1990) it cannot account for evanescent modes and, therefore, in the subsequent analysis the hydrodynamic interactions are modeled using a wide-spacing approximation.

- Beyond O(100) bodies, the size of the system to be solved using the Direct Matrix Method interaction theory by Kagemoto and Yue (1986) becomes excessive and extensions of the method for specific applications have been proposed.

1.3 Aims and objectives

In the previous section, a review of the numerical techniques to model the hydrodynamic interactions in arrays of bodies and with special focus on wave farms was presented.

To the author's knowledge, no study on a multi-body WEC composed of more than 50 floats, such as the Wavestar SC-Concept (Hansen et al., 2013) shown in Figure 1.1c, has been undertaken and the effect of hydrodynamic interactions on the performance of this type of device remains not well understood. The majority of studies on similar devices have been carried out using standard BEM solvers and have dealt only with $O(20)$ floats.

Amongst the alternatives to standard BEM solvers, the Direct Matrix Method by Kagemoto and Yue (1986) is identified as suitable for the investigation of compact clusters of $O(100)$ point absorber wave energy converters which comply with the spacing requirements of the interaction theory. However, the method is not bounded to the study of this particular case but can be used as well in sparse arrays of WECs.

It is unlikely that a wide-spacing approximation can provide accurate results for arrays of closely-spaced bodies. Thus, the methodology of Goo and Yoshida (1990) is selected to compute the isolated body solution required by the interaction theory of Kagemoto and Yue (1986). This is in spite of the fact that no commercial or open-source numerical tool incorporates the solution of Goo and Yoshida (1990) as opposed to the availability of the methodology by McNatt et al. (2015).

The interaction theory has been used in conjunction with other numerical techniques, for instance the transformation of cylindrical harmonics into plane waves, to study the variation of an angular wave spectrum when it propagates through a vast array of floating bodies such as ice floes. The similarities between the latter and a large cluster of WECs could potentially enable one to adapt and apply the aforementioned technique to improve the state-of-the-art in the numerical modeling of WEC arrays.

The objectives of the present work, defined based on the previous observations, are:

- The implementation and verification of the methodology by Goo and Yoshida (1990) in the open-source BEM solver NEMOH.
- The implementation and verification of the Direct Matrix Method interaction theory by Kagemoto and Yue (1986).
- The use of the Direct Matrix Method to investigate the power capture of a generic bottom-referenced heave-buoy array inspired by the Wavestar SC-Concept (Figure 1.1).
- The identification of synergies between the study of wave propagation through large clusters of wave energy converters and the marginal ice zone (MIZ).

1.4 Thesis outline

In line with the objectives stated in the previous section, the content of the present work is organized in the following manner:

- In **Chapter 2**, the finite-depth Direct Matrix Method interaction theory by Kagemoto and Yue (1986) is formulated and expressions for the radiation hydrodynamic coefficients and the excitation forces for bodies in array are provided.
- In **Chapter 3**, the methodology by Goo and Yoshida (1990) to compute the isolated body hydrodynamic operators required by the interaction theory is described and compared with the alternative approach proposed by McNatt et al. (2015). Results of the implementation are shown and verified with output from McNatt et al. (2015) and from a semi-analytical solution.
- In **Chapter 4**, the Direct Matrix Method interaction theory implementation is verified against direct simulations with the standard BEM solver NEMOH and semi-analytical results from the literature.
- In **Chapter 5**, the numerical tool developed in previous chapters is applied to the study of the hydrodynamic interactions' effect on the performance of a generic bottom-referenced heave-buoy array inspired by the Wavestar SC-Concept.

- In **Chapter 6**, a numerical technique to transform cylindrical harmonics into plane waves used in Montiel et al. (2015a) is described and the possibility of coupling it with spectral wave models is briefly discussed.

Chapter 2

Direct Matrix Method Interaction Theory in Finite-Depth

The methodology developed by Kagemoto and Yue (1986), known as Direct Matrix Method interaction theory and that we shall refer to herein as IT, enables one to accelerate the computation of the hydrodynamic coefficients, for multi-body arrays under certain circumstances, including finite water depth and under a specific spacing restriction. IT computations can generate the coefficients for large arrays, which could not be evaluated directly with a standard Boundary Element Method (BEM) code due to its excessive computational cost.

The IT computation is based on mathematically characterizing how an individual isolated device scatters and radiates waves. Because of that, this Chapter has been divided into two parts. In the first one, the solution to the Boundary Value Problem (BVP) for an isolated body is reviewed. Most commonly, such problem is solved in Cartesian coordinates. In this case, the focus is on the solution using cylindrical coordinates as this enables one to obtain a basis of cylindrical wave functions on which any incident, scattered or radiated wave field can be expressed. In the second one, the solution to the BVP in cylindrical coordinates for an isolated body is used to tackle the multiple-scattering in a large array of floating bodies. The formulae of the IT are derived and the procedure to compute the hydrodynamic coefficients of the array is shown.

2.1 Airy wave theory

In this section, a brief reminder of the linear wave theory is given. For a more detailed derivation the reader should see C.Mei et al. (2005) and Newman (1977) which have

been used as baseline.

Consider the BVP involving a perfect fluid (inviscid and incompressible) in a domain limited by the sea-bed and the free surface. The governing equations of the problem are given by the mass and the momentum conservation laws respectively:

$$\nabla \cdot \mathrm{u} = 0 \tag{2.1.1}$$

$$\left(\frac{\partial}{\partial t} + \mathrm{u} \cdot \nabla\right) \mathrm{u} = -\nabla \left(\frac{P}{\rho} + gz\right) \tag{2.1.2}$$

where $\mathrm{u}(\mathbf{x}, t)$ is the velocity vector, $P(\mathbf{x}, t)$ the pressure, ρ the density, g the gravitational acceleration and $\mathbf{x} = (x, y, z)$, with $z = 0$ at the free surface and $z > 0$ pointing upwards.

The irrotationality of the flow enables one to define a scalar field known as velocity potential such that:

$$\mathrm{u} = \nabla\Phi \tag{2.1.3}$$

where Φ is the velocity potential.

By combining (2.1.1) and (2.1.3), Laplace's equation is obtained:

$$\nabla^2\Phi = 0 \tag{2.1.4}$$

In addition, by substituting (2.1.3) into (2.1.2) and by using the following vector identity:

$$\mathrm{u} \cdot \nabla\mathrm{u} = \nabla\frac{\mathrm{u}^2}{2} - \mathrm{u} \times (\nabla \times \mathrm{u}) \tag{2.1.5}$$

equation (2.1.2) can be written as:

$$\nabla \left[\frac{\partial\Phi}{\partial t} + \frac{1}{2}|\nabla\Phi|^2\right] = -\nabla \left(\frac{P}{\rho} + gz\right) \tag{2.1.6}$$

After integration, (2.1.6) becomes Bernoulli equation which enables one to compute the pressure once the velocity potential is known:

$$-\frac{P}{\rho} = gz + \frac{\partial\Phi}{\partial t} + \frac{1}{2}|\nabla\Phi|^2 + C(t) \tag{2.1.7}$$

where P is the total pressure, $C(t)$ an integration constant which can be omitted by defining the potential appropriately and gz the hydrostatic contribution to the

pressure.

Apart from Laplace's equation, certain conditions at the domain boundaries need as well to be satisfied by the velocity potential. On the seabed, the non-permeability condition imposes a normal zero flow velocity and thus:

$$\left(\frac{\partial \Phi}{\partial n}\right)_{z=-d} = 0 \tag{2.1.8}$$

with d the constant water depth.

On the free-surface, two restrictions need to be adhered to. The equation describing the air-water interface may be written as:

$$F(\mathbf{x}, t) = z - \zeta(x, y, t) = 0 \tag{2.1.9}$$

where ζ is the height measured from $z = 0$.

On the one hand, the particles on the surface must remain on the surface. This statement is known as kinematic boundary condition and can be expressed as:

$$\frac{\partial \zeta}{\partial t} + \frac{\partial \Phi}{\partial x}\frac{\partial \zeta}{\partial x} + \frac{\partial \Phi}{\partial y}\frac{\partial \zeta}{\partial y} = \frac{\partial \Phi}{\partial z}, \quad \text{on} \quad z = \zeta \tag{2.1.10}$$

On the other hand, if surface tension is neglected (which is valid for the range of wavelengths considered herein) a constant pressure equal to the atmospheric must be imposed on the free-surface. This condition is known as dynamic boundary condition and can be obtained by applying (2.1.7) on the free surface:

$$-\frac{P_a}{\rho} = g\zeta + \frac{\partial \Phi}{\partial t} + \frac{1}{2}|\nabla \Phi|^2, \quad \text{on} \quad z = \zeta \tag{2.1.11}$$

Both the kinematic (2.1.10) and the dynamic (2.1.11) boundary conditions can be combined into a single condition expressed in the following manner if the atmospheric pressure is considered constant:

$$\frac{\partial^2 \Phi}{\partial t^2} + g\frac{\partial \Phi}{\partial z} + \frac{\partial}{\partial t}(\mathrm{u})^2 + \frac{1}{2}\mathrm{u} \cdot \nabla \mathrm{u}^2 = 0, \quad z = \zeta \tag{2.1.12}$$

In the previous expression, two different types of non-linearities arise (Ferrant, 2015): structural non-linearities, given by the non-linear differential terms, and position non-linearities, as the equation is valid on a boundary which is in turn an unknown quantity.

If waves of small slope are considered, i.e. $\epsilon \ll 1$ with ϵ the wave slope defined in terms of the wave amplitude ζ_a and the wave length λ as $\epsilon = 2\pi\zeta_a/\lambda$, the boundary

condition (2.1.12) can be linearized by expressing it on the known mean free-surface at plane $z = 0$. Thus, the linearized equations of the BVP under consideration follow as:

$$\nabla^2\Phi = 0, \quad -d < z < 0 \tag{2.1.13}$$

$$\frac{\partial\Phi}{\partial n} = 0, \quad z = -d \tag{2.1.14}$$

$$\frac{\partial^2\Phi}{\partial t^2} + g\frac{\partial\Phi}{\partial z} = 0, \quad z = 0 \tag{2.1.15}$$

If an harmonic time dependence is assumed, the spatial and time variation of Φ can be decoupled as:

$$\Phi = \Re\{\phi(x, y, z)\, e^{-i\omega t}\} \tag{2.1.16}$$

where Φ is the velocity potential in the domain, ϕ is its complex spatial part, (x, y, z) the spatial coordinates in a global Cartesian reference system and ω the angular frequency; ωessentially positive.

The simplest solution to the system of equations (2.1.13)-(2.1.15), obtained from separation of variables in Cartesian coordinates, is a plane wave with sinusoidal profile propagating along the x-axis given by the potential:

$$\phi^A(x, z) = -i\frac{g\zeta_a}{\omega}\frac{\cosh\left[k_0(z + d)\right]}{\cosh\left(k_0 d\right)}e^{ik_0 x} \tag{2.1.17}$$

where ϕ^A is the velocity potential of a plane wave, ζ_a is the wave amplitude, (x, z) the coordinates in a global Cartesian system and k_0 the wave number obtained from the dispersion relation:

$$k_0 \tanh(k_0 d) = \frac{\omega^2}{g} \tag{2.1.18}$$

2.2 Solution to the BVP for an isolated device

In the previous section, the BVP of a fluid bounded by the free-surface and the seabed was considered. Herein, additional boundary conditions are added to the system of equations (2.1.13)-(2.1.15) to account for the presence of a floating body. It will scatter incoming ambient waves (associated with the potential in (2.1.17)) which will exert dynamic forces on it and, as a consequence, the body will oscillate and radiate

waves.

Under the assumption of linearity, the total potential in this new domain (Figure (2.1)) limited by the sea-bed, the free-surface and the wetted surface of the body can be expressed as:

$$\phi = \phi^A + \phi^P \tag{2.2.1}$$

where ϕ is the total potential, ϕ^A the ambient wave potential and $\phi^P$the perturbation potential.

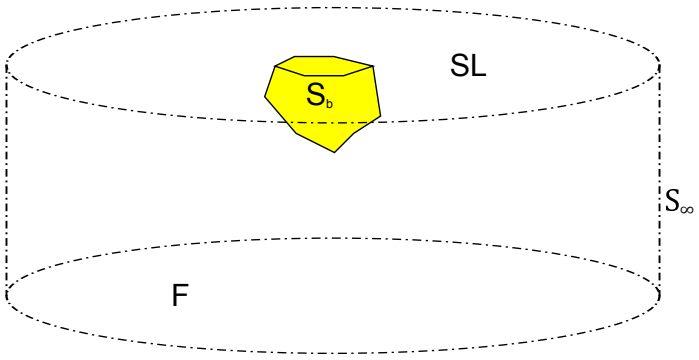

Figure 2.1: Schematic of the domain limited by the free surface (SL), the mean body's wetted surface (S_b), the seabed (F) and a control cylindrical surface at infinity (S_∞).

Besides satisfying (2.1.13)-(2.1.15), and since the body solid surface is considered impermeable to fluid, the perturbation potential is subject to an additional restriction which imposes no flux through the body surface. Similarly to the hypothesis made when linearizing the free-surface boundary condition, if small excursions of the floating body with respect to its characteristic dimensions are assumed, then the impermeable boundary condition can be applied in its mean position as:

$$\frac{\partial \phi^P}{\partial n} = -\frac{\partial \phi^A}{\partial n} + \mathrm{U} \cdot \mathrm{n}, \quad \text{on} \quad S_b \tag{2.2.2}$$

where S_b is the mean wetted surface of the body, U is the boundary velocity at the observed point and n its normal vector.

Moreover, it needs to be ensured that the generated waves, which perturb the incident wave field, will propagate away from the body and not towards it. This is represented by the so called Sommerfeld's radiation boundary condition which reads:

$$lim_{k_0 r \to \infty} \sqrt{r} \left(\frac{\partial \phi^P}{\partial r} - i k_0 \phi^P \right) = 0 \tag{2.2.3}$$

where r represents the radius of the cylindrical control surface shown in Figure 2.1.

To summarize, the linearized BVP of the perturbation potential is given by the following set of equations:

$$\nabla^2\phi^P = 0, \quad -d < z < 0 \tag{2.2.4}$$

$$\frac{\partial\phi^P}{\partial n} = 0, \quad z = -d \tag{2.2.5}$$

$$\frac{\partial^2\phi^P}{\partial t^2} + g\frac{\partial\phi^P}{\partial z} = 0, \quad z = 0 \tag{2.2.6}$$

$$\frac{\partial\phi^P}{\partial n} = -\frac{\partial\phi^A}{\partial n} + \mathrm{U}\cdot\mathrm{n}, \quad \text{on} \quad S_b \tag{2.2.7}$$

$$lim_{k_0 r\to\infty}\sqrt{r}\left(\frac{\partial\phi^P}{\partial r} - ik_0\phi^P\right) = 0 \tag{2.2.8}$$

The linearity of all the operators enables one to further decompose the perturbation potential in the following manner:

$$\phi^P = \phi^S + \sum_{k=1}^{Df} v_k\phi^{R,k} \tag{2.2.9}$$

where ϕ^S is the scattered potential by the body (also referred to as diffraction potential in the literature), $\phi^{R,k}$ is the radiated potential in a degree of freedom k, Df are the total number of degrees of freedom of the body and v_k is the amplitude of the generalized body velocity in its k^{th} degree of freedom.

By means of the decomposition in (2.2.9), two separated and independent BVP commonly referred to as diffraction and radiation problems are created. The former is associated with the scattering of the incident wave by the body when held fixed, whereas the latter with the generation of a wave due to the body motion in an otherwise still water surface. Both are given by the same set of equations (2.2.4) - (2.2.8) with the perturbation potential ϕ^P accordingly replaced by ϕ^S or $\phi^{R,k}$ and with the boundary condition (2.2.7) expressed as:

$$\frac{\partial\phi^S}{\partial n} = -\frac{\partial\phi^A}{\partial n}, \quad \text{on } S_b \quad \text{(diffraction BC)} \tag{2.2.10}$$

$$\frac{\partial\phi^{R,k}}{\partial n} = n_k, \quad \text{on } S_b \quad \text{(radiation BC)} \tag{2.2.11}$$

where n_k is the k^{th} component of the direction cosine vector explicitly defined in Chapter 3.

2.2.1 Outgoing waves

Both the scattered and radiated waves by an isolated body satisfy the radiation condition (2.2.3) and are, therefore, "outgoing" waves. For the solution of the array BVP, where waves emanating from each body due to scattering and radiation propagate and interact with its neighbours, it is very useful to be able to express both scattered and radiated waves by an isolated body as a linear combination of a set of basis functions that shall be referred to herein as outgoing partial cylindrical waves (Figure 2.2).

The outgoing basis functions, defined on the local cylindrical reference system of the body $Or\theta z$ (Figure 2.4), satisfy Laplace's equation (2.1.4) together with the seabed (2.1.8), free-surface (2.1.15) and radiation (2.2.3) BC and can be obtained using the technique of separation of variables in cylindrical coordinates (for a full derivation see Appendix A):

$$\left(\psi^S\right)_{nm} = \begin{cases} \frac{\cosh\left[k_0(z+d)\right]}{\cosh\ k_0 d}\, H_m^{(1)}(k_0 r)\, e^{im\theta} & n = 0,\ m \in \mathbb{Z} \\ \cos\left[k_n(z+d)\right] K_m(k_n r)\, e^{im\theta} & n \geq 1\,(n \in \mathbb{N}),\ m \in \mathbb{Z} \end{cases} \tag{2.2.12}$$

where $\left(\psi^S\right)_{nm}$ is the outgoing partial wave function associated with an angular-mode m and depth-mode n, $H_m^{(1)}$ is the m-th order Hankel function of the first kind, K_m is the m-th order modified Bessel function of the second kind, (z, r, θ) are the cylindrical coordinates local to the body and k_n are the solutions of the following dispersion equation:

$$k_n\ \tan\ k_n d = -\frac{\omega^2}{g} \tag{2.2.13}$$

By making use of (2.2.12), the scattered potential can be represented as:

$$\phi^S = \sum_{m=-\infty}^{\infty} \Bigg[(A)_{0m}\ \frac{\cosh\ k_0(z+d)}{\cosh\ k_0 d}\, H_m^{(1)}(k_0 r) + \sum_{n=1}^{\infty} (A)_{nm}\ \cos\ k_n(z+d)\, K_m(k_n r) \Bigg] e^{im\theta} \tag{2.2.14}$$

where $\left(A\right)_{nm}$ are complex coefficients that shall be referred to as scattered partial cylindrical wave coefficients.

Similarly, the radiated potential can be expressed as:

$$\phi^{R,k} = \sum_{m=-\infty}^{\infty} \Bigg[\left(R^k\right)_{0m} \frac{\cosh\, k_0(z+d)}{\cosh\, k_0 d} H_m^{(1)}(k_0 r) + \sum_{n=1}^{\infty} \left(R^k\right)_{nm} \cos\, k_n(z+d)\, K_m(k_n r) \Bigg] e^{im\theta} \quad (2.2.15)$$

where $\left(R^k\right)_{nm}$ are the complex radiated coefficients in a k^{th} mode of motion (with $k = 1, \ldots, 6$ in the general case) and are referred to as Radiation Characteristics.

The first term ($n = 0$) of the summation in (2.2.14) and (2.2.15) represents partial progressive waves, i.e., waves that propagate away from the body (Figures $1a, 1b, 1c$) and which bring energy to infinity as they decrease with $r^{-1/2}$. Contrarily, the second term ($n \geq 1$) produces standing waves known as evanescent modes (Figures $1d, 1e, 1f$) which enable the transition between the near and far wave fields and adapt the velocity potential to the body geometry so that the boundary conditions (2.2.10) and (2.2.11) are satisfied.

For convenience, (2.2.14) and (2.2.15) are represented as a scalar product of two infinite vectors of complex coefficients and partial cylindrical wave components (see section 2.4.1 for further details on the shape of the vectors):

$$\phi^S = A^T \psi^S; \quad \phi^{R,k} = \left(R^k\right)^T \psi^S \quad (2.2.16)$$

where superindex T indicates transpose.

The vectors of coefficients A and R^k need to be computed such that the body boundary conditions (2.2.10) and (2.2.11) are satisfied respectively and, therefore, they depend on the body geometry. For simple ones, such as a truncated vertical circular cylinder, semi-analytical techniques have been used to derive both the scattered (Garrett, 1971) and the radiated (Yilmaz, 1998) wave coefficients. A formulation by Sabuncu and Calisal (1981) which follows the procedure derived by (Garrett, 1971) is shown in Appendix C. In addition, the calculation of A and R^k using the formulae developed by Yilmaz (1998) and based on the recent work of Zeng and Tang (2013) is detailed in Appendix D. Beyond vertical truncated circular cylinders, for axysymetric geometries Kagemoto and Yue (1986) used a hybrid-element method (HEM). Finally, for bodies of arbitrary geometry, two different methodologies based on the use of a Boundary Element Method (BEM) code have been proposed (Goo and Yoshida, 1990; McNatt et al., 2015) and are the focus of Chapter 3.

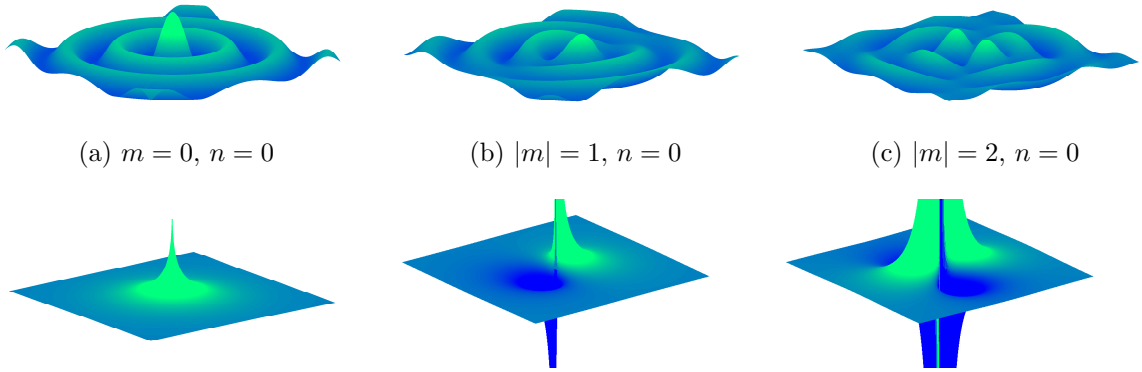

(a) $m = 0,\ n = 0$ (b) $|m| = 1,\ n = 0$ (c) $|m| = 2,\ n = 0$

(d) $m = 0,\ n = 1$ (e) $|m| = 1,\ n = 1$ (f) $|m| = 2,\ n = 1$

Figure 2.2: Partial waves modes. Progressive term $H_m^{(1)}(r)$ (a,b,c); evanescent term $K_m(r)$ (d,e,f).

2.2.2 Incident waves

In the previous section, a set of basis functions to express any kind of outgoing wave from a body was presented. In a large array, scattered and radiated waves generated by a body will propagate and become incident to the neighbouring ones. Intuitively, there is a need to be able to characterize incident waves by means of another set of basis functions that shall be referred to as incident partial cylindrical waves.

Take an ambient long-crested plane wave expressed in the form of (2.1.17) in a global Cartesian reference system $OXYZ$. To express such incident potential on an isolated body, its general form shall be adopted by considering the phase shift proportional to the distance between the origin of the global reference system (set as phase reference) and a line parallel to the wave crests passing through the center of the device:

$$\phi^A(x,\, y,\, z) = -i\frac{g\zeta_a}{\omega}\frac{\cosh\left[k_0(z+d)\right]}{\cosh\left(k_0 d\right)}e^{ik_0((x-X_0)\cos\beta+(y-Y_0)\sin\beta)} \tag{2.2.17}$$

where β is the wave propagation direction defined as shown in Figure 2.4 and (X_0, Y_0) are the coordinates of the center of the body in the global Cartesian reference system.

Now consider the following fundamental property of the Bessel functions (Watson (1966), p.14):

$$e^{\frac{1}{2}z(t-\frac{1}{t})} = \sum_{q=-\infty}^{\infty} t^q J_q(z) \tag{2.2.18}$$

where J_q is the q-th order Bessel function of the first kind.

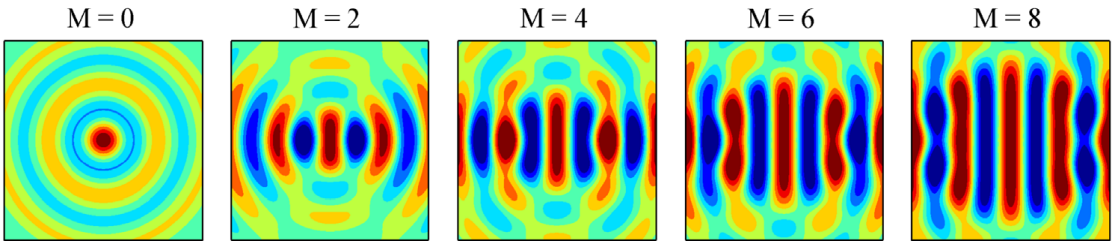

Figure 2.3: Incident plane wave as a summation of partial cylindrical waves plotted as the surface elevation for increasing truncation values M. Source: McNatt et al. (2015).

By means of (2.2.18), (2.2.17) can be written as:

$$\phi^A(r,\,\theta,\,z) = -i\frac{g\zeta_a}{\omega}\frac{\cosh\left[k_0(z+d)\right]}{\cosh\,k_0 d}e^{ik_0(X_0\cos\beta+Y_0\sin\beta)}\sum_{q=-\infty}^{\infty} i^q J_q(k_0 r)e^{iq(\theta-\beta)} \quad (2.2.19)$$

Equation (2.2.19) is a representation of an ambient plane wave by means of a superposition of cylindrical waves expressed in a local cylindrical reference system centered at the body. This is depicted in Figure 2.3 which shows, for different levels of truncation q (indicated as M in the figure), the free surface elevation associated with the velocity potential ϕ^A.

Apart from ambient long-crested plane waves, a body in array will be acted upon by scattered and radiated waves from other devices. As opposed to the ambient incident waves, which are purely progressive, outgoing waves are composed of both a progressive and an evanescent part as represented by equations (2.2.14) and (2.2.15). However, expression (2.2.19) allows one to express only progressive incident waves as a superposition of cylindrical harmonics. Thus, there is a need to generalize (2.2.19) so that it can account for standing waves and therefore can represent any form of incident wave.

The aforementioned generalization is achieved by applying Graf's addition theorem (Abramowitz and Segun A., 1964), which enables one to transform both progressive and evanescent components in an outgoing wave from a body as incident to a neighbouring one (see Appendix B), to the outgoing partial cylindrical wave functions (2.2.12). After this transformation, the generalized form of an incident wave expressed as a superposition of incident partial cylindrical waves reads:

$$\phi^I = \sum_{q=-\infty}^{\infty} \Bigg[\left(A^I\right)_{0q} \frac{\cosh\left[k_0(z+d)\right]}{\cosh\ k_0 d} J_q(k_0 r) + \sum_{l=1}^{\infty} \left(A^I\right)_{lq} \cos[k_l(z+d)]\, I_q(k_l r) \Bigg] e^{iq\theta} \quad (2.2.20)$$

where ϕ^I is the incident potential to the body (superindex A of "ambient" has been replaced by I "incident" as now any type of incident potential can be represented in this form), I_q is the q-th order modified Bessel function of the first kind, subindices q and l are the modes representing the angular and depth variation of the incident potential respectively and $\left(A^I\right)_{lq}$ are incident complex partial cylindrical wave coefficients.

To distinguish between an ambient long-crested plane wave and other forms of incident wave field, the partial cylindrical wave coefficients of the former are represented herein using the lower-case character a^I defined as:

$$\left(a^I\right)_{lq} = \begin{cases} -i\frac{g\zeta_a}{\omega} e^{ik_0(X_0\cos\beta + Y_0\sin\beta)} i^q e^{-iq\beta}, & l = 0 \\ 0 & l \geq 1 \end{cases} \quad (2.2.21)$$

As mentioned in section 2.2.1, for convenience it is worth expressing (2.2.20) as the scalar product of the infinite vectors of complex coefficients and partial incident cylindrical wave components:

$$\phi^I = \left(A^I\right)^T \psi^I \quad (2.2.22)$$

where the set of incident partial wave cylindrical basis functions ψ^I is given by:

$$\left(\psi^I\right)_{lq} = \begin{cases} \frac{\cosh\left[k_0(z+d)\right]}{\cosh\ k_0 d} J_q(k_0 r)\, e^{iq\theta}, & l = 0, q \in \mathbb{Z} \\ \cos[k_l(z+d)]\, I_q(k_l r)\, e^{iq\theta}, & l \geq 1\ (l \in \mathbb{N}), q \in \mathbb{Z} \end{cases} \quad (2.2.23)$$

For clarity of notation, indexes (n, m) are associated with outgoing waves and (l, q) with incident waves.

2.3 Solution of the array BVP: calculation of the scattering coefficients

Section 2.2 dealt with the representation of the different forms of the velocity potential (incident, scattered and radiated) for an isolated body using partial cylindrical waves.

We now use them to solve the multiple-scattering BVP problem where each body scatters ambient incident waves as well as scattered and radiated waves by the rest of devices in array. Intuitively, one can imagine that this succession of scattering events leads to a steady-state if the incident wave forcing is considered periodic with an harmonic time dependence. Once the steady-state reached, the solution to the multiple-scattering BVP is given by the scattered coefficients $(A_j)_{nm}$ for each body j in a large array.

One of the key aspects of the IT by Kagemoto and Yue (1986) is that the study of the wave scattering on the whole array is undertaken by focusing on one body at a time. Hereafter, this body will be referred to as j and its neighbours as i. The following analysis is based on the work by Kagemoto and Yue (1986) with the diffraction and radiation problems treated separately as in McNatt et al. (2015).

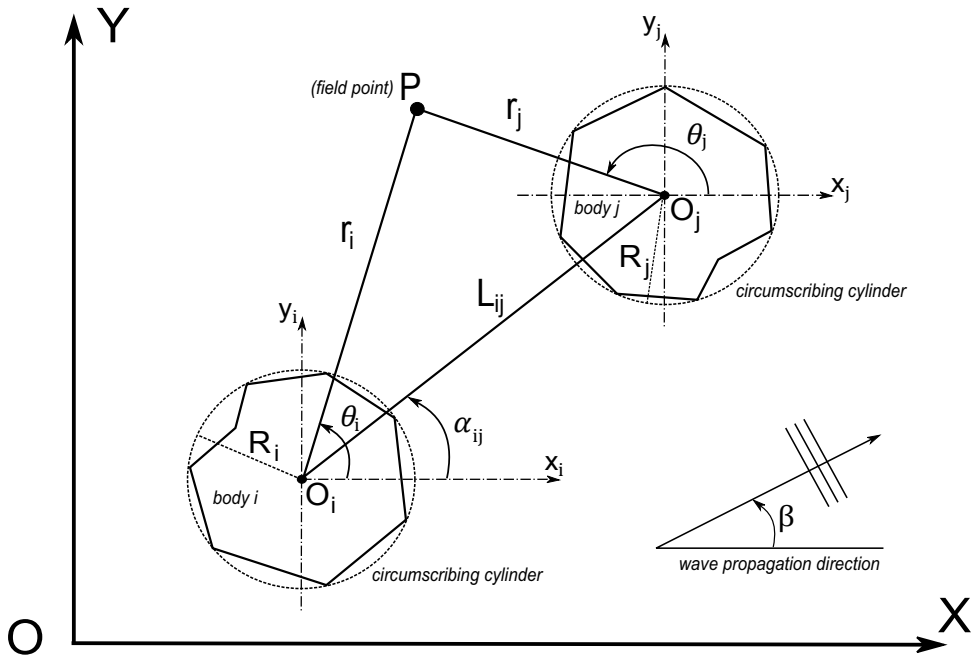

Figure 2.4: Schematic of the plane view of two bodies of arbitrary geometry with the nomenclature and reference systems used herein.

2.3.1 Diffraction Problem

We consider first the case where an incident long-crested plane wave acts upon the bodies of the array held fixed. The total incident wave to body j, represented by the potential ϕ_j^I, is the sum of the ambient incident plane wave and the initially unknown

waves scattered by all the neighbouring bodies i and incident on body j:

$$\phi_j^I = \left(a_j^I\right)^T \psi_j^I + \sum_{\substack{i=1 \\ i\neq j}}^{N} A_i^T \psi_i^S \tag{2.3.1}$$

where ϕ_j^I is the total incident potential to body j, $a_j^T \psi_j^I$ is the ambient incident wave to body j as defined in (2.2.21) and $A_i^T \psi_i^S$ is the scattered wave by a body i. To simplify notation, ambient incident waves to body j are represented by lower-case coefficient vectors a_j^I as opposed to incident waves generated by the neighbouring devices i which are represented by upper-case coefficient vectors A_i.

It is important to note that the terms in the summation on the right hand side of equation (2.3.1) representing the scattered potentials by bodies i are defined in their local cylindrical reference system. Now we wish to express them in the reference system of body j. For that, we make use of the transformation matrix $\mathbf{T}_{ij}$ defined as:

$$\psi_i^S = \mathbf{T}_{ij}\, \psi_j^I \tag{2.3.2}$$

From (2.3.2) it can be observed that the change of reference system between bodies i and j imposes additionaly the modification of the basis function, i.e. from scattered (S) to incident (I). Intuitively, the cylindrical wave scattered by body i is outgoing when observed from its local reference system but incident when viewed from the local reference system of body j.

The individual terms of the transformation matrix are given by (see Appendix B for derivation):

$$(\mathbf{T}_{ij})_{nn}^{mq} = \begin{cases} H_{m-q}(k_0 L_{ij}) e^{i\alpha_{ij}(m-q)} & n = 0 \\ K_{m-q}(k_n L_{ij})(-1)^q e^{i\alpha_{ij}(m-q)} & n \geq 1 \end{cases} \tag{2.3.3}$$

where L_{ij} is the distance between the centers of bodies i and j and α_{ij} is the angle at body i between the positive x-direction and the line joining the center of i to that of j in an anti-clockwise direction (Figure 2.4):

$$L_{ij} = \sqrt{(X_{0i} - X_{0j})^2 + (Y_{0i} - Y_{0j})^2} \tag{2.3.4}$$

$$\alpha_{ij} = \arctan \frac{(Y_{0j} - Y_{0i})}{(X_{0j} - X_{0i})} \tag{2.3.5}$$

where $(X_{0i},\, Y_{0i})$ and $(X_{0j},\, Y_{0j})$ are the center coordinates of bodies i and j respectively.

It is important to note that the use of the transformation matrix $\mathbf{T}_{ij}$, based on Graf's addition theorem for Bessel functions (Abramowitz and Segun A., 1964), imposes a restriction on the minimum separating distance that can exist between bodies (see Appendix B). Notwithstanding, as detailed in Chapter (3), it must be replaced by a stricter restriction which stems from the use of a specific form of Green's function.

By substituting (2.3.2) into (2.3.1):

$$\phi_j^I = \left(a_j^I\right)^T \psi_j^I + \sum_{\substack{i=1 \\ i\neq j}}^{N} A_i^T \mathbf{T}_{ij} \psi_j^I \tag{2.3.6}$$

Expression (2.3.6) can be rearranged by extracting the common factor ψ_j^I leading to:

$$\phi_j^I = \left(\left(a_j^I\right)^T + \sum_{\substack{i=1 \\ i\neq j}}^{N} A_i^T \mathbf{T}_{ij} \right) \psi_j^I \tag{2.3.7}$$

We note that (2.3.7) is of the form:

$$\phi_j^I = \left(A_j^I\right)^T \psi_j^I \tag{2.3.8}$$

where A_j^I, which represents the complex partial cylindrical wave coefficients vector of the total incident potential to body j, is given by:

$$A_j^I = a_j^I + \sum_{\substack{i=1 \\ i\neq j}}^{N} \mathbf{T}_{ij}^T A_i \tag{2.3.9}$$

The incident and scattered partial wave coefficients by an isolated body can be related by means of a linear operator known as Diffraction Transfer Matrix $\left(\mathbf{B}_j\right)$:

$$A_j = \mathbf{B}_j A_j^I \tag{2.3.10}$$

The elements $\left(\mathbf{B}_j\right)_{nl}^{mq}$ are defined as the coefficient of the partial wave of depth mode n and angular mode m in the scattered potential in response to a unit incident wave of depth mode l and angular mode q (Kagemoto and Yue, 1986). By substituting (2.3.9) into (2.3.10), the total incident partial wave coefficients can be related to the

scattered partial wave coefficients as:

$$A_j = \mathbf{B}_j \left(a_j^I + \sum_{\substack{i=1 \\ i \neq j}}^{N} \mathbf{T}_{ij}^T A_i \right) \tag{2.3.11}$$

If the same procedure that has been applied so far to body j is repeated for all devices in the array, (2.3.11) becomes a system of equations to solve for all the unknown scattered coefficients:

$$A = (\mathbf{I} - \mathbf{BT})^{-1} \mathbf{B}\, a^I \tag{2.3.12}$$

where $\mathbf{I}$ is the identity matrix and $\mathbf{B}$ and $\mathbf{T}$ are matrices containing respectively the diffraction transfer matrices and transformation matrices of the bodies in the array organised in the following manner:

$$\begin{bmatrix} A_1 \\ A_2 \\ \vdots \\ A_N \end{bmatrix} = \left(\mathbf{Id} - \begin{bmatrix} \mathbf{B}_1 & 0 & \dots & 0 \\ 0 & \mathbf{B}_2 & & \\ \vdots & & \ddots & 0 \\ 0 & \dots & 0 & \mathbf{B}_N \end{bmatrix} \begin{bmatrix} 0 & \mathbf{T}_{21}^T & \dots & \mathbf{T}_{N1}^T \\ \mathbf{T}_{12}^T & 0 & & \vdots \\ \vdots & & \ddots & \mathbf{T}_{N(N-1)}^T \\ \mathbf{T}_{1N}^T & \dots & \mathbf{T}_{(N-1)N}^T & 0 \end{bmatrix} \right)^{-1} \cdot \begin{bmatrix} \mathbf{B}_1 & 0 & \dots & 0 \\ 0 & \mathbf{B}_2 & & \\ \vdots & & \ddots & 0 \\ 0 & \dots & 0 & \mathbf{B}_N \end{bmatrix} \begin{bmatrix} a_1^I \\ a_2^I \\ \vdots \\ a_N^I \end{bmatrix} \tag{2.3.13}$$

The term $(\mathbf{I} - \mathbf{BT})^{-1}$ is usually referred to as the scattering matrix (Siddorn and Eatock Taylor, 2008). Prior to solving (2.3.12), the Diffraction Transfer Matrix (DTM) of the bodies in array needs to be evaluated. In case all the devices in array are identical, this needs to be performed only once. A detailed description and comparison of two different methodologies to compute the DTM of arbitrary geometries is given in Chapter 3.

2.3.2 Radiation Problem

The same methodology as the one described in section 2.3.1 can be applied to solve the radiation problem given by the motion of a body i of the array in one of its degrees of freedom k with all the others held fixed. In this case, by analogy with the diffraction problem, it can be considered that the "ambient waves" are the radiated

waves generated by the motion of body i in a mode of motion k. They will exist for all the bodies j besides the one i undergoing motion .

The radiated potential generated by a unitary velocity of body i in a degree of freedom k is defined as:

$$\phi_{ik}^R = R_{ik}^T \psi_i^S \tag{2.3.14}$$

where ϕ_{ik}^R is the radiated potential due to a motion of body i in mode k as if it was isolated (the scattered part of the radiated wave by the neighbouring bodies is not included), R_{ik}^T is the vector of complex radiated coefficients known as Radiation Characteristics and ψ_i^S is the vector of scattered partial waves expressed in the local reference system of body i.

Now, we wish to express the radiated potential by body i as incident potential to body j in its local cylindrical coordinate system. For that, we use the transformation matrix in (2.3.14) which reads:

$$\phi_{ik}^R = R_{ik}^T \mathbf{T}_{ij} \psi_j^I \tag{2.3.15}$$

Equation (2.3.15) is of the form:

$$\phi_{ik}^R = (a_j^{R,ik})^T \psi_j^I \tag{2.3.16}$$

where $a_j^{R,ik}$ is the vector of coefficients of the incident partial waves to body j representing the radiated potential by a body i moving in a degree of freedom k.

Thus, we can define the "ambient" incident waves to a body j of the array due to the motion of body i in a degree of freedom k as:

$$a_j^{R,ik} = \begin{cases} \mathbf{T}_{ij}^T R_{ik} & j \neq i \\ 0 & j = i \end{cases} \tag{2.3.17}$$

Then, using the same system of equations as in (2.3.12) with the "ambient" partial cylindrical wave coefficients defined as in (2.3.17), the initially unknown scattered coefficients of each body can be obtained.

Before being able to compute the solution of the system (2.3.12), as mentioned in section (2.3.1), the computation of the DTM of the bodies is needed. For the radiation problem, the Radiation Characteristics (RC) are required as well and a detailed description and comparison of two different methodologies to compute them for arbitrary geometries is given in Chapter 3.

2.3.3 Calculation of the radiation hydrodynamic coefficients and the excitation forces

The solution to the multiple scattering problem (2.3.12) enables one to reconstruct the total potential in the fluid domain and to compute the forces exerted on the bodies. McNatt et al. (2015) introduced a linear operator called Force Transfer Matrix ($\mathbf{G}_j$) which relates the forces acting in each degree of freedom of the body to the partial incident cylindrical wave coefficients. The procedure to compute it for arbitrary geometries is described in Chapter 3. Here we make use of the Force Transfer Matrix (FTM) to compute the excitation forces as:

$$F_j^E = \mathbf{G}_j \, A_j^I \tag{2.3.18}$$

where F_j^E is the vector of excitation forces with dimension Df_j and A_j^I are the cylindrical coefficients of the total wave incident to body j composed of the ambient incident wave and all the scattered waves by the fixed neighbouring bodies:

$$A_j^I = (a_j^I + \sum_{\substack{i=1 \\ i \neq j}}^{N} \mathbf{T}_{ij}^T A_i) \tag{2.3.19}$$

Similarly, following the procedure by McNatt et al. (2015), the radiation force can be computed as :

$$\left(F_j^R\right)^{ik} = \begin{cases} \mathbf{G}_j A_j^{I'} & j \neq i \\ -\left(-i\omega \left(\mathbf{AM}_j\right)^k + \left(\mathbf{D}_j\right)^k\right) + \mathbf{G}_j A_j^{I'} & j = i \end{cases} \tag{2.3.20}$$

where $\left(F_j^R\right)^{ik}$ is the vector of radiation forces on body j due to a motion of unit amplitude of body i in a degree of freedom k, $(\mathbf{AM})_j^k$ is the k^{th} column of the added mass matrix of the isolated body j , $(\mathbf{D})_j^k$ is the k^{th} column of the radiation damping matrix of the isolated body j and $A_j^{I'}$ are the cylindrical coefficients of the total wave incident to body j expressed as in (2.3.21) composed of the radiated wave cylindrical coefficients $a_j^{R,ik}$ generated by the motion of body i in the degree of freedom k plus all the scattered waves by the fixed neighbouring bodies:

$$A_j^{I'} = (a_j^{R,ik} + \sum_{\substack{i=1 \\ i \neq j}}^{N} \mathbf{T}_{ij}^T A_i) \tag{2.3.21}$$

The added mass and damping hydrodynamic coefficients are defined as terms of the radiation force proportional to the body acceleration and to its velocity respectively:

$$\left(F_{js}^{R}\right)^{ik} = -(-i\omega m_{js}^{ik} + b_{js}^{ik})\,\dot{X}_{ik} \tag{2.3.22}$$

where m_{js}^{ik} represents the added mass coefficient due to the radiation force generated by the motion of body i in a degree of freedom k acting on the degree of freedom s of body j and, similarly, b_{js}^{ik} is the damping coefficient due to the radiation force generated by the motion of body i in a degree of freedom k acting on the degree of freedom s of body j.

By rearranging (2.3.22), the following formulae for the hydrodynamic coefficients is obtained:

$$m_{js}^{ik} = \frac{1}{\omega}\,\Im\{\left(F_{js}^{R}\right)^{ik}\} \tag{2.3.23}$$

$$b_{js}^{ik} = -\Re\{\left(F_{js}^{R}\right)^{ik}\} \tag{2.3.24}$$

We note that the matrices of added mass and radiation damping hydrodynamic coefficients of each body in the array have dimensions $Df_j \times Df_a$, with Df_a the total number of degrees of freedom k of the array.

Expression (2.3.20) for the case $j = i$ differs from expression (15) in McNatt et al. (2015) as the partial cylindrical wave coefficients in the notation of the latter have amplitude and not velocity units. However, we note a typographical error on equation (15) in McNatt et al. (2015) where the term between brackets should be preceded by a minus sign.

2.4 Numerical Implementation

2.4.1 Vectors and Matrices shapes

Even though the vectors in (2.2.16) are theoretically infinitely long, for practical computations they need to be truncated. Their dimension is given as $(2M+1)\cdot(N+1)$ where the summations go from $m = -M$ to M and from $n = 0$ to N (the same expression will apply for modes q and l with truncation limits Q and L respectively).

The following mapping is used for the indexation of vectors containing elements

each corresponding to a pair (n, m) (or lq equivalently):

$$(n,m) \rightarrow (M+m)(N+1)+n+1; \quad n=0,...,N;\, m=-M,\ldots,0,\ldots,M \tag{2.4.1}$$

For matrices where each entry corresponds to two pairs of modes, such as the Transformation Matrix $\mathbf{T}_{ij}$, the previous mapping is applied to rows and columns:

$$\mathbf{T}_{ij} = \begin{bmatrix}
T_{0\,0}^{-M\,-Q} & 0 & \cdots & 0 & T_{0\,0}^{-M\,0} & 0 & & 0 & T_{0\,0}^{-M\,Q} & 0 & & 0 \\
0 & \ddots & & \vdots & 0 & \ddots & & \vdots & 0 & \ddots & & \vdots \\
\vdots & & \ddots & 0 & \vdots & & \ddots & 0 & \vdots & & \ddots & 0 \\
0 & \cdots & 0 & T_{N\,N}^{-M\,-Q} & 0 & \cdots & 0 & T_{N\,N}^{-M\,0} & 0 & \cdots & 0 & T_{N\,N}^{-M\,Q} \\
T_{0\,0}^{0\,-Q} & 0 & \cdots & 0 & T_{0\,0}^{0\,0} & 0 & & 0 & T_{0\,0}^{0\,Q} & 0 & & 0 \\
0 & \ddots & & \vdots & 0 & \ddots & & \vdots & 0 & \ddots & & \vdots \\
\vdots & & \ddots & 0 & \vdots & & \ddots & 0 & \vdots & & \ddots & 0 \\
0 & \cdots & 0 & T_{N\,N}^{0\,-Q} & 0 & \cdots & 0 & T_{N\,N}^{0\,-0} & 0 & \cdots & 0 & T_{N\,N}^{0\,Q} \\
T_{0\,0}^{M\,-Q} & 0 & \cdots & 0 & T_{0\,0}^{M\,0} & 0 & & 0 & T_{0\,0}^{M\,Q} & 0 & & 0 \\
0 & \ddots & & \vdots & 0 & \ddots & & \vdots & 0 & \ddots & & \vdots \\
\vdots & & \ddots & 0 & \vdots & & \ddots & 0 & \vdots & & \ddots & 0 \\
0 & \cdots & 0 & T_{N\,N}^{M\,-Q} & 0 & \cdots & 0 & T_{N\,N}^{M\,-0} & 0 & \cdots & 0 & T_{N\,N}^{M\,Q}
\end{bmatrix} \tag{2.4.2}$$

The specific arrangement of the $\mathbf{T}_{ij}$ terms, i.e. without coupling components between different depth modes, is explained as the depth variation is unchanged by the reference system transformation (Appendix B).

2.4.2 Bessel functions scaling

As mentioned in Kagemoto and Yue (1986), the disparate asymptotic nature of the Bessel functions makes it of paramount importance to normalize them with respect to both order and argument for numerical calculations. In the work of Child (2011), and based on Siddorn and Eatock Taylor (2008), this was done by dividing the radially-dependent functions by their value at a distance equal to the radius of the axysimmetric geometry considered, i.e., a truncated vertical cylinder. For arbitrary geometries, the same principle could be adopted by choosing as normalization distance the radius of the circumscribing cylinder to the body.

Following this strategy, expressions (2.2.23) and (2.2.12) for the incident and scattered partial waves respectively are reformulated as:

$$\left(\psi_j^I\right)_{lq} = \begin{cases} \frac{\cosh\left[k_0(z+d)\right]}{\cosh\, k_0 d}\, \frac{J_q(k_0 r_j)}{J_q(k_0 R_j)} e^{iq\theta_j}, & l = 0 \\ \cos[k_l(z+d)]\, \frac{I_q(k_l r_j)}{I_q(k_l R_j)} e^{iq\theta_j}, & l \geq 1 \end{cases}$$

$$\left(\psi_j^S\right)_{nm} = \begin{cases} \frac{\cosh\, k_0(z+d)}{\cosh\, k_0 d}\, \frac{H_m^{(1)}(k_0 r_j)}{H_m^{(1)}(k_0 R_j)} e^{im\theta_j} & n = 0 \\ \cos\, k_n(z+d)\, \frac{K_m(k_n r_j)}{K_m(k_n R_j)} e^{im\theta_j} & n \geq 1 \end{cases} \tag{2.4.3}$$

where R_j corresponds to the radius of the circumscribing cylinder of body j.

The changes in (2.4.3) are transfered to the partial wave coefficients of the ambient wave as:

$$(a_j)_{lq} = \begin{cases} -i\frac{g\zeta_a}{\omega}\, J_q(k_0 R_j) e^{ik_0(X_0\cos\beta + Y_0\sin\beta)} i^q e^{-iq\beta}, & l = 0 \\ 0 & l \geq 1 \end{cases} \tag{2.4.4}$$

Similarly, the elements of the transformation matrix are modified according to its definition, $\psi_i^S = \mathbf{T}_{ij}\psi_j^I$:

$$(\mathbf{T}_{ij})_{nn}^{mq} = \begin{cases} \frac{J_q(k_0 a_j)}{H_m^{(1)}(k_0 a_i)}\, H_{m-q}^{(1)}(k_0 L_{ij}) e^{i\alpha_{ij}(m-q)} & n = 0 \\ \frac{I_q(k_n a_j)}{K_m(k_n a_i)}\, K_{m-q}(k_n L_{ij})(-1)^q e^{i\alpha_{ij}(m-q)} & n \geq 1 \end{cases} \tag{2.4.5}$$

2.5 Summary

In the first section of this Chapter, the solution to the BVP for an isolated body in cylindrical coordinates has been presented. A generic form to express both the scattered and radiated wave fields based on the solution to the BVP has been derived. In addition, it has been shown that plane incident waves can be represented using a superposition of partial cylindrical waves by means of a fundamental property of Bessel functions.

In the second part, the solution to the BVP for a large number of bodies in array using the Direct Matrix Method interaction theory by Kagemoto and Yue (1986) has been presented. The generic form to represent incident, radiated and scattered wave fields derived in the first part of this Chapter has been used to construct a system of equations to solve for the unknown scattered partial cylindrical wave coefficients. In this process, a mathematical operator called Transformation Matrix which relies on Graf's addition theorem has been used. This imposes a spacing restriction which

affects the minimum distance allowed between two bodies in array.

Prior to solving the system of equations presented, two hydrodynamic operators (DTM and RC) which characterize the way an isolated body scatters and radiates waves respectively need to be evaluated. A third operator (FTM) is required for the computation of the efforts on the bodies in array and, therefore, for the generation of hydrodynamic coefficients. Details on the evaluation of these hydrodynamic operators for arbitrary geometries using a BEM solver will be given in the following Chapter.

Chapter 3

Hydrodynamic Operators of the Direct Matrix Method

In Chapter 2, the Direct Matrix Method interaction theory (IT) which enables one to efficiently solve the multiple-scattering problem was presented. It was shown that one of its fundamental parts is the computation of two hydrodynamic operators, the Diffraction Transfer Matrix (DTM) and the Radiation Characteristics (RC), which characterize the way an isolated body scatters and radiates waves respectively. In addition, an operator called Force Transfer Matrix (FTM) was used to evaluate the efforts on the bodies.

In this Chapter, two different methodologies derived by Goo and Yoshida (1990) and McNatt et al. (2015) to compute the DTM, FTM and RC for arbitrary geometries are presented and compared. We shall refer to the former, which has been implemented in the BEM code NEMOH as *Method I* and to the latter as *Method II*. Comparisons of both methodologies are undertaken by studying the hydrodynamic operators of two different geometries, a truncated vertical circular cylinder and a cube. This provides a valuable insight into the DTM, RC and FTM which have not received much attention in the literature but are required to implement the IT.

3.1 Method I

3.1.1 Diffraction Transfer Matrix

The methodology developed by Goo and Yoshida (1990) enables one to find each element $(\mathbf{B}_j)_{nl}^{mq}$ of the DTM following two steps. First, the solution to a diffraction problem where the incident wave is an incident cylindrical partial wave of angular

mode q and depth mode l is found. This involves solving for the unknown source strengths σ_{lqj} in the following integral equation:

$$\frac{1}{2}\sigma_{lqj}(r_j,\theta_j,z_j)+\iint_{S_j}\sigma_{lqj}(R_j,\Theta_j,\zeta_j)\frac{\partial G_j(R_j,\Theta_j,\zeta_j;r_j,\theta_j,z_j)}{\partial n}ds=-\frac{\partial\left(\psi_j^I\right)_{lq}(r_j,\theta_j,z_j)}{\partial n} \tag{3.1.1}$$

where G is the Green's function, (R_j,Θ_j,ζ_j) is the influencing or source point and (r_j,θ_j,z_j) the influenced or field point on S_j, $(\psi_j^I)_{lq}$ is the incident partial wave lq as defined in (2.2.23) and S_j the wetted surface of body j.

The right hand side of equation (3.1.1) expresses the diffraction boundary condition (2.2.10) on the wetted surface of the body due to an incident partial cylindrical wave of angular mode q and depth mode l. This boundary condition replaces the standard diffraction BC in BEM codes where the incident potential is simply the Airy potential of a planar wave (2.2.17). The derivatives with respect to the outward normal of $\left(\psi_j^I\right)_{lq}$ can be evaluated from:

$$\frac{\partial\left(\psi_j^I\right)_{lq}}{\partial n}=\frac{\partial\left(\psi_j^I\right)_{lq}}{\partial x_j}nx_j+\frac{\partial\left(\psi_j^I\right)_{lq}}{\partial y_j}ny_j+\frac{\partial\left(\psi_j^I\right)_{lq}}{\partial z_j}nz_j \tag{3.1.2}$$

where nx_j, ny_j and nz_j denote respectively the x, y and z components of the unit normal vector to the immersed surface of the body j. For the progressive ($l=0$) incident partial waves:

$$\frac{\partial\left(\psi_j^I\right)_{0q}}{\partial x_j}=\frac{\cosh\left[k_0(z_j+d)\right]}{\cosh\left(k_0d\right)}\left[k_0\frac{x_j}{r_j}J_{q-1}(k_0r_j)-\frac{q}{r_j^2}(x_j+i\,y_j)J_q(k_0r_j)\right]e^{iq\theta_j} \tag{3.1.3}$$

$$\frac{\partial\left(\psi_j^I\right)_{0q}}{\partial y_j}=\frac{\cosh\left[k_0(z_j+d)\right]}{\cosh\left(k_0d\right)}\left[k_0\frac{y_j}{r_j}J_{q-1}(k_0r_j)-\frac{q}{r_j^2}(y_j-i\,x_j)J_q(k_0r_j)\right]e^{iq\theta_j} \tag{3.1.4}$$

$$\frac{\partial\left(\psi_j^I\right)_{0q}}{\partial z_j}=\frac{\sinh\left[k_0(z_j+d)\right]}{\cosh\left(k_0d\right)}k_0J_q(k_0r_j)e^{iq\theta_j} \tag{3.1.5}$$

and for the evanescent ($l\geq 1$):

$$\frac{\partial\left(\psi_j^I\right)_{lq}}{\partial x_j} = \cos[k_l(z_j+d)]\left[k_l\frac{x_j}{r_j}I_{q-1}(k_l r_j) - \frac{q}{r_j^2}(x_j + i\,y_j)\,I_q(k_l r_j)\right]e^{iq\theta_j} \tag{3.1.6}$$

$$\frac{\partial\left(\psi_j^I\right)_{lq}}{\partial y_j} = \cos[k_l(z_j+d)]\left[k_l\frac{y_j}{r_j}I_{q-1}(k_l r_j) - \frac{q}{r_j^2}(y_j - i\,x_j)\,I_q(k_l r_j)\right]e^{iq\theta_j} \tag{3.1.7}$$

$$\frac{\partial\left(\psi_j^I\right)_{lq}}{\partial z_j} = -k_l\sin[k_l(z_j+d)]\,I_q(k_l r_j)e^{iq\theta_j} \tag{3.1.8}$$

Once the source strength distribution σ_{lqj} is known on the panelized surface of the body for all the possible combinations between l and q, the following step consists in expressing the scattered potential in the base of partial cylindrical wave functions (2.2.12). For that, it is worth recalling that the scattered potential at a field point in the fluid (r_j, θ_j, z_j) due to any source distribution σ_{lq} defined over a surface S_j can be expressed as:

$$\phi_j^S(r_j,\theta_j,z_j) = \iint_{S_j}\sigma_{lqj}(R_j,\Theta_j,\zeta_j)\,G_j(r_j,\theta_j,z_j;R_j,\Theta_j,\zeta_j)\,ds \tag{3.1.9}$$

In standard BEM codes, the Green function is expressed in Cartesian coordinates based on the form derived by (John, 1950). It can also be expressed in cylindrical coordinates as a Fourier series as presented by Black (1975) and further investigated by Fenton (1978):

$$\begin{aligned} G_j(r_j,\theta_j,z_j;R_j,\Theta_j,\zeta_j) = &\sum_{m=-\infty}^{\infty}\frac{i}{2}C_0\cosh[k_0(z_j+d)]\cosh[k_0(\zeta_j+d)] \\ &\times\left\{\begin{array}{l} H_m^{(1)}(k_0 r_j)J_m(k_0 R_j) \\ H_m^{(1)}(k_0 R_j)J_m(k_0 r_j)\end{array}\right\}e^{im(\theta_j-\Theta_j)} \\ &-\frac{1}{\pi}\sum_{n=1}^{\infty}C_n\cos[k_n(z_j+h)]\cos[k_n(\zeta_j+d)] \\ &\times\sum_{m=-\infty}^{\infty}\left\{\begin{array}{l} K_m(k_n r_j)I_m(k_n R_j) \\ K_m(k_n R_j)I_m(k_n r_j)\end{array}\right\}e^{im(\theta_j-\Theta_j)} \end{aligned} \tag{3.1.10}$$

where the upper terms in the curly brackets are used when $r_j > R_j$, the lower terms

when $r_j < R_j$ and C_0 and C_n are defined as:

$$C_0 = \frac{K^2 - k_0^2}{(k_0^2 - K^2)d + K}; \quad C_n = \frac{k_n^2 + K^2}{(k_n^2 + K^2)d - K}; \quad K = \frac{\omega^2}{g} \tag{3.1.11}$$

By substituting (3.1.10) into (3.1.9), and considering that the condition $r_j > R_j$ is always satisfied (i.e. the field point is always outside the circumscribing cylinder of the body), equation (3.1.9) can be expressed as:

$$\phi_j^S(r_j, \theta_j, z_j) = \frac{\cosh[k_0(z_j + d)]}{\cosh\ k_0 d} \sum_{m=-\infty}^{\infty} (\mathbf{B}_j)_{0l}^{mq} H_m^{(1)}(k_0 r_j) e^{im\theta_j} + \sum_{n=1}^{\infty} \cos[k_n(z_j + d)] \sum_{m=-\infty}^{\infty} (\mathbf{B}_j)_{nl}^{mq} K_m(k_n r_j) e^{im\theta_j} \tag{3.1.12}$$

where coefficients $(\mathbf{B}_j)_{0l}^{mq}$ and $(\mathbf{B}_j)_{nl}^{mq}$ are given by:

$$(\mathbf{B}_j)_{0l}^{mq} = \frac{i}{2} C_0\ \cosh\ k_0 d \iint_{S_j} \sigma_{lqj}(R_j, \Theta_j, \zeta_j)\, J_m(k_0 R_j)\ \cosh[k_0(\zeta_j + d)] e^{-im\Theta_j} ds \tag{3.1.13}$$

$$(\mathbf{B}_j)_{nl}^{mq} = -\frac{1}{\pi} C_n \iint_{S_j} \sigma_{lqj}(R_j, \Theta_j, \zeta_j)\, I_m(k_n R_j)\ \cos[k_n(\zeta_j + d)] e^{-im\Theta_j} ds \tag{3.1.14}$$

Equation (3.1.12) is exactly of the same form as (2.2.14) and it represents the scattered potential of the j^{th} body valid outside its circumscribed, bottom-mounted, imaginary vertical cylinder. Coefficients $(\mathbf{B}_j)_{nl}^{mq}$ represent the amplitudes of the partial scattered cylindrical waves of angular mode m and depth mode n due to a unitary incident partial wave of angular mode q and depth mode l $\left(\psi_j^I\right)_{lq}$. Hence, they are the elements of the DTM. In short, its lq^{th} column is obtained by solving the diffraction problem involving the incident cylindrical partial wave $\left(\psi_j^I\right)_{lq}$ and by embedding the corresponding source distribution σ_{lqj} in equations (3.1.13)-(3.1.14) to compute the element of the nm^{th} row.

3.1.2 Radiation Characteristics

The same principle applied for the calculation of the DTM can be used now to obtain the RC vector. First, the radiation problem associated with a degree of freedom k of the body under consideration is solved. In this case, the boundary-value problem is the same as the one solved by a standard BEM solver. Thus, the source strength

distribution can be obtained from the following equation:

$$\frac{1}{2}\sigma_{jk}(r_j,\theta_j,z_j)+\iint_{S_j}\sigma_{jk}(R_j,\Theta_j,\zeta_j)\frac{\partial G_j(R_j,\Theta_j,\zeta_j;r_j,\theta_j,z_j)}{\partial n}ds=n_{jk} \tag{3.1.15}$$

where the left hand side remains unchanged with respect to equation (3.1.1) and the right hand side represents the radiation BC (2.2.11) on the wetted surface of the body given by the direction cosine of a particular degree of freedom k ($k=1,\ldots,6$ in the general case) expressed as:

$$n_{1j}=n_x \tag{3.1.16}$$
$$n_{2j}=n_y \tag{3.1.17}$$
$$n_{3j}=n_z \tag{3.1.18}$$
$$n_{4j}=(y_j-y_{mj})n_{zj}-(z_j-z_{mj})n_{yj} \tag{3.1.19}$$
$$n_{5j}=(z_j-z_{mj})n_{xj}-(x_j-x_{mj})n_{zj} \tag{3.1.20}$$
$$n_{6j}=(x_j-x_{mj})n_{yj}-(y_j-y_{mj})n_{xj} \tag{3.1.21}$$

where (x_{mj},y_{mj},z_m) are the coordinates of the point about which the moment is taken.

Once known, the source strength distribution σ_{jk} is used in conjunction with the Green's function in cylindrical coordinates (3.1.10) to represent the radiated potential in terms of partial cylindrical waves leading to the following expressions for the Radiation Characteristics:

$$(R_j^k)_{0m}=\frac{i}{2}\,C_0\,\cosh\,k_0d\iint_{S_j}\sigma_{jk}(R_j,\Theta_j,\zeta_j)\,J_m(k_0R_j)\,\cosh[k_0(\zeta_j+d)]e^{-im\Theta_j}ds \tag{3.1.22}$$

$$(R_j^k)_{nm}=-\frac{1}{\pi}\,C_n\iint_{S_j}\sigma_{jk}(R_j,\Theta_j,\zeta_j)\,I_m(k_nR_j)\,\cos[k_n(\zeta_j+d)]e^{-im\Theta_j}ds \tag{3.1.23}$$

3.1.3 Force Transfer Matrix

The solution to the diffraction BVP (equation 3.1.1) given by the source strength distribution σ_{lqj} enables one to reconstruct the scattered potential by means of (3.1.9). The pressure associated to an incident partial wave $\left(\psi_j^I\right)_{lq}$ can then be computed from Bernouilli equation (2.1.7) leading to the following expression for the first order

excitation force:

$$\left(F_{jk}^{ex}\right)_{lq} = -i\rho\omega \iint_{S_j} \left[\left(\psi_j^I\right)_{lq} + \phi_j^S\right] n_{jk}\, ds \tag{3.1.24}$$

where $\left(F_{jk}^{ex}\right)_{lq}$ is the excitation force acting upon mode k due to an incident cylindrical partial wave of depth mode l and angular mode q and ϕ_j^S is the scattered potential as in (3.1.12).

The lq^{th} terms of the k^{th} row of the FTM (section 2.3.3) relate the forces acting in the degree of freedom k of the body due to a partial incident cylindrical wave coefficient $\left(\psi_j^I\right)_{lq}$ and, therefore, they are given by $\left(F_{jk}^{ex}\right)_{lq}$.

It is worth noting that the FTM, which is a frequency-dependent operator computed using the representation of the diffracted wave field on the basis of partial cylindrical wave functions, enables the computation of the excitation forces on an isolated body due to an incident long-crested progressive plane wave propagating in any arbitrary direction β and represented by means of the coefficients in (2.2.21). This is remarkably different than in a traditional BEM approach, where as many diffraction problems as incident wave directions need to be solved.

3.2 Method II

3.2.1 Diffraction Transfer Matrix

The *Method I* described in the previous section involves solving the diffraction BVP using incident partial cylindrical waves. Standard BEM codes such as the well-known WAMIT (Lee and Newman, 1999) do not enable, at present, to solve for this cylindrical representation of incident waves and can only deal with plane incident waves. McNatt et al. (2015) derived a methodology to circumvent this problem and to compute the elements of the DTM by solving multiple diffraction problems involving only incident plane waves. The procedure is detailed in the following paragraphs. An equivalent method that uses the Fourier transform can be found in McNatt (2015).

From the definition of the DTM (2.3.10), the following relationship applies:

$$A_j(\beta_n) = \mathbf{B}_j\, a_j(\beta_n) \tag{3.2.1}$$

where $A_j(\beta_n)$ is the vector of progressive scattered cylindrical wave coefficients , $\mathbf{B}_j$ the diffraction transfer matrix and $a_j(\beta_n)$ the vector of progressive ambient incident cylindrical wave coefficients. Subindex j refers to the body and β_n represents the

propagation direction of the plane incident wave.

Both vectors of coefficients are theoretically infinitely long but for practical computations a truncation is required. If we refer to the truncation value as M_j, vectors $A_j(\beta_n)$ and $a_j(\beta_n)$ have dimension $(2M_j + 1)$ whereas the diffraction transfer matrix $\mathbf{B}_j$ has dimensions $(2M_j + 1) \times (2M_j + 1)$.

As mentioned in section 2.2.2, incident plane waves travelling with a direction β_n can be represented by means of a superposition of partial progressive cylindrical waves. Thus, the vector of coefficients $a_j(\beta_n)$ is known and given by (2.2.21). Assuming that the vector of progressive scattered waves $A_j(\beta_n)$ is also a known quantity, it can be observed that equation (3.2.1) is an under-determined matrix equation to solve for the elements of the DTM. If instead of having only one set of coefficients $A_j(\beta_n)$ and $a_j(\beta_n)$ associated with a single wave direction β_n, a larger set of coefficients is available for as many wave directions β_n as the leading dimension of the diffraction transfer matrix $(2M_j+1)$, (3.2.1) becomes a full matrix equation from which the elements of the DTM can be obtained. McNatt et al. (2015) states that, to be more accurate, the number of coefficient vectors should be larger than the leading dimension of the diffraction transfer matrix creating as a result an over determined system.

So far it has been assumed that the coefficients $A_j(\beta_n)$ are known. The procedure to obtain them derived in McNatt et al. (2013) is briefly explained in the following paragraphs.

As has been shown in section 2.2.1, the solution to the diffraction problem for the scattered potential is of the form (2.2.14). Using the notation of McNatt et al. (2013):

$$\phi^S = i\frac{g}{\omega}\sum_{m=-\infty}^{\infty}(\chi^S)_m e^{im\theta} \tag{3.2.2}$$

where χ^S is given by:

$$(\chi^S)_m = (a^S)_m \frac{\cosh\, k_0(h+z)}{\cosh\, k_0 h} H_m^{(2)}(k_0 r) + \sum_{n=1}^{\infty}(b^S)_{nm}\, \cos\, k_n(h+z)\, K_m(k_n r) \tag{3.2.3}$$

where $H_m^{(2)}$ is the m^{th} order Hankel function of the second kind, m refers to the angular-mode, index n to the depth mode and h to the depth. a_{0m}^S and b_{nm}^S are the progressive and evanescent cylindrical wave coefficients respectively equivalent to A_{0m}^S and A_{nm}^S for the notation used in this work.

The term $(\chi^S)_m$ can be found as the Fourier transform of the velocity potential:

$$(\chi^S)_m = -\frac{i}{2\pi}\frac{\omega}{g}\int_0^{2\pi} \phi^S e^{-im\theta} d\theta \tag{3.2.4}$$

By equating (3.2.3) and (3.2.4) and by using the depth dependence orthogonality properties of the depth dependence functions:

$$\int_{-h}^{0} \cosh\, k_0(h+z)\, \cos\, k_l(h+z)\, dz = 0 \tag{3.2.5}$$

$$\int_{-h}^{0} \cos\, k_l(h+z)\, \cos\, k_n(h+z)\, dz = 0,\ l \neq n \tag{3.2.6}$$

the progressive and evanescent partial waves can be isolated. Then, if the potential due to a submerged body is known over a circular-cylindrical surface with radius r_0 the cylindrical coefficients can be calculated as:

$$a_{0m} = -\frac{i}{2\pi}\frac{\omega}{g}\frac{2\,\cosh\, k_0 h}{h\left(1+\frac{\sinh\, 2k_0h}{2k_0h}\right)}\frac{1}{H_m^{(2)}(k_0 r_0)}\int_{-h}^{0}\int_0^{2\pi} \phi(r_0,\,\theta,\,z)\, e^{-im\theta}\cosh\, k_0(h+z) d\theta dz \tag{3.2.7}$$

$$b_{nm} = -\frac{i}{2\pi}\frac{\omega}{g}\frac{2}{h\left(1+\frac{\sin\, 2k_nh}{2k_nh}\right)}\frac{1}{K_m(k_n r_0)}\int_{-h}^{0}\int_0^{2\pi} \phi(r_0,\,\theta,\,z) e^{-im\theta}\cos\, k_n(h+z) d\theta dz \tag{3.2.8}$$

3.2.2 Radiation Characteristics

The computation of the RC follows a similar procedure to the one used for the calculation of the DTM. First, the radiation problem associated with a specific mode of motion and frequency is solved with a standard BEM code. Then, by means of expressions (3.2.7) and (3.2.8), the radiated potential is expressed in terms of partial cylindrical wave functions. In this base, the coefficients are known as Radiation Characteristics and are denoted by $a_{0m}^{R,k}$ and $b_{nm}^{R,k}$ which correspond respectively to R_{0m}^k and R_{nm}^k in the notation of *Method I*.

3.2.3 Force Transfer Matrix

The same methodology applied for the calculation of the DTM can be applied to compute the FTM. From the definition of the latter, it can be observed that if one disposes of a sufficient set of excitation forces and incident partial wave coefficients,

equation (2.3.18) can be transformed into a system of equations which can be solved for the elements of the FTM. The pairs force/wave coefficients can be obtained by solving at least as many diffraction problems as the leading dimension of the FTM $(2M_j + 1)$ for different long-crested plane wave propagating directions.

3.3 Equivalence between Methods I and II

The formulation of *Method I* is based on the notation of Goo and Yoshida (1990) which makes use of a negative harmonic time dependence ($e^{-i\omega t}$), whereas *Method II* by McNatt et al. (2015) adopts a positive sign convention ($e^{i\omega t}$). In addition, in *Method I* amplitudes of partial wave coefficients have units of velocity potential (m^2/s). In *Method II* they have units of length (m) and get units of velocity potential by multiplying by $i\frac{g}{\omega}$. By taking into account such convention differences, the equivalence between both partial wave coefficients is given by (see Appendix (E) for full derivation):

$$(-1)^{-m}\frac{g}{\omega}\left[i(a_{-m}^{S,I})\right]^* = A_m^{S,I} \tag{3.3.1}$$

where super-index * denotes complex conjugate, $a_{-m}^{S,I}$ are the progressive partial waves coefficients in the notation of McNatt et al. (2015) and $A_m^{S,I}$ in the notation of Goo and Yoshida (1990).

By introducing (3.3.1) into the definition of the DTM in (3.2.1), the following expression relating their elements in both notations can be obtained:

$$\frac{(-1)^{-m}}{(-1)^{-q}}\,(\mathbf{B}^*)_{-m,-q}^{Method\,I} = (\mathbf{B})_{m,q}^{Method\,II} \tag{3.3.2}$$

The results presented in this work have been computed using the BEM solver NEMOH, in which *Method I* has been implemented. The results presented for *Method II* were computed using WAMIT. To solve the radiation problem, NEMOH employs unit-amplitude velocity as the boundary condition, while WAMIT uses unit-amplitude motions, which results in a difference in scaling of the resultant solutions. The relationship between the source strengths in the radiation problem is:

$$\sigma^{Nemoh} = \frac{1}{i\omega}\,\sigma^{Wamit} \tag{3.3.3}$$

As a consequence, by taking into account (3.3.3) and the notation convention differences in (3.3.1), the relationship between the RC in both notations follows as:

$$(-1)^{-m}\frac{g}{\omega^2}\left[(a^R_{-mk})\right]^* = R_{mk}$$

where a^R_{-mk} are the RC in the notation of McNatt et al. (2015) and R_{mk} in the notation of Goo and Yoshida (1990).

The formulae of the scattered and radiated potentials presented in this section and expressed on the basis of partial cylindrical waves are only valid outside the body's circumscribing cylinder of radius R_j. For *Method I*, the limitation stems from the use of the cylindrical Green's function form by Fenton (1978) valid only when $r_j > R_j$ whereas, for *Method II*, it is a consequence of performing a Fourier Transform of the potential on the body's circumscribing cylinder. Because of that, the use of the interaction theory requires that the relative distance between two bodies in the array has to be such that a circumscribing cylinder cannot intersect any other body (Figure (3.1)). This condition is more restrictive than the one imposed by the use of Graf's addition theorem in (2.3.2) which states that the circumscribing cylinder of a body cannot contain the geometrical center of any other body (Appendix B). In that sense, we note that the arrangement in Figure 5b by McNatt et al. (2015) falls out of the range of validity of the interaction theory.

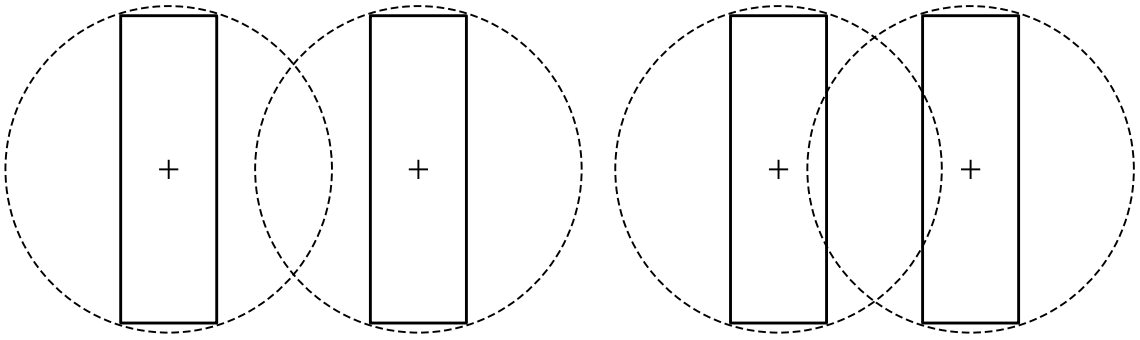

Figure 3.1: Authorized a) and unauthorized b) relative position between bodies when using the Direct Matrix Method interaction theory. Source: adapted from Chakrabarti (2001).

Even if evanescent terms from the scattered potential can be identified using (3.2.8), the use of only plane progressive incident waves (with no evanescent components) prevents the calculation of the DTM terms relating incident and scattered evanescent partial waves using *Method II*.

3.4 Rotation of the body

As shown by Peter and Meylan (2004a), for a non-axisymmetric body a rotation about its mean center position in the (x, y) plane varies the elements of the DTM, as well as the RC and the FTM.

With respect to the diffraction problem, the rotation of the body modifies the source distribution on its wetted surface. For this case, the rotation of the body is equivalent to keeping the body in its original position and rotating the incident potential. The latter can be expressed as:

$$\frac{\partial \phi^I_{q\gamma_j}}{\partial n} = \frac{\partial \phi^I_q}{\partial n} e^{iq\gamma_j} \tag{3.4.1}$$

where γ_j is the rotation of body j and ϕ^I_q is an incident potential of progressive mode q.

As the integral equation to determine the source strength is linear (3.1.1), the distribution of source strengths due to the rotated incident potential (3.4.1) can be expressed as:

$$\sigma^j_{q\gamma_j} = \sigma^j_q e^{iq\gamma_j} \tag{3.4.2}$$

where $\sigma^j_{q\gamma_j}$ is the distribution of source strengths due to the rotated incident potential.

If the rotated source strengths are introduced in (3.1.13), which is used to calculate the elements of the DTM, as well as a change in the angular dependence in the integral over the wetted surface of the body the following expression is obtained:

$$\left(\mathbf{B}^{\gamma_j}_{\mathbf{j}}\right)^{mq}_{0l} = \frac{i}{2} C_0 \cosh\, k_0 d \iint_{S_j} \sigma^j_{q\gamma_j}(R_j, \Theta_j, \zeta_j)\, J_m(k_0 R_j) \cosh[k_0(\zeta_j + d)] e^{-im(\Theta+\gamma_j)} ds \tag{3.4.3}$$

By substituting identity (3.4.2) into (3.4.3) we have:

$$\left(\mathbf{B}^{\gamma_j}_{\mathbf{j}}\right)^{mq}_{0l} = \frac{i}{2} C_0 \cosh\, k_0 d \iint_{S_j} \sigma^j_q(R_j, \Theta_j, \zeta_j)\, J_m(k_0 R_j) \cosh[k_0(\zeta_j + d)] e^{-im(\Theta+\gamma_j)} e^{iq\gamma_j} ds \tag{3.4.4}$$

The comparison between (3.4.4) and (3.1.13) leads to:

$$\left(\mathbf{B}^{\gamma_j}_{j}\right)^{mq}_{0l} = e^{i\gamma_j(q-m)} \left(\mathbf{B}_j\right)^{mq}_{0l} \tag{3.4.5}$$

It is worth noting that expression (3.4.5) is valid for both progressive and evanes-

cent modes as the rotation only changes angular variation and not depth dependence. Thus:

$$\left(\mathbf{B}_j^{\gamma_j}\right)_{nl}^{mq} = e^{i\gamma_j(q-m)}\left(\mathbf{B}_j\right)_{nl}^{mq} \tag{3.4.6}$$

Contrarily to the diffraction case, the body rotation does not change the source strength distribution associated with the radiation problem given by the motion of body j in a degree of freedom k:

$$\sigma_{q\gamma_j}^{jk} = \sigma_q^{jk} \tag{3.4.7}$$

The only effect is the modification of the angular dependence of the integral over the wetted surface in (3.1.22) which leads to:

$$\left(R_{jk}^{\gamma_j}\right)_{0m} = \frac{i}{2}C_0 \cosh\, k_0 d \iint_{S_j} \sigma_{q\gamma_j}^{jk}(R_j,\Theta_j,\zeta_j)\, J_m(k_0 R_j)\, \cosh[k_0(\zeta_j+d)] e^{-im(\Theta+\gamma_j)} ds \tag{3.4.8}$$

By comparing (3.4.8) and (3.1.22), the following relationship can be deduced:

$$\left(R_{jk}^{\gamma_j}\right)_{0m} = e^{-im\gamma_j}\left(R_{jk}\right)_{0m} \tag{3.4.9}$$

Using a more general notation including the evanescent modes (3.4.8) reads:

$$\left(R_{jk}^{\gamma_j}\right)_{nm} = e^{-im\gamma_j}\left(R_{jk}\right)_{nm} \tag{3.4.10}$$

The rotation of the incident potential (3.4.1) can be expressed in terms of the partial cylindrical wave coefficients as (McNatt et al., 2015):

$$\phi_{\gamma_j}^I = \left(A_{\gamma_j}^I\right)_{lq}\left(\psi^I\right)_{lq} \tag{3.4.11}$$

where $A_{\gamma_j}^I$ has been defined as:

$$\left(A_{\gamma_j}^I\right)_{lq} = e^{iq\gamma_j}\left(A^I\right)_{lq} \tag{3.4.12}$$

By substituting (3.4.12) into the definition of the FTM (2.3.18):

$$\left(F_j^{\gamma_j}\right)_{lq} = \left(\mathbf{G}_j\right)_{lq} e^{iq\gamma_j}\left(A^I\right)_{lq} \tag{3.4.13}$$

The comparison between expressions (3.4.13) and (2.3.18) leads to:

$$\left(\mathbf{G}_j^{\gamma_j}\right)_{lq} = e^{iq\gamma_j} \left(\mathbf{G}_j\right)_{lq} \tag{3.4.14}$$

3.5 Numerical Implementation

As mentioned in Babarit and Delhommeau (2015), the body boundary conditions in NEMOH can be defined by the user. Thus, for the diffraction problem, the code can easily accommodate a user-defined distribution of normal velocities at the centroid of each mesh panel. They have been implemented in the preprocessor module of the BEM code as the derivative of the incident partial wave functions (of angular mode q and depth mode l) presented in equations (3.1.3) - (3.1.8). The finite depth Green's function is expressed in Cartesian coordinates rather than the cylindrical coordinates of (3.1.1) as it is more convenient for the computations (Goo and Yoshida, 1990).

The asymptotic form of the term C_0 in (3.1.11) poses convergence problems when the water depth is increased. As mentioned in Peter and Meylan (2004a), the limitation can be circumvented if it is reformulated by means of the dispersion relation (C.1.11) leading to (derivation in Appendix F):

$$C_0 = -\frac{k_0}{2k_0 d + \sinh\, 2k_0 d} \tag{3.5.1}$$

No closed mathematical expression exists for the integrals (3.1.13)-(3.1.14) and (3.1.22)-(3.1.23), even when σ is constant over each panel. Therefore, they cannot be solved analytically but by using a quadrature scheme. In this work, results will be presented for a one-point and four-point Gaussian quadrature rules (Abramowitz and Segun A., 1964). Details of the numerical integration are shown in Appendix G. In the NEMOH BEM solver the source strengths are assumed to be constant over each flat quadrilateral panel. Nevertheless, the degree of variation of the other terms in the kernel of the integrals (3.1.13)-(D.1.113) and (3.1.22)-(3.1.23) is influenced by the discretization of the wetted surface of the body, as well as by the partial wave angular-mode m and by the frequency. The latter will determine the magnitude of the wave number. This can be qualitatively observed in Figure 3.2, which shows the variation, along the lateral side and the bottom of a cylinder, of the different functions the kernel of the DTM and RC integrals is composed of.

The normalization shown in section 2.4.2 propagates into the hydrodynamic operators in the following manner.

For the DTM:

$$(\tilde{\mathbf{B}}_j)_{0l}^{mq} = \frac{H_m(k_0 R_j)}{J_q(k_0 R_j)} (\mathbf{B}_j)_{0l}^{mq} \tag{3.5.2}$$

$$(\tilde{\mathbf{B}}_j)_{nl}^{mq} = \frac{K_m(k_n R_j)}{I_q(k_l R_j)} (\mathbf{B}_j)_{nl}^{mq} \tag{3.5.3}$$

where ˜ indicates a normalized operator.

For the RC, the progressive and evanescent terms should be scaled as:

$$(\tilde{R}_j^k)_{0m} = H_m(k_0 R_j)\,(R_j^k)_{0m} \tag{3.5.4}$$

$$(\tilde{R}_j^k)_{nm} = K_m(k_n R_j)\,(R_j^k)_{nm} \tag{3.5.5}$$

Finally, the normalized FTM terms read:

$$\left(\tilde{F}_{jk}^{ex}\right)_{0q} = \frac{1}{J_q(k_0 R_j)} \left(F_{jk}^{ex}\right)_{0q} \tag{3.5.6}$$

$$\left(\tilde{F}_{jk}^{ex}\right)_{lq} = \frac{1}{I_q(k_0 R_j)} \left(F_{jk}^{ex}\right)_{lq} \tag{3.5.7}$$

3.6 Results and Discussion

In this section, the main components of the DTM, the RC and the FTM for a truncated vertical cylinder (3 m radius and 6 m draft) and a cube (6 m side and 6 m draft) in a 10 m water depth are presented. The choice of two different bodies enables one to identify geometry specific features of the hydrodynamic operators. Only the most relevant results are shown herein and the rest has been compiled in Appendix I.

The two different discretizations shown in Figures 3.3 and 3.4 have been used for the computations. A mesh convergence study has been performed showing no significant improvement of accuracy by using 3.3b or 3.4b (see Appendix I).

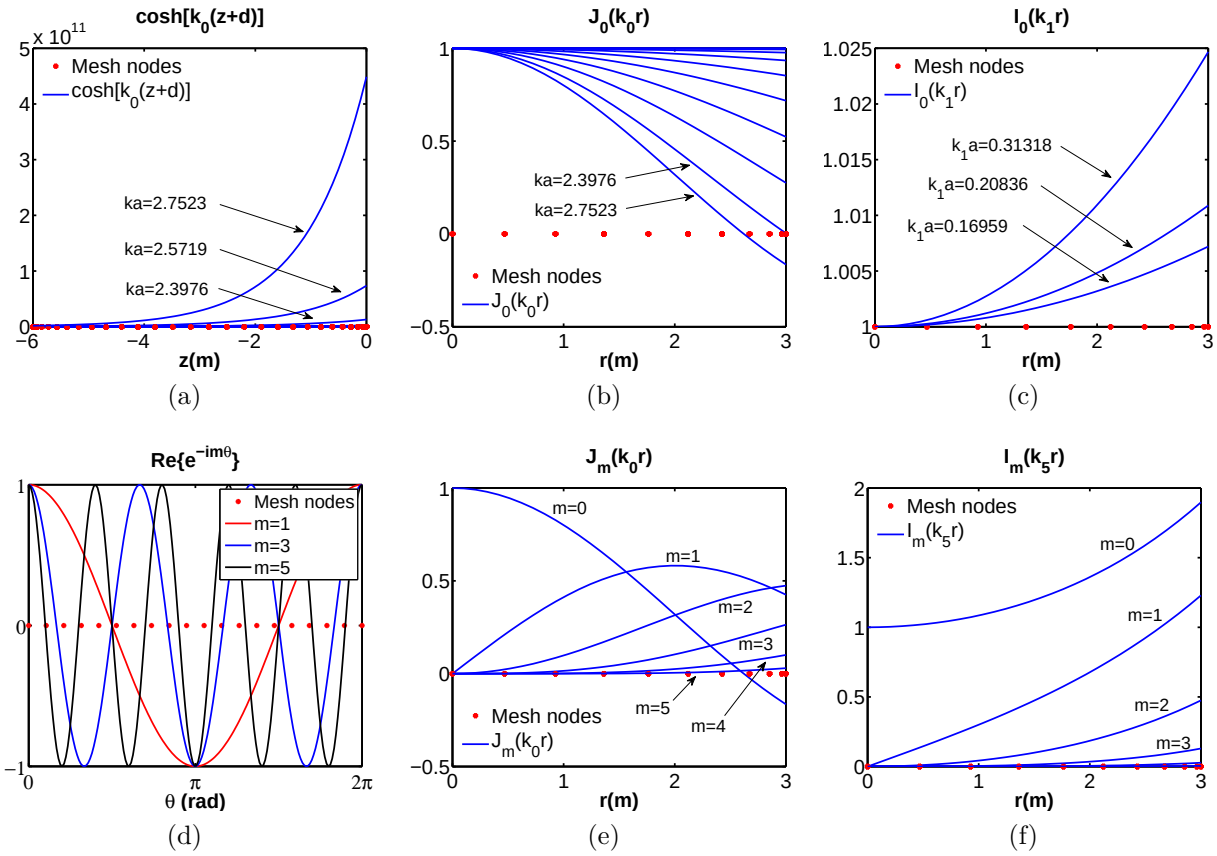

Figure 3.2: Variation of the hyperbolic cosine depth dependence (a), the Bessel function of the first kind (b, e) and the modified Bessel function of the first kind (c, f) along the lateral side and the bottom of a cylinder respectively (3m radius, 6m draft in a 30m water depth). Results in (e) are calculated for $k_0a = 2.7523$ and in (f) for k_5a= 1.7279. Variation of the sinusoindal term $e^{-im\theta}$ along the perimeter of the cylinder (d). Red points represent the nodes of a given mesh

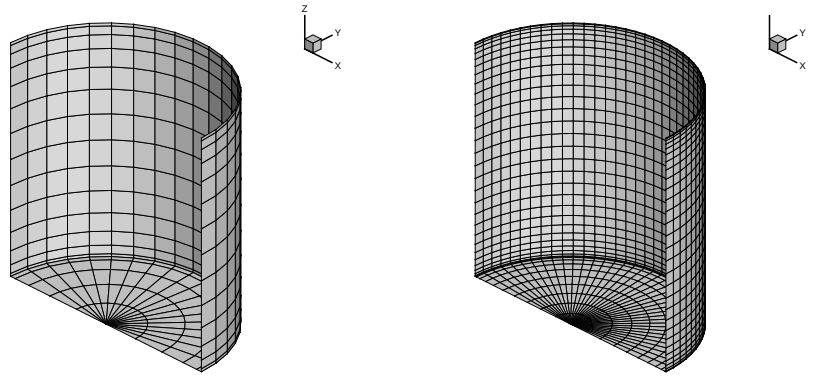

(a) (b)

Figure 3.3: Truncated vertical cylinder mesh. Only half of the geometry is shown due to symmetry. (a) - coarse mesh, 361 panels; (b) - fine mesh 1521 panels.

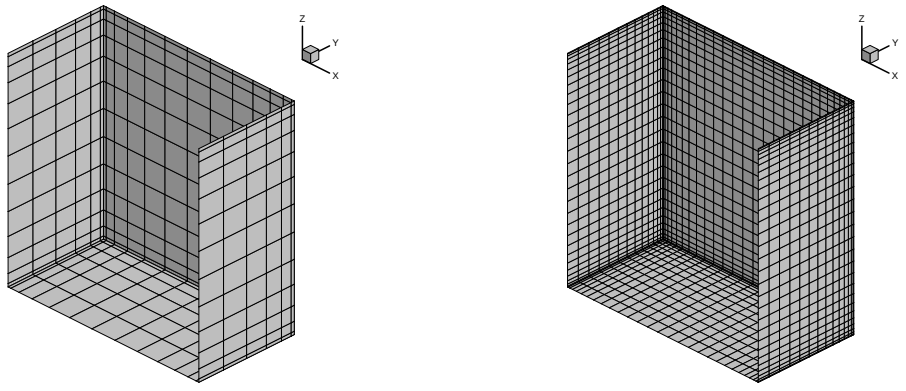

(a) (b)

Figure 3.4: Cube mesh. Only half of the geometry is shown due to symmetry. (a) - coarse mesh, 403 panels; (b) - fine mesh 2059 panels.

3.6.1 Diffraction Transfer Matrix

3.6.1.1 Cylinder

Figures 3.5a and 3.5b show the real and imaginary parts of the cylinder DTM components respectively. For clarity, only progressive terms are shown here. A very good agreement between results obtained using *Method I* (with both one-point and four-point quadrature schemes), *Method II* and the semi-analytical solution by Zeng and Tang (2013) (Appendix D) is found. It can be observed that the only non-zero DTM terms correspond to pairs of equal incident (q) and outgoing (m) angular modes. This is a particular feature of axisymmetric geometries such as the truncated vertical cylinder. In addition, it can be appreciated that the number of significant angular modes is frequency dependent. For instance, a truncation of only two angular modes is sufficient at $ka \sim 1$ but not at $ka \sim 2$ where three angular modes are required.

The numerical singularity observed at a ka of approximately 2.3 corresponds to an irregular frequency, not corrected in the version of NEMOH used.

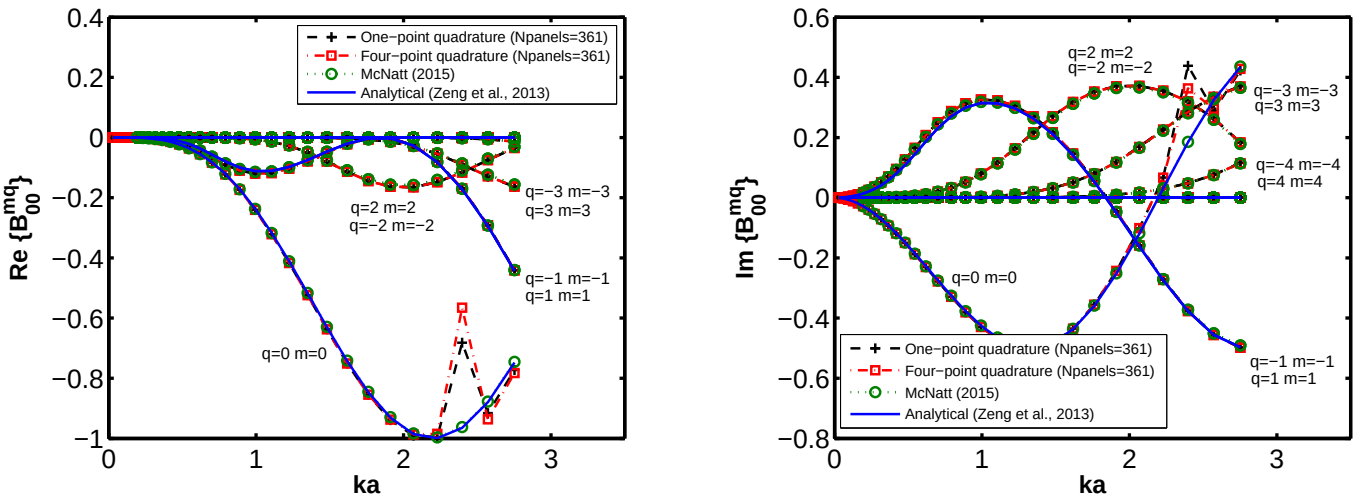

(a) (b)

Figure 3.5: Real and imaginary parts of the Diffraction Transfer Matrix progressive terms for a truncated vertical cylinder of 3m radius (a), 6m draft in a 10m water depth.

3.6.1.2 Cube

Figures 3.6a and 3.6b show the real and imaginary parts of the DTM components respectively. Similar to the truncated vertical cylinder, good agreement between the results obtained using *Method I* and *II* can be observed. For this non-axisymmetric geometry, terms of the DTM involving distinct incident and outgoing angular modes, such as the pair $(q = 1, m = -3)$, are non-zero as expected. In addition, it can be appreciated that for a wide range of ka values the angular mode truncation is higher than for the truncated vertical cylinder. No improvement of results is obtained whether using a one-point or four-point quadrature integration scheme.

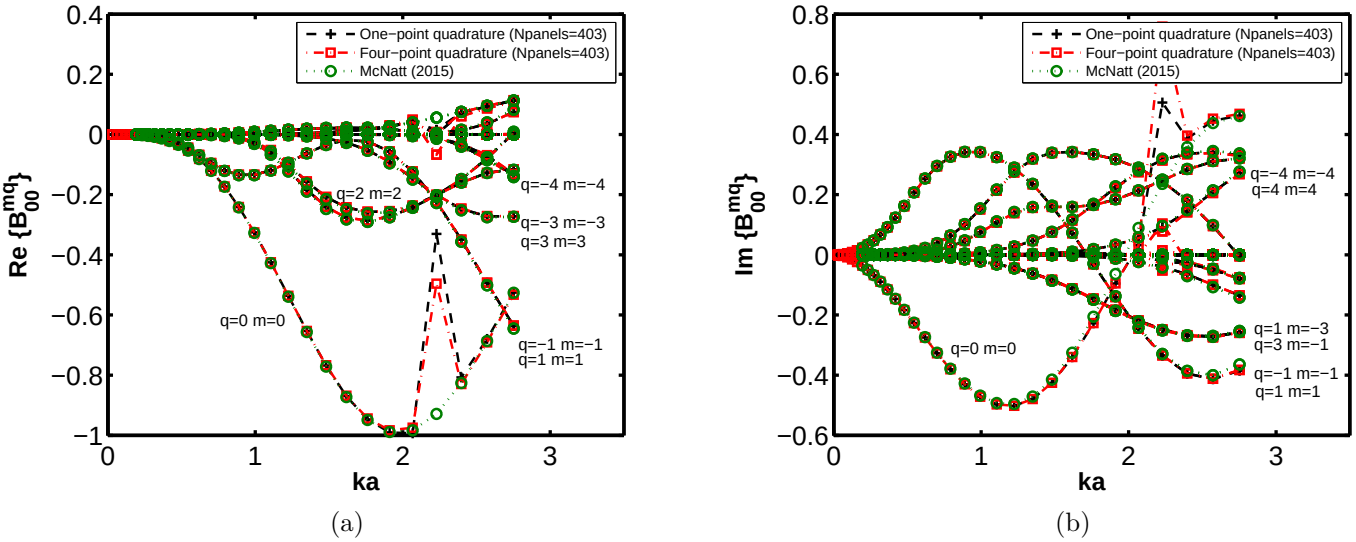

Figure 3.6: Real and imaginary parts of the Diffraction Transfer Matrix progressive terms for a cube of 6m side (2a), 6m draft in a 10m water depth.

3.6.2 Radiation Characteristics

3.6.2.1 Cylinder

The progressive terms of the surge RC of the cylinder are shown in Figure 3.7. Good agreement between both methods and the semi-analytical solution can be observed, as well as no significant differences between integration schemes. For this mode of motion, it can be observed that only modes $m = \pm 1$ are non-zero (see D.1.2). This is

explained as the wave generated by the motion of a cylinder in surge corresponds to the partial wave shown in Figure 2.2b.

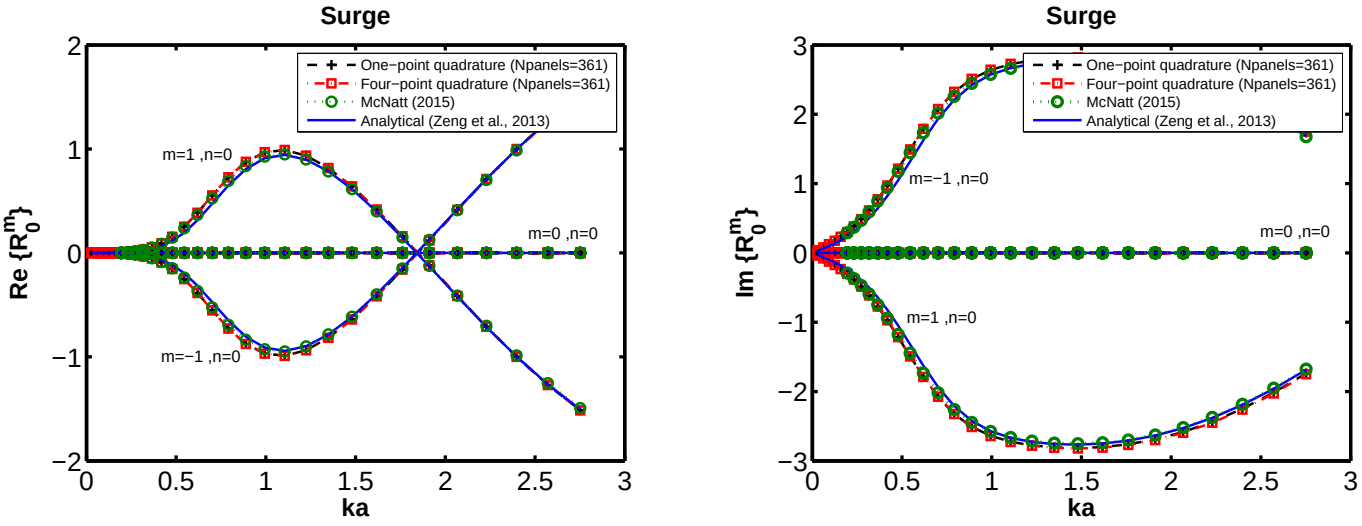

(a) (b)

Figure 3.7: Real and imaginary parts of the Radiation Characteristics progressive terms for a truncated vertical cylinder of 3m radius (a), 6m draft moving in surge in a 10m water depth.

For heave (Figure 3.8), only the mode $m = 0$, representing an isotropic wave (Figure 2.2a) is required (Appendix D). As for the DTM, the numerical singularity observed at a ka of approximately 2.3 corresponds to an irregular frequency.

There is a difference in the magnitude of both the real and the imaginary parts of the $m = 0$ wave between the outputs from *Method I*, *Method II*, and the semi-analytical results. There are several possible explanations for this discrepancy. On the one hand, the inherent differences between BEM and semi-analytical results. In that sense, deviations between hydrodynamic coefficients computed with a semi-analytical formulation and with a BEM code were observed by Chakrabarti (2000). On the other hand, differences between results of the two BEM codes used (NEMOH and WAMIT) as shown for instance by Crooks et al. (2016).

It is noteworthy to mention that the numerical scheme implemented in NEMOH to compute the RC is identical for all degrees of freedom. Thus, as a very good agreement is obtained for all modes but heave, the discrepancies for the latter seem to stem directly from inaccuracies of the source strengths provided by the BEM solver.

In that sense, we note that for this mode of motion the radiated wave is significantly smaller than for other modes (such as surge) as can be directly derived from the magnitude of the RC (the maximum value of its imaginary part is 2.8 for surge as opposite to 0.8 for heave).

One could argue that results are presented for the discretization shown in Figure 3.3a which seems rather coarse, specially at the base of the cylinder responsible for the generation of a velocity potential in heave. However, a mesh sensitivity study has been performed (as detailed in Appendix I) and a good convergence with results computed with a finer mesh has been found.

Finally, it is important to highlight that while it is true that the numerical integration is identical for all modes of motion when using a one-point quadrature scheme, the use of a four-point scheme requires the use of interpolation functions which depend on the geometry of the panel (quadrilateral or triangles). Hence, it is mandatory to distinguish between both panel geometries which are found at the cylinder base and which have an impact mainly on heave. However, as mentioned earlier we found no differences between the numerical integration approaches based on a single and 4 quadrature points. Additional validations for the heave mode of motion have been undertaken and are detailed in Chapter 4.

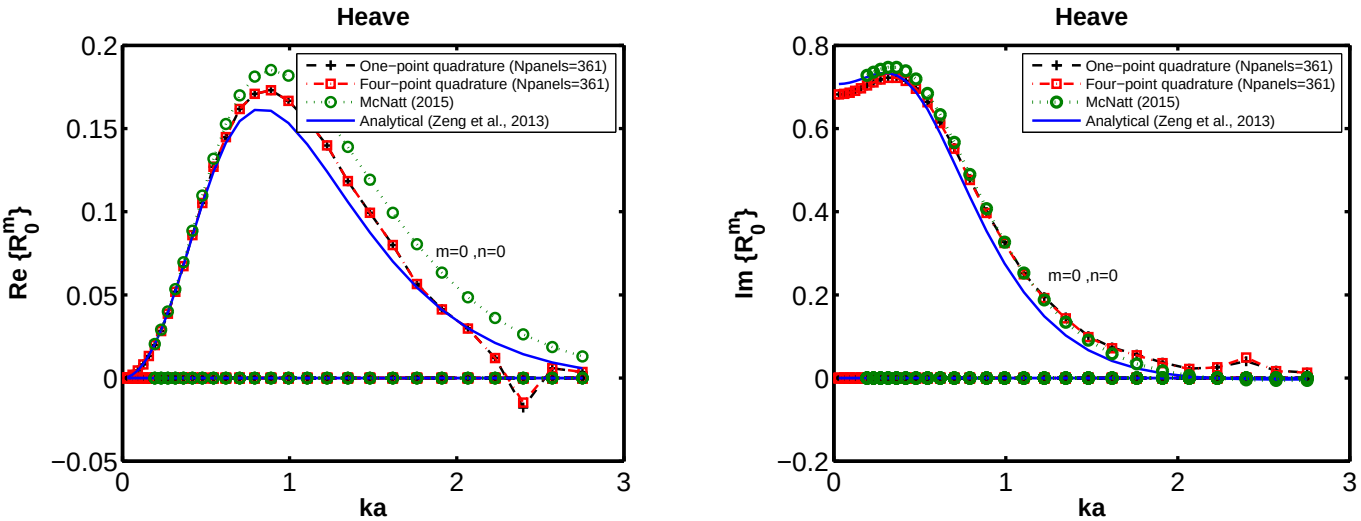

(a) (b)

Figure 3.8: Real and imaginary parts of the Radiation Characteristics progressive terms for a truncated vertical cylinder of 3m radius (a), 6m draft moving in heave in a 10m water depth.

3.6.2.2 Cube

Compared to the cylinder, additional angular modes of order three appear in the RC of the cube moving in surge (Figure 3.9). The radiated field for this geometry and for this mode of motion is more complex than the one generated by the truncated vertical cylinder and a superposition of partial waves is required to represent it. For heave (Figure 3.10), only the isotropic partial wave ($m = 0$) is needed.

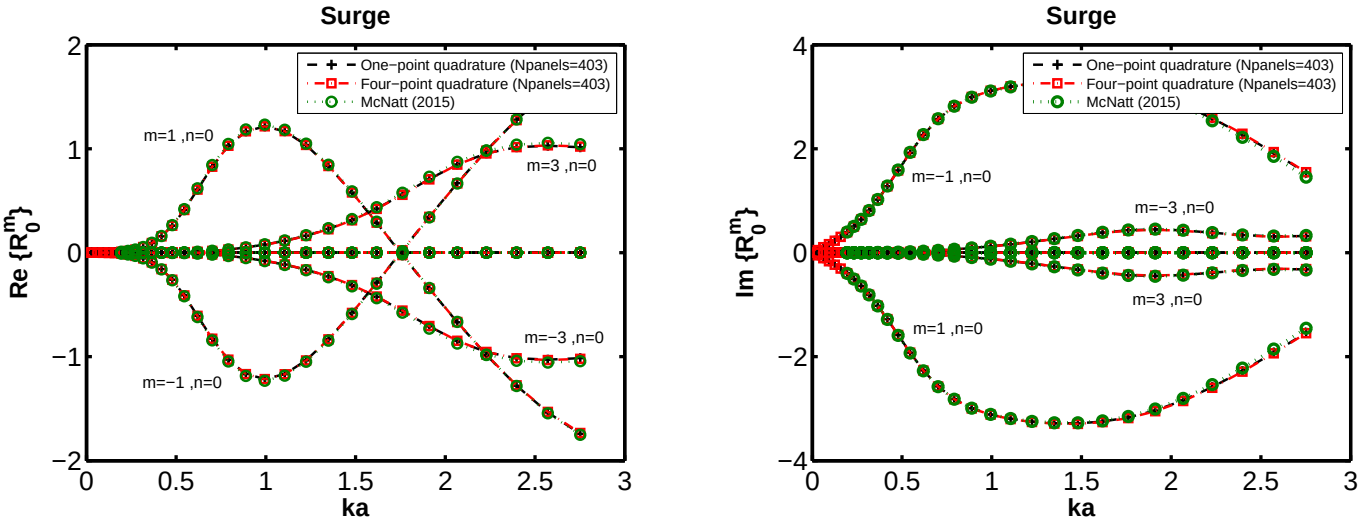

(a) (b)

Figure 3.9: Real and imaginary parts of the Radiation Characteristics progressive terms for a cube of 6m side (2a), 6m draft moving in surge in a 10m water depth.

3.6.3 Force Transfer Matrix

3.6.3.1 Cylinder

Plots of the real and imaginary parts of the FTM progressive terms for surge and heave are shown respectively in Figures 3.11 - 3.12. Good agreement between both methods can be observed, as well as no difference between integration schemes. It can be appreciated that such geometry is only excited by angular modes $q = \pm 1$ in surge and by mode $q = 0$ in heave. Moreover, it is noteworthy that the pattern of the FTM components is very similar to the RC behaviour. In Chapter 4, and by means of the

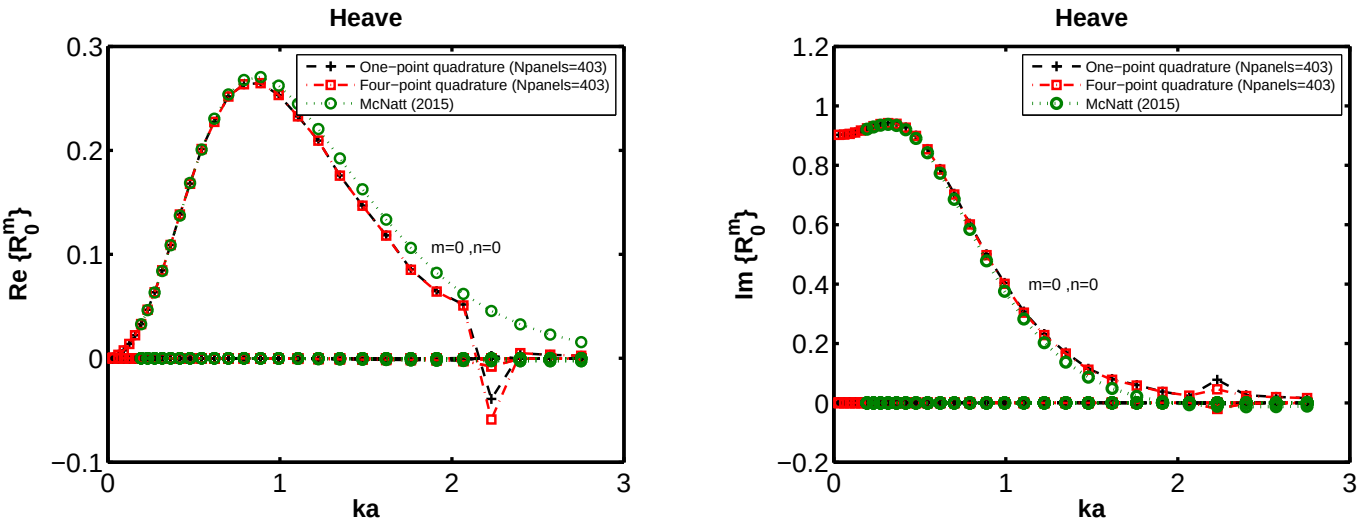

(a) (b)

Figure 3.10: Real and imaginary parts of the Radiation Characteristics progressive terms for a cube of 6m side (2a), 6m draft moving in heave in a 10m water depth.

Haskind's relation (Haskind, 1957), we show that the terms of the FTM and the RC are related by a frequency-dependent constant.

3.6.3.2 Cube

Plots of the real and imaginary parts of the FTM progressive terms for surge, heave and yaw are shown in Figures 3.13-3.15 respectively. Contrarily to the truncated vertical cylinder, the cube is excited by modes $q = \pm 3$ in addition to $q = \pm 1$ for surge. As in this case the geometry is not axisymmetric, the M_z force component is non-zero for relatively high ka values and is excited by mode $q = 4$. As for the cylindrical geometry, a very similar frequency-dependent pattern can be distinguished in both the FTM and the RC.

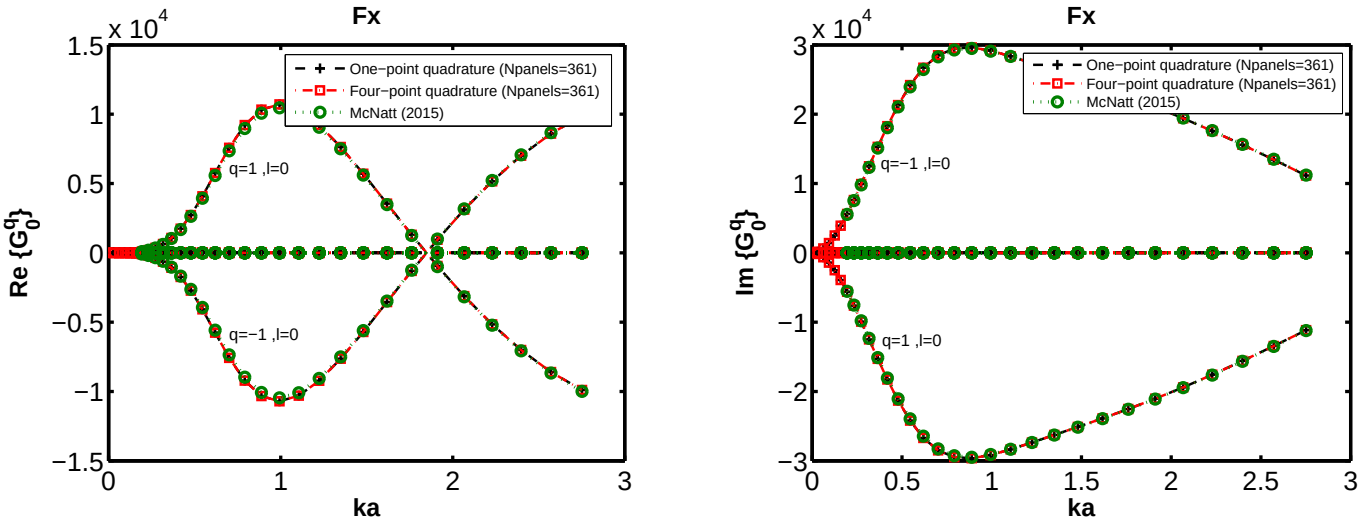

(a) (b)

Figure 3.11: Real and imaginary parts of the Force Transfer Matrix progressive F_x terms for a truncated vertical cylinder of 3m radius (a), 6m draft in a 10m water depth.

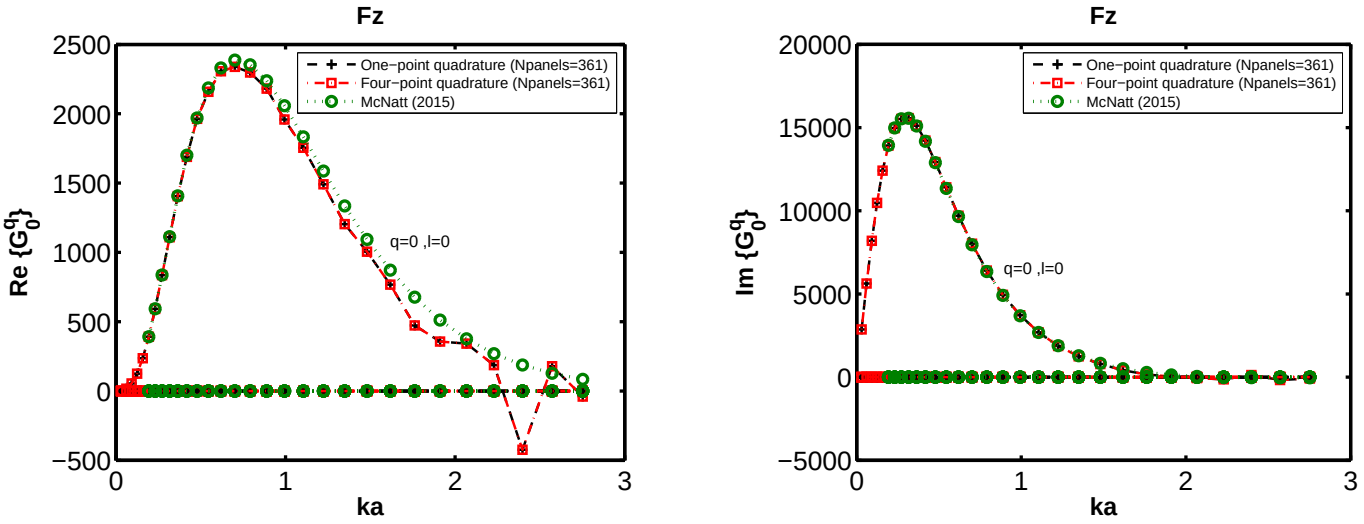

(a) (b)

Figure 3.12: Real and imaginary parts of the Force Transfer Matrix progressive F_z terms for a truncated vertical cylinder of 3m radius (a), 6m draft in a 10m water depth.

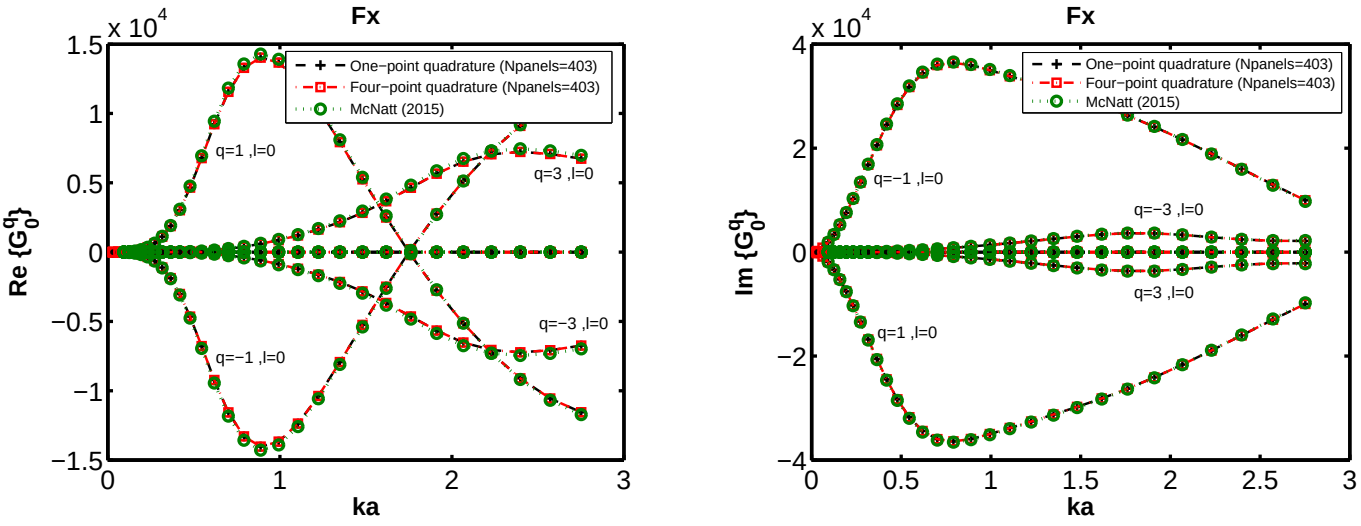

(a) (b)

Figure 3.13: Real and imaginary parts of the Force Transfer Matrix progressive F_x terms for a cube of 6m side (2a), 6m draft in a 10m water depth.

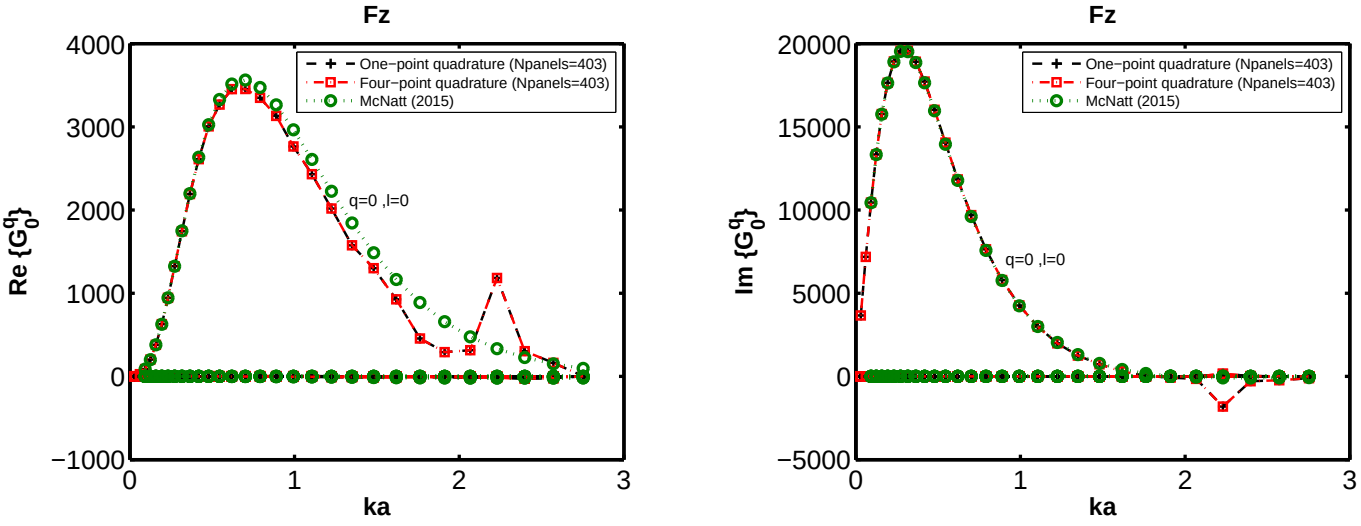

(a) (b)

Figure 3.14: Real and imaginary parts of the Force Transfer Matrix progressive F_z terms for a cube of 6m side (2a), 6m draft in a 10m water depth.

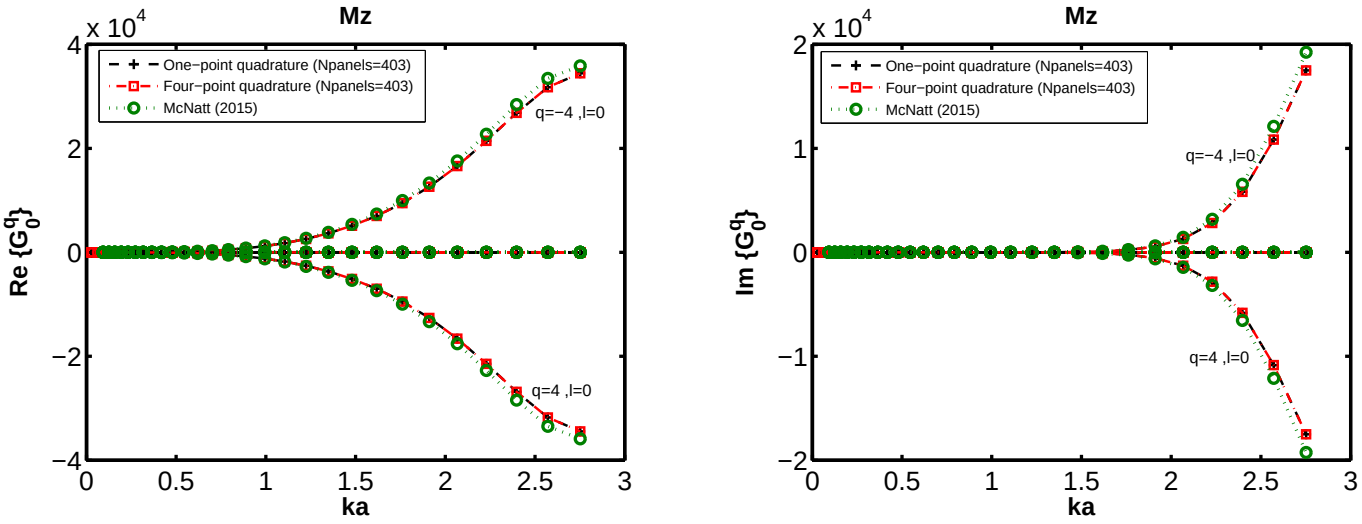

(a) (b)

Figure 3.15: Real and imaginary parts of the Force Transfer Matrix progressive M_z terms for a cube of 6m side (2a), 6m draft in a 10m water depth.

3.7 Conclusions

The calculation of the Diffraction Transfer Matrix and the Radiation Characteristics has been implemented in the open source BEM solver NEMOH using the methodology of Goo and Yoshida (1990). Results of the hydrodynamic operators for an isolated truncated vertical cylinder and a cube computed using two different numerical integration schemes have been contrasted with the methodology developed by McNatt et al. (2015) and a very good agreement has been found. In addition, the DTM and RC of the truncated vertical circular cylinder have been checked against the semi-analytical solution by Zeng and Tang (2013) and a very good match has been obtained.

For a truncated vertical cylinder, only the terms of the DTM corresponding to pairs of equal incident and outgoing angular modes have been observed to be different than zero. In contrast, for the cube, coupling terms between different incident and outgoing angular modes have been found to be significant. In both cases, the truncation of the angular terms has been shown to be frequency-dependent.

In addition, it has been checked that angular modes $m = -1, 0, 1$ are sufficient to represent the radiated waves of a truncated vertical circular cylinder in surge (odd terms) and heave (even term) for all frequencies. At the same time, it has been observed as expected that higher modes are required, particularly at the high frequency zone, to represent the radiated wave in surge by a cube.

Chapter 4

Validation of the Direct Matrix Method implementation

In Chapter 3, two different methodologies to compute the DTM, FTM and RC were presented and compared. It was observed that the frequency-dependent patterns of the RC and the FTM follow the same trends. In the first part of this Chapter, a novel set of relations between the FTM and the RC components is obtained using the Kochin functions specific to the cylindrical basis solutions. They extend the classical Haskind's relations valid with incident plane waves to the cylindrical components of the scattered and radiated fields. Moreover, an alternative demonstration of the identities which does not rely on the far-field asymptotic representation of the potential is given. Additional expressions relating the hydrodynamic coefficients and the RC for isolated bodies as well as for arrays are provided.

The relationships derived in the first part of this Chapter are based on the far-field representation of the potential, i.e. they take into account only the first term of the summation in expressions (2.2.14) and (2.2.20). Because of that, they are used to verify that good accuracy of results obtained from the implementation of the IT is achieved with a finite angular-mode truncation. Details are provided in the first part of this Chapter results section.

The validation effort would be incomplete if the influence of the evanescent modes truncation was not addressed as well, i.e. the second term of the summation in expressions (2.2.14) and (2.2.20). The last part of this Chapter's results section focuses on their effect on the hydrodynamic coefficients and the free surface.

4.1 Isolated body

4.1.1 Haskind's Relation

Haskind's Relation (Haskind, 1957) enables the excitation force to be expressed in terms of radiation parameters. In this section we provide a brief reminder of its derivation, which can be found for instance in Newman (1962).

The excitation force acting on a body with wetted surface S_b (Figure 4.1) can be written as:

$$F_{ex}^k = i\omega\rho \int_{S_b} (\phi^I + \phi^S) n^k dS \tag{4.1.1}$$

where ϕ^I is the incident potential, ϕ^S the scattered and n^k the generalized direction cosine with respect to S_b.

The boundary condition on the radiation potential $\phi^{R,k}$, corresponding to degree of freedom k, is:

$$n^k = \frac{\partial \phi^{R,k}}{\partial n} \tag{4.1.2}$$

where $\phi^{R,k}$ is the radiated potential in the k degree of freedom.

In addition, the radiation boundary condition at infinity on $\phi^{R,k}$ reads:

$$\frac{\partial \phi^{R,k}}{\partial r} = ik_0\phi^{R,k} + O(k_0 r)^{-3/2} \quad k_0 r \to \infty \tag{4.1.3}$$

As both the scattered (ϕ^S) and the radiated (ϕ^R) potentials satisfy both the free surface boundary condition and the Sommerfeld condition at infinity, it follows from Green's theorem that:

$$\int_{S_b} \left(\phi^S \frac{\partial \phi^{R,k}}{\partial n} - \frac{\partial \phi^S}{\partial n} \phi^{R,k} \right) dS = 0 \tag{4.1.4}$$

By substituting (4.1.2) into (4.1.1) and by making use of (4.1.4), we have:

$$F_{ex}^k = i\omega\rho \int_{S_b} \left(\phi^I \frac{\partial \phi^{R,k}}{\partial n} + \phi^{R,k} \frac{\partial \phi^S}{\partial n} \right) dS \tag{4.1.5}$$

Finally, expression (4.1.5) can be rewritten by making use of the diffraction boundary condition on the wetted surface of the body:

$$\frac{\partial \phi^S}{\partial n} = -\frac{\partial \phi^I}{\partial n} \tag{4.1.6}$$

leading to the Haskind relation::

$$F_{ex}^{k} = i\omega\rho \int_{S_b} \left(\phi^{I} \frac{\partial \phi^{R,k}}{\partial n} - \phi^{R,k} \frac{\partial \phi^{I}}{\partial n} \right) dS \tag{4.1.7}$$

even more simply:

$$F_{ex}^{k} = i\omega\rho \int_{S_b} \left(\phi^{I} n^{k} - \phi^{R,k} \frac{\partial \phi^{I}}{\partial n} \right) dS \tag{4.1.8}$$

- a powerful formula that allows evaluation of the excitation force without solving the diffraction problem explicitly.

4.1.2 Relationship between the Force Transfer Matrix and the Radiation Characteristics

The Haskind relation (4.1.7) in section 4.1.1 is used as a starting point for the following derivation. To begin with, the excitation force (F_{ex}^{k}) is expressed using the definition of the Force Transfer Matrix ($\mathbf{G}$) given by McNatt et al. (2015):

$$F_{ex}^{k} = \sum_{m=-\infty}^{\infty} \mathbf{G}_{0m}^{k} a_{0m}^{I} \tag{4.1.9}$$

where $\mathbf{G}_{m}^{k}$ corresponds to the mth element of the kth row of the Force Transfer Matrix and a_{m}^{I} represents the mth term of the ambient incident wave cylindrical coefficients vector given by (2.2.21).

Direct substitution of (4.1.9) into (4.1.7) leads to:

$$\sum_{m=-\infty}^{\infty} \mathbf{G}_{0m}^{k} a_{0m}^{I} = i\omega\rho \int_{S_b} \left(\phi^{I} \frac{\partial \phi^{R,k}}{\partial n} - \phi^{R,k} \frac{\partial \phi^{I}}{\partial n} \right) dS \tag{4.1.10}$$

The expressions of the incident, scattered and radiated potentials using the base of partial cylindrical wave functions are only valid outside the circumscribing cylinder of the body (Ω_{out}). Thus, by means of Green's theorem, we seek to express the surface integral in expression (4.1.10) on a control surface instead of on the body's wetted surface (S_b). Generally, a cylinder of infinite radius is used together with the asymptotic expression of the potential. In this case, we have chosen a cylindrical surface infinitesimally larger than the body's circumscribing cylinder (S_c^{ϵ}) to allow for the use of Green's theorem in the fluid domain (Ω_{int}) limited by S_b, S_c^{ϵ}, the free-surface

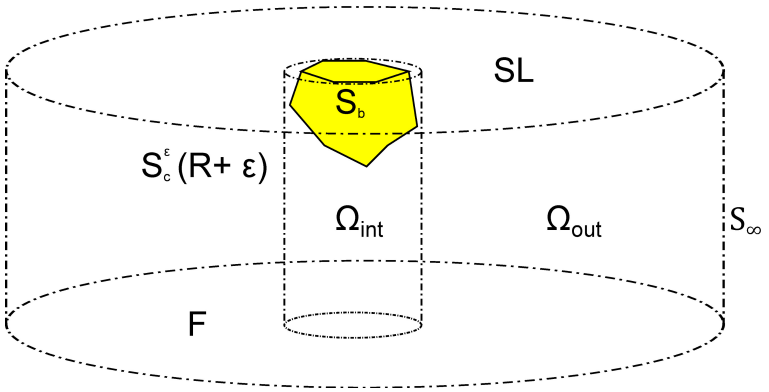

Figure 4.1: Schematic of the domains used for the application of the Green's theorem. Free surface (SL); body's wetted surface (S_b); body's circumscribing cylinder radius (R_c); cylindrical surface infinitesimally larger than the body's circumscribing cylinder (S_c^ϵ), seabed (F); limit of the domain at infinity (S_∞); domain interior to the circumscribing cylinder (Ω_{int}); domain comprised between the circumscribing cylinder and the cylindrical surface at infinity (Ω_{out}).

and the seabed (Figure 4.1):

$$\int_{S_c^\epsilon + S_b} \left(\phi^I \frac{\partial \phi^{R,k}}{\partial n} - \phi^{R,k} \frac{\partial \phi^I}{\partial n} \right) dS = 0 \tag{4.1.11}$$

in which it is implicit that the contribution from the integrals on the free surface and the seabed are zero.

By using (4.1.11), expression (4.1.10) can be written as:

$$\sum_{m=-\infty}^{\infty} \mathbf{G}_{0m}^k a_{0m}^I = -i\rho\omega \int_{S_c^\epsilon} \left(\phi^I \frac{\partial \phi^{R,k}}{\partial n} - \phi^{R,k} \frac{\partial \phi^I}{\partial n} \right) dS \tag{4.1.12}$$

Take now the expression of the incident (2.2.20) and the radiated (2.2.15) potentials, that we shall reformulate for convenience as:

$$\phi^I(r,\theta,z) = \phi_F^I(r,\theta,z) + \phi_N^I(r,\theta,z) = f_0(z)\Lambda^I(r,\,\theta) + \Gamma^I(r,\,\theta,\,z) \tag{4.1.13}$$

$$\phi^{R,k}(r,\theta,z) = \phi_F^{R,k}(r,\theta,z) + \phi_N^{R,k}(r,\theta,z) = f_0(z)\Lambda^{R,k}(r,\,\theta) + \Gamma^{R,k}(r,\,\theta,\,z) \tag{4.1.14}$$

where ϕ^I and $\phi^{R,k}$ are respectively the incident and the radiated potential due to a motion in a degree of freedom k and ϕ_F and ϕ_N are its far-field and near-field contributions respectively with:

$$f_0(z) = \frac{\cosh\, k_0(z+d)}{\cosh\, k_0 d} \tag{4.1.15}$$

$$f_n(z) = \cos\, k_n(z+d) \tag{4.1.16}$$

$$\Lambda^I(r,\,\theta) = \sum_{m=-\infty}^{\infty} (a^I)_{0m}\, J_m(k_0 r)\, e^{im\theta} \tag{4.1.17}$$

$$\Gamma^I(r,\,\theta,\,z) = \sum_{m=-\infty}^{\infty} \sum_{n=1}^{\infty} f_n(z)\, (a^I)_{nm}\, I_m(k_n r)\, e^{im\theta} \tag{4.1.18}$$

$$\Lambda^{R,k}(r,\,\theta) = \sum_{m=-\infty}^{\infty} (R^k)_{0m}\, H_m(k_0 r)\, e^{im\theta} \tag{4.1.19}$$

$$\Gamma^{R,k}(r,\,\theta,\,z) = \sum_{m=-\infty}^{\infty} \sum_{n=1}^{\infty} f_n(z)\, (R^k)_{nm}\, K_m(k_n r)\, e^{im\theta} \tag{4.1.20}$$

Substituting (4.1.13) and (4.1.14) into (4.1.12), and taking into account that ambient incident waves are composed of only progressive terms ($\Gamma^I = 0$), we have:

$$\sum_{m=-\infty}^{\infty} \mathbf{G}^k_{0m} a^I_{0m} = -i\rho\omega \int_{-d}^{0} f_0(z)^2 dz \int_0^{2\pi} \left(\Lambda^I \frac{\partial \Lambda^{R,k}}{\partial n} - \Lambda^{R,k} \frac{\partial \Lambda^I}{\partial n} \right) R^\epsilon\, d\theta - i\rho\omega \int_{-d}^{0} \int_0^{2\pi} \left(f_0(z) \Lambda^I \frac{\partial \Gamma^{R,k}}{\partial n} - \Gamma^{R,k} f_0(z) \frac{\partial \Lambda^I}{\partial n} \right) R^\epsilon\, d\theta dz \tag{4.1.21}$$

where R^ϵ is the radius of a cylindrical surface infinitesimally larger than the body's circumscribing cylinder.

With respect to the first term on the right hand side of (4.1.21), the depth integral is evaluated using:

$$\omega \int_{-d}^{0} f_0(z)^2 dz = \frac{c_g}{k_0} \frac{\omega^2}{g} \tag{4.1.22}$$

where c_g is the group velocity given by:

$$c_g = \frac{1}{2} \frac{\omega}{k_0} \left(1 + \frac{2k_0 h}{\sinh\, 2k_0 h} \right) \tag{4.1.23}$$

For convenience we define the first integral in θ to be I:

$$I = \int_0^{2\pi} \left(\Lambda^I \frac{\partial \Lambda^{R,k}}{\partial n} - \Lambda^{R,k} \frac{\partial \Lambda^I}{\partial n} \right) R\, d\theta \tag{4.1.24}$$

Substituting the definitions of Λ^I and $\Lambda^{R,k}$ into the previous expression:

$$I = \int_0^{2\pi} \left(\sum_{m=-\infty}^{\infty} a_{0m}^I J_m(k_0 r) \sum_{q=-\infty}^{\infty} R_{0q}^k \frac{\partial H_q(k_0 r)}{\partial n} \mid_{r=R^\epsilon} \right) e^{i(m+q)\theta} R^\epsilon d\theta - \int_0^{2\pi} \left(\sum_{m=-\infty}^{\infty} a_{0m}^I \frac{\partial J_m(k_0 r)}{\partial n} \mid_{r=R^\epsilon} \sum_{q=-\infty}^{\infty} R_{0q}^k H_q(k_0 r) \right) e^{i(m+q)\theta} R^\epsilon d\theta \quad (4.1.25)$$

The only non-zero contributions of the terms $e^{i(m+n)\theta}$ to the integral in θ come from the case where $m = -n$ and they are equal to 2π. Thus, (4.1.25) can be rewritten:

$$I = 2\pi R^\epsilon \sum_{m=-\infty}^{\infty} a_{0m}^I R_{0-m}^k \left(J_m(k_0 r) \frac{\partial H_{-m}(k_0 r)}{\partial n} - \frac{\partial J_m(k_0 r)}{\partial n} H_{-m}(k_0 r) \right) \quad (4.1.26)$$

The expression in parentheses in (4.1.26) can be rewritten using the following identities for Bessel and Hankel functions (Abramowitz and Segun A., 1964):

$$J_m = \frac{1}{2}(H_m^{(1)} + H_m^{(2)}) \quad (4.1.27)$$

$$H_{-m}^{(1)} = (-1)^m H_m^{(1)} \quad (4.1.28)$$

leading to:

$$I = 2\pi R^\epsilon \sum_{m=-\infty}^{\infty} a_{0m}^I R_{0-m}^k \frac{1}{2}(-1)^m \left(H_m^{(2)}(k_0 r) \frac{\partial H_m^{(1)}(k_0 r)}{\partial r} \mid_{r=R^\epsilon} - \frac{\partial H_m^{(2)}(k_0 r)}{\partial r} \mid_{r=R^\epsilon} H_m^{(1)}(k_0 r) \right) \quad (4.1.29)$$

The term in brackets can now be related to the Wronskian of $H_m^{(1)}$ and $H_m^{(2)}$ (Abramowitz and Segun A., 1964):

$$-W(H_m^{(1)}, H_m^{(2)}) = H_m^{(2)}(k_0 r) \frac{\partial H_m^{(1)}(k_0 r)}{\partial r} \mid_{r=R^\epsilon} - \frac{\partial H_m^{(2)}(k_0 r)}{\partial r} \mid_{r=R^\epsilon} H_m^{(1)}(k_0 r) = -\frac{4i}{\pi R^\epsilon} \quad (4.1.30)$$

Substituting (4.1.30) into (4.1.29):

$$I = 4i \sum_{m=-\infty}^{\infty} (-1)^m a_{0m}^I R_{0-m}^k \quad (4.1.31)$$

Let us now evaluate the second term of the summation on the right hand side of equation (4.1.21). We define the first and second terms of the integral in θz to be:

$$I_2 = \int_{-d}^{0}\int_{0}^{2\pi} f_0(z)\Lambda^I \frac{\partial \Gamma^{R,k}}{\partial r}\, R^\epsilon d\theta dz \tag{4.1.32}$$

$$I_3 = \int_{-d}^{0}\int_{0}^{2\pi} f_0(z)\Gamma^{R,k} \frac{\partial \Lambda^I}{\partial r}\, R^\epsilon d\theta dz \tag{4.1.33}$$

Considering I_2 first, we substitute the definitions of Λ^I and $\Gamma^{R,k}$ given by (4.1.17) and (4.1.20) respectively to obtain:

$$I_2 = \int_{-d}^{0}\int_{0}^{2\pi} \Big(\sum_{m=-\infty}^{\infty} f_0(z)\, a^I{}_{0m}\, J_m(k_0 r)\, |_{r=R^\epsilon} \times \sum_{q=-\infty}^{\infty}\sum_{n=1}^{\infty} f_n(z)(R^k)_{nq} \frac{\partial K_q(k_n r)}{\partial r}\, |_{r=R^\epsilon} \Big) e^{i(m+q)\theta}\, R^\epsilon d\theta dz \tag{4.1.34}$$

The only non-zero contributions of the terms $e^{i(m+q)\theta}$ to the integral in θ arise where $m = -q$ and they are equal to 2π. Thus, (4.1.34) reads:

$$I_2 \;=\; 2\pi R^\epsilon \sum_{m=-\infty}^{\infty}\sum_{n=1}^{\infty} a^I{}_{0m}\,(R^k)_{n,-m} J_m(k_0 r) \frac{\partial K_{-m}(k_n r)}{\partial r} \;\; |_{r=R^\epsilon} \;\; \int_{-d}^{0} f_0(z)\sigma_n(z) dz \tag{4.1.35}$$

By means of the orthogonality properties of the depth functions:

$$\int_{-d}^{0} \cosh\, k_0(d+z) \cos\, k_n(d+z)\, dz = 0 \tag{4.1.36}$$

the depth integral in (4.1.35) vanishes. An analogous derivation for I_3 finally leads to:

$$I_2 = I_3 = 0 \tag{4.1.37}$$

This shows that the second term of the summation on the right hand side of equation (4.1.21), i.e. the near-field contribution of the radiated potential, has no effect on the excitation force.

Finally, (4.1.12) becomes:

$$\sum_{m=-\infty}^{\infty} \mathbf{G}_{0m}^{k} a_{0m}^{I} = 4\frac{\rho c_g \omega^2}{g k_0} \sum_{m=-\infty}^{\infty} (-1)^m R_{0-m}^{k} a_{0m}^{I} \tag{4.1.38}$$

This relation between the FTM and the RC expresses the original Haskind relation in the framework of cylindrical wave fields theory. Furthermore, as each partial wave is an eigenfunction of an orthogonal set, the identity (4.1.38) holds element-wise and reads:

$$\mathbf{G}_{m}^{k} = 4\frac{\rho c_g \omega^2}{g k_0} (-1)^m R_{-m}^{k} \tag{4.1.39}$$

In (4.1.39), the subindex n referring to evanescent terms has been omitted to simplify notation. Hereafter, a single subindex will indicate that only the far-field contribution to the potential is considered.

In the derivation above, the integration surface was chosen to be the circumscribing cylinder to the body. However, it was observed that the radius of the cylindrical control surface ultimately cancels out when the integral is evaluated. Thus, it would have been equivalent to consider a cylinder at infinity and retain only the leading terms of the asymptotic expression of the potential.

The expression of the excitation force in terms of the far-field radiation potential is a classical result of hydrodynamics, which can be found for instance in expression (8.6.41) in C.Mei et al. (2005) (or 5.147 in Falnes (2002)):

$$F_{ex}^{k} = -\frac{4}{k_0} \rho g A \mathcal{A}^{k}(\theta_I + \pi) c_g \tag{4.1.40}$$

where F_{ex}^{k} is the excitation force and $\mathcal{A}^{k}(\theta)$, generally known as the Kochin function, corresponds to the angular variation of the radially spreading wave in the far-field representation of the potential. At leading order of the asymptotic expansion for large r, the potential may be expressed as:

$$\phi \sim -\frac{ig}{\omega} \frac{\cosh k_0(z+h)}{\cosh k_0 h} \mathcal{A}(\theta) \left(\frac{2}{\pi k_0 r}\right)^{\frac{1}{2}} e^{ik_0 r - i\pi/4} \tag{4.1.41}$$

Expression (4.1.40) could have been used as well to obtain (4.1.38) taking into account that the Kochin function can be directly related to the asymptotic form of the cylindrical solution:

$$\mathcal{A}^{k}(\theta) = \sum_{m=-\infty}^{\infty} (-i)^m \frac{i\omega}{g} R_{m}^{k} e^{im\theta} \tag{4.1.42}$$

Equation (4.1.42) has been adapted to the notation and the far-field potential representation of C.Mei et al. (2005), and differs slightly from that given by McNatt et al. (2013). Substituting (4.1.42) into (4.1.40) returns the same expression as in (4.1.38).

The author would like to note that the contents of this Chapter have been published in the journal paper Fàbregas Flavià and Clément (2017).

4.1.3 Radiation Damping Coefficients in terms of the far-field radiation potential

By applying Green's theorem to two radiation potentials, the radiation damping coefficients may be expressed in terms of the far-field radiation potential. This is a classic result of hydrodynamics, whose derivation is briefly reviewed in this section and can be found for instance in Falnes (2002).

We consider the two radiation potentials $\phi^{R,p}$ and $(\phi^{R,k})^*$. By application of Green's theorem in the domain $\Omega_{int}\,\mathrm{U}\,\Omega_{out}$:

$$\int_{S_b}\left(\phi^{R,p}n_k - (\phi^{R,k})^* n_p\right) dS = -\int_{S_\infty}\left(\phi^{R,p}\frac{\partial(\phi^{R,k})^*}{\partial n} - (\phi^{R,k})^*\frac{\partial\phi^{R,p}}{\partial n}\right) dS \tag{4.1.43}$$

where the super-index * represents the complex conjugate.

Now, if we apply Green's theorem again to the same domain and to the same radiation potentials (now without taking the complex conjugate of $\phi^{R,k}$) we can deduce that:

$$\int_{S_b}\phi^{R,p}\,n_k dS = \int_{S_b}\phi^{R,k}\,n_p dS \tag{4.1.44}$$

Thus:

$$\int_{S_b}(\phi^{R,p})^*\,n_k dS = \int_{S_b}(\phi^{R,k})^*\,n_p dS \tag{4.1.45}$$

By substituting (4.1.45) into (4.1.43) we obtain:

$$\mathbf{D}^{pk} = -\frac{\rho\omega}{2i}\int_{S_\infty}\left(\phi^{R,p}\frac{\partial(\phi^{R,k})^*}{\partial n} - (\phi^{R,k})^*\frac{\partial\phi^{R,p}}{\partial n}\right) dS \tag{4.1.46}$$

where $\mathbf{D}^{pk}$ represents the element p,k in the radiation damping coefficient matrix, with p the direction of the force and k the degree of freedom.

Expression (4.1.46) can be simplified using (4.1.3):

$$\mathbf{D}^{pk} = \rho\omega k\int_{S_\infty}\phi^{R,p}\left(\phi^{R,k}\right)^* dS \tag{4.1.47}$$

from which the symmetry of $\mathbf{D}^{pk}$ and the positivity of $\mathbf{D}^{pp}$ are easily deduced.

4.1.4 Relationship between the Force Transfer Matrix and the Damping coefficients

Now(4.1.47) can be used to derive a relationship between the diagonal terms of the radiation damping coefficients matrix and the FTM.

By using the definition of the radiated potential in cylindrical coordinates, equation (4.1.47) can be expressed as:

$$\mathbf{D}^{pk} = \rho\omega k_0 \int_{-d}^{0} f_0(z)^2 dz \cdot \int_0^{2\pi} \left(\sum_{m=-\infty}^{\infty} R_m^p H_m^{(1)}(k_0 R_\infty) \sum_{n=-\infty}^{\infty} \left(R_n^k\right)^* H_n^{(2)}(k_0 R_\infty) \right) e^{i(m-n)\theta} R_\infty d\theta \quad (4.1.48)$$

where R_∞ represents the radius of a cylindrical control surface at infinity.

The only non-zero contributions of the terms $e^{i(m-n)\theta}$ to the integral in θ occur where $m = n$ and they are equal to 2π. Thus, the previous expression can be written as:

$$\mathbf{D}^{pk} = 2\pi R_\infty \rho c_g \frac{\omega^2}{g} \sum_{m=-\infty}^{\infty} R_m^p \left(R_m^k\right)^* H_m^{(1)}(k_0 R_\infty) H_m^{(2)}(k_0 R_\infty) \quad (4.1.49)$$

where the depth integral has been evaluated using (4.1.22).

The product of Hankel functions of the first and the second kind can be rewritten using their definition in terms of the Bessel functions of the first and the second kind:

$$H_m^{(1)} H_m^{(2)} = (J_m + iY_m)(J_m - iY_m) = J_m^2 + Y_m^2 \quad (4.1.50)$$

where the argument of the functions has been omitted for simplicity.

The asymptotic forms ($z \to \infty$) of the Bessel functions of the first and the second kind are (Abramowitz and Segun A., 1964):

$$J_m(z) = \sqrt{\frac{2}{\pi z}} \cos(z - \frac{1}{2}m\pi - \frac{1}{4}\pi) + \mathbf{O}(|z|^{-1}) \quad (4.1.51)$$

$$Y_m(z) = \sqrt{\frac{2}{\pi z}} \sin(z - \frac{1}{2}m\pi - \frac{1}{4}\pi) + \mathbf{O}(|z|^{-1}) \quad (4.1.52)$$

Thus:

$$J_m^2(z) + Y_m^2(z) = \left(\sqrt{\frac{2}{\pi z}}\right)^2 (\cos^2(z - \frac{1}{2}m\pi - \frac{1}{4}\pi) + \sin^2(z - \frac{1}{2}m\pi - \frac{1}{4}\pi)) = \frac{2}{\pi z} \quad (4.1.53)$$

where the higher order terms of the asymptotic form have been neglected.

By using (4.1.53), expression (4.1.49) becomes:

$$\mathbf{D}^{pk} = 4\rho c_g \frac{\omega^2}{k_0 g} \sum_{m=-\infty}^{\infty} (R_m^p) \left(R_m^k\right)^* \quad (4.1.54)$$

For the diagonal terms of the damping matrix, i.e. $p = k$, using the fact that the product of a complex number and its conjugate is $z\bar{z} = |z|^2$ we have:

$$\mathbf{D}^{kk} = 4\rho c_g \frac{\omega^2}{k_0 g} \sum_{m=-\infty}^{\infty} |R_m^k|^2 \quad (4.1.55)$$

where we note that the term $4\rho c_g \frac{\omega^2}{k_0 g}$ is exactly the same as in (4.1.39).

An equivalent form for expression (4.1.54) can be derived from equation 8.6.13 in C.Mei et al. (2005), which relates the damping coefficients with the Kochin function:

$$\mathbf{D}^{pk} = \frac{2}{\pi k_0} \rho g c_g \int_0^{2\pi} \mathcal{A}_p(\theta) \mathcal{A}_k^*(\theta) d\theta \quad (4.1.56)$$

where $\mathcal{A}(\theta)$ is as defined in (4.1.42).

The result in (4.1.55) gives a relationship between the diagonal terms of the radiation damping coefficients matrix and the RC. Commonly this relationship is expressed in terms of the excitation forces as (Newman, 1977, eq(173) p.304):

$$\mathbf{D}^{kk} = \frac{k}{8\pi \rho g c_g} \int_0^{2\pi} |F_{ex}^k(\theta)|^2 d\theta \quad (4.1.57)$$

where $F_{ex}^k(\theta)$ is the excitation force on the fixed body due to an incident wave propagating at an angle $\pi + \theta$ to the positive x-axis.

A similar expression can be obtained by using (4.1.39), which relates the elements of the FTM and the RC, and substituting it into (4.1.55), leading to:

$$\mathbf{D}^{kk} = \frac{g k_0}{4\rho c_g \omega^2} \sum_{m=-\infty}^{\infty} |\mathbf{G}_m^k|^2 \quad (4.1.58)$$

From expression (4.1.55) it can be directly inferred that there exist a finite number of non-zero partial wave coefficients or, in other words, that their magnitude tends to zero when the angular-mode truncation is increased.

4.2 Array

4.2.1 Generalisation of Haskind's relation for an array of bodies

Expression (4.1.7) can be generalized to an array composed of N_b bodies by following a similar derivation to that shown in section 4.1.1 (see for instance Falnes (1980)). In this case, the radiation boundary condition (4.1.2) is expressed as:

$$\frac{\partial \Phi_i^{R,k_i}}{\partial n} = \begin{cases} n^{k_i} & \text{on} \quad S_i \\ 0 & \text{on} \quad S_j \, (j \neq i) \end{cases} \tag{4.2.1}$$

where Φ_i^{R,k_i} is the potential of a wave radiated by body i in a mode of motion k_i and scattered by all the neighbouring bodies j, and n^{k_i} the boundary condition on the radiation potential Φ_i^{R,k_i} .

Then, the excitation force acting on a body i of an array composed of N_b bodies can be written in terms of only the ambient and radiation potentials:

$$F_{ex,i}^{k_i} = i\rho\omega \int_S \left(\phi^I \frac{\partial \Phi_i^{R,k_i}}{\partial n} - \Phi_i^{R,k_i} \frac{\partial \phi^I}{\partial n} \right) dS \tag{4.2.2}$$

where ϕ^I represents the ambient incident potential and $S = \bigcup S_i$

By applying Green's theorem to a domain limited by surface S and a control surface at infinity (S_∞), the excitation force can be evaluated using only the far field potentials as:

$$F_{ex,i}^{k_i} = -i\rho\omega \int_{S_\infty} \left(\phi^I \frac{\partial \Phi_i^{R,k_i}}{\partial n} - \Phi_i^{R,k_i} \frac{\partial \phi^I}{\partial n} \right) dS \tag{4.2.3}$$

4.2.2 Relationship between the Excitation Force and the Radiation Characteristics

The representation of the incident and radiated potentials in expression (4.2.3) relating the excitation force with the far-field potentials follows as:

$$\phi_i^I(r_i,\theta_i,z) = f_0(z)\,\Lambda^I(r,\theta); \quad \phi_i^{R,k}(r_i,\theta_i,z) = f_0(z)\,\Lambda^{R,k}(r,\theta) \tag{4.2.4}$$

However, as the body is no longer in isolation, the radiated potential of a body i moving in mode of motion k_i will be written as a sum of two contributions:

$$\Phi_i^{R,k_i} = \phi_i^{R,k_i} + \sum_{j=1}^{N_b} \phi_j^{S,k_i} \tag{4.2.5}$$

where Φ_i^{R,k_i} is the total radiated potential, ϕ_i^{R,k_i} is the radiated potential by body i in motion mode k_i as if it was isolated and ϕ_j^{S,k_i} is the potential scattered by a body j in the array due to the wave radiated by body i moving in mode of motion k_i.

Using (4.2.4), together with the fact that the scattered potential can be expressed in terms of the same partial cylindrical wave functions as the radiated potential, we obtain:

$$\phi_i^{R,k_i}(r_i,\theta_i,z_i) = f_0(z) \sum_{m=-\infty}^{\infty} (R_i^{k_i})_m\, H_m(k_0 r_i)\, e^{im\theta_i} \tag{4.2.6}$$

$$\phi_j^{S,k_i}(r_j,\theta_j,z_j) = f_0(z) \sum_{m=-\infty}^{\infty} (A_j^{k_i})_m\, H_m(k_0 r_j)\, e^{im\theta_j} \tag{4.2.7}$$

where $A_j^{k_i}$ represent the cylindrical coefficients of the scattered potential by body j due to the motion of body i in motion mode k_i.

As the potentials are expressed with respect to the local cylindrical reference system centered at each body, we must apply a coordinate transformation to express all potentials with respect to the local reference system of body i. To express the far-field coefficients from different sources with respect to a common origin, Falnes (2002) uses the asymptotic approximations for the relationship between local and global coordinates. In this case, we make use of the multipole expansion matrix $\mathbf{M}_{ij}$ from Graf's addition theorem, which expresses the scattered potential of body i around the origin of the jth coordinate system (Kashiwagi, 2000):

$$\Upsilon_i^S(r_i,\theta_i,z_i) = \mathbf{M}_{ij}\,\Upsilon_j^S(r_j,\theta_j,z_j) \tag{4.2.8}$$

where $\Upsilon^S = H_m(k_0 r)\, e^{im\theta}$ and the progressive terms of the multipole expansion matrix are given by:

$$(\mathbf{M}_{ij})^{mq}_{nn} = J_{m-q}(k_0 L_{ij})\, e^{i(m-q)\alpha_{ij}}; \quad n = 0 \tag{4.2.9}$$

where L_{ij} is the separating distance between bodies i and j, α_{ij} the angle at body i between the positive x-direction and the line joining the center of i to that of j in an anti-clockwise direction (Figure (2.4)), indices m, q the angular-mode, and n the depth-mode.

By applying (4.2.8) and using (4.2.6) and (4.2.7), equation (4.2.5) can be expressed as:

$$\Phi_i^{R,k_i}(r_i, \theta_i, z_i) = f_0(z) \sum_{m=-\infty}^{\infty} (\mathcal{R}_i^{k_i})_m H_m(k_0 r_i) e^{im\theta_i} \tag{4.2.10}$$

where $\mathcal{R}_i^{k_i}$ is the vector of cylindrical coefficients expressing the radiated wave by body i in a motion mode k and including all the scattered waves by all the bodies in the array:

$$(\mathcal{R}_i^{k_i})_m = \left(R_i^{k_i} + \sum_{j=1}^{N_b} [\mathbf{M}_{ji}]^T A_j^{k_i} \right)_m \tag{4.2.11}$$

Finally, expression (4.2.3) can be evaluated in the same manner as (4.1.12), leading to:

$$F_{ex,i}^{k_i} = 4 \frac{\rho c_g \omega^2}{g k_0} \sum_{m=-\infty}^{\infty} (-1)^m a_m^{I,i} \, (\mathcal{R}_i^{k_i})_{-m} \tag{4.2.12}$$

By separating the contributions from vector (4.2.11), the excitation force acting on body i in direction k_i can also be expressed as:

$$F_{ex,i}^{k_i} = \sum_{m=-\infty}^{\infty} \left(\mathbf{G}_m^{k_i} + \tilde{\mathbf{G}}_m^{k_i} \right) a_m^{I,i} \tag{4.2.13}$$

where $\tilde{\mathbf{G}}_m^{k_i}$ is defined as:

$$\tilde{\mathbf{G}}_m^{k_i} = 4 \frac{\rho c_g \omega^2}{g k_0} (-1)^m \left(\sum_{j=1}^{N_b} [\mathbf{M}_{ji}]^T A_j^{k_i} \right)_m \tag{4.2.14}$$

In (4.2.13) we have separated the contributions to the excitation force from the body itself, as if it was isolated (first term of the summation), and from the hydrodynamic interactions with the rest of bodies in the array (second term).

Equation (4.2.12) could also have been derived, for instance, from expression 5.203 in Falnes (2002), which is a generalization of (4.1.40) for an array of bodies and relates

the excitation force on a body to the radiation far-field expressed at a global origin, by substituting in it the expression of the Kochin function defined in (4.1.42). In this case, the RC of the isolated body should be replaced by the vector of cylindrical coefficients expressing the radiated wave by a body in the array, including all the scattered waves by the neighbours, as in (4.2.11).

4.2.3 Relationship between the Damping coefficients and the Radiation Potential

Similarly to the result presented in section 4.1.3, the radiation damping of a body in the array can be expressed in terms of the far-field radiation potential. Using this generalization, the damping force on oscillator i in a direction k_i due to a unit velocity motion of body j moving in a mode of motion k_j can be expressed as (Falnes, 1980):

$$\mathbf{D}_{ij}^{p_i,k_j} = \rho\omega k_0 \int_{S_\infty} \Phi_j^{R,k_j} \left(\Phi_i^{R,p_i}\right)^* dS \tag{4.2.15}$$

where $\mathbf{D}_{ij}^{p_i,k_j}$ is the radiation damping force on body i in a degree of freedom p_i due to a unitary velocity of body j in a degree of freedom k_j and Φ_j^{R,k_j} and Φ_i^{R,p_i} are respectively the radiated potentials from body j in a mode of motion k_j and body i in a mode of motion p_i and scattered by the rest of the bodies in the array.

As in section 4.2.2, we express both potentials in the reference system local to body i of the array, and thus:

$$\Phi_i^{R,p_i}(r_i,\theta_i,z_i) = f_0(z) \sum_{m=-\infty}^{\infty} \left(\mathcal{R}_i^{p_i}\right)_m H_m(k_0 r_i)\, e^{im\theta_i} \tag{4.2.16}$$

$$\Phi_j^{R,k_j}(r_i,\theta_i,z_i) = f_0(z) \sum_{m=-\infty}^{\infty} \left(\mathcal{R}_j^{k_j}\right)_m H_m(k_0 r_i)\, e^{im\theta_i} \tag{4.2.17}$$

where $\mathcal{R}_i^{p_i}$ and $\mathcal{R}_j^{k_j}$ are:

$$\mathcal{R}_i^{p_i} = R_i^{p_i} + \sum_{j=1}^{N_b} [\mathbf{M}_{ji}]^T A_j^{p_i} \tag{4.2.18}$$

$$\mathcal{R}_j^{k_j} = [\mathbf{M}_{ji}]^T R_j^{k_j} + \sum_{j=1}^{N_b} [\mathbf{M}_{ji}]^T A_j^{k_j} \tag{4.2.19}$$

(4.2.15) can then be evaluated in a similar manner to (4.1.47), leading to:

$$\mathbf{D}_{ij}^{p_i,k_j} = 4\frac{\rho c_g \omega^2}{g k_0} \sum_{m=-\infty}^{\infty} \left(\mathcal{R}_j^{k_j}\right)_m (\mathcal{R}_i^{p_i})_m^* \tag{4.2.20}$$

If we set $i = j$ and $p = k$, by separating the contributions from vectors (4.2.16) and (4.2.17), expression (4.2.20) can be rewritten as:

$$\mathbf{D}_{ii}^{k_i,k_i} = \frac{g k_0}{4\rho c_g \omega^2} \sum_{m=-\infty}^{\infty} |\mathbf{G}_m^{k_i}|^2 + \frac{g k_0}{4\rho c_g \omega^2} \sum_{m=-\infty}^{\infty} \left(\mathbf{G}_{-m}^{k_i} (\tilde{\mathbf{G}}_m^{k_i})^* + (\mathbf{G}_{-m}^{k_i})^* \tilde{\mathbf{G}}_m^{k_i} + |\tilde{\mathbf{G}}_m^{k_i}|^2 \right) \tag{4.2.21}$$

where the first term of the summation corresponds to the term of the damping coefficient matrix $\mathbf{D}^{k,k}$ of the body in isolation (4.1.54), and the remaining terms correspond to the contribution from the multiple-scattering from the rest of bodies in the array.

Expression (4.2.20) can also be obtained, for instance, from equation 5.182 in Falnes (2002), using the expression for the Kochin function defined in (4.1.42), in which the RC of the isolated body is replaced by the vector of cylindrical coefficients that expresses the radiated wave by a body in the array including all the scattered waves by the neighbours, as in (4.2.11).

4.3 Results and Discussion

In the first part of this section, entitled *Progressive terms*, the relationships derived in sections 4.1.2 and 4.1.4 are verified numerically. Results are presented for a truncated vertical circular cylinder of radius a, draft $2a$ in water depth $4a$. In addition, the excitation forces and radiation damping coefficients are computed using the identities derived in sections 4.2.2 and 4.2.3 for an array composed of four truncated vertical circular cylinders of the same geometry separated by distance $4a$ (Figure 4.5). This particular configuration was studied by Siddorn and Eatock Taylor (2008) using the IT with semi-analytical expressions for the hydrodynamic operators and showed that, for certain wave numbers, it is prone to the phenomenon of near-trapped modes. The mesh used for the calculations is the same as in 3.3a.

In the second part, entitled *Evanescent terms*, both the hydrodynamic coefficients and the free surface elevation are computed using different values of the evanescent modes truncation to study its impact on the results. In this case, both a small array

of two truncated vertical cylinders and an array of 4 are considered. As in the first section, the mesh used is the same as in Figure 3.3a. In addition, the cube geometry characterized in Chapter 3 is utilized to validate the rotation of the hydrodynamic operators detailed in section 3.4.

Finally, in the third part, special emphasis is put on the importance of normalizing the Bessel functions as explained in section 2.4.2. A comparison of the system's scattering matrix (2.3.13) condition number computed with and without normalization is shown. In addition, a comparison of the computational cost of both direct BEM computations using NEMOH and the IT is shown and analyzed.

4.3.1 Progressive terms

4.3.1.1 Isolated body

Figures 4.2 - 4.3 show the progressive terms of the FTM in surge and roll respectively, computed both by means of NEMOH, using its capability to solve the diffraction problem for partial cylindrical waves, and by means of the RC (also computed with NEMOH using the methodology of Goo and Yoshida (1990)), using the identity (4.1.39). Excellent agreement between the two approaches is observed. As mentioned in 3.6.2.1, only partial waves associated with angular modes $m = \pm 1$ are required to express the wave field radiated by a cylinder moving in surge. The RC are directly related to the FTM terms by expression (4.1.39) from which it follows that only the same modes of the incident cylindrical waves will generate a force on the body.

Figure 4.4 shows the diagonal radiation damping coefficients for surge and roll computed in the standard manner using NEMOH and by means of the FTM terms using the far-field identity in (4.1.58). A very good match between results can be appreciated with a slight numerical inaccuracy of 2% for roll at the region of wavenumbers ($ka > 1.5$).

4.3.1.2 Array

Figure 4.6 shows the variation of the excitation force with wave number in surge and heave for cylinders 1-2 (Figure 4.5) and for an incident wave propagating with direction $\beta = 0$. Results obtained by Siddorn and Eatock Taylor (2008) are shown, and compared to our computation using the IT, for which hydrodynamic operators obtained using NEMOH. Very good agreement between them is found. In addition, the excitation forces computed by means of the relationship (4.2.12) are shown as a numerical verification of the extended cylindrical Haskind relations. Again, very good

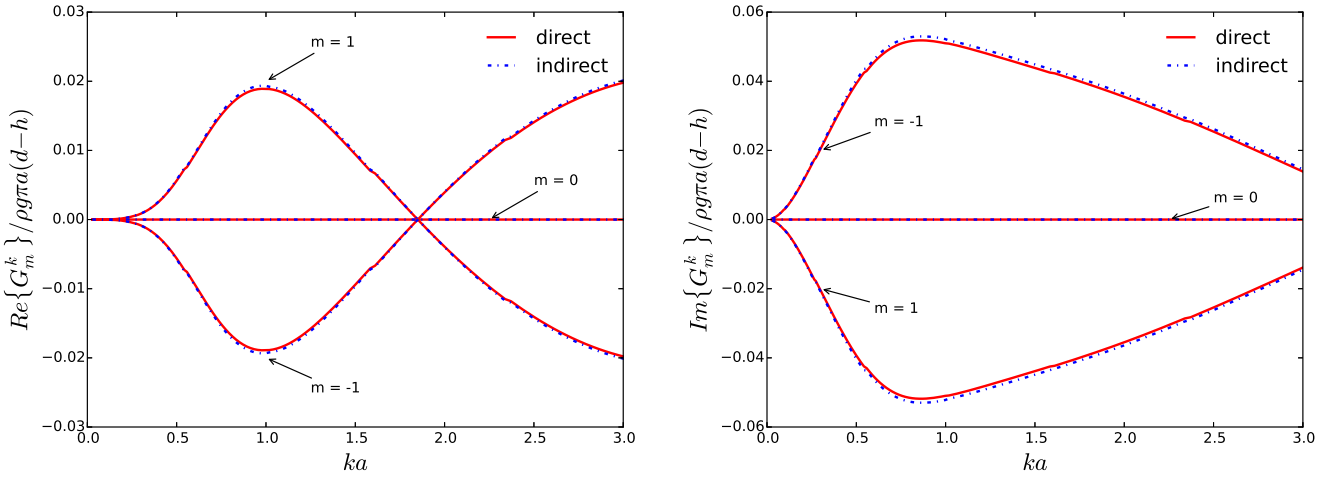

(a) (b)

Figure 4.2: Real (a) and Imaginary (b) parts of the FTM progressive terms in the surge (k=1) degree of freedom for an isolated cylinder of radius a, draft ($d - h = 2a$) in a water depth ($d = 4a$). The solid line (direct) corresponds to the direct calculation of the FTM using NEMOH. The dotted line (indirect) is obtained from the RC computed with NEMOH and by using the right-hand side of equation (4.1.39).

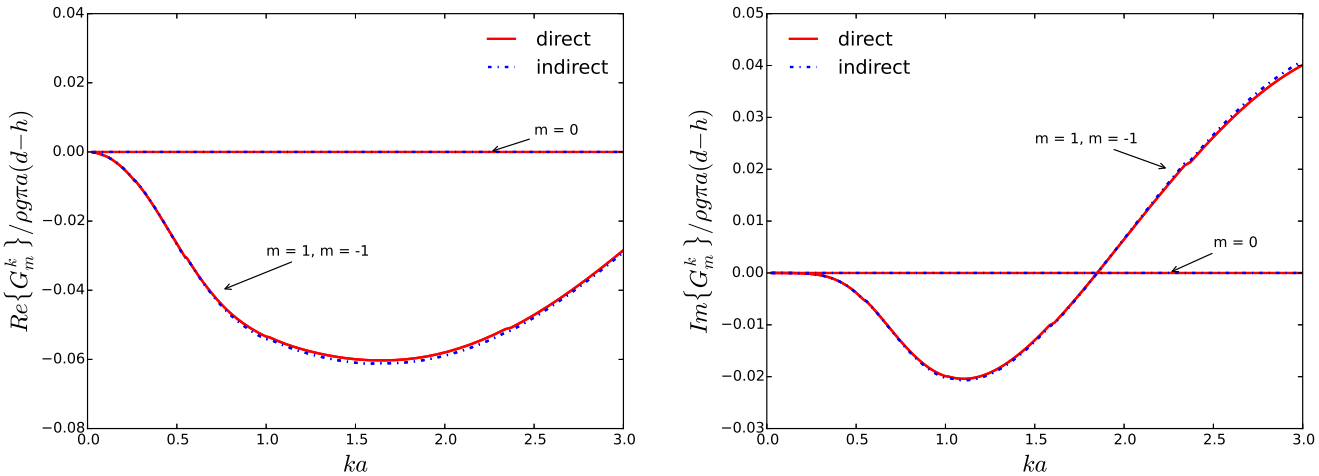

(a) (b)

Figure 4.3: Real (a) and Imaginary (b) parts of the FTM progressive terms in the Roll (k=4) degree of freedom for an isolated cylinder of radius a, draft ($d - h = 2a$) in a water depth ($d = 4a$). The solid line (direct) corresponds to the direct calculation of the FTM using NEMOH. The dotted line (indirect) is calculated from the RC computed with NEMOH and by using the right-hand side of equation (4.1.39).

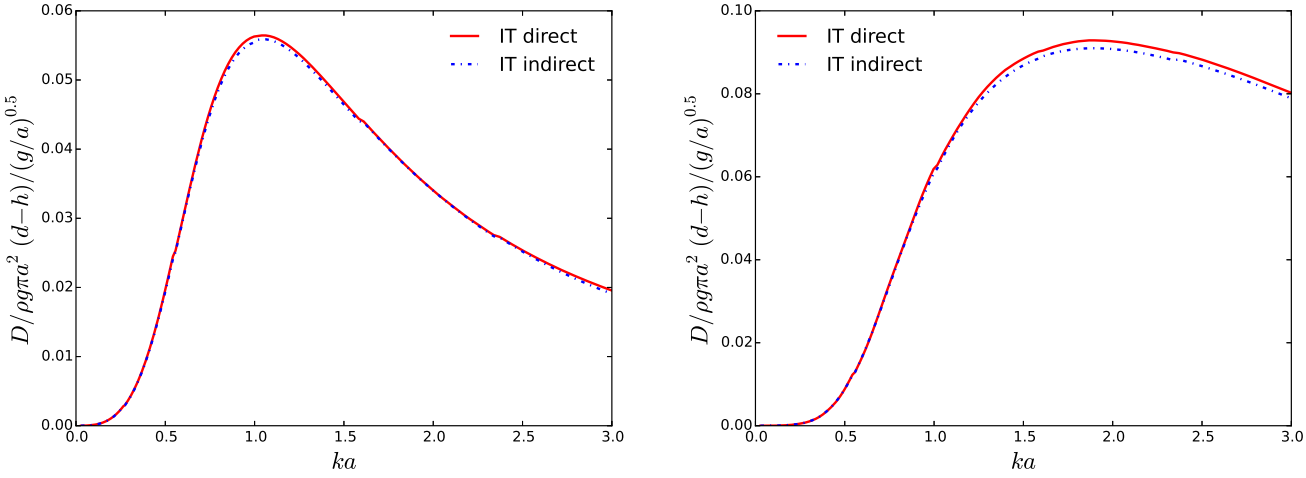

(a) (b)

Figure 4.4: Diagonal radiation damping coefficients for the degrees of freedom Surge (a) and Roll (b) of a cylinder of radius a, draft $(d-h=2a)$ in a water depth $(d=4a)$. The solid line (direct) corresponds to the direct calculation of the damping coefficients using NEMOH. The dotted line (indirect) is calculated from the RC computed with NEMOH and by using the right-hand side of equation (4.1.58).

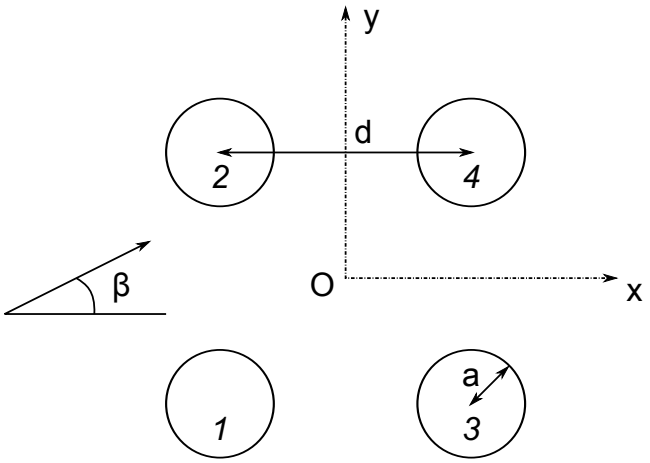

Figure 4.5: Schematic representation of an array composed of four truncated vertical cylinders of radius a and separated by a distance between centers d. $\beta = 0$ corresponds to the positive $x-axis$.

agreement with the previous methodologies is observed, despite a slight overestimation of the peaks for surge, mainly at low wave numbers ($ka < 1$). An irregular frequency at $ka = 3.8$ (surge) and $ka = 2.4$ (heave) can also be observed. Also shown are the contributions to the total excitation force from the isolated body on one hand and from the hydrodynamic interactions on the other hand, which were computed separately using expression (4.2.13). Only the modulus is displayed here, so the curves cannot be directly summed.

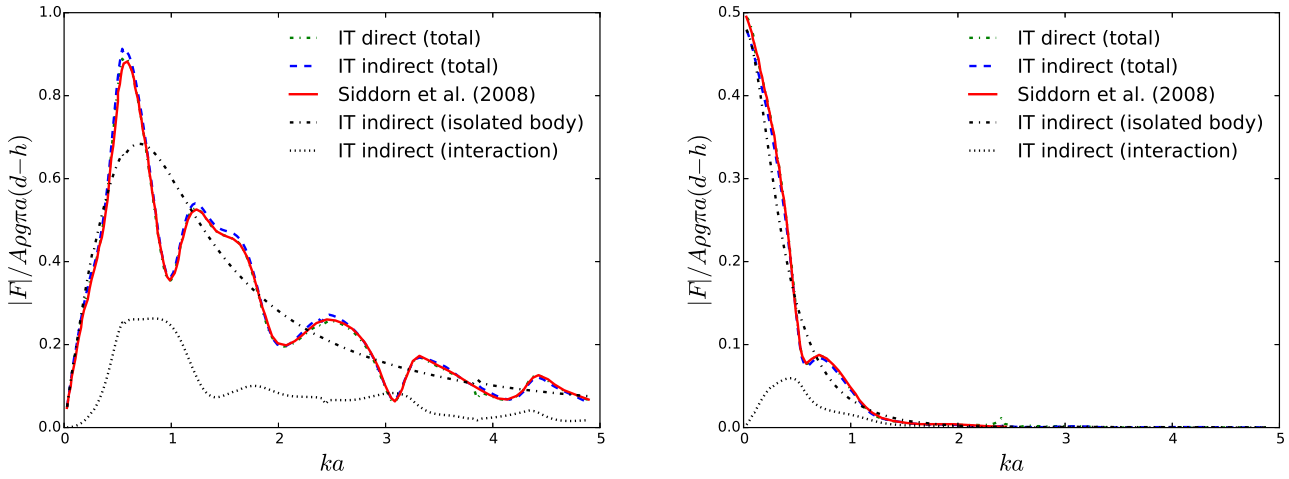

Figure 4.6: Non-dimensional excitation forces in Surge (a) and Heave (b) for the cylinders 1-2 in the array shown in Figure 4.5 from an incident plane wave with propagation direction ($\beta = 0$) and amplitude A . The solid line reproduces the results by Siddorn and Eatock Taylor (2008); the dotted green line has been computed with the IT by Kagemoto and Yue (1986) using NEMOH to compute the required hydrodynamic operators and the dotted blue line by means of the right-hand side of the extended cylindrical Haskind relation (4.2.12). The black dotted lines ($- \cdot -\cdot$) and ($\cdots$) correspond respectively to the contribution to the total excitation force from the isolated body and from the hydrodynamic interactions with the neighbours and have been computed from the first and second terms of equation (4.2.13) respectively.

One would normally compute the excitation forces using the FTM, which sums the individual contributions to the total excitation force from each partial incident wave by solving a diffraction problem. The verification provided by equation (4.2.12) is powerful from two points of view. First, it does not make use of diffraction, but rather the cylindrical coefficients of a radiation problem. Second, a summation of all the cylindrical coefficients is performed prior to multiplication by a scalar quantity,

which can be, for instance, in the order of 10^7 times higher in magnitude than each individual partial wave coefficient, improving the global accuracy of the computation.

The near-trapped modes phenomenon only occurs at specific propagating directions of the incident waves, in this case for $\beta = \pi/4$, and for specific wavenumbers for the layout analyzed. As shown in Figure 4.7, the excitation force in surge for cylinders 1-2 has a sharp peak at $ka = 1.66$. Similarly to Figure 4.6, a very good match is observed between the results by Siddorn and Eatock Taylor (2008) and those obtained from the present application of the IT. A slight overestimation of the peaks for surge, mainly at low wave numbers ($ka < 1$), is observed for the results computed using expression (4.2.12). The irregular frequencies in both surge and heave cases can be identified at the same wave numbers as in the case $\beta = 0$.

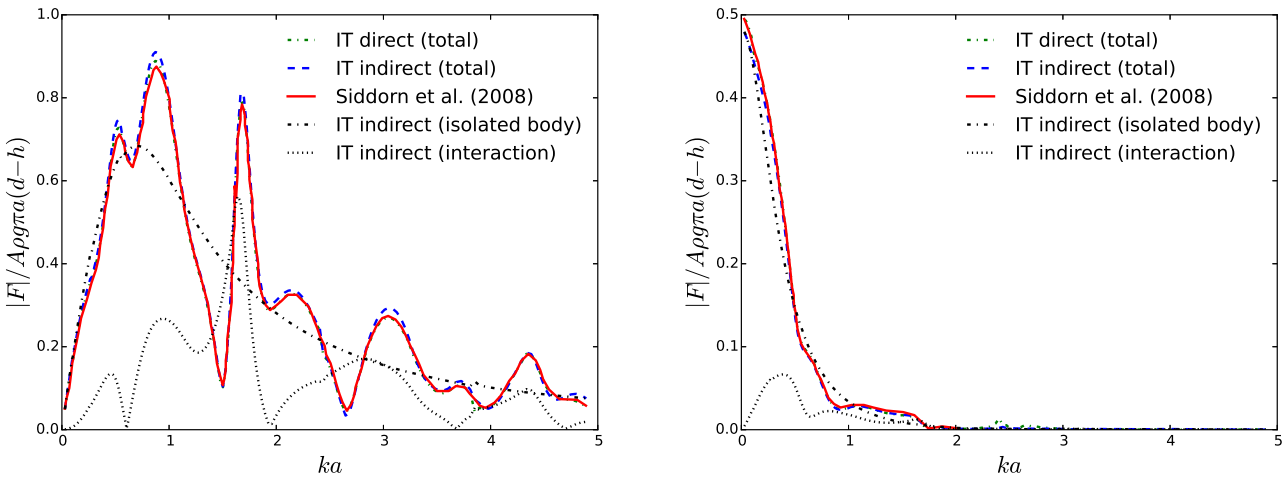

Figure 4.7: Non-dimensional excitation forces in Surge (a) and Heave (b) for the cylinder 1 in the array shown in Figure 4.5 from an incident plane wave with propagation direction ($\beta = \pi/4$) and amplitude A . The legend follows as in Figure 4.6.

Figures 4.8 - 4.11 show the variation of the radiation damping coefficients with wave number. Results are computed with the IT, making use of the hydrodynamic operators obtained with our BEM code, as well as from expression (4.2.20), and compared to Siddorn and Eatock Taylor (2008). In general, good agreement between the three methodologies can be observed, apart from slight under and overestimation of the results computed using the relationship (4.2.20) at several wave numbers. Slight frequency irregularities can be detected at the same wave numbers detailed for the excitation forces. Figure 4.11 shows the separate contributions from the isolated body

and from the hydrodynamic interaction to the diagonal radiation damping coefficients computed by means of expression (4.2.21). For the surge mode of motion, the effect of the hydrodynamic interactions is clearly observed at $ka = 1.66$.

The differences in the results by Siddorn and Eatock Taylor (2008) obtained at low wavenumbers ($ka \leq 1$) are mainly attributable to discrepancies between the semi-analytical solution and the BEM solver, which has also been shown by Cruz et al. (2010). For the rest of the wave number range, discrepancies are due to numerical inaccuracies in the calculations performed with the methodology implemented.

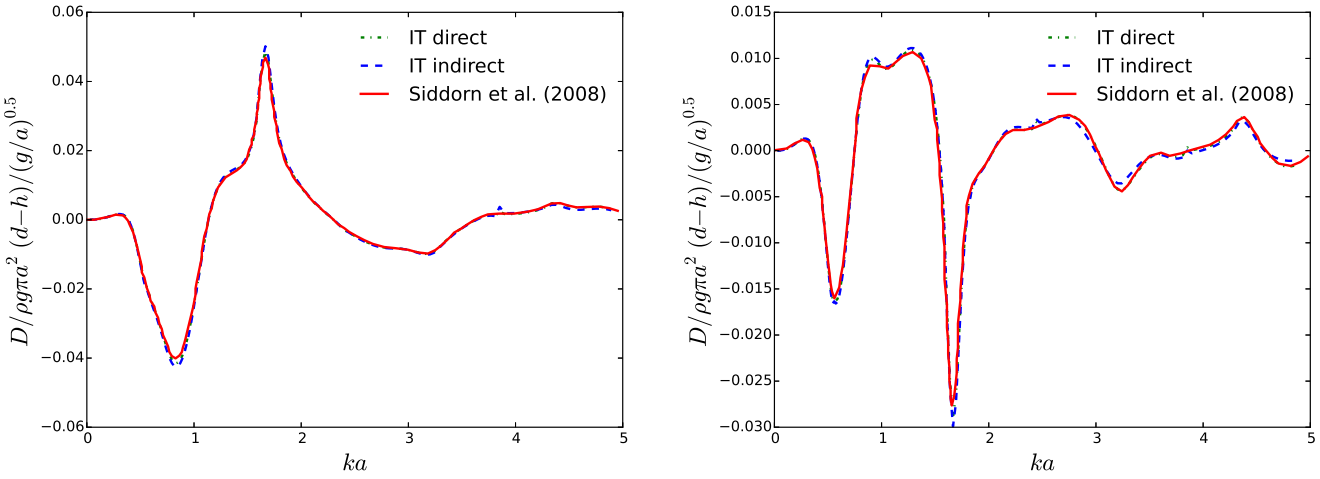

(a) (b)

Figure 4.8: Non-dimensional Surge coupling radiation damping coefficients between two cylinders (1-3 in *a)*; 1-4 in *b)*) in the array shown in Figure 4.5. The first index indicates the cylinder on which the radiation force is evaluated due to the motion of the body indicated by the second index. The solid line reproduces the results by Siddorn and Eatock Taylor (2008); the dotted green line has been computed with the IT by Kagemoto and Yue (1986) using NEMOH to compute the required hydrodynamic operators and the dotted blue line by means of the right-hand side of equation (4.2.3).

4.3.2 Evanescent terms

Results for the hydrodynamic coefficients obtained using the IT are shown in Figure 4.13 for a small array of two cylinders of $3m$ radius (a), $6m$ draft in a $50m$ water depth (Figure 4.12). They are compared to direct calculations performed with NEMOH.

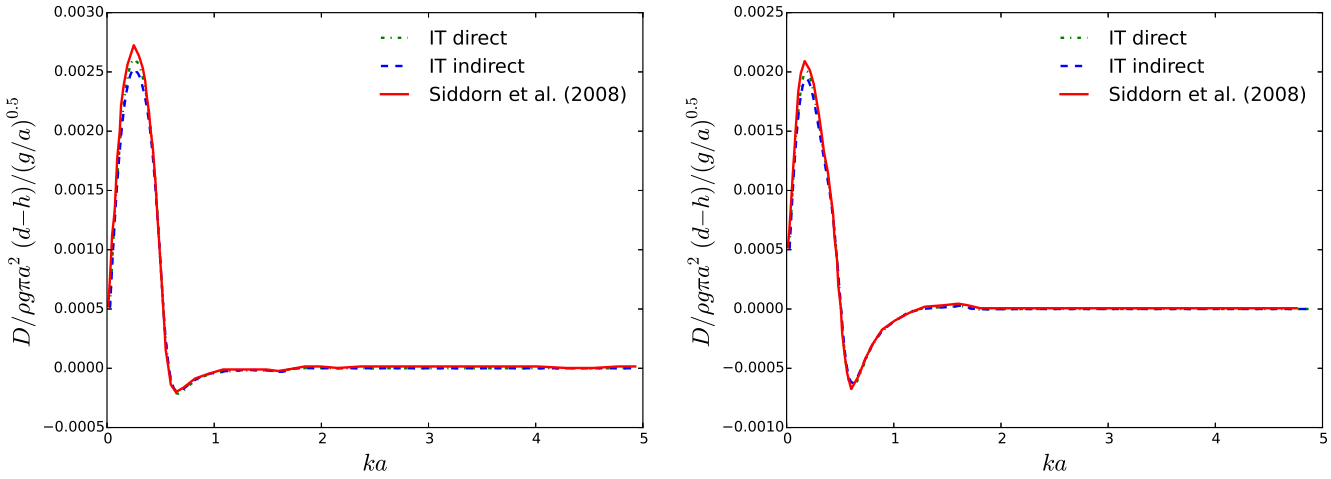

(a) (b)

Figure 4.9: Non-dimensional Heave coupling radiation damping coefficients between two cylinders (1-3 in *a)*; 1-4 in *b)*) in the array shown in Figure 4.5. The legend follows as in Figure 4.8.

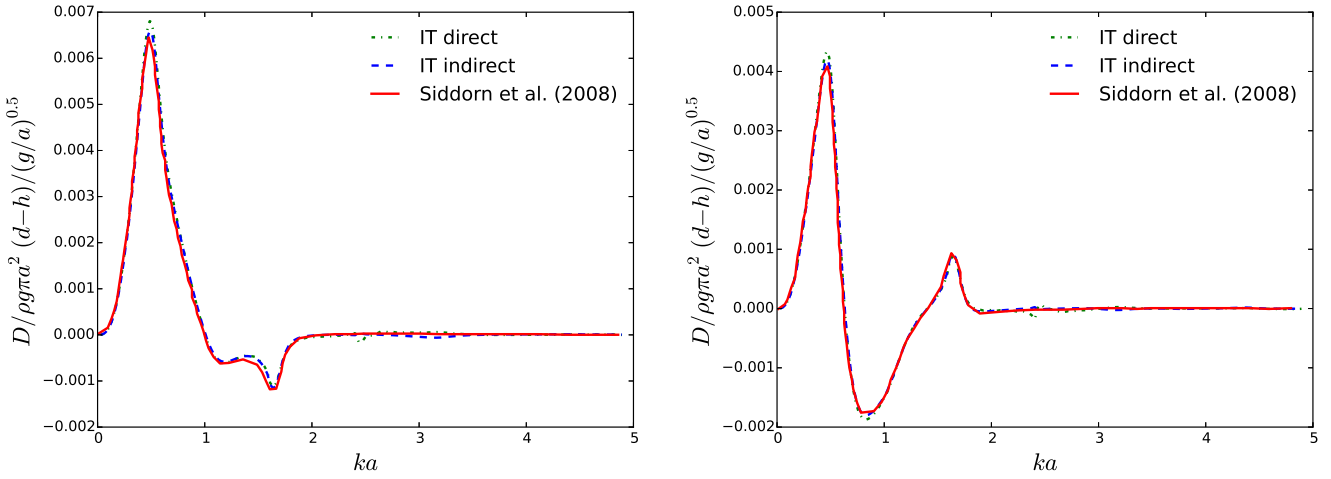

(a) (b)

Figure 4.10: Non-dimensional Heave-Surge coupling radiation damping coefficients between two cylinders (1-3 in *a)*; 1-4 in *b)*) in the array shown in Figure 4.5. The legend follows as in Figure 4.8.

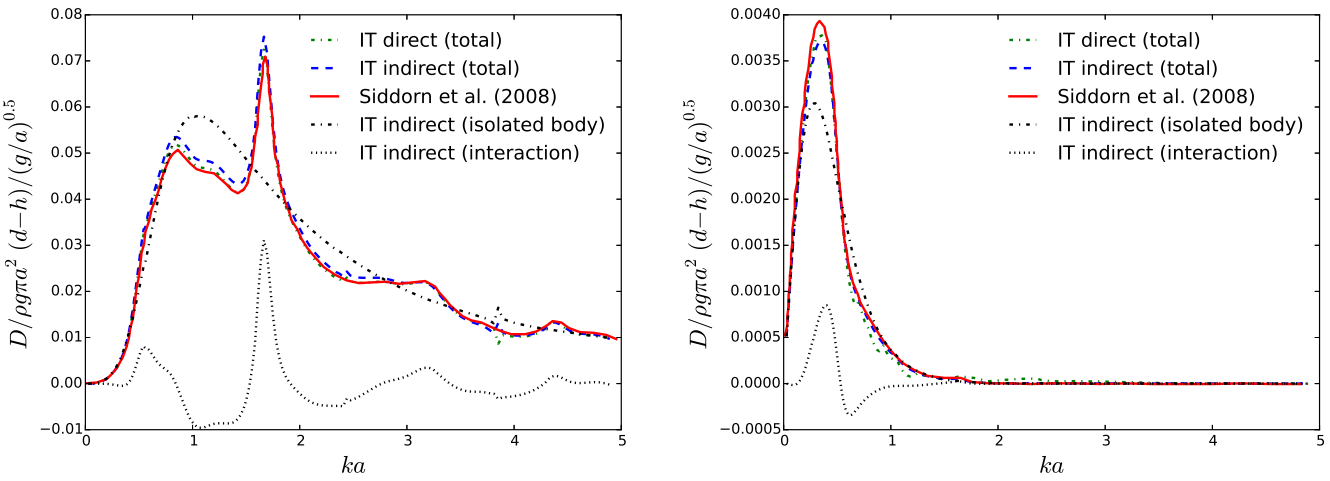

Figure 4.11: Non-dimensional diagonal Surge (a) and Heave (b) radiation damping coefficients of cylinder 1 in the array shown in Figure 4.5. The solid line reproduces the results by Siddorn and Eatock Taylor (2008); the dotted green line has been computed with the IT by Kagemoto and Yue (1986) using NEMOH to compute the required hydrodynamic operators and the dotted blue line by means of the right-hand side of equation (4.2.3). The black dotted lines $(- \cdot - \cdot)$ and $(\cdot \cdots)$ correspond respectively to the contribution to the total radiation force from the isolated body and from the hydrodynamic interactions with the neighbours and have been computed from the first and second terms of equation (4.2.20) respectively.

Several separating distance cases are considered. When only a single line is visible, it means that the other lines lie underneath it and there is a perfect match from visual accuracy.

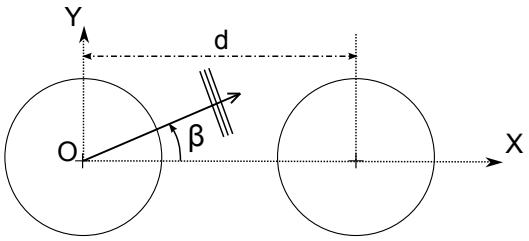

Figure 4.12: Schematic of an array composed of two truncated vertical cylinders. $\beta = 0$ corresponds to the positive $x - axis$.

First, both bodies are set far away from each other at a distance $d/a = 5000$. As expected, the hydrodynamic coefficients are the same as if the cylinders were in isolation. Moreover, for such a long separating distance the evanescent modes do not play an important role. This can be derived from the fact that in their absence ($L = 0$) a perfect match of results between the IT and the direct computations (Figure (4.13a)) is obtained, with L being the truncation order of the series related to the near-field components of the potentials.

When bodies are set closer, in this case at a distance of $d/a = 5$, hydrodynamic interactions become important as can be observed in Figures (4.13b) and (4.13c). For $ka > 0.2$, the added mass and damping coefficients in isolation are altered. A similar behaviour was shown by Siddorn and Eatock Taylor (2008) for the heave coupling radiation hydrodyamic coefficients. At this separating distance ($d/a = 5$) and for the surge mode of motion, the influence of the evanescent modes is still negligible.

Finally, for a fixed frequency corresponding to a wave length of ($\lambda/a = 10$), the coupling heave-heave added mass coefficient $(3, 9)$ is shown (Figure 4.14) at several separating distances which span from $d/a = 10$ to the limit case where the perimeters of both cylinders are externally tangent ($d/a = 2$). The full direct BEM solution is also plotted for comparison. The influence of the evanescent modes for the heave-heave coupling can be clearly observed, as well as convergence of the IT results to direct calculation when the truncation of evanescent modes is increased. It has been observed that their importance to ensure accuracy of the radiation hydrodynamic coefficients (both added mass and damping) for close separating distances is mainly dependent on the motion mode and the frequency. For instance, for the surge-surge coupling, their influence at $\lambda/a = 10$ (Figure 4.15a) is negligible but not at $\lambda/a = 30$ (Figure 4.15b).

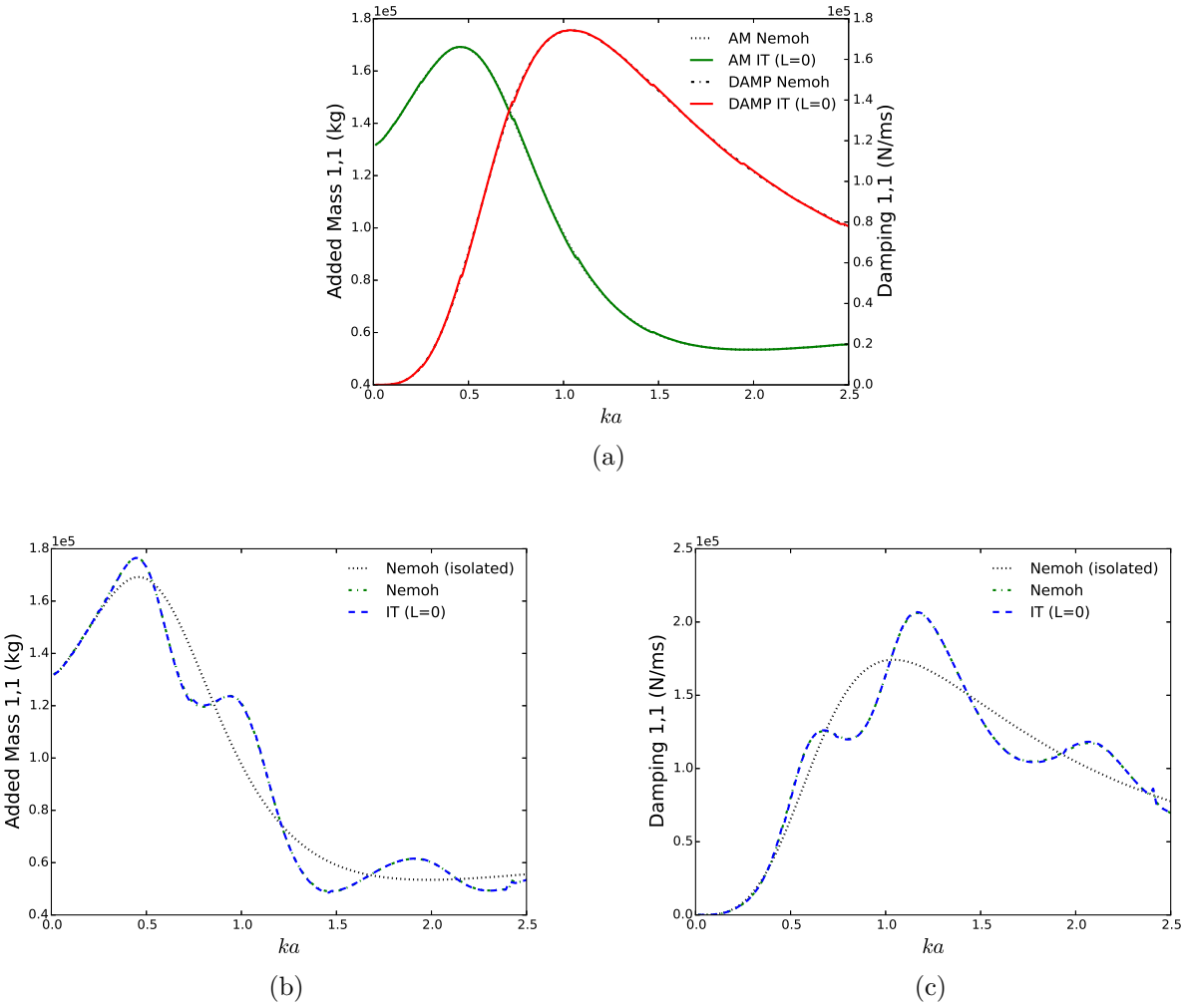

Figure 4.13: Added mass and damping coefficients for the first truncated vertical cylinder ($3m$ radius, $6m$ draft in a $50m$ water depth) in the two body array (Figure 4.12) for different separating distances ($d/a = 5000$ - (a), $d/a = 5$ - (b), $d/a = 5$ - (c)). First index corresponds to the direction of the force and the second to the degree of freedom.

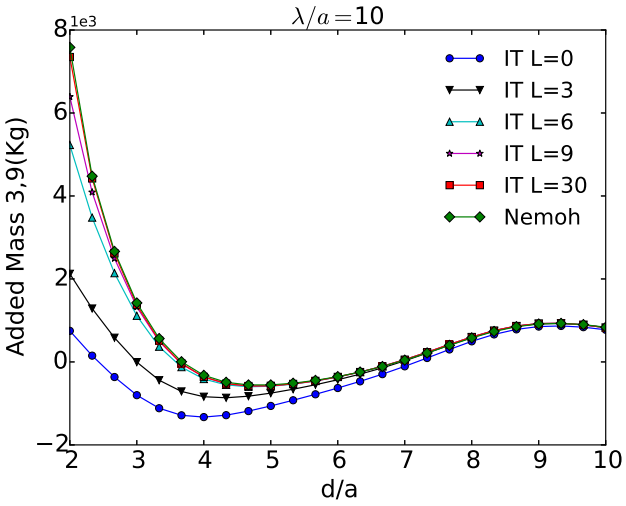

Figure 4.14: Heave-heave coupling added mass coefficient as a function of the evanescent modes truncation L and for a small array of two truncated vertical circular cylinders of radius 3m, draft 6m in water depth of 50m.

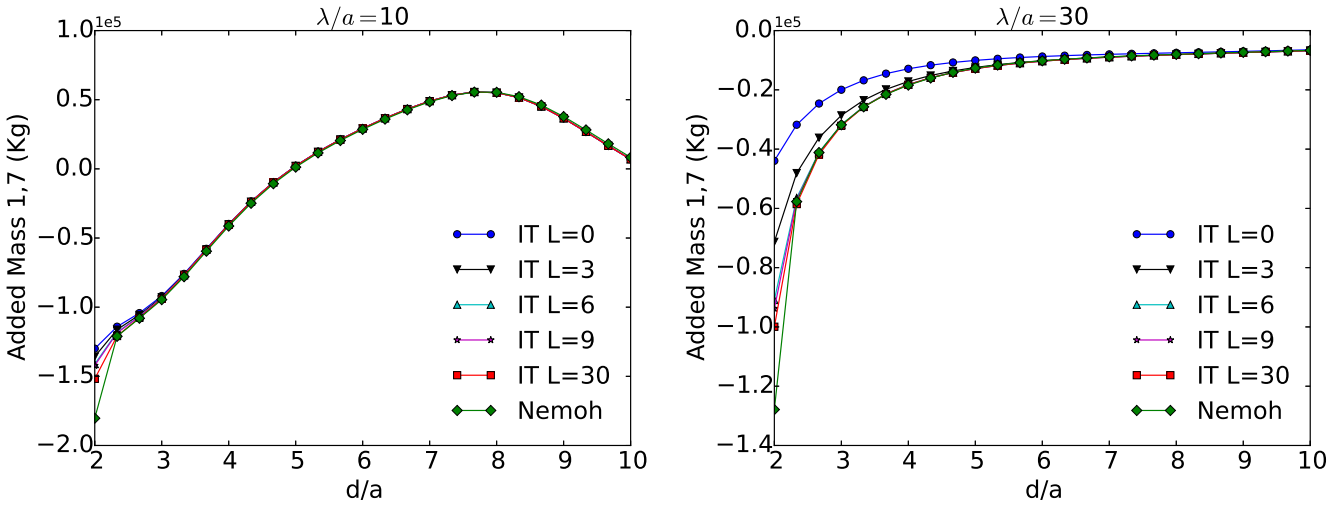

(a) (b)

Figure 4.15: Surge-surge coupling added mass coefficient as a function of the evanescent modes truncation L for two different wavelengths for a small array of two truncated vertical circular cylinders of radius 3m, draft 6m in water depth of 50m.

Another way to visualize the effect of the evanescent modes truncation consists of studying the free surface elevation (η). Figures 4.16a - 4.16b show the total wave elevation, i.e. the sum of incident, scattered and radiated wave elevations including the computed body motions (see section 5.1.2 for a more detailed description of the equation of motion of a floating body), obtained with NEMOH and with the IT respectively for a small array of 4 freely floating truncated vertical cylinders in a regular wavetrain of propagation direction $\beta = 0$ and wavelength $\lambda/a = 10$ with a the radius of the cylinders. The IT free surface elevation has been calculated using its definition $\eta = -\frac{1}{g}\frac{\partial\phi}{\partial t}|_{z=0}$, where the velocity potential in the fluid domain has been reconstructed from the solution of the multiple-scattering problem by means of expressions (2.2.20), (2.2.14) - (2.2.15).

It can be observed that a very good agreement between results is obtained for the whole domain (Figure 4.16c) when no evanescent modes are used with the highest discrepancies being located at the vicinity of the bodies. The use of a higher evanescent modes truncation (Figures 4.16d - 4.16f) reduces the error at these regions and results computed with the interaction theory converge with those obtained from direct calculations with the standard BEM code.

Figures 4.17a - 4.17b show the total wave elevation obtained with NEMOH and with the IT respectively for a small array of 4 freely floating cubes for a regular wave of propagation direction $\beta = 0$ and wavelength $\lambda/a = 10$ with a the radius of the circumscribing cylinder to the cubes. On two of the bodies a rotation of 45 degrees has been applied. On NEMOH, this has been accounted for by providing the mesh-files of each individual body separately. The software *Meshmagick* by Rongère (2016) has been used to apply the required translations and rotations to the original mesh file of a cube centered at the origin. In contrast, in the IT computation the relationships derived in section 3.4 have been applied, i.e. a single mesh of a cube centered at the origin has been employed to compute all the hydrodynamic operators. As for the cylinder array, a very good agreement between results is obtained in the whole domain (Figure 4.17c) when no evanescent modes are used with the highest discrepancies being located at the vicinity of the bodies. The latter are reduced when a higher number of evanescent modes is used (Figures 4.17d - 4.17f).

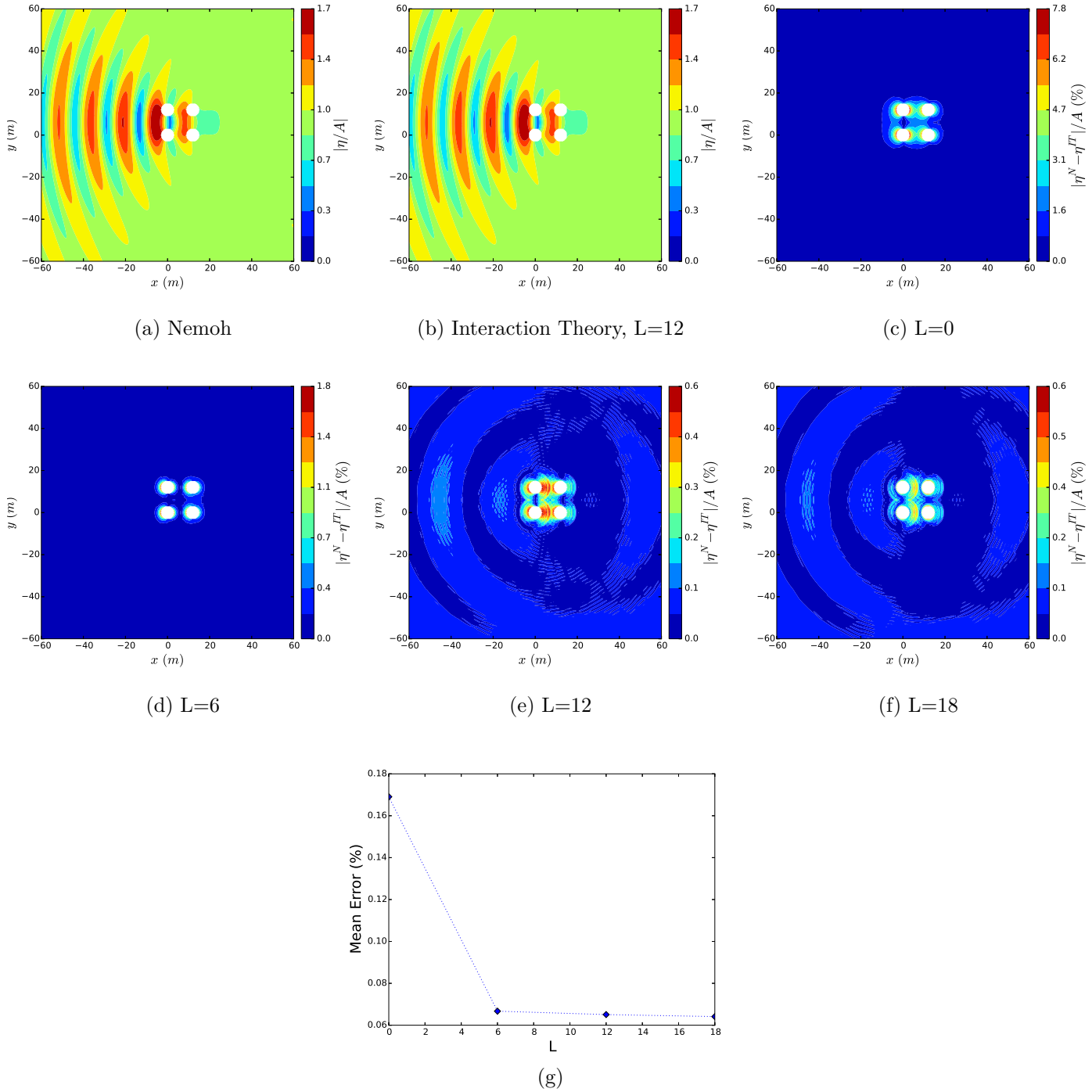

(a) Nemoh (b) Interaction Theory, L=12 (c) L=0

(d) L=6 (e) L=12 (f) L=18

(g)

Figure 4.16: Magnitude of surface elevation for an array of 4 cylinders of $3m$ radius, $6m$ draft in a $50m$ water depth with a separation distance of 12m. Plots c, d, e, f show the percentage difference between the wave fields computed with the interaction theory (b) indicated by IT and the direct calculation using NEMOH (a) indicated by N as a function of the evanescent modes truncation L ((c) - $L = 0$, (d) - $L = 6$, (e) - $L = 12$, (f) - $L = 18$). Results are normalized by the amplitude of the incident wave (A). Propagation direction is defined from left to right.

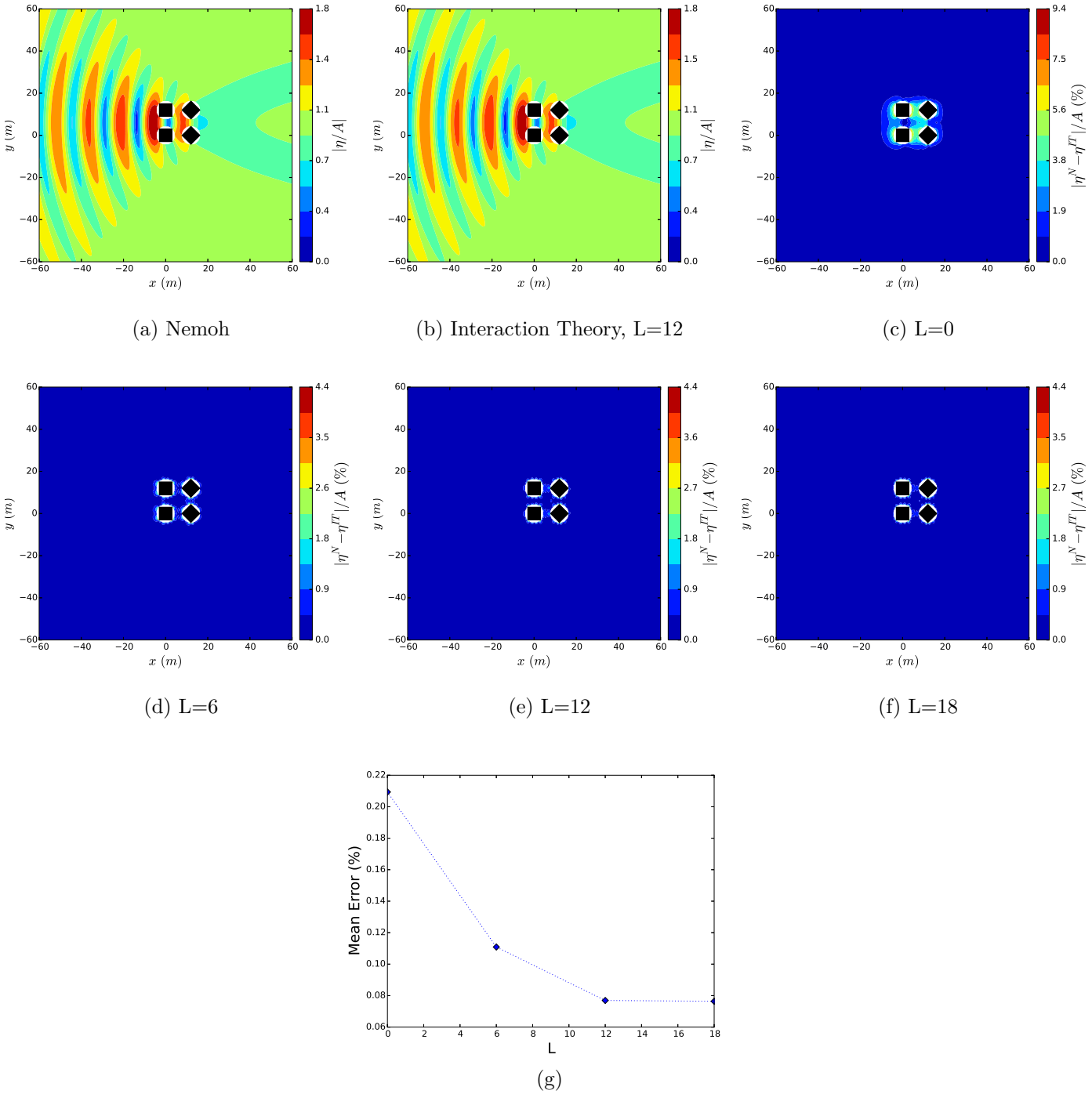

(a) Nemoh (b) Interaction Theory, L=12 (c) L=0

(d) L=6 (e) L=12 (f) L=18

(g)

Figure 4.17: Magnitude of surface elevation for an array of 4 cube boxes of $6m$ side, $6m$ draft in a $50m$ water depth with a separation distance of 12m. Plots c, d, e, f show the percentage difference between the wave fields computed with the interaction theory (b) indicated by IT and the direct calculation using NEMOH (a) indicated by N as a function of the evanescent modes truncation L ((c) - $L = 0$, (d) - $L = 6$, (e) - $L = 12$, (f) - $L = 18$). Results are normalized by the amplitude of the incident wave (A). Propagation direction is defined from left to right.

4.3.3 Condition Number

In section 2.4.2, the importance of normalizing Bessel functions with respect to both order and argument was evoked. Normalized formulae for the incident and outgoing basis functions were given and the changes propagated to the rest of expressions. In particular, in section 3.5 normalizing terms for the hydrodynamic operators (DTM, RC and FTM) were detailed. Herein, a comparison of the system scattering matrix condition number (see section C.4 for a detailed description) computed with and without normalization of the Bessel functions is shown. Results are presented for a configuration of four truncated vertical cylinders, as in Figure 4.5, for different frequencies, separating distances and evanescent modes truncation.

In Figure 4.18 the scattering matrix condition number, computed without having applied the normalization to Bessel functions, is shown to increase with the frequency, when the separating distance between bodies is reduced and when the evanescent modes truncation is increased. While the differences in condition number are small amongst the two different evanescent modes truncation used for all frequencies and separating distances, they are significant with respect to the case where only progressive terms are considered. This is remarkable specially at high frequencies where values of the condition number reach values on the order of 10^{20} when evanescent modes are used, leading to a matrix rank of 1140, and of 10^4 with only progressive terms, reducing the matrix rank to 60.

A different trend of results is observed in Figure 4.19, which shows the condition number of the same scattering matrix but now with normalized Bessel functions. Even if an increasing trend is kept when the gap between bodies is reduced, the condition number remains lower than 10 in almost all cases which is excellent in terms of numerical stability. In addition, and contrarily to the previous case, the behaviour is shown to be quite independent of the evanescent modes truncation.

4.3.4 Wall Clock Execution Time

In this section, the time savings of the Direct Matrix Method interaction theory are examined by comparison with direct computations using the BEM code NEMOH. The two case studies chosen consist of an array of truncated vertical circular cylinders and flap-type converters discretized as shown in Figure 4.21 and deployed in inline

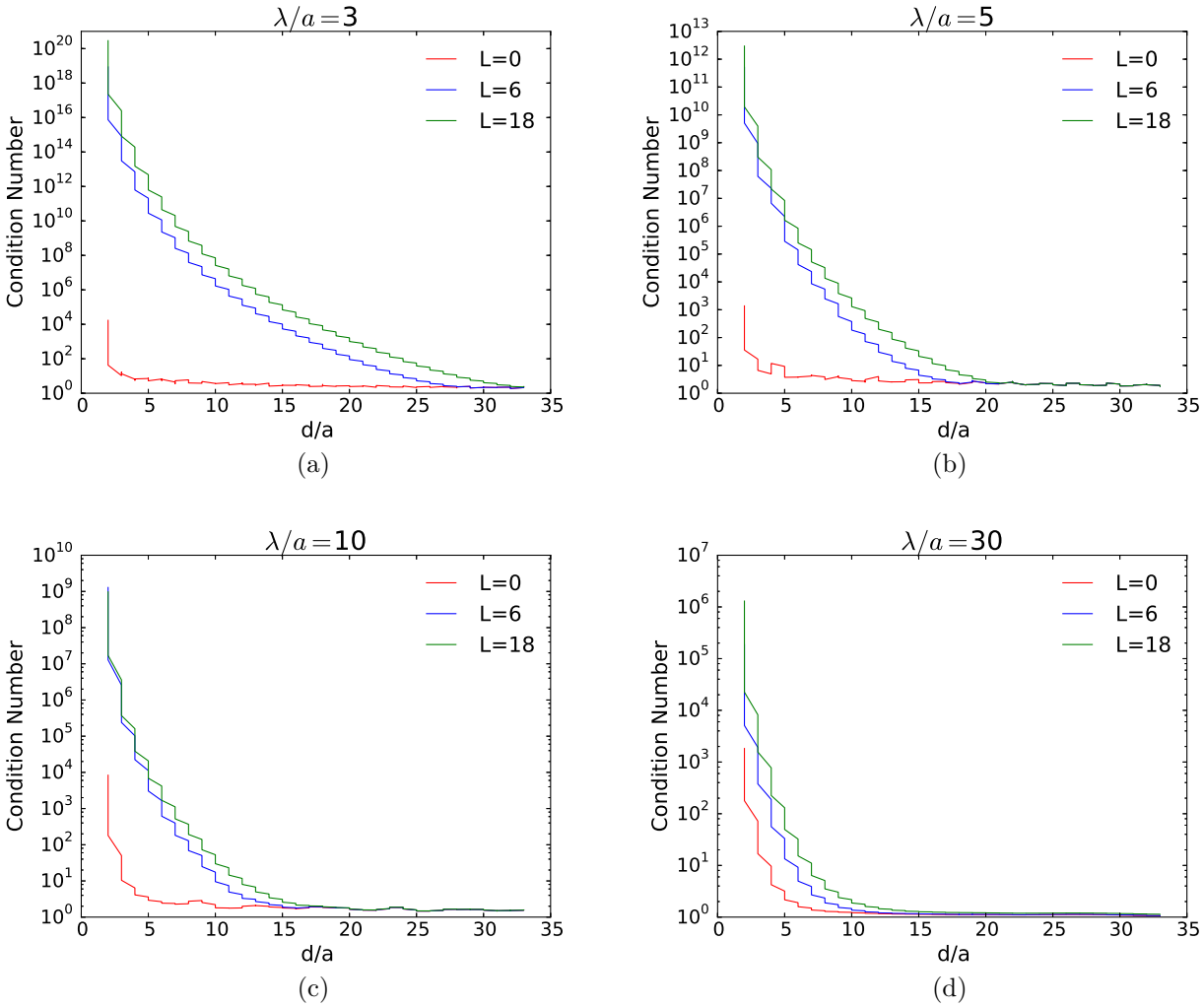

Figure 4.18: Condition number of the system scattering matrix of a 4 cylinder array (without Bessel functions normalization).

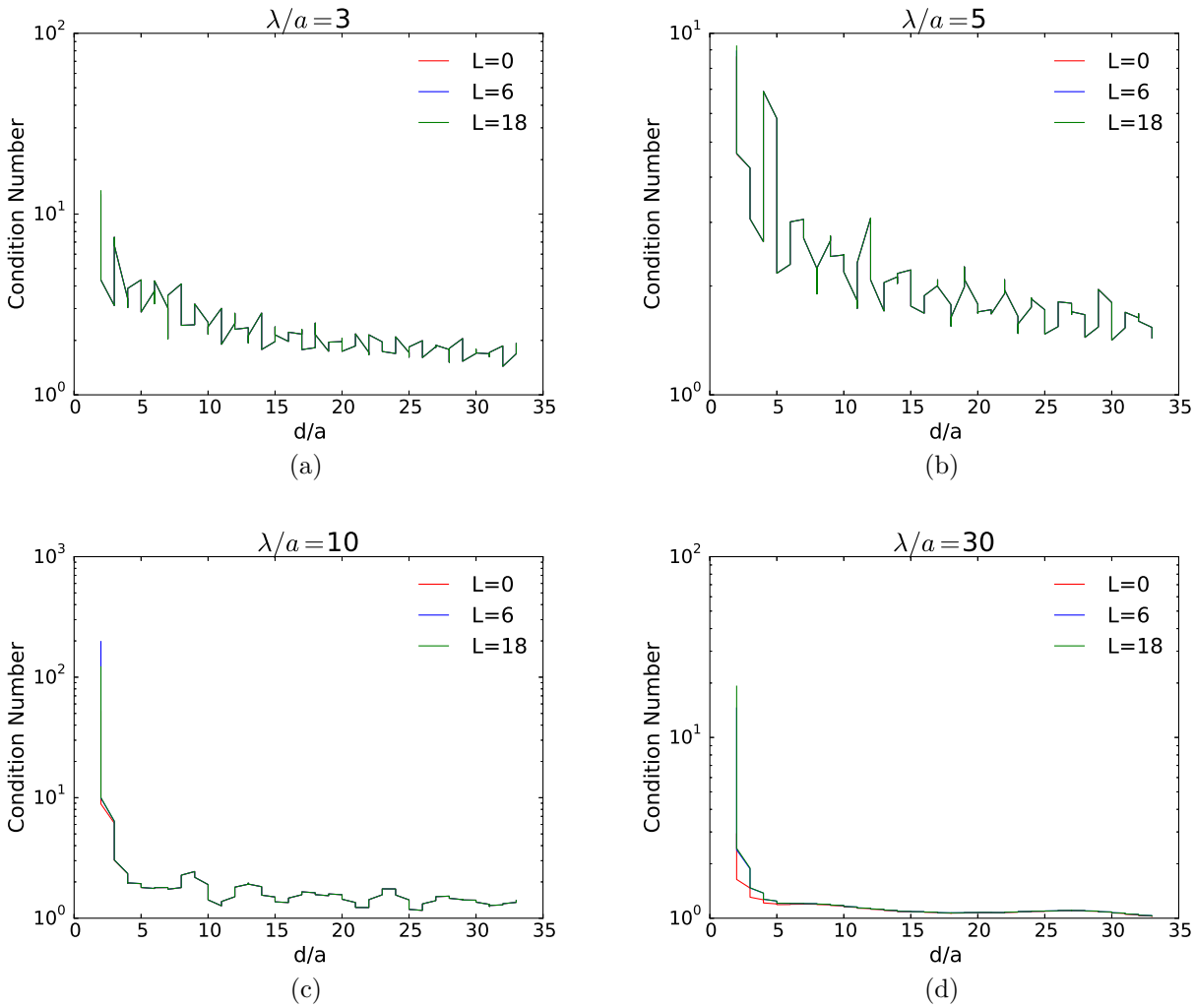

Figure 4.19: Condition number of the system scattering matrix of a 4 cylinder array (with Bessel functions normalization).

layout as depicted in Figure 4.20. The computations are performed using a total of 30 frequencies in the range $0.2 - 1.5$ rad/s ($\sim 4 - 30\,s$ of period), 5 wave propagation directions in the range $(-\pi/2,\ \pi/2\,rad)$ and a water depth of 50 m. Both the diffraction and radiation problems are solved, the latter for the general case with 6 degrees of freedom per body.

Figures 4.22a and 4.22b show the wall clock time associated with direct NEMOH and IT simulations as a function of the number of inline cylinders and flap-type converters respectively. The interaction theory requires the evaluation of the isolated body hydrodynamic characteristics prior to solving the multiple-scattering problem. Thus, both the time used to solve the multiple-scattering only (indicated as "IT") and the time spent to compute the individual body hydrodynamic characteristics and the multiple-scattering (indicated as "IT + HC") are shown. In addition, the computations with the IT can be performed including evanescent modes whose number is indicated as "L".

For both case studies with an evanescent modes truncation $L = 0$, it can be observed that the acceleration provided by the IT is remarkable. Indeed, for the layout with 10 inline bodies NEMOH computations are on the order of $\sim 10h$ in contrast with $\sim 10min$ for the IT. A significant part of the latter is dedicated to evaluate the individual body solution, which takes on the order of minutes. This cost becomes negligible compared to the computational time involved in solving the multiple-scattering problem when the number of bodies increases. Indeed, for the 60-body configuration the markers of the "IT" and "IT+HC" overlap completely.

When the number of evanescent modes used increases, it can be observed that the computations with the IT are considerably slowed-down. While for $L = 0$ and for both geometries the computational time associated with 60 inline bodies is $\sim 1h$, the transition to $L = 2$ makes it go beyond $10h$. This is caused by the fact that the number of unknowns in the IT depends on both the angular-mode (M) and the depth-mode (L) truncations, the latter referred as well to as evanescent modes truncation, used to represent the isolated body solution in the base of partial cylindrical wave functions. As mentioned in section 2.4, the size of the vectors of unknowns of each body is $(2M + 1)(L + 1)$ and, therefore, the size of the total system to be solved by the IT is $(2M + 1)(L + 1)N_b$ provided that all the body geometries are the same.

Table 4.1 shows a comparison of the total number of unknowns associated with direct NEMOH computations and the IT for the 60 inline bodies case. The advantages of expressing the solution in the basis of partial cylindrical wave functions can be clearly observed. It is worth noting that, while in direct NEMOH computations the

number of unknowns is higher for the cylinder whose mesh is slightly finer than the one used for the flap, in IT computations this trend is inverted and a higher number of modes is used for the flap. As mentioned in Chapter 3, a higher number of angular-modes is required to represent the wave field around a non-axisymmetric geometry contrarily to the case of axisymmetric bodies such as truncated vertical cylinders. This has an impact on the computational time as can be derived from Figure 4.22 where, for the 60-body configuration, the wall clock times associated with both the cylinder and the flap are slightly below and over $1h$ respectively. In addition to depending on the type of body geometry, the number of cylindrical harmonics required by the interaction theory is as well frequency-dependent. The highest and lowest truncations required in the frequency range of the present case study have been indicated as IT_{max} and IT_{min} respectively.

Finally, direct NEMOH computations for the 60-body case have not been attempted but the wall clock time they would take has been estimated as 124 and 119 days for the truncated vertical cylinder and the flap arrays respectively. For that, the trend of the computational times taken by the simulations of up to 10 bodies has been used. Figure 4.23 shows the wall clock time per problem as a function of the number of panels and, as expected, it can be observed that the numerical complexity grows proportional to the square of the size of the system.

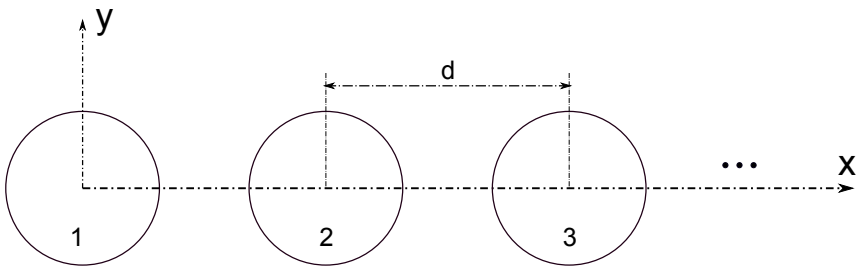

Figure 4.20: Schematic of an array of inline bodies separated by a distance d.

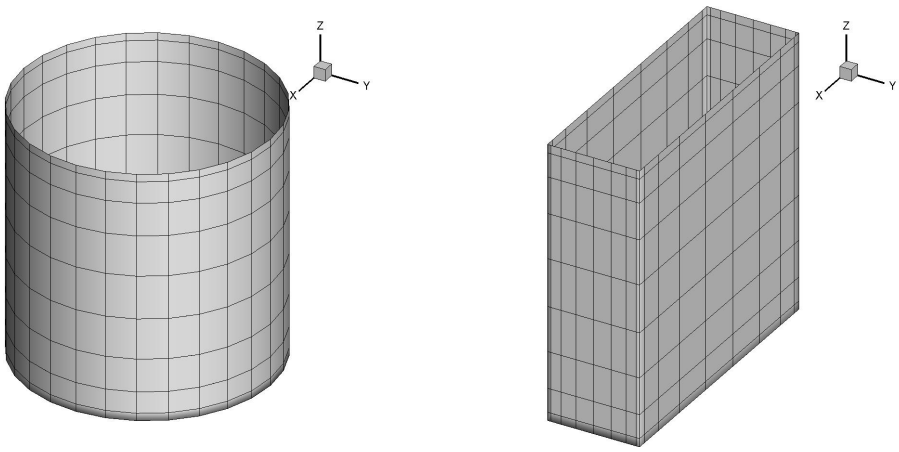

(a) 392 Panels (b) 378 Panels

Figure 4.21: Discretization of *a*) a truncated vertical cylinder of $3m$ radius and $6m$ draft, *b*) a flap-type converter of $6m$ width by $2m$ side.

$N_{bodies} = 60$	$N_{unknowns}$	
	Cylinder	Flap
$NEMOH$	23520	22680
$IT_{min}\,(L = 0)$	300	420
$IT_{max}\,(L = 0)$	660	780
$IT_{min}\,(L = 2)$	900	1260
$IT_{max}\,(L = 2)$	1980	2340

Table 4.1: Size of the Boundary Value Problem to be solved using both a direct NEMOH simulation and the interaction theory (IT) for different values of evanescent modes truncation (L). The highest and lowest truncation levels required for the IT in the frequency range of the case study are indicated as IT_{max} and IT_{min} respectively. The problem size is defined based on the discretizations of two different geometries, a truncated vertical circular cylinder and a flap-type converter shown in Figures 4.21a and 4.21b respectively.

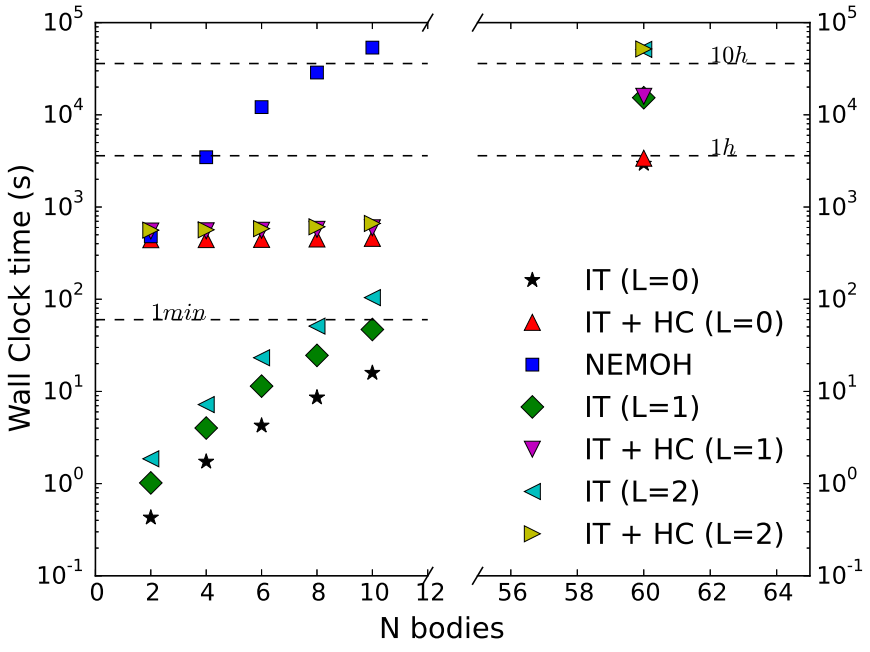

(a)

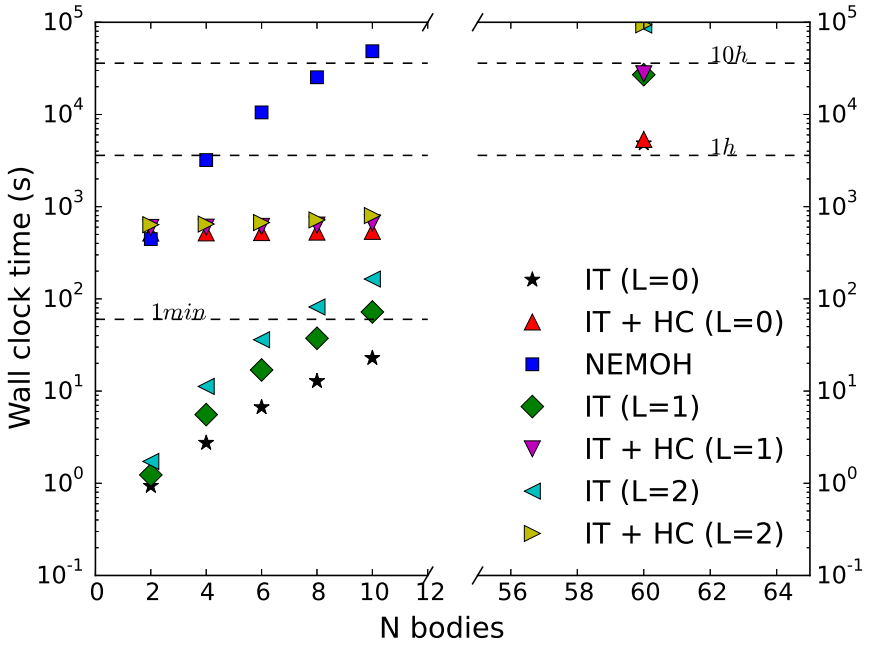

(b)

Figure 4.22: Comparison of wall clock computational times between the Direct Matrix Method interaction theory (IT) and direct NEMOH simulations for both a truncated vertical cylinder *a*) and a flap-type converter *b*), shown respectively in Figures 4.21a and 4.21b, as a function of the number of bodies positioned successively in line and separated by a distance of 60 meters. Calculations using the interaction theory require, first, the evaluation of the isolated body hydrodynamic characteristics and, then, the solution to the multiple scattering problem. The time associated with the former is indicated as "HC" and with the latter as "IT". The evanescent modes truncation is referred to as "L". Simulations were performed with 6 dofs per body, 30 frequencies (0.2 - 2.0 rad/s) and 5 propagation directions and both the diffraction and radiated problems were solved.

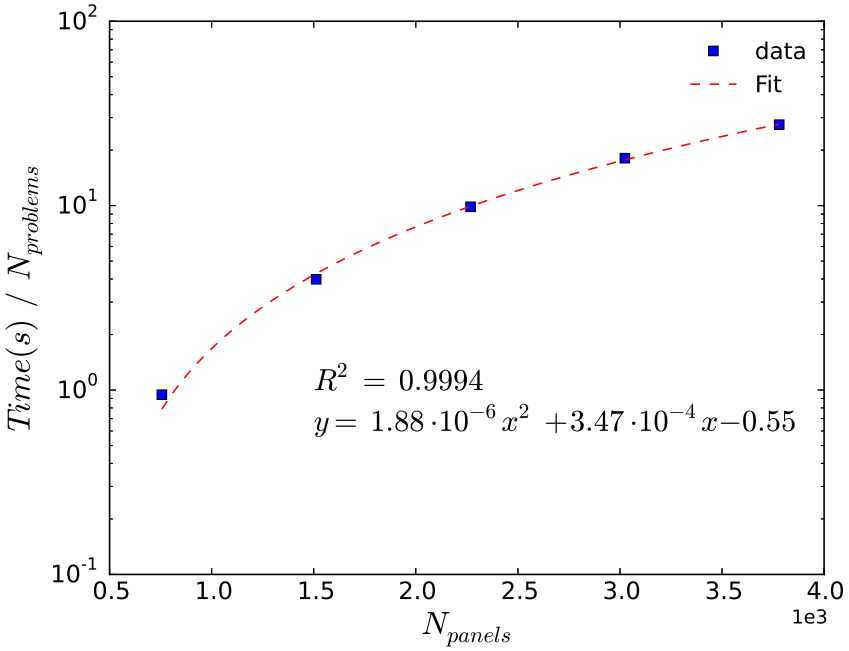

(a)

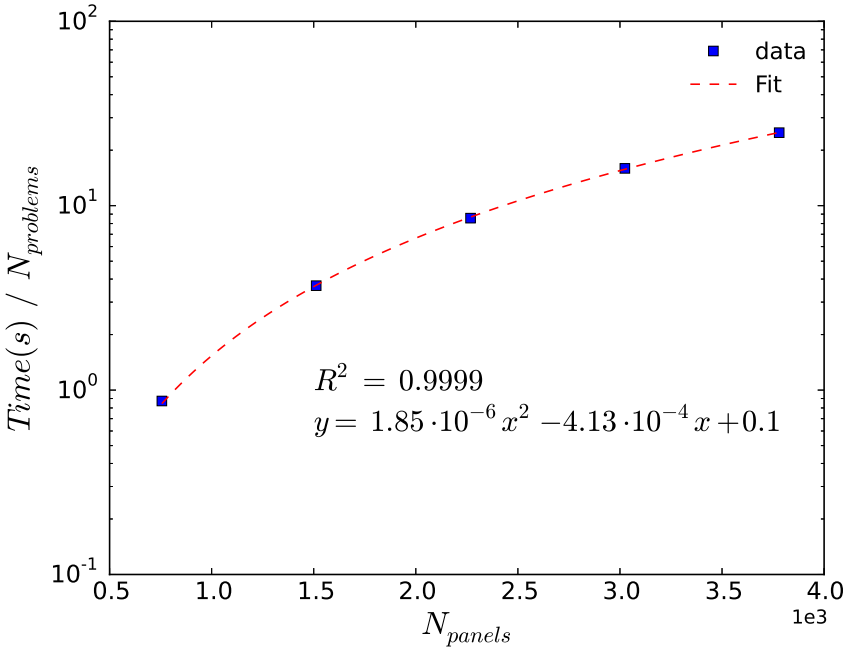

(b)

Figure 4.23: Curve fitting of the wall clock computational time of direct NEMOH simulations for both a truncated vertical cylinder *a*) and a flap-type converter *b*) shown in Figures 4.21a and 4.21b respectively.

4.4 Conclusions

4.4.1 Relationships for progressive terms

Simple relationships between the Force Transfer Matrix (FTM) and the Radiation Characteristics (RC), and between the radiation damping coefficients and the FTM were obtained following two different derivations. They extend the classical Haskind relations to the cylindrical wave field components. The first identity enables faster calculation of the RC, as it removes the need to solve any radiation problem or to numerically integrate the source strengths over the wetted surface of the body, as is required by the methodology of Goo and Yoshida (1990).

Numerical validations of the relationships for a truncated vertical circular cylinder were carried out. Very good agreement was observed between the FTM and radiation damping coefficients computed with NEMOH and the same quantities obtained from the RC and the FTM respectively by means of the new relationships derived.

The excitation force for a body in the array was expressed as a function of its RC and the scattering coefficients of a radiation multiple-scattering problem. In addition, the radiation damping coefficients for the bodies in an array have been related to both their RC and the scattering coefficients of a radiation problem. Numerical verifications of these identities were performed using the array of four truncated vertical circular cylinders studied by Siddorn and Eatock Taylor (2008). Good agreement has been obtained between their results, the standard calculation of both the excitation forces and the radiation damping coefficients using the IT with its associated hydrodynamic operators computed with NEMOH, and the same quantities calculated from both the RC and the scattering coefficients associated with a radiation problem.

The derived expressions were used to compute the separate contributions to the excitation force in surge and to the surge coupling radiation damping coefficients on a body in the array, from the body itself as if it was isolated, and from the hydrodynamic interactions with its neighbours. The effect of trapped modes at specific wavelengths, characterized by a large increase in the force on the body caused by hydrodynamic interactions, has been clearly observed, as expected.

It is beleived that the novel relationships derived herein can be used to speed up computation of the RC of the body, as well as to test the accuracy of the interaction theory implemented.

4.4.2 Influence of the evanescent terms

Radiation hydrodynamic coefficients computed with the IT by Kagemoto and Yue (1986) have been verified against direct BEM computations for a small array of two truncated vertical circular cylinders and a very good match of results has been observed. For closely spaced configurations, the effect of the hydrodynamic interactions on the radiation coefficients has been identified to be significant. In addition, the impact of the evanescent modes truncation on the added-mass coefficients has been shown. It has been found that the influence of the evanescent modes on their accuracy computed using the IT is strongly dependent on the separating distance between the bodies, on the mode of motion as well as on the frequency.

Finally, the free surface elevation of an array of four freely floating truncated vertical circular cylinders and cubes computed with the IT has been verified with direct BEM calculations. The effect of the evanescent modes truncation has been clearly shown to be significant only at the vicinity of the bodies.

4.4.3 Condition number

High condition numbers are directly related to precision losses and, therefore, special measures ought to be put in place to modify the terms responsible for the ill-conditioning. Bessel functions normalization has been found to be beneficial to reduce the system's scattering matrix condition number specially when the evanescent modes truncation is non-zero and when bodies are placed in close proximity.

4.4.4 Wall clock time

The time savings offered by the Direct Matrix Method interaction theory have been shown to be remarkable when compared to direct BEM solver simulations on a large number of bodies. Indeed, for a case study of 60 truncated vertical cylinders and flap-type converters the computational time of direct NEMOH calculations has been estimated as 124 and 119 days respectively in contrast with the 49 and 80 minutes of the IT with a truncation of zero evanescent modes. While BEM solvers are hampered by an increase of the number of bodies, computations with the IT are slowed down considerably when the number of evanescent modes used is incremented.

Chapter 5

Numerical modeling and optimization of a bottom-referenced heave-buoy WEC array

A great variety of technologies to extract power from ocean waves have been proposed, some of which are currently under development. These wave energy converters (WECs) may be classified by several methods (Falcão, 2010), for example on the basis of size: devices whose characteristic length is much smaller than the wave length of the incoming waves are referred to as point absorbers, and have been the object of numerous studies. Their responses are characterized by a resonant peak over a narrow band of frequencies of the incident wave spectra, and control strategies can be applied to increase their energy absorption (Falnes, 2001).

Another category, often referred to as multi-body WECs, consists of a group of multiple closely-spaced point absorbers attached to a common fixed or floating support structure. Within this category, several configurations have been proposed, including the FO^3 platform (Taghipour and Moan, 2008), the Manchester Bobber (Weller et al., 2010) and the Wavestar (Hansen and Kramer, 2011). The former two consist of a square lattice of floats linked to a common supporting structure through a Power Take-Off (PTO) system. In contrast, floats in the latter are distributed with a linear arrangement and connected to both sides of a fixed bridge structure through rigid arms.

Inspired by the FO^3 device, Garnaud and Mei (2009) analyzed the performance of compact square and circular arrays of cylindrical point absorbers and compared them

to a bigger float having an equivalent displacement. They found that, unlike the large buoy, the circular array of multiple point absorbers had good efficiency over a broad range of frequencies. They made use of the method of homogenization, which offers great savings in computational time, and is valid when both the device size and the separating distance between units is small in comparison to the incident wave length.

A different acceleration technique, a mode expansion method (Newman, 1994), was used by Taghipour and Moan (2008) to study the FO^3 device. They evaluated both the response of the floating rig supporting 21 floats and the wave energy absorption capabilities of the WEC. For this particular configuration, they found that the power produced was independent of the mean wave direction for short-crested ocean waves. In addition, they observed significant differences in power production between floats.

A comparison of two FO^3-type WECs, one with 21 aligned buoys and the other with a staggered grid configuration of twelve buoys, was performed by De Backer et al. (2010). Calculations were undertaken in the frequency domain and the hydrodynamic coefficients were calculated using the Boundary Element Method (BEM) code WAMIT. They observed that the 21-unit configuration was able to produce only 25% more power than the 12-unit configuration. A similar result was observed in experiments carried out by Garnaud and Mei (2009) in which an increase in the density of floats for tight configurations led to a relatively small increase in capture width. The work of De Backer et al. (2010) addressed the impact of constraints and several PTO optimization strategies. It was found that the former reduced the power production of the arrays whereas the application of individual optimization led to a significant increase in energy capture when compared to other less sophisticated strategies. The same conclusion was reached by Nambiar et al. (2015) after a study of three buoys of the Wavestar prototype that compared different types of resistive and reactive PTO control strategies using a dedicated time domain model including PTO damping force constraints.

Different versions of the Wavestar multi-body WEC device have been presented in Hansen et al. (2013). In this Chapter, as we wish to illustrate the interest of the Direct Matrix Method when dealing with very large groups of floating bodies, we choose the 60-float *SC-concept* as a working example. The objectives are i) to examine the power capture of a generic bottom-referenced heave-buoy array (BF-HBA) inspired by this WEC, and ii) to conduct an optimization of both its layout and the size of the floats.

The study is carried out in the frequency domain using linear potential theory. No constraints nor sophisticated Power Take-Off tuning strategies have been considered herein and, as in De Backer et al. (2010), the effect of waves diffracted by the sup-

porting piles of the structure has not been addressed. Therefore, results should be regarded as preliminary estimates of the power generation potential of this type of technology.

In the following sections, a detailed description of the system is provided and the numerical modeling in the frequency domain is detailed, with particular emphasis on the procedure used for efficient computation of the hydrodynamic coefficients of the floats in the array. Some results are then presented, detailing the response of both an individual and a small cluster of three floats. Following the analysis of individual units, relevant layout configurations derived from optimization studies on the reference 60-unit configuration are analyzed in detail. Finally, results concerning the impact of float size on power capture are presented.

5.1 Methodology

5.1.1 Description of the System

The bottom-referenced heave-buoy array WEC studied herein is composed of 60 hemispherical floats regularly distributed along both sides of each of the three arms of a fixed bridge structure. Each individual float is rigidly connected to an arm mounted on the supporting frame by means of a hinge joint. In our modeling, the hydraulic Power Take-Off (PTO), which transforms the rotation into electrical power in the real device, is modelled by a basic linear damper.

A global Cartesian reference system (X, Y, Z) is used to define the ambient incident wave propagation angle (β) with respect to the multi-body WEC. In addition, a local Cartesian reference system (x, y, z) centered at each float is used to redefine the incident wave angle with respect to each individual unit. Figure 5.1 shows a schematic of the system, and the main parameters are specified in Table 5.1.

5.1.2 Equation of Motion

Assuming the same harmonic time dependence as in (2.1.16) for the time-varying variables, the linear first-order equation of motion of a single hemispherical point absorber float in the frequency domain can be written as:

$$(J + A)\ddot{\gamma} + (B + B_{pto})\dot{\gamma} + K^h\gamma = M^{ex} \tag{5.1.1}$$

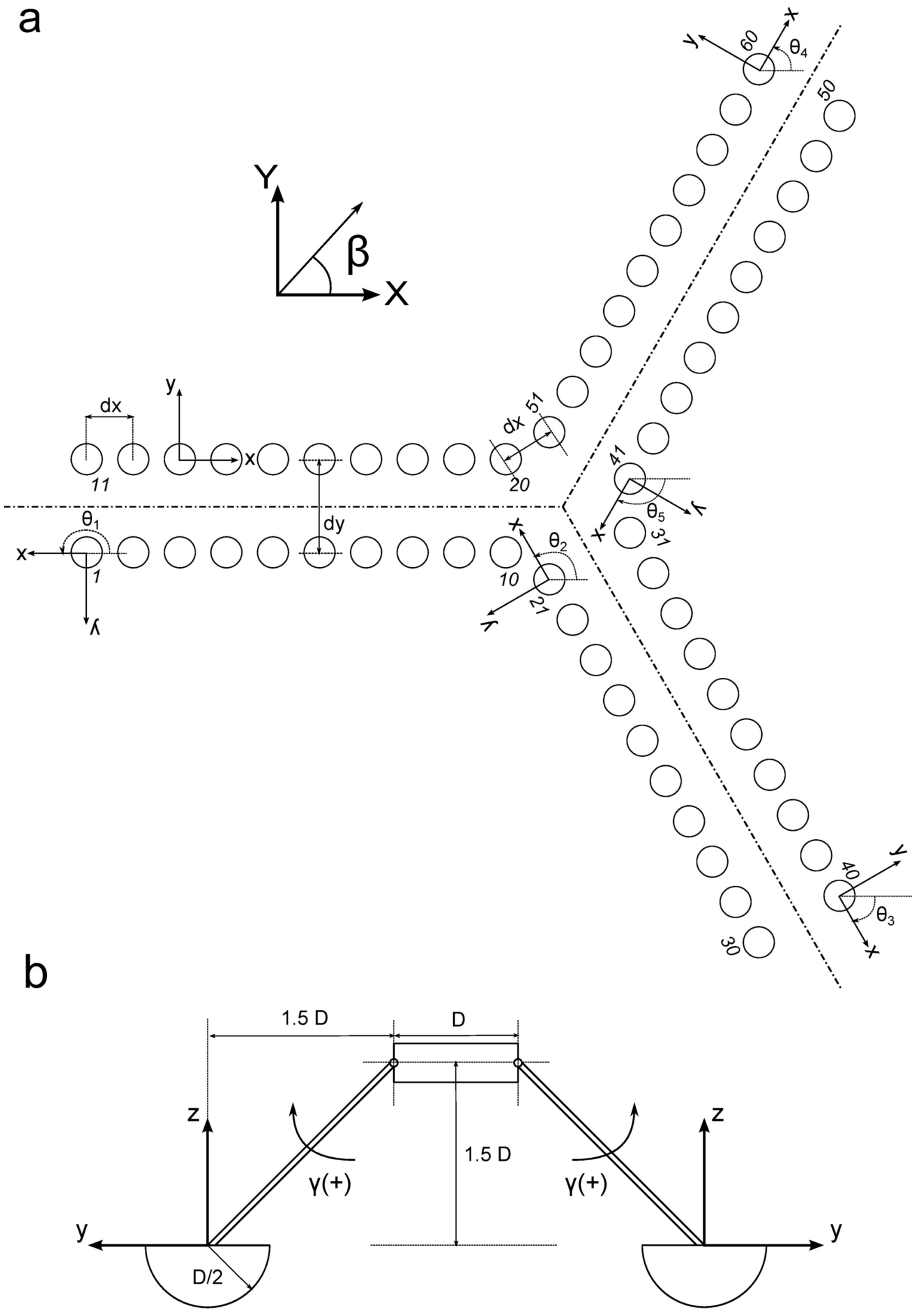

Figure 5.1: Top (a) and Side (b) schematic views of the bottom-referenced heave-buoy array Wave Energy Converter.

Parameter	Value
dx	$7.2\ m$
dy	$24\ m$
D	$6\ m$
γ_{max}	$0.28\ rad$
θ_1	$\pi\, rad$
θ_2	$2\pi/3 rad$
θ_3	$-\pi/3\, rad$
θ_4	$\pi/3\, rad$
θ_5	$-2\pi/3 rad$

Table 5.1: Main parameters of the bottom-referenced heave-buoy array Wave Energy Converter.

where γ is the angle of rotation along the bearing axis, J the inertia of the float, A and B the radiation hydrodynamic coefficients of added-inertia and damping moment respectively, B_{pto} the damping moment of the PTO system, K^h the hydrostatic stiffness and M^{ex} the excitation moment.

The radiation hydrodynamic coefficients of the float can be computed either as a result of the combination of two translations and one rotation of the body with respect to its center of rotation, or from single rotation along the bearing axis. In this work, the latter strategy has been used and the normal velocities of the radiation problem have been set accordingly.

Assuming that the rigid arm connecting the float to the bearing is weightless, the hydrostatic stiffness coefficient K^h expressed with respect to the axis of rotation can be computed as (Babarit et al., 2012b):

$$K^h = K_B^{h,roll} + \rho g V(z_B - z_A) - mg(z_G - z_A) + K_B^{h,heave}(y_B - y_A)^2 \tag{5.1.2}$$

where $K_B^{h,roll}$ and $K_B^{h,heave}$ are the hydrostatic stiffness related to the roll and heave motions, respectively, along the axis passing through the center of buoyancy of the float, ρ the water density, g the gravity acceleration, V the volume of the float, (x_B, y_B, z_B) the coordinates of the center of buoyancy, (x_G, y_G, z_G) the coordinates of the center of gravity and (x_A, y_A, z_A) the coordinates of the bearing. Table 5.2 summarizes the values of the parameters for an hemispheric float of the configuration shown in Figure 5.1.

Equation (5.1.1) can be generalized to include the motion of all the multi-body

Parameter	Expression	Value
V	$2/3\pi\frac{D^3}{8}$	56.55 m^3
$K_B^{h,heave}$	$\rho g\pi\frac{D^2}{4}$	284305 $kg\cdot m/s^2$
$K_B^{h,roll}$	$\rho g\pi 6/24\frac{R^4}{16}$	639687 $kg\cdot m/s^2$
(x^G, y^G, z^G)	$(0, 0, -\frac{3}{8}\frac{D}{2})$	(0,0,-1.125) m
(x^B, y^B, z^B)	$(0, 0, -\frac{3}{8}\frac{D}{2})$	(0,0,-1.125) m
(x^A, y^A, z^A)	$(0, -1.5D, 1.5D)$	(0,-9,9) m
J	$\frac{83}{320}\rho V\frac{D^2}{4} + \rho V d^2$	$1.08\cdot 10^7$ $kg\cdot m^2$
d	$\sqrt{(1.5D)^2 + (1.5D + \frac{3}{8}\frac{D}{2})^2}$	13.55 m

Table 5.2: Main parameters of an hemispheric float.

WEC floats:

$$(\mathbf{J} + \mathbf{A})\ddot{\Gamma} + (\mathbf{B} + \mathbf{B}_{pto})\dot{\Gamma} + \mathbf{K}^h\Gamma = \mathbf{M}^{ex} \tag{5.1.3}$$

where Γ is the vector of rotations, $\mathbf{J}$ is the diagonal inertia matrix of the system, $\mathbf{A}$ and $\mathbf{B}$ are the matrices of hydrodynamic added-inertia and radiation damping moment coefficients respectively, $\mathbf{B}_{pto}$ is the diagonal matrix of PTO damping moments, $\mathbf{K}^h$ the matrix of hydrostatic stiffness and $\mathbf{M}^{ex}$ the vector of excitation moments. All the matrices have dimensions $(N_b \times N_b)$, where N_b is the total number of floats.

5.1.3 Computation of the Hydrodynamic Coefficients

The use of standard Boundary Element Method (BEM) solvers to evaluate the hydrodynamic coefficient matrices for large arrays of bodies, such as the bottom-fixed heave-buoy array WEC, is associated with very high computational costs. This hampers analysis of such systems and precludes the use of layout optimization, which requires constant recomputation of the hydrodynamic coefficients to account for modifications to the position of the floats.

To avoid the limitations imposed by the use of standard BEM solvers in the current study, the hydrodynamic coefficients were evaluated using the implementation of the Direct Matrix Method Interaction Theory (IT) by Kagemoto and Yue (1986), described in Chapter 2. As opposed to standard BEM solvers, in which the multiple-scattering problem is solved by treating all the bodies in the array simultaneously, in the Direct Matrix Method the diffraction/radiation boundary conditions are first imposed on an isolated float and then combined with an interaction theory to take into account the effect of the neighbouring devices. As in the present case, where all the floats have the same geometry, the boundary value problem (BVP) needs to be solved only once, thus leading to an additional gain in computational speed.

The transfer from the diffraction/radiation problem of an isolated geometry to the BVP of the whole array is achieved by expressing the wave fields in a base of partial cylindrical wave functions. This enables the waves diffracted and radiated by a float to be mathematically characterized in terms of two hydrodynamic operators known as Diffraction Transfer Matrix (DTM) and Radiation Characteristics (RC). The advantage of this transformation is that the number of cylindrical modes required to represent the perturbation of the wave field by an arbitrary geometry is significantly smaller than the number of panels required to discretize its wetted surface. The reduction in the number of unknowns associated to an individual float enables a drastic reduction of the computational time for the whole array, as shown in section 5.2.4.

5.1.4 Performance evaluation

The total annual power generated by a float j in the multi-body WEC (P_y^j) can be computed by summing up the contribution from each of the wave climate sea states as:

$$P_y^j = \sum_{i=1}^{N_s} O_i(H_s, T_p) \cdot P_i^j(H_s, T_p) \tag{5.1.4}$$

where P_y^j is the total annual power produced by float j, N_s is the number of sea states considered, (H_s, T_p) are the significant wave height and the peak period of the sea state, O_i its probability of occurrence and P_i^j the power produced by unit j in the ith sea state.

Under the assumptions of linear potential flow theory the power generated by a float in a given sea state can be evaluated using the following expression:

$$P_i^j(H_s, T_p) = \int_0^{2\pi} \int_0^{\infty} 2\, S_i(\omega, \beta) p^j(\omega, \beta)\, d\omega d\beta \tag{5.1.5}$$

where $S_i(\omega, \theta)$ is the directional wave spectrum and $p^j(\omega, \theta)$ the power function of body j defined as:

$$p^j(\omega, \beta) = \frac{1}{2} B_{pto} \omega^2 \Gamma^j(\omega, \beta)^2 \tag{5.1.6}$$

where B_{pto} is the Power Take-Off (PTO) damping and $\Gamma^j(\omega, \beta)$ is the response amplitude operator (RAO) of the productive degree of freedom of the hemispheric float obtained by solving the equation of motion of the system (5.1.3).

The total annual power (P_y) produced by all units is obtained simply as:

$$P_y = \sum_{j=1}^{N_b} P_y^j \tag{5.1.7}$$

The effect of the hydrodynamic interactions among floats in the multi-body WEC on the power generation is quantified using the interaction factor, generally referred to as q-factor, defined as the ratio between the power produced by the float in the array and the power it would produce if isolated:

$$q_i^j = \frac{P_i^j}{P_i^{j,\,isol}} \tag{5.1.8}$$

where q_i^j is the interaction factor of float j in the i^{th} sea state and $P_i^{j,isol}$ the power that an isolated float j would produce in the ith sea state.

The significant amplitude of rotation of float j, γ_s^j, can be computed as (De Backer et al., 2010):

$$\gamma_s = 2\sqrt{\int_0^\infty \int_0^{2\pi} S_\gamma^j(f,\beta) df d\beta} \tag{5.1.9}$$

where $S_\gamma^j(f,\beta)$ is the rotation spectrum of float j evaluated as:

$$S_\gamma^j(f,\beta) = \frac{\Gamma^j(f,\beta)^2}{2\Delta f \Delta\beta} \tag{5.1.10}$$

5.1.5 Wave Climate

A total of eleven sea states (Table 5.3) representing 80% of the wave conditions at Hanstholm (Hansen and Kramer, 2011) were used for the computations. It was considered that the other 20% fall outside of the range of operation of the multi-body WEC, i.e. production is stopped when $H_s < 0.75m$ and protection mode is activated for cases with $H_s > 2.75m$.

The wave field was modeled as a two-dimensional frequency-direction Bretschneider spectrum with a generalized cosine angular spreading function as defined in Holthuijsen (2010):

$$S(f,\,\theta) = \frac{A}{f^5} e^{-\frac{B}{f^4}} C\,\cos^m(\beta - \bar{\beta}) \tag{5.1.11}$$

Seastate	$H_s(m)$	$T_p(s)$	$Prob(\%)$
1	0.75	4.10	19.2
2	0.75	5.27	11.4
3	0.75	6.44	2.21
4	1.25	4.10	6.84
5	1.25	5.27	13.0
6	1.25	6.44	2.96
7	1.75	5.27	9.58
8	1.75	6.44	3.05
9	2.25	5.27	3.34
10	2.25	6.44	4.6
11	2.75	6.44	3.89

Table 5.3: Wave climate series used in the simulations.

where $\omega = 2\pi f$ and constants A, B and C are given by:

$$A = \frac{5}{16}\frac{H_s^2}{T_p^4}; \quad B = \frac{5}{4}\frac{1}{T_p^4}; \quad C = \frac{\Gamma(\frac{1}{2}m+1)}{\Gamma(\frac{1}{2}m+\frac{1}{2})\sqrt{\pi}} \tag{5.1.12}$$

The coefficient of the angular spreading function has been set as $m = 20$, a value representative of wind seas. The spectrum was discretized using 30 frequencies and five directions making a total of 150 wave components per sea state. The water depth was set to 20m.

5.2 Results and Discussion

5.2.1 Individual float response

The solution to the equation of motion (5.1.1) of an individual articulated hemispherical float is shown in Figure 5.2 together with the power extracted, the latter computed using equation (5.1.6). The response of the float shows the typical features of a point absorber, namely a steady response at low frequencies, an increased motion at the resonant frequency which is greatly reduced when reaching the higher frequency zone. A particularity of the arm-float system studied herein is that, in spite of the axisymmetry of the float, its response is highly dependent on the incident angle of the waves. This is because the components of the excitation force in both y and z directions contribute to the moment along the axis of rotation (x). An incident wave with $\beta = 90°$ will generate y and z force components which will produce rotation moments acting in the same direction. Contrarily, at $\beta = 270°$ the rotation moments will act in opposite

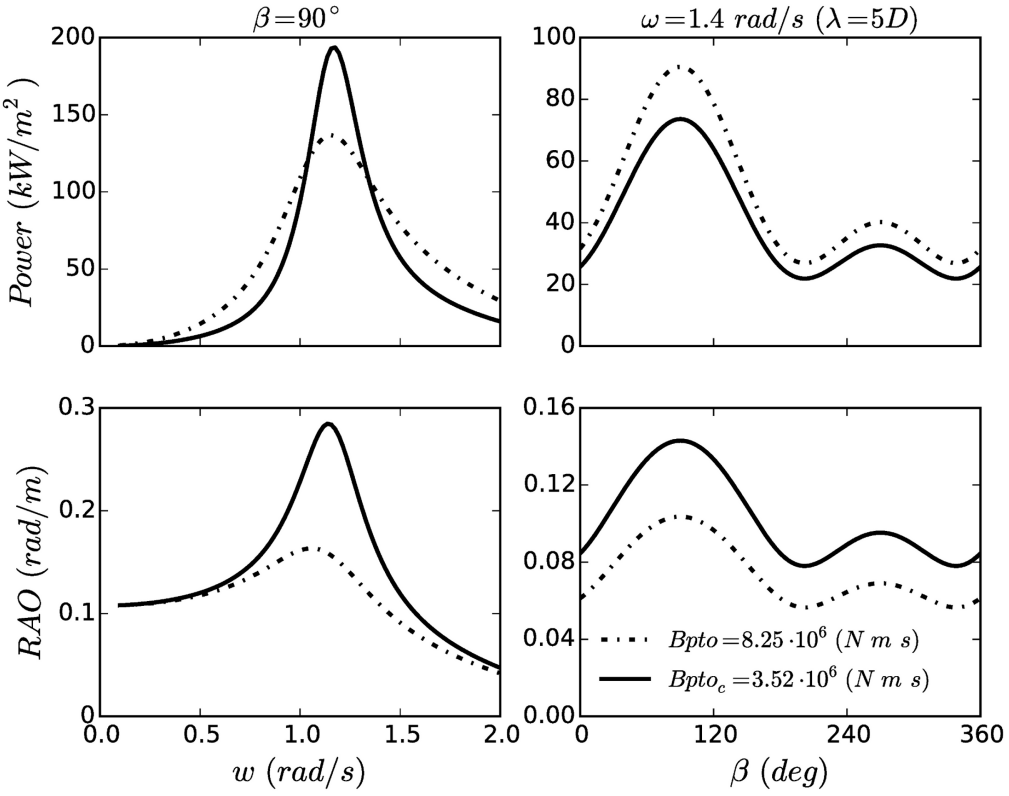

Figure 5.2: Response Amplitude Operator (RAO) and power function of an individual isolated hemispherical float as a function of the Power Take-Off damping (B_{pto}) and for both a range of incoming wave frequencies and directions.

directions. From Figure 5.2 it can be observed that the maximum response is achieved for an incident wave angle of $\beta = 90°$, which corresponds to the situation where the moments of rotation generated by the forces in y and z direction are aligned. The incident angle for which the minimum response occurs also depends on the balance between the magnitudes of the y and z forces.

Both the power and the response of the float are shown for two different values of B_{pto}, indicated as $Bpto_c$ and $Bpto$ on the graphs. The former is the value that maximises the response allowed (γ_{max}) at the resonant frequency and for an incident wave angle of $\beta = 90°$. The latter has been tuned to reduce the float motion to 20% of the critical value at the same conditions.

5.2.2 Three-float cluster

The presence of adjacent units affects the hydrodynamic forces acting on a float and, as a consequence, its response is different to that where it is in isolation. This is illustrated in Figure 5.3b which shows a comparison between, on the one hand, the response of an isolated float under the action of regular waves traveling at $\beta = 90°$ (the same displayed in section 5.2.1 with damping B_{pto}) and; on the other hand, the response of the float when located in the middle of a three-unit group (Figure 5.3a) representing part of the bottom-fixed heave-buoy array WEC. It can be observed that the peak of the rotation along the bearing axis is reduced and shifted towards lower frequencies. As mentioned in Nambiar et al. (2015), the close proximity of the floats means that hydrodynamic interactions are expected to be very important.

The motion of float-2 was obtained by solving equation (5.1.3), for which the matrices of hydrodynamic coefficients were computed using both the standard BEM solver NEMOH (Babarit and Delhommeau, 2015) and the IT. Figure 5.3c compares the percentage difference between the amplitude of the float response obtained from NEMOH (used as reference) and from the IT using different evanescent mode truncation L. As shown in section 4.3.2, special attention to this truncation is required for cases where bodies are placed in close proximity. Despite being separated by a small distance relative to their radius, the maximum discrepancy of the response amplitude for float-2 when the evanescent mode truncation is set to zero is only of 2.5% (this remarkable finding is discussed in detail in Appendix J). A similar result was obtained by Chakrabarti (2001) who observed no significant influence of the evanescent mode truncation on the forces acting on two floating modules. Only a small effect on the motions was reported.

The differences in Figure 5.3c are highly frequency-dependent and, although not shown here, they also vary as a function of the incident wave propagation angle. It is not clear how to extrapolate from this analysis of three floats under regular waves to draw conclusions about the influence of the evanescent mode truncation in a 60-float case study with irregular sea state; therefore, additional sensitivity studies were performed (detailed in section 5.2.3).

5.2.3 60-float Configuration

This section presents a series of simulations of the bottom-referenced heave-buoy array WEC (Figure 5.1) installed in a location with the wave climate detailed in Table 5.3. Both the annual power production (P_y) of the multi-body WEC and the performance

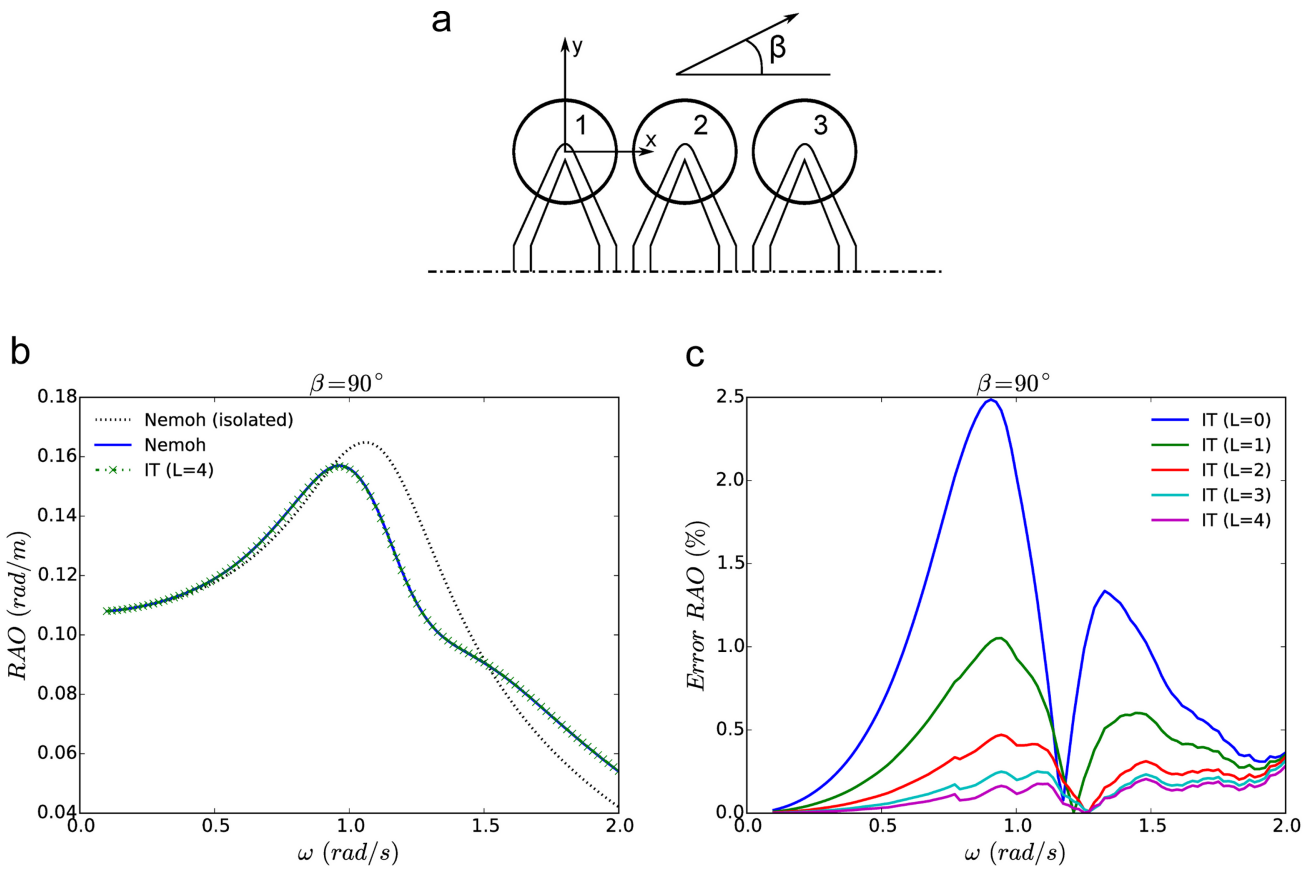

Figure 5.3: (a) Top view of a section of a three-float WEC; (b) Comparison of the Response Amplitude Operator (RAO) of float 2 computed using both a direct BEM calculation (both when isolated and in array) and with the Direct Matrix Method interaction theory (IT) using 4 evanescent modes (L) and a $\beta = 90°$ wave incidence; (c) relative difference between the (RAO) of float 2 computed using both a direct BEM calculation and with the Direct Matrix Method interaction theory (IT) for different values of the evanescent modes truncation (L) and a wave incidence of $\beta = 90°$.

of each individual float were evaluated, the latter defined based on its interaction factor as well as on its significant motion amplitude. In addition, the free-surface disturbance coefficient, defined as the ratio between the actual and the undisturbed incident significant wave height, was calculated to allow for a visualization of the wave field.

For the sake of simplicity, the same value of PTO damping moment was used for all units and all given sea states, and was chosen in such a way as to maximize the annual power production of the WEC at the reference site. This strategy is referred to as diagonal optimization De Backer et al. (2010) or scalar optimization (Ricci et al., 2007). It is worth noting that other more sophisticated optimization strategies out of scope in this study, as shown for instance by De Backer et al. (2010) and Nambiar et al. (2015), could improve the energy yield of the multi-body WEC studied here. For example, for a realistic wave climate, De Backer et al. (2010) observed energy absorption increases of 16% and 18% for each unit of a 12-buoy and 21-buoy multi-body WEC respectively when the control parameters were optimized individually and not diagonally.

Figure 5.4 shows both the interaction factor of each float and the free-surface disturbance coefficient (H_s/H_s^I) for the most probable sea state ($H_s = 0.75m$, $T_p = 4s$). Results are presented for 2 main propagation directions ($\beta = 0$ and $\beta = \pi/3$) of the incident wave spectrum. For the former, it can be observed that the interaction factor of the front floats (f_1 and f_{11}) is significantly greater than 1 and gradually decreases as waves travel along the units in branches b_1^{10} and b_{11}^{20}. At floats f_{10} and f_{20}, behind the wake produced by the preceding units, most of the available energy has been captured and the value of the interaction factor is very low. The same occurs at floats f_{21} and f_{51}. An increase in interaction factor is only observed when moving away from the horizontal axis of symmetry of the WEC and towards the end of branches b_{51}^{60} and b_{21}^{30}. Notwithstanding, the values remain significantly lower than 1. It is in this part of the domain where the highest disturbance coefficients are observed. In contrast, the wake behind the floats significantly affects the units at branches b_{31}^{40} and b_{41}^{50} which have interaction factors close to zero.

For $\beta = \pi/3$ it can be observed that floats in branches b_1^{10} and b_{21}^{30} benefit from higher interaction factors than elsewhere, although they do not exceed unity. In addition, a region with high disturbance coefficients can be clearly distinguished in front of the device, as opposed to the wake area behind characterized by a reduced wave elevation. Only floats $f_{11} - f_{12}$ and $f_{39} - f_{40}$ are not shadowed by the units in the front branches for this particular alignment of the incident wave field and the WEC.

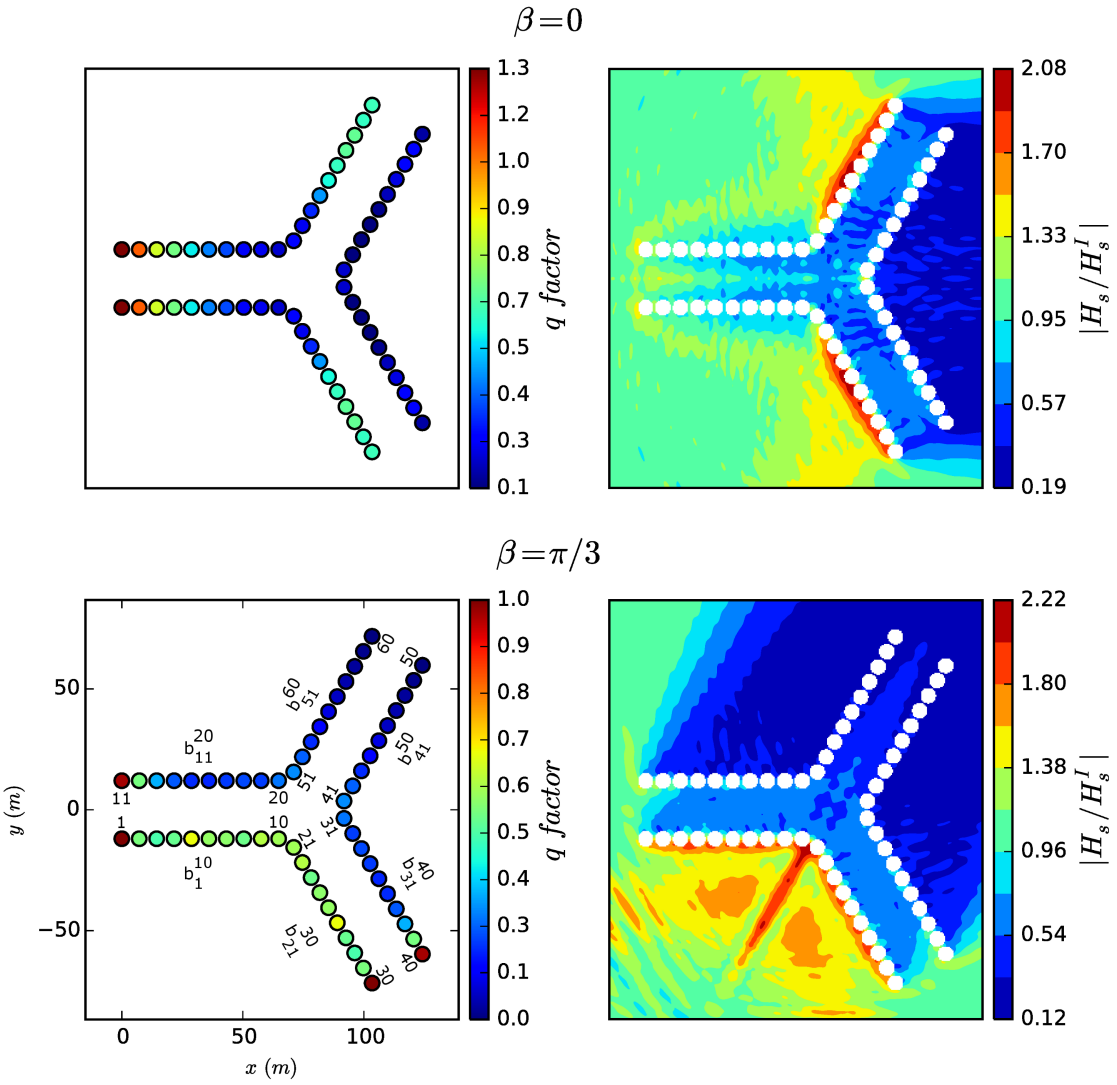

Figure 5.4: Float interaction factors (q-factor) of the bottom-fixed heave-buoy array WEC and disturbance coefficient (H_s/H_s^I) of the wave field for a sea state with ($H_s = 0.75m$, $T_p = 4s$) and two mean propagation directions (0 and $\pi/3\,rad$) of the incident wave spectra.

Truncation (n)	0	1	2
$\max(\text{abs}[(P_n^i - P_2^i)/P_2^i])$ (%)	0.55	0.41	Reference

Table 5.4: Influence of the evanescent modes truncation on the power generated.

The pattern of interaction factor among the floats is similar for all sea states, with the only significant difference being an increase in the power produced by the units in branches b_{11}^{20} and b_{31}^{40} for wave conditions with longer peak periods propagating with a main direction $\beta = \pi/3$. As the B_{pto} damping moment (identically applied to all units) was optimized to maximize the annual power extracted, the interaction factors and the significant motions are closely related. From the left column of Figure 5.7, which shows the significant motions of each float for the most energetic sea state ($H_s = 2.75m$, $T_p = 6.44s$), it can be noted that floats in branches b_{11}^{20} - b_{31}^{40} undergo motions on the same order of magnitude as the ones in branches b_1^{10} - b_{21}^{30}. In contrast, for $\beta = 0$ the pattern observed is similar to that for the interaction factors shown in Figure 5.4. Assuming the motions of the floats are governed by a Rayleigh distribution, as used in De Backer et al. (2010), and assuming the maximum significant motion to be $0.17rad$, it can be predicted that the design condition γ_{max} prescribed in Table 5.1 will be exceeded $\sim 25\%$ of the time when the WEC operates in the most energetic sea state. This point is further investigated in section 5.2.6.

The main findings from a sensitivity study of the impact of the evanescent mode truncation on the annual power production of the bottom-fixed heave-buoy array WEC are summarized in Table 5.4. The greatest discrepancy in power extracted from a sea state, when computed using 2 evanescent modes and without accounting for them, is only 0.55%. As the difference is not significant, and given that the lower the truncation used the higher the computational speed of the IT method, the evanescent modes were dispensed with in the calculations presented in the following sections. As shown in section 4.3.2, calculations of free surface elevation using zero-truncated IT display inaccuracies only in close proximity to the bodies. However, they are not discernible to the naked eye, and are included here for qualitative purposes only.

5.2.4 Power versus Number of Floats

The underproduction of the majority of the multi-body WEC floats, described in the preceding section, suggests that layout modifications may improve the yield of individual units. The strategy adopted here consists of successively increasing the number of floats on each branch from two to the initial ten, while keeping them

equally distributed along both sides of the distinctive fixed three-arm bridge structure. At each step, the separating distance between floats was optimized. A minimum and maximum separating distance were also determined: the minimum distance being $7.2m$ - the separating distance between floats for the original 60-unit WEC - and the maximum distance being the greatest separation possible without exceeding the footprint of the original WEC. The value of the PTO damping moment (B_{pto}) used in the preceding section was preserved, and was the same for all units. As shown in section 5.2.6, this parameter does not have a significant effect on the results.

Figure 5.5 shows the results of the optimization process, i.e. the annual power produced by each configuration and the separating distance between units, for the two main propagation directions of the incident wave spectra. With the exception of the 12-float configuration, average annual power is slightly greater when $\beta = \pi/3$; for the 48-float configuration, the difference is only 2.6%. However, for both values of β the change in average annual power as a function of number of floats (N) follows a similar trend: it increases linearly for $N \leq 30$; continues to increase nonlinearly until an inflection point is reached at $N = 48$; then decreases towards the average anual power produced by the initial 60-float WEC configuration studied in the preceding section.

For both main propagation directions of the incident wave spectra (β), the optimal separating distance for the 12 and 18-float configurations falls within the bounds imposed, although it is much closer to the upper limit than to the lower. This is also true for the 24-float configuration when $\beta = 0$. For all other cases, the optimal distance is the upper limit, which decreases as the number of units increases until merging with the separating distance ($7.2m$) of the 60-float WEC.

The above observations of average annual power and separating distance clearly show that increasing the number (and hence density) of floats in this particular three-arm structure layout has diminishing return in terms of power production. Indeed, a remarkable result is that the same annual power can be obtained with a 60-float and 36-float configuration, the latter being studied in more detail in the following section. Obviously, this has important implications with respect to the cost of the WEC and the LCOE (levelized cost of energy).

These results are in line with observations by De Backer et al. (2010) who showed differences of only 25% in annual power production between two multi-body WECs of 21 and 12 floats. However, the size of the floats and their arrangement were not the same for both devices.

Table 5.5 compares the wall clock execution time required to obtain the results in

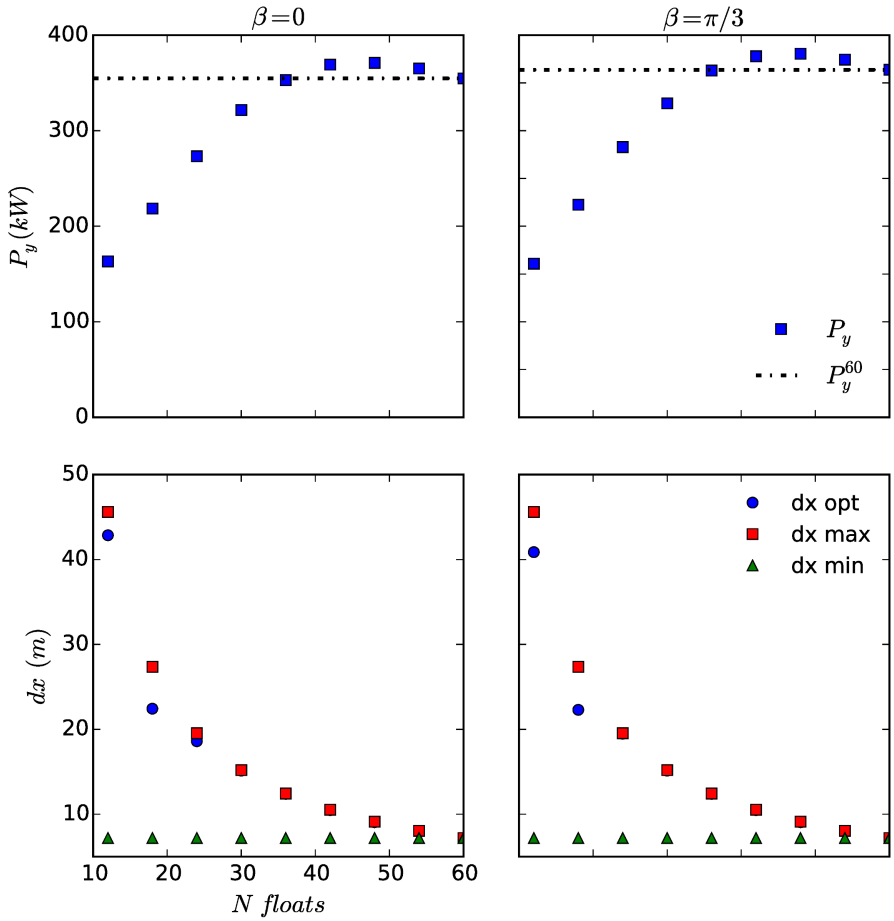

Figure 5.5: Annual power (P_y) and separating distance between floats (dx) as a function of the number of units used in the bottom-referenced heave-buoy array WEC for two main propagation directions of the incident wave spectra. The annual power has been computed using the optimized separating distance ($dx\,opt$) between floats for each configuration comprised between the limits ($dx\,max$) and ($dx\,min$).

N bodies	N function evaluations	IT (hours)	Direct NEMOH (years)
12	10	0.6	0.1
18	10	1.3	0.3
24	11	2.7	0.9
30	10	3.7	1.6
36	10	5.1	2.7
42	9	6.4	3.8
48	7	6.6	4.4
54	6	7.3	5.4
60	1	1.7	1.2

Table 5.5: Comparison of wall clock execution time between the IT and direct NEMOH calculations for each of the optimized configurations in Figure 5.5. The execution time of the direct BEM simulations has been estimated following the procedure detailed in section 4.3.4.

Figure 5.5 between the IT and standard direct NEMOH BEM calculations. Values are presented based on computations on a Dell[1] machine with two Intel(R) Xeon(R)[2] 64-bit 2.27GHz processors and 8GB random access memory running the Microsoft Windows 7 Professional [3] operating system. The computational advantage of using the IT over standard BEM solvers is clear.

5.2.5 36-float Configuration

In this section, details of the 36-float bottom-referenced heave-buoy array WEC simulations are given. Figure 5.6 shows the interaction factor for each float and the free-surface disturbance coefficient for the most probable sea state ($H_s = 0.75m$, $T_p = 4s$). Results are presented for the two main propagation directions ($\beta = 0$ and $\pi/3$) of the incident wave spectrum considered. For the former, it can be observed that the interaction factor of floats f_1 and f_7 is significantly higher than unity and gradually decreases as waves propagate along branches b_1^6 and b_7^{12}. At floats f_6 and f_{12}, shadowed by the units up front, most of the available energy has been absorbed and the values of the interaction factor are very low. The decreasing trend is reversed at branches b_{31}^{36} and b_{13}^{18}, where the interaction factor gradually increases from low values at units f_{13} and f_{31} until reaching levels as high as at the front of branches b_1^6 and b_7^{12} for floats f_{29} and f_{35}. This differs from the 60-unit configuration, whose floats at this part of the multi-body WEC had interaction factors significantly less than one (Figure 5.4).

[1]Dell is a registered trademark of Dell, Inc.
[2]Intel Xeon is a registered trademark of Intel Corp.
[3]Microsoft Windows 7 Professional is a registered trademark of Microsoft Corp.

The wake behind branches b_1^6 and b_7^{12}, observed to be a region of low disturbance coefficient, diminishes the power production of floats in b_{25}^{30} and b_{19}^{24} close to the horizontal axis of symmetry of the device. However, it is higher than for the 60-unit case. The interaction factor increases at the ends of branches b_{25}^{30} and b_{19}^{24} which benefit from a smaller shadowing effect.

For $\beta = \pi/3$, similar trend is observed as in the 60-float configuration, i.e. floats in branches b_1^6 and b_{13}^{18} have interaction factors significantly higher than the rest. However, in this case they are all greater than unity. In addition, floats in branches b_7^{12} and b_{19}^{24} are less shadowed by units in b_1^6 and b_{13}^{18}. Disturbance coefficients close to unity are observed in this area due to both the reduced number of units and increased spacing between them. In contrast, an area of wave concentration can be distinguished in front of the device as opposed to a region of wave attenuation behind. The range of disturbance coefficients is significantly lower for the 36-float configuration than for the 60-unit tight cluster as the structure is more "transparent" to the incident waves.

As for the 60-float configuration, the pattern of interaction factors among the floats is similar for all sea states, with the only significant difference being an increase in power produced by the units in branches b_7^{12} and b_{19}^{24} for wave conditions with longer peak periods propagating with main direction $\beta = \pi/3$. As mentioned in section 5.2.3, the interaction factors and the significant motions are closely related. From the right column of Figure 5.7, which shows the significant motions of each float for the most energetic sea state ($H_s = 2.75m$, $T_p = 6.44s$), it can be observed that the significant motions of floats in branches b_7^{12} and b_{19}^{24} are of the same order of magnitude as those in b_1^6 and b_{13}^{18}. In contrast, for $\beta = 0$ the pattern of significant motions is similar to that of the interaction factors.

For both the 60-float and the 36-float configurations, the highest significant motion is found to be $\gamma_s = 0.17$ rad (9.74 deg). This indicates that the similar average annual power generated by both configurations is not due to the fact that the 36-float WEC undergoes significantly higher motions than the 60-float WEC. In addition, if the float motions are assumed to be governed by a Rayleigh distribution, as in section 5.2.3, it can be predicted that the design condition γ_{max} prescribed in Table 5.1 will be exceeded 25% of the time when the 36-float WEC operates in the most energetic sea state - similar to the case of the 60-float WEC.

5.2.6 Radius optimization

In section 5.2.4, the effect of the number of floats on the annual power production of the three-arm bottom-referenced heave-buoy array WEC was inspected. The 36-float

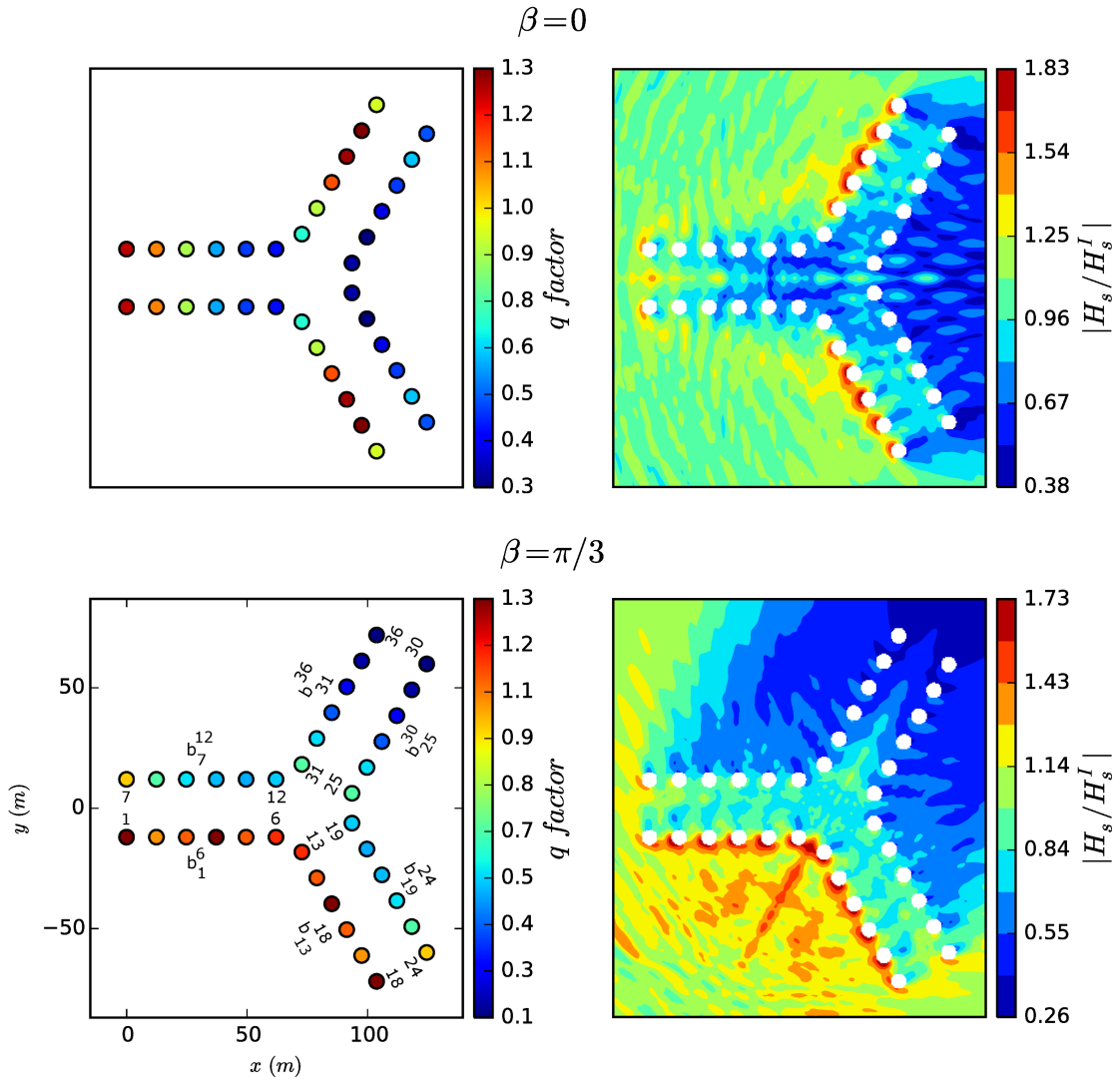

Figure 5.6: Float interaction factors (q-factor) of the 36-unit bottom-referenced heave-buoy array WEC and disturbance coefficient (H_s/H_s^I) of the wave field for a sea state with ($H_s = 0.75m$, $T_p = 4s$) and two mean propagation directions (0 and $\pi/3\,rad$) of the incident wave spectra.

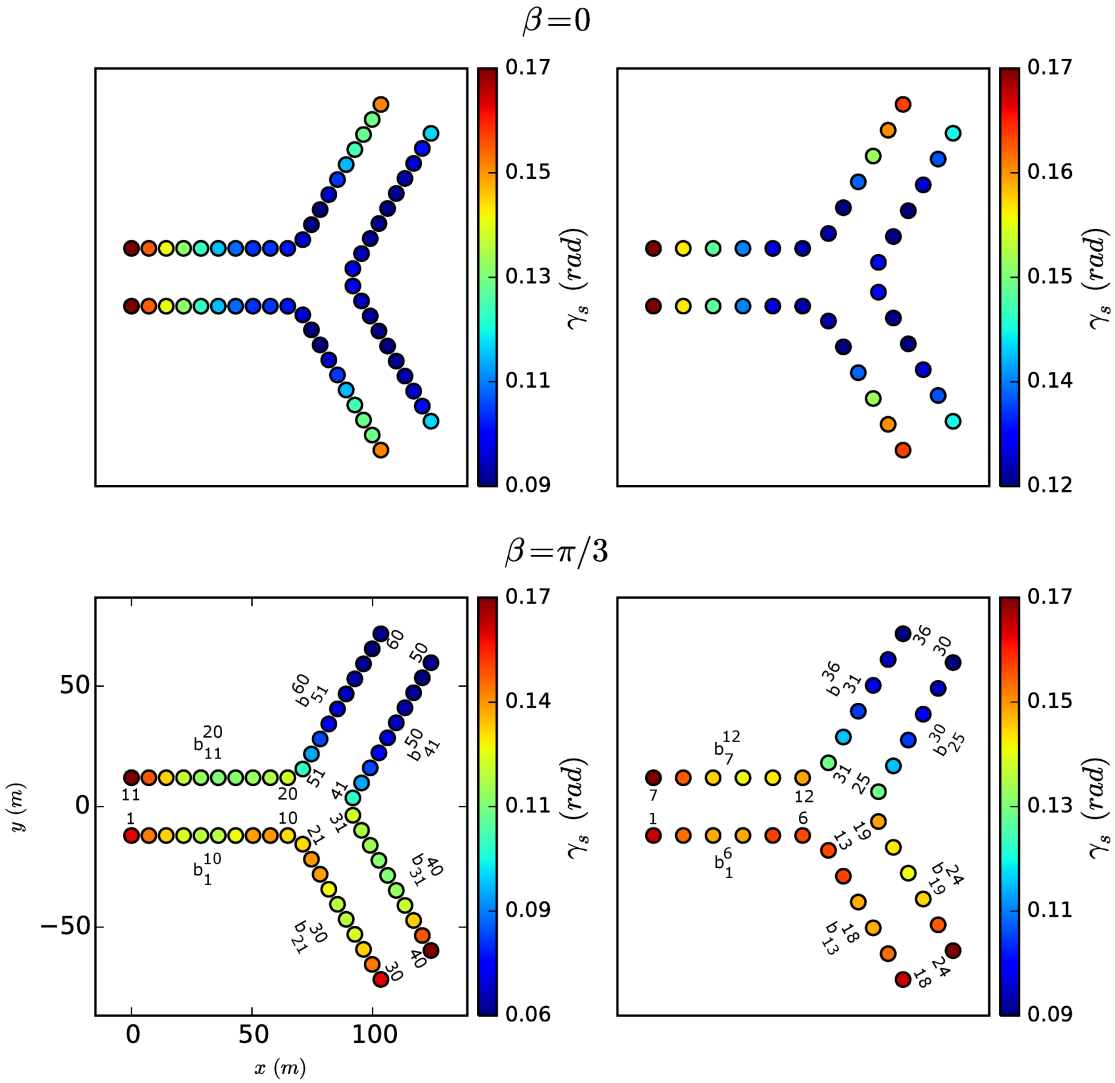

Figure 5.7: Float significant motions (γ_s) of the 60 and 36-unit bottom-referenced heave-buoy array WEC for the sea state with ($H_s = 2.75m$, $T_p = 6.44s$) and two mean propagation directions (0 and $\pi/3\,rad$) of the incident wave spectra.

configuration analyzed in the preceding section was found to generate as much power as the initial 60-float WEC with the same float size. In this section, the impact of float size on the total power output of the 36-unit configuration is investigated. The procedure adopted consists of gradually increasing the radius of the hemispheres from $2m$ to $5.5m$, the latter being the value that assures that the minimum edge-to-edge distance between floats is always greater than in the 60-float configuration. For each radius, the value of the PTO damping moment (B_{pto}), equally applied to all the floats and sea states, is optimized to maximize the annual power output.

Figure 5.8 shows the annual power (P_y^{36}) and the PTO damping moment optimized for each hemisphere radius ($B^r_{pto,36}$). In addition, the annual power computed with the PTO damping moment used in section 5.2.3, which optimizes the power generated by the 60-float configuration ($B^{r=3m}_{pto,60}$), is provided for comparison. Results are shown for the two main propagation directions (β) of the incident wave spectrum.

Average annual power is observed to be a concave function of hemisphere radius, with a global maximum observed at $r = 3.5$m for both values of β, using the PTO damping moment ($B^r_{pto,36}$) optimized for each float size. The value is 4.6% higher for $\beta = \pi/3$ than for $\beta = 0$. A remarkable result is that almost the same amount of power is produced for configurations with floats of radius $3m$ or $4.5m$, the difference between them being of only 2.3% and 1.4% for $\beta = 0$ and $\pi/3$ respectively. Using the PTO damping moment optimized for the 60-float configuration ($B^{r=3m}_{pto,60}$), a similar concave function is observed; however, the slope of the increasing and decreasing parts of the curve is significantly higher than for ($B^r_{pto,36}$).

It is noteworthy that at a radius of 3m, for both main propagation directions (β), no significant differences were observed between average annual power computed using the two different values of PTO damping. Using the fact that PTO damping moment is proportional to r^5, it can be inferred that the principal determinant of its optimization is not the number of floats but their size. When the PTO damping moment optimized for a radius of $3m$ is applied ($B^{r=3m}_{pto,60}$), the average annual power produced in cases $r < 3m$ or $r > 3m$ deviates significantly from its maximum. The value of B_{pto} is too high and the float motions too small when $r < 3m$ and vice versa when $r > 3m$. This can be observed for the case $r = 4.5m$ in Figure 5.9, which shows the significant motions of each unit of the 36-float configuration for both β propagation directions. When ($B^{r=3m}_{pto,60}$) is used, float motions become significantly higher than when ($B^{r=4.5m}_{pto,36}$) is used. In the latter case, assuming the motions of the floats are governed by a Rayleigh distribution and the maximum significant motion is $0.1rad$, it can be predicted that the design condition γ_{max} prescribed in Table 5.1 will

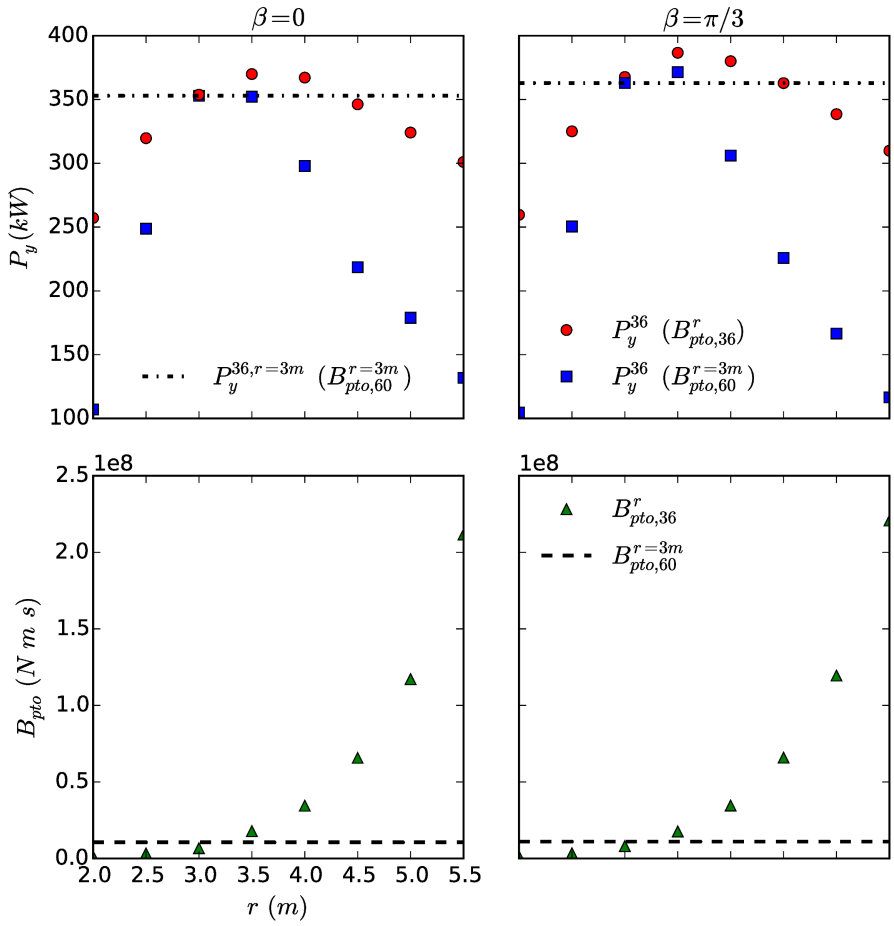

Figure 5.8: Annual power (P_y) produced by a 36-unit bottom-referenced heave-buoy array WEC as a function of both the radius of the hemispheric floats and the value of PTO damping (B_{pto}) used for two main propagation directions of the incident wave spectra (β). The values of PTO damping optimized for each float radius of the 36-unit configuration are indicated as ($B_{pto,36}^{r}$) whereas ($B_{pto,60}^{r=3m}$) refers to the PTO damping which optimizes the annual power produced by the 60-unit configuration with $3m$ radius floats.

be exceeded only $\sim 2\%$ of the time (for specific floats) when the WEC operates in the most energetic sea state. Although not shown here, for the same sea state the design condition is exceeded $\sim 20\%$ of the time for the configuration with radius $3.5m$ and its associated optimized B_{pto}.

An economic assessment should be performed to identify the most advantageous design solution. On the one hand, despite satisfying the motion constraints imposed by the Power Take-Off configuration considered in this study, the use of units of radius $4.5m$ would increase the total submerged volume by 102% compared to the initial 60-float WEC with hemispheres of radius $3m$. In addition, the cost of the hydraulic rams for the $4.5m$ units would be much higher than for $3m$ units, as can be inferred from Figure 5.8, which shows that the damping provided for the former is ~ 7 times higher than for the latter. On the other hand, the $3.5m$ radius floats could be selected on the basis that the overall power is maximized. In that case, the increase in total submerged volume with respect to the initial 60-float configuration would only be 5%; however, it would be necessary to limit the motion of the units that exceed the mechanical bounds imposed by the hydraulic rams using other means, such as increasing the B_{pto} damping. This would both reduce the total power produced and significantly increase the cost of the PTO units, which in order to be economically viable should not be required to withstand very large control moments.

5.3 Conclusions

The performance of a generic 60-float bottom-fixed heave-buoy array WEC has been established in irregular waves with directional spreading. No significant difference in energy capture was found for the two mean propagation directions of the incident waves considered. This result would have been difficult to anticipate prior to numerical calculations, as the arrangement of the floats relative to the propagation direction is not the same.

Similar to other studies on closely spaced point absorbers, important differences in energy capture between floats were found. This behaviour has important implications for their structural design as, despite all having the same hemispheric geometry, they will be acted upon by different loading conditions.

The most remarkable result was found by tuning both the separating distance and the number of floats of the device. It was observed that if the structure's footprint is limited to that of the initial 60-float configuration, the energy capture increase due to the addition of new floats "saturates" at 36 float. Beyond this number, adding more

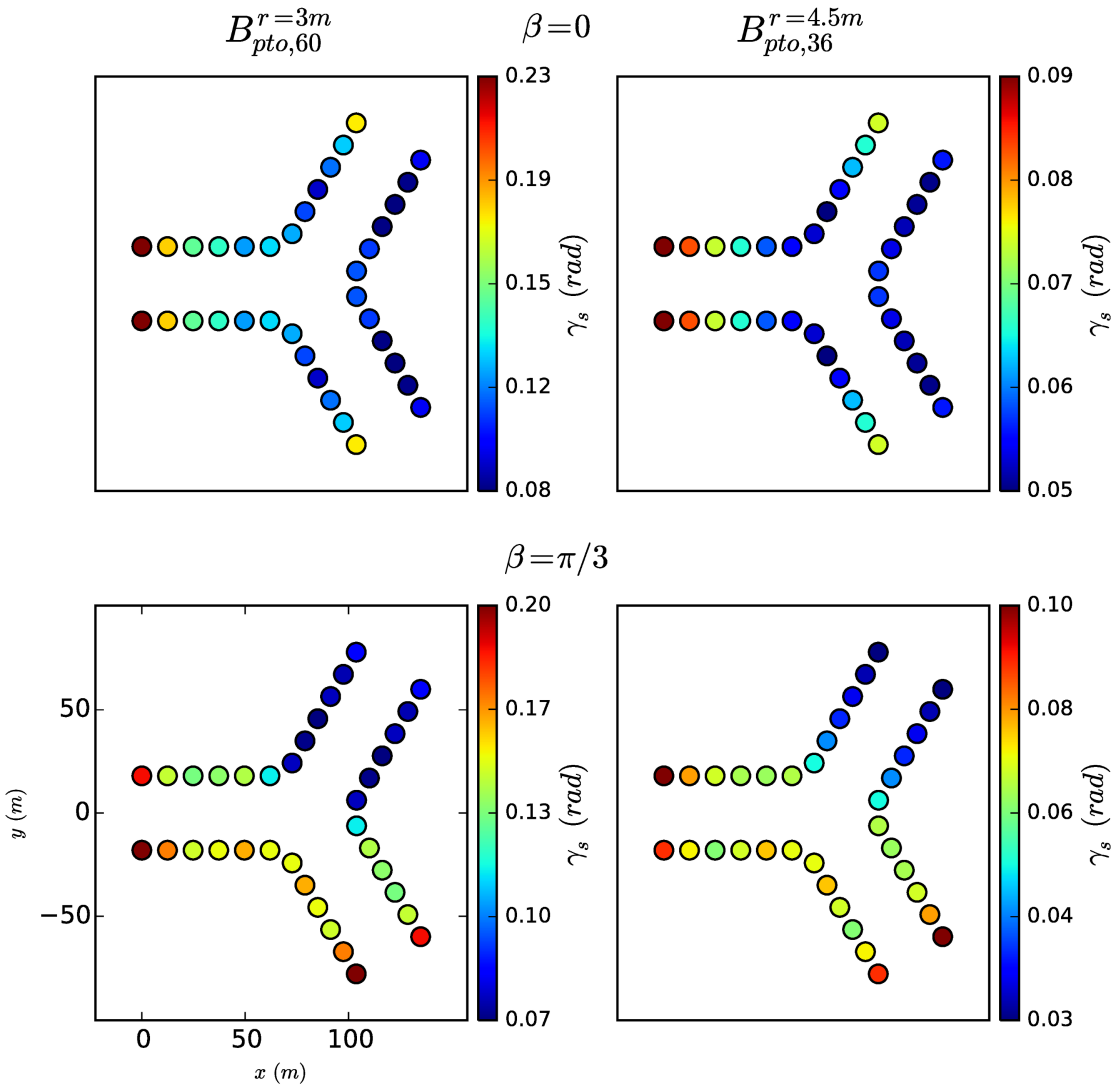

Figure 5.9: Float significant motions (γ_s) of the 36-unit bottom-referenced heave-buoy array WEC with float radius $4.5m$ for the sea state with ($H_s = 2.75m$, $T_p = 6.44s$) and two mean propagation directions (0 and $\pi/3\,rad$) of the incident wave spectra. Results are presented for two different values of PTO damping ($B^{r=3m}_{pto,60}$) and ($B^{r=4.5m}_{pto,36}$). The former is optimized to maximize the energy capture of a 60-unit configuration with $3m$ radius floats and the latter of a 36-unit with $4.5m$ radius floats.

floats does not significantly increase the power production, which in fact decreases such that the mean annual energy capture of the 36 and the 60-unit configurations are the same.

Finally, a sensitivity analysis was performed on the radius of the floats, from which it was found that optimal energy capture is achieved for a float radius of $3.5m$.

The author would like to note that the contents of this Chapter have been published in the journal paper Fàbregas Flavià et al. (2017).

Chapter 6

Impact of a large WEC farm on the ambient wave spectrum

The focus of Chapter 5 was on the annual energy capture of a multi-body WEC. Beside power production, it is of paramount importance to assess the potential impact large clusters of wave energy converters may have on the ambient wave climate, and particularly in the shore zone where modifications of the coastal processes may have important consequences.

Folley et al. (2012) compared different tools to model WEC arrays based on a defined set of characteristics. As opposed to spectral wave models, highly suitable to study the distal environmental impact, potential flow solvers were found to be unsuitable for this task. However, they clearly outperformed spectral wave models as far as the evaluation of localised effects amongst WECs is concerned.

Based on these observations, Babarit et al. (2013) presented a methodology to couple a BEM solver with either a phase resolved or a spectral wave model by making use of Kochin functions. The proposed BEM-spectral solver coupling was based on the implementation of the modified wave average energy flux around the WECs, characterized by the Kochin function and derived from the BEM solver, in the spectral wave model.

In this Chapter, an alternative procedure is outlined. As in Babarit et al. (2013), the far-field representation of the perturbed incident waves is used. However, in this case it is not used to compute the modified wave energy flux around the WECs but to evaluate, at the outlet of the wave farm domain set as interface, the resultant transmitted spectrum. The latter can then be used as input BC for the spectral model to solve the spatial wave propagation to the shoreline.

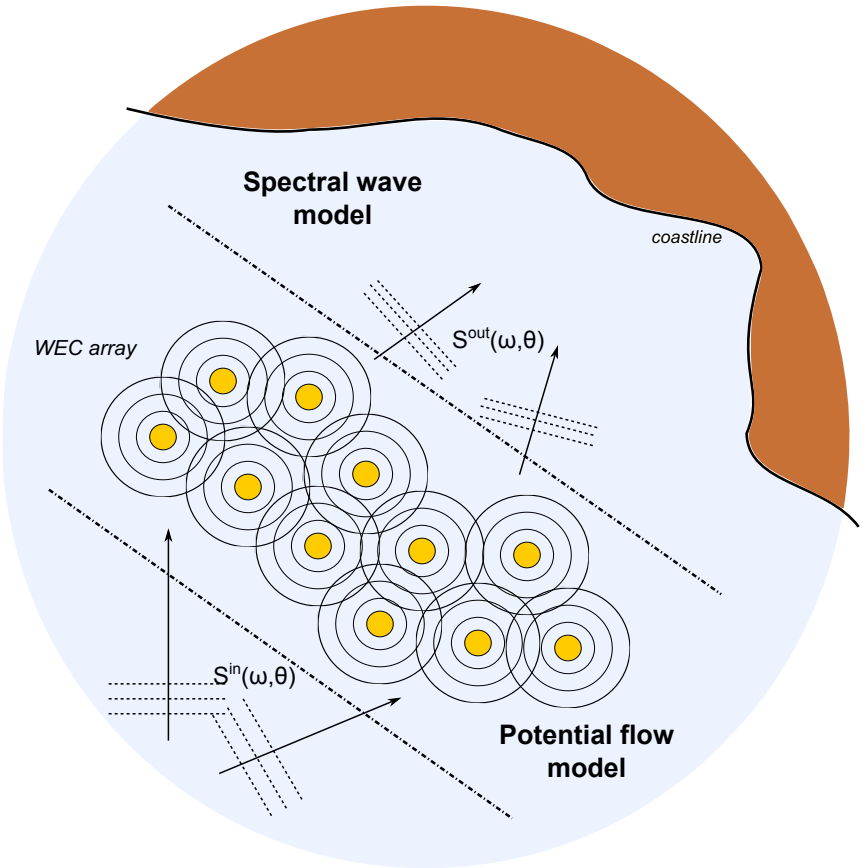

Figure 6.1: Schematic of the coupling between the IT and a Spectral wave model. Filled circles represent the array WECs whereas the empty ones the scattered and radiated wave fields given as a superposition of cylindrical harmonics by the IT (Kagemoto and Yue, 1986). S^{in} and S^{out} represent both the incident and transmitted spectra at the inlet and outlet of the wave farm respectively indicated as dotted lines.

Despite not requiring the addition of modifications to a standard spectral wave model, the proposed coupling methodology is not exempt from limitations. Some of them are discussed at the end of this Chapter, as the main focus is on the computation of the transmitted wave spectrum carried out in two steps. First, the linear first-order wave-structure interaction on a large array of WECs acted upon by an incident wave spectrum is efficiently solved by using the implementation of the IT described in Chapters 2 - 4. The use of this method provides both the scattered and radiated potentials by each body in the array, as a result of the multiple-scattering, on the basis of partial cylindrical wave functions. Then, by employing the procedure described in Montiel et al. (2015a), the cylindrical harmonics are transformed into plane waves. The latter, given that linearity is assumed, are superposed to the undisturbed incident plane waves to derive the perturbed transmitted spectrum at the outlet of the wave farm. A schematic of the procedure is depicted in Figure 6.1.

In the first part of this Chapter, the transformation of outgoing progressive partial cylindrical waves into a superposition of plane waves is presented. This expansion is then used to characterize the solution of the IT (both the scattered and the radiated cylindrical wave fields) in the form of transmitted and reflected spectra. Details on the numerical implementation of the expressions derived are given with special emphasis on the angular variables sampling. Finally, in the results section both the transmission and reflection coefficients of an array of truncated vertical cylinders are shown as a function of different parameters. A comparison of the free surface elevation evaluated with the IT (as described in Chapter 4) and by means of the transformation of cylindrical harmonics into plane waves is shown for a small array of two truncated vertical cylinders. At the end, the perspectives offered by this methodology and its limitations are discussed.

6.1 Plane wave expansion of cylindrical harmonics

We shall recall that solutions to the multiple-scattering problem obtained by means of the IT (Kagemoto and Yue, 1986) detailed in Chapter 2, i.e. radiated and scattered waves by each body in the array, are expressed in the base of outgoing partial cylindrical wave functions as:

$$\phi_j^S = \left(A_j\right)^T \psi_j^S; \quad \phi_j^{R,k} = \left(R_j^k\right)^T \psi_j^S \tag{6.1.1}$$

where A_j are the complex scattered partial wave coefficients, R_j^k the radiated partial cylindrical wave coefficients in a k^{th} mode of motion (with $k = 1, \ldots, 6$ in the general case) referred to as radiation characteristics (RC) and ψ_j^S the outgoing partial cylindrical wave functions given by:

$$\left(\psi_j^S\right)_{nm} = \begin{cases} \frac{\cosh\left[k_0(z_j+d)\right]}{\cosh\ k_0 d}\, H_m^{(1)}(k_0 r_j)\, e^{im\theta_j} & n = 0,\ m \in \mathbb{Z} \\ \cos\left[k_n(z_j+d)\right] K_m(k_n r_j)\, e^{im\theta_j} & n \geq 1\,(n \in \mathbb{N}),\ m \in \mathbb{Z} \end{cases} \tag{6.1.2}$$

where subindex j refers to a body j in the array with local cylindrical reference system defining a point p in the fluid domain with the coordinates $(r_j,\ \theta_j,\ z_j)$. The relationship of the latter with the Cartesian coordinates in a global Cartesian reference system $OXYZ$ is given by $(x,\ y,\ z) = (X_{0j} + r_j \cos\theta_j,\ Y_{0j} + r_j \sin\theta_j,\ z_j)$ with $O_j(X_{0j},\ Y_{0j},\ 0)$ the Cartesian coordinates of the jth body center in the horizontal plane (Figure 2.4).

Hereafter in this section, without loss of generality, it is considered that only a single body centered at the origin is present and, therefore, subindex j is not used to simplify notation. The analysis follows the work by Montiel et al. (2015a).

While evanescent modes are required to accurately represent the velocity potential in the vicinity of the array bodies (as shown in Figures 4.16 - 4.17), given their fast decay far from the farm domain their influence is negligible. Thus, as the objective is to enable one to study the impact of the wave farm located far offshore from the coast on its wave climate, in this Chapter the focus is only on the progressive part of the velocity potential given by cylindrical harmonics $H_m^{(1)}(k_0 r)\, e^{im\theta}$ (Figures 2.2a - 2.2c). We seek to express them as a superposition of plane waves. This transformation was introduced by Cincotti et al. (1993) based on the Sommerfeld's integral representation of the Hankel function of the first kind:

$$H_m^{(1)}(k_0 r) = \frac{(-i)^m}{\pi} \int_c e^{ik_0 r \cos w + imw} dw \tag{6.1.3}$$

where $H_m^{(1)}$ is the Hankel function of the first kind and C is the integration path in the plane of the complex variable $w = u + iv$. The integration path needs to (i) pass through the origin; (ii) have an upper part ($v > 0$) in the strip $-\pi < u \leq 0$; (iii) have a lower part ($v < 0$) in the strip $0 \leq u < \pi$. The path chosen is shown in Figure 6.2 and has $\gamma_l + i\infty$ and $\gamma_u - i\infty$ as lower and upper limits respectively.

By multiplying $e^{im\theta}$ on both right and left hand sides of expression (6.1.3) and by applying the change of variable $w = \chi - \theta$ to the integral, the following expression is

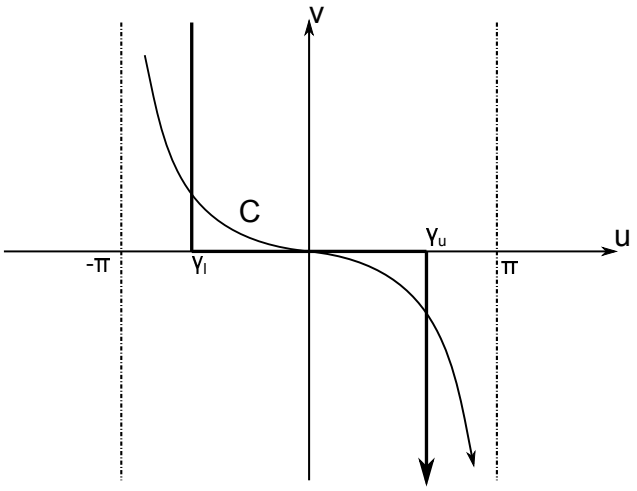

Figure 6.2: Schematic of the integration contours in the complex χ plane. The arrows indicate direction.

obtained:

$$H_m^{(1)}(k_0 r)e^{im\theta} = \frac{(-i)^m}{\pi}\int_{\gamma_l+i\infty+\theta}^{\gamma_u-i\infty+\theta} e^{im\chi}e^{ik_0(x\cos\chi+y\sin\chi)}d\chi \tag{6.1.4}$$

Limits γ_l and γ_u are chosen as $-\pi/2-\theta$ and $\pi/2-\theta$ respectively for the case where $x \geq 0$. By following the same procedure for the case $x \leq 0$, this time by applying the change of variable $w = -(\chi+\theta)+\pi$ and by selecting the limits as $\gamma_l = \pi/2-\theta$ and $\gamma_u = 3\pi/2-\theta$, the following expression can be derived:

$$H_m^{(1)}(k_0 r)e^{im\theta} = \begin{cases} \frac{(-i)^m}{\pi}\int_{-\pi/2+i\infty}^{\pi/2-i\infty} e^{im\chi}e^{ik_0(x\cos\chi+y\sin\chi)}d\chi & (x \geq 0) \\ \frac{i^m}{\pi}\int_{-\pi/2+i\infty}^{\pi/2-i\infty} e^{-im\chi}e^{ik_0(-x\cos\chi+y\sin\chi)}d\chi & (x \leq 0) \end{cases} \tag{6.1.5}$$

Equation (6.1.5) enables one to represent outgoing partial cylindrical waves as a continuous superposition of plane waves traveling in the positive and negative x directions, as indicated by the first and second expressions respectively. Figure 6.4 schematically depicts this representation. We note that, as mentioned earlier, we are considering a single body with $O = O_j$, and thus $(x,\, y) = (x_j,\, y_j)$.

At this point, it may be of interest to clarify the effect of the complex branches on the integrals in (6.1.5). For that, we evaluate their separate contribution by decom-

posing the integration domain in the following manner:

$$\int_{-\pi/2+i\infty}^{-\pi/2} d\chi + \int_{-\pi/2}^{\pi/2} d\chi + \int_{\pi/2}^{\pi/2-i\infty} d\chi \tag{6.1.6}$$

Let us define the following complex variable change:

$$\chi = \begin{cases} -\frac{\pi}{2} - i(1+t); & t < -1 \\ \frac{\pi}{2}t; & -1 \leq t \leq 1 \\ \frac{\pi}{2} + i(1-t); & t > 1 \end{cases} \tag{6.1.7}$$

where t is an integration contour parametrization variable with $t \in \mathbb{R}$.

The integral in (6.1.5) for the case $x \geq 0$ can be expressed using (6.1.7) as:

$$H_m^{(1)}(k_0 r)e^{im\theta} = \frac{(-i)^m}{\pi}\left[-i\int_{-\gamma-1}^{-1}(-i)^m e^{m(1+t)}e^{k_0 x\sinh(1+t)}e^{-ik_0 y\cosh(1+t)}dt + \right.$$
$$\left.\frac{\pi}{2}\int_{-1}^{1} e^{im\frac{\pi}{2}t}e^{ik_0(x\cos\frac{\pi}{2}t + y\sin\frac{\pi}{2}t)}dt - i\int_{1}^{1+\gamma}(i)^m e^{-m(1-t)}e^{k_0 x\sinh(1-t)}e^{ik_0 y\cosh(1-t)}dt\right] \tag{6.1.8}$$

where γ represents the truncation of the complex integration contour.

By direct inspection of the integrands in (6.1.8), it can be observed that the plane wave terms associated with the complex branches, i.e. first and third terms of the summation in (6.1.8), decay exponentially with x, the larger the value of t the faster the decay. These components correspond to evanescent plane waves and it is important to differentiate them from the evanescent waves in (6.1.2). The former are a result of the plane wave expansion of cylindrical harmonics representing the progressive part of the scattered/radiated potential by the body.

This is illustrated in Figure 6.3, which shows the influence of the truncation parameter γ on the evaluation of (6.1.8). It can be observed that an increase of γ enables one to accurately represent the imaginary part of the Hankel function for relatively small values of $k_0 r$. As $k_0 r$ increases, the influence of γ, and thus of the evanescent plane waves, becomes less important until they are no longer required.

As opposed to the variation with respect to x, the behaviour of the integrands in the complex integrals of (6.1.8) with respect to y is not straightforward to interpret. From direct inspection, it could seem that there is no decay in y direction which contradicts

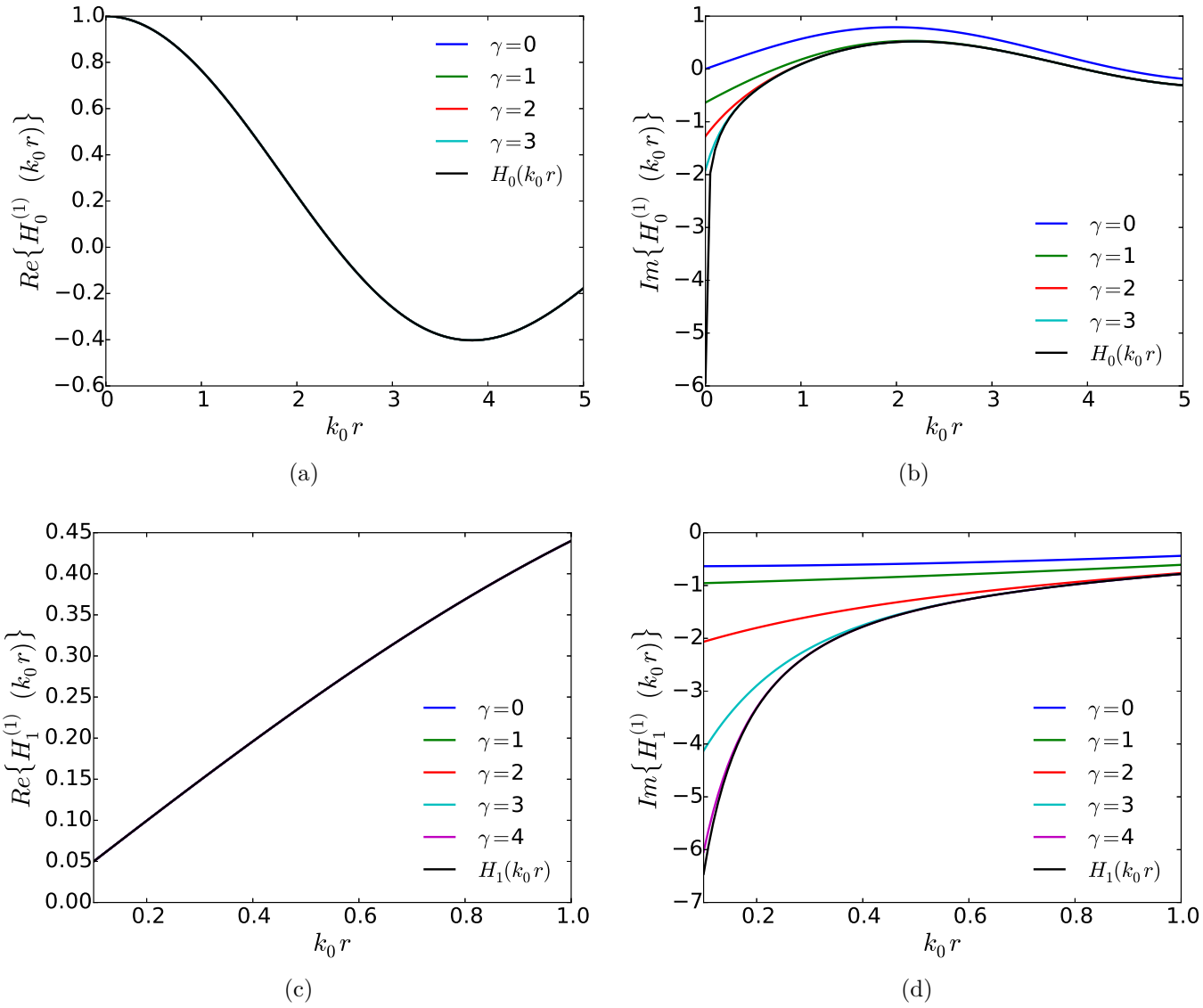

Figure 6.3: Influence of the truncation parameter γ on the evaluation of the Hankel function of the first kind for the case $x \geq 0$ and with $r = x$ ($\theta = 0$). When only a single line is visible it means that a perfect match of results is obtained.

the asymptotic behaviour $\sqrt{\frac{1}{r}}$ of the Hankel function when $r \to \infty$ (Abramowitz and Segun A., 1964). The method of stationary phase can be used to put light on this. It relies on the cancellation of sinusoids with rapidly varying phase, such that the integrals of the following type:

$$I = \int_{-\infty}^{\infty} F(x) e^{-i\phi(x)} dx \tag{6.1.9}$$

where $\phi(x)$ is a rapidly varying function of x over most of the range of integration and $F(x)$ is a slowly varying function in comparison with $\phi(x)$, can be evaluated as (Ursell, 1960):

$$I \approx \sqrt{\frac{2\pi}{i\phi''(x_s)}} F(x_s) e^{-i\phi(x_s)} \tag{6.1.10}$$

where x_s is a point of stationary phase, i.e., a point where $d\phi/dx = 0$.

By taking the first integral in (6.1.8) with the change of variable $t = -\alpha - 1$ and by setting the truncation limit as ∞ with $x = 0$, it can be rewritten as:

$$I = -\int_{0}^{\infty} (-i)^m e^{-m\alpha} e^{-ik_0 y \cosh\alpha} d\alpha \tag{6.1.11}$$

The term $k_0 y \cosh\alpha$ varies much faster than $e^{-m\alpha}$ and, therefore, they can be identified as $\phi(\alpha)$ and $F(\alpha)$ respectively. Then, as $\phi' = k_0 y \sinh\alpha$, it follows that $\alpha_s = 0$. The second derivative $\phi'' = k_0 y \cosh\alpha$ evaluated at the point of stationary phase is equal to $k_0 r$ where it has been used that $y = r\sin\theta$ and that $\theta = \pi/2$ for the positive branch of y. By subsituting the values in expression (6.1.10), the value of the integral (6.1.11) reads:

$$I \approx \sqrt{\frac{2\pi}{i(k_0 r)}} e^{-ik_0 r} \tag{6.1.12}$$

As expected, the expression obtained follows the same trend $\sqrt{\frac{1}{r}}$ as the asymptotic behaviour of the Hankel function of the first kind. The same reasoning can be applied to the last integral of the summation in (6.1.8) leading to the same result.

6.2 Transmitted and reflected spectra

In section 6.1, the representation of progressive cylindrical harmonics as a continuous superposition of plane waves with amplitudes that depend continuously on the direction was presented. In this section, the transformation is utilized to define the sum of

incident, radiated and scattered wave fields as transmitted and reflected angular spectra on both sides of the wave farm domain limited by two arbitrary infinite vertical planes parallel to the y axis ($x = \xi_0$ and $x = \xi_1$) inside which all the WEC centers O_j are contained (Figure 6.4):

$$\phi^{Ref}(\mathbf{x}) = \frac{\cosh k_0(z+d)}{\cosh k_0 d} \int_{-\pi/2+i\infty}^{\pi/2-i\infty} A^{Ref}(\chi)\, e^{ik_0(-(x-\xi_0)\cos\chi + y\sin\chi)} d\chi \quad (x \leq \xi_0) \tag{6.2.1}$$

$$\phi^{Trans}(\mathbf{x}) = \frac{\cosh k_0(z+d)}{\cosh k_0 d} \int_{-\pi/2+i\infty}^{\pi/2-i\infty} A^{Trans}(\chi)\, e^{ik_0((x-\xi_1)\cos\chi + y\sin\chi)} d\chi \quad (x \geq \xi_1) \tag{6.2.2}$$

where $\mathbf{x} = (x,\, y,\, z)$, ϕ^{Ref} and ϕ^{Trans} are the reflected and transmitted velocity potential respectively and $A^{Ref}(\chi)$ and $A^{Trans}(\chi)$ are the reflected and transmitted spectra respectively. The former represents the angular distribution at $x = \xi_0$ of plane waves propagating along the negative x direction. The latter describes the angular distribution at $x = \xi_1$ of plane waves traveling in the positive x direction.
The ambient incident wave forcing reads:

$$\phi^{In}(\mathbf{x}) = \frac{\cosh k_0(z+d)}{\cosh k_0 d} \int_{-\pi/2}^{\pi/2} A^{In}(\tau)\, e^{ik_0(x\cos\tau + y\sin\tau)} d\tau \tag{6.2.3}$$

where $A^{In}(\tau)$ is the incident spectra and characterizes the angular distribution of incoming energy at the origin. The representation of a plane wave propagating in a single direction τ_0 is expressed as $A^{In}(\tau) = \delta(\tau - \tau_0)$, with δ the Dirac delta function. It is useful to separate the contribution of the incident transmitted spectra in the following manner:

$$A^{T}(\chi) = \tilde{A}^{T}(\chi) + e^{ik\xi_1\cos\chi} A^{In}(\chi) \tag{6.2.4}$$

where $\tilde{A}^{T}(\chi)$ is the transmitted spectrum due to radiation and scattering only.
It can be observed that the integration limits of (6.2.3) differ from those in (6.2.1) and (6.2.2). The former are real as no decaying waves are present in the propagating ambient incident wave. In contrast, decaying plane waves are present in the reflected and transmitted potentials as a result of the decomposition of the diffracted and radiated progressive cylindrical harmonics into plane waves.

For completeness, the reader should refer to Montiel et al. (2016), who assessed the influence of evanescent modes on the wave propagation through the MIZ by means of the slab-clustering method (Montiel et al., 2015a). In the former, a detailed analysis

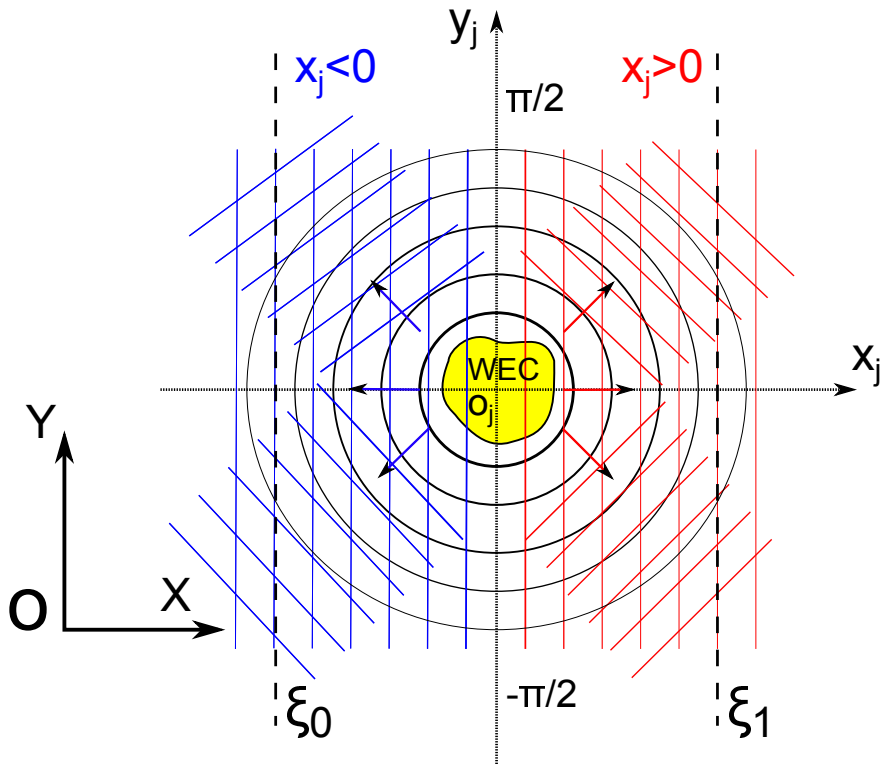

Figure 6.4: Schematic representation of the cylindrical harmonics transformation into plane waves in the horizontal plane. (x_j, y_j) represent the Cartesian reference system local to body j and OXY the global Cartesian reference system in which the jth body center O_j is expressed $O_j = (X_{0j}, Y_{0j})$. ξ_0 and ξ_1 are vertical planes parallel to the y axis and containing the centers of all the bodies in the array.

of the transformation of both the progressive and evanescent parts of the velocity potential as a superposition of plane waves is given.

Apart from characterizing the angular distribution of the transmitted and reflected plane waves, $A^{Ref}(\chi)$ and $A^{Trans}(\chi)$ define the reflected and transmitted energies respectively relative to the normalized incident energy:

$$E^{Ref} = \int_{-\pi/2}^{\pi/2} |\mathbf{A}^{Ref}(\chi)|^2 d\chi; \quad E^{Trans} = \int_{-\pi/2}^{\pi/2} |\mathbf{A}^{Trans}(\chi)|^2 d\chi \tag{6.2.5}$$

where E^{Ref} and E^{Trans} are the normalized reflected and transmitted energies respectively.

For the diffraction problem, given here by an array of fixed bodies acted upon by an incident wave spectrum, the following relationship which expresses energy conservation in the system needs to hold:

$$\int_{-\pi/2}^{\pi/2} |\mathbf{A}^{Ref}(\chi)|^2 d\chi + \int_{-\pi/2}^{\pi/2} |\mathbf{A}^{Trans}(\chi)|^2 d\chi = \int_{-\pi/2}^{\pi/2} |\mathbf{A}^{In}(\chi)|^2 d\chi \tag{6.2.6}$$

Based on reflected and transmitted energies, transmission (T) and reflection (R) coefficients can be defined as:

$$R = \sqrt{\left(\int_{-\pi/2}^{\pi/2} |\mathbf{A}^{Ref}(\chi)|^2 d\chi\right) / \left(\int_{-\pi/2}^{\pi/2} |\mathbf{A}^{In}(\chi)|^2 d\chi\right)} \tag{6.2.7}$$

$$T = \sqrt{\left(\int_{-\pi/2}^{\pi/2} |\mathbf{A}^{Trans}(\chi)|^2 d\chi\right) / \left(\int_{-\pi/2}^{\pi/2} |\mathbf{A}^{In}(\chi)|^2 d\chi\right)} \tag{6.2.8}$$

For the general case, i.e. WECs in energy production regime with diffracted and radiated wave fields being generated, (6.2.6) would read:

$$E^{Abs} = \int_{-\pi/2}^{\pi/2} |\mathbf{A}^{In}(\chi)|^2 d\chi - \int_{-\pi/2}^{\pi/2} |\mathbf{A}^{Ref}(\chi)|^2 d\chi - \int_{-\pi/2}^{\pi/2} |\mathbf{A}^{Trans}(\chi)|^2 d\chi \tag{6.2.9}$$

where E^{Abs} is the normalized energy absorbed by the WECs.

We note that an expression analogous to (6.2.9) was used by Garnaud and Mei (2009) to compute the power-extraction efficiency of a long array of energy-absorbing buoys.

6.2.1 Diffraction

In (6.2.1) and (6.2.2), the general representation of the reflected and transmitted potentials was given. In this section, the procedure to compute the reflected $A^{Ref}(\chi)$ and transmitted $A^{Trans}(\chi)$ angular spectra, which characterize the scattered waves by the bodies in the array held fixed, is detailed

As opposed to section 6.1, where only a single isolated body was considered, hereafter subindex j is used to refer to a body j in a large array of WECs.
Take the ambient incident potential in cylindrical coordinates local to body j defined as:

$$\phi^{In}(r_j, \theta_j, z_j) \approx \frac{\cosh\, k_0(z_j + d)}{\cosh\, k_0 d} \sum_{m=-M}^{M} f_m^j\, J_m(k_0 r_j)\, e^{im\theta_j} \tag{6.2.10}$$

where f_m^j is given by:

$$f_m^j = i^m \int_{-\pi/2}^{\pi/2} A^{In}(\tau)\, e^{-im\tau} e^{ik_0(X_{0j}\cos\tau + Y_{0j}\sin\tau)} d\tau \tag{6.2.11}$$

We note that (6.2.11) is of the same form as (2.2.21). The solution (considering only progressive modes) to the diffraction multiple scattering problem given by the scattered potentials by each body can be written as:

$$\phi_j^S(r_j, \theta_j, z_j) \approx \frac{\cosh\, k_0(z_j + d)}{\cosh\, k_0 d} \sum_{m=-M}^{M} c_m^j H_m^{(1)}(k_0 r_j)\, e^{im\theta_j} \tag{6.2.12}$$

where c_m^j are complex coefficients.
Now, we wish to substitute the expansion of cylindrical harmonics into plane waves (6.1.5) for $(x \geq 0)$ into (6.2.12). Given the fact that (6.1.5) was presented for an isolated body located at the origin of the global Cartesian reference system, it is required to adapt the expression taking into account the phase difference with respect to the origin of the jth body O_j. In addition, as the objective is to express the resultant transmitted potential with respect to a common phase reference point for all the bodies given by $(x, y) = (\xi_1, 0)$, a phase change is applied to (6.1.5) for $(x \geq 0)$ which now reads:

$$H_m(kr_j)\, e^{im\theta_j} = \frac{(-i)^m}{\pi} \int_{-\pi/2+i\infty}^{\pi/2-i\infty} e^{im\chi} e^{ik_0([(x-\xi_1)+(\xi_1-X_{0j})]\cos\chi + (y-Y_{0j})\sin\chi)} d\chi \tag{6.2.13}$$

By substituting (6.2.13) into (6.2.12), and by adding up the contributions from all

bodies which have now a common phase reference, the transmitted potential due to scattering in the array can be expressed as :

$$\phi^{Trans}(\mathbf{x}) = \frac{\cosh\, k_0(z_j+d)}{\cosh\, k_0 d}\int_{-\pi/2+i\infty}^{\pi/2-i\infty}\sum_{m=-M}^{M}\frac{(-i)^m}{\pi}e^{im\chi}e^{ik_0((x-\xi_1)\cos\chi+y\sin\chi)}\times$$
$$\sum_{j=1}^{N_b}c_m^j e^{ik_0((\xi_1-X_{0j})\cos\chi-Y_{0j}\sin\chi)}d\chi + \frac{\cosh\, k_0(z_j+d)}{\cosh\, k_0 d}\int_{-\pi/2}^{\pi/2}A^{In}(\tau)e^{ik_0(x\cos\tau+y\sin\tau)}d\tau \tag{6.2.14}$$

where N_b represents the total number of bodies.
Then, by means of the DTM of the array defined as:

$$\mathcal{D} = (\mathbf{I}-\mathbf{BT})^{-1}\,\mathbf{B} \tag{6.2.15}$$

with dimensions $N_b(2M+1)\times N_b(2M+1)$ and where $\mathbf{B}$ and $\mathbf{T}$ are defined as in section 2.3.1, the complex scattered coefficients c_m^j can be related to the incident coefficients f_m^j as:

$$c_m^j = \mathcal{D}_m^j\, f_m^j \tag{6.2.16}$$

Hence, by substituting expression (6.2.16) into (6.2.14) we have:

$$\phi^{Trans}(\mathbf{x}) = \frac{\cosh\, k_0(z_j+d)}{\cosh\, k_0 d}\int_{-\pi/2+i\infty}^{\pi/2-i\infty}\sum_{m=-M}^{M}\frac{(-i)^m}{\pi}e^{im\chi}e^{ik_0((x-\xi_1)\cos\chi+y\sin\chi)}\times$$
$$\sum_{j=1}^{N_b}\mathcal{D}_{mj}\,i^m\left[\int_{-\pi/2}^{\pi/2}A^{In}(\tau)\,e^{-im\tau}e^{ik_0(X_{0j}\cos\tau+Y_{0j}\sin\tau)}d\tau\right]\times$$
$$e^{ik_0((\xi_1-X_{0j})\cos\chi-Y_{0j}\sin\chi)}d\chi + \frac{\cosh\, k_0(z_j+d)}{\cosh\, k_0 d}\int_{-\pi/2}^{\pi/2}A^{In}(\tau)e^{ik_0(x\cos\tau+y\sin\tau)}d\tau \tag{6.2.17}$$

With some algebraic manipulations, the transmitted potential due to scattering in the array can be expressed as in (6.2.2) with the transmitted spectra given by :

$$A^{Trans}(\chi) = \int_{-\pi/2}^{\pi/2}\mathcal{T}(\chi:\tau)\,A^{In}(\tau)\,d\tau \tag{6.2.18}$$

where $\mathcal{T}(\chi:\tau)$ is the transmission kernel defined as:

$$\mathcal{T}(\chi:\tau) = (\mathbf{V}^{Trans}(\chi))^T\mathcal{D}\mathbf{V}^{In}(\tau) + e^{ik_0\xi_1\cos\chi}\delta(\chi-\tau) \tag{6.2.19}$$

where the elements of $\mathbf{V}^{Trans}$ and $\mathbf{V}^{In}$are:

$$[\mathbf{V}^{Trans}(\chi)]_{(j-1)(2M+1)+M+m+1} = \frac{(-i)^m}{\pi} e^{-ik_0((X_{0j}-\xi_1)\cos\chi+Y_{0j}\sin\chi)} e^{im\chi} \tag{6.2.20}$$

with $1 \leq j \leq N_b$, $-M \leq m \leq M$, and:

$$[\mathbf{V}^{In}(\tau)]_{(j-1)(2M+1)+M+m+1} = i^m e^{ik_0(X_{0j}\cos\tau+Y_{0j}\sin\tau)} e^{-im\tau} \tag{6.2.21}$$

with $1 \leq j \leq N_b$, $-M \leq m \leq M$.
Following the same procedure, the reflected spectra can be computed as:

$$A^{Ref}(\chi) = \int_{-\pi/2}^{\pi/2} \mathcal{R}(\chi:\tau)\, A^{in}(\tau)\, d\tau \tag{6.2.22}$$

where $\mathcal{R}(\chi:\tau)$ is the reflection kernel given by:

$$\mathcal{R}(\chi:\tau) = (\mathbf{V}^{Ref}(\chi))^T \mathcal{D} \mathbf{V}^{In}(\tau) \tag{6.2.23}$$

where the elements of $\mathbf{V}^{Ref}$ read:

$$[\mathbf{V}^{Ref}(\chi)]_{(j-1)(2M+1)+M+m+1} = \frac{i^m}{\pi} e^{ik_0((X_{0j}-\xi_0)\cos\chi-Y_{0j}\sin\chi)} e^{-im\chi} \tag{6.2.24}$$

It is noteworthy that the integration limits of (6.2.18) and (6.2.22) are real as no decaying plane waves are present in the ambient incident spectrum.

6.2.2 Radiation

A similar procedure as the one described in section 6.2.1 for the diffraction problem can be applied to compute the radiated transmitted and reflected spectra which characterize the wave field created by the motion of the bodies in array. In this case, instead of being given by the terms f_m^j which describe ambient incident plane waves as a superposition of cylindrical waves, the incident potential acting upon each body j of the array reads:

$$\phi^{In}(r_j, \theta_j, z_j) \approx \frac{\cosh\, k_0(z_j+d)}{\cosh\, k_0 d} \sum_{m=-M}^{M} g_m^j\, J_m(k_0 r_j)\, e^{im\theta_j} \tag{6.2.25}$$

with g_m^j expressed as:

$$g_m^j = \int_{-\frac{\pi}{2}}^{\frac{\pi}{2}} A^{In}(\tau, \omega_0) \left(\sum_{\substack{i=1 \\ i \neq j}}^{N_b} \sum_k -i\omega_0 \Gamma_{ik}(\tau,\, \omega_0) \mathbf{T}_{ij}^T(\omega_0)\, R_{ik}(\omega_0) \right)_m d\tau \tag{6.2.26}$$

where g_m^j represents the partial cylindrical waves incident to body j due to the radiated fields by the rest of bodies in array in their respective degrees of freedom k. Only the radiated fields, given by the Radiation Characteristics (RC) of each body i in motion mode k (R_{ik}) as if it was isolated and without including the resulting scattered waves in the array are considered. As mentioned in section 3.3, the RC are computed for a unitary velocity and therefore they are scaled here with the velocity term $-i\omega_0\Gamma_{ik}(\tau,\, \omega_0)$ with $\Gamma_{ik}(\tau,\, \omega_0)$ the Response Amplitude Operator of body i in the array in its k^{th} mode of motion for an excitation at angle τ and an angular frequency ω_0. $\mathbf{T}_{ij}$ is the Transformation Matrix as defined in (2.3.3).

Expressions (6.2.18), (6.2.20) and (6.2.22) - (6.2.24) are identical for the radiation problem, whereas the second term of the summation in (6.2.19) should be removed for the transmission kernel to represent the transmitted radiated wave field. Finally, $\mathbf{V}^{In}(\tau)$ can be identified directly from (6.2.26) as:

$$[\mathbf{V}^{In}(\tau)]_{(j-1)(2M+1)+M+m+1} = \left(\sum_{\substack{i=1 \\ i \neq j}}^{N_b} \sum_k -i\omega_0 \Gamma_{ik}(\tau,\, \omega_0) \mathbf{T}_{ij}^T(\omega_0)\, R_{ik}(\omega_0) \right)_m \tag{6.2.27}$$

6.3 Numerical Implementation

In sections (6.2.1) and (6.2.2), the expressions to evaluate $A^{Ref}(\chi)$ and $A^{Trans}(\chi)$ were shown as integral mappings of the incident spectrum. For practical computations, they need to be approximated by means of a discretization of the transmitted $\mathcal{T}(\chi : \tau)$ and reflected $\mathcal{R}(\chi : \tau)$ kernels. This is achieved by sampling the angular variables χ and τ. The former take values in the complex angular domain shown in Figure 6.2, such that $-\frac{\pi}{2} + i\infty \leq \chi \leq \frac{\pi}{2} - i\infty$, whereas the latter are real and defined as $-\frac{\pi}{2} \leq \tau \leq \frac{\pi}{2}$. The complex variable χ is parameterized as in (6.1.7) and the improper integrals truncated as $-\frac{\pi}{2} + i\gamma \leq \chi \leq \frac{\pi}{2} - i\gamma$ with $\gamma \geq 0$. A number of N_t samples are used for the real part of the domain, $-\frac{\pi}{2} \leq \chi \leq \frac{\pi}{2}$, and N_v samples for the imaginary branches $-\frac{\pi}{2} + i\gamma \leq \chi < -\frac{\pi}{2}$ and $\frac{\pi}{2} < \chi \leq \frac{\pi}{2} - i\gamma$.

By using this discretization, transmitted and reflected kernels become matrices of dimensions $(2N_v + N_t) \times N_t$. Consequently, vectors $\mathbf{A}^{Ref}$ and $\mathbf{A}^{Trans}$ have lengths $2N_v + N_t$, while $\mathbf{A}^{In}$ is composed of N_t terms:

$$\mathbf{A}^{Ref} = \mathcal{R}\mathbf{A}^{In} \quad ; \mathbf{A}^{Trans} = \mathcal{T}\mathbf{A}^{In} \tag{6.3.1}$$

The numerical integration is performed using a trapezoidal scheme with a nonuniform grid which is the most suited to the present problem (Montiel et al., 2015a).

6.4 Results

In this section, reflection and transmission coefficients of an array of truncated vertical cylinders are shown. In addition, the free surface elevation computed by means of the transformation of cylindrical harmonics into plane waves, and thus using transmitted and reflected spectra, is shown for a small array of two truncated vertical cylinders.

Results are presented for a water depth of 50m and for the same geometry descretization as shown in Figure 3.3a.

6.4.1 Reflection and transmission coefficients

In this section, we analyze the influence of the angular variable sampling on the transmission and reflection coefficients. For that, two arrays of 3 and 51 truncated vertical cylinders disposed parallel to the Y axis as shown in Figure 6.5a, i.e. symmetrically arranged with respect to the x axis, are considered. The bodies are acted upon by a normalized incident directional spectrum given by:

$$S(\tau) = \frac{2}{\pi}\cos^2(\tau); \quad \int_{-\pi/2}^{\pi/2} S(\tau)\, d\tau = 1 \tag{6.4.1}$$

where the angular variable τ is comprised in the interval $-\pi/2 \leq \tau \leq \pi/2$ and the incident wave amplitudes are given by $\mathbf{A}^{In}(\tau) = \sqrt{S(\tau)}$.

Figure 6.6 shows the reflection and transmission coefficients at different incident wave lengths for the small array of 3 truncated vertical cylinders shown in Figure 6.5a with $d/a = 4$. It can be observed that a converged value is reached for all wave lengths if a sufficient number of samples is used. In particular, the higher the frequency, the higher the number of discretization samples required. It is found that, as expected, more energy is transmitted for long incident waves. As the wave length decreases, the majority of the incident energy is reflected.

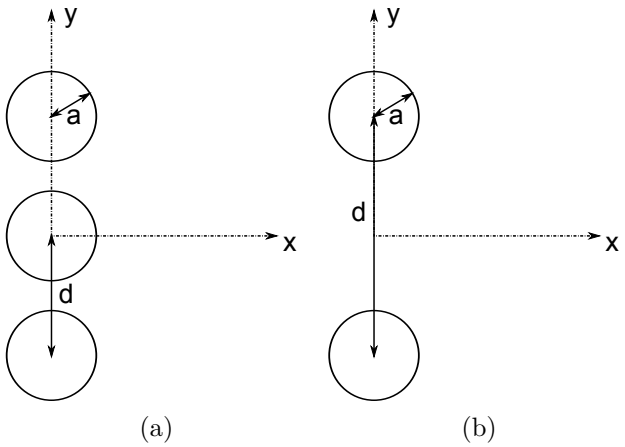

Figure 6.5: Schematic of three and two truncated vertical cylinder array configurations.

Results in Figure 6.6 are presented for a fixed separating distance between bodies. In Figure 6.7, the angular variable sampling required to achieve a precision of 10^{-4} in energy balance (6.2.6) for the transmission and reflected coefficients as a function of the separation distance between body centers d is shown. It can be observed that the longer the separating distance, the higher the number of samples required in particular for short wave lengths. The number of samples seems to increase linearly with the separating distance.

In Figure 6.8 the reflection and transmission coefficients are plotted as a function of the wave number and for two arrays composed of 3 and 51 cylinders disposed as in Figure 6.5a with $d = 3a$. No significant differences between both cases can be observed. This is in agreement with the results obtained by Montiel et al. (2015b) who showed that, for a similar layout, the response of a long array of circular ice floes could be well approximated using just a small number of them. As observed previously in Figure 6.6, the transmission coefficient is higher for long waves and decreases with wave length. The angular variable sampling employed to obtain these results is detailed in Figure 6.9. It can be observed that, in agreement with the trend displayed in Figure 6.6, the higher the distance from the phase reference the higher the number of samples required. In spite of the oscillatory behaviour shown in Figure 6.9, the trend of both the transmission and reflection coeffcients is continuous and relatively smooth.

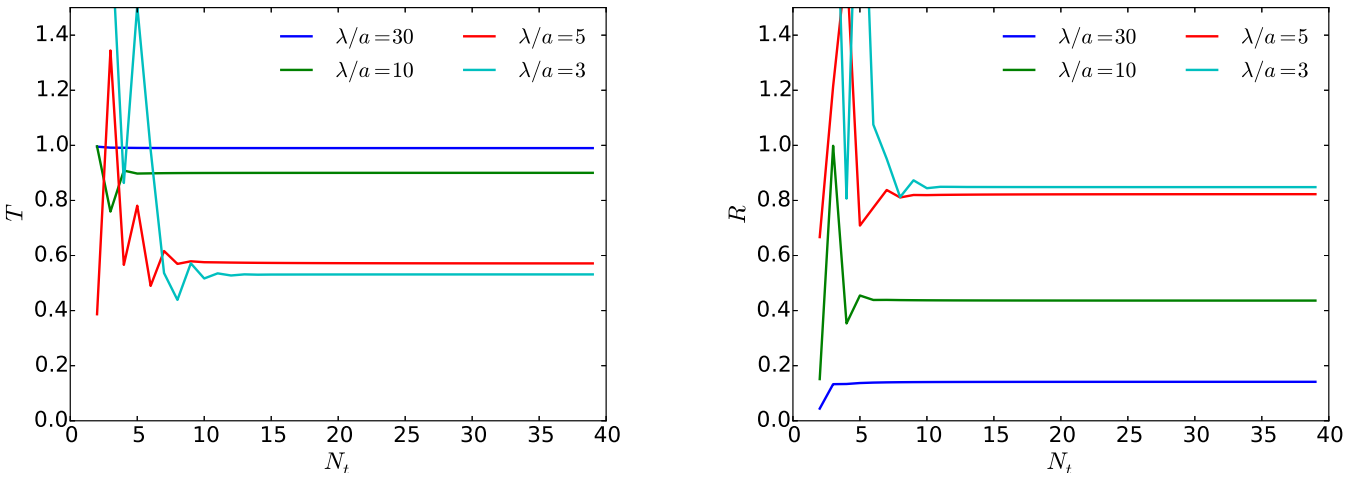

Figure 6.6: Transmission a) and reflection b) coefficient as a function of the angular variable sampling N_t for an array of 3 truncated vertical cylinders disposed parallel to the Y axis as in Figure 6.5a and with $d/a = 4$

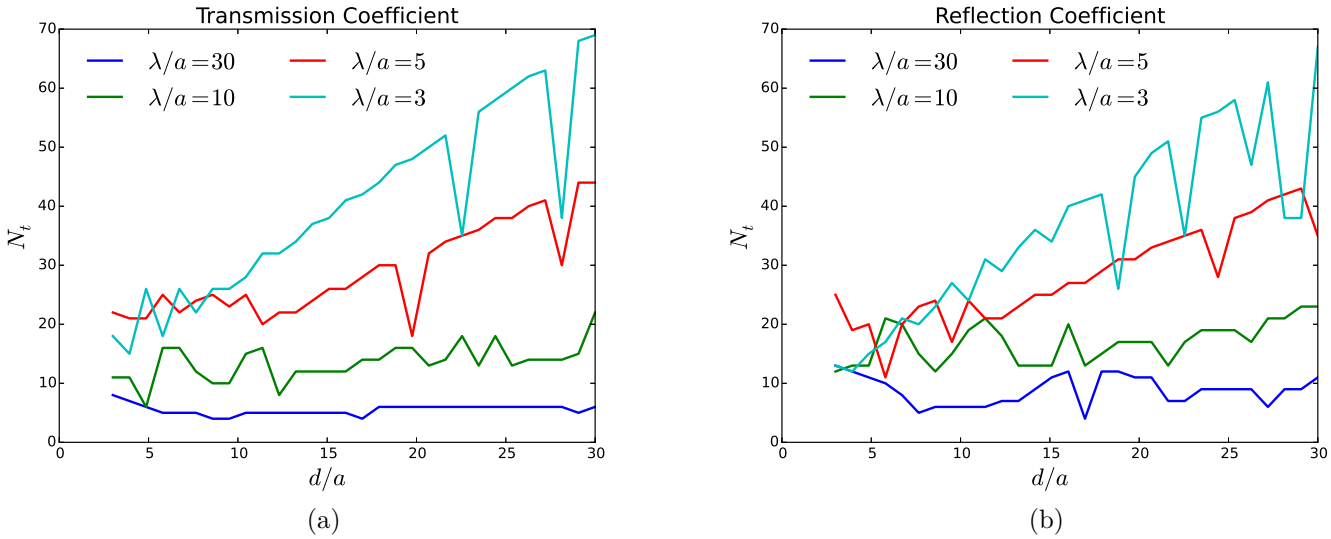

Figure 6.7: Number of angular discretization samples N_t as a function of the separating distance between bodies d for both the transmission a) and reflection b) coefficients of an array of 3 truncated vertical cylinders as shown in Figure 6.5a.

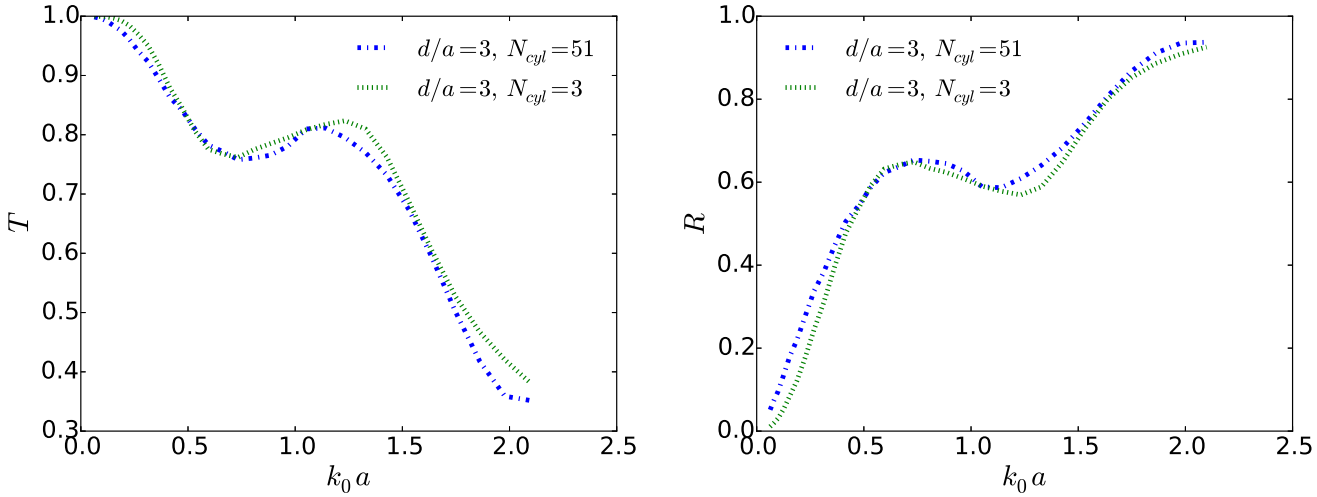

(a) (b)

Figure 6.8: Transmitted a) and reflected b) coefficients for an array of both 3 and 51 cylinders displayed parallel to axis Y as shown in Figure 6.5a.

6.4.2 Free surface elevation

In 6.4.1, the sensitivity of the angular discretization on the transmission and reflection coefficients was investigated. In this section, we seek to verify the implementation of the integral mappings of the incident spectrum (6.2.18) and (6.2.22) to compute respectively the transmitted $A^{Trans}(\chi)$ and reflected $A^{Ref}(\chi)$ spectra. Using expressions (6.2.1) and (6.2.2), the free surface elevation ($\eta = -\frac{1}{g}\frac{\partial \phi}{\partial t}|_{z=0}$) for a small array composed of two truncated vertical cylinders (Figure 6.5b with $d = 6a$) with a wave forcing of the form (6.4.1) is evaluated and compared to calculations performed using the IT as described in Chapter 4.

Two different cases are considered: the scattered potential of the two cylinders as a result of the incident spectrum as in (6.4.1) and the radiated potential by the freely floating bodies under the same incident waves. With respect to the former, Figure 6.10 shows the reflected $\mathbf{A}^{Ref}(\chi)$ and transmitted $\mathbf{A}^{Trans}(\chi)$ energy spectra derived from expressions (6.2.18) and (6.2.22). For the latter, they have been computed using the procedure described in section 6.2.2 and are shown in Figure 6.11.

As mentioned in section 6.1, the improper integrals in expressions (6.2.1) and

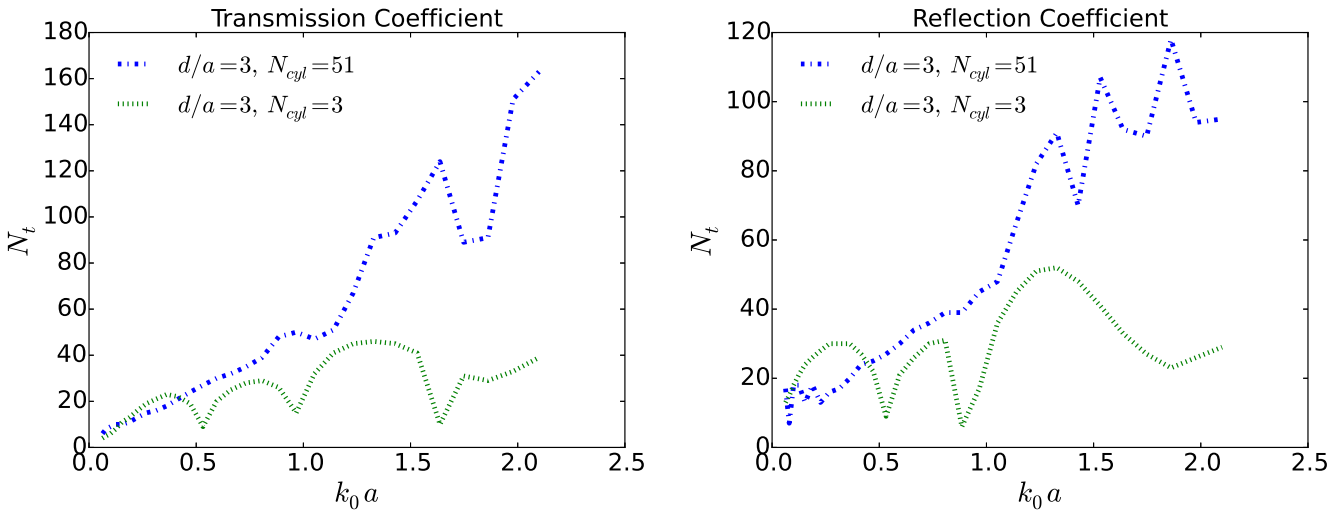

(a) (b)

Figure 6.9: Sensitivity of the angular variable discretization on the transmission a) and reflection b) coefficients as a function of the wave length to satisfy (6.2.6) with a precision of 10^{-5} .

(6.2.2) need to be truncated. The influence of the truncation parameter, referred to as γ, on the free surface elevation has been investigated for both the diffraction and radiation cases and results are displayed in Figures 6.12 and 6.13 respectively. On the left column, the free surface elevation's absolute value is depicted. On the right column the relative difference in percentage between the free surface elevation computed using equations (6.2.1) and (6.2.2) (referred to as η^{PC}) and by means of the IT (indicated by η^{IT}) is shown.

From the left column in Figures 6.12 and 6.13 it can be observed that continuity in free surface elevation η between the transmitted and reflected domains (separated by a vertical white line) is always achieved for a truncation value $\gamma > 2$. From the right column, it can be observed that the free surface elevation discrepancy between the two methodologies employed is reduced when the truncation parameter γ is increased. In addition, it is noteworthy that the differences are concentrated at the transition region between the transmitted and reflected domains. Indeed, it is in this region where plane decaying waves are significant. We note that few terms γ are required to accurately describe the free surface elevation in the domain. This result is in agreement with the observations by Montiel et al. (2015a).

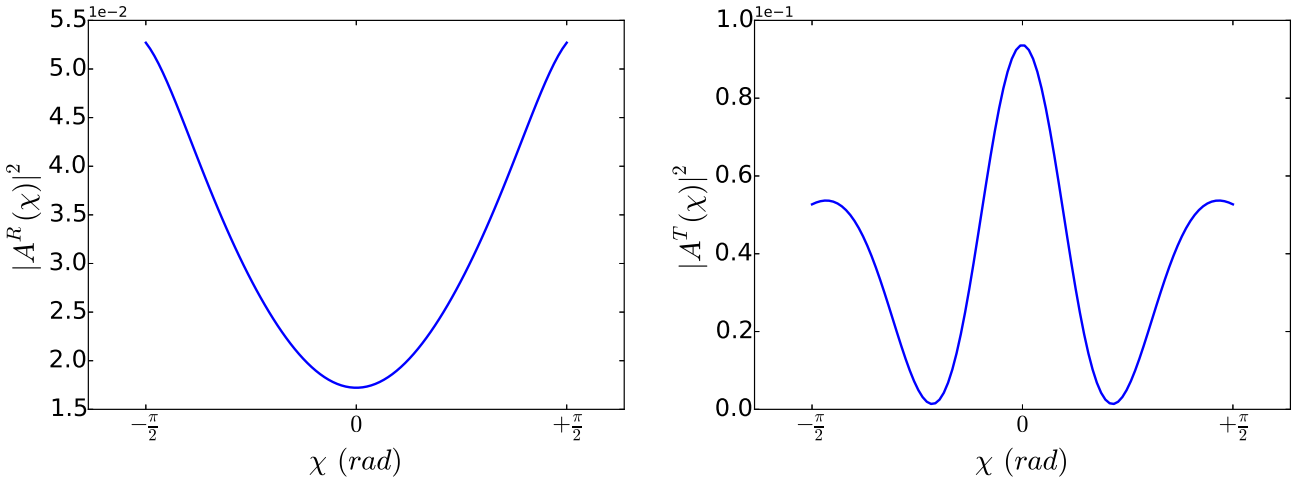

(a) (b)

Figure 6.10: Reflected a) and transmitted b) energy spectra of the scattered wave field for a two cylinder array with separating distance $d = 6a$ between bodies with a the cylinder radius. The wave forcing is as in (6.4.1) with a wave length $\lambda/a = 10$.

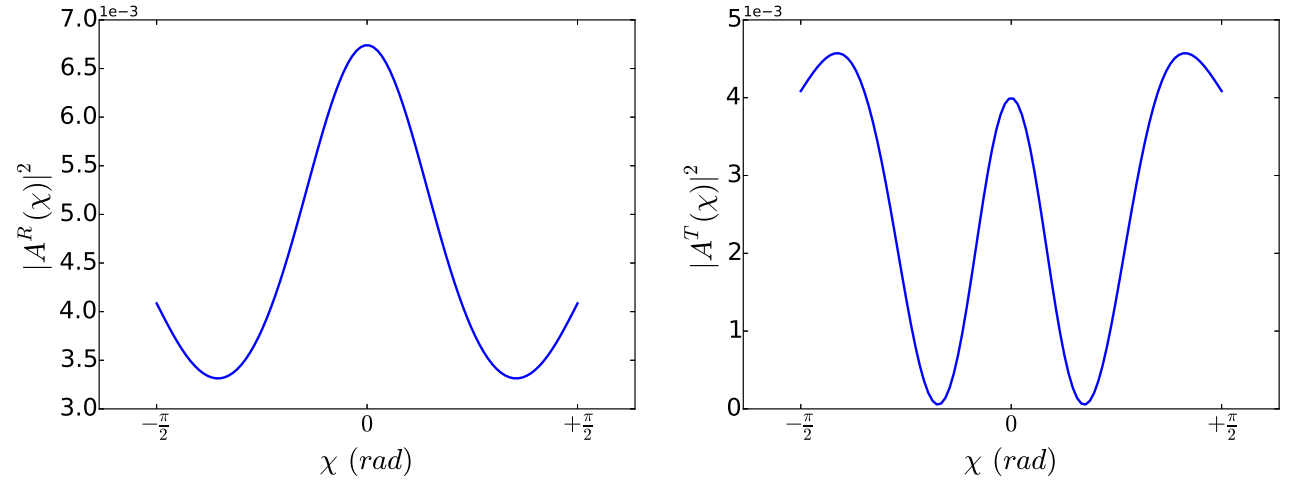

(a) (b)

Figure 6.11: Reflected a) and transmitted b) energy spectra of the radiated wave field for a two cylinder array with separating distance d between bodies with a the cylinder radius. The wave forcing is as in (6.4.1) with a wave length $\lambda/a = 10$.

6.5 Discussion and conclusions

In this Chapter, a methodology to transform cylindrical harmonics into plane waves has been presented based on the work by Montiel et al. (2015a). It enables one to characterize the modified wave field at the outlet of a large wave farm as a result of the interaction between ambient incident waves and the WECs. Thus, one can compute the resultant transmitted spectrum to be given as input boundary condition to a spectral wave model to study its propagation to the shoreline.

It has been observed that with a fine enough angular variable sampling, converged transmission and reflection coefficients which satisfy the diffraction energy conservation equation with a precision of $10^{-4}/10^{-5}$ are obtained. The number of samples has been found to be dependent on both the frequency and the distance of the bodies from the common phase reference. In particular, the higher the latter two the finer the discretization required. In addition, the computation of the reflected and transmitted spectra has been verified by means of a comparison of the free surface elevation evaluated with both the IT only and using the transformation of cylindrical harmonics to plane waves. The dependance of the transmitted and reflected potential on the complex branches truncation parameter has been analyzed showing that few terms are required to achieve a converged result.

Due to time limitations, the scope of work of this Chapter has been bounded to the verification of the cylindrical-plane wave transformation implemented and the coupling with a spectral wave model has not been addressed in detail. However, some considerations with respect to the latter are given in the following paragraphs.

One of the assumptions inherent to the use of a BEM solver is that the water depth is constant. This enables one to define an impermeable boundary condition on the perfectly flat seabed. While for a single WEC, with a characteristic length say on the order of ~ 10 m, this hypothesis can be considered valid; for large wave farms composed of O(100) devices separated by distances say on the order of ~ 100 m and hence occupying an area of several km^2, significant bathymetry variations are to be expected.

In addition to the constant water depth hypothesis, the fact of characterizing the angular distribution of transmitted plane waves at a single point of the wave farm outlet $(x,\, y) = (\xi_1,\, 0)$ is implicitly linked to two assumptions. First, an homogeneous

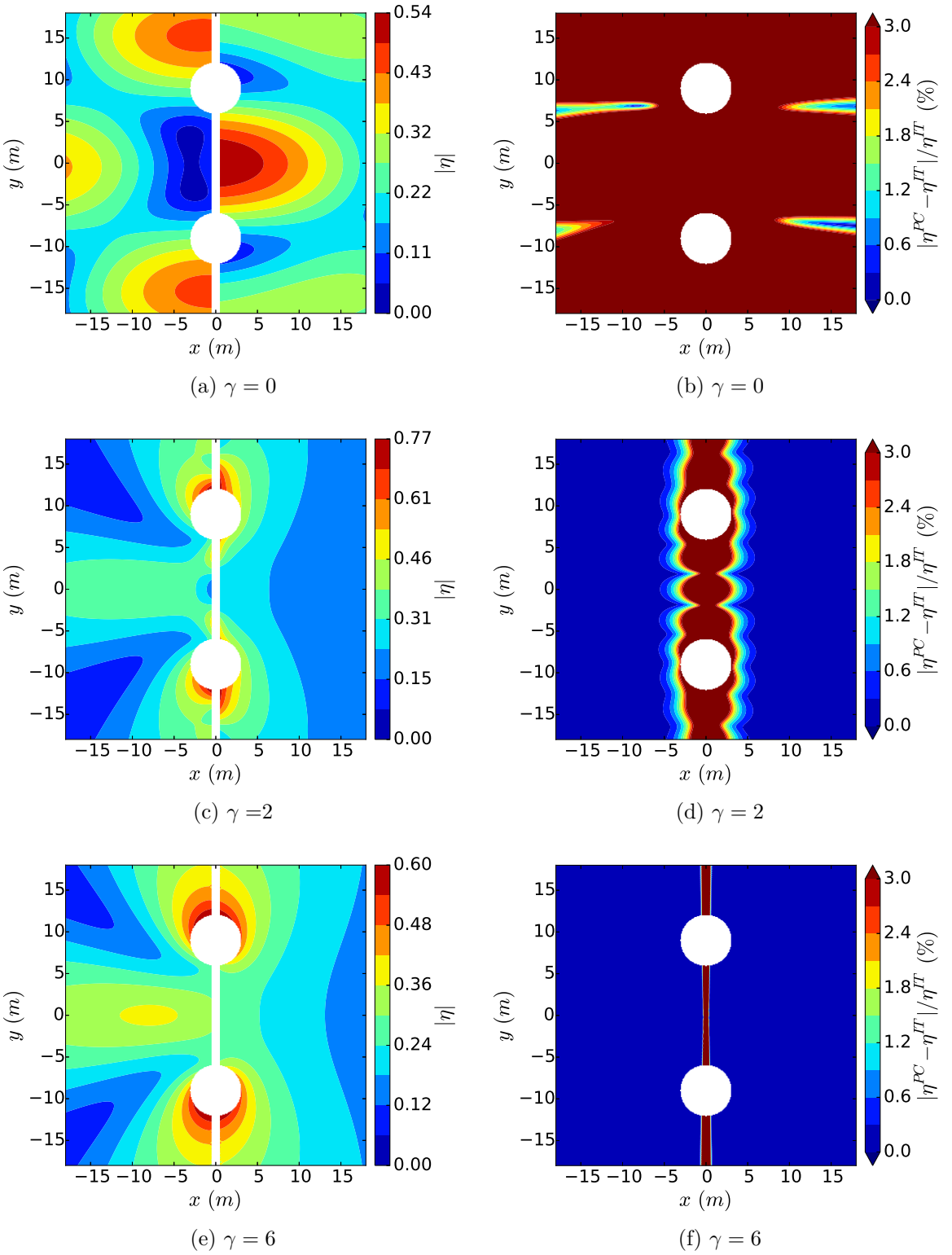

(a) $\gamma = 0$ (b) $\gamma = 0$

(c) γ =2 (d) $\gamma = 2$

(e) $\gamma = 6$ (f) $\gamma = 6$

Figure 6.12: Sensitivity study of the improper integral truncation parameter γ on the scattered free surface elevation (η). Plots on the left column (a, c, e) represent the absolute value of the scattered free surface elevation; right column (b, d, f) show the difference in percentage between the free surface elevation computed with the interaction theory (η^{IT}) and with the transformation of cylindrical harmonics to plane waves (η^{PC}). The incident wave forcing is as in (6.4.1) and the wave length $\lambda/a = 10$.

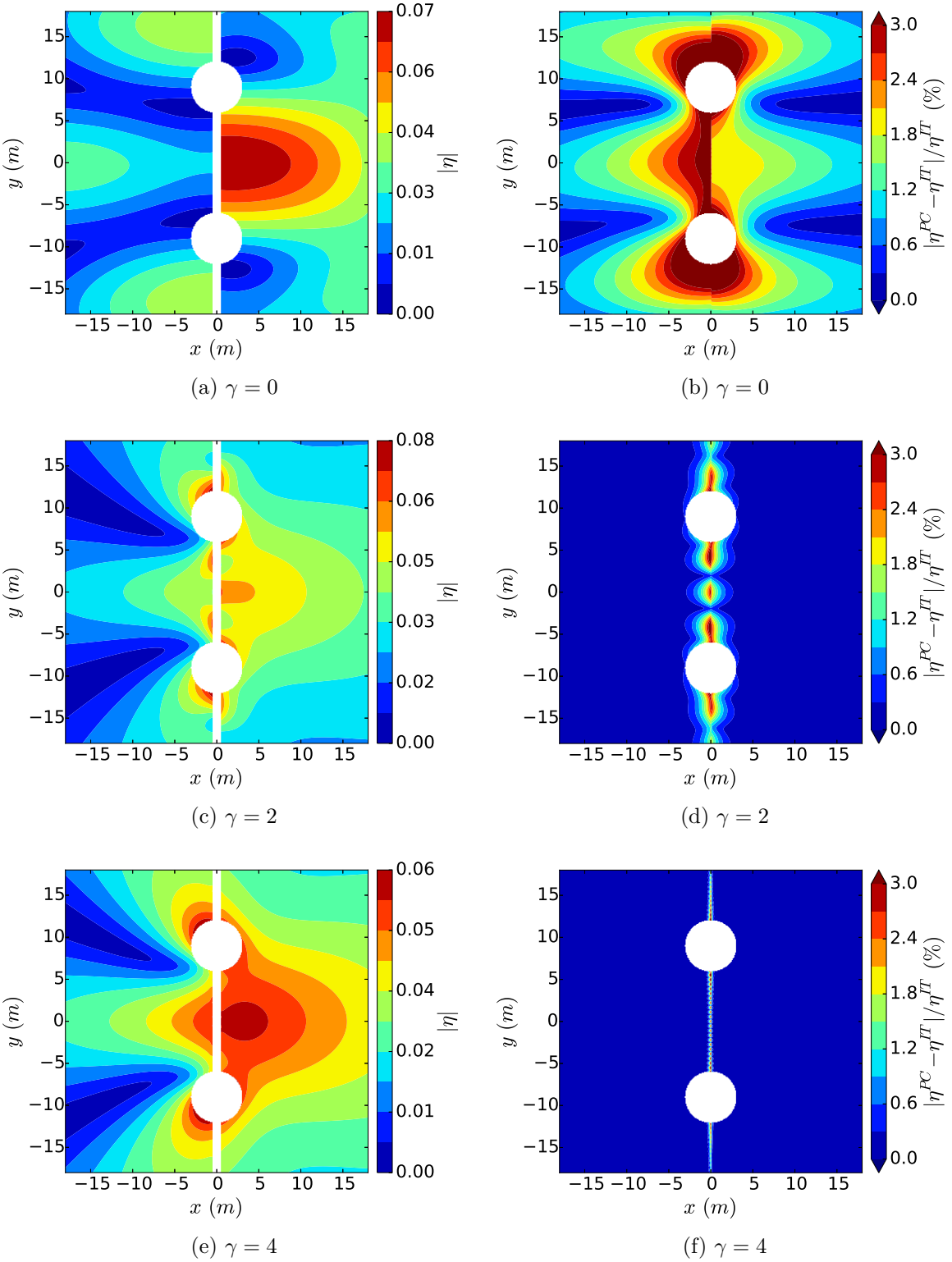

(a) $\gamma = 0$ (b) $\gamma = 0$

(c) $\gamma = 2$ (d) $\gamma = 2$

(e) $\gamma = 4$ (f) $\gamma = 4$

Figure 6.13: Sensitivity study of the improper integral truncation parameter γ on the radiated free surface elevation (η). Plots on the left column (a, c, e) represent the absolute value of the scattered free surface elevation; right column (b, d, f) show the difference in percentage between the free surface elevation computed with the interaction theory (η^{IT}) and with the transformation of cylindrical harmonics to plane waves (η^{PC}). The incident wave forcing is as in (6.4.1) and the wave length $\lambda/a = 10$.

distribution of the WECs on the wave farm region and, second, a domain whose length along the y direction can be considered as "infinitely" large. Intuitively, with respect to the former, one can imagine that if the WECs arrangement is not regular, as can happen in case several clusters of multiple bodies are formed, the spectrum at the outlet of the wave farm will vary significantly whether it is measured behind a cluster or in the spacing between two of them. With regard to the extension along the y-direction, if the domain is finite the angular distribution of plane waves at the transition area between the array and the open sea will be governed by the incident spectrum, as opposed to the transmitted spectrum at the wave farm area which is highly influenced by the presence of the WECs.

In order to avoid this limitation, the angular distribution of the transmitted wave field should be characterized at different points of the wave farm domain outlet as if being perceived by different "observers". With the procedure shown in this Chapter, which offers great computation savings as a consequence of utilizing an integral mapping of the incident spectrum to express the reflected and transmitted wave fields, the characterization of the transmitted spectrum at different points cannot be achieved. This is because the superposition of the wave fields generated by each of the units in the array is done on a plane wave basis by imposing a common phase reference, in this case at $(x,\, y) = (\xi_1,\, 0)$. However, an alternative procedure could be envisaged. It would consist in transferring the scattered and radiated cylindrical wave fields generated by each unit to a common origin, i.e. the points at which the spectrum is to be characterized. This transformation was shown in section 4.2.2 by means of the multipole expansion matrix $\mathbf{M}$ from Graf's addition theorem. Once this step accomplished, the transformation of the cylindrical harmonics at each point into plane waves could take place using equation (6.1.5).

While the use of this alternative procedure could enable one to circumvent the limitation of characterizing the wave field at the outlet of the wave farm with a unique spectrum, tests on the sensitivity of the number of points considered and their location at the interface between the BEM solver and the spectral wave model should be carried out. In addition, the use of the multipole expansion from Graf's addition theorem is associated with an increase in the number of angular modes required to achieve a converged solution. Thus, depending on both the number of points required at the farm domain outlet and the increase in angular mode truncation, for wave farms composed of a large number of units $O(100)$ the applicability of the proposed BEM-spectral wave model coupling methodolgy could be hampered.

Chapter 7

Conclusions

In the present work we have implemented and verified a numerical tool based on the Direct Matrix Method interaction theory. It enables one to compute the hydrodynamic interactions amongst a large number of bodies $O(100)$ of arbitrary shape, such as Wave Energy Converters (WECs), provided they satisfy a special spacing requirement. Such configurations cannot be evaluated with standard Boundary Element Method (BEM) solvers, which are the state-of-the-art in wave-structure interaction, due to their excessive computational complexity.

The savings in computational time provided by the interaction theory have allowed us to study the impact of hydrodynamic interactions on the energy capture of a generic bottom-referenced heave-buoy array composed of 60 hemispheric floats.

In addition, we have implemented a numerical technique which transforms the interaction theory output such that it could be input to a spectral wave model to study the impact large clusters of bodies may have on the local coast wave climate.

Based on a thorough literature review and in line with the objectives defined in Chapter 1, the **main contributions** of this work are:

- The implementation in the open-source BEM solver NEMOH of a methodology to compute the isolated body hydrodynamic characteristics, including both the far-field and the near-field contributions, in the form required by the Direct Matrix Method interaction theory and which allows individuals to use it in a straightforward manner.

- The verification of the modifications introduced to the standard NEMOH BEM solver with comparisons to, on the one hand, the output from an alternative methodology to compute the isolated body hydrodynamic operators accounting only for the far-field contribution and, on the other hand, a semi-analytical

solution for truncated vertical circular cylinders.

- To display the frequency-dependent patterns of the isolated body hydrodynamic operators which, despite the fundamental role they play in the interaction theory, had not been plotted before.

- The derivation and numerical verification of novel expressions relating the components of two hydrodynamic operators of the isolated body, the Force Transfer Matrix and the Radiation Characteristics, as well as relations between the Radiation Characteristics with the radiation damping coefficients and the excitation forces for a single body and a body in array. While based on the Haskind's relation, they had not been given before in the context of the interaction theory and they can be useful to test its accuracy.

- The verification of the interaction theory implementation with a comparison of its output against results from both direct NEMOH calculations and a semi-analytical solution. The comparisons have clearly shown the effect of the near-field on the accuracy of the added-mass hydrodynamic coefficients when the bodies are set in close proximity.

- To address the inaccuracies introduced by the wide-spacing approximation, i.e. no near-field contribution accounted for, in the estimation of the energy capture of a multi-body wave energy converter composed of 60 closely-spaced floats. It has been shown that the incorrect added-mass coefficients, as a result of dispensing with evanescent modes, are compensated by the magnitude of the Power Take-Off damping and that their impact on the total energy capture of the device is not significant.

- The implementation of a methodology to transform cylindrical harmonics into plane waves and a critical evaluation of the possibilities it offers to address the impact large clusters of WECs may have on the distal coast wave climate.

Amongst all the results produced in this body of work, we shall highlight as **key finding**:

- The "saturation" of the power production increase of a generic bottom-referenced heave-buoy array WEC when a certain threshold in terms of the number of floats installed in a given device footprint is exceeded. It has been found that forming a tight cluster of too many units for the multi-body WEC layout analysed has a negative impact on the power production. Indeed, the same annual energy

capture can be obtained with a 60-float and a 36-float configuration. This has very important implications for cost reduction.

The numerical tool developed and the subsequent analysis carried out in this body of work are entirely based on linear potential wave theory and have been bounded to the frequency domain. However, further studies in time domain are required to accurately address the impact of motion limitations and sophisticated control strategies on the performance of the generic multi-body WEC floats. In that case, the transformation of the base of hydrodynamic coefficients in the frequency domain into impulse response functions in time domain must be achieved. For that, the interaction theory used herein may present some **limitations**:

- The use of evanescent modes has been found to be essential for an accurate evaluation of the added-mass coefficient matrices for closely-spaced bodies, in particular their off-diagonal terms. However, an increase of the evanescent modes truncation has been observed to slow down computations quite significantly. Thus, for cases involving a large number $O(100)$ of closely-spaced floats such as in multi-body WECs, the computation of accurate added-mass hydrodynamic coefficients may be associated with excessive computational times, let apart the tedious task of checking numerical convergence for each individual term of the hydrodynamic coefficient matrix. A detailed analysis of the effect of spurious added-mass coefficients on the float's response in the time domain should be performed.

Finally, if the development of multi-body WECs is pursued it might be required to perform simulations on arrays composed of several clusters of closely-spaced floats, i.e. $\gg O(100)$ bodies, and to address their potential impact on the distal wave climate. **Further research** is needed in these areas, in particular the present body of work has opened the possibility:

- To apply the transformation of cylindrical harmonics into plane waves to couple a potential flow solver and a spectral wave model.

- To couple, on the one hand, the methodology implemented in this work to compute the solution to the boundary value problem of an isolated body of arbitrary geometry and, on the other hand, alternative methodologies to the interaction theory used herein which are more suitable to deal with the hydrodynamic interactions amongst several clusters of bodies.

References

Abramowitz, M. and Segun A., I. (1964). *Handbook of mathematical functions with Formulas, Graphs, and Mathematical Tables*. Dover Publications, Inc, first edition.

A.Martin, P. (2006). Multiple Scattering: Interaction of Time-Harmonic Waves with N Obstacles.

ANSYS Aqwa (2016). BEM Software.

Babarit, A. (2010). Impact of long separating distances on the energy production of two interacting wave energy converters. *Ocean Engineering*, 37(8-9):718–729.

Babarit, A. (2013). On the park effect in arrays of oscillating wave energy converters. *Renewable Energy*, 58:68–78.

Babarit, A. and Delhommeau, G. (2015). Theoretical and numerical aspects of the open source BEM solver NEMOH. In *Proceedings of the 11th European Wave and Tidal Energy Conference 6-11th Sept 2015, Nantes, France*, pages 1–12.

Babarit, A., Folley, M., Charrayre, F., Peyrard, C., and Benoit, M. (2013). On the modelling of WECs in wave models using far field coefficients. In *European Wave and Tidal Energy Conference, EWTEC*, pages 1–9.

Babarit, A., Gendron, B., Singh, J., Melis, C., and Jean, P. (2012a). Numerical and experimental modeling of an electro-active deformable wave energy converter. In *13èmes Journées de l'Hydrodynamique*, Chatou.

Babarit, A., Hals, J., Muliawan, M. J., Kurniawan, A., Moan, T., and Krokstad, J. (2012b). Numerical benchmarking study of a selection of wave energy converters (with corrigendum in Renewable Energy 2015). *Renewable Energy*, 41:44–63.

Black, J. L. (1975). Wave forces on vertical axisymmetric bodies. *Journal of Fluid Mechanics*, 67(02):369–376.

Borgarino, B. (2011). *Résolution accélérée du problème de tenue à la mer appliquée à l'étude paramétrique de fermes de récupérateur d'énergie des vagues*. PhD thesis, Ecole Centrale de Nantes.

Borgarino, B., Babarit, A., and Ferrant, P. (2012a). An implementation of the fast multipole algorithm for wave interaction problems on sparse arrays of floating bodies. *Journal of Engineering Mathematics*, 77(1):51–68.

Borgarino, B., Babarit, A., and Ferrant, P. (2012b). Impact of wave interactions effects on energy absorption in large arrays of wave energy converters. *Ocean Engineering*, 41:79–88.

Budal, K. (1977). Theory for Absorption of Wave Power by a System of Interacting Bodies. *Journal of Ship Research*, 21(4):248–253.

Bureau Veritas (2016). HYDROSTAR.

Chakrabarti, S. (2000). Hydrodynamic interaction forces on multi-moduled structures. *Ocean Engineering*, 27(10):1037–1063.

Chakrabarti, S. (2001). Response due to moored multiple structure interaction. *Marine Structures*, 14(1-2):231–258.

Cheney, W. and Kincaid, D. (2008). *Numerical Mathematics and Computing*. Bob Pirtle, sixth edition.

Child, B. (2011). *On the configuration of arrays of floating wave energy converters*. PhD thesis, The University of Edinburgh.

Child, B. and Venugopal, V. (2010). Optimal configurations of wave energy device arrays. *Ocean Engineering*, 37(16):1402–1417.

Cincotti, G., G, F., and Santarsiero, M. (1993). Plane wave expansion of cylindrical functions. 95:192–198.

C.Mei, C., Stiassnie, M., and K.P.Yue, D. (2005). *Theory and applications of ocean surface waves. Part 1: Linear Aspects*. World Scientific Publishing.

Cody, W. and Stoltz, L. (2013). Special Function Evaluation.

COP21 (2015). Conférence des Nations Unies sur les Changements Climatiques.

Crooks, D., Hoff, J. V., Folley, M., and Elsaesser, B. (2016). Oscillating Wave Surge Converter Forced Oscillation Tests. In *Proceedings of the ASME 2016 35th International Conference on Ocean, Offshore and Arctic Engineering*, pages 1–10.

Cruz, J. (2008). *Ocean Wave Energy: Current Status and Future Prespectives*. Springer-Verlag Berlin Heidelberg.

Cruz, J., Sykes, R., Siddorn, P., and Taylor, R. (2010). Estimating the loads and energy yield of arrays of wave energy converters under realistic seas. *IET Renewable Power Generation*, 4(November 2009):488–497.

D.Cook, R., S.Malkus, D., E.Plesha, M., and J.Witt, R. (2002). *Concepts and Applications of Finite Element Analysis*. John Wiley & Sons, Hoboken, 4th edition.

De Backer, G., Vantorre, M., Beels, C., De Rouck, J., and Frigaard, P. (2010). Power absorption by closely spaced point absorbers in constrained conditions. *IET Renewable Power Generation*, 4(6):579.

Delhommeau, G. (1987). *Les problèmes de diffraction-radiation et de résistance de vagues étude théorique et résolution numerique par la méthode des singularités*. PhD thesis.

Delhommeau, G. (1989). Amélioration des performances des codes de calcul de diffraction-radiation au premier ordre.

Delhommeau, G. (1993). Numerical Simulation of Hydrodynamics : Ships and Offshore Structures. In *Nineteenth WEGMENT School*, Nantes.

Developers, S. (2016). SciPy.org.

DTOcean Project (2017). Optimal Design Tools for Ocean Energy Arrays.

Duclos, G. and Clément, A. H. (2004). Wave propagation through arrays of unevenly spaced vertical piles. *Ocean Engineering*, 31(13):1655–1668.

Engström, J., Eriksson, M., Göteman, M., Isberg, J., and Leijon, M. (2013). Performance of large arrays of point absorbing direct-driven wave energy converters. *Journal of Applied Physics*, 114(20).

Evans, D. (1980). Some analytical results for two and three dimensional wave-energy absorbers. In *Proceedings of power from sea waves*, pages p.213–49.

Fàbregas Flavià, F., Babarit, A., and Clément, A. H. (2017). On the numerical modeling and optimization of a bottom-referenced heave-buoy array of wave energy converters. *International Journal of Marine Energy*.

Fàbregas Flavià, F. and Clément, A. H. (2017). Extension of Haskind's relations to cylindrical wave fields in the context of an interaction theory. *Applied Ocean Research*.

Fàbregas Flavià, F., McNatt, C., Rongère, F., Babarit, A., and Clément, A. H. (2016a). A numerical tool for the frequency domain simulation of large arrays of identical floating bodies. *Ocean Engineering*.

Fàbregas Flavià, F., McNatt, C., Rongère, F., Babarit, A., and Clément, A. H. (2016b). Computation of the diffraction transfer matrix and the radiation characteristics in the open-source BEM code NEMOH. In *Proceedings of the ASME 2016 35th International Conference on Ocean, Offshore and Arctic Engineering*.

Falcão, A. F. d. O. (2010). Wave energy utilization: A review of the technologies. *Renewable and Sustainable Energy Reviews*, 14(3):899–918.

Falcao, A. F. O. and Henriques, J. C. C. (2016). Oscillating-water-column wave energy converters and air turbines: A review. *Renewable Energy*, 85:1391–1424.

Falnes, J. (1980). Radiation impedance matrix and optimum power absorption for interacting oscillators in surface waves. *Applied Ocean Research*, 2(2):75–80.

Falnes, J. (1984). Wave-power absorption by an array of attenuators oscillating with unconstrained amplitudes. *Applied Ocean Research*, 6(1):16 – 22.

Falnes, J. (2001). Optimum control of oscillation of wave energy converters. *International Journal of Offshore and Polar Engineering*, 12.

Falnes, J. (2002). *Ocean Waves and Oscillating Systems*. Cambridge University Press.

Falnes, J. and Budal, K. J. (1982). Wave-power absorption by parallel rows of interacting oscillating bodies. *Applied Ocean Research*, 4:194 – 207.

Felippa, C. U. o. C. (2014). Introduction to Finite Element Methods (ASEN 5007).

Fenton, J. (1978). Wave forces on vertical bodies of revolution. *Journal of Fluid Mechanics*, 85:241–255.

Ferrant, P. (2015). Tenue à la mer, cours ECN, option Hydrodynamique et Génie Océanique.

Fitzgerald, C. J. and Thomas, G. (2007). A preliminary study on the optimal formation of an array of wave power devices. In *Proceedings of the 7th European Wave and Tidal Energy Conference*, number Proc. of the 7th European Wave and Tidal Energy Conf., Porto, Portugal.

Folley, M., Babarit, A., Child, B., Forehand, D., Boyle, L. O., Silverthorne, K., Spinneken, J., Stratigaki, V., and Troch, P. (2012). A review of numerical modelling of wave energy converter arrays. In *Proceedings of the ASME 2012 31st International Conference on Ocean, Offshore and Arctic Engineering*, pages 1–11.

Folley, M. and Whittaker, T. (2009). The effect of sub-optimal control and the spectral wave climate on the performance of wave energy converter arrays. *Applied Ocean Research*, 31(4):260–266.

Fouilloux, A. and Corde, P. (2014). *Cours IDRIS Fortran: notions de base.*

Fred Olsen Ltd (2009). FO3 Platform artist impression.

G., T. and D., E. (1981). Arrays of three-dimensional wave-energy aborbers. *Journal of Fluid Mechanics*, 108:67–88.

Garnaud, X. and Mei, C. C. (2009). Wave-power extraction by a compact array of buoys. *Journal of Fluid Mechanics*, 635:389–413.

Garrett, C. (1971). Wave forces on a circular dock. *Journal of Fluid Mechanics*, 46.

Goo, J.-S. and Yoshida, K. (1990). A Numerical Method for Huge Semisubmersible Responses in Waves. *Society of Naval Architects and Marine Engineers*, 98:365–387.

Göteman, M., Engström, J., Eriksson, M., and Isberg, J. (2015). Fast Modeling of Large Wave Energy Farms Using Interaction Distance Cut-Off. *Energies*, 8(12):13741–13757.

Guo, J. (2002). Simple and explicit solution of wave dispersion equation. *Coastal Engineering*, 45:71–74.

Hansen, R. H. and Kramer, M. M. (2011). Modelling and Control of the Wavestar Prototype. *Proceedings of the 9th European Wave and Tidal Energy Conference*, pages 1–10.

Hansen, R. H., Kramer, M. M., and Vidal, E. (2013). Discrete displacement hydraulic power take-off system for the wavestar wave energy converter. *Energies*, 6(8):4001–4044.

Haskind, M. (1957). The Exciting Forces and Wetting of Ships in Waves, (in Russian), Izvestia Akademii Nauk S.S.S.R., Otdelenie Tekhnicheskikh Nauk, No. 7 (English translation available as David Taylor Model Basin Translation No. 307, March 1962).

Holthuijsen, L. H. (2010). *Waves in Oceanic and Coastal Waters*. Cambridge University Press.

IPCC (1988). Intergovernmental Panel on Climate Change.

IPCC (2014). Climate Change 2014: Synthesis Report. contribution of Working Groups I, II and III to the Fifth Assessment Report of the Intergovenmental Panel on Climate Change [Core Writing Team, R.K. Pachauri and L.A. Meyer (eds.)]. Technical report, Geneva, Switzerland.

Jean, P., Wattez, A., Ardoise, G., Melis, C., Van Kessel, R., Fourmon, A., Barrabino, E., Heemskerk, J., and Queau, J. P. (2012). Standing wave tube electro active polymer wave energy converter. In *Proc. SPIE*, pages 83400C–83400C–21.

John, F. (1950). On the motion of floating bodies II. Simple harmonic motions. *Communications on Pure and Applied Mathematics*, 3:45–101.

Kagemoto, H. and Yue, D. K. P. (1986). Interactions among multiple three-dimensional bodies in water waves: an exact algebraic method. *Journal of Fluid Mechanics*, 166(-1):189.

Kagemoto, H. and Yue, D. K. P. (1993). Hydrodynamic interaction analyses of very large floating structures. *Marine Structures*, 6(2-3):295–322.

Kashiwagi, M. (1998). A B-Spline Galerkin scheme for calculating the hydroelastic response of a Very Large Floating Structure in waves. *Journal of Marine Science and Technology*, pages 37–49.

Kashiwagi, M. (2000). Hydrodynamic interactions among a great number of columns supporting a very large flexible structure. *Journal of Fluids and Structures*, 14:1013–1034.

Kashiwagi, M. (2002). Wave-Induced Local Steady Forces on a Column-Supported Very Large Floating Structure. *International Journal of Offshore and Polar Engineering*, 12(2):98–104.

Kashiwagi, M. and Kohjoh, T. (1995). A method of computing hydrodynamic interactions in Large Floating Structures composed of multiple bodies. In *Proceedings of 13th Ocean Engineering Symposium*, pages 247–254. Society of Naval Architects of Japan.

Kashiwagi, M. and Yoshida, S. (2001). Wave Drift Force and Moment on VLFS Supported by a Great Number of Floating Columns. *International Journal of Offshore and Polar Engineering*, 11(3):176–183.

Kramer, M., Marquis, L., and Frigaard, P. (2011). Performance Evaluation of the Wavestar Prototype. In *Proceedings of the 9th European Wave and Tidal Conference*, Southampton.

Kring, D., Korsmeyer, T., Singer, J., and White, J. (2000). Analyzing mobile offshore bases using accelerated boundary-element methods. *Marine Structures*, 13(4-5):301–313.

Lee, C.-H. and Newman, J. (1999). WAMIT.

Linton, C. M. and McIver, P. (2001). *Handbook of mathematical techniques for wave/structure interactions*.

MacCamy, R. C. and Fuchs, R. A. (1954). Wave Forces on Piles: A Diffraction Theory.

Manchester Bobber (2008). Manchester Bobber artist impression.

Mavrakos, S. A. (1991). Hydrodynamic coefficients for groups of interacting vertical axisymmetric bodies. *Ocean Engineering*, 18(5):485–515.

Mavrakos, S. A. and Koumoutsakos, P. (1987). Hydrodynamic interaction among vertical axisymmetric bodies restrained in waves. *Applied Ocean Research*, 9(3):128–140.

Mavrakos, S. A. and McIver, P. (1997). Comparison of methods for computing hydrodynamic characteristics of arrays of wave power devices. *Applied Ocean Research*, 1187(97):283–291.

McIver, P. and Evans, D. V. (1984). Approximation of wave forces on cylinder arrays. *Applied Ocean Research*, 6(2):101–107.

McNatt, J. C. (2015). *Cylindrical Linear Water Waves and their Application to the Wave-body Problem*. PhD thesis, The University of Edinburgh.

McNatt, J. C., Venugopal, V., and Forehand, D. (2013). The cylindrical wave field of wave energy converters. *International Journal of Marine Energy*, 3-4:e26–e39.

McNatt, J. C., Venugopal, V., and Forehand, D. (2015). A novel method for deriving the diffraction transfer matrix and its application to multi-body interactions in water waves. *Ocean Engineering*, 94:173–185.

Mei, C. C. (1989). *The Applied Dynamics of Ocean Surface Waves*. World Scientific.

Montiel, F., Squire, V. A., and Bennetts, L. G. (2015a). Evolution of directional wave spectra through finite regular and randomly perturbed arrays of scatterers. *Journal of Applied Mathematics*, 75(2):630–651.

Montiel, F., Squire, V. A., and Bennetts, L. G. (2015b). Reflection and transmission of ocean wave spectra by a band of randomly distributed ice floes. *Annals of Glaciology*, (10):1–9.

Montiel, F., Squire, V. A., and Bennetts, L. G. (2016). Attenuation and directional spreading of ocean wave spectra in the marginal ice zone. *Journal of Fluid Mechanics*, 790:492–522.

Moreau, J.-P. (2014). Bessel Programs in Fortran 90.

Nambiar, A. J., Forehand, D. I. M., Kramer, M. M., Hansen, R. H., and Ingram, D. M. (2015). Effects of hydrodynamic interactions and control within a point absorber array on electrical output. *International Journal of Marine Energy*, 9:20–40.

Newman, J. (1962). The Exciting Forces on Fixed Bodies in Waves. *Journal of Ship Research*, 6(10).

Newman, J. N. (1977). *Marine Hydrodynamics*. The Massachusetts Institute of Technology, 9th edition.

Newman, J. N. (1994). Wave effects on deformable bodies. *Applied Ocean Research*, 16(1):47–59.

Ohkusu, M. (1974). Hydrodynamic forces on multiple cylinders in waves. In *International Symposium on the Dynamics of Marine Vehicles and Structures in Waves*, pages 107–112.

Pecher, A. and Kofoed, J. P. (2017). *Handbook of Ocean Wave Energy*. Springer Open.

Peter, M. a. and Meylan, M. H. (2004a). Infinite-depth interaction theory for arbitrary floating bodies applied to wave forcing of ice floes. *Journal of Fluid Mechanics*, 500:145–167.

Peter, M. a. and Meylan, M. H. (2004b). The eigenfunction expansion of the infinite depth free surface Green function in three dimensions. *Wave Motion*, 40(1):1–11.

Peterson, P. (2007). F2PY: Fortran to Python interface generator.

Principia (2016). DIODORE.

Quarteroni, A., Sacco, R., and Saleri, F. (2007). *Méthodes Numériques: Algorithmes, analyse et applications*.

REN21 (2016). Renewables 2016: Global Status Report. Technical report.

Ricci, P., Saulnier, J., and Falcao, A. (2007). Point-absorber arrays: a configuration study off the Portuguese west-coast. In *Proceedings of the 7th European Wave Tidal Energy Conference*, Porto (Portugal).

Rongère, F. (2016). Meshmagick User Manual, Ecole Centrale de Nantes (ECN).

Sabuncu, T. and Calisal, S. (1981). Hydrodynamic coefficients for vertical circular cylinders at finite depth. *Ocean Engineering*, 8:25–63.

Sharp, C. and DuPont, B. (2016). A multi-objective real-coded genetic algorithm method for wave energy converter array optimization. In *Proceedings of the ASME 2016 35th International Conference on Ocean, Offshore and Arctic Engineering*, pages 1–10.

SI Ocean (2013). Ocean Energy: Cost of Energy and Cost Reduction Opportunities. Technical Report May.

SI Ocean (2014). Wave and Tidal Energy Market Deployment Strategy for Europe, Strategic Initiative for Ocean Energy. Technical Report June.

Siddorn, P. and Eatock Taylor, R. (2008). Diffraction and independent radiation by an array of floating cylinders. *Ocean Engineering*, 35(13):1289–1303.

Simon, M. J. (1982). Multiple scattering in arrays of axisymmetric wave-energy devices. Part 1. A matrix method using a plane-wave approximation. *Journal of Fluid Mechanics*, 120(-1):1.

Singh, J. and Babarit, A. (2014). A fast approach coupling Boundary Element Method and plane wave approximation for wave interaction analysis in sparse arrays of wave energy converters. *Ocean Engineering*, 85:12–20.

Spring, B. H. and Monkmeyer, P. L. (1974). Interaction of Plane Waves With Vertical Cylinders. *Proceedings of the 14th Coastal Engineering Proceedings*, 3:1828–1847.

Taghipour, R. and Moan, T. (2008). Efficient Frequency-Domain Analysis of Dynamic Response for the Multi-Body Wave Energy Converter in Multi-Directional Waves. *Proceedings of the Eighteenth (2008) International Offshore and Polar Engineering Conference*, 8:357–365.

Thomas, P. and Evans, V. (1981). Arrays of three-dimensional wave-energy absorbers. *Journal of Fluid Mechanics*, 108:67–88.

Topper, M. (2010). Numerical Modelling of Flows Free Surfaces.

TPOcean (2016). Strategic Research Agenda for Ocean Energy, European Technology and Innovation Platform for Ocean Energy. Technical report.

Twersky, V. (1952). Multiple scattering and radiation by an arbitrary configuration of parallel cylinders. *Journal of the Acoustical Society of America*, 24:42–46.

Ursell, F. (1960). On Kelvin ' s ship-wave pattern. *Journal of Fluid Mechanics*, 8-3:418–431.

Watson, G. (1966). *A treatise on the theory of Bessel functions*. Cambridge University Press.

WAVESTAR (2015). Wavestar concept.

Weller, S., Stallard, T., and Stansby, P. (2010). Experimental measurements of irregular wave interaction factors in closely spaced arrays. *IET Renewable Power Generation*, 4(6):628.

Wolgamot, H. A., Taylor, P. H., and Eatock Taylor, R. (2012). The interaction factor and directionality in wave energy arrays. *Ocean Engineering*, 47:65–73.

Yeung, R. W. (1981). Added mass and damping of a vertical cylinder in finite-depth waters. *Applied Ocean Research*, 3(3):119–133.

Yilmaz, O. (1998). Hydrodynamic Interaction of Waves with Group of Truncated Vertical Cylinders. *Jounal of waterway, port, coastal, and ocean engineering*, pages 272–279.

Yilmaz, O. and Incecik, A. (1998). Analytical solutions of the diffraction problem of a group of truncated vertical cylinders. *Ocean engineering*, 25(6):385–394.

Yilmaz, O., Incecik, A., and Barltrop, N. (2001). Wave enhancement due to blockage in semi-submersible and TLP structures. *Ocean Engineering*, 28(5):471–490.

Zeng, X.-h. and Tang, S.-y. (2013). The hydrodynamic interactions of an array of truncated circular cylinders as each cylinder oscillates independently with different prescribed modes. *Journal of Hydrodynamics, Ser. B*, 25(1):27–38.

Appendix A

Derivation of outgoing partial wave functions

The following analysis has been extracted and adapted from section 3.4.1 in Child (2011).

Take Laplace's equation (2.1.4) in cylindrical polar coordinates:

$$\frac{\partial^2\phi}{\partial r^2} + \frac{1}{r}\frac{\partial\phi}{\partial r} + \frac{1}{r^2}\frac{\partial^2\phi}{\partial\theta^2} + \frac{\partial^2\phi}{\partial z^2} = 0 \tag{A.0.1}$$

Assume a separable solution for the potential of the form:

$$\phi = \sigma_r(r)\,\sigma_\theta(\theta)\,\sigma_z(z) \tag{A.0.2}$$

Substitution of (A.0.2) into (A.0.1), with the introduction of a separation constant $-\mu^2$ leads to:

$$\frac{\sigma_r^{''}}{\sigma_r} + \frac{\sigma_r^{'}}{\sigma_r r} + \frac{\sigma_\theta^{''}}{r^2\sigma_\theta} = -\frac{\sigma_z^{''}}{\sigma_z} = -\mu^2, \quad \mu \in \mathbb{C} \tag{A.0.3}$$

where the prime $'$ denotes differentiation with respect to the functional variable.

A.1 Separation of the z-coordinate

Take the middle and right-hand side of expression (A.0.3):

$$\sigma_z^{''} - \mu^2\sigma_z = 0 \tag{A.1.1}$$

The general solution for $\sigma_z(z)$ of (A.1.1) is:

$$c_1 \cosh \mu z + c_2 \sinh \mu z, \quad c_1, c_2 \in \mathbb{C} \tag{A.1.2}$$

Application of the boundary condition on the seabed (2.1.8) implies $c_2 = 0$, and the free surface BC (2.2.6) leads to:

$$\frac{\omega^2}{g} = \mu \tanh \mu d \tag{A.1.3}$$

for non-trivial solutions. Equation (A.1.3) defines the eigenvalues μ in the vertical direction and is known as dispersion relation. Solutions of the equation are either purely real or imaginary (Mei, 1989, 4.2,4). Those with negative real or imaginary parts will be abandoned, since the corresponding velocity potentials do not satisfy the radiation condition (2.2.3). If μ is real, a unique solution $\mu = k_0$ is obtained, known as the progressive wave number which corresponds to travelling wave solutions and satisfies:

$$\frac{\omega^2}{g} = k_0 \tanh k_0 d, \quad k_0 \geq 0 \, (k_0 \in \mathbb{R}) \tag{A.1.4}$$

If, on the other hand, μ is purely imaginary then there exists a countably infinite set of solutions $\mu = ik_q \, (q = 1, 2, \dots)$ to (A.1.3). The values k_q are known as the evanescent wave numbers and are given by:

$$\frac{\omega^2}{g} = -k_q \tan k_q d, \quad k_q \geq 0 \, (k_q \in \mathbb{R}), \, q \geq 1 \, (q \in \mathbb{N}) \tag{A.1.5}$$

The spatial functions associated with the eigenvalues take the form:

$$\sigma_z^q(z) = \begin{cases} \cosh \, k_0 z, & q = 0 \\ \cos \, k_q z, & q \geq 1 \, (q \in \mathbb{N}) \end{cases} \tag{A.1.6}$$

A.2 Separation of the θ-coordinate

From the outermost expressions in (A.0.3), a further separation constant $-v^2$ may be introduced to give:

$$-\mu^2 r^2 - \frac{\sigma_r'' r^2}{\sigma_r} - \frac{\sigma_r'}{\sigma_r} = \frac{\sigma_\theta''}{\sigma_\theta} = -v^2, \quad v \in \mathbb{C} \tag{A.2.1}$$

The middle and right-hand expressions of this yield:

$$\sigma_\theta^{''} + v^2\sigma_\theta = 0 \tag{A.2.2}$$

If $v \neq 0$, equation (A.2.2) has the following solution for σ_θ:

$$c_1 e^{iv\theta} + c_2 e^{-iv\theta}, \quad c_1,\, c_2 \in \mathbb{C} \tag{A.2.3}$$

However, continuity of the potential as θ increases from 2π to 0 requries that $v = n$ be an integer. Hence the values that v may take form a further set of eigenvalues. In the degenerate case where $v = 0$, equation (A.2.2) may be integrated directly to give the solution:

$$c_1\theta + c_2, \quad c_1,\, c_2 \in \mathbb{C} \tag{A.2.4}$$

Applying continuity of the potential again means that $c_1 = 0$, with the (constant) remainder of this solution capable of being incorporated into (A.2.3) as the $v = 0$ case. The eigenfunctions in the angular coordinate are therefore given by:

$$\sigma_\theta^{n\pm}(\theta) = e^{\pm in\theta}, \quad n \in \mathbb{Z} \tag{A.2.5}$$

A.3 Separation of the r-coordinate

The outermost expressions of (A.2.1) lead to:

$$-\mu^2 r^2 - \frac{\sigma_r^{''} r^2}{\sigma_r} - \frac{\sigma_r^{'} r}{\sigma_r} = -v^2 \tag{A.3.1}$$

Inserting the eigenvalues μ and v gives an equation for every pair of values. In the progressive case, the transformation $\hat{r}(r) = k_0 r$ with $\hat{\sigma}_r(\hat{r}(r)) = \sigma_r(r)$ then leads to:

$$\hat{\sigma}_r^{''}\hat{r}^2 + \hat{\sigma}_r^{'}\hat{r} + (\hat{r}^2 - n^2)\hat{\sigma}_r = 0 \tag{A.3.2}$$

This is Bessel's equation in the variable $\hat{r}$, which has linearly independent solutions $J_n(\hat{r})$and $Y_n(\hat{r})$ (Bessel functions of the first and second kind of order n). It will in fact be convenient to express the solution using the Hankel function of the first kind of order n:

$$H_n = H_n^{(1)} = J_n + iY_n \tag{A.3.3}$$

The required space is still spanned if the function H_n is used instead of Y_n. Furthermore this choice of function allows the radiation condition (2.2.3) to be satisfied. Hence the solution for σ_r in the original variable is:

$$c_1 J_n(k_0 r) + c_2 H_n(k_0 r), \quad c_1,\, c_2 \in \mathbb{C} \tag{A.3.4}$$

which exists for each n. The evanescent case involves substitution of the imaginary eigenvalues into (A.3.1). Using the transformation $\hat{r}(r) = k_q r$ with $\hat{\sigma_r}(\hat{r}(r)) = \sigma_r(r)$, this gives:

$$\hat{\sigma}_r^{''}\hat{r}^2 + \hat{\sigma}_r^{'}\hat{r} + (-\hat{r}^2 - n^2)\hat{\sigma_r} = 0 \tag{A.3.5}$$

This is the modified Bessel equation in $k_q r$, so we have the following solution for σ_r:

$$c_1 I_n(k_q r) + c_2 K_n(k_q r), \quad c_1,\, c_2 \in \mathbb{C},\, q \geq 1 \tag{A.3.6}$$

for each pair q, n. I_n and K_n are the modified Bessel functions of the first and second kind of order n. Application of the radiation condition (2.2.3) to solutions (A.3.4) and (A.3.6) for large argument prohibits inclusion of the functions J_n and I_n. The permitted solution in the r-coordinate are:

$$\sigma_r^{q,n}(r) = \begin{cases} H_n(k_0 r), & q = 0,\, n \in \mathbb{Z} \\ K_n(k_q r), & q \geq 1\,(q \in \mathbb{N}),\, n \in \mathbb{Z} \end{cases} \tag{A.3.7}$$

A.4 General solution

For each pair of eigenvalues (μ, v), the separable solution for ϕ may be reconstructed as the product of spatial functions (A.1.6), (A.2.5) and (A.3.7) in each coordinate. After some manipulation, the solutions containing σ_θ^{n-} may be seen to differ from those containing $\sigma_\theta^{n+}$by only a scalar factor and so are subsequently omitted. The general soltuion for ϕ may then be written as a linear combination of outgoing partial wave functions:

$$\left(\psi^S\right)_{nm} = \begin{cases} \frac{\cosh\, k_0 z}{\cosh\, k_0 d}\, H_n(k_0 r)\, e^{in\theta}, & q = 0,\, n \in \mathbb{Z} \\ \cos\, k_q z\, K_n(k_q r)\, e^{in\theta}, & q \geq 1\,(q \in \mathbb{N}),\, n \in \mathbb{Z} \end{cases} \tag{A.4.1}$$

where it has been taken into account that any solution can be written as a linear combination of eigenfunctions of the form (A.1.6) regardless of the pre-factor used. In

this case, $\frac{1}{\cosh k_0 d}$ has been chosen.

Appendix B

Transformation Matrix

The method of solution of the Direct Matrix Method interaction theory involves treating the outgoing waves from body i, i.e. diffracted and radiated waves, as incident waves to the other bodies of the array. It is important to note that the diffracted and radiated wavefields from body i are expressed in its local reference system. Hence, there is a need to transform them into incident waves to another body j in its local reference system. The transformation is based on the Graf's addition theorem for Bessel functions (Abramowitz and Segun A., 1964) which states that:

$$H_m(k_0 r_i)e^{im(\theta_i-\alpha_{ij})} = \sum_{q=-\infty}^{\infty} H_{m+q}(k_0 L_{ij})J_q(k_0 r_j)e^{iq(\pi-\theta_j+\alpha_{ij})} \tag{B.0.1}$$

$$K_m(k_n r_i)e^{im(\theta_i-\alpha_{ij})} = \sum_{q=-\infty}^{\infty} K_{m+q}(k_n L_{ij})I_q(k_n r_j)e^{iq(\pi-\theta_j+\alpha_{ij})} \tag{B.0.2}$$

where L_{ij} is the distance between the centers of bodies i and j and α_{ij} is the angle at body i between the positive x-direction and the line joining the center of i to that of j in an anti-clockwise direction (Figure 2.4). They are expressed respectively as in (2.3.4) and (2.3.5).

Expressions (B.0.1) and (B.0.2) are valid only if $r_i < L_{ij}$ which is ensured by satisfying that the circumscribing cylinder of body i does not contain the center of the circumscribing cylinder of body j (Figure B.1). By replacing index q by $-q$, and by noting that:

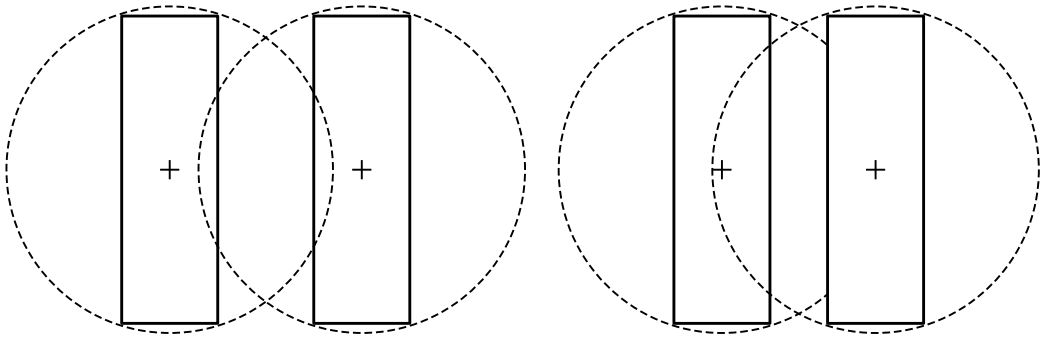

(a) (b)

Figure B.1: Authorized a) and unauthorized b) relative position between bodies to comply with Graff's addition theorem restriction.

$$J_{-q} = (-1)^q J_q \tag{B.0.3}$$

$$I_{-q} = I_q \tag{B.0.4}$$

expressions (B.0.1)-(B.0.2) can be rewritten as:

$$H_m(k_0 r_i)e^{im(\theta_i)} = \sum_{q=-\infty}^{\infty} H_{m-q}(k_0 L_{ij})e^{i\alpha_{ij}(m-q)} J_q(k_0 r_j)e^{iq\theta} \tag{B.0.5}$$

$$K_m(k_n r_i)e^{im(\theta_i)} = \sum_{q=-\infty}^{\infty} K_{m-q}(k_n L_{ij})(-1)^q e^{i\alpha_{ij}(m-q)} I_q(k_n r_j)e^{iq\theta_j} \tag{B.0.6}$$

The terms on the left hand side are the functions representing the scattered partial waves of angular mode m and depth mode n in the local cylindrical reference system of body i (2.2.12), whereas the last two terms on the right hand side are the functions representing the incident partial wave of angular mode q and depth mode n in the local reference system of body j (2.2.23). Thus, the following applies:

$$\psi_i^S = \mathbf{T}_{ij}\psi_j^I \tag{B.0.7}$$

where ψ_i^S is the vector of scattered partial wave functions in the local reference system of body i, ψ_j^I is the vector of incident partial wave functions in the local reference system of body j and $\mathbf{T}_{ij}$ is referred to as "transformation matrix" whose

elements are:

$$(\mathbf{T}_{ij})_{nn}^{mq} = \begin{cases} H_{m-q}(k_0 L_{ij}) e^{i\alpha_{ij}(m-q)} & n = 0 \\ K_{m-q}(k_n L_{ij})(-1)^q e^{i\alpha_{ij}(m-q)} & n \geq 1 \end{cases} \tag{B.0.8}$$

As the transformation in (B.0.1)-(B.0.2) does not affect the depth variation of the partial cylindrical waves, a single index n is used in (B.0.8).

Appendix C

Single truncated vertical cylinder at finite depth

The work by Sabuncu and Calisal (1981) presents an analytical formulation of the hydrodynamic coefficients for vertical circular cylinders at finite depth. The analysis follows Garrett's method (Garrett, 1971) and divides the fluid into an inner and an outer region as shown in Figure (C.1). A potential formulation is used based on the hypothesis of irrotationality and incompressibility of the flow. The solution of the potential is found separately for each region and, by means of imposing its continuity at the boundary as well as continuity of the velocity, the solution for the whole domain is found.

C.1 System of equations

The following formulation has been extracted from the work by Sabuncu and Calisal (1981) but has been slightly modified in order to correct several typographical errors encoutered in the original work[1]. The changes have been highlighted with red colour. The added mass and damping coefficients for heave mode are calculated using:

$$\frac{a_{22}}{\rho D}+i\frac{b_{22}}{\omega\rho D}=\frac{d}{h-d}\left\{\frac{1}{2}-\frac{1}{8}\left(\frac{a}{d}\right)^2+\frac{1}{2}A_0+\frac{2}{\pi}\left(\frac{d}{a}\right)\sum_{n=1}^{\infty}\frac{A_n(-1)^n}{n}\frac{I_1\left(\frac{n\pi a}{d}\right)}{I_0\left(\frac{n\pi a}{d}\right)}\right\} \quad \text{(C.1.1)}$$

where a_{22} and b_{22} are the added mass and damping coefficients for heave, D is the

[1]The author would like to thank Sander Calisal for having provided an original copy of the equations through direct communication which has been very useful to identify the typographical errors.

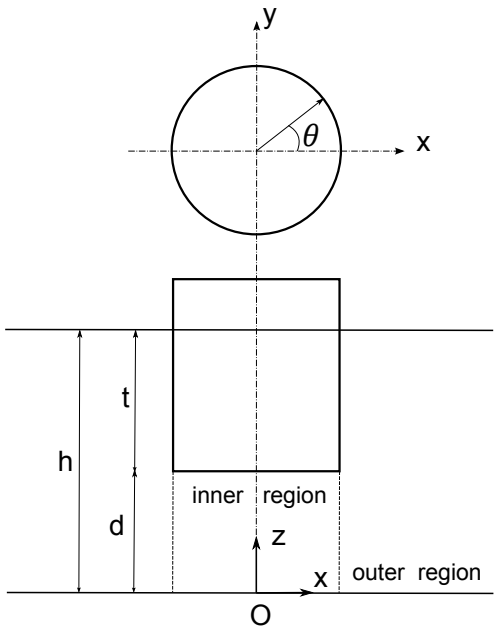

Figure C.1: Coordinate system. Source: Sabuncu and Calisal (1981)

volume of the cylinder in water and A_n are the complex coefficients which are solution of the following linear set of equations:

$$\gamma_{nj}\, A_j = h_n \tag{C.1.2}$$

Expressions for γ_{nj} and h_n are:

$$\gamma_{nj} = \left(\delta_{nj} + 16\, U_j (L\, P_0(n,j) + \sum_{q=1}^{\infty} \frac{K_0(m_q a)}{K_1(m_q a)} P_q(n,j)\right) + i\, \frac{32 U_j T P_0(n,j)}{\pi m_0 a} \tag{C.1.3}$$

$$h_n = \frac{4a}{d}\left(L P_0(n,0) + \sum_{q=1}^{\infty} \frac{K_0(m_q a)}{K_1(m_q a)}\, P_q(n,0)\right) - \frac{2(-1)^n}{(n\pi)^2} + i\, \frac{8}{\pi m_0 d} T P_0(n,0)$$

$$h_0 = \frac{4a}{d}\left(L P_0(0,0) + \sum_{q=1}^{\infty} \frac{K_0(m_q a)}{K_1(m_q a)}\, P_q(0,0)\right) - \left(\frac{1}{3} - \frac{1}{2}\left(\frac{a}{d}\right)^2\right) + i\, \frac{8}{\pi m_0 d} T P_0(n,0) \tag{C.1.4}$$

where:

$$\delta_{nj} = \begin{cases} 1 & \text{if } n = j \\ 0 & \text{if } n \neq j \end{cases} \tag{C.1.5}$$

$$U_j = \frac{j\pi}{2} \frac{I_1\left(j\frac{\pi a}{d}\right)}{I_0\left(j\frac{\pi a}{d}\right)} \quad j = 1, 2, 3, ... \quad U_0 = 0 \tag{C.1.6}$$

$$P_0(n,j) = \frac{(-1)^{n+j}(m_0 d\, sh(m_0 d))^2}{[(2m_0 h) + sh(2m_0 h)]\,[(m_0 d)^2 + (n\pi)^2]\,[(m_0 d)^2 + (j\pi)^2]} \tag{C.1.7}$$

$$P_q(n,j) = \frac{(-1)^{n+j}(m_q d\, sin(m_q d))^2}{[(2m_q h) + sin(2m_q h)]\,[(m_q d)^2 - (n\pi)^2]\,[(m_q d)^2 - (j\pi)^2]} \tag{C.1.8}$$

$$L = \frac{J_0(m_0 a)\, J_1(m_0 a) + Y_0(m_0 a)\, Y_1(m_0 a)}{[J_1(m_0 a)]^2 + [Y_1(m_0 a)]^2} \tag{C.1.9}$$

$$T = \frac{1}{[J_1(m_0 a)]^2 + [Y_1(m_0 a)]^2} \tag{C.1.10}$$

The values m_0 and m_q are the solution of the following dispersion equations:

$$m_0 \tanh(m_0 h) = \frac{\omega^2}{g} \tag{C.1.11}$$

$$m_q \tanh(m_q h) = -\frac{\omega^2}{g} \tag{C.1.12}$$

C.2 Numerical implementation

The equations presented in Section C.1 have been implemented in the programming language *Fortran*. It is obvious that the infinite series cannot be handled numerically and that a finite truncation is required. In the work of Sabuncu and Calisal (1981) a total of 20 terms were used for the computations. In Section C.4 the impact of the truncation order will be analysed by performing a convergence analysis.

In order to solve the dispersion equations (C.1.11 and C.1.12), which do not have an explicit analytical solution, numerical methods have been used. With respect to the former, it has been solved using the Newton-Raphson iterative algorithm. Briefly, this method enables to successively find better approximations to the roots of the function to be solved. In this case:

$$f(m_0) = m_0 \tanh(m_0 h) - \frac{\omega^2}{g} \tag{C.2.1}$$

To do so, the initial guess is replaced by:

$$m_0^1 = m_0^0 - \frac{f(m_0^0)}{f'(m_0^0)} \tag{C.2.2}$$

where the supperindexs represent the iteration.

In order to start the iterations as close as possible to the solution, the approximate analytical solution to Equation(C.2.1) provided by Guo (2002) has been used to generate m_0^0:

$$y = x^2(1 - e^{-x^\beta})^{-\frac{1}{\beta}} \tag{C.2.3}$$

where $x = h\omega/\sqrt{gh}$, $y = m_0 h$ and $\beta = 2.4908$.

With respect to (C.1.12), it has been solved using the bisection algorithm. Briefly, this method enables to find the root of a continuous function defined in an interval $[a, b]$ where $f(a)$ and $f(b)$ have opposite signs. For the particular case of the function:

$$f(m_q) = m_q \tan(m_q h) + \frac{\omega^2}{g} \tag{C.2.4}$$

the interval is $[\pi/2h + (j-1)\pi/h + \epsilon, \pi/h + j\pi/h - \epsilon]$, with j the truncation and ϵ a small value defined to to ensure that all the solutions are found (Section C.5).

For both Newton and bisection iterative algorithms, some parameters to control the precision of the solution as well as the maximum number of iterations allowed have been incorporated in the numerical routine.

Most of the functions used in the formulae are included in the Intel® Math Kernel Library, such as Bessel functions $J_\nu(x)$ and $Y_\nu(x)$. Others, such as the modified Bessel functions $K_\nu(x)$ and $I_\nu(x)$ have been obtained from the library SPECFUN (Cody and Stoltz, 2013).

To solve the linear complex system of equations (C.1.2), the LAPACK routine ZGESV based on a LU decomposition has been used. Other LAPACK routines that have been utilized include DGELS (to solve an overdetermined real linear system) and ZGESVD (to obtain the singular value decomposition of a complex matrix). Details of these numerical procedures can be found in Quarteroni et al. (2007).

C.3 Results

The graphs in Figures (C.2)-(C.7) show a comparison between the results obtained from the implementation of equations listed in (C.1) and the values provided by

Sabuncu and Calisal (1981). It is important to remind that, in both computations, the number of truncation terms used is 20. It can be observed that the agreement between the resutls is in general very good. It has to be precised that the data by Sabuncu and Calisal (1981) has been digitalized and this may have introduced some error with respect to the original values. This is particularly important for the added mass rather than for the damping coefficients.

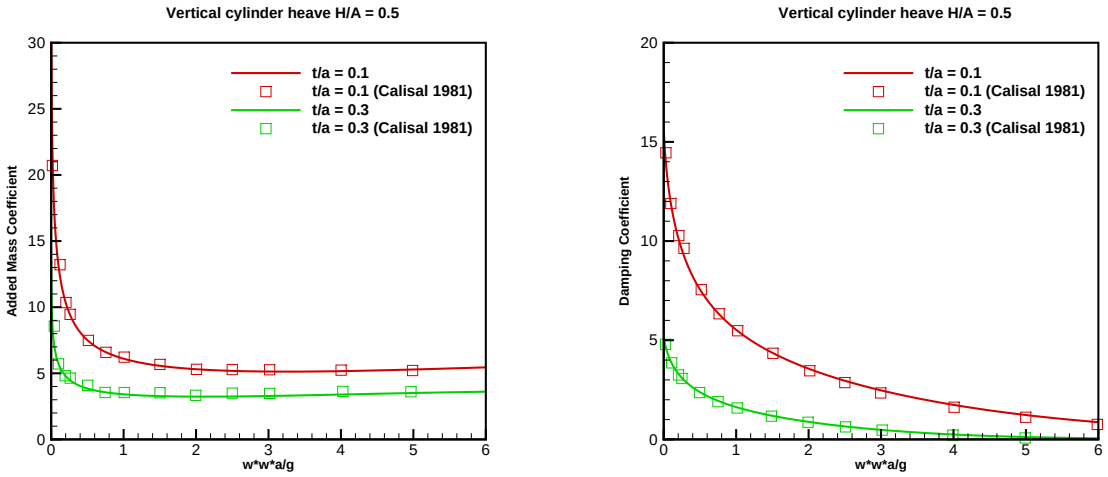

(a) (b)

Figure C.2

In addition, by taking advantage of the analytical expressions for the limiting case $\omega \to 0$ (C.3.1), a comparison showing analytical and numerical results for $\omega = 10^{-3}$ has been undertaken (Table C.1). Similarly to the previous case, the agreement is very good.

$$Im\, A_0 = \frac{\pi a^2}{2dh}; \quad \frac{b_{22}}{\omega \rho D} = \frac{\pi a^2}{4h(h-d)} \tag{C.3.1}$$

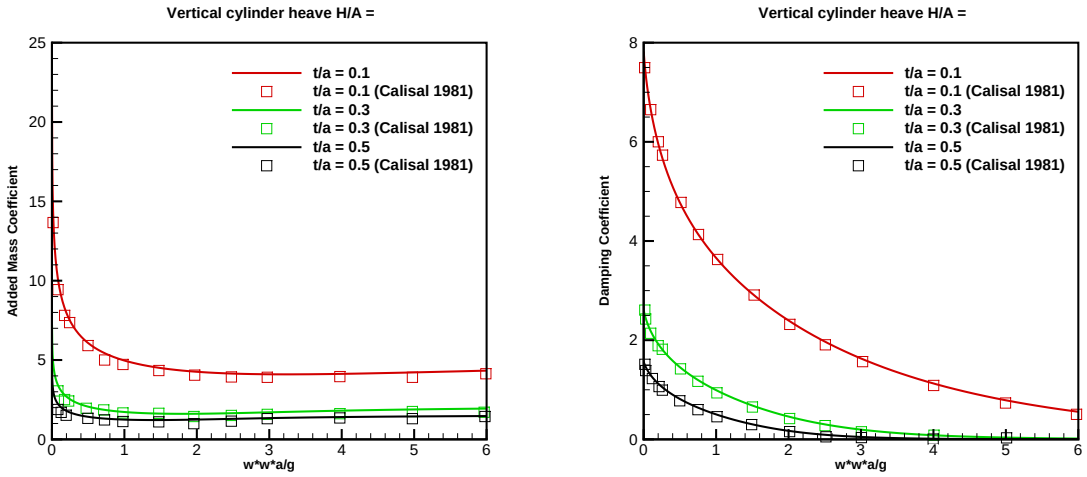

(a) (b)

Figure C.3

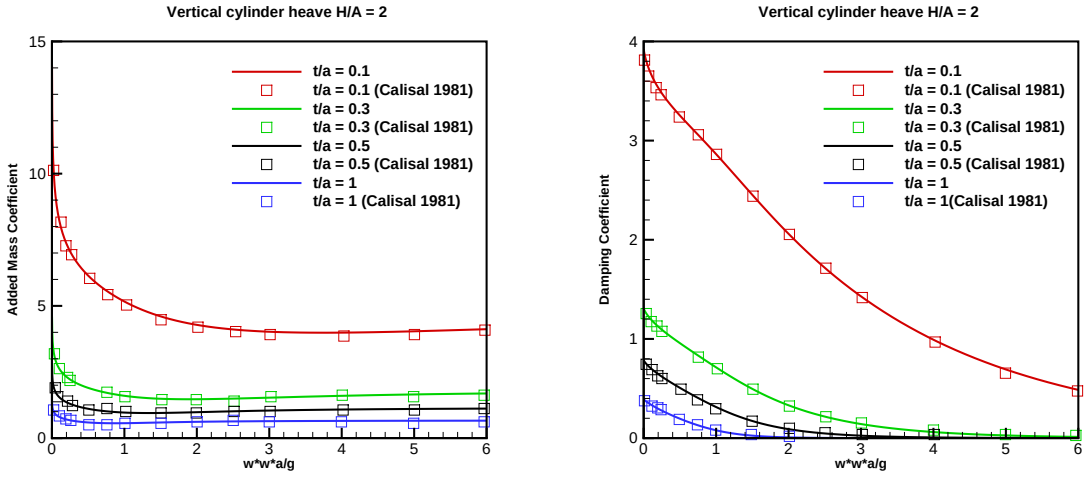

(a) (b)

Figure C.4

C.4 Accuracy

The solution of the system of equations (C.1.2) is not exempt from numerical errors. The objective of this section is to identify their source and try to quantify them so as to have a precision-controlled final result.

As stated in Quarteroni et al. (2007, pg.44), numerical errors arise from two sources: the rounding errors introduced by the computer while solving the problem and the

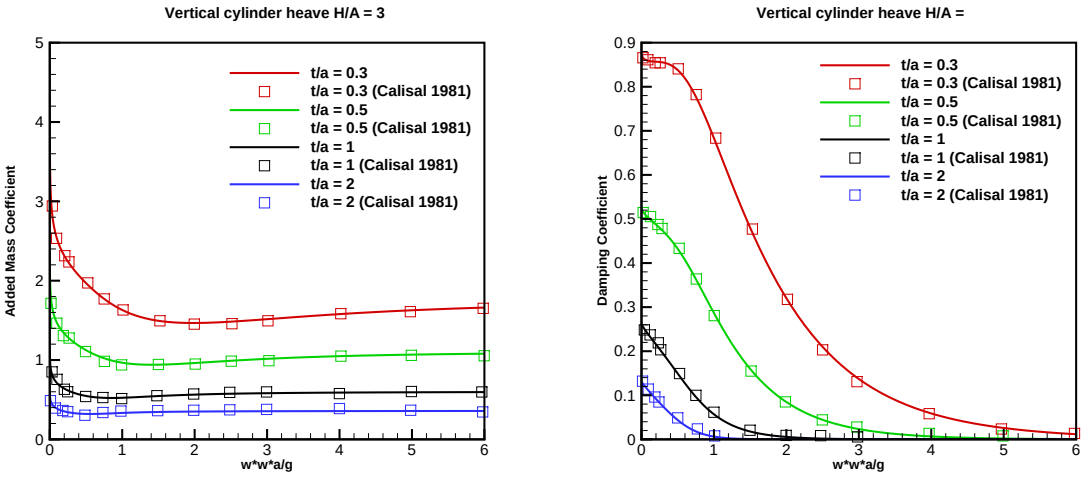

(a) (b)

Figure C.5

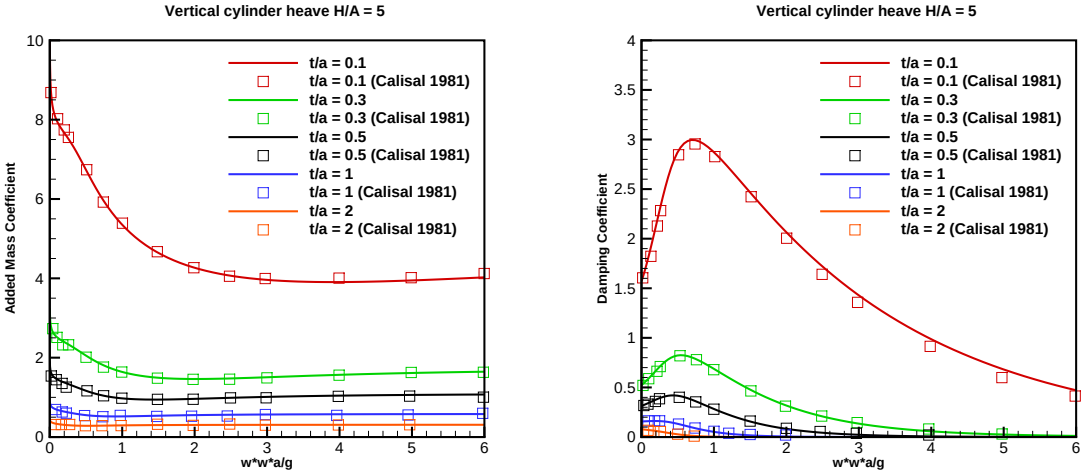

(a) (b)

Figure C.6

truncation of infinite operations that have to be completed in a finite number of steps. With respect to the former, the computations have been performed using double precision which enables to dispose of up to 15 significant digits.

As has already been mentioned in Section C.4, the solution of the dispersions equations (C.1.11) and (C.1.12) involves a numerical error which can be controlled in the routine by establishing the desired difference between their left and right sides by

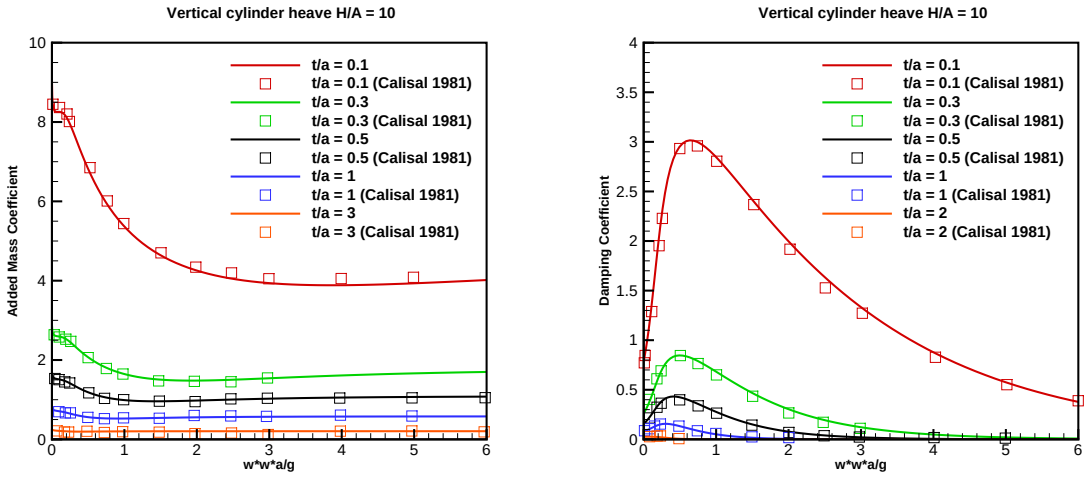

(a) (b)

Figure C.7

means of a parameter.

Another source of rounding error may come from the resolution of the linear system of equations. An important quantity to take into account when solving such systems, i.e. $Ax = b$, is the condition number. It gives an indication of how sensitive is the result of the system (x) to errors of the data (b). As a general rule of thumb, as stated by Cheney and Kincaid (2008, pg.321), it can be considered that the number of digits of precision lost in the resolution of the system is equal to $log_{10}(k(A))$ where $k(A)$ represents the condition number of the matrix A. Ideally, we are interested in having a small condition number to lose as less precision digits as possible. The graphs in Figures (C.8) to (C.13) provide the value of the condition number for different

h/a	t/a	$\pi a^2/2dh$	$Im(A_0)$	$\pi a^2/4h(h-d)$	$b_{22}/\omega\rho D$
0.5	0.1	7.85398163	7.85398149	15.70796326	15.70796299
0.5	0.3	15.70796326	15.70796298	5.23598775	5.23598766
1	0.1	1.74532925	1.74532926	7.85398163	7.85398167
1	0.3	2.24399475	2.24399471	2.61799387	2.61799383
1	0.5	3.14159265	3.14159250	1.57079632	1.57079625
2	0.1	0.41336745	0.41336745	3.92699081	3.92699077
2	0.3	0.46199891	0.46199890	1.30899693	1.30899691
2	0.5	0.52359877	0.52359879	0.78539816	0.78539818
2	1	0.78539816	0.78539818	0.39269908	0.39269909
3	0.3	0.19392547	0.19392547	0.87266462	0.87266461
3	0.5	0.20943951	0.20943951	0.52359877	0.52359879
3	1	0.26179938	0.26179939	0.26179938	0.26179939
3	2	0.52359877	0.52359879	0.13089969	0.13089969
5	0.1	0.06411413	0.06411413	1.57079632	1.57079639
5	0.3	0.06684239	0.06684239	0.52359877	0.52359879
5	0.5	0.06981317	0.06981316	0.31415926	0.31415926
5	1	0.07853981	0.07853981	0.15707963	0.15707963
5	2	0.10471975	0.10471975	0.07853981	0.07853981
10	0.1	0.01586662	0.01586662	0.78539816	0.78539817
10	0.3	0.01619377	0.01619377	0.26179938	0.26179940
10	0.5	0.01653469	0.01653469	0.15707963	0.15707962
10	1	0.01745329	0.01745329	0.07853981	0.07853981
10	3	0.02243994	0.02243994	0.02617993	0.02617993

Table C.1: Comparison between analytical and numerically calculated values ($\omega = 10^{-3}$)

levels of truncation. It can be observed that the matrix of the system (C.1.2) is well conditioned meaning that the lost of precision related to its resolution is insignificant. The condition number can be computed using the following expression (Quarteroni et al., 2007, pg.63):

$$k(A) = \frac{\sigma_{max}}{\sigma_{min}} \tag{C.4.1}$$

where σ_{max} and σ_{min} represent the highest and lowest singular values of the matrix A.

With respect to the infinite series truncation, a convergence analysis has been performed and some of its results are presented in Figures (C.8) to (C.13). It can be observed that the convergence curves follow different trends depending on the combination of input parameters. In all the cases analysed the level of convergence is very satisfactory as at the beginning of the iterations the difference with respect to

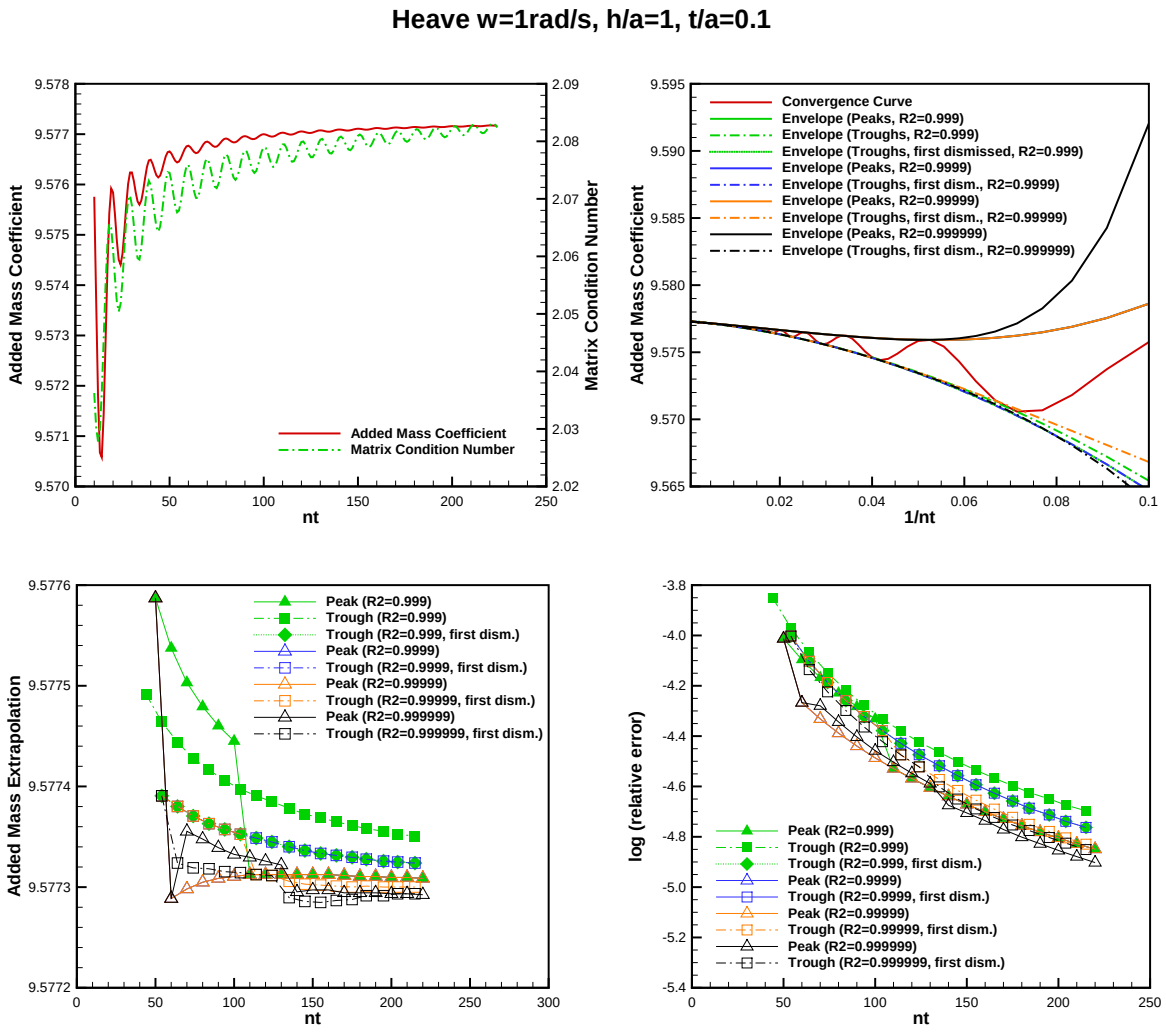

Figure C.8

the converged value is already less than 0.2%.

For an accurate estimation of the error, the envelopes of the convergence curve (for the oscillating trends) and the curve itself (for the non-oscillating) have been expressed in terms of the inverse of the truncation $(1/nt)$ and fitted by means of a polynome $P(1/nt)$:

$$P(1/nt) = a_0 + a_1(1/nt) + a_2(1/nt)^2 + a_3(1/nt)^3 + ... \qquad \text{(C.4.2)}$$

That way, the term a_0 provides an extrapolation of the hydrodynamic coefficients values which would correspond to having infinite nt (bottom left graph of Figures (C.8) to (C.13)).

The coefficients of the polynome have been obtained solving the following overde-

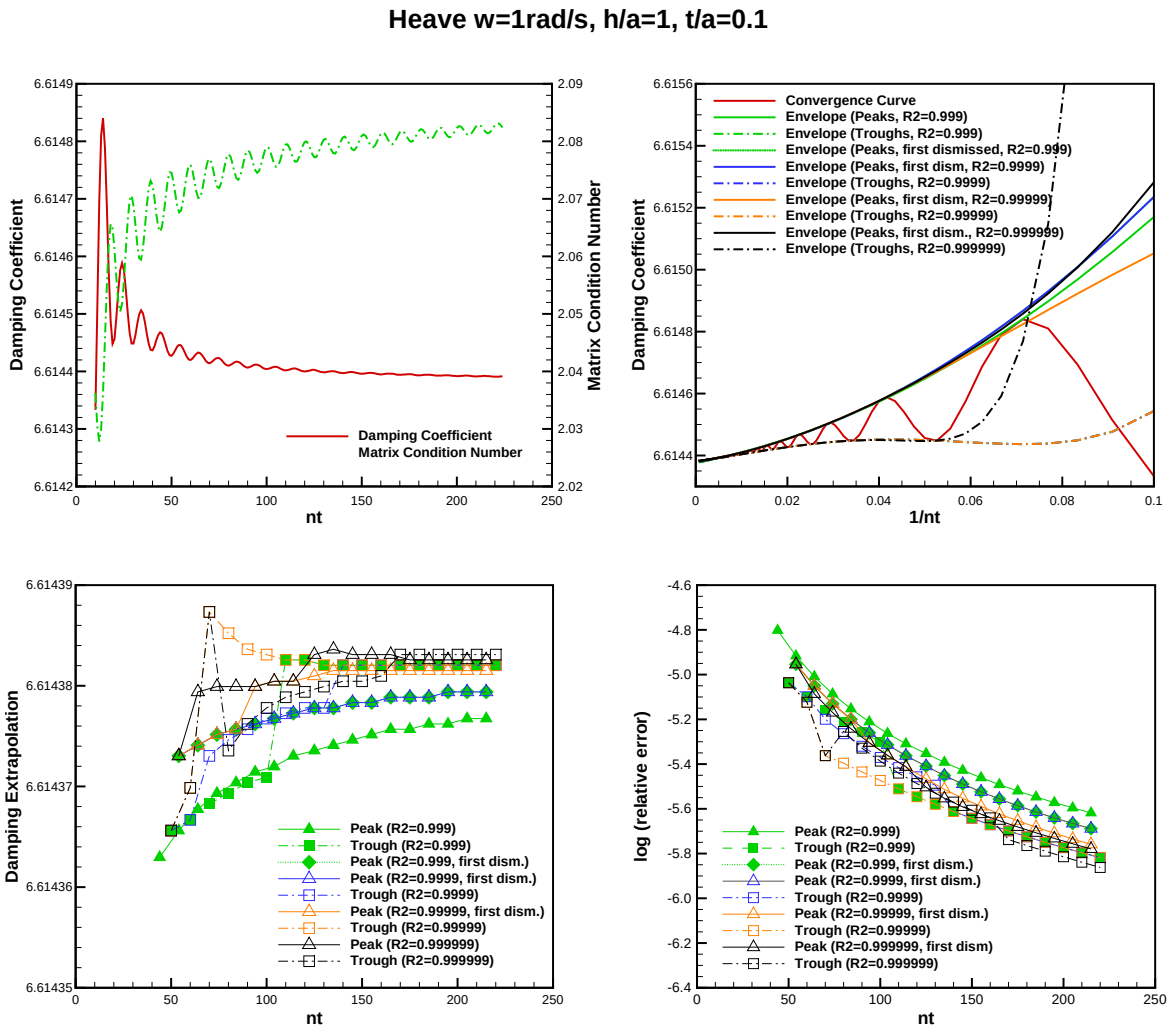

Figure C.9

termined system using a least-squares method:

$$\begin{bmatrix} c_1 \\ c_2 \\ \vdots \\ c_n \end{bmatrix} = \begin{bmatrix} 1 & \frac{1}{nt_1} & \left(\frac{1}{nt_1}\right)^2 & \cdots & \left(\frac{1}{nt_1}\right)^k \\ 1 & \frac{1}{nt_2} & \left(\frac{1}{nt_2}\right)^2 & \cdots & \left(\frac{1}{nt_2}\right)^k \\ \vdots & \vdots & \vdots & \ddots & \vdots \\ 1 & \frac{1}{nt_n} & \left(\frac{1}{nt_n}\right)^2 & \cdots & \left(\frac{1}{nt_n}\right)^k \end{bmatrix} \begin{bmatrix} a_0 \\ a_1 \\ \vdots \\ a_k \end{bmatrix} \tag{C.4.3}$$

where c_1,c_2,..., c_n represent the hydrodynamic coefficients for different truncation values $1, 2, .., n$, and $a_0, a_1, ..., a_k$ represent the unknown coefficients of the polynome of order k.

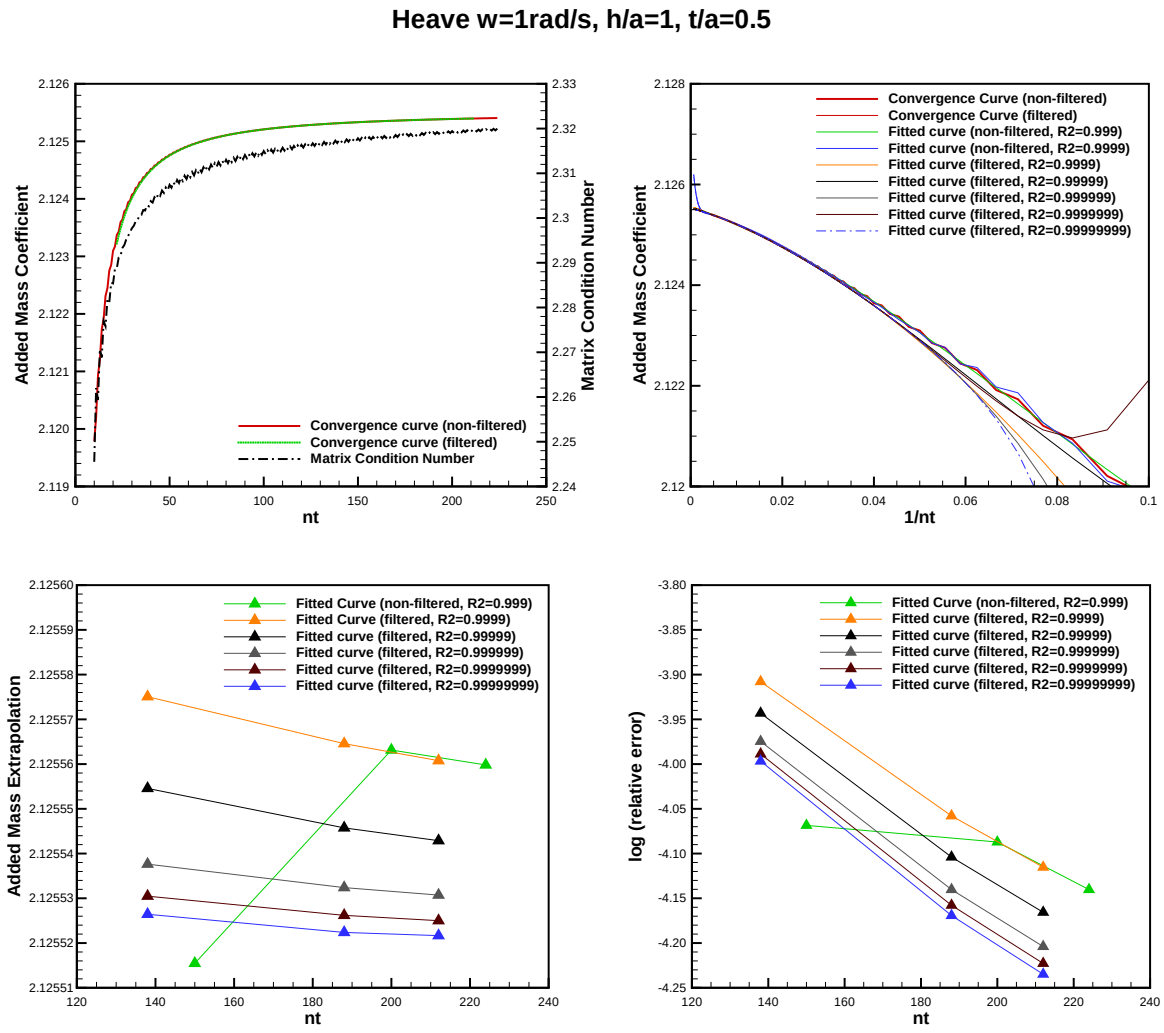

Figure C.10

The accuracy of the fitting has been controlled by means of the R^2 coefficient of the regression defined as:

$$R^2 = 1 - \frac{SS_{res}}{SS_{tot}} \tag{C.4.4}$$

where SS_{res} represents the total sum of squares of residuals and SS_{tot} the total sum of squares.

In Figures (C.10, C.11) convergence of the extrapolated hydrodynamic coefficients when increasing R^2 can be observed. Another important aspect is that the trend of the extrapolated values does not change considerably when the truncation is increased (for high enough R^2). This is valuable for the cases where the values of parameters d

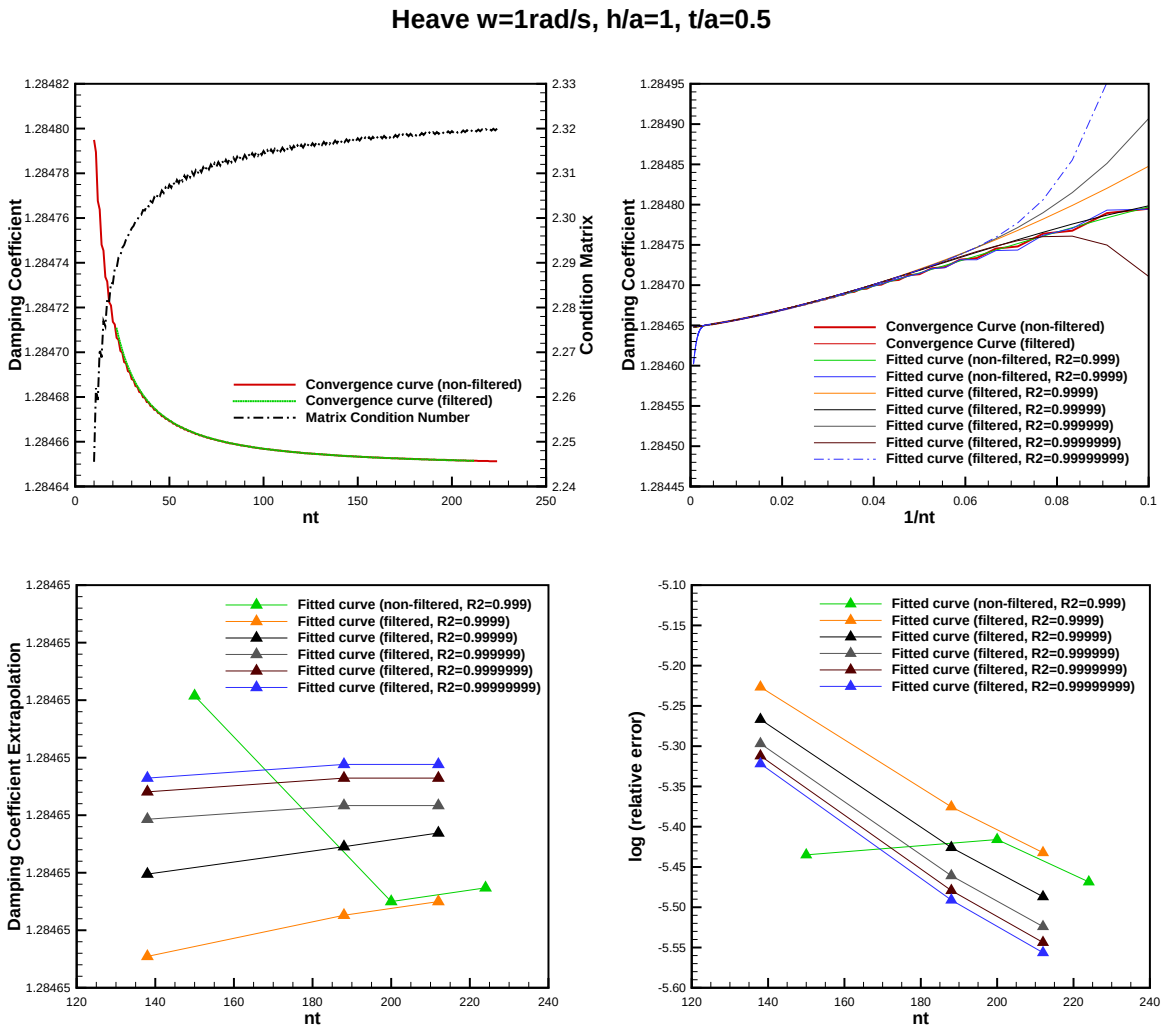

Figure C.11

and h restrict the truncation index j as will be seen in Section C.4.

A similar trend can be observed in Figures (C.8-C.9, C.12-C.13). The values of the extrapolation converge for high values of R^2 and they do not change significantly when the truncation is increased. However, it is observed that for certain cases there is no smooth transition but an abrupt change of the extrapolated value. This is due to a change in the order of the polynome to adapt to the R^2 coefficient imposed.

It is worth mentioning that a moving-average filter has been used to smooth the small disturbances in the non-oscillating curves which difficult the fitting process. This is shown in Figures (C.10) and (C.11) where a clear deviation from the trend for values of nt close to zero is observed for the non-filtered fitted curve. This filter

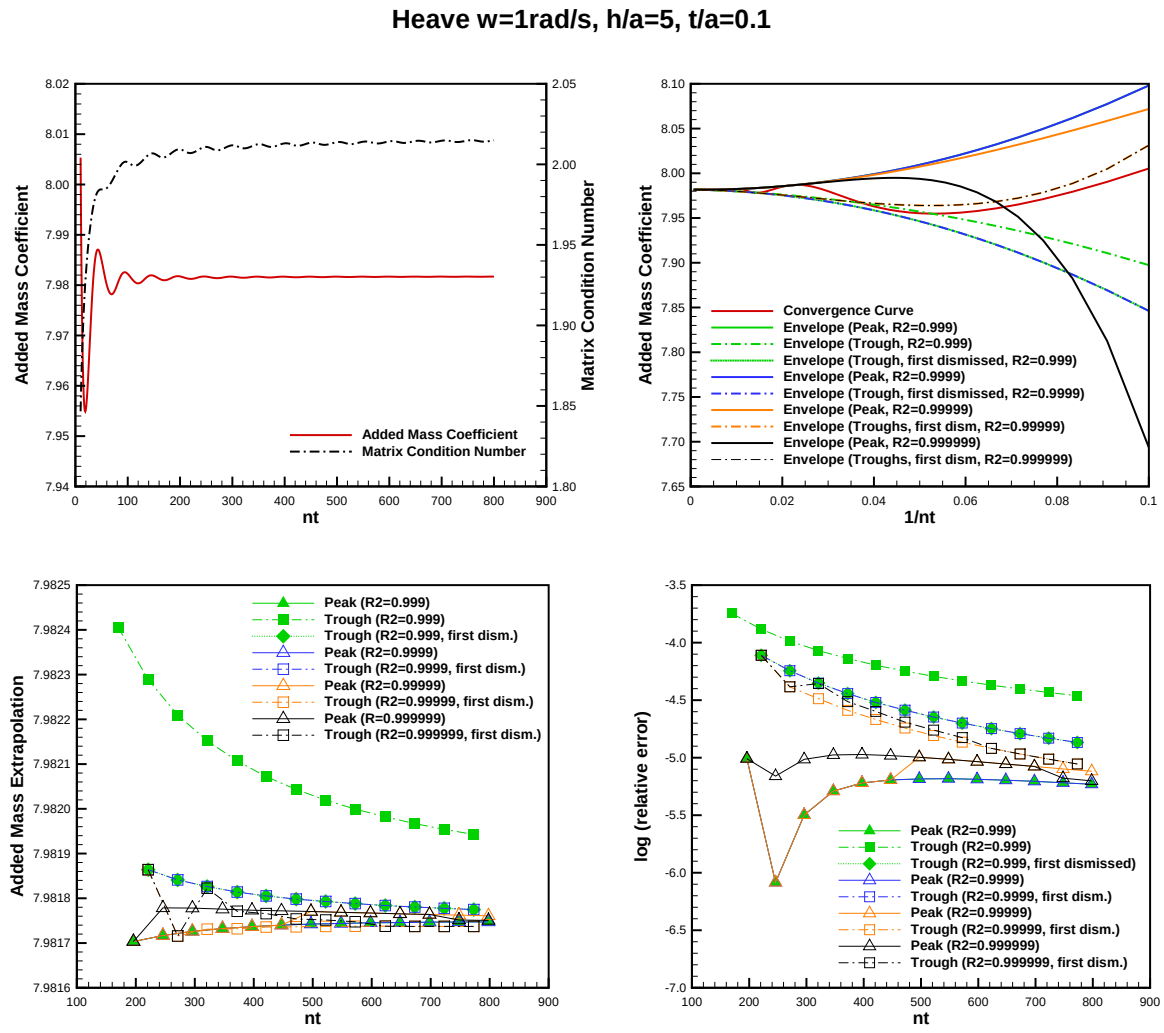

Figure C.12

involves loosing some of the data at the extremes, but this is not a problem provided sufficient data points are available.

C.5 Parameters sensitivity analysis

The objective of this section is to identify potential numerical singularities that could arise if some restrictions with respect to the input parameters' value (w, h, d, a) were not respected.

By inspecting the formulae, it can be observed that the value m_0 appears in the denominator of the imaginary term of γ_{nj} and h_n, as well as in the first term of the

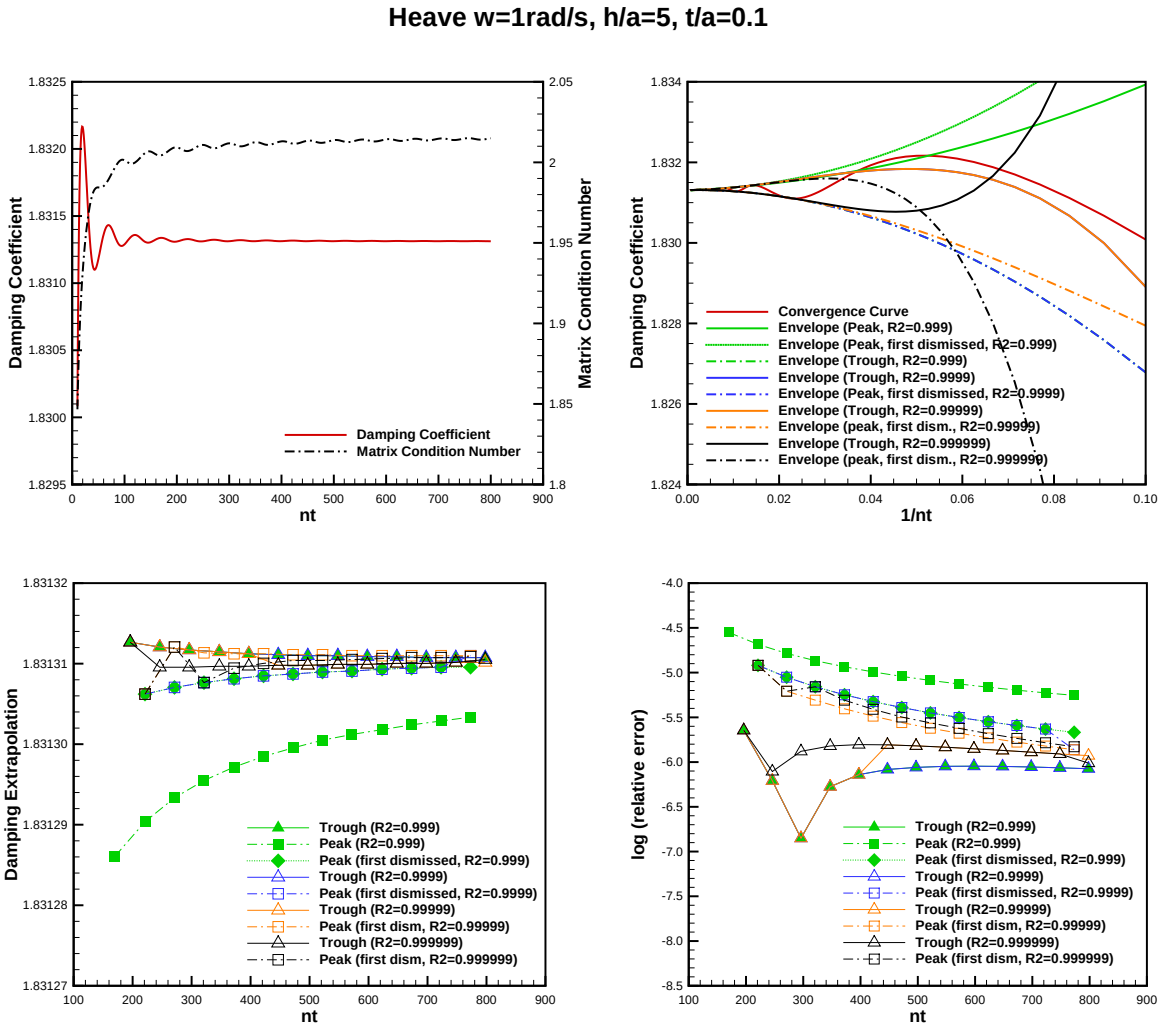

Figure C.13

denominator of $P_0(n, j)$. This directly suggests that the value of the angular frequency cannot be input as zero as in such case, the solution of the dispersion equation (C.1.11) would be $m_0 = 0$.

A source of numerical singularity could arise from the second term in the numerator $(m_0 d\, sh(m_0 d))^2$ or the first term of the denominator $(sh(2m_0 h))$ of $P_0(n, j)$. In case the hyperbolic sinus argument was too big, the previous expressions would have a value out of the range r that can be represented with an architecture of 64bits (Fouilloux and Corde, 2014):

$$2.2 \times 10^{-308} \leqslant |r| \leqslant 1.8 \times 10^{308} \tag{C.5.1}$$

Therefore the following restrictions have been imposed:

$$\left(x\,\frac{e^{x}-e^{-x}}{2}\right)^{2} < c \tag{C.5.2}$$

$$\frac{e^{y}-e^{-y}}{2} < c \tag{C.5.3}$$

where $x = m_0 d$, $y = 2m_0 h$ and $c = 1.8\,10^{308}$. If expression (C.5.2) is developed, we have:

$$x\frac{e^{x}-e^{-x}}{2} < c^{\frac{1}{2}};\ ln(x)+ln\left(\frac{e^{x}-e^{-x}}{2}\right) < ln(c)^{\frac{1}{2}};\ ln(x)+ln\left(e^{x}-e^{-x}\right)-ln(2) < ln(c)^{\frac{1}{2}}$$

if $x \to \infty \Rightarrow e^{-x} \sim 0$ then:

$$ln(x)+x < ln(c)^{\frac{1}{2}}+ln(2);\ \ x < ln(c)^{\frac{1}{2}}+ln(2)-ln(x);\ \ x < b-ln(x)$$

where $b = ln(c)^{\frac{1}{2}}+ln(2)$.

As x has to be at least $< b$, from that follows that $ln(x)$ will always be $< ln(b)$. Therefore we can write in a conservative way:

$$x < b-ln(b);\ m_0 d < b^{*} \tag{C.5.4}$$

where x has been substituted by its value and $b^{*} = b-ln(b)$. A similar development is applicable to expression (C.5.3) and it leads to :

$$m_0 h < \beta^{*} \tag{C.5.5}$$

where $\beta^{*} = 0.5\ [ln(c)+ln(2)]$

For very large values of the term $m_0 h$, equation (C.1.11) admits as solution:

$$m_0 = \frac{w^2}{g} \tag{C.5.6}$$

If (C.5.6) is substituted into (C.5.4) and (C.5.5) then:

$$\frac{w^2}{g}\,d < b^{*};\ \frac{w^2}{g}\,h < \beta^{*} \tag{C.5.7}$$

Rearranging (C.5.7):

$$d < b^* \frac{g}{\omega^2};\ h < \beta^* \frac{g}{\omega^2} \tag{C.5.8}$$

At this point it is worth using the condition defined in Section C.2 which establishes that a solution to the dispersion equation can be found provided that :

$$\frac{\pi}{2h} > 2\epsilon \tag{C.5.9}$$

Taking into account that $\epsilon = 10^{-9}$, the depth is limited to an approximate maximum value of $7\,x10^4$ km. This result has to be combined with the restriction for h in (C.5.8)

Another possible source of numerical difficulties can arise from the use of the Bessel functions. Intuitively, it can be deduced from the observation of figure (C.14) that if the argument of the functions becomes too big or too small their value may fall out of the range (C.5.1). For $Y(x)$ and $J(x)$, with $x = m_0 a$, if $x \to \infty$ and $a \simeq d$, the problem arises from the term $sinh(m_0 d)$ which grows much faster than $Y(x)$ and $J(x)$ and that has already been dealt with. Contrarily, in case $a >> d$, the numerical singularity will come from function $K(m_q a)$. Therefore, it can be concluded that functions $J(x)$ and $Y(x)$ will not generate numerical problems before $K(x)$ when $x \to \infty$.

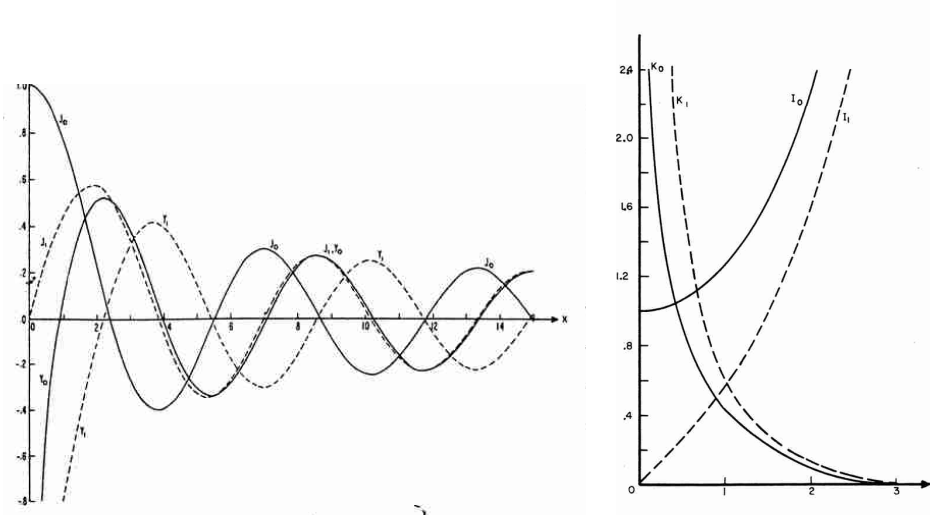

(a) J_0, J_1, Y_0, Y_1 (b) I_0, I_1, K_0, K_1

Figure C.14: Bessel functions of the first kind and second kind (a); Modified Bessel functions of the first and second kind (b). Source: Abramowitz and Segun A. (1964)

The function $K_\nu(z)$ can be expressed using the following development for values of $z \to \infty$ (Abramowitz and Segun A., 1964, 9.7.2):

$$K_\nu(z) \sim \sqrt{\frac{\pi}{2z}}\, e^{-z} \left\{ 1 + \frac{4\nu^2 - 1}{8z} + \frac{(4\nu^2 - 1)(4\nu^2 - 9)}{2!(8z)^2} + \frac{(4\nu^2 - 1)(4\nu^2 - 9)(4\nu^2 - 25)}{3!(8z)^3} + ... \right\} \tag{C.5.10}$$

The first term previous to the brackets reaches the lowest limit of the range (C.5.1) when z takes a value of 705.342. Therefore it is imposed that:

$$m_q\, a < 705.342 \tag{C.5.11}$$

The term m_q is the solution of the dispersion equation (C.1.12) and approaches the value $j\frac{\pi}{h}$ for $m_q \to \infty$. Therefore:

$$j\, \frac{\pi}{h}\, a < g^* \tag{C.5.12}$$

where $g^* = 705.342$ and j corresponds to the number of truncation terms.

A development of the bessel function $I_\nu(z)$ similar to (C.5.10) exists for values of $z \to \infty$ (Abramowitz and Segun A., 1964, 9.7.1):

$$I_\nu(z) \sim \frac{e^z}{\sqrt{2\pi z}} \left\{ 1 + \frac{4\nu^2 - 1}{8z} + \frac{(4\nu^2 - 1)(4\nu^2 - 9)}{2!(8z)^2} + \frac{(4\nu^2 - 1)(4\nu^2 - 9)(4\nu^2 - 25)}{3!(8z)^3} + ... \right\} \tag{C.5.13}$$

The first term before the brackets approaches the highest limit of the range (C.5.1) for values of $z = 713.987$. The following condition is then defined:

$$j\, \frac{\pi}{d}\, a < \gamma^* \tag{C.5.14}$$

where $\gamma^* = 713.987$.

It is worth noting that $K_\nu(x)$ decreases much faster than $I_\nu(x)$ increases when $x \to \infty$ and, therefore, (C.5.12) has been used in the routine to limit the truncation j. By comparing Figures (C.8)-(C.9) ($h = 1$) and (C.12)-(C.13) ($h = 5$) a difference in the number of truncation terms used can be observed. From equation (C.5.12) it can be deduced that the higher the value of the depth (h) the higher the truncation limit will be.

Rearanging (C.5.12) and (C.5.14) we have:

$$h > \frac{j\pi}{g^*}\, a;\ d > \frac{j\pi}{\gamma^*} a \tag{C.5.15}$$

By combining (C.5.15) and (C.5.8):

$$\boxed{\begin{array}{c} \dfrac{j\pi}{\gamma^*}\, a < d < \dfrac{1}{w^2}\, b^*\, g \\ \dfrac{j\pi}{g^*}\, a < h < \dfrac{1}{w^2}\, \beta^*\, g \\ h > d \end{array}} \tag{C.5.16}$$

The constants b^* and β^* can be calculated as follows:

$$\begin{aligned} b^* &= ln(c)^{\frac{1}{2}} + ln(2) - ln\left(ln(c)^{\frac{1}{2}} + ln(2)\right) = \\ &= ln\left(1.8^{\frac{1}{2}}\, 10^{154}\right) + ln(2) - ln\left(ln\left(1.8^{\frac{1}{2}}\, 10^{154}\right) + ln(2)\right) = \\ &= 0.5\, ln(1.8) + 154\, ln(10) + ln(2) - ln\left(0.5\, ln(1.8) + 154\, ln(10) + ln(2)\right) = \\ &= 349.71138 \end{aligned}$$

$$\begin{aligned} \beta^* &= 0.5\, \left[ln(1.8\, 10^{308} + ln(2)\right] = \\ &= 0.5\, [ln(1.8) + 308\, ln(10) + ln(2)] = \\ &= 355.2386 \end{aligned}$$

Expression (C.5.16) is valid for large values of a and w and limits their maximum value with respect to d and h. Moreover, it relates the truncation and the value of h. Notwithstanding, (C.5.16) does not provide any limits to a and w concerning the smallest values they can take. This is because so far the analysis has been focused on the acceptable largest arguments of the bessel functions. However, potential numerical problems may also arise if the arguments become too small, as represented in figure (C.14).

Functions $K_\nu(x)$ and $Y_\nu(x)$ have similar trends when $x \to 0$ as can be deduced from the following expressions (Abramowitz and Segun A., 1964, 9.6.8 and 9.1.8):

$$K_0(z) \sim -ln(z); \quad K_\nu(z) \sim \frac{1}{2}\, \Gamma(\nu) \left(\frac{1}{2}\, z\right)^{-\nu} \quad \nu \neq 0 \tag{C.5.17}$$

$$Y_0(z) \sim \left(\frac{2}{\pi}\right) ln(z); \quad Y_\nu(z) \sim -\frac{1}{\pi}\Gamma(\nu)\left(\frac{1}{2}\,z\right)^{-\nu} \quad \nu \neq 0 \tag{C.5.18}$$

Similarly, for $I_\nu(z)$ and $J_\nu(z)$ for $z \to 0$ (Abramowitz and Segun A., 1964, 9.1.7 and 9.6.7):

$$J_\nu(z) \sim \left(\frac{1}{2}z\right)^\nu / \Gamma(\nu+1) \quad \nu = 0, 1, 2, ... \tag{C.5.19}$$

$$I_\nu(z) \sim \left(\frac{1}{2}z\right)^\nu / \Gamma(\nu+1) \quad \nu = 0, 1, 2... \tag{C.5.20}$$

From expression (C.5.17):

$$|ln(z)| < 1.8\,10^{308};\ z > e^{-1.8\,10^{308}} \quad for \quad \nu = 0 \tag{C.5.21}$$

$$\frac{1}{z} < 1.8\,10^{308}; \quad z > \frac{1}{1.8\,10^{308}} = 0.\dot{5}\,10^{-308} \quad for \quad \nu = 1 \tag{C.5.22}$$

It is clear that (C.5.22) is more restrictive than (C.5.21). At the same time, (C.5.22) falls out of range (C.5.1) and therefore it is substituted by:

$$m_q a > 2.2\,10^{-308}; \quad for \quad \nu = 1$$

where z has been substituted by the argument of the bessel function $K_\nu(z)$.

The solution of the dispersion equation (C.1.12) will be comprised between $j\pi/2h$ and π/h. Therefore it is imposed that:

$$\frac{j\pi}{2h}\,a > 2.2\,10^{-308} \tag{C.5.23}$$

The case of $Y_\nu(z)$ is analysed as it appears in the expression (C.1.10). Thus:

$$\frac{1}{[Y_1(m_0 a)]^2} > 2.2\,10^{-308}; \quad \left(\frac{2}{\pi}\,|ln(m_0 a)|\right)^2 < \frac{1}{2.2}\,10^{308}; \quad m_0 a > e^{(-\pi/2)\left(1/\sqrt{2.2}\right)10^{154}} \tag{C.5.24}$$

It is only interesting to check expression (C.5.24) for small values of m_0 as if a is very small, it will be the bessel function $K_\nu(m_q a)$ which will lead to a numerical problem as it tends to grow faster than Y for small values of its argument.

The solution of the dispersion equation (C.1.11) when $m_0 h$ is small can be assumed

to be $w/\sqrt{gh}$. Therefore, substituting this result in (C.5.24):

$$\frac{w}{\sqrt{gh}}\, a > e^{(-\pi/2)\left(1/\sqrt{2.2}\right)\, 10^{154}} \tag{C.5.25}$$

Expression (C.5.25) is always valid independently of the value of w, h, a provided they satisfy expression (C.5.1).
Eventually, from expressions (C.5.20) and (C.5.19):

$$\frac{j\pi a}{d} > 2\left(2.2\, 10^{-308}\right) \tag{C.5.26}$$

$$\frac{wa}{\sqrt{gh}} > 2\left(2.2\, 10^{-308}\right) \tag{C.5.27}$$

The expression (C.5.25) should be replaced by (C.5.27) as the latter is more restrictive. Both (C.5.26) and (C.5.27) provide limits to the lowest values the parameters a and w can take with respect to d and h.

Appendix D

Hydrodynamic interactions in an array of truncated circular cylinders

D.1 Formulation

The following formulation, adapted from (Child, 2011; Zeng and Tang, 2013) and completed, is based on the Direct Matrix Method interaction theory (IT) by Kagemoto and Yue (1986) detailed in Chapter 2. As mentioned in the latter, several hydrodynamic operators are required to perform computations with the IT. In this Appendix, the focus is on the generation of the Diffraction Transfer Matrix (DTM) and Radiation Characteristics (RC) for a truncated vertical cylinder. For such a simple geometry, they can be expressed using a semi-analytical solution. For more complex shapes, methodologies which rely on the use of Boundary Element Method (BEM) solvers must be used and are detailed in Chapter 3. The contents of this Appendix are organized in the following manner:

- In section D.1.1 the notation convention used in this body of work is specified.
- In section D.1.2 the formulae to compute the RC of a truncated vertical cylinder are provided.
- In section D.1.3 the components of the DTM of a truncated vertical cylinder are derived.
- In section D.1.4 expressions for the hydrodynamic forces, which were not specified in Zeng and Tang (2013), are fully detailed.

- Finally, section D.2 shows numerical verifications of the formulae presented in the preceding sections.

D.1.1 Notation

The notation and the reference system adopted, shown in Figure (D.1), follow Zeng and Tang (2013):

- The cylinder mode of motion is indicated by index s, with surge ($s = 1$); sway (2); heave (3); roll (4) and pitch (5). Yaw mode (6) will not be considered as it has no effect on the radiated field around the cylinder.
- Subindexs R and D refer to radiated and diffracted wave fields respectively, and E and C to the exterior and core regions.
- Index m represents the angular-mode of cylindrical partial waves, whereas n as well as q and p represent depth-modes. For the RC (section D.1.2), index n represents the depth-modes of the core region and q the ones of the exterior region. For the DTM (section D.1.3), index n is associated with the depth-mode of an incident wave, whereas q and p represent the depth-modes of outgoing waves in the exterior and core regions respectively.
- Variables with a tilde, such as $\tilde{R}$, refer to the core region.
- One of the key aspects of the IT is that the study of the wave scattering on the whole array is undertaken by focusing on one body at a time. This body is referred to as j and its neighbours as i.
- Variable ζ_s^i represents the oscillation ampitude of mode s for cylinder i. Similarly, v_s^i is the velocity of cylinder i in mode s ($v_s^i = -i\omega_0\zeta_s^i$).
- Wave numbers k_0 and k_q are the solutions of the dispersion equations A.1.4 and A.1.5 respectively.
- The spatial part of the total velocity potential Φ is represented by ϕ.
- H_m is the Hankel function of the first kind of order m, K_m is the modified Bessel function of the second kind of order m and I_q is the modified Bessel function of the first kind of order q.
- Superindex $'$ represents derivative.

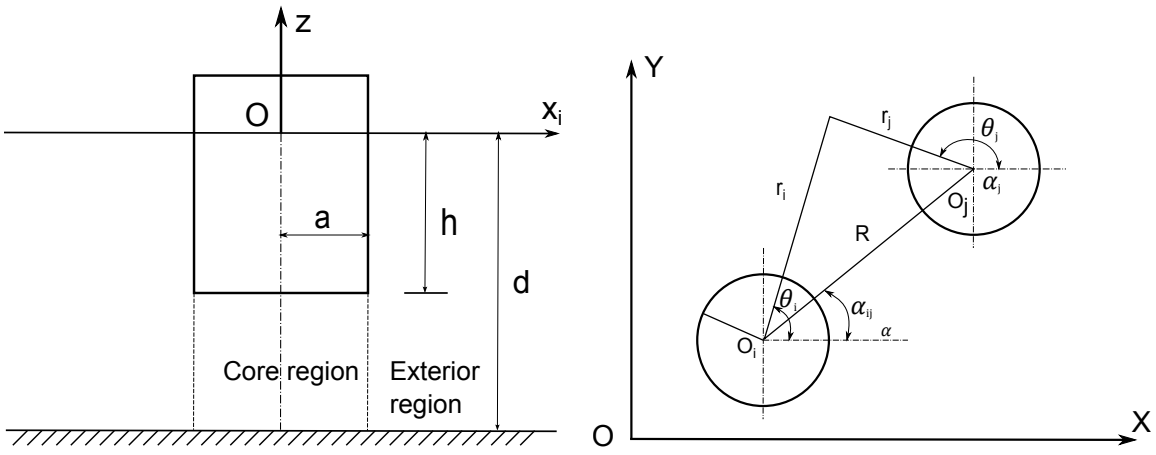

(a) Reference system individual cylinder (b) Reference system cylinder array

Figure D.1: Source: adapted from Zeng and Tang (2013)

D.1.2 Radiation Characteristics

The radiated potential in the exterior region of the cylinder due to a motion in mode s and amplitude ζ_s can be defined as:

$$\phi_{Rs-E} = -i\omega_0\zeta_s \sum_{m=-\infty}^{\infty} R^E e^{im\theta} \tag{D.1.1}$$

with:

$$R^E = D_{0m}^{Rs}\frac{H_m(k_0r)}{H'_m(k_0a)}\frac{\cosh\ k_0(z+d)}{N_0^{1/2}} + \sum_{q=1}^{\infty} D_{qm}^{Rs}\frac{K_m(k_qr)}{K'_m(k_qa)}\frac{\cos\ k_q(z+d)}{N_q^{1/2}} \tag{D.1.2}$$

$$N_0 = \frac{1}{2}\left(1+\frac{\sinh\ 2k_0d}{2k_0d}\right) \tag{D.1.3}$$

$$N_q = \frac{1}{2}\left(1+\frac{\sin\ 2k_qd}{2k_qd}\right); \quad q \geq 1 \tag{D.1.4}$$

where R^E represents a linear combination of basis functions which enable one to represent any outgoing wave potential in the exterior region. For a complete derivation see Child (2011, 3.4.1.1).

In compact form, (D.1.1) can be expressed as:

$$\phi_{Rs-E} = -i\omega_0\zeta_s^i R_{is}^T \psi_i^{D-E} \tag{D.1.5}$$

with:

$$R_{is}(0,m) = \frac{D^s_{0m}\cosh\, k_0 d}{H'_m(k_0 a_i) N_0^{1/2}}, \quad m = \pm 1,\, n = 0 \tag{D.1.6}$$

$$R_{is}(n,m) = \frac{D^s_{nm}}{K'_m(k_n a_i) N_n^{1/2}}, \quad m = \pm 1,\, n > 0 \tag{D.1.7}$$

$$\left(\psi_i^{D-E}\right)_n^m = \begin{cases} \frac{\cosh\, k_0(z+d)}{\cosh\, k_0 d} H_m(k_0 r_i) e^{im\theta_i}, & n = 0,\, n \in \mathbb{Z} \\ \cos\, k_n(z+d)\, K_m(k_n r_i) e^{im\theta_i}, & n \geq 1,\, n \in \mathbb{Z} \end{cases} \tag{D.1.8}$$

The terms of vector ψ_i^{D-E} are referred to as partial cylindrical wave functions (see section (2.2.1)) and are depicted in Figure 2.2 for specific values of the angular-modes m and depth-modes n. The terms of vector R_{is} enable one to express the radiated potential in the base of outgoing cylindrical harmonics and are defined as Radiation Characteristics (RC).

An equivalent formulation exists for the core region. In this case, as in (D.1.1), the radiated potential can be expressed as:

$$\phi_{Rs-C} = -i\omega_0 \zeta_s \sum_{m=-\infty}^{\infty} \widetilde{R} e^{im\theta} \tag{D.1.9}$$

with:

$$\widetilde{R} = \widetilde{R}_h + \widetilde{R}_p \tag{D.1.10}$$

$$\widetilde{R}_p = \Lambda_s \lambda_{ms} \tag{D.1.11}$$

$$\widetilde{R}_h = \frac{C^s_{0m}}{2}\left(\frac{r}{a}\right)^{|m|} + \sum_{n=1}^{\infty} C^s_{nm} \frac{I_m\left(\frac{n\pi r}{d-h}\right)}{I_m\left(\frac{n\pi a}{d-h}\right)} \cos\left(\frac{n\pi(z+d)}{d-h}\right) \tag{D.1.12}$$

where $\widetilde{R}$ is a linear combination of cylindrical basis functions which, in this case, enables one to express the scattered potential in the core region. For a complete derivation see Child (2011, 3.4.1.2).

Expression (D.1.9) can be represented in compact form as:

$$\phi_{Rs-C} = -i\omega_0 \zeta_s^i \left[\tilde{R}_{js}(n,m)(\psi_j^{D-C})_n^m + \Lambda_s \sum_{m=-\infty}^{\infty} \lambda_{ms} e^{im\theta}\right] \tag{D.1.13}$$

with:

$$\tilde{R}_{js}(0,m) = \frac{C^s_{0m}}{2}\frac{1}{a^{|m|}}; \quad n=0 \tag{D.1.14}$$

$$\tilde{R}_{js}(n,m) = \frac{C^s_{nm}}{I_m\left(\frac{n\pi a}{d-h}\right)}\cos\left(\frac{n\pi(z+d)}{d-h}\right); \quad n\geq 1 \tag{D.1.15}$$

$$\left(\psi_j^{D-C}\right)^m_n = \begin{cases} r^{|m|}e^{im\theta_i}, & n=0,\, n\in\mathbb{Z} \\ I_m\left(\frac{n\pi r_j}{d-h}\right)e^{im\theta_i}, & n\geq 1,\, n\in\mathbb{Z} \end{cases} \tag{D.1.16}$$

$$\Lambda_s = 0, \quad s=1,2 \tag{D.1.17}$$

$$\Lambda_s = \frac{1}{2(d-h)}\left[(z+d)^2 - \frac{r_j^2}{2}\right], \quad s=3 \tag{D.1.18}$$

$$\Lambda_s = \frac{r_j}{2(d-h)}\left[(z+d)^2 - \frac{r_j^2}{4}\right], \quad s=4 \tag{D.1.19}$$

$$\Lambda_s = -\frac{1}{2(d-h)}\left[(z+d)^2 - \frac{r_j^2}{4}\right], \quad s=5 \tag{D.1.20}$$

Both (D.1.1) and (D.1.9) need to satisfy the impenetrable body surface conditions:

$$\frac{\partial\varphi^i_{Rs-E}}{\partial r} = v^i_s\, f_s(z)\sum_{m=-\infty}^{\infty}\lambda_{ms}e^{im\theta} \quad on \quad r=a; \quad -h\leq z\leq 0 \tag{D.1.21}$$

$$\frac{\partial\varphi^i_{Rs-C}}{\partial z} = v^i_s\, g_s(r_i)\sum_{m=-\infty}^{\infty}\lambda_{ms}e^{im\theta} \quad on \quad z=-h, \quad r\leq a \tag{D.1.22}$$

where $v^i_s = -i\omega_0\zeta^i_s$ is the velocity of the cylinder i in mode s. Expressions $f_s(z)$, $g_s(r_i)$ and λ_{ms} are:

$$f_s(z)=1, \quad g_s(r_i)=0, \quad s=1,\,2 \tag{D.1.23}$$

$$f_s(z)=0, \quad g_s(r_i)=1, \quad s=3 \tag{D.1.24}$$

$$f_s(z)=-(z-\bar{z}), \quad g_s(r_i)=r_i, \quad s=4 \tag{D.1.25}$$

$$f_s(z)=(z-\bar{z}), \quad g_s(r_i)=-r_i, \quad s=5 \tag{D.1.26}$$

$$\lambda_{11} = \lambda_{15} = \frac{1}{2}, \quad \lambda_{13} = 0, \quad \lambda_{12} = \lambda_{14} = \frac{1}{2i} \tag{D.1.27}$$

$$\lambda_{01} = \lambda_{05} = 0, \quad \lambda_{03} = 1, \quad \lambda_{02} = \lambda_{04} = 0 \tag{D.1.28}$$

$$\lambda_{-11} = \lambda_{-15} = \frac{1}{2}, \quad \lambda_{-13} = 0, \quad \lambda_{-12} = \lambda_{-14} = -\frac{1}{2i} \tag{D.1.29}$$

$$\lambda_{ms} = 0, \quad m \neq 0, \pm 1 \tag{D.1.30}$$

By imposing (D.1.21) and (D.1.22), the following expressions for the unknown coefficients of the RC vector are obtained:

$$C_{nm}^{Rs} = \frac{2}{d-h} \int_{-d}^{-h} \widetilde{R}_h(a,z) \cos\left(\frac{n\pi(z+d)}{d-h}\right) dz \tag{D.1.31}$$

$$D_{0m}^{Rs} = \frac{1}{k_0 d} \int_{-d}^{0} \frac{\partial R}{\partial r}(a,z)\, N_0^{-\frac{1}{2}} \cosh\,(k_0(z+d))\, dz\,; \quad q = 0 \tag{D.1.32}$$

$$D_{qm}^{Rs} = \frac{1}{k_q d} \int_{-d}^{0} \frac{\partial R}{\partial r}(a,z)\, N_q^{-\frac{1}{2}} \cos\,(k_q(z+d))\, dz\,; \quad q \geq 1 \tag{D.1.33}$$

They are derived using the orthogonality properties of the depth functions. For the exterior region:

$$\frac{1}{d} \int_{-d}^{0} \sigma_z^q(z)\, \sigma_z^m(z)\, dz = \begin{cases} 1, & q = m \\ 0, & q \neq m \end{cases} \tag{D.1.34}$$

where:

$$\sigma_z^q(z) = \begin{cases} N_0^{-\frac{1}{2}} \cosh\, k_0(z+d), & q = 0 \\ N_q^{-\frac{1}{2}} \cos\, k_q(z+d), & q \geq 1\,(\mathrm{q} \in \mathbb{N}) \end{cases} \tag{D.1.35}$$

Similarly, for the core region:

$$\frac{2}{d-h} \int_{-d}^{-h} \sigma_z^t(z) \cos\left(\frac{m\pi(z+d)}{d-h}\right) dz = \begin{cases} 1, & t = m\,(s,m \in \mathbb{N}) \\ 0, & t \neq m\,(s,m \in \mathbb{N}) \end{cases} \tag{D.1.36}$$

where:

$$\sigma_z^t(z) = \begin{cases} \frac{1}{2}, & t = 0 \\ \cos\left(\frac{t\pi(z+d)}{d-h}\right), & t \neq 0\,(t \in \mathbb{N}) \end{cases} \tag{D.1.37}$$

To check the derivation of (D.1.31), we take $\widetilde{R}_h(a,z)$ and express it using (D.1.37):

$$\widetilde{R}_h(a,z) = C_{0m}^{Rs}\sigma_z^0(z) + \sum_{s=1}^{\infty} C_{nm}^{Rs}\sigma_z^t(z) \tag{D.1.38}$$

If (D.1.38) is multiplied by the term $\cos(s\pi z/h)$, i.e. $\sigma_z^s(z)$, then we have:

$$\widetilde{R}_h(a,z)\sigma_z^t(z) = C_{0m}^{Rs}\sigma_z^0\sigma_z^t(z) + \sum_{s=1}^{\infty} C_{nm}^{Rs}\sigma_z^t(z)\sigma_z^t(z) \tag{D.1.39}$$

Now, (D.1.39) is substituted into (D.1.31) and the role of the orthogonality functions becomes explicit:

$$\begin{aligned} C_{nm}^{Rs} = \frac{2}{d-h}\int_{-d}^{-h} \tilde{R}_h(a,z)\,\cos\left(\frac{n\pi(z+d)}{d-h}\right)dz = \\ = \frac{2}{d-h}\left[\int_{-d}^{-h} C_{0m}^{Rs}\sigma_z^0\sigma_z^t(z) + \sum_{s=1}^{\infty}\int_{-d}^{-h} C_{nm}^{Rs}\sigma_z^t(z)\sigma_z^t(z)\right] \end{aligned} \tag{D.1.40}$$

where the integral and the summation have been exchanged.

A similar result would be obtained by developping $\frac{\partial R}{\partial r}(a,z)$ in expressions (D.1.32) and (D.1.33) using orthogonal functions.

By applying the following matching conditions at the interface $r = a$, the interior and exterior potentials can be related to each other (Child, 2011, pg.54):

$$R = \tilde{R} \quad r = a; \quad -d \leq z \leq -h \tag{D.1.41}$$

$$\frac{\partial R}{\partial r} = \frac{\partial \tilde{R}}{\partial r} \quad r = a; \quad -d \leq z \leq -h \tag{D.1.42}$$

$$\frac{\partial R}{\partial r} = f(s)\,\lambda_{ms} \quad r = a; \quad -h \leq z \leq 0 \tag{D.1.43}$$

Condition (D.1.43) differs from (Child, 2011, 3.104) as the latter was only valid for heave mode. Using (D.1.43) ensures that the boundary conditions for the radiation potential in both the exterior and core regions (D.1.21, D.1.22) are satisfied. Using

(D.1.1):

$$\left.\frac{\partial \phi^i_{Rs-E}}{\partial r}\right|_{r_i=a_i} = -iw_0\zeta^i_s \sum_{m=-\infty}^{\infty} \left.\frac{\partial R^E}{\partial r}\right|_{r_i=a_i} e^{im\theta} = v^i_s\, f_s(z) \sum_{m=-\infty}^{\infty} \lambda_{ms} e^{im\theta} \tag{D.1.44}$$

Similarly, using (D.1.22) and (D.1.10):

$$\begin{aligned}\left.\frac{\partial \phi^i_{Rs-C}}{\partial z}\right|_{z=-h} &= -iw_0\zeta^i_s \sum_{m=-\infty}^{\infty} \left.\frac{\partial \tilde{R}}{\partial z}\right|_{z=-h} e^{im\theta} = -iw_0\zeta^i_s \sum_{m=-\infty}^{\infty} \left.\frac{\partial}{\partial z}\right|_{z=-h} (\tilde{R}_h + \Lambda_s\lambda_{ms}) e^{im\theta} = \\ &= -iw_0\zeta^i_s \sum_{m=-\infty}^{\infty} \left.\frac{\partial}{\partial z}\right|_{z=-h} (\Lambda_s\lambda_{ms})\, e^{im\theta} = v^i_s\, g_s(r_i) \sum_{m=-\infty}^{\infty} \lambda_{ms} e^{im\theta}\end{aligned} \tag{D.1.45}$$

where $\left.\frac{\partial \tilde{R}_h}{\partial z}\right|_{z=-h} = 0$ and $\left.\frac{\partial \Lambda_s}{\partial z}\right|_{z=-h} = g_s(r_i)$ have been used.

It is worth mentioning that Zeng and Tang (2013, 25e) does not satisfy $\left.\frac{\partial \Lambda_s}{\partial z}\right|_{z=-h} = g_s(r_i)$ which is due to a typographical error. Instead, Λ_5 (D.1.20) should be:

$$\Lambda_5 = -\frac{r_i}{2(d-h)}\left[(z+d)^2 - \frac{r_j^2}{4}\right] \tag{D.1.46}$$

To further verify expression (D.1.46), it is checked that the potential representing the particular solution (D.1.46) satisfies Laplace equation. Such potential is expressed as:

$$\phi_p = \sum_{m=-\infty}^{\infty} \Lambda_s \lambda_{ms} e^{im\theta} \tag{D.1.47}$$

If (D.1.47) is introduced into Laplace's equation in cylindrical coordinates we have:

$$\frac{1}{r}\frac{\partial}{\partial r}\left(r\frac{\partial \phi}{\partial r}\right) + \frac{1}{r^2}\frac{\partial^2 \phi}{\partial \theta^2} + \frac{\partial^2 \phi}{\partial z^2} = 0 \tag{D.1.48}$$

with:

$$\frac{1}{r}\frac{\partial}{\partial \mathrm{r}}\left(r\frac{\partial \phi}{\partial r}\right) = \left[-\frac{(z+d)^2}{2r(d-h)} + \frac{9r}{8(d-h)}\right]\cos\theta \tag{D.1.49}$$

$$\frac{1}{r^2}\frac{\partial^2 \phi}{\partial \theta^2} = \frac{1}{2r(d-h)}\left[(z+d)^2 - \frac{r^2}{4}\right]\cos\theta \tag{D.1.50}$$

$$\frac{\partial^2 \phi}{\partial z^2} = -\frac{r}{d-h}\cos\theta \tag{D.1.51}$$

Substituting (D.1.49 - D.1.51) into (D.1.48):

$$\nabla^2\phi_p = \left[-\frac{(z+d)^2}{2r(d-h)} + \frac{9r}{8(d-h)}\right]\cos\theta + \frac{1}{2r(d-h)}\left[(z+d)^2 - \frac{r^2}{4}\right]\cos\theta - \frac{r}{d-h}\cos\theta = 0$$

By using the decomposition of the core potential (D.1.10) and the matching conditions (D.1.41 - D.1.43), equations (D.1.31-D.1.33) can be rewritten as:

$$C^R_{nm} = \frac{2}{d-h}\int_{-d}^{-h}(R - \Lambda_s\lambda_{ms})(a,z)\,\cos\left(\frac{n\pi(z+d)}{d-h}\right)dz \tag{D.1.52}$$

$$D^R_{0m} = \frac{1}{k_0 d}\int_{-d}^{0}\left[\frac{\partial\tilde{R}_h(a,z)}{\partial r} + \lambda_{ms}\frac{\partial\Lambda_s(a,z)}{\partial \mathrm{r}}\right] N_0^{-\frac{1}{2}}\cosh\,(k_0(z+d))\,dz + \\ + \frac{1}{k_0 d}\int_{-h}^{0} f_s(z)\lambda_{ms}N_0^{-\frac{1}{2}}\cosh(k_0(z+d))dz \tag{D.1.53}$$

$$D^R_{qm} = \frac{1}{k_q d}\int_{-d}^{0}\left[\frac{\partial\tilde{R}_h(a,z)}{\partial r} + \lambda_{ms}\frac{\partial\Lambda_s(a,z)}{\partial \mathrm{r}}\right] N_q^{-\frac{1}{2}}\cos\,(k_q(z+d))\,dz + \\ + \frac{1}{k_q d}\int_{-h}^{0} f_s(z)\lambda_{ms}N_q^{-\frac{1}{2}}\cos(k_q(z+d))dz \tag{D.1.54}$$

Then, by substituting (D.1.52 - D.1.54) in the expressions of R (D.1.6 - D.1.7), $\tilde{R}_h$ (D.1.12) and Λ_s (D.1.17 - D.1.20):

$$C^R_{nm} = \frac{2}{d-h}\int_{-d}^{-h} R(a,z)\,\cos\left(\frac{n\pi(z+d)}{d-h}\right)dz - \frac{2}{d-h}\int_{-d}^{-h}\Lambda_s(a,z)\lambda_{ms}\,\cos\left(\frac{n\pi(z+d)}{d-h}\right)dz = \\ \frac{2}{d-h}\int_{-d}^{-h}\left[D^R_{0m}\frac{H_m(k_0a)}{H'_m(k_0a)}\frac{cosh\,k_0(z+d)}{N_0^{1/2}}\cos\left(\frac{n\pi(z+d)}{d-h}\right) + \right. \\ \left. + \sum_{q=1}^{\infty} D^R_{qm}\frac{K_m(k_qa)}{K'_m(k_qa)}\frac{cos\,k_q(z+d)}{N_q^{1/2}}\cos\left(\frac{n\pi(z+d)}{d-h}\right)\right]dz - \\ - \frac{2}{d-h}\int_{-d}^{-h}\Lambda_s(a,z)\lambda_{ms}\cos\left(\frac{n\pi(z+d)}{d-h}\right)dz \tag{D.1.55}$$

$$
\begin{aligned}
D^R_{0m} = \frac{1}{k_0 d}\int_{-d}^{-h} \frac{\partial \tilde{R}_h(a,z)}{\partial r} N_0^{-1/2}\cosh(k_0(z+d))dz + \\
+ \frac{1}{k_0 d}\int_{-d}^{-h} \lambda_{ms}\frac{\partial \Lambda_s(a,z)}{\partial r} N_0^{-1/2}\cosh(k_0(z+d))dz + \\
+ \frac{1}{k_0 d}\int_{-h}^{0} f_s(z)\lambda_{ms} N_0^{-1/2}\cosh(k_0(z+d))dz = \\
= \frac{1}{k_0 d}\int_{-d}^{-h}\left[\frac{C^R_{0m}}{2}\frac{1}{a^{|m|}}|m|a^{|m|-1}N_0^{-1/2}\cosh(k_0(z+d)) + \right. \\
\left. + \sum_{n=1}^{\infty} C^R_{nm}\frac{n\pi}{d-h}\frac{I'_m\left(\frac{n\pi a}{d-h}\right)}{I'_m\left(\frac{n\pi a}{d-h}\right)}\cos\left(\frac{n\pi(z+d)}{d-h}\right)N_0^{-1/2}\cosh(k_0(z+d))\right]dz + \\
\frac{1}{k_0 d}\int_{-d}^{-h}\frac{\partial \Lambda_s(a,z)\lambda_{ms}}{\partial r} N_0^{-1/2}\cosh(k_0(z+d))dz + \\
+ \frac{1}{k_0 d}\int_{-h}^{0} f_s(z)\lambda_{ms} N_0^{-1/2}\cosh(k_0(z+d))dz \quad \text{(D.1.56)}
\end{aligned}
$$

$$
\begin{aligned}
D^R_{qm} = \frac{1}{k_q d}\int_{-d}^{-h} \frac{\partial \tilde{R}_h(a,z)}{\partial r} N_q^{-1/2}\cos(k_q(z+d))dz + \\
+ \frac{1}{k_q d}\int_{-d}^{-h} \lambda_{ms}\frac{\partial \Lambda_s(a,z)}{\partial r} N_q^{-1/2}\cos(k_q(z+d))dz + \\
+ \frac{1}{k_q d}\int_{-h}^{0} f_s(z)\lambda_{ms} N_q^{-1/2}\cos(k_q(z+d))dz = \\
= \frac{1}{k_0 d}\int_{-d}^{-h}\left[\frac{C^R_{0m}}{2}\frac{1}{a^{|m|}}|m|a^{|m|-1}N_q^{-1/2}\cos(k_q(z+d)) + \right. \\
\left. + \sum_{n=1}^{\infty} C^R_{nm}\frac{n\pi}{d-h}\frac{I'_m\left(\frac{n\pi a}{d-h}\right)}{I'_m\left(\frac{n\pi a}{d-h}\right)}\cos\left(\frac{n\pi(z+d)}{d-h}\right)N_q^{-1/2}\cosh(k_q(z+d))\right]dz + \\
\frac{1}{k_q d}\int_{-d}^{-h}\frac{\partial \Lambda_s(a,z)\lambda_{ms}}{\partial r} N_q^{-1/2}\cos(k_q(z+d))dz + \\
+ \frac{1}{k_q d}\int_{-h}^{0} f_s(z)\lambda_{ms} N_q^{-1/2}\cos(k_q(z+d))dz \quad \text{(D.1.57)}
\end{aligned}
$$

Expressions (D.1.55 - D.1.57) form a system of equations of the form:

$$\begin{cases} C^s_{nm} + \sum_{q=0}^{\infty} F^m_{nq} D^s_{qm} = R^{nm}_s \\ D^s_{qm} - \sum_{n=0}^{\infty} G^m_{qn} C^s_{nm} = S^{qm}_s \end{cases} \tag{D.1.58}$$

where:

$$F^m_{n0} = -\frac{2}{d-h}\int_{-d}^{-h} \frac{H_m(k_0 a)}{H'_m(k_0 a)} \frac{\cosh\, k_0(z+d)}{N_0^{1/2}} \cos\left(\frac{n\pi(z+d)}{d-h}\right) dz \tag{D.1.59}$$

$$F^m_{nq} = -\frac{2}{d-h}\int_{-d}^{-h} \frac{K_m(k_q a)}{K'_m(k_q a)} \frac{\cos\, k_q(z+d)}{N_q^{1/2}} \cos\left(\frac{n\pi(z+d)}{d-h}\right) dz \tag{D.1.60}$$

$$G^m_{00} = \frac{1}{k_0 d}\int_{-d}^{-h} \frac{|m|}{2a} N_0^{-1/2} \cosh\, k_0(z+d) dz \tag{D.1.61}$$

$$G^m_{q0} = \frac{1}{k_q d}\int_{-d}^{-h} \frac{|m|}{2a} N_q^{-1/2} \cos\, k_q(z+d) dz \tag{D.1.62}$$

$$G^m_{0n} = \frac{1}{k_0 d}\int_{-d}^{-h} \frac{n\pi}{d-h} \frac{I'_m\left(\frac{n\pi a}{d-h}\right)}{I_m\left(\frac{n\pi a}{d-h}\right)} \cos\left(\frac{n\pi(z+d)}{d-h}\right) N_0^{-1/2} \cosh\, k_0(z+d) dz \tag{D.1.63}$$

$$G^m_{qn} = \frac{1}{k_q d}\int_{-d}^{-h} \frac{n\pi}{d-h} \frac{I'_m\left(\frac{n\pi a}{d-h}\right)}{I_m\left(\frac{n\pi a}{d-h}\right)} \cos\left(\frac{n\pi(z+d)}{d-h}\right) N_q^{-1/2} \cosh\, k_q(z+d) dz \tag{D.1.64}$$

$$R^{nm}_s = -\frac{2}{d-h}\int_{-d}^{-h} \lambda_{ms} \Lambda_s(a,z) \cos\left(\frac{n\pi(z+d)}{d-h}\right) dz \tag{D.1.65}$$

$$\begin{aligned} S^{0m}_s = {} & \frac{\lambda_{ms}}{k_0 d}\int_{-d}^{-h} \frac{\partial \Lambda_s(a,z)}{\partial r} N_0^{-1/2} \cosh\, k_0(z+d) dz + \\ & + \frac{1}{k_0 d}\int_{-h}^{0} f_s(z) \lambda_{ms} N_0^{-1/2} \cosh\, k_0(z+d) dz \end{aligned} \tag{D.1.66}$$

$$\begin{aligned} S^{qm}_s = {} & \frac{\lambda_{ms}}{k_q d}\int_{-d}^{-h} \frac{\partial \Lambda_s(a,z)}{\partial r} N_q^{-1/2} \cos\, k_q(z+d) dz + \\ & + \frac{1}{k_q d}\int_{-h}^{0} f_s(z) \lambda_{ms} N_q^{-1/2} \cos\, k_q(z+d) dz \end{aligned} \tag{D.1.67}$$

Expressions (D.1.59) - (D.1.67) are idential to Zeng and Tang (2013, A1a-A4b) if the terms $Z_0(z)$ and $Z_q(z)$ are defined as:

$$Z_0(z) = N_0^{-1/2} \cosh\, k_0(z+d) \tag{D.1.68}$$

$$Z_q(z) = N_q^{-1/2} \cos\, k_q(z+d) \tag{D.1.69}$$

The previous expressions differ from Zeng and Tang (2013, 11a,11b) and this is most probably due to a difference in the notation for the main body of their work and the appendices. Thus:

$$F_{n0}^m = -\frac{2H_m(k_0a)\, k_0(d-h)(-1)^n \sinh\, k_0(d-h)}{H_m'(k_0a) N_0^{1/2} \left[k_0^2(d-h)^2 + (n\pi)^2\right]}, \quad q=0,\, n \geq 0 \tag{D.1.70}$$

$$F_{nq}^m = -\frac{2K_m(k_qa)\, k_q(d-h)(-1)^n \sin\, k_q(d-h)}{K_m'(k_qa)\, N_q^{1/2} \left[k_q^2(d-h)^2 - (n\pi)^2\right]}, \quad q \neq 0,\, n \geq 0 \tag{D.1.71}$$

$$G_{00}^m = \frac{|m| \sinh\, k_0(d-h)}{2ak_0^2 d N_0^{1/2}}, \quad q=0,\, n=0 \tag{D.1.72}$$

$$G_{q0}^m = \frac{|m| \sin\, k_q(d-h)}{2ak_q^2 d N_q^{1/2}}, \quad q \geq 1,\, n=0 \tag{D.1.73}$$

$$G_{0n}^m = \frac{I_m'\left(\frac{n\pi a}{d-h}\right)}{I_m\left(\frac{n\pi a}{d-h}\right)} \frac{n\pi(d-h)(-1)^n \sinh\, k_0(d-h)}{(n^2\pi^2 + k_0^2(d-h)^2) d N_0^{1/2}}, \quad q=0,\, n \geq 1 \tag{D.1.74}$$

$$G_{qn}^m = \frac{I_m'\left(\frac{n\pi a}{d-h}\right)}{I_m\left(\frac{n\pi a}{d-h}\right)} \frac{n\pi(d-h)(-1)^n \sin\, k_q(d-h)}{(-n^2\pi^2 + k_q^2(d-h)^2) d N_q^{1/2}}, \quad q \geq 1,\, n \geq 1 \tag{D.1.75}$$

Expressions (D.1.59) - (D.1.64) are explicitly defined in Zeng and Tang (2013, A1a-A3d) but not (D.1.65) - (D.1.67). The solution of the integrals is detailed below. It is worth mentioning that h (draft of the cylinder) should be interpreted as h_j.

- **Case** $s = 1$

As $\Lambda_1 = 0$, then $R_1^{nm} = 0$. For S_1^{qm}:

$$S_1^{q0} = 0 \quad (\lambda_{01} = 0) \tag{D.1.76}$$

$$S_1^{01} = \frac{\frac{1}{2}}{k_0 d} \int_{-h}^{0} \frac{\cosh\, k_0(z+d)}{N_0^{1/2}} dz = \frac{1}{2k_0^2 d N_0^{1/2}} \left[\sinh(k_0 d) - \sinh\, k_0(d-h)\right] \quad m=1, q=0 \tag{D.1.77}$$

where it has been used:

$$\begin{gathered}\int \cosh\, x\, dx = \sinh\, x \\ \left[\begin{array}{cc} k_0 z + k_0 d & = p \\ k_0 dz & = dp \end{array}\right] \\ \int_{-h}^{0} \cosh\, k_0(z+d) dz = \int_{-k_0 h + k_0 d}^{k_0 d} \frac{\cosh\, p}{k_0} dp\end{gathered} \tag{D.1.78}$$

As $\lambda_{11} = \lambda_{-11}$then $S_1^{01} = S_1^{0(-1)}$. For S_1^{q1} :

$$S_1^{q1} = \frac{\frac{1}{2}}{k_q d} \int_{-h}^{0} \frac{\cos\, k_q(z+d)}{N_q^{1/2}} dz = \frac{1}{2k_q^2 d N_q^{1/2}} \left[\sin(k_q d) - \sin\, k_q(d-h)\right] \quad q \geq 1, m = 1 \tag{D.1.79}$$

As previously, $S_1^{q1} = S_1^{q(-1)}$.

- **Case** $s = 2$

As $\Lambda_2 = 0$, then $R_2^{nm} = 0$. For S_2^{qm}:

$$S_2^{q0} = 0 \quad (\lambda_{02} = 0) \tag{D.1.80}$$

$$S_2^{01} = \frac{\frac{1}{2i}}{k_0 d} \int_{-h}^{0} \frac{\cosh\, k_0(z+d)}{N_0^{1/2}} dz = \frac{1}{2ik_0^2 d N_0^{1/2}} \left[\sinh(k_0 d) - \sinh\, k_0(d-h)\right] \quad m = 1, q = 0 \tag{D.1.81}$$

where (D.1.78) has been used. As $\lambda_{12} = -\lambda_{-12}$then $S_2^{01} = -S_2^{0(-1)}$. For S_2^{q1}:

$$S_2^{q1} = \frac{\frac{1}{2i}}{k_q d} \int_{-h}^{0} \frac{\cos\, k_q(z+d)}{N_q^{1/2}} dz = \frac{1}{2ik_q^2 d N_q^{1/2}} \left[\sin(k_q d) - \sin\, k_q(d-h)\right] \quad q \geq 1, m = 1 \tag{D.1.82}$$

As previously, $S_2^{q1} = -S_2^{q(-1)}$.

- **Case** $s = 3$

Using $\Lambda_3 = \frac{1}{2(d-h)} \left[(z+d)^2 - \frac{r_j^2}{2}\right]$we have:

$$R_3^{n0} = -\frac{2}{d-h}\int_{-d}^{-h}\frac{1}{2(d-h_j)}\left[(z+d)^2-\frac{a_j^2}{2}\right]\cos\left[\frac{n\pi(z+d)}{d-h}\right]dz =$$
$$= -\frac{1}{(d-h)}\left[\int_{-d}^{-h}(z+d)^2\cos\left[\frac{n\pi(z+d)}{d-h}\right]dz - \int_{-d}^{-h}\frac{r_j^2}{2}\cos\left[\frac{n\pi(z+d)}{d-h}\right]dz\right] =$$
$$= \frac{-2(d-h)(-1)^n}{(n\pi)^2} \quad n \geq 1 \quad \text{(D.1.83)}$$

where (D.1.84) and (D.1.85) have been used:

$$\int_{-d}^{-h}(z+d)^2\cos\left[\frac{n\pi(z+d)}{d-h}\right]dz$$
$$\left[\begin{array}{c} p = z+d; \quad d-h = h^* \\ dp = dz \end{array}\right] \qquad \text{(D.1.84)}$$
$$\int_0^{h^*} p^2\cos\left[\frac{n\pi p}{h^*}\right]dp = \frac{2(h^*)^3(-1)^n}{(n\pi)^2}$$

$$\frac{r_j^2}{2}\int_{-d}^{-h}\cos\left[\frac{n\pi(z+d)}{d-h}\right]dz = \frac{r_j^2}{2}\frac{d-h}{n\pi}\sin\left[\frac{n\pi(z+d)}{d-h}\right]_{-d}^{-h} = 0 \qquad \text{(D.1.85)}$$

Substituting $n = 0$ in (D.1.83):

$$R_3^{00} = -\frac{2}{d-h}\int_{-d}^{-h}\frac{1}{2(d-h)}\left[(z+d)^2-\frac{r_j^2}{2}\right]dz =$$
$$-\frac{1}{(d-h)^2}\left[\int_{-d}^{-h}(z+d)^2dz - \int_{-d}^{-h}\frac{r_j^2}{2}dz\right] = -\frac{1}{(d-h)^2}\left[\frac{(d-h)^3}{3}-\frac{a_j^2}{2}(d-h)\right] \quad n=0 \qquad \text{(D.1.86)}$$

where the same variable change as in (D.1.84) has been used.

With respect to S_3^{qm}, for $m = \pm 1$ ($q \geq 0$):

$$S_3^{q1} = S_3^{q(-1)} = 0; \quad (\lambda_{13} = \lambda_{-13} = 0) \qquad \text{(D.1.87)}$$

For $q = m = 0$ then:

$$S_3^{00} = \frac{1}{k_0 d}\int_{-d}^{-h} \frac{-a}{2(d-h)} \frac{\cosh\, k_0(z+d)}{N_0^{1/2}} dz = \frac{-a}{2(d-h)k_0^2 d N_0^{1/2}} \left[\sinh\, k_0(d-h)\right] \tag{D.1.88}$$

where the following has been used:

$$\begin{gathered} \left.\frac{\partial \Lambda_3(r,z)}{\partial r}\right|_{r=a} = \frac{-a}{2(d-h)} \\ \int \cosh\, x\, dx = \sinh\, x \\ \left[\begin{array}{c} k_0 z + k_0 d = p \\ k_0 dz = dp \end{array}\right] \\ \int_{-d}^{-h} \cosh\, k_0(z+d) dz = \int_0^{k_0(k-h)} \cosh(p) \frac{dp}{k_0} = \frac{1}{k_0}\left[\sinh\, k_0(d-h)\right] \end{gathered} \tag{D.1.89}$$

For $q \neq 0$:

$$S_3^{q0} = \frac{1}{k_q d}\int_{-d}^{-h} \frac{-a}{2(d-h)} \frac{\cosh\, k_q(z+d)}{N_q^{1/2}} dz = \frac{-a}{2(d-h)k_q^2 d N_q^{1/2}} \left[\sin\, k_q(d-h)\right] \quad q \geq 1, m = 0 \tag{D.1.90}$$

where a similar change of variable and integral as in (D.1.89) has been used.

- **Case** $s = 4$

As $\lambda_{04} = 0$ then $R_4^{n0} = 0$. Using $\Lambda_4 = \frac{r_j}{2(d-h)}\left[(z+d)^2 - \frac{r_j^2}{4}\right]$we have for $n = 0, m = 1$:

$$\begin{aligned} R_4^{01} = -\frac{2}{d-h}\int_{-d}^{-h} \lambda_{14}\Lambda_4(a,z) dz = -\frac{2}{d-h}\int_{-d}^{-h} \frac{1}{2i}\frac{a_j}{2(d-h)}\left[(z+d)^2 - \frac{a_j^2}{4}\right] dz = \\ -\frac{a_j}{2i(d-h)^2}\left[\int_{-d}^{-h}(z+d)^2 dz - \int_{-d}^{-h}\frac{a_j^2}{4} dz\right] = \\ -\frac{a_j}{2i(d-h)^2}\left[\frac{(d-h)^3}{3} - \frac{a_j^2}{4}(d-h)\right] \quad n = 0, m = 1 \end{aligned} \tag{D.1.91}$$

As $\lambda_{14} = -\lambda_{-14}$ then $R_4^{0(-1)} = -R_4^{01}$. For $n \geq 1, m = 1$:

$$R_4^{n1} = -\frac{2}{d-h}\int_{-d}^{-h}\frac{1}{2i}\frac{a_j}{2(d-h)}\left[(z+d)^2-\frac{a_j^2}{4}\right]\cos\left[\frac{n\pi(z+d)}{d-h}\right]dz =$$
$$= -\frac{a_j}{2i(d-h)^2}\int_{-d}^{-h}\left[(z+d)^2-\frac{a_j^2}{4}\right]\cos\left[\frac{n\pi(z+d)}{d-h}\right]dz =$$
$$= -\frac{a_j}{2i(d-h)^2}\left(\frac{2(d-h)^3(-1)^n}{(n\pi)^2}\right) = -\frac{a_j(d-h)(-1)^n}{i(n\pi)^2} \quad n\geq 1, m=1 \quad \text{(D.1.92)}$$

where (D.1.84) and (D.1.85) have been used. Similarly as before, $R_4^{n1} = -R_4^{n(-1)}$. For S_4^{qm}, $S_4^{00} = 0$ as $\lambda_{04} = 0$. For S_4^{01}, using $\frac{\partial\Lambda_4(a,z)}{\partial r}\Big|_{r=a} = \frac{(z+d)^2}{2(d-h)} - \frac{3a^2}{8(d-h)}$:

$$S_4^{01} = \frac{\lambda_{14}}{k_0 d}\int_{-d}^{-h}\left[\frac{(z+d)^2}{2(d-h)}-\frac{3a^2}{8(d-h)}\right]\frac{\cosh\ k_0(z+d)}{N_0^{1/2}}dz - \frac{\lambda_{14}}{k_0 d}\int_{-h}^{0} z\frac{\cosh\ k_0(z+d)}{N_0^{1/2}}dz =$$
$$= \frac{\lambda_{14}}{k_0 d N_0^{1/2}}\left[\int_{-d}^{-h}\frac{(z+d)^2}{2(d-h)}\cosh\ k_0(z+d)dz - \int_{-d}^{-h}\frac{3a^2}{8(d-h)}\cosh\ k_0(z+d)dz\right] -$$
$$- \frac{\lambda_{14}}{k_0 d N_0^{1/2}}\int_{-h}^{0} z\cosh\ k_0(z+d)dz \quad \text{(D.1.93)}$$

Using:

$$\int x^2\cosh\ ax\,dx = -\frac{2x\cosh\ ax}{a^2} + \left(\frac{x^2}{a}+\frac{2}{a^3}\right)\sinh\ ax$$
$$\int_{-d}^{-h}(z+d)^2\cosh\ k_0(z+d)dz = \int_0^{d-h} p^2\cosh(k_0 p)dp =$$
$$= -\frac{2p\cosh\ k_0 p}{k_0^2} + \left(\frac{p^2}{k_0}+\frac{2}{k_0^3}\right)\sinh\ k_0 p\Big]_0^{d-h} =$$
$$-\frac{2(d-h)\cosh\ k_0(d-h)}{k_0^2} + \left(\frac{(d-h)^2}{k_0}+\frac{2}{k_0^3}\right)\sinh\ k_0(d-h)$$
$$\int_{-d}^{-h}\cosh\ k_0(z+d)dz = \int_0^{d-h}\cosh(p)\frac{dp}{k_0} = \frac{1}{k_0}\sinh(p)\Big]_0^{k_0(d-h)} = \frac{1}{k_0}\sinh\ k_0(d-h)$$
$$\int_{-h}^{0} z\cosh\ k_0(z+d)dz = -\frac{1}{k_0^2}\cosh(k_0 d) + \frac{h}{k_0}\sinh\ k_0(d-h) + \frac{1}{k_0^2}\cosh\ k_0(d-h)$$

Equation (D.1.93) can be expressed:

$$S_4^{01} = \frac{\lambda_{14}}{k_0 d N_0^{1/2}} \frac{1}{2(d-h)} \left[-\frac{2(d-h)\cosh\, k_0(d-h)}{k_0^2} + \left(\frac{(d-h)^2}{k_0} + \frac{2}{k_0^3} \right) \sinh\, k_0(d-h) \right] -$$
$$\frac{\lambda_{14}}{k_0 d N_0^{1/2}} \frac{3a^2}{8(d-h)} \frac{1}{k_0} \sinh\, k_0(d-h) -$$
$$\frac{\lambda_{14}}{k_0 d N_0^{1/2}} \left[-\frac{1}{k_0^2} \cosh(k_0 d) + \frac{h}{k_0} \sinh\, k_0(d-h) + \frac{1}{k_0^2} \cosh\, k_0(d-h) \right] \quad m = 1, q = 0 \tag{D.1.94}$$

As $\lambda_{14} = -\lambda_{-14}$ then $S_4^{01} = -S_4^{0(-1)}$. For $q \neq 0, m = 0$, $S_4^{q0} = 0$. For $q \neq 0, m = 1$:

$$S_4^{q1} = \frac{\lambda_{14}}{k_q d} \int_{-d}^{-h} \left[\frac{(z+d)^2}{2(d-h)} - \frac{3a^2}{8(d-h)} \right] \frac{\cos\, k_q(z+d)}{N_q^{1/2}} dz + \frac{\lambda_{14}}{k_q d} \int_{-h}^{0} -z \frac{\cos\, k_q(z+d)}{N_q^{1/2}} dz \tag{D.1.95}$$

Using:

$$\int x^2 \cos\, ax\, dx = \frac{x^2 \sin\, ax}{a} - \frac{2}{a} \left[\frac{\sin\, ax}{a^2} - \frac{x \cos\, ax}{a} \right]$$
$$\int_{-d}^{-h} (z+d)^2 \cos k_q(z+d) dz = \int_0^{d-h} p^2 \cos(k_q p) dp =$$
$$= \left[\frac{p^2 \sin\, k_q p}{k_q} - \frac{2}{k_q} \left[\frac{\sin\, k_q p}{k_q^2} - \frac{p \cos\, k_q p}{k_q} \right] \right]_0^{d-h} =$$
$$= \frac{(d-h)^2 \sin\, k_q(d-h)}{k_q} - \frac{2}{k_q} \left[\frac{\sin\, k_q(d-h)}{k_q^2} - \frac{(d-h)\cos\, k_q(d-h)}{k_q} \right]$$

we have:

$$S_4^{q1} = \frac{\lambda_{14}}{k_q d}\left[\frac{1}{2N_q^{1/2}(d-h)}\int_{-d}^{-h}(z+d)^2\cos\,k_q(z+d)dz - \frac{3a^2}{8(d-h)N_q^{1/2}}\int_{-d}^{-h}\cos\,k_q(z+d)dz\right] - \frac{\lambda_{14}}{k_q d N_q^{1/2}}\int_{-h}^{0} z\cos\,k_q(z+d)dz =$$
$$\frac{\lambda_{14}}{2k_q d N_q^{1/2}(d-h)}\left[\frac{(d-h)^2\sin\,k_q(d-h)}{k_q} - \frac{2}{k_q}\left[\frac{\sin\,k_q(d-h)}{k_q^2} - \frac{(d-h)\cos\,k_q(d-h)}{k_q}\right]\right] -$$
$$\frac{3a^2}{8(d-h)N_q^{1/2}}\frac{\lambda_{14}}{k_q^2 d}\sin\,k_q(d-h) - \frac{\lambda_{14}}{k_q d N_q^{1/2}}\left[\frac{1}{k_q^2}\cos\,k_q d - \frac{1}{k_q^2}\cos\,k_q(d-h) + \frac{h}{k_q}\sin\,k_q(d-h)\right] \tag{D.1.96}$$

Again, $S_4^{q1} = -S_4^{q(-1)}$.

- **Case** $s = 5$

For $m = 0$, $R_5^{n0} = 0$ as $\lambda_{05} = 0$. Using $\Lambda_5 = -\frac{r}{2(d-h)}\left[(z+d)^2 - \frac{r_j^2}{4}\right]$:

$$R_5^{01} = -\frac{2}{d-h}\int_{-d}^{-h}\frac{1}{2}\left(-\frac{a_j}{2(d-h)}\right)\left[(z+d)^2 - \frac{a_j^2}{4}\right]dz =$$
$$\frac{r}{2(d-h)^2}\int_{-d}^{-h}\left[(z+d)^2 - \frac{a_j^2}{4}\right]dz = \frac{a_j}{2(d-h)^2}\left[\frac{(d-h)^3}{3} - \frac{a_j^2}{4}(d-h)\right] \quad n = 0, m = 1 \tag{D.1.97}$$

For $n \geq 1$and $m = 1$, R_5^{n1} :

$$R_5^{n1} = -\frac{2}{d-h}\int_{-d}^{-h}\frac{1}{2}\left(\frac{-a_j}{2(d-h)}\right)\left[(z+d)^2 - \frac{a_j^2}{4}\right]\cos\left[\frac{n\pi(z+d)}{d-h}\right]dz =$$
$$= \frac{a_j}{2(d-h)^2}\int_{-d}^{-h}\left[(z+d)^2 - \frac{a_j^2}{4}\right]\cos\left[\frac{n\pi(z+d)}{d-h}\right]dz = \frac{a_j(d-h)(-1)^n}{(n\pi)^2} \tag{D.1.98}$$

As $\lambda_{15} = \lambda_{-15}$, then we have that $R_5^{n(-1)} = R_5^{n1}$.

For S_5^{qm}, when $q = 0, m = 0$ then $S_5^{00} = 0$ as $\lambda_{05} = 0$. Similarly, $S_5^{q0} = 0$. For S_5^{01}:

$$S_5^{01} = \frac{\lambda_{15}}{k_0 d}\int_{-d}^{-h}\left[\frac{-(z+d)^2}{2(d-h)} + \frac{3a_j^2}{8(d-h)}\right]\frac{\cosh\ k_0(z+d)}{N_0^{1/2}}dz + \frac{\lambda_{15}}{k_0 d}\int_{-h}^{0} z\frac{\cosh\ k_0(z+d)}{N_0^{1/2}}dz =$$

$$= \frac{-\lambda_{15}}{2k_0 N_0^{1/2}(d-h)}\int_{-d}^{-h}(z+d)^2\cosh\ k_0(z+d)dz + \frac{3\lambda_{15}a_j^2}{8(d-h)k_0 d N_0^{1/2}}\int_{-d}^{-h}\cosh\ k_0(z+d)dz +$$

$$\frac{\lambda_{15}}{k_0 d N_0^{1/2}}\int_{-h}^{0} z\cosh\ k_0(z+d)dz =$$

$$\frac{-\lambda_{15}}{2k_0 d N_0^{1/2}(d-h)}\left[-\frac{2(d-h)\cosh\ k_0(d-h)}{k_0^2} + \left(\frac{(d-h)^2}{k_0} + \frac{2}{k_0^3}\right)\sinh\ k_0(d-h)\right] +$$

$$\frac{\lambda_{15}}{8(d-h)}\frac{3a_j^2}{k_0^2 d N_0^{1/2}}\sinh\ k_0(d-h) +$$

$$\frac{\lambda_{15}}{k_0 d N_0^{1/2}}\left[-\frac{1}{k_0^2}\cosh\ k_0 d + \frac{h}{k_0}\sinh\ k_0(d-h) + \frac{1}{k_0^2}\cosh\ k_0(d-h)\right] \quad \text{(D.1.99)}$$

as $\lambda_{15} = \lambda_{-15}$, $S_5^{01} = S_5^{0(-1)}$. For S_5^{q1}:

$$S_5^{q1} = \frac{\lambda_{15}}{k_q d}\int_{-d}^{-h}\left[\frac{-(z+d)^2}{2(d-h)} + \frac{3a_j^2}{8(d-h)}\right]\frac{\cos\ k_q(z+d)}{N_q^{1/2}}dz + \frac{\lambda_{15}}{k_q d}\int_{h}^{0} z\frac{\cos\ k_q(z+d)}{N_q^{1/2}}dz =$$

$$= \frac{-\lambda_{15}}{2k_q d(d-h)N_q^{1/2}}\int_{-h}^{-h}(z+d)^2\cos\ k_q(z+d)dz + \frac{\lambda_{15}3a_j^2}{8k_q d(d-h)N_q^{1/2}}\int_{-d}^{-h}\cos\ k_q(z+d)dz +$$

$$\frac{\lambda_{15}}{k_q d N_q^{1/2}}\int_{-h}^{0} z\cos\ k_q(z+d)dz =$$

$$= \frac{-\lambda_{15}}{2k_q d(d-h)N_q^{1/2}}\left[\frac{(d-h)^2\sin\ k_q(d-h)}{k_q} - \frac{2}{k_q}\left(\frac{\sin\ k_q(d-h)}{k_q^2} - \frac{(d-h)\cos\ k_q(d-h)}{k_q}\right)\right] +$$

$$\frac{\lambda_{15}3a^2}{8k_q d(d-h)N_q^{1/2}}\left[\frac{1}{k_q}\sin\ k_q(d-h)\right] +$$

$$\frac{\lambda_{15}}{k_q d N_q^{1/2}}\left[\frac{1}{k_q^2}\cos\ k_q d - \frac{1}{k_q^2}\cos\ k_q(d-h) + \frac{h}{k_q}\sin\ k_q(d-h)\right] \quad \text{(D.1.100)}$$

D.1.3 Diffraction Transfer Matrix

Any incident wave potential, whether representing an ambient plane wave or scattered/radiated waves generated by cylinders in array, can be expressed as a linear

combination of the following basis functions (see section 2.2.2):

$$\left(\psi^I\right)_n^m = \begin{cases} \frac{\cosh\, k_0(z+d)}{\cosh\, k_0 d} J_m(k_0 r) e^{im\theta}, & n = 0,\, n \in \mathbb{Z} \\ \cos\, k_n(z+d)\, I_m(k_n r) e^{im\theta}, & n \geq 1,\, n \in \mathbb{Z} \end{cases} \tag{D.1.101}$$

Using as definition of the incident potential (Child, 2011, pg.48):

$$\left(\phi^I\right)_n^m = \begin{cases} i^m \left(\psi_j^I\right)_0^m, & n = 0 \\ \left(\psi_j^I\right)_n^m, & n \geq 1 \end{cases} \tag{D.1.102}$$

the resulting diffracted wave field in the exterior region of the cylinder can be expressed in a general form as:

$$\left(\phi^D\right)_{qn}^m = \chi_{qn}^m(r,\, z) e^{im\theta}, \quad r \geq a \tag{D.1.103}$$

with:

$$\begin{aligned} \chi_{q0}^m = i^m \frac{\cosh\, k_0(z+d)}{\cosh\, k_0 d} \left\{ J_m(k_0 r) - \frac{J_m'(k_0 a)}{H_m'(k_0 a)} H_m(k_0 r) \right\} \\ + D_{00}^m \frac{H_m(k_0 r)}{H_m'(k_0 a)} \frac{\cosh\, k_0(z+d)}{N_0^{1/2}} + \sum_{q=1}^{\infty} D_{q0}^m \frac{K_m(k_q r)}{K_m'(k_q a)} \frac{\cos\, k_q(z+d)}{N_q^{1/2}} \end{aligned} \tag{D.1.104}$$

$$\begin{aligned} \chi_{qn}^m = \cos\, k_n(z+d) \left\{ I_m(k_n r) - \frac{I_m'(k_n a)}{K_m'(k_n a)} K_m(k_n r) \right\} \\ + D_{0n}^m \frac{H_m(k_0 r)}{H_m'(k_0 a)} \frac{\cosh\, k_0(z+d)}{N_0^{1/2}} + \sum_{q=1}^{\infty} D_{qn}^m \frac{K_m(k_q r)}{K_m'(k_q a)} \frac{\cos\, k_q(z+d)}{N_q^{1/2}} \end{aligned} \tag{D.1.105}$$

Expression (D.1.104) represents the vertical and radial variation of the exterior potential due to an incident progressive wave (z-mode $n = 0$), whereas (D.1.105) is caused by an evanescent incident wave of z-mode $n \geq 1$. Because of the symmetry of the body, the scattered wave will have the same angular variation of the incident wave.

Using the basis functions (D.1.8), which can be linearly combined to express any general solution for the scattered potential in the exterior region of the cylinder, the diffracted potential in (D.1.103) can be expressed as:

$$\left(\phi^{D-E}\right)_{q0}^{m} = i^m \left(\psi_j^I\right)_0^m - i^m \frac{J_m^{'}(k_0 a)}{H_m^{'}(k_0 a)} \left(\psi_j^{D-E}\right)_0^m + D_{00}^m \frac{\cosh\, k_0 d}{H_m^{'}(k_0 a) N_0^{1/2}} \left(\psi_j^{D-E}\right)_0^m + \sum_{q=1}^{\infty} D_{q0}^m \frac{1}{K_m^{'}(k_q a) N_q^{1/2}} \left(\psi_j^{D-E}\right)_q^m \quad \text{(D.1.106)}$$

$$\left(\phi^{D-E}\right)_{qn}^{m} = \left(\psi_j^I\right)_n^m - \frac{I_m^{'}(k_n a)}{K_m^{'}(k_n a)} \left(\psi_j^{D-E}\right)_n^m + D_{0n}^m \frac{\cosh\, k_0 d}{H_m^{'}(k_0 a) N_0^{1/2}} \left(\psi_j^{D-E}\right)_0^m + \sum_{q=1}^{\infty} D_{qn}^m \frac{1}{K_m^{'}(k_q a) N_q^{1/2}} \left(\psi_j^{D-E}\right)_q^m \quad \text{(D.1.107)}$$

Similarly to the exterior region, the diffracted wave field in the core region can be expressed as:

$$\left(\tilde{\phi}^D\right)_{pn}^{m} = \tilde{\chi}_{pn}^m(r,\, z) e^{im\theta}, \quad r \leq a \quad \text{(D.1.108)}$$

with:

$$\tilde{\chi}_{pn}^m = \frac{C_{0n}^m}{2} \left(\frac{r}{a}\right)^{|m|} + \sum_{p=1}^{\infty} C_{pn}^m \frac{I_m\left(\frac{p\pi r_j}{d-h}\right)}{I_m\left(\frac{p\pi a}{d-h}\right)} \cos\left(\frac{p\pi(z+d)}{d-h}\right) \quad \text{(D.1.109)}$$

By means of the following basis functions (Zeng and Tang, 2013, 26a-26b):

$$\left(\psi_j^{D-C}\right)_p^m = \begin{cases} r_j^{|m|} e^{im\theta_j}, & p = 0 \\ I_m\left(\frac{p\pi r_j}{d-h}\right) e^{im\theta_j}, & p \geq 1 \end{cases} \quad \text{(D.1.110)}$$

potential (D.1.108) can be expressed as:

$$\left(\phi^{D-C}\right)_p^m = \frac{C_{0n}^m}{2} \frac{1}{a^{|m|}} \left(\psi_j^{D-C}\right)_0^m + \sum_{p=1}^{\infty} \frac{C_{pn}^m}{I_m\left(\frac{p\pi a}{d-h}\right)} \cos\left(\frac{p\pi(z+d)}{d-h}\right) \left(\psi_j^{D-C}\right)_p^m \quad \text{(D.1.111)}$$

Using the definition of the Diffraction Transfer Matrix (DTM) from Kagemoto and Yue (1986), which states that the entry $(\mathbf{B})_{q\,n}^{m\,m}$corresponds to "the coefficient of the partial wave of z-mode q and θ-mode m in the scattered velocity potential exterior to the cylinder in response to a unit incident wave of z-mode n and θ-mode m", the elements of matrix $\mathbf{B}$ can be obtained by dividing the coefficients of $\left(\psi^S\right)_q^m$ by those

of $\left(\psi^I\right)_n^m$. Thus:

$$\mathbf{B}_{0\,0}^{m\,m} = -\frac{J_m^{'}(k_0a)}{H_m^{'}(k_0a)} + D_{00}^m \frac{\cosh\, k_0 d}{i^m H_m^{'}(k_0a) N_0^{1/2}}, \quad n=0;\, q=0 \tag{D.1.112}$$

$$\mathbf{B}_{q\,0}^{m\,m} = \frac{D_{q0}^m}{i^m K_m^{'}(k_qa) N_q^{1/2}}, \quad n=0;\, q\geq 1 \tag{D.1.113}$$

$$\mathbf{B}_{0\,n}^{m\,m} = D_{0n}^m \frac{\cosh\, k_0 d}{H_m^{'}(k_0a) N_0^{1/2}}, \quad n\geq 1;\, q=0 \tag{D.1.114}$$

$$\mathbf{B}_{q\,n}^{m\,m} = D_{qn}^m \frac{1}{K_m^{'}(k_qa) N_q^{1/2}}, \quad n\geq 1;\, q\geq 1;\, q\neq n \tag{D.1.115}$$

$$\mathbf{B}_{q\,n}^{m\,m} = -\frac{I_m^{'}(k_na)}{K_m^{'}(k_na)} + D_{qn}^m \frac{1}{K_m^{'}(k_qa) N_q^{1/2}}, \quad n\geq 1;\, q\geq 1;\, q=n \tag{D.1.116}$$

A similar definition for $\left(\tilde{\mathbf{B}}\right)_{p\,m}^{n\,n}$stands, whose elements represent "the coefficient in the interior diffracted potential in z-mode p due to the same incident disturbance" (Child, 2011, pg.61). Therefore, $\left(\tilde{\mathbf{B}}\right)_{p\,m}^{n\,n}$ is obtained by dividing coefficients of $\left(\tilde{\psi}^D\right)_p^m$ by those of $\left(\psi^I\right)_n^m$.

$$\tilde{\mathbf{B}}_{0\,0}^{m\,m} = \frac{C_{00}^m}{2i^m a^{|m|}}, \quad n=0;\, p=0 \tag{D.1.117}$$

$$\tilde{\mathbf{B}}_{p\,0}^{m\,m} = \frac{C_{p0}^m}{i^m I_m\left(\frac{p\pi a}{d-h}\right)} \cos\left(\frac{p\pi(z+d)}{d-h}\right), \quad n=0;\, p\neq 0 \tag{D.1.118}$$

$$\tilde{\mathbf{B}}_{0\,n}^{m\,m} = \frac{C_{0n}^m}{2a^{|m|}}, \quad n\neq 0;\, p=0 \tag{D.1.119}$$

$$\tilde{\mathbf{B}}_{p\,n}^{m\,m} = \frac{C_{pn}^m \cos\left(\frac{p\pi(z+d)}{d-h}\right)}{I_m\left(\frac{p\pi a}{d-h}\right)}, \quad n\neq 0;\, p\neq 0 \tag{D.1.120}$$

As stated by Child (2011, p.62) "all coefficients for which the angular mode of the scattered potential is not equal to that of the incident potentail are zero due to the radial symmetry of the device".

Expressions (D.1.114) - (D.1.120) are identical to Zeng and Tang (2013, A5a-A6d) except from (D.1.112) and (D.1.113) which have an additional term in the denominator related to the incident plane wave's propagation angle. This may correspond to a typographical error.

In order to find the unknown coefficients of potentials (D.1.103) and (D.1.108), a similar procedure to the one explained in Section D.1.2 is followed. Orthogonality of

depth functions is used together with the mathing conditions at the interface between the core and the external region to obtain the following system of equations (see (Child, 2011, pg.51) or (Yilmaz et al., 2001, pg.487)):

$$\begin{cases} C^m_{pn} + \sum_{q=0}^{\infty} E^m_{pq} D^m_{qn} = U^m_{pn} \\ D^m_{qn} = \sum_{p=0}^{\infty} G^m_{qp} C^m_{pn} \end{cases} \tag{D.1.121}$$

where:

$$E^m_{pq} = -\frac{2}{d-h}\frac{H_m(k_0a)}{H'_m(k_0a)}\frac{(d-h)^2 k_0(-1)^p \sinh\, k_0(d-h)}{N_0^{1/2}(p^2\pi^2 + k_0^2(d-h)^2)}, \quad p \geq 0,\, q = 0 \tag{D.1.122}$$

$$E^m_{pq} = -\frac{2}{d-h}\frac{K_m(k_qa)}{K'_m(k_qa)}\frac{(d-h)^2 k_q(-1)^p \sin\, k_q(d-h)}{N_q^{1/2}(-p^2\pi^2 + k_q^2(d-h)^2)}, \quad p \geq 0,\, q \geq 1 \tag{D.1.123}$$

$$G^m_{qp} = \frac{|m| \sinh\, k_0(d-h)}{2ak_0^2 d N_0^{1/2}}, \quad q = 0,\, p = 0 \tag{D.1.124}$$

$$G^m_{qp} = \frac{|m| \sin\, k_q(d-h)}{2ak_q^2 d N_q^{1/2}}, \quad q \geq 1,\, p = 0 \tag{D.1.125}$$

$$G^m_{qp} = \frac{I'_m\left(\frac{p\pi a}{d-h}\right)}{I_m\left(\frac{p\pi a}{d-h}\right)}\frac{p\pi(d-h)(-1)^p \sinh\, k_0(d-h)}{(p^2\pi^2 + k_0^2(d-h)^2) d N_0^{1/2}}, \quad q = 0,\, p \geq 1 \tag{D.1.126}$$

$$G^m_{qp} = \frac{I'_m\left(\frac{p\pi a}{d-h}\right)}{I_m\left(\frac{p\pi a}{d-h}\right)}\frac{p\pi(d-h)(-1)^p \sin\, k_q(d-h)}{(-p^2\pi^2 + k_q^2(d-h)^2) d N_q^{1/2}}, \quad q \geq 1,\, p \geq 1 \tag{D.1.127}$$

$$U^m_{pn} = \frac{4i^{m+1}(-1)^p (d-h) \sinh\, k_0(d-h)}{\pi a(p^2\pi^2 + k_0^2(d-h)^2) H'_m(k_0a) cosh\, k_0 d}, \quad p \geq 0,\, n = 0 \tag{D.1.128}$$

$$U^m_{pn} = \frac{2(d-h)(-1)^{p+1} \sin\, k_n(d-h)}{a(-p^2\pi^2 + k_n^2(d-h)^2) K'_m(k_na)}, \quad p \geq 0,\, n \geq 1 \tag{D.1.129}$$

D.1.4 Hydrodynamic forces

Sections D.1.2 and D.1.3 provided the formulae to compute the RC and the DTM respectively of a truncated vertical circular cylinder. These hydrodynamic operators are required to solve the multiple-scattering problem using the Direct Matrix Method interaction theory by Kagemoto and Yue (1986) detailed in Chapter 2. Here, the focus

is only on the radiation problem and its associated scattered partial cylindrical wave coefficients A_R for each body j in the array can be obtained by solving the following system of equations:

$$A_{Rj} = \mathbf{B}_j^E \sum_{i=1, i\neq j}^{N} \mathbf{T}_{ij}^T \left[\sum_{s=1}^{5} (-i\omega_0 \zeta_s^i \, R_{is}) + A_{Ri} \right] \tag{D.1.130}$$

where R_{is} is the RC vector of body i moving in a mode of motion s and A_{Ri} are the scattered partial cylindrical wave coefficients describing the scattered wave field by each body i generated as a consequence of the radiated field by bodies i.

The total velocity potential in both exterior and core regions of each cylinder j in array can be reconstructed from the scattering coefficients (A_R) obtained from (D.1.130) as:

$$\phi_{RD-E}^j = \left[\sum_{s=1}^{5} (-i\omega_0 \zeta_s^j \, R_{js}^T) + A_{Rj}^T \right] \psi_j^{D-E} + \sum_{i=1, i\neq j}^{N} \left[\sum_{s=1}^{5} (-i\omega_0 \zeta_s^j \, R_{is}^T) + A_{Ri}^T \right] \mathbf{T}_{ij} \psi_j^I \tag{D.1.131}$$

$$\phi_{RD-C}^j = \sum_{s=1}^{5} \left[-i\omega_0 \zeta_s^j \, \phi_{Rs-C} \right] + \left\{ \sum_{i=1, i\neq j}^{N} \left[\sum_{s=1}^{5} (-i\omega_0 \zeta_s^i \, R_{is}^T) + A_{Ri}^T \right] \mathbf{T}_{ij} \right\} \left(\mathbf{B}_j^C \right)^T \psi_j^{D-C} \tag{D.1.132}$$

where ϕ_{RD-E}^j and ϕ_{RD-C}^j represent the total velocity potential in the exterior and core regions of cylinder j respectively.

It is noteworthy to mention that the multiple-scattering problem is solved in the exterior region only as can be derived from the use of $\mathbf{B}^E$ in (D.1.130). The scattered coefficients on the exterior region are transferred to the core one by means of the $\mathbf{B}^C$ as can be observed in (D.1.132).

After having obtained ϕ_{RD-E}^j and ϕ_{RD-C}^j, the first-order hydrodynamic forces and moments can be obtained by integrating the pressure overt the wetted surface of the cylinder j. Thus:

$$F = -\int p_H \, n \, dS; \quad M = -\int p_H \, (L \times n) \, dS \tag{D.1.133}$$

where F and M are the hydrodynamic force and moment, n the normal to the surface, L the lever arm and p_H the hydrodynamic pressure calculated as:

$$p_H = Re\left\{-\rho \frac{\partial \phi_{RD}}{\partial t}\right\} \tag{D.1.134}$$

The complete expressions for the forces are not defined in Zeng and Tang (2013) and have been developed in the following sections.

D.1.4.1 Force direction z

$$F_z^j = -i\rho\omega \iint \phi_{RD}^j n \, dS = i\rho\omega \int_0^{a_i} \int_0^{2\pi} \phi_{RD}^j r_j d\theta_j dr_j = i\rho\omega \int_0^{a_j} \int_0^{2\pi} \phi_{RD-C}^j \Big|_{z=-h} r_j d\theta_j dr_j =$$
$$= i\rho\omega \int_0^{a_j} \int_0^{2\pi} \sum_{s=1}^{5} -i\omega_0 \zeta_S^i (R_{js-C}^T \psi_j^{D-C} + \Lambda_s \sum_{m=-\infty}^{\infty} \lambda_{ms} e^{im\theta_j}) r_j d\theta_j dr_j +$$
$$i\rho\omega \int_0^{a_j} \int_0^{2\pi} \left\{ \sum_{\substack{i=1 \\ i\neq j}}^{n} \left[\sum_{s=1}^{5} (-i\omega_0 \zeta_s^i R_{is}^T) + A_{Ri}^T \right] T_{ij} \right\} (B_j^C)^T (\psi_j^{D-C}) r_j d\theta_j dr_j =$$
$$i\rho\omega_0 \sum_{s=1}^{5} -i\omega_0 \zeta_s^j Y_{js-C}^R + i\rho\omega_0 \left\{ \sum_{\substack{i=1 \\ i\neq j}}^{n} \left[\sum_{s=1}^{5} (-i\omega_0 \zeta_s^i R_{is}^T) + A_{Ri}^T \right] T_{ij} \right\} (B_j^C)^T Y_j^{D-C} \tag{D.1.135}$$

where:

$$Y_{js-C}^R = \int_0^{a_j} \int_0^{2\pi} (R_{js-C}^T \psi_j^{D-C} + \Lambda_s \sum_{m=-\infty}^{\infty} \lambda_{ms} e^{im\theta_j}) r_j d\theta_j dr_j \tag{D.1.136}$$

$$Y_j^{D-C} = \int_0^{a_j} \int_0^{2\pi} \psi_j^{D-C} r_j d\theta_j dr_j \tag{D.1.137}$$

Developing (D.1.137):

$$Y_j^{D-C} = \int_0^{a_j}\int_0^{2\pi} r_j d\theta_j dr_j = 2\pi \left.\frac{r^2}{2}\right|_0^{a_j} = \pi a_j^2 \quad p=0,\, m=0 \tag{D.1.138}$$

$$Y_j^{D-C} = \int_0^{a_j}\int_0^{2\pi} r_j^{|m|} e^{im\theta_j} r_j d\theta_j dr_j = \int_0^{a_j} r_j^{|m|+1} dr_j \int_0^{2\pi} e^{im\theta_j} d\theta = \tag{D.1.139}$$

$$= \left.\frac{r_j^{|m|+2}}{|m|+2}\right|_0^{a_j} \left.\frac{e^{im\theta_j}}{im}\right|_0^{2\pi} = \frac{a_j^{|m|+2}}{|m|+2}\cdot 0 = 0 \quad p=0,\, m\neq 0 \tag{D.1.140}$$

$$Y_j^{D-C} = \int_0^{a_j}\int_0^{2\pi} I_m\left(\frac{p\pi r_j}{d-h}\right) e^{im\theta_j} r_j d\theta_j dr_j = 0 \quad p\geq 1, m\neq 0 \tag{D.1.141}$$

$$Y_j^{D-C} = \int_0^{a_j}\int_0^{2\pi} I_0\left(\frac{p\pi r_j}{d-h}\right) r_j d\theta_j dr_j = 2\pi\int_0^{a_j} I_0\left(\frac{p\pi r_j}{d-h}\right) r_j dr_j = \tag{D.1.142}$$

$$= 2a_j\frac{d-h}{p} I_1\left(\frac{p\pi a_j}{d-h}\right) = 2a_j\frac{d-h}{p} I_1\left(\frac{p\pi a_j}{d-h}\right) \quad p\geq 1,\, m=0 \tag{D.1.143}$$

expression (D.1.143) has been derived using Abramowitz and Segun A. (1964, 9.6.28):

$$\left(\frac{1}{x}\frac{d}{dx}\right)\{xI_1(x)\} = I_0(x) \rightarrow \int I_0\left(\frac{p\pi r_j}{d-h}\right) r_j dr = \frac{d-h}{p\pi} a_j I_1\left(\frac{p\pi a_j}{d-h}\right)$$

Results (D.1.140) and (D.1.141) show that there is no contribution from non-symmetrical angular modes ($m \neq 0$).

Developing (D.1.136):

$$Y^R_{js-C} = R^T_{js-C} Y^{D-C}_j + \int_0^{a_j} \Lambda_s r_j dr_j \int_0^{2\pi} \sum_{m=-\infty}^{\infty} \lambda_{ms} e^{im\theta_j} d\theta_j \tag{D.1.144}$$

$$s = 1,\, 2 \rightarrow \Lambda_s = 0 \tag{D.1.145}$$

$$s = 3 \rightarrow \int_0^{2\pi} d\theta \int_0^{a_j} r_j \frac{1}{2(d-h)} \left[(z+d)^2 - \frac{r_j^2}{2} \right] dr_j =$$

$$2\pi \left[\int_0^{a_j} \frac{(z+d)^2}{2(d-h)} r_j dr - \int_0^{a_j} \frac{r_j^3}{4(d-h)} dr \right] = \tag{D.1.146}$$

$$= \pi \frac{(z+d)^2}{d-h} \frac{a_j^2}{2} - \frac{\pi}{2} \frac{1}{d-h} \frac{a_j^4}{4} = \frac{\pi}{2(d-h)} \left[(z+d)^2 a_j^2 - \frac{a_j^4}{4} \right] \tag{D.1.147}$$

$$s = 4 \rightarrow \int_0^{2\pi} \sum_{m=-\infty}^{\infty} \lambda_{ms} e^{im\theta_j} d\theta = \int_0^{2\pi} \left(\frac{1}{2i} e^{i\theta_j} - \frac{1}{2i} e^{i(-\theta_j)} \right) d\theta = \int_0^{2\pi} \sin\theta \, d\theta = 0 \tag{D.1.148}$$

$$s = 5 \rightarrow \int_0^{2\pi} \sum_{m=-\infty}^{\infty} \lambda_{ms} e^{im\theta_j} d\theta = \int_0^{2\pi} \left(\frac{1}{2} e^{i\theta} + \frac{1}{2} e^{-i\theta} \right) d\theta = \int_0^{2\pi} \cos\theta \, d\theta = 0 \tag{D.1.149}$$

Therefore:

$$Y^R_{j1-C} = R^T_{j1-C} Y^{D-C}_j \tag{D.1.150}$$

$$Y^R_{j2-C} = R^T_{j2-C} Y^{D-C}_j \tag{D.1.151}$$

$$Y^R_{j3-C} = R^T_{j3-C} Y^{D-C}_j + \frac{\pi}{2(d-h)} \left[(d-h)^2 a_j^2 - \frac{a_j^4}{4} \right] \tag{D.1.152}$$

$$Y^R_{j4-C} = R^T_{j4-C} Y^{D-C}_j \tag{D.1.153}$$

$$Y^R_{j5-C} = R^T_{j5-C} Y^{D-C}_j \tag{D.1.154}$$

Only the particular solution of heave mode contributes to the heave force as can be derived from (D.1.145) - (D.1.149).

D.1.4.2 Force direction x

$$
\begin{aligned}
F_x^j = -i\rho\omega_0 \iint \phi_{RD} n_x dS = -i\rho\omega_0 \iint \phi_{RD-E} n_x dS = \\
= -i\rho\omega_0 \int_{-h}^{0}\int_{0}^{2\pi} \phi_{RD-E}|_{r=a_j}\, a_j d\theta_j dz\, \cos\theta_j = \\
= -i\rho\omega_0 \int_{-h}^{0}\int_{0}^{2\pi} \left[\sum_{s=1}^{5}(-i\omega_0\zeta_s^j R_{js}^T) + A_{Rj}^T\right] \psi_j^{D-E} a_j \cos\theta_j d\theta_j dz - \\
i\rho\omega_0 \int_{-h}^{0}\int_{0}^{2\pi} \sum_{\substack{i=1\\ i\neq j}}^{N} \left[\sum_{s=1}^{5}(-i\omega_0\zeta_s^j R_{is}^T) + A_{Ri}^T\right] T_{ij}\psi_j^I a_j \cos\theta_j d\theta_j dz = \\
= -i\rho\omega_0 \left[\sum_{s=1}^{5}(-i\omega_0\zeta_s^j R_{js}^T) + A_{Rj}^T\right] Y_j^{D-E} - i\rho\omega_0 \sum_{\substack{i=1\\ i\neq j}}^{N} \left[\sum_{s=1}^{5}(-i\omega_0\zeta_s^i R_{is}^T) + A_{Ri}^T\right] T_{ij} Y_j^I
\end{aligned}
\tag{D.1.155}
$$

where:

$$
Y_{jF_x}^{D-E} = \int_{-h}^{0}\int_{0}^{2\pi} \psi_j^{D-E} a_j \cos\theta_j d\theta_j dz \tag{D.1.156}
$$

$$
Y_{jF_x}^{I} = \int_{-h}^{0}\int_{0}^{2\pi} \psi_j^{I} a_j \cos\theta_j d\theta_j dz \tag{D.1.157}
$$

Then, expanding (D.1.156):

$$
\begin{aligned}
Y_{jF_x}^{D-E} = \int_{-h}^{0}\int_{0}^{2\pi} \frac{\cosh\, k_0(z+d)}{\cosh\, k_0 d} H_0(k_0 r_j) a_j \cos\theta_j d\theta_j dz = \\
= \frac{H_0(k_0 a_j)}{cosh\, k_0 d} \int_{-h}^{0} \cosh\, k_0(z+d) dz \int_{0}^{2\pi} \cos\theta_j d\theta_j = 0; \quad n = 0,\, m = 0
\end{aligned}
\tag{D.1.158}
$$

$$
\begin{aligned}
Y_{jF_x}^{D-E} = \int_{-h}^{0}\int_{0}^{2\pi} \frac{\cosh\, k_0(z+d)}{\cosh(k_0 d)} H_m(k_0 r_j) e^{im\theta_j} a_j \cos\theta_j d\theta_j dz = \\
= \frac{H_m(k_0 a_j) a_j}{\cosh(k_0 d)} \int_{-h}^{0} \cosh\, k_0(z+d) dz \int_{0}^{2\pi} e^{im\theta_j} \cos\theta_j d\theta_j = \\
= \frac{H_m(k_0 a_j) a_j}{\cosh(k_0 d) k_0} \pi(\sinh(k_0 d) - \sinh(k_0(d-h))); \quad n = 0\, m \neq 0
\end{aligned}
\tag{D.1.159}
$$

$$Y_{jF_x}^{D-E} = \int_{-h}^{0}\int_{0}^{2\pi} \cosh\ k_n(z+d)K_0(k_n a_j)a_j \cos\theta_j d\theta_j dz = \\ = K_0(k_n a_j)a_j \int_{-h}^{0} \cos\ k_n(z+d)dz \int_{0}^{2\pi} \cos\ \theta_j d\theta_j = 0; \quad n \neq 0, m = 0 \quad \text{(D.1.160)}$$

$$Y_{jF_x}^{D-E} = \int_{-h}^{0}\int_{0}^{2\pi} \cos\ k_n(z+d)K_m(k_n r_j)e^{im\theta_j}a_j \cos\theta_j d\theta_j dz = \\ = a_j K_m(k_n a_j) \int_{-h}^{0} \cos\ k_n(z+d)dz \int_{0}^{2\pi} e^{im\theta_j} \cos\theta_j d\theta_j = \\ = \frac{a_j K_m(k_n a_j)\pi}{k_n} \left[\sin(k_n d) - \sin(k_n(d-h))\right]; \quad n \neq 0,\ m \neq 0 \quad \text{(D.1.161)}$$

To derive (D.1.159) the following has been used:

$$\int_{-h}^{0} \cosh\ k_0(z+d)dz \overset{p=k_0(z+d)}{=} \int_{-k_0 h+k_0 d}^{k_0 d} \cosh(p)\frac{1}{k_0}dp = \\ = \frac{1}{k_0}\sinh(p)\Big|_{-k_0 h+k_0 d}^{k_0 d} = \frac{1}{k_0}\left[\sinh\ k_0 d - \sinh\ k_0(d-h)\right] \\ \int_{0}^{2\pi} e^{im\theta_j}\cos\theta_j d\theta_j = \int_{0}^{2\pi} (\cos(m\theta)\cos\theta + j\sin(m\theta)\cos\theta)d\theta = \\ = \int_{0}^{2\pi} (\cos^2\theta + j\,m\,\sin\theta\,\cos\theta)d\theta = \pi$$

Similarly for (D.1.157):

$$Y_{jF_x}^{I} = \int_{-h}^{0}\int_{0}^{2\pi} \frac{\cosh\ k_0(z+d)}{cosh\, k_0 d} J_0(k_0 a_j)a_j \cos\theta_j d\theta_j dz = \\ = \frac{J_0(k_0 a_j)a_j}{\cosh\ k_0 d} \int_{-h}^{0} \cosh\ k_0(z+d)dz \int_{0}^{2\pi} \cos\theta_j d\theta_j = 0; \quad n = 0,\ m = 0 \quad \text{(D.1.162)}$$

$$Y^I_{jF_x} = \int_{-h}^{0}\int_{0}^{2\pi} \frac{\cosh\ k_0(z+d)}{\cosh\ k_0 d} J_m(k_0 a_j) e^{im\theta_j} a_j \cos\theta_j d\theta_j dz = \\ = \frac{J_m(k_0 a_j)}{\cosh\ k_0 d} a_j \int_{-h}^{0} \cosh\ k_0(z+d) dz \int_{0}^{2\pi} e^{im\theta_j} \cos\theta_j d\theta_j = \\ = \frac{J_m(k_0 a_j) a_j}{\cosh(k_0 d) k_0} \pi \left[\sinh(k_0 d) - \sinh\ k_0(d-h)\right]; \quad n=0,\ m\neq 0 \quad \text{(D.1.163)}$$

$$Y^I_{jF_x} = \int_{-h}^{0}\int_{0}^{\pi} \cos\ k_n(z+d) I_0(k_n a_j) a_j \cos\theta_j d\theta_j dz = \\ = I_0(k_n a_j) a_j \int_{-h}^{0} \cos\ k_n(z+d) dz \int_{0}^{2\pi} \cos\theta_j d\theta_j = 0; \quad n\neq 0,\ m=0 \quad \text{(D.1.164)}$$

$$Y^I_{jF_x} = \int_{-h}^{0}\int_{0}^{2\pi} \cos\ k_n(z+d) I_m(k_n r_j) e^{im\theta_j} a_j \cos\theta_j d\theta dz = \\ = a_j I_m(k_n a_j) \int_{-h}^{0} \cos\ k_n(z+d) dz \int_{0}^{2\pi} e^{im\theta_j} \cos\theta_j d\theta = \\ = \frac{a_j I_m(k_n a_j)\pi}{k_n} \left[\sin(k_n d) - \sin\ k_n(d-h)\right]; \quad n\neq 0,\ m\neq 0 \quad \text{(D.1.165)}$$

D.1.4.3 Force direction y

$$F^j_y = -i\rho\omega_0 \left[\sum_{s=1}^{5}(-i\omega_0 \zeta^j_s R^T_{js}) + A^T_{Rj}\right] Y^{D-E}_j - i\rho\omega_0 \sum_{\substack{i=1\\ i\neq j}}^{N} \left[\sum_{s=1}^{5}(-i\omega_0 \zeta^i_s R^T_{is}) + A^T_{Ri}\right] T_{ij} Y^I_j \quad \text{(D.1.166)}$$

where:

$$Y^{D-E}_{jF_y} = \int_{-h}^{0}\int_{0}^{2\pi} \psi^{D-E}_j a_j \sin\theta_j d\theta_j dz \quad \text{(D.1.167)}$$

$$Y^I_{jF_y} = \int_{-h}^{0}\int_{0}^{2\pi} \psi^I_j a_j \sin\theta_j d\theta_j dz \quad \text{(D.1.168)}$$

Developping (D.1.167):

$$Y_{jF_y}^{D-E} = \int_{-h}^{0}\int_{0}^{2\pi} \frac{\cosh\ k_0(z+d)}{\cosh\ k_0 d} H_0(k_0 a_j) a_j \sin\theta d\theta_j dz = \\ = \frac{a_j H_0(k_0 a_j)}{\cosh\ k_0 d} \int_{-h}^{0} \cosh\ k_0(z+d) dz \int_{0}^{2\pi} \sin\theta d\theta = 0; \quad n = 0\,, m = 0 \quad \text{(D.1.169)}$$

$$Y_{jF_y}^{D-E} = \int_{-h}^{0}\int_{0}^{2\pi} \frac{\cosh\ k_0(z+d)}{\cosh\ k_0 d} H_m(k_0 r_j) e^{im\theta_j} a_j \sin\theta d\theta_j dz = \\ = \frac{H_m(k_0 a_j) a_j}{\cosh\ k_0 d} \int_{-h}^{0} \cosh\ k_0(z+d) dz \int_{0}^{2\pi} e^{im\theta_j} \sin\theta_j d\theta_j = \\ = \frac{H_m(k_0 a_j) a_j}{\cosh\ k_0 d} \frac{m\pi i}{k_0} \left[\sinh\ k_0 d - \sinh\ k_0(d-h)\right]; \quad n = 0,\ m \neq 0 \quad \text{(D.1.170)}$$

$$Y_{jF_y}^{D-E} = \int_{-h}^{0}\int_{0}^{2\pi} \cos\ k_n(z+d) K_0(k_n a_j) a_j \sin\theta_j d\theta_j dz = \\ = K_0(k_n a_j) a_j \int_{-h}^{0} \cos\ k_n(z+d) dz \int_{0}^{2\pi} \sin\theta_j d\theta_j = 0; \quad n \neq 0,\ m = 0 \quad \text{(D.1.171)}$$

$$Y_{jF_y}^{D-E} = \int_{-h}^{0}\int_{0}^{2\pi} \cos\ k_n(z+d) K_m(k_n a_j) e^{im\theta_j} a_j \sin\theta_j d\theta_j dz = \\ = a_j K_m(k_n a_j) \int_{-h}^{0} \cos\ k_n(z+d) dz \int_{0}^{2\pi} e^{im\theta_j} \sin\theta_j d\theta_j = \\ = \frac{a_j K_m(k_n a_j)}{k_n} m\pi i \left[\sin\ k_n d - \sin\ k_n(d-h)\right]; \quad n \neq 0,\ m \neq 0 \quad \text{(D.1.172)}$$

To derive (D.1.170) the following has been used:

$$\int e^{im\theta_j} \sin\theta_j d\theta_j = \int (\cos(m\theta) + j\sin(m\theta)) \sin\theta = m\pi$$

Similarly for (D.1.168):

$$Y_{jF_y}^{I} = \int_{-h}^{0}\int_{0}^{2\pi} \psi_j^I a_j \sin\theta_j d\theta_j dz = \int_{-h}^{0}\int_{0}^{2\pi} \frac{\cosh\ k_0(z+d)}{\cosh\ k_0 d} J_0(k_0 a_j) a_j \sin\theta_j d\theta_j dz = \\ = \frac{a_j J_0(k_0 a_j)}{\cosh\,(k_0 d)} \int_{-h}^{0} \cosh\ k_0(z+d) dz \int_{0}^{2\pi} \sin\theta_j d\theta = 0; \quad n = 0,\ m = 0 \quad \text{(D.1.173)}$$

$$Y^I_{jF_y} = \int_{-h}^{0}\int_{0}^{2\pi} \frac{\cosh\, k_0(z+d)}{\cosh\, k_0 d} J_m(k_0 a_j) e^{im\theta_j} a_j \sin\theta_j d\theta_j dz = \\ = \frac{J_m(k_0 a_j) a_j}{\cosh\, k_0 d} \int_{-h}^{0} \cosh\, k_0(z+d) dz \int_{0}^{2\pi} e^{im\theta_j} \sin\theta_j d\theta = \\ = \frac{J_m(k_0 a_j) a_j}{\cosh\, k_0 d} \frac{m\pi i}{k_0} \left[\sinh\, k_0 d - \sinh\, k_0(d-h)\right]; \quad n=0,\, m\neq 0 \quad \text{(D.1.174)}$$

$$Y^I_{jF_y} = \int_{-h}^{0}\int_{0}^{2\pi} \cos\, k_n(z+d) I_0(k_n a_j) a_j \sin\theta d\theta_j dz = \\ = I_0(k_n a_j) a_j \int_{-h}^{0} \cos\, k_n(z+d) dz \int_{0}^{2\pi} \sin\theta d\theta_j = 0, \quad n\neq 0,\, m=0 \quad \text{(D.1.175)}$$

$$Y^I_{jF_y} = \int_{-h}^{0}\int_{0}^{2\pi} \cos\, k_n(z+d) I_m(k_n a_j) e^{im\theta_j} a_j \sin\theta_j d\theta_j dz = \\ = I_m(k_n a_j) a_j \int_{-h}^{0} \cos\, k_n(z+d) dz \int_{0}^{2\pi} e^{im\theta_j} \sin\theta_j d\theta_j = \\ = \frac{a_j I_m(k_n a_j)}{k_n} m\pi i \left[\sin\, k_n d - \sin\, k_n(d-h)\right]; \quad n\neq 0,\, m\neq 0 \quad \text{(D.1.176)}$$

The strategy to calculate the moments has been extracted from the work by Yilmaz (1998, pg.274). Although the sign of the lever to calculate the contribution from the z Force has been kept the same, the signs corresponding to the levers to calculate the contributions from F_y and F_x have been modified.

D.1.4.4 Moment direction y

$$M_y = \underbrace{-i\rho\omega_0 \int_{-h}^{0}\int_{0}^{2\pi} \phi^j_{RD-E}\Big|_{r=a_j} a_j d\theta_j dz\, \cos\theta_j \overbrace{(z)}^{lever}}_{F_x contribution} + \\ \underbrace{i\rho\omega_0 \int_{0}^{a_j}\int_{0}^{2\pi} \phi^j_{RD-C}\Big|_{z=-h} r_j d\theta_j dr_j \overbrace{(-r\cos\theta)}^{lever}}_{F_z contribution} \quad \text{(D.1.177)}$$

With respect to the F_z contribution to $M_y(M_{yF_z})$:

$$M_{yF_z} = i\rho\omega_0 \sum_{s=1}^{5} -i\omega_0 \zeta_s^j Y_{js-C}^{M_y R} + i\rho\omega_0 \left\{ \sum_{\substack{i=1 \\ i\neq j}}^{N} \left[\sum_{s=1}^{5} (-i\omega_0 \zeta_s^i R_{is}^T) + A_{Ri}^T \right] T_{ij} \right\} (B_j^C)^T Y_{jM_y}^{D-C} \tag{D.1.178}$$

where:

$$Y_{js-C}^{M_y R} = \int_0^{a_j} \int_0^{2\pi} -(R_{js-C}^T \psi_j^{D-C} + \Lambda_s \sum_{m=-\infty}^{\infty} \lambda_{ms} e^{im\theta_j}) r^2 \cos\theta d\theta dr \tag{D.1.179}$$

$$Y_{jM_y}^{D-C} = \int_0^{a_j} \int_0^{2\pi} -(\psi_j^{D-C}) r^2 \cos\theta d\theta dr \tag{D.1.180}$$

By developping (D.1.179):

$$Y_{jM_y}^{D-C} = \int_0^{a_j} \int_0^{2\pi} -r^2 \cos\theta d\theta dr = 0; \quad p = 0,\, m = 0$$

$$Y_{jM_y}^{D-C} = \int_0^{a_j} \int_0^{2\pi} -r_j^{|m|} e^{im\theta_j} r^2 d\theta dr \, \cos\theta = -\int_0^{a_j} r_j^{|m|+2} dr \int_0^{2\pi} e^{im\theta_j} \cos\theta d\theta =$$
$$= -\frac{r_j^{|m|+3}}{|m|+3}\bigg|_0^{a_j} \pi = -\pi \frac{a_j^{|m|+3}}{|m|+3}; \quad p = 0,\, m \neq 0$$

$$Y_{jM_y}^{D-C} = -\int_0^{a_j} \int_0^{2\pi} I_m \left(\frac{p\pi r_j}{d-h} \right) e^{im\theta_j} r^2 \cos\theta d\theta dr =$$
$$= -\int_0^{a_j} I_m \left(\frac{p\pi r_j}{d-h} \right) r^2 dr \int_0^{2\pi} e^{im\theta_j} \cos\theta d\theta =$$
$$= -\pi \frac{d-h}{p\pi} \left[r^2 I_2 \left(\frac{p\pi r}{d-h} \right) \right]_0^{a_j} = -\frac{d-h}{p} a^2 I_2 \left(\frac{p\pi a}{d-h} \right); \quad p \geq 1,\, m \neq 0$$

$$Y_{jM_y}^{D-C} = \int_0^{a_j} \int_0^{2\pi} -I_0 \left(\frac{p\pi r}{d-h} \right) r^2 \cos\theta d\theta dr =$$
$$= \int_0^{a_j} -I_0 \left(\frac{p\pi r}{d-h} \right) r^2 dr \int_0^{2\pi} \cos\theta d\theta = 0; \quad p \geq 1,\, m = 0$$

Similarly for (D.1.180):

$$Y_{js-C}^{M_yR} = \int_0^{a_j}\int_0^{2\pi} -(R_{js-C}^T\psi_j^{D-C} + \Lambda_s(z,r)\sum_{m=-\infty}^{\infty}\lambda_{ms}e^{im\theta})r^2\cos\theta d\theta dr =$$
$$= R_{js-C}^T Y_{jM_y}^{D-C} - \int_0^{a_j}\Lambda_s(z,r)r^2dr\int_0^{2\pi}\sum_{m=-\infty}^{\infty}\lambda_{ms}e^{im\theta}\cos\theta d\theta$$

$$s = 1,2 \rightarrow \Lambda_s(z,r) = 0$$
$$s = 3 \rightarrow \int_0^{a_j}\Lambda_S(z,r)r^2dr\int_0^{2\pi}\cos\theta d\theta = 0$$
$$s = 4 \rightarrow \int_0^{a_j}\Lambda_4(z,r)r^2dr\int_0^{2\pi}\left(\frac{1}{2i}e^{i\theta} - \frac{1}{2i}e^{i(-\theta)}\right)\cos\theta d\theta = 0$$
$$s = 5 \rightarrow \int_0^{a_j}\Lambda_5(z,r)r^2dr\int_0^{2\pi}\left(\frac{1}{2}e^{i\theta} + \frac{1}{2}e^{-i\theta}\right)\cos\theta d\theta = \pi\left[-\frac{a_j^4(d-h)}{8} + \frac{a_j^6}{48(d-h)}\right]$$

Therefore:

$$Y_{j1-C}^{M_yR} = R_{j1-C}^T Y_{jM_y}^{D-C}$$
$$Y_{j2-C}^{M_yR} = R_{j2-C}^T Y_{jM_y}^{D-C}$$
$$Y_{j3-C}^{M_yR} = R_{j3-C}^T Y_{jM_y}^{D-C}$$
$$Y_{j4-C}^{M_yR} = R_{j4-C}^T Y_{jM_y}^{D-C}$$
$$Y_{j5-C}^{M_yR} = R_{j5-C}^T Y_{jM_y}^{D-C} - \pi\left[-\frac{a_j^4(d-h)}{8} + \frac{a_j^6}{48(d-h)}\right]$$

With respect to the F_x contribution to $M_y(M_{yF_x})$:

$$M_{yF_x} = -i\rho\omega_0\left[\sum_{s=1}^{5}(-i\omega_0\zeta_s^j R_{js}^T) + A_{Rj}^T\right]Y_{jM_y}^{D-E} - i\rho\omega_0\sum_{\substack{i=1\\i\neq j}}^{N}\left[\sum_{s=1}^{5}(-i\omega_0\zeta_s^i R_{is}^T) + A_{Ri}^T\right]T_{ij}Y_{jM_y}^I$$

where:

$$Y_{jM_y}^{D-E} = \int_{-h}^{0}\int_0^{2\pi}\psi_j^{D-E}a_j\,z\,\cos\theta_j d\theta_j dz \tag{D.1.181}$$
$$Y_{jM_y}^{I} = \int_{-h}^{0}\int_0^{2\pi}\psi_j^{I}a_j\,z\,\cos\theta_j d\theta_j dz \tag{D.1.182}$$

Developping (D.1.181):

$$Y_{jM_y}^{D-E} = \int_{-h}^{0}\int_{0}^{2\pi} \frac{\cosh\ k_0(z+d)}{\cosh\ k_0 d} H_0(k_0 r_j) a_j z\ \cos\theta_j d\theta_j dz =$$
$$= \frac{H_0(k_0 a_j) a_j}{\cosh\ k_0 d} \int_{-h}^{0} \cosh\ k_0(z+d)\, z\, dz \int_{0}^{2\pi} \cos\theta_j d\theta_h = 0; \quad n=0,\, m=0 \quad \text{(D.1.183)}$$

$$Y_{jM_y}^{D-E} = \int_{-h}^{0}\int_{0}^{2\pi} \frac{\cosh\ k_0(z+d)}{\cosh\ k_0 d} H_m(k_0 r_j) e^{im\theta_j} a_j\ z\ \cos\theta_j d\theta_j dz =$$
$$= \frac{H_m(k_0 a_j) a_j}{cosh\, k_0 d} \int_{-h}^{0} \cosh\ k_0(z+d)\, z\, dz \int_{0}^{2\pi} e^{im\theta_j} \cos\theta_j d\theta_j =$$
$$= \frac{H_m(k_0 a_j) a_j}{\cosh\ k_0 d} \pi \left[\frac{1}{k_0^2} \cosh\ k_0(d-h) + \frac{h}{k_0} \sinh\ k_0(d-h) - \frac{1}{k_0^2} \cosh(k_0 d) \right]; \quad n=0,\, m\neq 0$$
(D.1.184)

$$Y_{jM_y}^{D-E} = \int_{-h}^{0}\int_{0}^{2\pi} \cos\ k_n(z+d)\, k_0(k_n a_j) a_j \cos\theta_j\, z\, d\theta dz =$$
$$= K_0(k_n a_j) a_j \int_{-h}^{0} \cos\ k_n(z+d) dz \int_{0}^{2\pi} \cos\theta_j d\theta = 0; \quad n\neq 0,\, m=0 \quad \text{(D.1.185)}$$

$$Y_{jM_y}^{D-E} = \int_{-h}^{0}\int_{0}^{2\pi} \cos\ k_n(z+d) K_m(k_n r_j) e^{im\theta_j} a_j\ z\ \cos\theta_j d\theta_j dz =$$
$$= K_m(k_n a_j) a_j \int_{-h}^{0} \cos\ k_n(z+d)\, z\, dz \int_{0}^{2\pi} e^{im\theta_j} \cos\theta_j d\theta =$$
$$= K_m(k_n a_j) a_j \pi \left[\frac{1}{k_n^2} \cos k_n d - \frac{1}{k_n^2} \cos\ k_n(d-h) + \frac{h}{k_n} \sin\ k_n(d-h) \right]; \quad n\neq 0,\, m\neq 0$$
(D.1.186)

For (D.1.184) it has been used:

$$\int_{-h}^{0} \cosh\ k_0(z+d)\, z\, dz \overset{p=k_0(z+d)}{=} \int_{k_0(d-h)}^{k_0 d} \cosh(p) \left(\frac{p}{k_0} - d\right) \frac{dp}{k_0} =$$

$$= \frac{1}{k_0^2} \int_{k_0(d-h)}^{k_0 d} \cosh(p)\, p\, dp - \frac{d}{k_0} \int_{k_0(d-h)}^{k_0 d} \cosh(p) dp =$$

$$= \frac{1}{k_0^2} \left[p\ \sinh(p) - \cosh(p)\right]_{k_0(d-h)}^{k_0 d} - \frac{d}{k_0} \sinh(p)\Big|_{k_0(d-h)}^{k_0 d} =$$

$$= \frac{1}{k_0^2} \left[k_0 d\ \sinh(k_0 d) - \cosh(k_0 d) - k_0(d-h) \sinh\ k_0(d-h) + \cosh\ k_0(d-h)\right] =$$

$$= -\frac{1}{k_0^2} \cosh(k_0 d) + \frac{h}{k_0} \sinh\ k_0(d-h) + \frac{1}{k_0^2} \cosh\ k_0(d-h)$$

Similarly for (D.1.182):

$$\int_{-h}^{0} \cos\ k_n(z+d)\, z\, dz \overset{p=k_n(z+d)}{=} \int_{k_n(d-h)}^{k_n d} \cos(p) \left(\frac{p}{k_n} - d\right) \frac{dp}{k_n} =$$

$$= \frac{1}{k_n^2} \int_{k_n(d-h)}^{k_n d} \cos(p)\, p\, dp - \frac{d}{k_n} \int_{k_n(d-h)}^{k_n d} \cos(p) dp =$$

$$= \frac{1}{k_n^2} \left[\cos p + p \sin p\right]_{k_n(d-h)}^{k_n d} - \frac{d}{k_n} \sin(p)\Big|_{k_n(d-h)}^{k_n d} =$$

$$= \frac{1}{k_n^2} \left[\cos\ k_n d + k_n d\ \sin k_n d - \cos\ k_n(d-h) - k_n(d-h)\ \sin\ k_n(d-h)\right]$$

$$- \frac{d}{k_n} \left[\sin(k_n d) - \sin\ k_n(d-h)\right] = \frac{1}{k_n^2} \cos k_n d - \frac{1}{k_n^2} \cos\ k_n(d-h) + \frac{h}{k_n} \sin\ k_n(d-h)$$

Developping (D.1.182):

$$Y_{jM_y}^I = \int_{-h}^{0} \int_{0}^{2\pi} \frac{\cosh\ k_0(z+d)}{\cosh\ k_0 d} J_0(k_0 a_j) a_j\, z\, \cos\theta_j d\theta_j dz =$$

$$= \frac{J_0(k_0 a_j) a_j}{\cosh\ k_0 d} \int_{-h}^{0} \cosh\ k_0(z+d)\, z \int_{0}^{2\pi} \cos\theta_j d\theta = 0; \quad n = 0,\ m = 0$$

$$Y^I_{jM_y} = \int_{-h}^{0}\int_{0}^{2\pi} \frac{\cosh\ k_0(z+d)}{\cosh\ k_0 d} J_m(k_0 a_j) e^{im\theta_j} a_j\ z\ \cos\theta_j d\theta_j dz =$$
$$= \frac{J_m(k_0 a_j) a_j}{\cosh\ k_0 d} \int_{-h}^{0} \cosh\ k_0(z+d)\, z\, dz \int_{0}^{2\pi} e^{im\theta_j} \cos\theta_j d\theta_j =$$
$$= \frac{J_m(k_0 a_j) a_j}{cosh\, k_0 d} \pi \left[\frac{1}{k_0^2} cosh\, k_0(d-h) + \frac{h}{k_0} \sinh\ k_0(d-h) - \frac{1}{k_0^2} \cosh\ k_0 d \right]; \quad n=0,\ m \neq 0$$

$$Y^I_{jM_y} = \int_{-h}^{0}\int_{0}^{2\pi} \cos\ k_n(z+d) I_0(k_n a_j) a_j\ z\ \cos\theta d\theta dz =$$
$$= I_0(k_n a_j) a_j \int_{-h}^{0} \cos\ k_n(z+d)\, z\, dz \int_{0}^{2\pi} \cos\theta d\theta = 0; \quad n \neq 0,\ m = 0$$

$$Y^I_{jM_y} = \int_{-h}^{0}\int_{0}^{2\pi} \cos\ k_n(z+d) I_m(k_n r_j) e^{im\theta_j} a_j\ z\ \cos\theta\, d\theta\, dz =$$
$$= I_m(k_n a_j) a_j \int_{-h}^{0} \cos\ k_n(z+d)\, z\, dz \int_{0}^{2\pi} e^{im\theta_j} \cos\theta d\theta =$$
$$= I_m(k_n a_j) a_j \pi \left[\frac{1}{k_n^2} \cos\ k_n d - \frac{1}{k_n^2} \cos\ k_n(d-h) + \frac{h}{k_n} \sin\ k_n(d-h) \right]; \quad n \neq 0,\ m \neq 0$$

D.1.4.5 Moment direction x

$$M_x = \underbrace{-i\rho\omega_0 \int_{-h}^{0}\int_{0}^{2\pi} \phi^j_{RD-E}\Big|_{r=a_j} a_j d\theta_j \sin\theta_j \overbrace{(-z)}^{lever}\, dz}_{F_y contribution} +$$
$$\underbrace{i\rho\omega_0 \int_{0}^{a_j}\int_{0}^{2\pi} \phi^j_{RD-C}\Big|_{z=-h} r_j d\theta_j dr_j \overbrace{(r\sin\theta)}^{lever}}_{F_z contribution} \quad \text{(D.1.187)}$$

With respect to the F_z contribution:

$$M_{xF_z} = i\rho\omega_0 \sum_{s=1}^{5} -i\omega_0 \zeta_s^j Y^{M_x R}_{js-C} + i\rho\omega_0 \left\{ \sum_{\substack{i=1 \\ i\neq j}}^{N} \left[\sum_{s=1}^{5} (-i\omega_0 \zeta_s^i R^T_{is}) + A^T_{Ri} \right] T_{ij} \right\} (B^C_j)^T Y^{D-C}_{jM_x}$$

where:

$$Y_{js-c}^{M_xR} = \int_0^{a_j}\int_0^{2\pi}(R_{js-C}^T\psi_j^{D-C} + \Lambda_s\sum_{m=-\infty}^{\infty}\lambda_{ms}e^{im\theta})r^2\sin\theta d\theta dr \tag{D.1.188}$$

$$Y_{jM_x}^{D-C} = \int_0^{a_j}\int_0^{2\pi}\psi_j^{D-C}r^2\sin\theta d\theta dr \tag{D.1.189}$$

Developping (D.1.188):

$$Y_{jM_x}^{D-C} = \int_0^{a_j}\int_0^{2\pi}r^2\sin\theta d\theta dr = 0; \quad p=0,\, m=0 \tag{D.1.190}$$

$$Y_{jM_x}^{D-C} = \int_0^{a_j}\int_0^{2\pi}r_j^{|m|}e^{im\theta_j}r^2\sin\theta d\theta dr = \\ = \int_0^{a_j}r^{|m|+2}dr\int_0^{2\pi}e^{im\theta_j}\sin\theta d\theta = \frac{a_j^{|m|+3}}{|m|+3}m\pi i; \quad p=0,\, m\neq 0 \tag{D.1.191}$$

$$Y_{jM_x}^{D-C} = \int_0^{a_j}\int_0^{2\pi}I_0\left(\frac{p\pi r_j}{d-h}\right)r^2\sin\theta d\theta dr = \\ = \int_0^{a_j}I_0\left(\frac{p\pi r}{d-h}\right)r^2dr\int_0^{2\pi}\sin\theta d\theta = 0; \quad p\geq 1,\, m=0$$

$$Y_{jM_x}^{D-C} = \int_0^{a_j}\int_0^{2\pi}I_m\left(\frac{p\pi r_j}{d-h}\right)e^{im\theta_j}r^2\sin\theta d\theta dr = \int_0^{a_j}I_m\left(\frac{p\pi r_j}{d-h}\right)r^2dr\int_0^{2\pi}e^{im\theta_j}\sin\theta_j d\theta = \\ = m\pi\frac{d-h}{p\pi}a^2I_2\left(\frac{p\pi a}{d-h}\right) = \frac{mi}{p}(d-h)a^2I_2\left(\frac{p\pi a}{d-h}\right); \quad p\geq 1,\, m\neq 0 \tag{D.1.192}$$

Similarly, for (D.1.189):

$$s = 1, 2 \rightarrow \Lambda_s(z, r) = 0 \tag{D.1.193}$$

$$s = 3 \rightarrow \int_0^{a_j} \Lambda_3(z, r) r^2 dr \int_0^{2\pi} \sin\theta d\theta = 0 \tag{D.1.194}$$

$$s = 4 \rightarrow \int_0^{2\pi} \Lambda_4(z, r) r^2 dr \int_0^{2\pi} \left(\frac{1}{2i} e^{i\theta} - \frac{1}{2i} e^{i(-\theta)} \right) \sin\theta d\theta = \\ = \pi \left[\frac{d-h}{8} a_j^4 - \frac{1}{48} \frac{1}{d-h} a_j^6 \right] \tag{D.1.195}$$

$$s = 5 \rightarrow \int_0^{a_j} \Lambda_5(z, r) r^2 dr \int_0^{2\pi} \left(\frac{1}{2} e^{i\theta} + \frac{1}{2} e^{-i\theta} \right) \sin\theta d\theta = 0 \tag{D.1.196}$$

Therefore:

$$Y_{j1-C}^{M_x R} = R_{j1-C}^T Y_{jM_x}^{D-C} \tag{D.1.197}$$

$$Y_{j2-C}^{M_x R} = R_{j2-C}^T Y_{jM_x}^{D-C} \tag{D.1.198}$$

$$Y_{j3-C}^{M_x R} = R_{j3-C}^T Y_{jM_x}^{D-C} \tag{D.1.199}$$

$$Y_{j4-C}^{M_x R} = R_{j4-C}^T Y_{jM_x}^{D-C} + \pi \left[\frac{d-h}{8} a_j^4 - \frac{1}{48} \frac{1}{d-h} a_j^6 \right] \tag{D.1.200}$$

$$Y_{j5-C}^{M_x R} = R_{j5-C}^T Y_{jM_x}^{D-C} \tag{D.1.201}$$

With regard to the F_y contribution:

$$M_{xF_y} = -i\rho\omega_0 \left[\sum_{s=1}^{5} (-i\omega_0 \zeta_s^j R_{js}^T) + A_{Rj}^T \right] Y_{jM_x}^{D-E} - i\rho\omega_0 \sum_{\substack{i=1 \\ i \neq j}}^{N} \left[\sum_{s=1}^{5} (-i\omega_0 \zeta_s^j R_{is}^T) + A_{Ri}^T \right] T_{ij} Y_{jM_x}^I \tag{D.1.202}$$

where:

$$Y_{jM_x}^{D-E} = \int_{-h}^{0} \int_0^{2\pi} \psi_j^{D-E} a_j \sin\theta_j d\theta_j dz(-z) \tag{D.1.203}$$

$$Y_{jM_x}^{IF_y} = \int_{-h}^{0} \int_0^{2\pi} \psi_j^I a_j \sin\theta_j d\theta dz(-z) \tag{D.1.204}$$

Developping (D.1.203):

$$Y_{jM_x}^{D-E} = \int_{-h}^{0}\int_{0}^{2\pi} \frac{\cosh\ k_0(z+d)}{\cosh\ k_0 d} H_0(k_0 a_j) a_j \sin\theta d\theta_j (-z) dz =$$
$$= \frac{H_0(k_0 a_j) a_j}{\cosh\ k_0 d} \int_{-h}^{0} \cosh\ k_0(z+d)(-z)dz \int_{0}^{2\pi} \sin\theta d\theta = 0; \quad n=0,\ m=0$$

$$Y_{jM_x}^{D-E} = \int_{-h}^{0}\int_{0}^{2\pi} \frac{\cosh\ k_0(z+d)}{\cosh\ k_0 d} H_m(k_0 r_j) e^{im\theta_j} a_j \sin\theta d\theta dz(-z) =$$
$$= \frac{H_m(k_0 a_j) a_j}{\cosh\ k_0 d} \int_{-h}^{0} \cosh\ k_0(z+d)(-z)dz \int_{0}^{2\pi} e^{im\theta_j} \sin\theta d\theta =$$
$$= \frac{H_m(k_0 a_j) a_j}{\cosh\ k_0 d} m\pi i \left[\frac{1}{k_0^2}\cosh(k_0 d) - \frac{h}{k_0}\sinh\ k_0(d-h) - \frac{1}{k_0^2}\cosh\ k_0(d-h)\right]; \quad n=0,\ m\neq 0$$

$$Y_{jM_x}^{D-E} = \int_{-h}^{0}\int_{0}^{2\pi} \cos\ k_n(z+d) K_0(k_n a_j) a_j \sin\theta_j d\theta_j dz(-z) =$$
$$= K_0(k_n a_j) a_j \int_{-h}^{0} \cos\ k_n(z+d)(-z)dz \int_{0}^{2\pi} \sin\theta d\theta = 0; \quad n\neq 0,\ m=0$$

$$Y_{jM_x}^{D-E} = \int_{-h}^{0}\int_{0}^{2\pi} \cos\ k_n(z+d) K_m(k_n a_j) e^{im\theta_j} a_j \sin\theta d\theta_j dz(-z) =$$
$$= K_m(k_n a_j) a_j \int_{-h}^{0} \cos\ k_n(z+d)(-z)dz \int_{0}^{2\pi} e^{im\theta_j} \sin\theta_j d\theta =$$
$$= K_m(k_n a_j) a_j m\pi i \left[\frac{-1}{k_n^2}\cos k_n d + \frac{1}{k_n^2}\cos\ k_n(d-h) - \frac{h}{k_n}\sin\ k_n(d-h)\right]; \quad n\neq 0,\ m\neq 0$$

Developping D.1.204:

$$Y_{jM_x}^{IF_y} = \int_{-h}^{0}\int_{0}^{2\pi} -\frac{\cosh\ k_0(z+d)}{\cosh\ k_0 d} J_0(k_0 a_j)\ a_j\ \sin\theta_j d\theta_j dz(z) =$$
$$- \frac{J_0(k_0 a_j)}{\cosh\ k_0 d} a_j \int_{-h}^{0} \cosh\ k_0(z+d)\, z\, dz \int_{0}^{2\pi} \sin\theta_j d\theta_j = 0; \quad n=0,\ m=0$$

$$Y_{jM_x}^{IF_y} = \int_{-h}^{0}\int_{0}^{2\pi} -\frac{\cosh\ k_0(z+d)}{cosh\, k_0 d} J_m(k_0 a_j) e^{im\theta_j} a_j \sin\theta_j d\theta_j dz(z) =$$
$$-\frac{J_m(k_0 a_j)}{\cosh\ k_0 d} a_j \int_{-h}^{0} \cosh\ k_0(z+d)\, z\, dz \int_{0}^{2\pi} e^{im\theta_j} \sin\theta_j d\theta_j =$$
$$\frac{J_m(k_0 a_j)}{\cosh\ k_0 d} a_j m\pi i \left[\frac{1}{k_0^2}\cosh\ k_0 d - \frac{h}{k_0}\sinh\ k_0(d-h) - \frac{1}{k_0^2}\cosh\ k_0(d-h)\right]; \quad n=0,\, m\neq 0$$

$$Y_{jM_x}^{IF_y} = \int_{-h}^{0}\int_{0}^{2\pi} \cos\ k_n(z+d) I_0(k_n r_j)\, a_j \sin\theta_j d\theta_j dz(-z) =$$
$$I_0(k_n a_j) a_j \int_{-h}^{0} \cos\ k_n(z+d)(-z) dz \int_{0}^{2\pi} \sin\theta_j d\theta_j = 0; \quad n\neq 0,\, m=0$$

$$Y_{jM_x}^{IF_y} = \int_{-h}^{0}\int_{0}^{2\pi} \cos\ k_n(z+d) I_m(k_n a_j) e^{im\theta_j} a_j \sin\theta_j d\theta dz(-z) =$$
$$I_m(k_n a_j) a_j \int_{-h}^{0} \cos\ k_n(z+d)(-z) dz \int_{0}^{2\pi} e^{im\theta_j} \sin\theta_j d\theta_j =$$
$$I_m(k_n a_j) a_j m\pi i \left[\frac{-1}{k_n^2}\cos\ k_n d + \frac{1}{k_n^2}\cos\ k_n(d-h) - \frac{h}{k_n}\sin\ k_n(d-h)\right]; \quad n\neq 0,\, m\neq 0$$

D.1.4.6 Hydrodynamic coefficients

The hydrodynamic coefficients can be computed using::

$$m_{ds} = \frac{1}{\omega^2 \zeta_s} \Re\left\{F_{ds}\right\} \tag{D.1.205}$$

$$b_{ds} = \frac{1}{\omega \zeta_s} \Im\left\{F_{ds}\right\} \tag{D.1.206}$$

where subindex d represents direction of the force and s the motion mode. In adimensionalized form, (D.1.205) for modes $s = 1, 2, 3$ is multiplied by $(\rho a^2 \pi h)^{-1}$whereas modes $s = 4, 5$ are multiplied by $(\rho a^2 \pi h a^2)^{-1}$. With respect to (D.1.206), modes $s = 1, 2, 3$ are multiplied by $(\rho a^2 \pi h \omega)^{-1}$ and $s = 4, 5$ by $(\rho a^2 \pi h a^2 \omega)^{-1}$.

D.1.4.7 Summary of Force Formulae

The forces and moments are calculated as follows:

$$F_x^j = -i\rho\omega_0 \left[\sum_{s=1}^{5}(-i\omega_0\zeta_s^j R_{js}^T) + A_{Rj}^T\right] Y_{jF_x}^{D-E} - i\rho\omega_0 \sum_{\substack{i=1\\ i\neq j}}^{N} \left[\sum_{s=1}^{5}(-i\omega_0\zeta_s^i R_{is}^T) + A_{Ri}^T\right] T_{ij} Y_{jF_x}^I$$

$$\begin{cases} Y_{jF_x}^{D-E} = 0 & n \geq 0,\ m = 0 \\ Y_{jF_x}^{D-E} = \frac{H_m(k_0 a_j)a_j}{\cosh(k_0 d)k_0}\pi(\sinh(k_0 d) - \sinh(k_0(d-h))) & n = 0\, m \neq 0 \\ Y_{jF_x}^{D-E} = \frac{a_j K_m(k_n a_j)\pi}{k_n}\left[\sin(k_n d) - \sin(k_n(d-h))\right] & n \neq 0,\ m \neq 0 \end{cases}$$

$$\begin{cases} Y_{jF_x}^{I} = 0 & n \geq 0,\ m = 0 \\ Y_{jF_x}^{I} = \frac{J_m(k_0 a_j)a_j}{\cosh(k_0 d)k_0}\pi\left[\sinh(k_0 d) - \sinh\ k_0(d-h)\right] & n = 0,\ m \neq 0 \\ Y_{jF_x}^{I} = \frac{a_j I_m(k_n a_j)\pi}{k_n}\left[\sin(k_n d) - \sin(k_n(d-h))\right] & n \neq 0,\ m \neq 0 \end{cases}$$

$$F_y^j = -i\rho\omega_0 \left[\sum_{s=1}^{5}(-i\omega_0\zeta_s^j R_{js}^T) + A_{Rj}^T\right] Y_{jF_y}^{D-E} - i\rho\omega_0 \sum_{\substack{i=1\\ i\neq j}}^{N} \left[\sum_{s=1}^{5}(-i\omega_0\zeta_s^i R_{is}^T) + A_{Ri}^T\right] T_{ij} Y_{jF_y}^I$$

$$\begin{cases} Y_{jF_y}^{D-E} = 0 & n \geq 0,\ m = 0 \\ Y_{jF_y}^{D-E} = \frac{H_m(k_0 a_j)a_j}{\cosh\ k_0 d}\frac{m\pi i}{k_0}\left[\sinh\ k_0 d - \sinh\ k_0(d-h)\right] & n = 0,\ m \neq 0 \\ Y_{jF_y}^{D-E} = \frac{a_j K_m(k_n a_j)}{k_n} m\pi i\left[\sin\ k_n d - \sin\ k_n(d-h)\right] & n \neq 0,\ m \neq 0 \end{cases}$$

$$\begin{cases} Y_{jF_y}^{I} = 0 & n \geq 0,\ m = 0 \\ Y_{jF_y}^{I} = \frac{J_m(k_0 a_j)a_j}{\cosh\ k_0 d}\frac{m\pi i}{k_0}\left[\sinh\ k_0 d - \sinh\ k_0(d-h)\right] & n = 0,\ m \neq 0 \\ Y_{jF_y}^{I} = \frac{a_j I_m(k_n a_j)}{k_n} m\pi i\left[\sin\ k_n d - \sin\ k_n(d-h)\right] & n \neq 0,\ m \neq 0 \end{cases}$$

$$F_z^j = i\rho\omega_0 \sum_{s=1}^{5} -i\omega_0\zeta_s^j Y_{js-C}^{RF_z} + i\rho\omega_0 \left\{\sum_{\substack{i=1\\ i\neq j}}^{n} \left[\sum_{s=1}^{5}(-i\omega_0\zeta_s^i R_{is}^T) + A_{Ri}^T\right] T_{ij}\right\} (B_j^C)^T Y_{jF_z}^{D-C}$$

$$\begin{cases} Y_{jF_z}^{D-C} = \pi a_j^2 & p = 0,\ m = 0 \\ Y_{jF_z}^{D-C} = 2a_j\frac{d-h}{p} I_1\left(\frac{p\pi a_j}{d-h}\right) & p \geq 1,\ m = 0 \\ Y_{jF_z}^{D-C} = 0 & p \geq 0,\ m \neq 0 \end{cases}$$

$$\begin{cases} Y_{js-C}^{RF_z} = \widetilde{R}_{js}^T Y_{jF_z}^{D-C} & s = 1,2,4,5 \\ Y_{j3-C}^{RF_z} = \widetilde{R}_{j3}^T Y_{jF_z}^{D-C} + \frac{\pi}{2(d-h)} \left[(d-h)^2 a_j^2 - \frac{a_j^4}{4} \right] & s = 3 \end{cases}$$

$$M_y = i\rho\omega_0 \sum_{s=1}^{5} -i\omega_0 \zeta_s^j Y_{js-C}^{M_y R} + i\rho\omega_0 \left\{ \sum_{\substack{i=1 \\ i\neq j}}^{N} \left[\sum_{s=1}^{5} (-i\omega_0 \zeta_s^i R_{is}^T) + A_{Ri}^T \right] T_{ij} \right\} (B_j^C)^T Y_{jM_y}^{D-C} -$$
$$i\rho\omega_0 \left[\sum_{s=1}^{5} (-i\omega_0 \zeta_s^j R_{js}^T) + A_{Rj}^T \right] Y_{jM_y}^{D-E} - i\rho\omega_0 \sum_{\substack{i=1 \\ i\neq j}}^{N} \left[\sum_{s=1}^{5} (-i\omega_0 \zeta_s^i R_{is}^T) + A_{Ri}^T \right] T_{ij} Y_{jM_y}^I$$

$$\begin{cases} Y_{jM_y}^{D-C} = 0 & p \geq 1,\ m = 0 \\ Y_{jM_y}^{D-C} = -\pi \frac{a_j^{|m|+3}}{|m|+3} & p = 0,\ m \neq 0 \\ Y_{jM_y}^{D-C} = -\frac{d-h}{p} a^2 I_2 \left(\frac{p\pi a}{d-h} \right) & p \geq 1,\ m \neq 0 \end{cases}$$

$$\begin{cases} Y_{jM_y}^{D-E} = 0 & n \geq 0,\ m = 0 \\ Y_{jM_y}^{D-E} = \frac{H_m(k_0 a_j) a_j}{\cosh\ k_0 d} \pi \left[\frac{1}{k_0^2} \cosh\ k_0(d-h) + \frac{h}{k_0} \sinh\ k_0(d-h) - \frac{1}{k_0^2} \cosh(k_0 d) \right] & n = 0,\ m \neq 0 \\ Y_{jM_y}^{D-E} = K_m(k_n a_j) a_j \pi \left[\frac{1}{k_n^2} \cos k_n d - \frac{1}{k_n^2} \cos\ k_n(d-h) + \frac{h}{k_n} \sin\ k_n(d-h) \right] & n \neq 0,\ m \neq 0 \end{cases}$$

$$\begin{cases} Y_{jM_y}^{I} = 0 & n \geq 0,\ m = 0 \\ Y_{jM_y}^{I} = \frac{J_m(k_0 a_j) a_j}{\cosh\ k_0 d} \pi \left[\frac{1}{k_0^2} \cosh\ k_0(d-h) + \frac{h}{k_0} \sinh\ k_0(d-h) - \frac{1}{k_0^2} \cosh\ k_0 d \right] & n = 0,\ m \neq 0 \\ Y_{jM_y}^{I} = I_m(k_n a_j) a_j \pi \left[\frac{1}{k_n^2} \cos\ k_n d - \frac{1}{k_n^2} \cos\ k_n(d-h) + \frac{h}{k_n} \sin\ k_n(d-h) \right] & n \neq 0,\ m \neq 0 \end{cases}$$

$$\begin{cases} Y_{js-C}^{M_y R} = \widetilde{R}_{js}^T Y_{jM_y}^{D-C} & s = 1,2,3,4 \\ Y_{j5-C}^{M_y R} = \widetilde{R}_{j5}^T Y_{jM_y}^{D-C} - \pi \left[-\frac{a_j^4 (d-h)}{8} + \frac{a_j^6}{48(d-h)} \right] & s = 5 \end{cases}$$

$$M_x = i\rho\omega_0 \sum_{s=1}^{5} -i\omega_0 \zeta_s^j Y_{js-C}^{M_x R} + i\rho\omega_0 \left\{ \sum_{\substack{i=1 \\ i\neq j}}^{N} \left[\sum_{s=1}^{5} (-i\omega_0 \zeta_s^i R_{is}^T) + A_{Ri}^T \right] T_{ij} \right\} (B_j^C)^T Y_{jM_x}^{D-C} -$$
$$i\rho\omega_0 \left[\sum_{s=1}^{5} (-i\omega_0 \zeta_s^j R_{js}^T) + A_{Rj}^T \right] Y_{jM_x}^{D-E} - i\rho\omega_0 \sum_{\substack{i=1 \\ i\neq j}}^{N} \left[\sum_{s=1}^{5} (-i\omega_0 \zeta_s^i R_{is}^T) + A_{Ri}^T \right] T_{ij} Y_{jM_x}^I$$

$$\begin{cases} Y_{jM_x}^{D-C} = 0 & p \geq 0,\ m = 0 \\ Y_{jM_x}^{D-C} = \frac{a_j^{|m|+3}}{|m|+3} m\pi i & p = 0,\ m \neq 0 \\ Y_{jM_x}^{D-C} = \frac{mi}{p}(d-h)a^2 I_2\left(\frac{p\pi a}{d-h}\right) & p \geq 1,\ m \neq 0 \end{cases}$$

$$\begin{cases} Y_{jM_x}^{D-E} = 0 & n \geq 0,\ m = 0 \\ Y_{jM_x}^{D-E} = \frac{H_m(k_0 a_j)a_j}{\cosh\, k_0 d} m\pi i \left[\frac{1}{k_0^2}\cosh(k_0 d) - \frac{h}{k_0}\sinh\, k_0(d-h) - \frac{1}{k_0^2}\cosh\, k_0(d-h)\right] & n = 0,\ m \neq 0 \\ Y_{jM_x}^{D-E} = K_m(k_n a_j)a_j m\pi i \left[\frac{-1}{k_n^2}\cos k_n d + \frac{1}{k_n^2}\cos\, k_n(d-h) - \frac{h}{k_n}\sin\, k_n(d-h)\right] & n \neq 0,\ m \neq 0 \end{cases}$$

$$\begin{cases} Y_{jM_x}^{I} = 0 & n \geq 0,\ m = 0 \\ Y_{jM_x}^{I} = \frac{J_m(k_0 a_j)}{\cosh\, k_0 d} a_j m\pi i \left[\frac{1}{k_0^2}\cosh\, k_0 d - \frac{h}{k_0}\sinh\, k_0(d-h) - \frac{1}{k_0^2}\cosh\, k_0(d-h)\right] & n = 0,\ m \neq 0 \\ Y_{jM_x}^{I} = I_m(k_n a_j)a_j m\pi i \left[\frac{-1}{k_n^2}\cos\, k_n d + \frac{1}{k_n^2}\cos\, k_n(d-h) - \frac{h}{k_n}\sin\, k_n(d-h)\right] & n \neq 0,\ m \neq 0 \end{cases}$$

$$\begin{cases} Y_{js-C}^{M_x R} = \widetilde{R}_{js}^T Y_{jM_x}^{D-C} & s = 1,2,3,5 \\ Y_{j4-C}^{M_x R} = \widetilde{R}_{j4}^T Y_{jM_x}^{D-C} + \pi\left[\frac{d-h}{8}a_j^4 - \frac{1}{48}\frac{1}{d-h}a_j^6\right] & s = 4 \end{cases}$$

D.2 Numerical results

In this section, a verification of the formulae derived in the preceding sections is presented. For their implementation, both *Fortran* and *Python* languages have been used and interfaced by means of *F2PY* (Peterson, 2007). The computation of all the operators required by the IT has been implemented in *Fortran*. This includes the Radiation Characteristics (RC), the Diffraction Transfer Matrix (DTM) and the Transformation Matrix. Vectors containing the terms resulting from the integration of the partial wave functions on the cylindrical surface (referred to as Y in section D.1.4.7) have been also implemented in *Fortran*. Details on the resolution of the dispersion equations and on the evaluation of Bessel functions are given in (C.2). The IT system of equations (2.3.13) has been assembled and solved using *Python* as well as the computation of the forces and the hydrodynamic coefficients.

D.2.1 Isolated Cylinder

A first verification is carried out by considering a single isolated cylinder. This is done by setting to zero both the interaction coefficients (A_{Rj}) as well as the RC vectors

(R_{is}) in the expressions of the forces shown in section D.1.4.7. This simplification enables one to "switch off" the effect of hydrodynamic interactions and to calculate the radiation hydrodynamic coefficients of an isolated cylinder due only to its own motion. Results obtained using this procedure have been compared against the semi-analytical solution of Sabuncu and Calisal (1981) presented in (C) and are displayed in Figures D.2 - D.5. A truncation of 20 evanescent terms has been used as indicated in Sabuncu and Calisal (1981). A very good match between results is found for all modes of motion and geometric parameters of the system. We note a slight offset for both the added mass and damping coefficients in sway for thin plate geometries, i.e. $t/a = 0.1 - 0.5$. Additional verifications for this mode of motion are presented in the following sections.

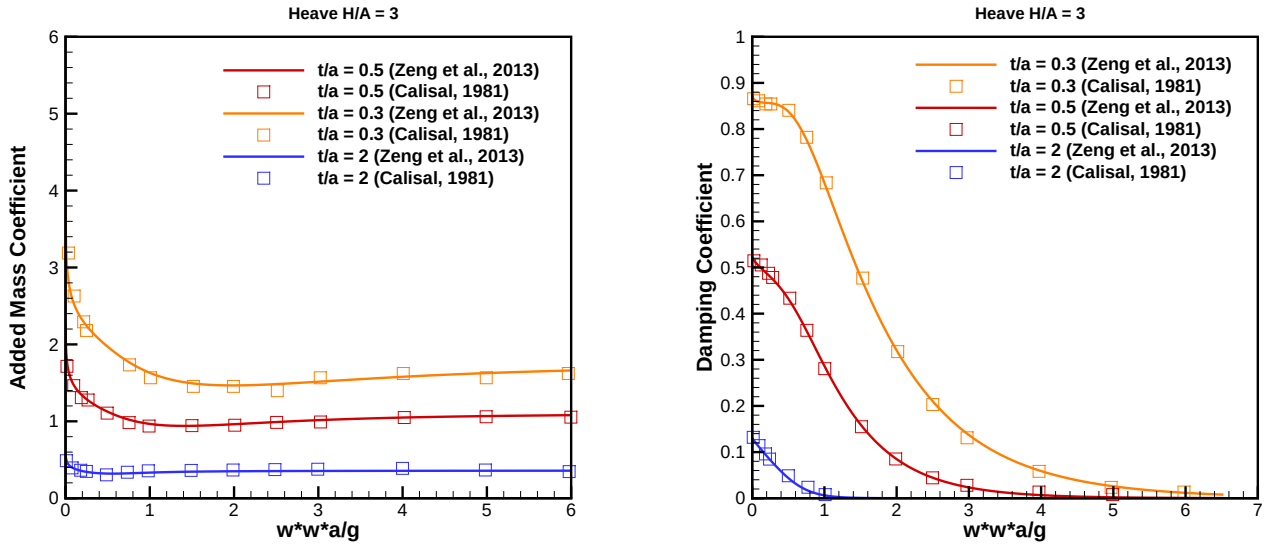

(a) (b)

Figure D.2

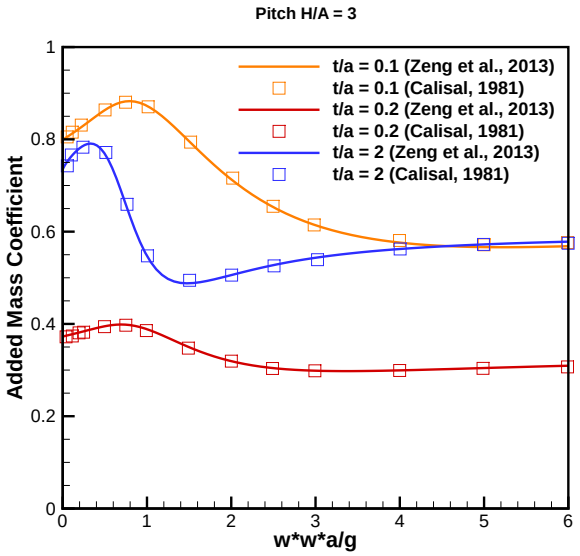

(a)

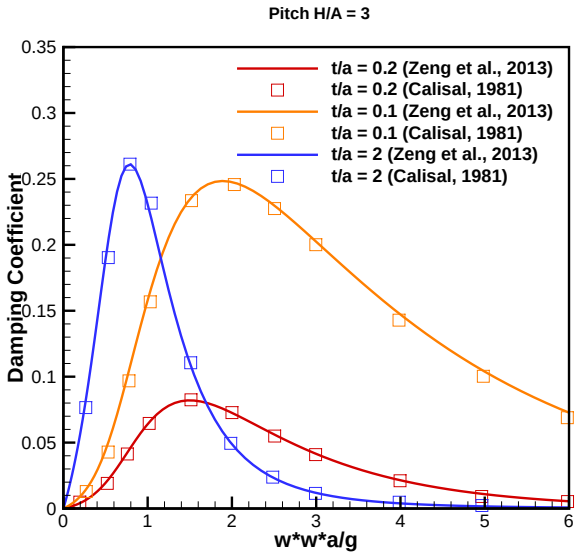

(b)

Figure D.3

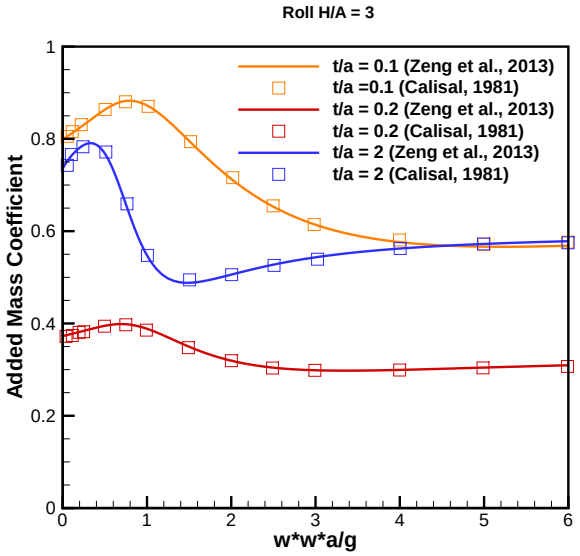

(a)

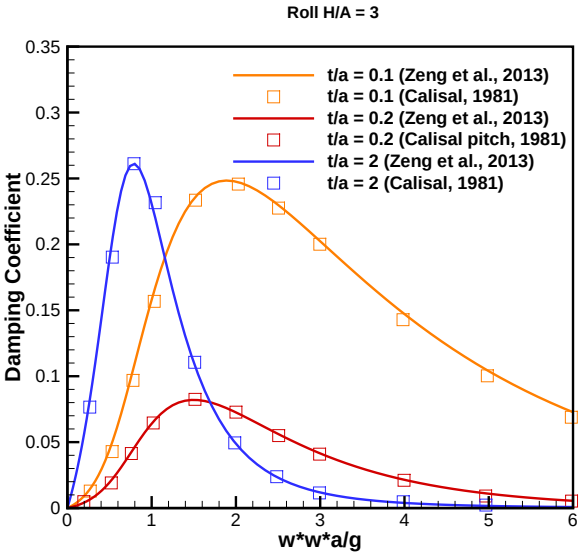

(b)

Figure D.4

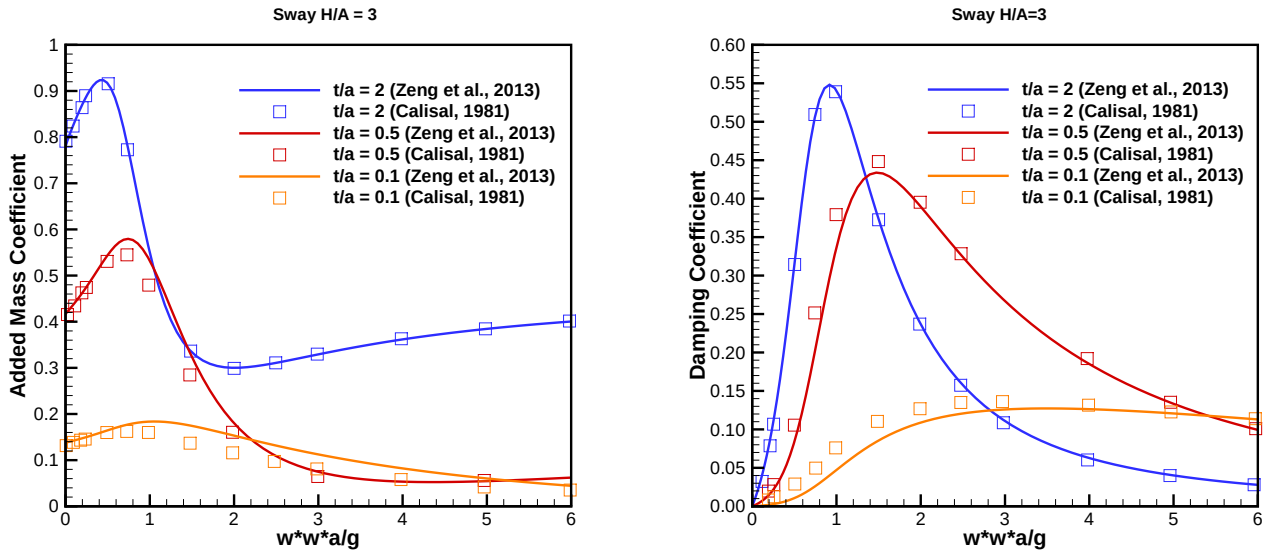

(a) (b)

Figure D.5

D.2.2 Four cylinder array

The results shown in the previous section validate the derivation and implementation of the partial wave functions integrals on the surface of the cylinder as well as the RC evaluation. Herein, the results of the work by Zeng and Tang (2013) for a small array of four cylinders (Figure D.6a) with a radius a, draft $5a$ in a water depth of $20a$ and separated by a distance $d = 5a$ have been replicated to verify the implementation of the full multiple-scattering problem. Cylinders 1 and 2 are forced to oscillate in phase in roll mode, and at the same time an oscillation out of phase for cylinders 3 and 4 is imposed in pitch mode. The amplitudes of oscillation are kept the same.

Contrarily to the case of Sabuncu and Calisal (1981), in Zeng and Tang (2013) the truncation is not specified. Results presented in Figures D.7 - D.11 have been generated using 10 evanescent modes as for this number the values provided by Zeng and Tang (2013) are replicated with good accuracy. Notwithstanding, a sensitivity analysis of the evanescent modes truncation is performed in section D.2.3.

In spite of the good accuracy observed for all modes, a difference of a factor 10 is observed in F_z (Figures D.9). It is hypothesized it may stem from the use of a different motion amplitude in the adimensionalization factor. To confirm it is not due to an

error of the formulation/implementation, the radiation hydrodynamic coefficients in heave have been compared in section (D.2.3) to calculations performed using NEMOH and the IT with the hydrodynamic operators generated as described in Chapter I.

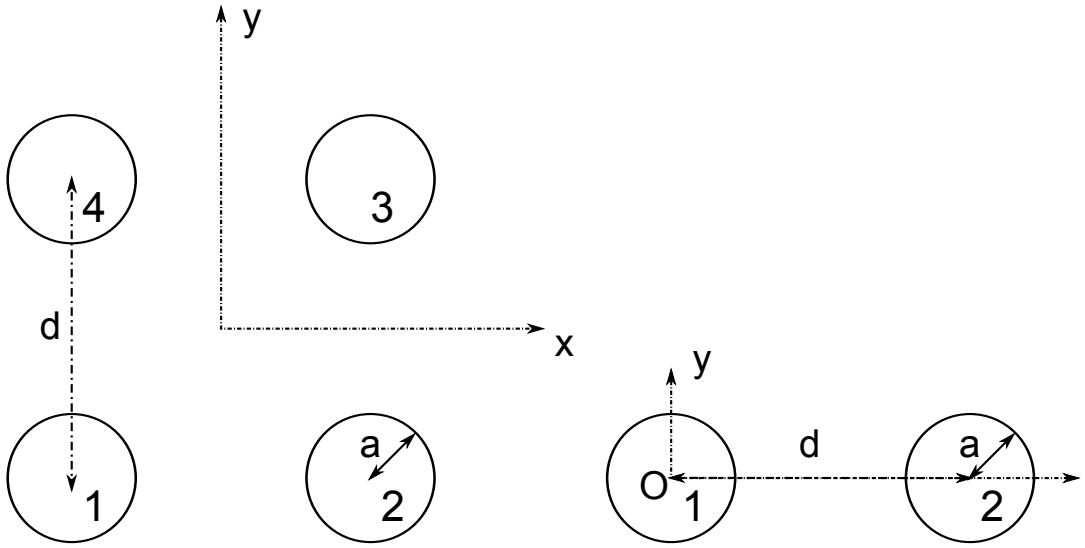

(a) Schematic of a four cylinder array. (b) Schematic of a two cylinder array.

Figure D.6

D.2.3 Sensitivity to evanescent modes truncation

A case consisting of two in-line cylinders (Figure D.6b) of radius $a = 3m$, draft $6m$ in a water depth of $10m$ is chosen to study the sensitivity of the hydrodynamic coefficients with respect to the number of evanescent modes used. Results for the diagonal added mass and damping coefficients are shown as a function of the separating distance between cylinders and for two different wave lengths ($\lambda/a = 10$, Figure D.12; $\lambda/a = 30$,

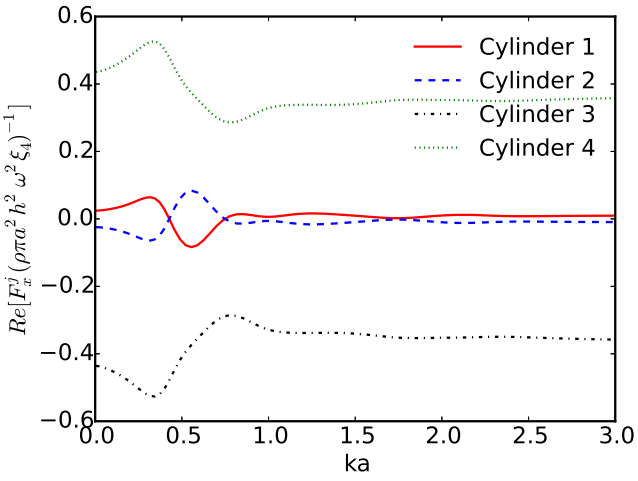

(a)

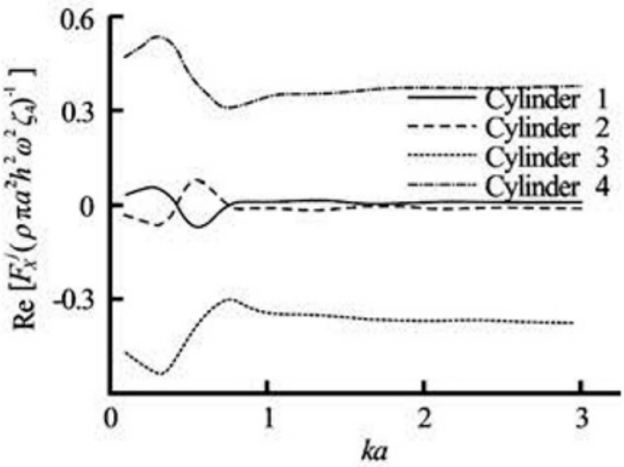

(b)

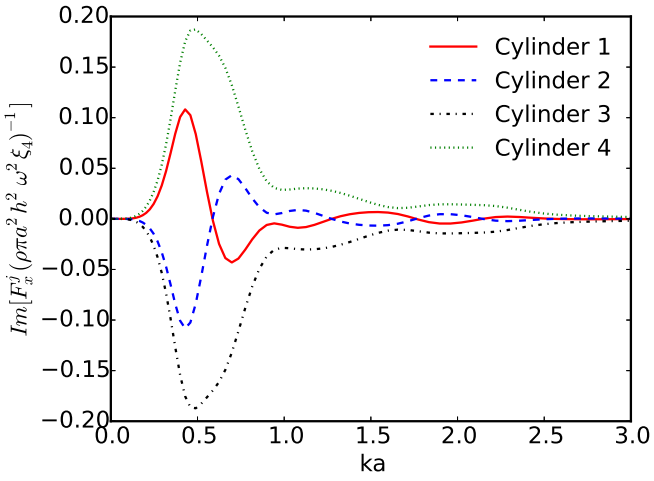

(c)

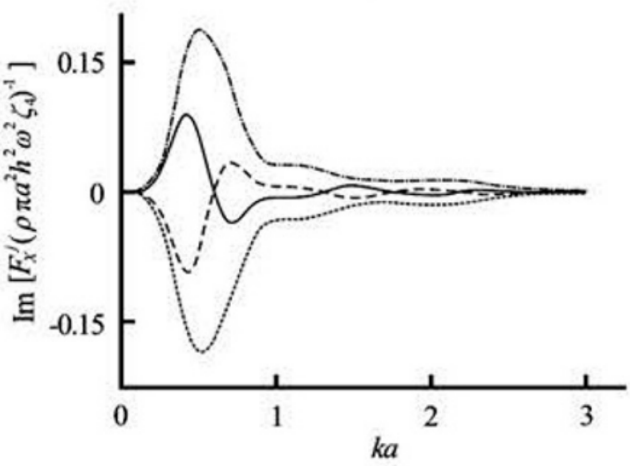

(d)

Figure D.7

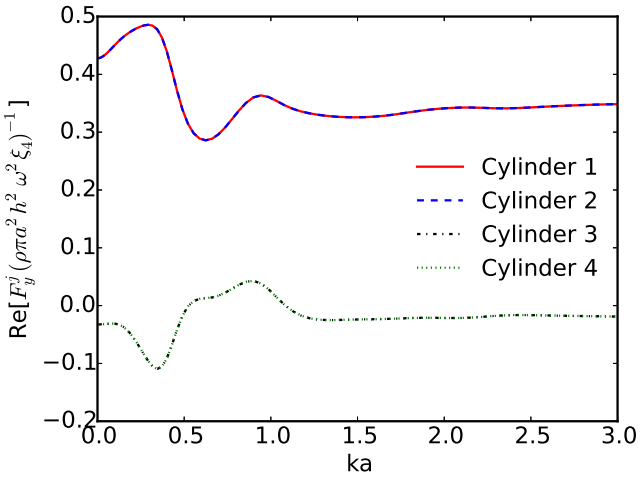

(a)

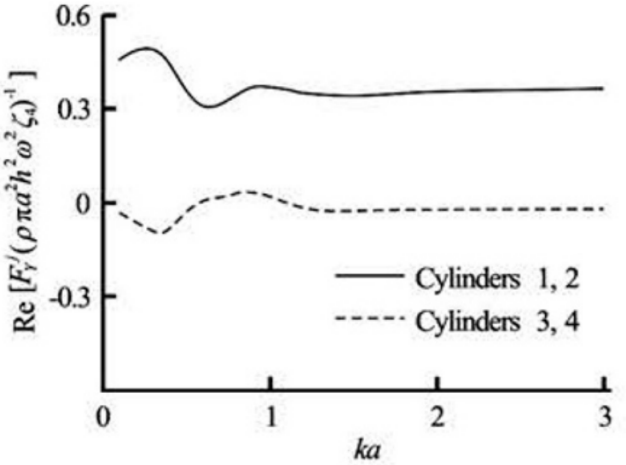

(b)

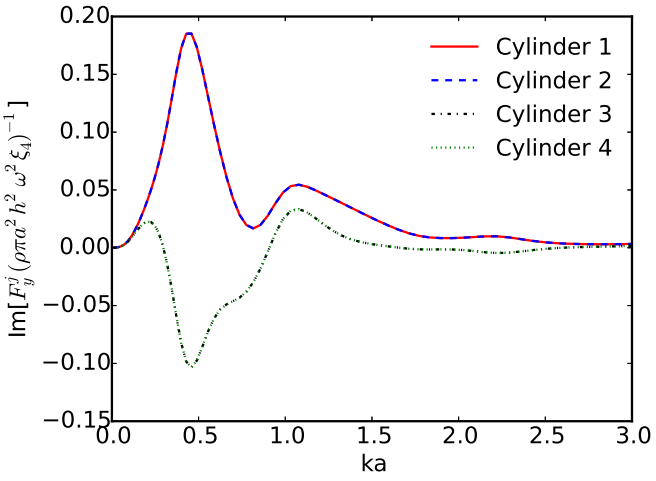

(c)

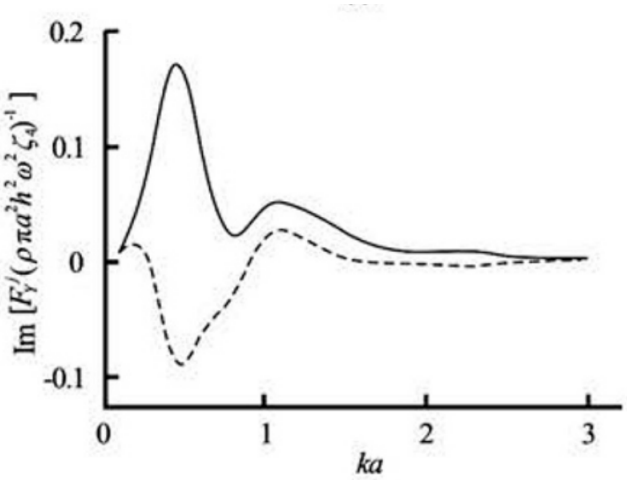

(d)

Figure D.8

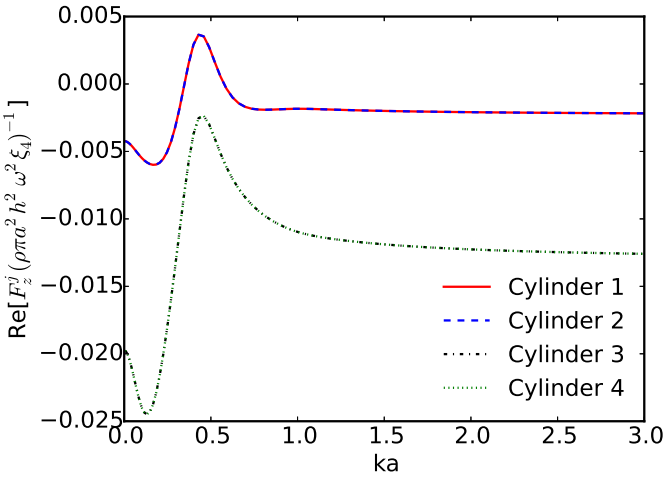

(a)

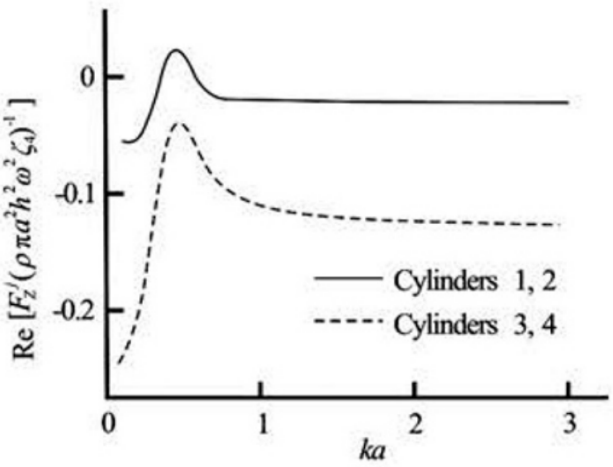

(b)

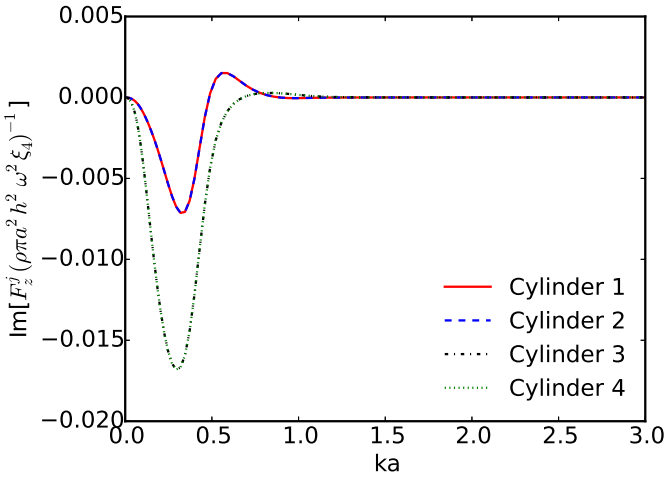

(c)

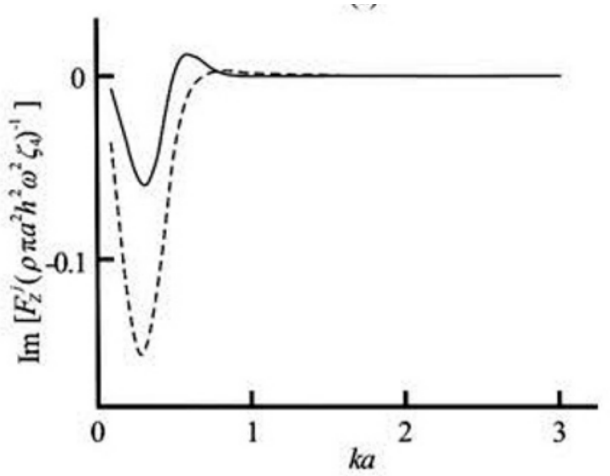

(d)

Figure D.9

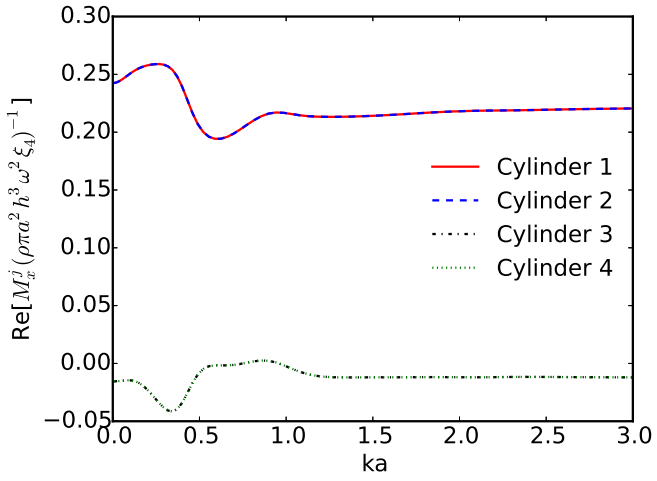

(a)

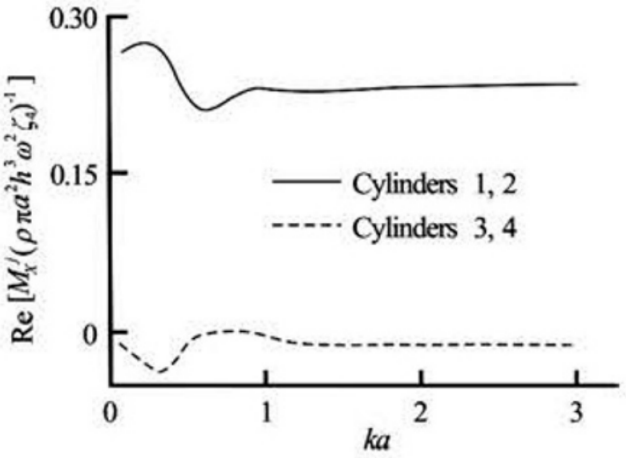

(b)

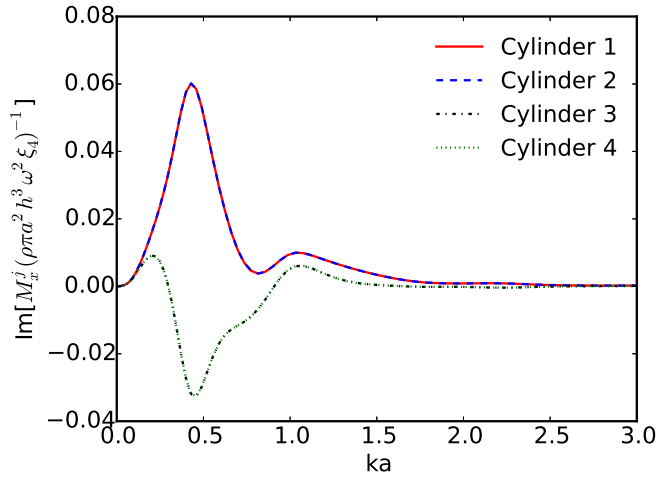

(c)

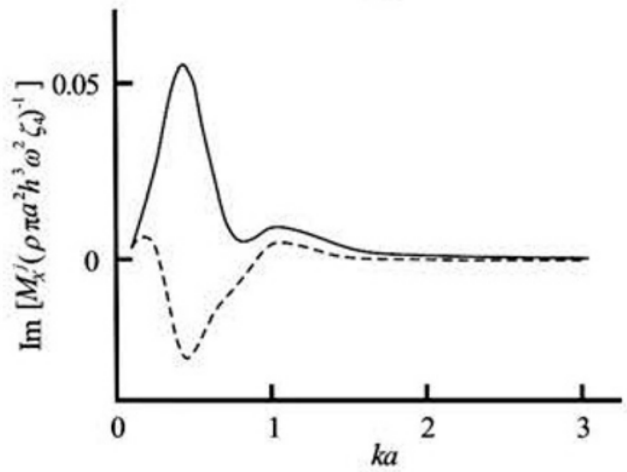

(d)

Figure D.10

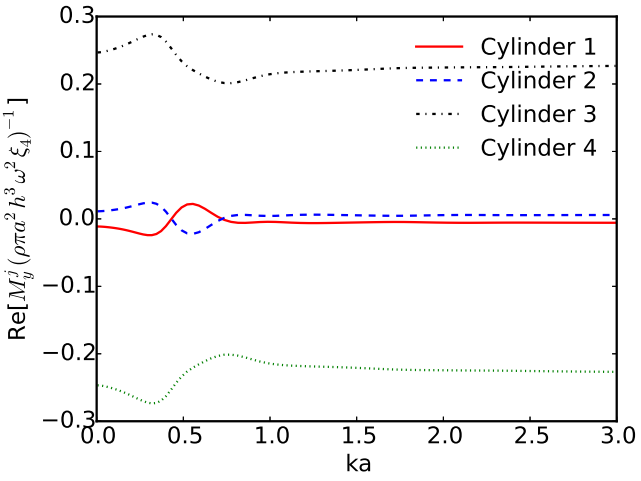

(a)

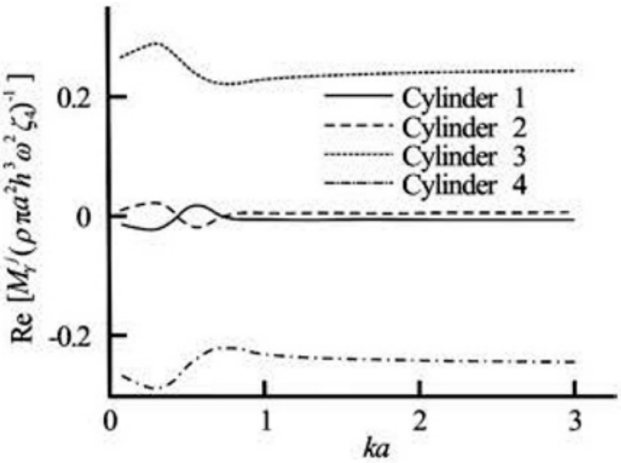

(b)

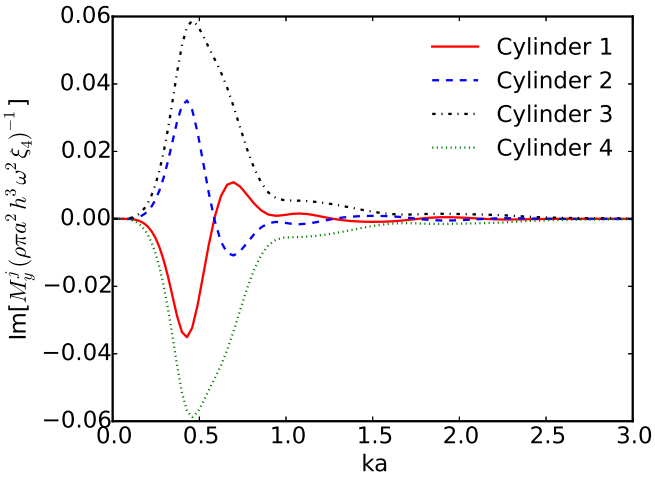

(c)

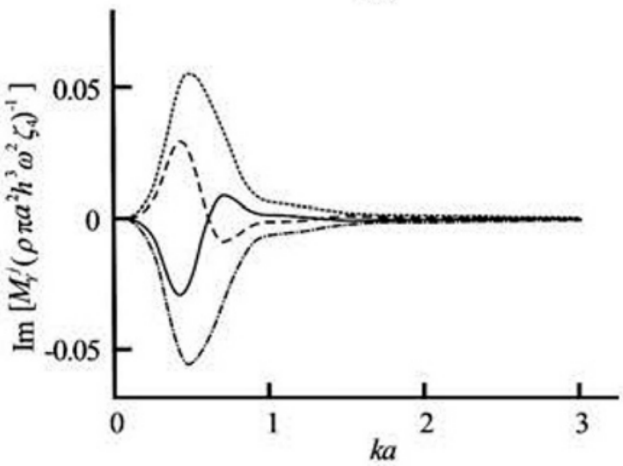

(d)

Figure D.11

Figure D.13). In all cases, it can be observed that a truncation of 30 terms ensures a good level of precision. A lower sensitivity of results has been found for the off-diagonal terms (not shown herein).

Results given in the work by Zeng and Tang (2013) and presented as reference in section D.2.2 are not exempt from uncertainties as the truncation used to generate them is not specified in the original work. In the previous section it has been found that they can be replicated with good agreement using 10 modes. However, results in Figures D.12 and D.13 indicate that they may not be converged. Because of that, an additional set of verifications has been undertaken.

They consist of comparing the results obtained from the implementation of the formulae in section D.1.4.7 against direct calculations with the BEM code NEMOH and the IT. For the latter, the required hydrodynamic operators have been generated as described in Chapter I. Results are presented as a function of the separating distance for two different wave lengths ($\lambda/a = 10$, Figure D.14; $\lambda/a = 30$, Figure D.15), and as a function of the wave frequency for a fixed separating distance (Figure D.16).

With respect to Figures D.14 and D.15, it can be observed that a finer discretization of the wetted surface of the cylinder reduces the differences between the semi-analytical solution and the BEM as expected. A perfect match between the direct NEMOH calculations and the IT is found. A very good agreement is as well observed between the BEM and the semi-analytical solution, with the highest discrepancy ($\sim 6\%$) observed for the damping coefficients in the longest wave length and for the highest separating distance between bodies. With respect to the F_z force, a maximum difference of $\sim 3\%$ is found between the semi-analytical solution and the BEM with the highest refinement.

In Figure D.16, a very good match between the diagonal and coupled radiation hydrodynamic coefficients in heave computed with the implementation of the semi-analytical solution by Zeng and Tang (2013) and with the IT can be observed. We note a discrepancy of $\sim 6\%$ of results for the damping coefficient at the interval of wave frequencies $0.6-0.8\,rad/s$ and the presence of an irregural frequency at $2.2 rad/s$.

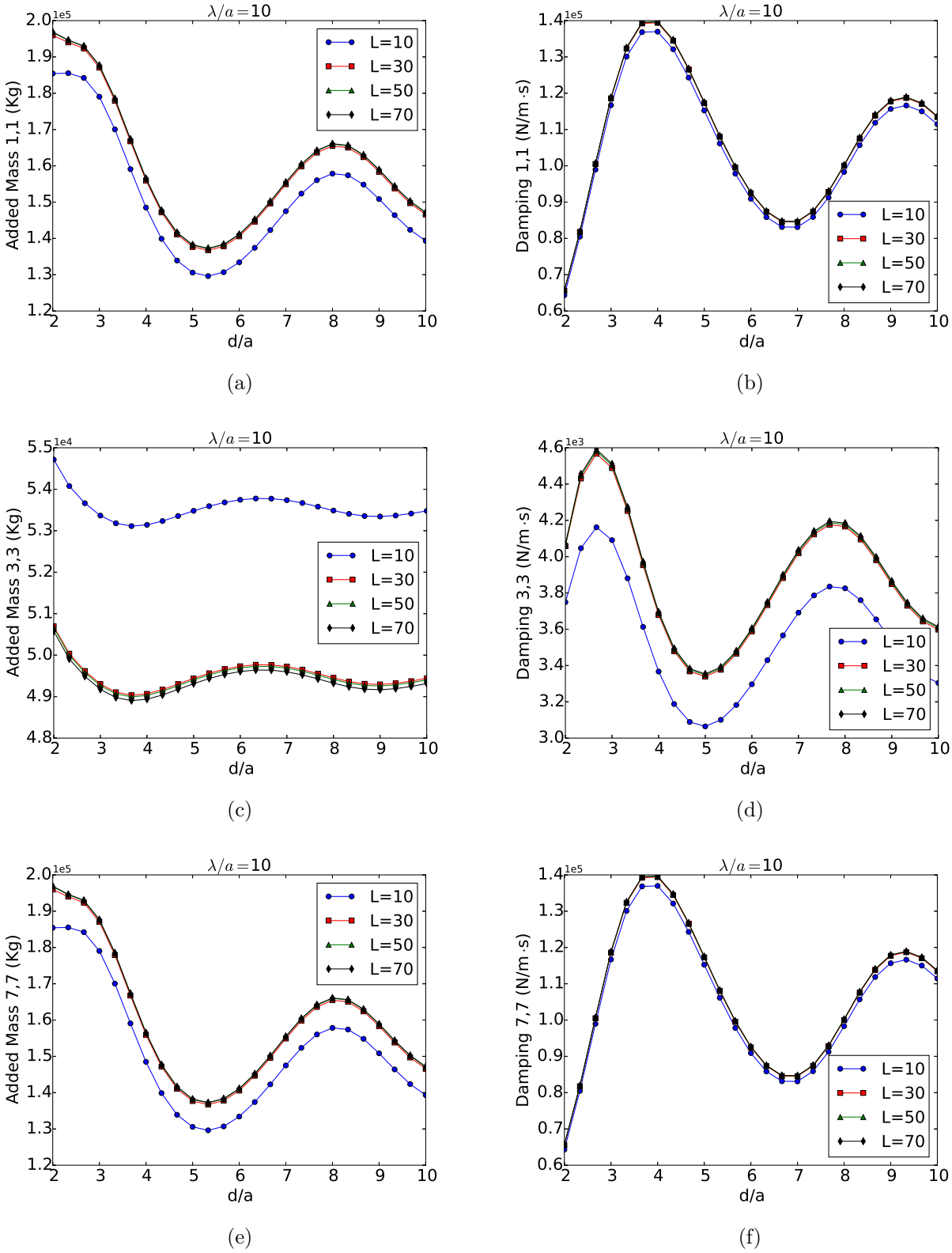

Figure D.12: Comparison between diagonal added mass and damping coefficients for two cylinders (Figure D.6b) of radius $3m$, draft $6m$ in a $10m$ water depth at several separation distances and for several truncation values (represented as L). First index corresponds to the direction of the force and the second to the degree of freedom.

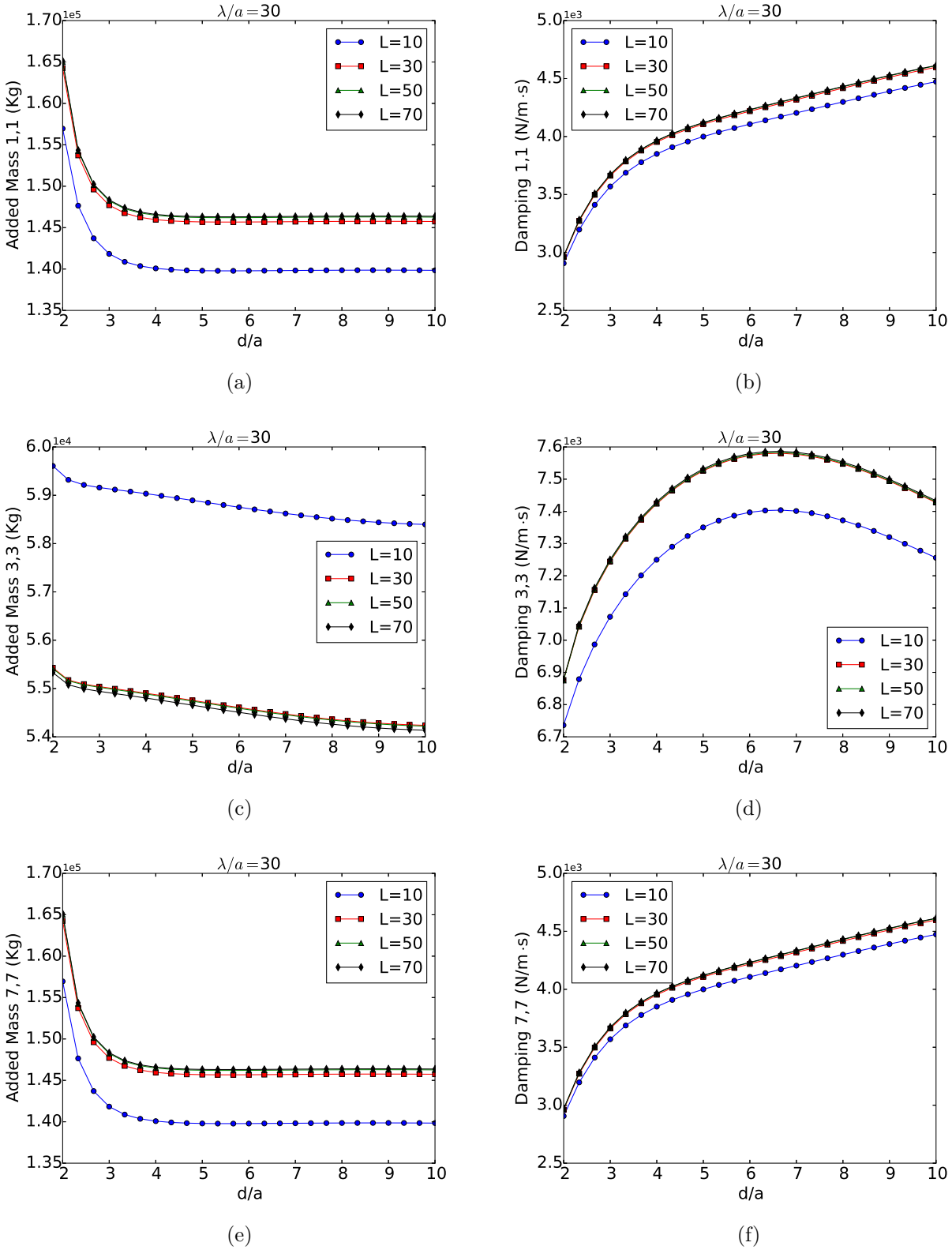

Figure D.13: Comparison between diagonal added mass and damping coefficients for two cylinders (Figure D.6b) of radius $3m$, draft $6m$ in a $10m$ water depth at several separation distances and for several truncation values (represented as L). First index corresponds to the direction of the force and the second to the degree of freedom.

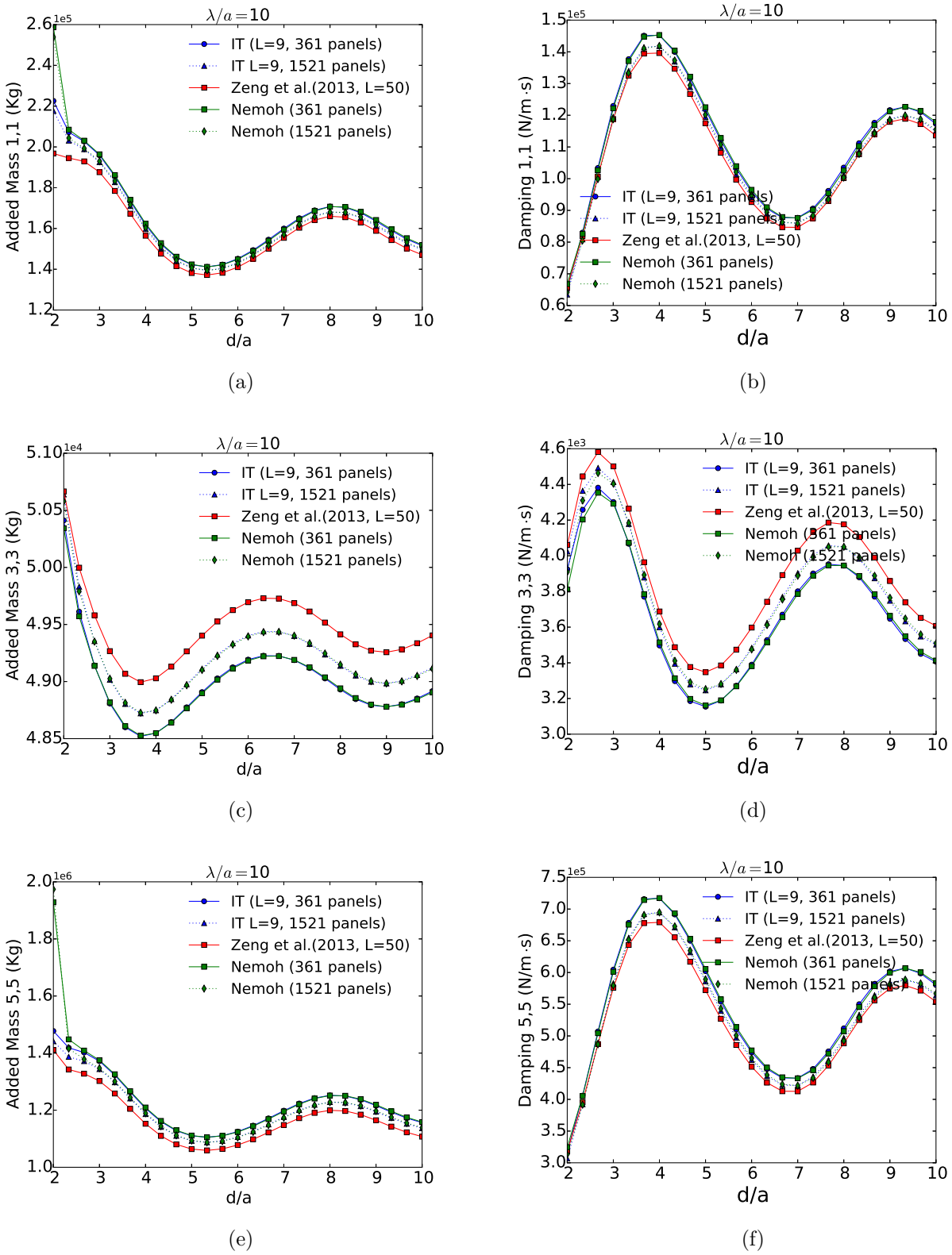

Figure D.14: Comparison between diagonal added mass coefficients computed with NEMOH, with the IT and a semi-analytical solution for two truncated vertical cylinders (Figure D.6b) of radius $3m$, draft $6m$ in a $10m$ water depth at several separation distances. First index corresponds to the direction of the force and the second to the degree of freedom.

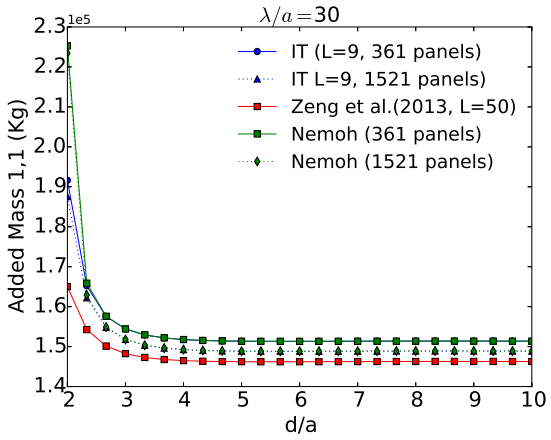

(a)

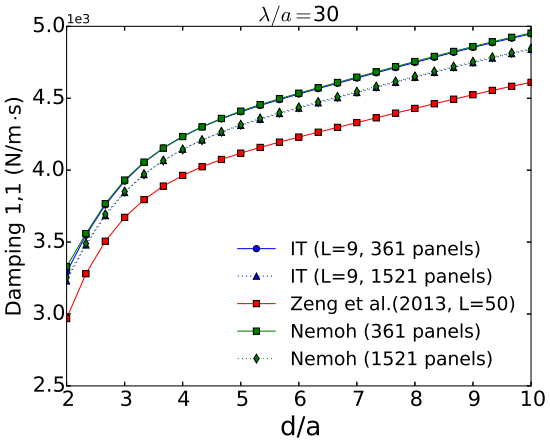

(b)

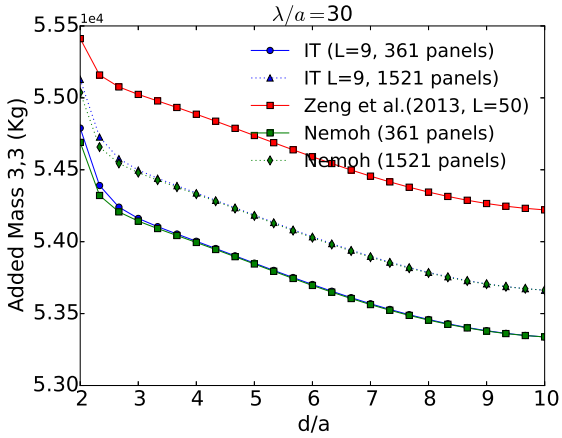

(c)

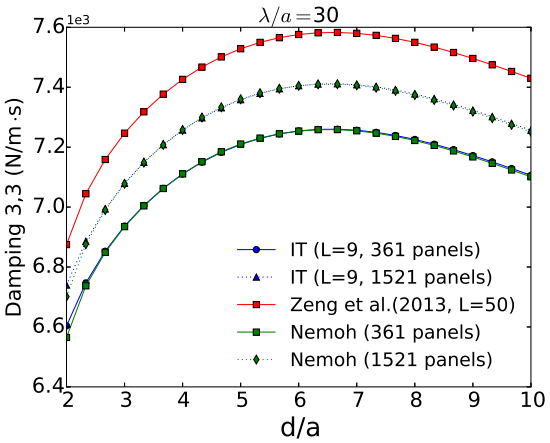

(d)

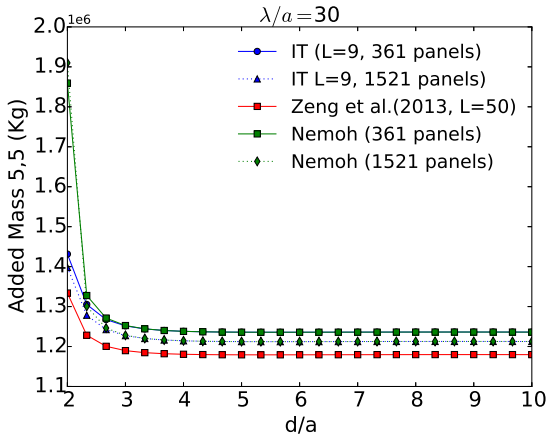

(e)

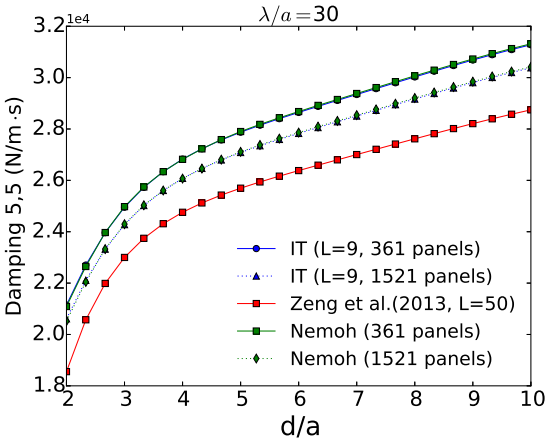

(f)

Figure D.15: Comparison between diagonal added mass coefficients computed with NEMOH, with the IT and a semi-analytical solution for two truncated vertical cylinders (Figure D.6b) at several separation distances. First index corresponds to the direction of the force and the second to the degree of freedom.

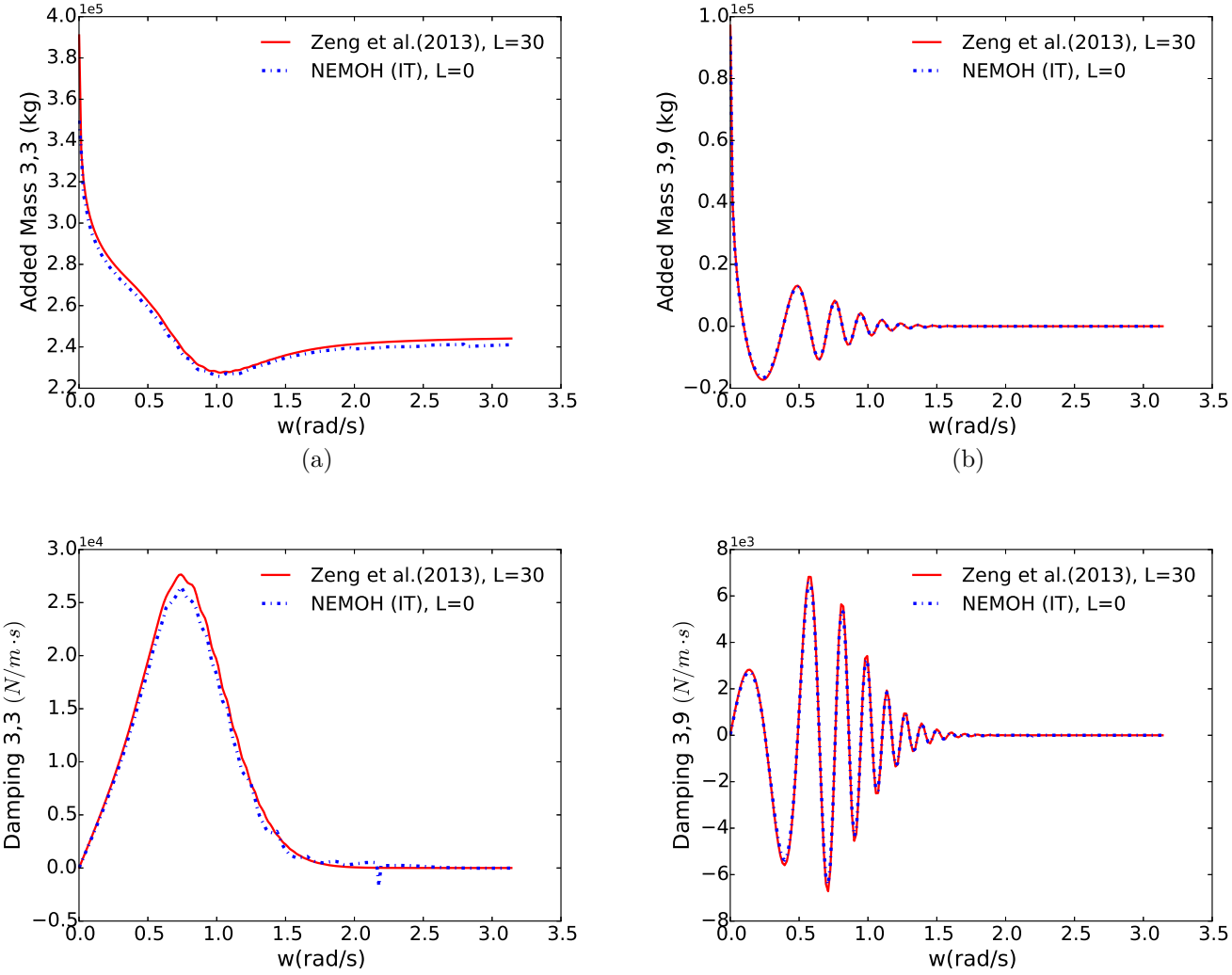

Figure D.16: Diagonal and coupled added-mass and damping radiation coefficients in heave for two truncated vertical cylinders (Figure D.6b) as a function of the frequency. Two sets of results computed with a semi-analytical solution and with the IT are presented. The bodies have a radius of $5m$, a $10m$ draft in $50m$ water depth and are separated by $200m$. First index corresponds to the direction of the force and the second to the degree of freedom.

Appendix E

Equivalence between Method I and II

E.1 Diffraction Transfer Matrix

On the one hand, the representation of the progressive part of the scattered potential using the notation of McNatt et al. (2015) follows as:

$$\Phi^S = \sum_{m=-\infty}^{\infty} i\frac{g}{\omega}\, a_m^S \frac{\cosh\, k_0(h+z)}{\cosh\, k_0 h}\, H_m^{(2)}(k_0 r)\, e^{im\theta} e^{i\omega t} \tag{E.1.1}$$

where h is the water depth, $H_m^{(2)}$ the Hankel function of the second kind and a_m^S the progressive complex scattered partial wave coefficients.

On the other hand, the convention used by Goo and Yoshida (1990) reads:

$$\Phi^S = \sum_{m=-\infty}^{\infty} A_m^S \frac{\cosh\, k_0(z+d)}{\cosh\, k_0 d} H_m^{(1)}(k_0 r)\, e^{im\theta} e^{-i\omega t} \tag{E.1.2}$$

where d stands for the water depth, $H_m^{(1)}$ is the Hankel function of the first kind and A_m^S the progressive complex scattered partial wave coefficients.

In (E.1.1), a positive sign convention ($e^{i\omega t}$) is adopted and amplitudes of partial wave coefficients have units of length. Contrarily, (E.1.2) makes use of a negative harmonic time dependence ($e^{-i\omega t}$) and amplitudes of partial wave coefficients have units of velocity potential (m^2/s). The use of Hankel functions of the first and the second kind is a consequence of the time dependence conventions chosen.

If indexs m and $-m$ are exchanged in (E.1.2) we have:

$$\Phi^S = \sum_{m=-\infty}^{\infty} A^S_{-m} \frac{\cosh\ k_0(z+d)}{\cosh\ k_0 d} H^{(1)}_{-m}(k_0 r)\, e^{-im\theta} e^{-i\omega t} \tag{E.1.3}$$

By using the identity (Abramowitz and Segun A., 1964, 9.1.6):

$$H^{(1)}_{-m}(z) = e^{im\pi} H^{(1)}_m(z) \tag{E.1.4}$$

Expression (E.1.3) can be simplified as:

$$\Phi^S = \sum_{m=-\infty}^{\infty} (-1)^m\, A^S_{-m} \frac{\cosh\ k_0(z+d)}{\cosh\ k_0 d} H^{(1)}_m(k_0 r)\, e^{-im\theta} e^{-i\omega t} \tag{E.1.5}$$

Both (E.1.5) and (E.1.1) are complex conjugates and the following relationship between the coefficients applies:

$$(-1)^m \frac{g}{\omega} \left[i(a^S_m) \right]^* = A^S_{-m} \tag{E.1.6}$$

With respect to the incident potential, it is expressed using the notation of McNatt et al. (2015) as:

$$\Phi^I = \sum_{q=-\infty}^{\infty} i\frac{g}{\omega}\, a^I_q \frac{\cosh\ k_0(h+z)}{\cosh\ k_0 h}\, J_q(k_0 r)\, e^{iq\theta} e^{i\omega t} \tag{E.1.7}$$

whereas in the convention of Goo and Yoshida (1990) it follows as:

$$\Phi^I = \sum_{q=-\infty}^{\infty} A^I_q \frac{\cosh\ k_0(z+d)}{\cosh\ k_0 d}\, J_q(k_0 r)\, e^{iq\theta} e^{-i\omega t} \tag{E.1.8}$$

As has been done previously, by exchanging indexs q and $-q$ equation (E.1.8) can be expressed as:

$$\Phi^I = \sum_{q=-\infty}^{\infty} A^I_{-q} \frac{\cosh\ k_0(z+d)}{\cosh\ k_0 d}\, J_{-q}(k_0 r)\, e^{-iq\theta} e^{-i\omega t} \tag{E.1.9}$$

Using the identity (Abramowitz and Segun A., 1964, 9.1.5):

$$J_{-q}(z) = (-1)^q J_q(z) \tag{E.1.10}$$

Expression (E.1.8) becomes:

$$\Phi^I = \sum_{q=-\infty}^{\infty} (-1)^q A^I_{-q} \frac{\cosh\ k_0(z+d)}{\cosh\ k_0 d}\, J_q(k_0 r)\, e^{-iq\theta} e^{-i\omega t} \tag{E.1.11}$$

Thus, it can be observed that (E.1.11) and (E.1.7) are complex conjugates and that the incident partial waves coefficients of both conventions can be related by:

$$(-1)^q \frac{g}{\omega} \left[i(a_q^I) \right]^* = A_{-q}^I \tag{E.1.12}$$

From the definition of the Diffraction Transfer Matrix given by (2.3.10):

$$a_m^S = \mathbf{B}_{\mathbf{m,q}}^{\mathbf{Method\,II}}\, a_q^I \tag{E.1.13}$$

$$A_m^S = \mathbf{B}_{\mathbf{m,q}}^{\mathbf{Method\,I}}\, A_q^I \tag{E.1.14}$$

By substituting (E.1.12) and (E.1.6) into (E.1.14):

$$(-1)^{-m} \frac{g}{\omega} \left[i(a_{-m}^S) \right]^* = \mathbf{B}_{\mathbf{m,q}}^{\mathbf{Method\,I}} (-1)^{-q} \frac{g}{\omega} \left[i(a_{-q}^I) \right]^* \tag{E.1.15}$$

Rearranging terms, (E.1.15) gives:

$$(a_{-m}^S)^* = \frac{(-1)^{-q}}{(-1)^{-m}} \mathbf{B}_{\mathbf{m,q}}^{\mathbf{Method\,I}} (a_{-q}^I)^* \tag{E.1.16}$$

From comparison of (E.1.13) and (E.1.16), it can be deduced that:

$$\left(\mathbf{B}_{\mathbf{-m,-q}}^{\mathbf{Method\,II}} \right)^* = \frac{(-1)^{-q}}{(-1)^{-m}} \mathbf{B}_{\mathbf{m,q}}^{\mathbf{Method\,I}} \tag{E.1.17}$$

Finally, rearranging (E.1.17):

$$\boxed{\frac{(-1)^{-m}}{(-1)^{-q}} \left(\mathbf{B}_{\mathbf{-m,-q}}^{\mathbf{Method\,II}} \right)^* = \mathbf{B}_{\mathbf{m,q}}^{\mathbf{Method\,I}}} \tag{E.1.18}$$

E.2 Radiation Characteristics

In an analogous manner as in section E.1, the notation of the progressive part of the radiation potential given by McNatt et al. (2015) and Goo and Yoshida (1990) is compared to obtain a relationship between the RC expressed in both notation conventions. As mentioned in section 2.2.1, the scattered and radiated potentials can be expressed using the same partial cylindrical wave functions:

$$\phi^R = i\frac{g}{\omega}(a^R_{mk})^T \psi^S_{Method\,II} \tag{E.2.1}$$

$$\phi^R = (R_{mk})^T \psi^S_{Method\,I} \tag{E.2.2}$$

where R_{mk} and a^R_{mk} are the RC in a mode of motion k in the notation of Methods I and II respectively, ψ the scattered partial wave functions and T indicates transpose.

As the scattered and radiated potentials have analogous expressions, the relationship (E.1.6) applies as well to the radiation characteristics:

$$(-1)^m \frac{g}{\omega}\left[i(a^R_{mk})\right]^* = R_{-mk} \tag{E.2.3}$$

It is noteworthy to mention that depending on whether the radiation characteristics are calculated using the BEM solver NEMOH or WAMIT, (E.2.3) should be slightly modified. This is due to the different radiation boundary conditions applied by both BEM codes when solving the radiation problem. In NEMOH, the normal velocities on the wetted body surface are defined as unitary vectors:

$$\frac{\partial \phi}{\partial n} = 1 \tag{E.2.4}$$

whereas in WAMIT the definition is as follows:

$$\frac{\partial \phi}{\partial n} = i\omega \tag{E.2.5}$$

Thus, as coefficients a^R_{mk} are calculated with WAMIT and R_{-mk} in NEMOH, a^R_{mk} in (E.2.3) should be divided by $i\omega$ leading to:

$$\boxed{(-1)^m \frac{g}{\omega^2}\left[(a^R_{mk})\right]^* = R_{-mk}} \tag{E.2.6}$$

E.3 Force Transfer Matrix

From the definition of the Force Transfer Matrix given by (2.3.18):

$$F^{Method\,II} = \mathbf{G^{Method\,II}_q} a^I_q \tag{E.3.1}$$

$$F^{Method\,I} = \mathbf{G^{Method\,I}_q} A^I_q \tag{E.3.2}$$

By substituting (E.1.12) into (E.3.2):

$$F^{Method\,I} = \mathbf{G_q^{Method\,I}}(-1)^{-q}\frac{g}{\omega}\left[i(a^I_{-q})\right]^* \tag{E.3.3}$$

Both F^{McNatt} and F^{Goo} would be the same if calculated with the same BEM code. In case both NEMOH and WAMIT are used for the calculations, it is worth highlighting the following difference with respect to the excitation force:

$$\left(F^{WAMIT}\right)^* = F^{Nemoh} \tag{E.3.4}$$

Taking into account that WAMIT has been used to derive the excitation force on the methodology of McNatt et al. (2015) and NEMOH for the convention of Goo and Yoshida (1990), then the following applies:

$$\left(F^{Method\,II}\right)^* = F^{Method\,I} \tag{E.3.5}$$

If (E.3.5) is substituted into (E.3.3):

$$\left(F^{Method\,II}\right)^* = \mathbf{G_q^{Method\,I}}(-1)^{-q}\frac{g}{\omega}\left[i(a^I_{-q})\right]^* \tag{E.3.6}$$

By comparing (E.3.6) and (E.3.1), it can be deduced that:

$$\left(\mathbf{G_{-q}^{Method\,II}}\right)^* = \mathbf{G_q^{Method\,I}}(-1)^{-q}\frac{g}{\omega}(-i) \tag{E.3.7}$$

Therefore, by rearranging (E.3.7):

$$\boxed{\mathbf{G_q^{Method\,I}} = (-1)^q\, i\frac{\omega}{g}\left(\mathbf{G_{-q}^{Method\,II}}\right)^*} \tag{E.3.8}$$

Appendix F

Reformulation of Green's function constant

As mentioned in Peter and Meylan (2004a), the term $K^2 - k_0^2$ of the constant C_0 (3.1.11) associated with the propagating modes of the Green's function poses convergence problems when the depth is increased. To avoid this hurdle, it is advised to rewrite C_0 making use of the dispersion equation:

$$k_0 \tanh k_0 d = \frac{\omega_0^2}{g}; \quad K = \frac{\omega_0^2}{g} \tag{F.0.1}$$

From (3.1.13), the focus is on the outer part of the integral over the wetted surface of the body which is defined here as Q for convenience:

$$Q = \frac{i}{2} C_0 \cosh k_0 d = \frac{i}{2} \frac{K^2 - k_0^2}{(k_0^2 - K^2)d + K} \cosh k_0 d \tag{F.0.2}$$

By substituting (F.0.1) into (F.0.2) and by multiplying numerator and denominator by $\cosh(k_0 d)$ the following is obtained:

$$Q = \frac{i}{2} \frac{k_0^2(\sin^2(k_0 d) - \cosh^2(k_0 d)}{[(k_0^2 - K^2)d + K] \cosh k_0 d} \tag{F.0.3}$$

By making use of the trigonometric relationship:

$$\cosh^2(z) - \sinh^2(z) = 1 \tag{F.0.4}$$

Expression (F.0.3) can be simplified:

$$Q = -\frac{i}{2} \frac{k_0^2}{[(k_0^2 - K^2)d + K] \cosh k_0 d} \tag{F.0.5}$$

Now, by substituting (F.0.1) into (F.0.5) and by multiplying numerator and denominator by $\cosh(k_0 d)$ the following expression is obtained:

$$Q = -\frac{i}{2}\frac{k_0^2}{\left[(k_0^2 - k_0^2\tanh^2(k_0 d))\,d + K\right]}\frac{\cosh\, k_0 d}{\cosh^2 k_0 d} = -\frac{i}{2}\frac{k_0^2\cosh\, k_0 d}{k_0^2 d + K\cosh^2 k_0 d} = \\ -\frac{i}{2}\frac{k_0\cosh\, k_0 d}{k_0 d + \sinh k_0 d\,\cosh\, k_0 d} = -i\frac{k_0\cosh\, k_0 d}{2k_0 d + \sinh\, 2k_0 d} \quad \text{(F.0.6)}$$

By using (F.0.6) the divergence problems due to the depth increase can be circumvented. The effect of constant C_0 reformulation is shown in Figures (F.1) and (F.2).

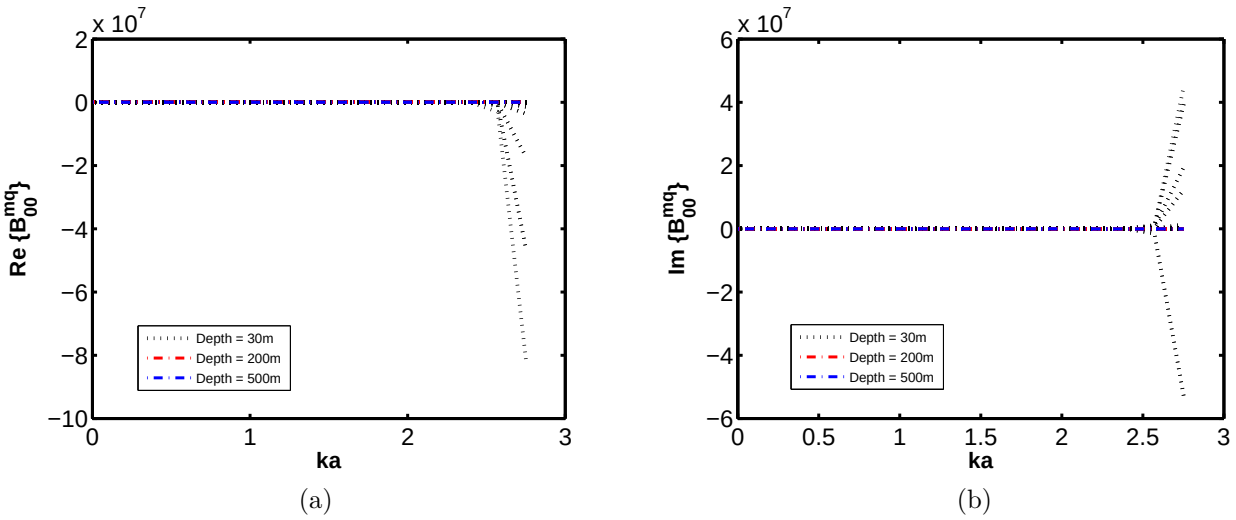

(a) (b)

Figure F.1: Real and imaginary parts of the Diffraction Transfer Matrix progressive terms for a truncated vertical cylinder of 3m radius (a), 6m draft in three different water depths. For $30m$ the Green's function constant used is in its original form.

In Figure F.1, the progressive terms of the DTM for the truncated vertical cylinder described in Chapter 3 are shown for water depths spanning from $30m$ to $500m$. The correction to the Green's function constant has only been applied to the 200 and $500m$ results. Contrarily, to exemplify the effect of the correction, the original term (F.0.2) has been kept for the $30m$ depth and a divergence trend at the high wave number

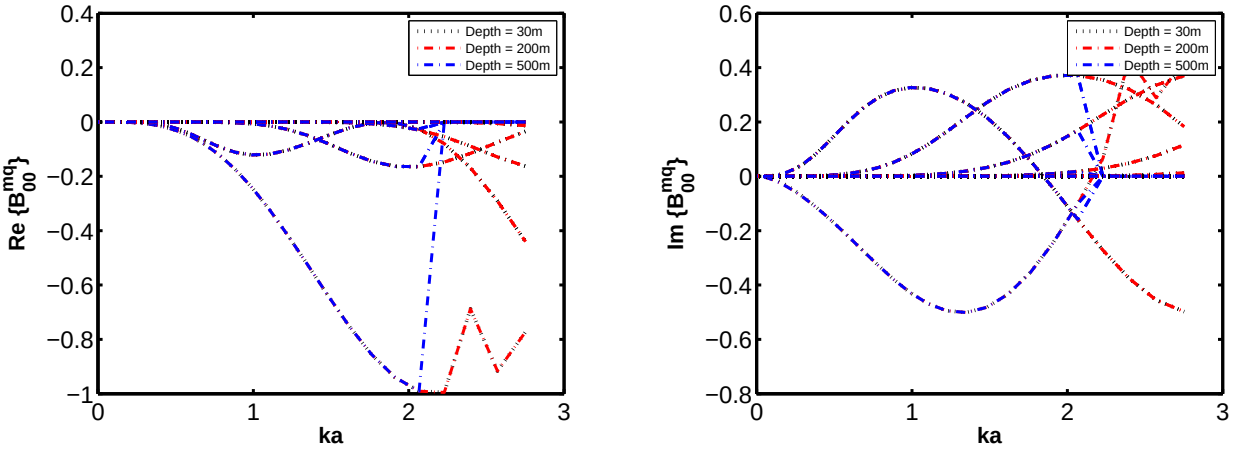

(a) (b)

Figure F.2: Real and imaginary parts of the Diffraction Transfer Matrix progressive terms for a truncated vertical cylinder of 3m radius (a), 6m draft in three different water depths. For all water depths the Green's function constant has been reformulated.

region can be clearly distinguished. In Figure F.2, the correction has been applied to all depths and very good agreement amongst the curves is observed. However, we note a sudden collapse of the results for $500m$ to zero value for a wave number of $k_0 a \sim 2.22$. In this case, the behaviour is caused by the denominator in (F.0.6) reaching values which fall out of the range r that can be represented with an architecture of 64bits (Fouilloux and Corde, 2014):

$$2.2 \cdot 10^{-308} \leq |r| \leq 1.8 \cdot 10^{308} \tag{F.0.7}$$

By substituting the denominator of (F.0.6) into (F.0.7) we have:

$$\frac{e^{x} - e^{-x}}{2} \leq 1.8 \cdot 10^{308} - x \tag{F.0.8}$$

where the definition of the hyperbolic sinus has been used and $x = 2k_0 d$.

By applying the natural logarithm to each side of (F.0.8):

$$x \lessapprox ln\,(2 \cdot\ 1.8 \cdot 10^{308}) \tag{F.0.9}$$

where terms e^{-x} on the left hand side of (F.0.8) and x on the right hand side are

considered negligible. Then,

$$x \lessapprox 710 \quad \text{or equivalently} \quad k_0 a \lessapprox 2.13 \tag{F.0.10}$$

Appendix G

Numerical Integration

Integrals in (3.1.13)-(3.1.14) and (3.1.22)-(3.1.23) cannot be solved analytically, as there exists no closed mathematical expression for the source strengths. Indeed, the latter are only known at the centroids of each facet of the discretization. Thus, they need to be evaluated numerically. To do so, there exist several methods some of which are explained in this section.

The simplest approach consists of evaluating the kernel of the integral only at the panel's centroid and multiplying it by the panel's surface. This is equivalent to assuming that the kernel of the integral is constant over the panel. For instance, (3.1.13) would be computed as:

$$(\mathbf{B}_j)_{0l}^{mq} = \frac{i}{2} C_0 \cosh(k_0 d) \sum_{i=1}^{Np} \sigma_{lqj}(R_j^{Ci}, \Theta_j^{Ci}, \zeta_j^{Ci})\, J_m(k_0 R_j^{Ci}) \cosh[k_0(\zeta_j^{Ci} + d)] e^{-im\Theta_j} S^{Ci} \tag{G.0.1}$$

where $(R_j^{Ci}, \Theta_j^{Ci}, \zeta_j^{Ci})$ are the centroid coordinates of the ith panel, S^{Ci} represents its surface and Np is the total number of panels of the discretization.

An alternative procedure consists of using a quadrature scheme which is defined as any formula which enables one to calculate an approximation of an integral (Quarteroni et al., 2007). The idea is to evaluate the function at specific points and to multiply them by an appropriate weighting factor. Finally, results are added up.

There exist many different quadrature rules (D.Cook et al., 2002). A commonly used quadrature scheme is known as Gauss quadrature and has the following form to perform multidimensional integration over a 2D surface (Abramowitz and Segun A.,

1964):

$$\frac{1}{C}\iint_S f(x,y)\,dxdy = \sum_{i=1}^{Nq} \omega_i\, f(x_i, y_i) + R \tag{G.0.2}$$

where C is a constant that depends on the geometry of the 2D domain, Nq is the number of quadrature points, $f(x,y)$ is the function to integrate, $f(x_i, y_i)$ is the function value on the quadrature point of coordinates (x_i, y_i), ω_i are the weights given at each quadrature point and R the residual.

Abramowitz and Segun A. (1964) compiled several gaussian quadrature schemes and its weights for several canonical domain geometries such as a square and a triangle, some of which are reproduced in Figure G.1.

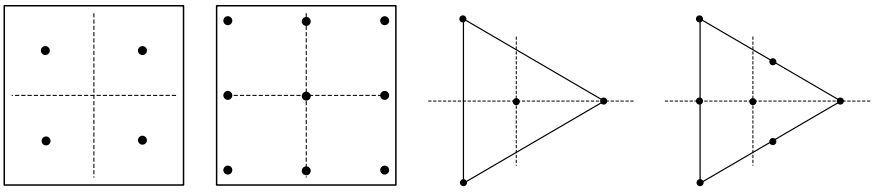

Figure G.1: Points of quadrature for a multidimensional integration. The square has limits $|x| \leq h$, $|y| \leq h$ whereas the triangle is inscribed in a circle of radius h. Source: Abramowitz and Segun A. (1964)

The discretization of the wetted surface of a body using the BEM code NEMOH is performed using flat quadrilateral panels that can degenerate into triangles (Delhommeau, 1987, Annex 5). If a Gaussian quadrature scheme is to be applied to each of the body facets, they need to have a canonical form (Figure G.4) and, therefore, a parametrisation is required. The latter enables one to transform a three-dimensional flat quadrilateral or triangle into a standard two-dimensional square or triangle with specified limits as shown in Figure G.2.

The transformation from the physical space of cartesian coordinates $(x,\, y,\, z)$ into parametric space (s,t) is performed as:

$$(x,\, y,\, z) = \left(\sum_{i=1}^{Np} \psi_i x_i, \sum_{i=1}^{Np} \psi_i y_i, \sum_{i=1}^{Np} \psi_i z_i \right) \tag{G.0.3}$$

where Np is the total number of nodes of the panel and ψ_i are the interpolation functions defined on each node i.

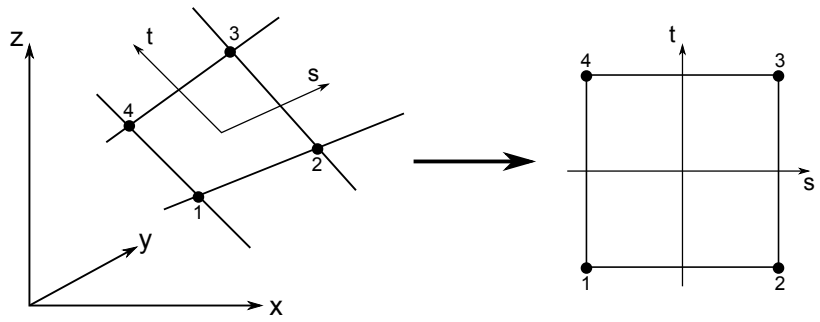

Figure G.2: Four node bilinear quadrilateral and its image in parametric space. Source: adapted from Topper (2010).

The interpolation functions are defined so that their value is one only at their associated node, i.e., the value of ψ_1 will be one at node 1 and zero elsewhere. As each quadrilateral panel is flat and composed of four nodes (3 in case of a triangle), a linear parametrisation is used. If instead of being flat the panels were curved and described by means of 9 nodes for instance, a biquadratic parametrisation should be used. Figure G.3 shows a comparison of both types of interpolation functions.

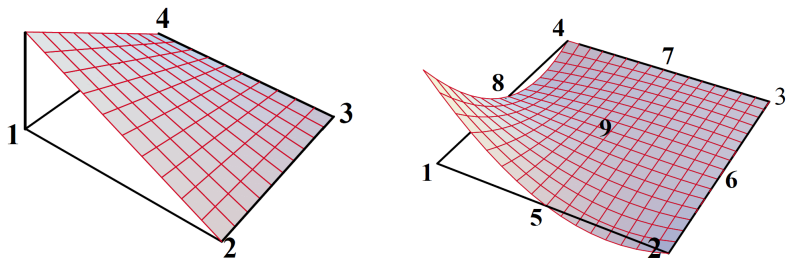

(a) 4-node bilinear element (b) 9-node biquadratic element

Figure G.3: Interpolation functions for node 1 of a quadrilateral element. Source: adapted from Felippa (2014)

With respect to the case of a quadrilateral element, the canonical domain is described as in Figure G.4 (a) and its associated interpolation functions for a linear parametrisation are defined as:

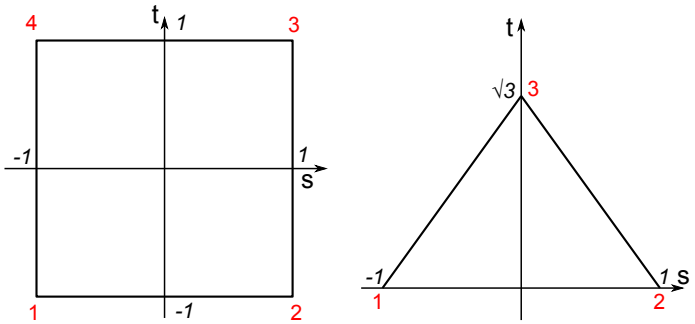

(a) Canonical quadrilateral. (b) Canonical triangle. Its circumscribing circle has a radius of $2\sqrt{3}/3$

Figure G.4: Red numbers indicate node number and the limits of the domain are indicated in italic. Adapted from: Topper (2010)

$$\psi_1(s,t) = \frac{1}{4}(1-s)(1-t); \quad \frac{\partial \psi_1}{\partial s} = -\frac{1}{4}(1-t); \quad \frac{\partial \psi_1}{\partial t} = -\frac{1}{4}(1-s) \tag{G.0.4}$$

$$\psi_2(s,t) = \frac{1}{4}(1+s)(1-t); \quad \frac{\partial \psi_2}{\partial s} = \frac{1}{4}(1-t); \quad \frac{\partial \psi_2}{\partial t} = -\frac{1}{4}(1+s) \tag{G.0.5}$$

$$\psi_3(s,t) = \frac{1}{4}(1+s)(1+t); \quad \frac{\partial \psi_3}{\partial s} = \frac{1}{4}(1+t); \quad \frac{\partial \psi_3}{\partial t} = \frac{1}{4}(1+s) \tag{G.0.6}$$

$$\psi_4(s,t) = \frac{1}{4}(1-s)(1+t); \quad \frac{\partial \psi_4}{\partial s} = -\frac{1}{4}(1+t); \quad \frac{\partial \psi_4}{\partial t} = \frac{1}{4}(1-s) \tag{G.0.7}$$

Similarly for the triangular elements (Figure G.4 b), and following the notation of Topper (2010) the interpolation functions are defined as:

$$\tilde{\psi}_1(s,t) = \frac{\sqrt{3}(1-s)-t}{2\sqrt{3}}; \quad \frac{\partial \tilde{\psi}_1}{\partial s} = -\frac{1}{2}; \quad \frac{\partial \tilde{\psi}_1}{\partial t} = -\frac{\sqrt{3}}{6} \tag{G.0.8}$$

$$\tilde{\psi}_2(s,t) = \frac{\sqrt{3}(1+s)-t}{2\sqrt{3}}; \quad \frac{\partial \tilde{\psi}_2}{\partial s} = \frac{1}{2}; \quad \frac{\partial \tilde{\psi}_2}{\partial t} = -\frac{\sqrt{3}}{6} \tag{G.0.9}$$

$$\tilde{\psi}_3(s,t) = \frac{t}{\sqrt{3}}; \quad \frac{\partial \tilde{\psi}_3}{\partial s} = 0; \quad \frac{\partial \tilde{\psi}_3}{\partial t} = \frac{\sqrt{3}}{3} \tag{G.0.10}$$

The relationship between the area of the element in physical space and in the parameterised space is given by the Jacobian as:

$$dA = J(s,t)\, ds dt \tag{G.0.11}$$

where $J(s,t)$ is the Jacobian evaluated at the point of the parametric space (s,t) and dA is the differential of area of the quadrilateral physical space.

The Jacobian can be computed as (Topper, 2010):

$$J(s,t) = |Q_s \times Q_t| \tag{G.0.12}$$

where expressions Q_s and Q_t are:

$$Q_s = \left(\sum_{i=1}^{4} \frac{\partial \psi_i(s,t)}{\partial s} x_i, \sum_{i=1}^{4} \frac{\partial \psi_i(s,t)}{\partial s} y_i, \sum_{i=1}^{4} \frac{\partial \psi_i(s,t)}{\partial s} z_i \right) \tag{G.0.13}$$

$$Q_t = \left(\sum_{i=1}^{4} \frac{\partial \psi_i(s,t)}{\partial t} x_i, \sum_{i=1}^{4} \frac{\partial \psi_i(s,t)}{\partial t} y_i, \sum_{i=1}^{4} \frac{\partial \psi_i(s,t)}{\partial t} z_i \right) \tag{G.0.14}$$

By introducing (G.0.11) into (G.0.2), the following expression for the integral over the physical quadrilateral is obtained:

$$\iint_S f(x,y)\, dxdy = C \sum_{i=1}^{Nq} J(s,t)\, \omega_i\, f(s_i,t_i) \tag{G.0.15}$$

Appendix H

Formulation of the Direct Matrix Method interaction theory for infinite depth

The content of the following sections has been extracted and adapted from the work by Peter and Meylan (2004a). It extends the Direct Matrix Method interaction theory formulae derived by Kagemoto and Yue (1986) to infinite-depth. Although not used in this body of work, it is provided for comparison with the Finite-Depth methodology detailed in Chapter 2 and as a formulae summary which might be useful for future implementations. The notation conventions follow as in Chapter 2.

H.1 Array wave fields

In water of infinite depth, the generic scattered and incident potentials outside the circumscribing cylinders of bodies i and j can be expressed in cylindrical coordinates referred to its local reference system as:

$$\phi_i^S(r_i,\, \theta_i,\, z) = e^{\alpha z} \sum_{m=-\infty}^{\infty} (A_i)_m^0 H_m^{(1)}(\alpha r_i)\, e^{im\theta_i} + \int_0^{\infty} \Psi(z,\eta) \sum_{m=-\infty}^{\infty} (A_i)_m^{\eta} K_m(\eta r_i)\, e^{im\theta_i} d\eta \tag{H.1.1}$$

$$\phi_j^I(r_j,\, \theta_j,\, z) = e^{\alpha z} \sum_{q=-\infty}^{\infty} (D_j)_q^0 J_q(\alpha r_j)\, e^{iq\theta_j} + \int_0^{\infty} \Psi(z,\xi) \sum_{q=-\infty}^{\infty} (D_j)_q^{\xi} I_q(\xi r_j)\, e^{iq\theta_j} d\xi \tag{H.1.2}$$

where coefficients $(A_i)_m^0$ and $(D_j)_q^0$ for the propagating modes are discrete and $(A_i)_m^\eta$ and $(D_j)_q^\xi$ for the decaying modes are functions. $H_m^{(1)}$ is the Hankel function of the first kind of order m, K_m is the modified Bessel function of the second kind of order m, J_q is the Bessel function of the first kind of order q and I_q is the modified Bessel function of the first kind of order q. Contrarily to the finite-depth interaction theory, the sum over the discrete roots of the dispersion equation is replaced by an integral in the infinite-depth theory. The vertical eigenfunctions corresponding to the decaying modes are given by:

$$\Psi(z,\eta) = cos\,\eta z + \frac{\alpha}{\eta} sin\,\eta z; \quad \alpha = \frac{\omega^2}{g} \tag{H.1.3}$$

where ω is the angular frequency.

It is noteworthy that the radiated potential by a body j moving in a mode of motion k can be formulated using the same expression (H.1.1) with coefficients $(A_i)_m^0$ and $(A_i)_m^\eta$ replaced by R_{0m}^{jk} and $R_m^{jk}(\eta)$, the latter two referred to as Radiation Characteristics (RC).

By means of the Graf's addition theorem for Bessel functions (Abramowitz and Segun A., 1964) which reads:

$$H_m^{(1)}(\alpha r_i)e^{im(\theta_i)} = \sum_{q=-\infty}^{\infty} H_{m-q}(\alpha L_{ij})e^{i\theta_{ij}(m-q)} J_q(\alpha r_j)e^{iq\theta} \tag{H.1.4}$$

$$K_m(\eta r_i)e^{im(\theta_i)} = \sum_{q=-\infty}^{\infty} K_{m-q}(\eta L_{ij})(-1)^q e^{i\theta_{ij}(m-q)} I_q(\eta r_j)e^{iq\theta_j} \tag{H.1.5}$$

the scattered potential by a body i can be expressed as incident to body j in its local reference system. This is done by substituting (H.1.4) and (H.1.5) into (H.1.1):

$$\phi_i^S(r_j,\,\theta_j,\,z) = e^{\alpha z} \sum_{q=-\infty}^{\infty} \left[\sum_{m=-\infty}^{\infty} (A_i)_m^0 H_{m-q}^{(1)}(\alpha L_{ij})\, e^{i(m-q)\theta_{ij}} \right] J_q(\alpha r_j)\, e^{iq\theta_j} + \int_0^\infty \Psi(z,\,\eta) \sum_{q=-\infty}^{\infty} \left[\sum_{m=-\infty}^{\infty} (A_i)_m^\eta\, K_{m-q}(\eta L_{ij})\, e^{i(m-q)\theta_{ij}} (-1)^q \right] I_q(\eta r_j)\, e^{iq\theta_j} d\eta \tag{H.1.6}$$

Following the same procedure described in section 2.3, for an array of N bodies the total incident potential to a body j will be composed of the incident wave acting on the array, given by either an ambient incident wave or by the radiated wave by a body j moving in a degree of freedom k whether a diffraction or a radiation problem

is considered respectively, and the resulting scattered potentials by the $i(i \neq j)$ neighbouring bodies, written as $\sum_{\substack{i=1 \\ i\neq j}}^{N} \phi_i^S(r_j, \theta_j, z)$. Thus, the total incident potential to j is expressed as:

$$\phi_j^I(r_j,\, \theta_j,\, z) = e^{\alpha z} \sum_{q=-\infty}^{\infty} \left[(D_j)_q^0 + \sum_{\substack{i=1 \\ i\neq j}}^{N} \sum_{m=-\infty}^{\infty} (A_i)_m^0 H_{m-q}^{(1)}(\alpha L_{ij})\, e^{i(m-q)\theta_{ij}} \right] J_q(\alpha r_j)\, e^{iq\theta_j} +$$
$$\int_0^{\infty} \Psi(z,\, \eta) \sum_{q=-\infty}^{\infty} \left[(D_j)_q^{\eta} + \sum_{\substack{i=1 \\ i\neq j}}^{N} \sum_{m=-\infty}^{\infty} (A_i)_m^{\eta} K_{m-q}(\eta L_{ij})\, e^{i(m-q)\theta_{ij}} (-1)^q \right] I_q(\eta r_j)\, e^{iq\theta_j} d\eta \tag{H.1.7}$$

By comparison of expressions (H.1.2) and (H.1.7), it can be derived that the total incident potential coefficients D_j^T are given by:

$$(D_j^T)_q^0 = (D_j)_q^0 + \sum_{\substack{i=1 \\ i\neq j}}^{N} \sum_{m=-\infty}^{\infty} (A_i)_m^0\, H_{m-q}^{(1)}(\alpha L_{ij})\, e^{i(m-q)\theta_{ij}} \tag{H.1.8}$$

$$(D_j^T)_q^{\xi} = (D_j)_q^{\xi} + \sum_{\substack{i=1 \\ i\neq j}}^{N} \sum_{m=-\infty}^{\infty} (A_i)_m^{\xi}\, K_{m-q}(\xi L_{ij})\, e^{i(m-q)\theta_{ij}} (-1)^q \tag{H.1.9}$$

where variable ξ is used intead of η to represent incident potential and $(D_j^T)_q^0$ and $(D_j^T)_q^{\xi}$ are incident discrete coefficients and functions respectively.

By means of the Diffraction Transfer Matrix $\mathbf{B}_j$, which relates the total incident and scattered partial waves from an isolated body, the scattered potential from body j due to the incident potential (H.1.7) can be obtained. As mentioned in Peter and Meylan (2004a), when the depth is finite and a countable number of modes exist $\mathbf{B}_j$ is an infinite dimensional matrix. Contrarily, when the modes are functions of a continuous variable as in infinite depth, $\mathbf{B}_j$ is the kernel of an integral operator. The definition of the Diffraction Transfer Matrix elements in infinite depth follows as:

$$(A_j)_m^0 = \sum_{q=-\infty}^{\infty} (\mathbf{B}_j)_{mq}^{00} (D_j)_q^0 + \int_0^{\infty} \sum_{q=-\infty}^{\infty} (\mathbf{B}_j)_{mq}^{0\xi} (D_j)_q^{\xi} d\xi \tag{H.1.10}$$

$$(A_j)_m^{\eta} = \sum_{q=-\infty}^{\infty} (\mathbf{B}_j)_{mq}^{\eta 0} (D_j)_q^0 + \int_0^{\infty} \sum_{q=-\infty}^{\infty} (\mathbf{B}_j)_{mq}^{\eta\xi} (D_j)_q^{\xi} d\xi \tag{H.1.11}$$

By substituting (H.1.8) and (H.1.9) into (H.1.10) and (H.1.11), the system of equations to solve for the partial wave coefficients of the scattered wave fields by all bodies can be obtained:

$$(A_j)_m^0 = \sum_{q=-\infty}^{\infty} (\mathbf{B}_j)_{mq}^{00} \left[(D_j)_q^0 + \sum_{\substack{i=1 \\ i\neq j}}^{N} \sum_{m=-\infty}^{\infty} (A_i)_m^0 \, H_{m-q}^{(1)}(\alpha L_{ij}) \, e^{i(m-q)\theta_{ij}} \right] +$$
$$\int_0^{\infty} \sum_{q=-\infty}^{\infty} (\mathbf{B}_j)_{mq}^{0\xi} \left[(D_j)_q^{\xi} + \sum_{\substack{i=1 \\ i\neq j}}^{N} \sum_{m=-\infty}^{\infty} (A_i)_m^{\xi} \, K_{m-q}(\xi L_{ij}) \, e^{i(m-q)\theta_{ij}} (-1)^q \right] d\xi \quad \text{(H.1.12)}$$

$$(A_j)_m^{\eta} = \sum_{q=-\infty}^{\infty} (\mathbf{B}_j)_{mq}^{\eta 0} \left[(D_j)_q^0 + \sum_{\substack{i=1 \\ i\neq j}}^{N} \sum_{m=-\infty}^{\infty} (A_i)_m^0 \, H_{m-q}^{(1)}(\alpha L_{ij}) \, e^{i(m-q)\theta_{ij}} \right] +$$
$$\int_0^{\infty} \sum_{q=-\infty}^{\infty} (\mathbf{B}_j)_{mq}^{\eta\xi} \left[(D_j)_q^{\xi} + \sum_{\substack{i=1 \\ i\neq j}}^{N} \sum_{m=-\infty}^{\infty} (A_i)_m^{\xi} \, K_{m-q}(\xi L_{ij}) \, e^{i(m-q)\theta_{ij}} (-1)^q \right] d\xi \quad \text{(H.1.13)}$$

H.2 Diffraction Transfer Matrix and Radiation Characteristics

The derivation of the DTM in infinite-depth given by Peter and Meylan (2004a) follows the methodology of Goo and Yoshida (1990). The difference with the latter is that instead of using the free-surface Green's function in cylindrical coordinates presented by Black (1975) and further investigated by Fenton (1978) it makes use of the infinite-depth version of the same Green's function representation derived by Peter and Meylan (2004b) which reads:

$$G_j(r_j, \theta_j, z_j; R_j, \Theta_j, \zeta_j) = \frac{1}{2} i\alpha e^{\alpha(z+\zeta_j)} \sum_{m=-\infty}^{\infty} H_m^{(1)}(\alpha r_j) J_m(\alpha R_j) \, e^{im(\theta_j - \Theta_j)} +$$
$$\frac{1}{\pi^2} \int_0^{\infty} \Psi(z,\eta) \frac{\eta^2}{\eta^2 + \alpha^2} \Psi(\zeta_j, \eta) \sum_{m=-\infty}^{\infty} K_m(\eta r_j) \, I_m(\eta R_j) \, e^{im(\theta_j - \Theta_j)} d\eta \quad \text{(H.2.1)}$$

where G is the Green's function infinite-depth form valid for $r > R_j$ with R_j being the circumscribing cylinder of body j, (R_j, Θ_j, ζ_j) is the influencing or source point

and (r_j, θ_j, z_j) is the influenced or field point.

Take the representation of the scattered potential in terms of a source strength distribution given by:

$$\phi_j^S(r_j, \theta_j, z_j) = \iint_{S_j} \sigma_j(R_j, \Theta_j, \zeta_j)\, G_j(r_j, \theta_j, z_j;\, R_j, \Theta_j, \zeta_j) ds \tag{H.2.2}$$

where S_j is the wetted surface of body j and σ_j the source strength distribution on the wetted surface of body j.

If (H.2.1) is substituted into (H.2.2):

$$\phi_j^S(r_j, \theta_j, z) = e^{\alpha z} \sum_{m=-\infty}^{\infty} \left[\frac{1}{2} i\alpha \int_{S_j} e^{\alpha\zeta_j} J_m(\alpha R_j)\, e^{-im\Theta_j} \sigma_j(R_j, \Theta_j, \zeta_j) ds \right] H_m^{(1)}(\alpha r_j)\, e^{im\theta_j} + \int_0^{\infty} \Psi(z, \eta) \sum_{m=-\infty}^{\infty} \left[\frac{1}{\pi^2} \frac{\eta^2}{\eta^2 + \alpha^2} \int_{S_j} \Psi(\zeta_j, \eta)\, I_m(\eta R_j)\, e^{-im\Theta_J} \sigma_j(R_j, \Theta_j, z_j)\, ds \right] K_m(\eta r_j)\, e^{im\theta_j} d\eta \tag{H.2.3}$$

Expression (H.2.3) is of the form (H.1.1). The procedure described enables one to express the scattered potential represented by a source distribution σ in the cylindrical eigenfunction expansion basis. If the source distribution is due to a unit amplitude incident potential of the form:

$$\phi_j^I(r_j, \theta_j, z) = \begin{cases} e^{\alpha z}\, J_q(\alpha r_j)\, e^{iq\theta_j} & progressive \\ \Psi(z, \xi)\, I_q(\xi r_j)\, e^{iq\theta_j} & evanescent \end{cases} \tag{H.2.4}$$

then the coefficients in (H.2.3) are the elements of the Diffraction Transfer Matrix which read:

$$(\mathbf{B}_j)_{mq}^{0\xi} = \frac{1}{2} i\alpha \int_{S_j} e^{\alpha\zeta_j} J_m(\alpha R_j)\, e^{-im\Theta_j} (\sigma_j)_q^{\xi}(R_j, \Theta_j, \zeta_j)\, ds \tag{H.2.5}$$

$$(\mathbf{B}_j)_{mq}^{\eta\xi} = \frac{1}{\pi^2} \frac{\eta^2}{\eta^2 + \alpha^2} \int_{S_j} \Psi(\zeta_j, \eta)\, I_m(\eta R_j)\, e^{-im\Theta_j} (\sigma_j)_q^{\xi}(R_j, \Theta_j, \zeta_j)\, ds \tag{H.2.6}$$

If instead, the source distribution is given by a unit amplitude motion of the body j in calm water with a motion mode k, then coefficients (H.2.5) and (H.2.6) represent the radiation characteristics and can be written as:

$$(R_j^k)_m^0 = \frac{1}{2} i\alpha \int_{S_j} e^{\alpha\zeta_j} J_m(\alpha R_j)\, e^{-im\Theta_j} \sigma_j^k(R_j, \Theta_j, \zeta_j)\, ds \tag{H.2.7}$$

$$(R_j^k)_m^\eta = \frac{1}{\pi^2} \frac{\eta^2}{\eta^2 + \alpha^2} \int_{S_j} \Psi(\zeta_j, \eta)\, I_m(\eta R_j)\, e^{-im\Theta_j} \sigma_j^k(R_j, \Theta_j, \zeta_j)\, ds \tag{H.2.8}$$

H.3 Numerical implementation

For numerical calculations, the infinite sums need to be truncated and the integrals must be discretized to be solved using an appropriate numerical scheme. As mentioned in Peter and Meylan (2004a), the number of decaying roots of the dispersion relation must be chosen in finite depth, whereas in infinite depth the discretization of a continuous variable must be selected. Thus, in the infinite-depth case one is free to choose the number of points as well as the points themselves. From the work of Peter and Meylan (2004a), the discretization of the scattered potential follows as:

$$\phi_j^S(r_j, \theta_j, z) = e^{\alpha z} \sum_{m=-M}^{M} (A)_m^0 H_m^{(1)}(\alpha r_j)\, e^{im\theta_j} + \sum_{n=1}^{N} h_n \Psi(z, \eta_n) \sum_{m=-M}^{M} (A)_m^{\eta_n} K_m(\eta_n r_j)\, e^{im\theta_j} \tag{H.3.1}$$

The discretization of the infinite integral is done by defining a set of nodes $0 \leq \eta_1 < \cdots < \eta_n < \cdots < \eta_N$ with weights h_n given by the mid-point quadrature rule:

$$h_n = \frac{1}{2}(\eta_{n+1} - \eta_{n-1}); \quad n = 2, \ldots, N-1 \tag{H.3.2}$$

$$h_1 = \eta_2 - \eta_1 \tag{H.3.3}$$

$$h_N = \eta_N - \eta_{N-1} \tag{H.3.4}$$

As stated by Peter and Meylan (2004a), the mid-point rule allows a clever choice of the discretization points so that the convergence with Gaussian quadrature is no better. The choice of the integration limit is driven, as mentioned in Peter and Meylan (2004b), by the fast decay of the modified Bessel function of the second kind which causes the integrand to decay quickly for a large argument. This enables one to calculate the integral for a small interval. The latter is chosen from zero until the point at which the integrand is strictly less than 10^{-6}. Because of the quick decay of the integrand, more nodes are placed near the zero limit and the number is gradually reduced while reaching the upper limit of the integral. This seems to be achieved

by means of a cosine spacing of the nodes in the work of Peter and Meylan (2004a) although it is not explicitly mentioned.

From the discretized form of the potential in (H.3.1), we can conceive an analogous formulation to the finite-depth one making use of infinite-depth basis functions to represent the incident, scattered and radiated potentials. These are detailed in the following subsections.

H.3.1 Array wave fields

Expressions (H.1.2) and (H.1.1) for the generic representation of the incident and scattered (radiated) potentials can be formulated as a scalar product after discretization of the infinite integral and the truncation of the infinite series:

$$\phi_j^S = (A_j^S)^T \psi_j^{S\infty}; \quad \phi_j^R = (R_j^k)^T \psi_j^{S\infty}; \quad \phi_j^I = (D_j^I)^T \psi_j^{I\infty} \tag{H.3.5}$$

$$\left(\psi_j^{S\infty}\right)_m^n = \begin{cases} e^{\alpha z}\, H_m(\alpha r_j)\, e^{im\theta_j} & n = 0 \\ h_n \Psi(z,\eta_n)\, K_m(\eta_n r_j)\, e^{im\theta_j} & n \geq 1 \end{cases} \tag{H.3.6}$$

$$\left(\psi_j^{I\infty}\right)_q^l = \begin{cases} e^{\alpha z}\, J_m(\alpha r_j)\, e^{im\theta_j} & l = 0 \\ h_l \Psi(z,\eta_l)\, I_m(\eta_l r_j)\, e^{im\theta_j} & l \geq 1 \end{cases} \tag{H.3.7}$$

where $\psi_j^{S\infty}$ and $\psi_j^{I\infty}$ are the outgoing and incident partial wave functions in infinite-depth, A_j^S are scattered partial wave coefficients, R_j^k is the vector of radiated partial wave coefficients referred to as Radiation Characteristics (RC) and D_j^I the vector of incident partial wave coefficients.

For the particular case of the ambient incident wave field, the elements of the coefficient vector D_j^∞ are given by:

$$\left(D_j^\infty\right)_q^l = \begin{cases} -i\frac{g\zeta_a}{\omega} e^{i\alpha(X_{0j}cos\beta + Y_{0j}sin\beta)} i^q e^{-iq\beta} & l = 0 \\ 0 & l \geq 1 \end{cases} \tag{H.3.8}$$

By means of (H.1.4) and (H.1.5), the scattered potential by a body i can be expressed as incident to body j in its local reference system:

$$\psi_i^{S\infty} = \mathbf{T}_{ij}^\infty \psi_j^{I\infty} \tag{H.3.9}$$

$$\left(\mathbf{T}_{ij}^{\infty}\right)_{mq}^{nn} = \begin{cases} H_{m-q}^{(1)}(\alpha L_{ij})\, e^{i(m-q)\theta_{ij}} & n = 0 \\ (-1)^q K_{m-q}(\eta_n L_{ij})\, e^{i(m-q)\theta_{ij}} & n \geq 1 \end{cases} \tag{H.3.10}$$

The system of equations given by (H.1.12) - (H.1.13) can be expressed in its discretized form as:

$$A_j = \mathbf{B}_j^{\infty}(D_j + \sum_{\substack{i=1 \\ i\neq j}}^{N} \mathbf{T}_{ij}^{\infty^T} A_i) \tag{H.3.11}$$

The vector of incident partial waves coefficients D_j can be set as:

$$D_{j,ik} = \begin{cases} (\mathbf{T}_{ij}^{\infty})^T R_{ik} & j \neq i \\ 0 & j = i \end{cases} \tag{H.3.12}$$

for the radiation problem where a body i of the array undergoes a motion in a motion mode k or as D_j^{∞} for a diffraction problem with a plane incident wave of propagation direction β, pulsation ω and amplitude ζ_a.

H.3.2 Diffraction Transfer Matrix and Radiation Characteristics

The expressions of the DTM elements after discretization are as follows:

$$(\mathbf{B}_j)_{mq}^{0l} = \frac{1}{2} i\alpha \int_{S_j} e^{\alpha\zeta_j} J_m(\alpha R_j)\, e^{-im\Theta_j} (\sigma_j)_0^l(R_j, \Theta_j, \zeta_j)\, ds$$

$$(\mathbf{B}_j)_{mq}^{nl} = \frac{1}{\pi^2} \frac{\eta_n^2}{\eta_n^2 + \alpha^2} \int_{S_j} \Psi(\zeta_j, \eta_n)\, I_m(\eta_n R_j)\, e^{-im\Theta_j} (\sigma_j)_q^l(R_j, \Theta_j, \zeta_j)\, ds$$

The numerical evaluation of the integrals over the wetted surface of the body by means of a quadrature scheme has been detailed in Appendix G. The same procedure can be applied to the infinite-depth. The source-strength distribution $(\sigma_j)_q^l$ can be obtained by solving the following integral equation:

$$\frac{1}{2}\sigma_j(r_j, \theta_j, z_j) + \iint_{S_j} \sigma_j(R_j, \Theta_j, \zeta_j) \frac{\partial G_j(R_j, \Theta_j, \zeta_j; r_j, \theta_j, z_j)}{\partial n} ds_j = -\frac{\partial \left(\psi_j^{I\infty}\right)_{lq}(r_j, \theta_j, z_j)}{\partial n} \tag{H.3.13}$$

where $\frac{\partial\left(\psi_j^{I\infty}\right)(r_j,\theta_j,z_j)}{\partial n}$ are the derivatives of the unit amplitude partial cylindrical wave in infinite-depth given by:

$$\frac{\partial\left(\psi_j^{I\infty}\right)_{lq}}{\partial n} = \frac{\partial\left(\psi_j^{I\infty}\right)_{lq}}{\partial x_j} nx_j + \frac{\partial\left(\psi_j^{I\infty}\right)_{lq}}{\partial y_j} ny_j + \frac{\partial\left(\psi_j^{I\infty}\right)_{lq}}{\partial z_j} nz_j \tag{H.3.14}$$

For progressive modes:

$$\frac{\partial\left(\psi_j^{I\infty}\right)_{0q}}{\partial x_j} = e^{\alpha z_j}\left[\alpha\frac{x_j}{r_j}J_{q-1}(\alpha r_j) - \frac{q}{r_j^2}(x_j + i\,y_j)\,J_q(\alpha r_j)\right]e^{iq\theta} \tag{H.3.15}$$

$$\frac{\partial\left(\psi_j^{I\infty}\right)_{0q}}{\partial y_j} = e^{\alpha z_j}\left[\alpha\frac{y_j}{r_j}J_{q-1}(\alpha r_j) - \frac{q}{r_j^2}(y_j - i\,x_j)\,J_q(\alpha r_j)\right]e^{iq\theta_j} \tag{H.3.16}$$

$$\frac{\partial\left(\psi_j^{I\infty}\right)_{0q}}{\partial z_j} = e^{\alpha z_j}\alpha J_q(\alpha r_j)\,e^{iq\theta_j} \tag{H.3.17}$$

Similarly, for evanescent modes:

$$\frac{\partial\left(\psi_j^{I\infty}\right)_{lq}}{\partial x_j} = h_l\Psi(z,\eta_l)\left[\eta_l\frac{x_j}{r_j}I_{q-1}(\eta_l r_j) - \frac{q}{r_j^2}(x_j + i\,y_j)\,I_q(\eta_l r_j)\right]e^{iq\theta_j} \tag{H.3.18}$$

$$\frac{\partial\left(\psi_j^{I\infty}\right)_{lq}}{\partial y_j} = h_l\Psi(z,\eta_l)\left[\eta_l\frac{y_j}{r_j}I_{q-1}(\eta_l r_j) - \frac{q}{r_j^2}(y_j - i\,x_j)\,I_q(\eta_l r_j)\right]e^{iq\theta} \tag{H.3.19}$$

$$\frac{\partial\left(\psi_j^{I\infty}\right)_{lq}}{\partial z_j} = h_l\left[\alpha\cos(\eta_l z) - \eta_l\sin(\eta_l z)\right]I_q(\eta_l r_j)\,e^{iq\theta} \tag{H.3.20}$$

With respect to the expressions of the RC elements after discretization:

$$(R_j^k)_m^0 = \frac{1}{2}i\alpha\int_{S_j} e^{\alpha\zeta_j}J_m(\alpha R_j)\,e^{-im\Theta_j}\sigma_j^k(R_j,\Theta_j,\zeta_j)\,ds \tag{H.3.21}$$

$$(R_j^k)_m^n = \frac{1}{\pi^2}\frac{\eta_n^2}{\eta_n^2+\alpha^2}\int_{S_j}\Psi(\zeta_j,\eta_n)\,I_m(\eta_n R_j)\,e^{-im\Theta_j}\sigma_j^k(R_j,\Theta_j,\zeta_j)\,ds \tag{H.3.22}$$

where the source strength distribution σ_j^k is obtained by solving the same integral equation in (3.1.15).

Appendix I

Hydrodynamic operators of a truncated vertical circular cylinder and a cube

I.1 Mesh Sensitivity

I.1.1 Cylinder

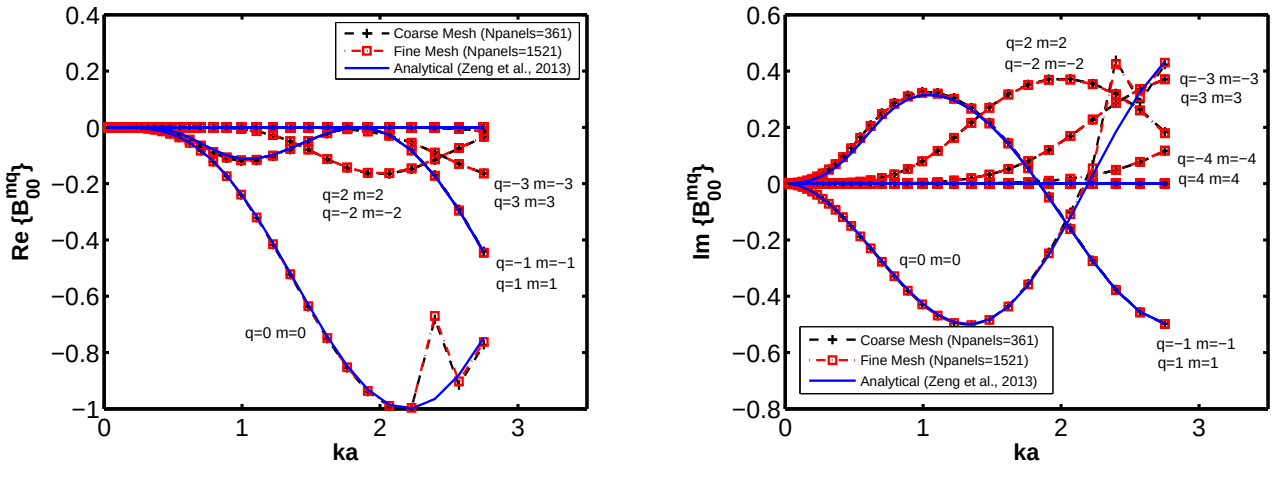

(a) (b)

Figure I.1: Real and imaginary parts of the Diffraction Transfer Matrix progressive terms for a truncated vertical cylinder of 3m radius (a), 6m draft in a 10m water depth.

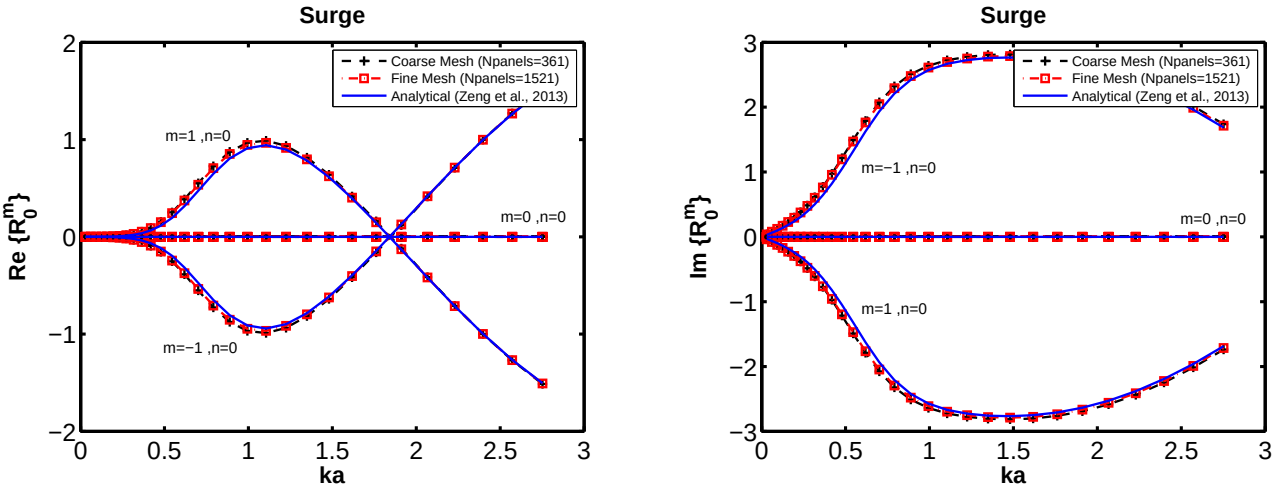

(a) (b)

Figure I.2: Real and imaginary parts of the Radiation Characteristics progressive terms for a truncated vertical cylinder of 3m radius (a), 6m draft moving in surge in a 10m water depth.

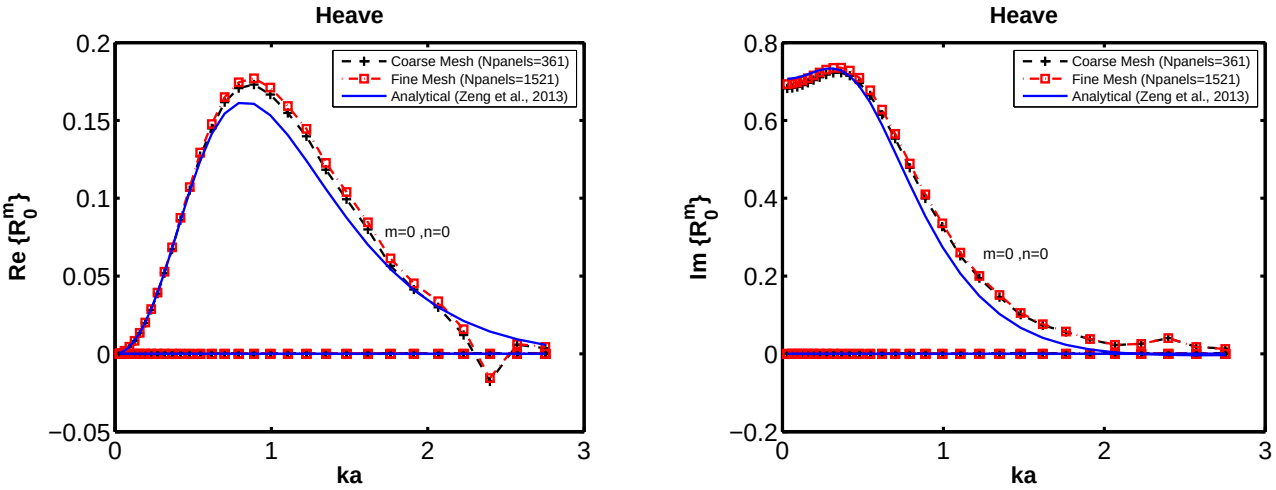

(a) (b)

Figure I.3: Real and imaginary parts of the Radiation Characteristics progressive terms for a truncated vertical cylinder of 3m radius (a), 6m draft moving in heave in a 10m water depth.

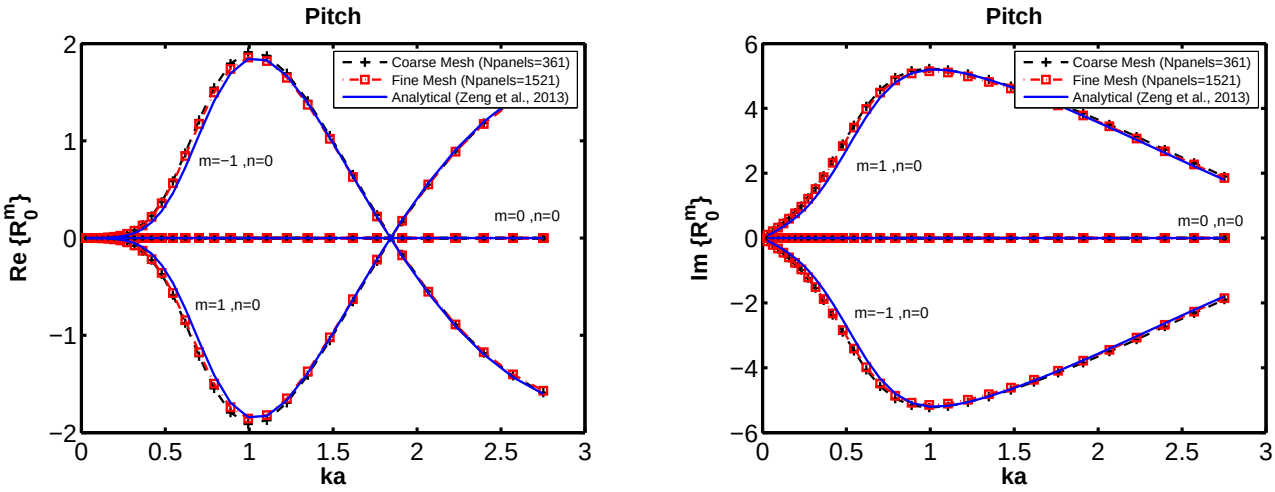

(a) (b)

Figure I.4: Real and imaginary parts of the Radiation Characteristics progressive terms for a truncated vertical cylinder of 3m radius (a), 6m draft moving in pitch in a 10m water depth.

I.1.2 Cube

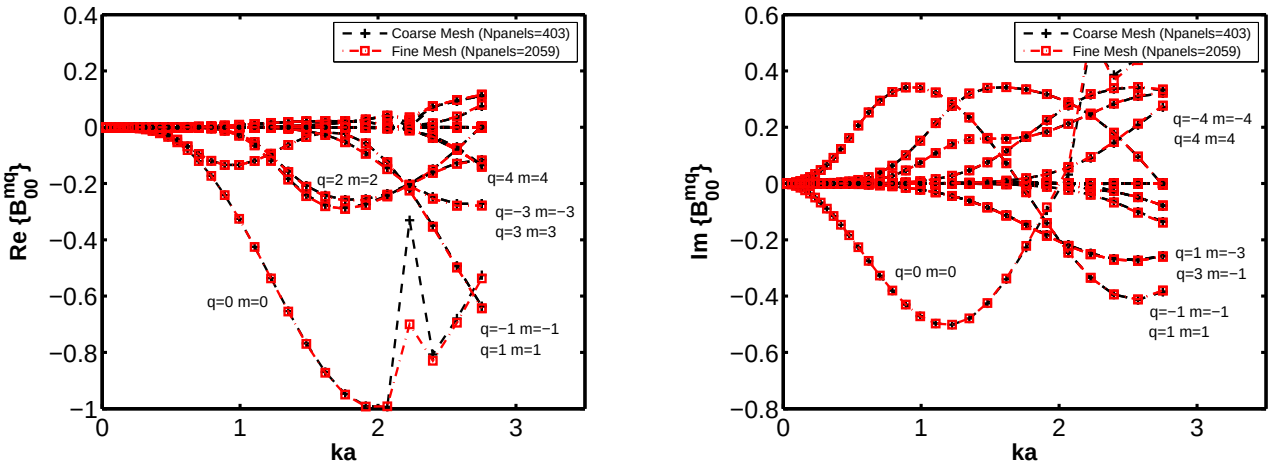

(a) (b)

Figure I.5: Real and imaginary parts of the Diffraction Transfer Matrix progressive terms for a square box of 6m side (2a), 6m draft in a 10m water depth.

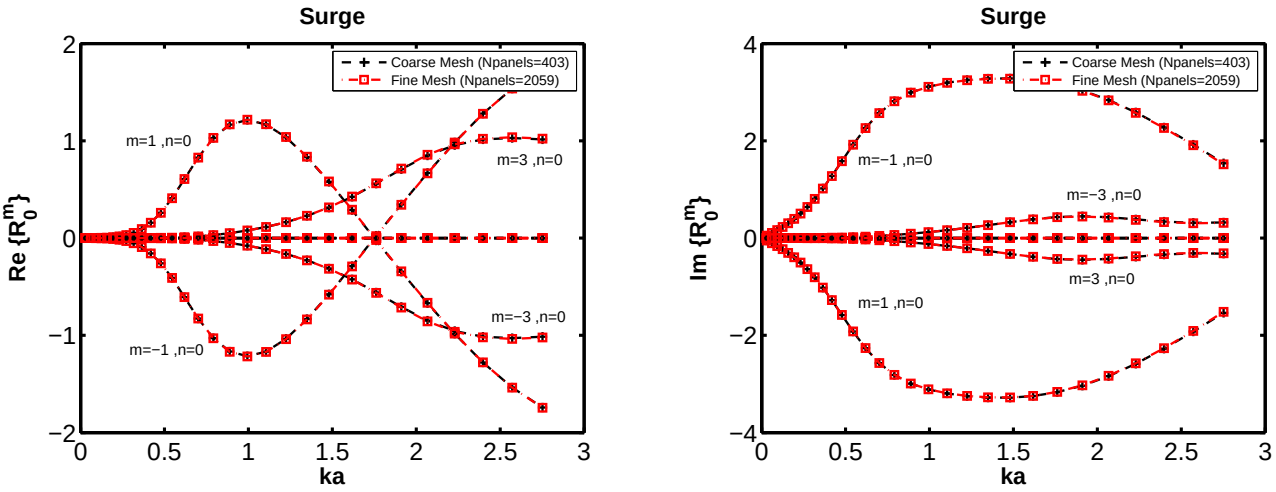

(a) (b)

Figure I.6: Real and imaginary parts of the Radiation Characteristics progressive terms for a square box of 6m side (2a), 6m draft moving in surge in a 10m water depth.

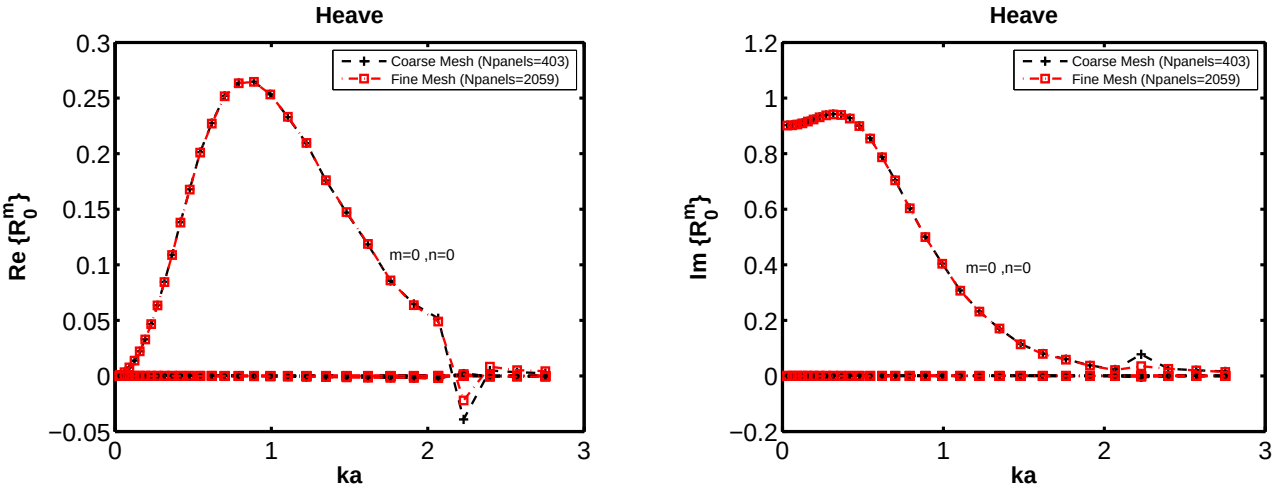

(a) (b)

Figure I.7: Real and imaginary parts of the Radiation Characteristics progressive terms for a square box of 6m side (2a), 6m draft moving in heave in a 10m water depth.

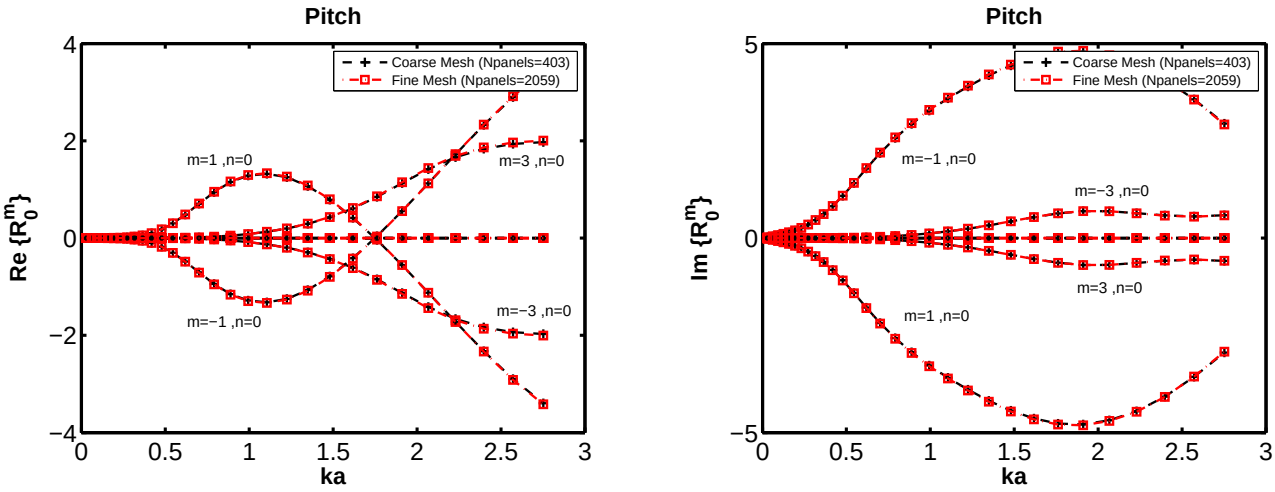

(a) (b)

Figure I.8: Real and imaginary parts of the Radiation Characteristics progressive terms for a square box of 6m side (2a), 6m draft moving in pitch in a 10m water depth.

I.2 Radiation Characteristics

I.2.1 Cylinder

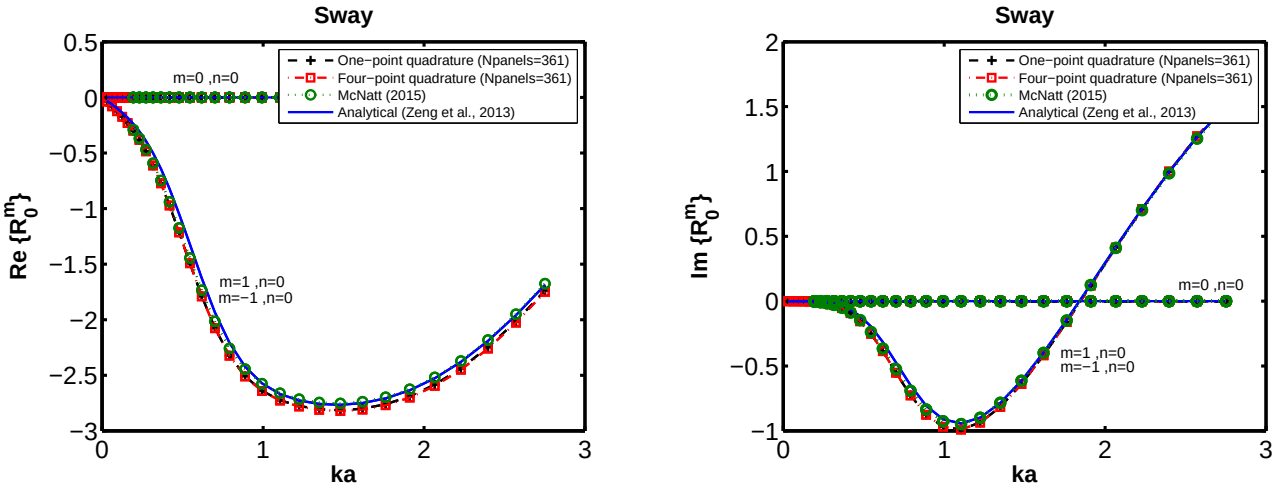

(a) (b)

Figure I.9: Real and imaginary parts of the Radiation Characteristics progressive terms for a truncated vertical cylinder of 3m radius (a), 6m draft moving in sway in a 10m water depth.

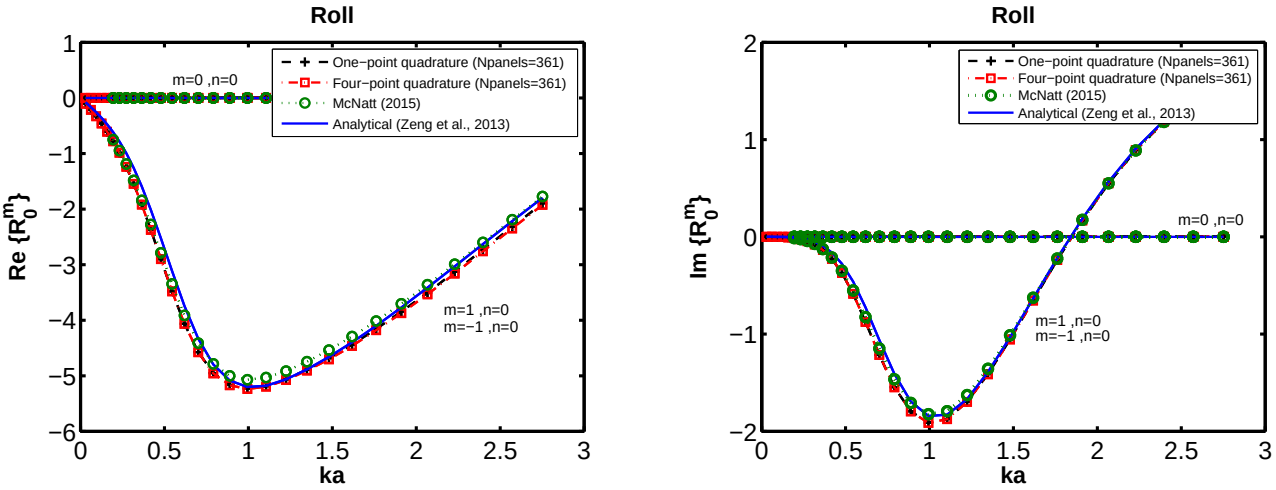

Figure I.10: Real and imaginary parts of the Radiation Characteristics progressive terms for a truncated vertical cylinder of 3m radius (a), 6m draft moving in roll in a 10m water depth.

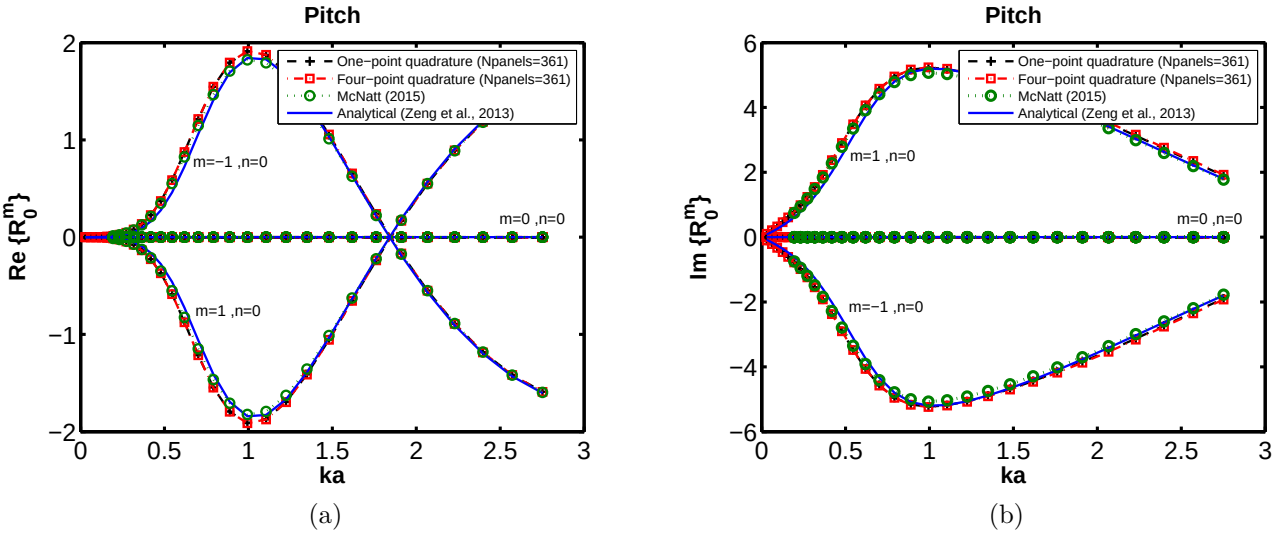

Figure I.11: Real and imaginary parts of the Radiation Characteristics progressive terms for a truncated vertical cylinder of 3m radius (a), 6m draft moving in pitch in a 10m water depth.

I.2.2 Cube

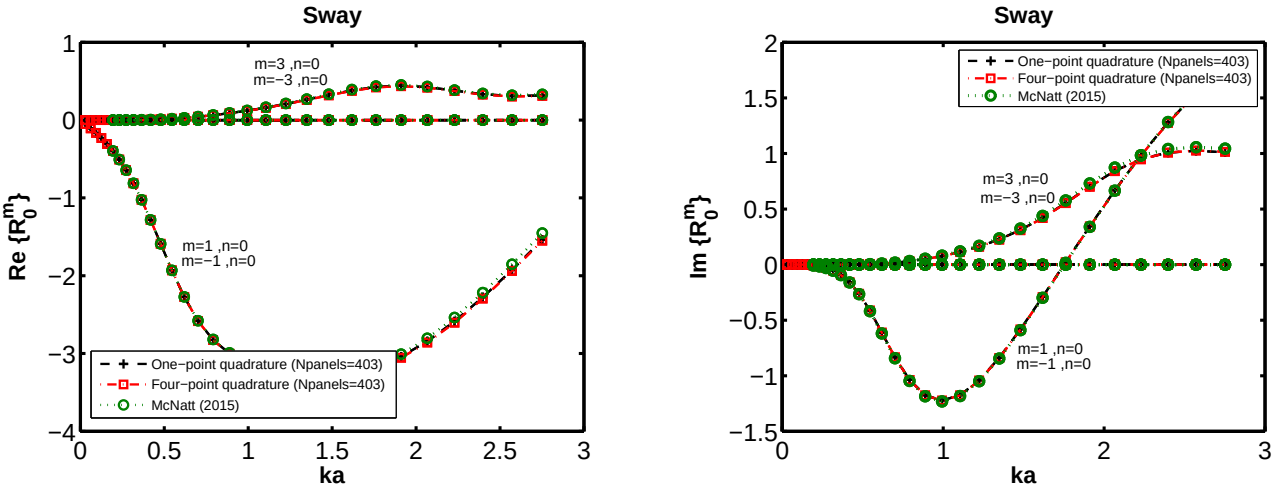

(a) (b)

Figure I.12: Real and imaginary parts of the Radiation Characteristics progressive terms for a square box of 6m side (2a), 6m draft moving in sway in a 10m water depth.

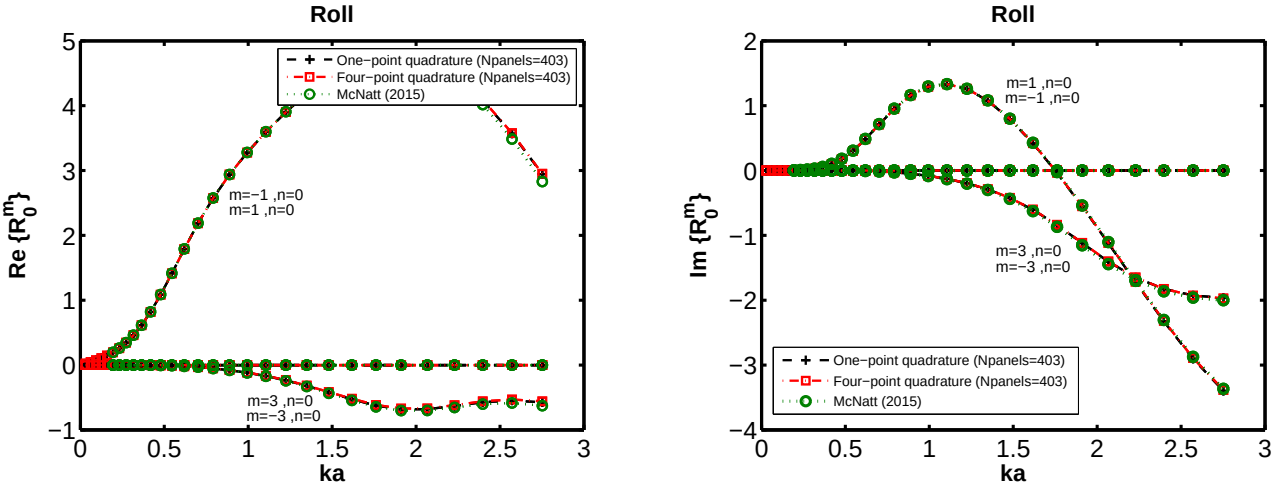

(a) (b)

Figure I.13: Real and imaginary parts of the Radiation Characteristics progressive terms for a square box of 6m side (2a), 6m draft moving in roll in a 10m water depth.

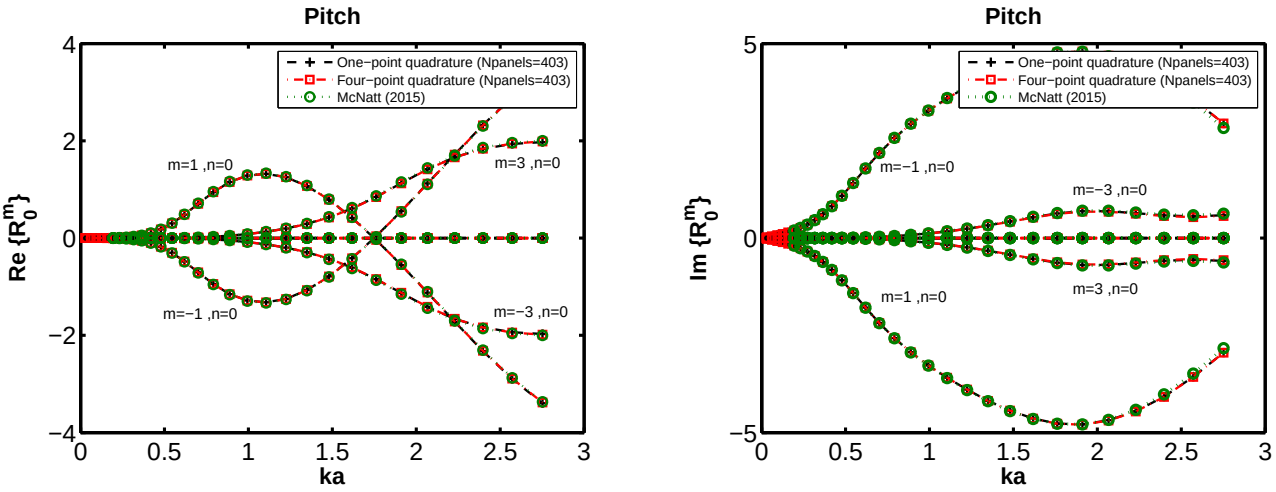

(a) (b)

Figure I.14: Real and imaginary parts of the Radiation Characteristics progressive terms for a square box of 6m side (2a), 6m draft moving in pitch in a 10m water depth.

I.3 Force Transfer Matrix

I.3.1 Cylinder

I.3.2 Cube

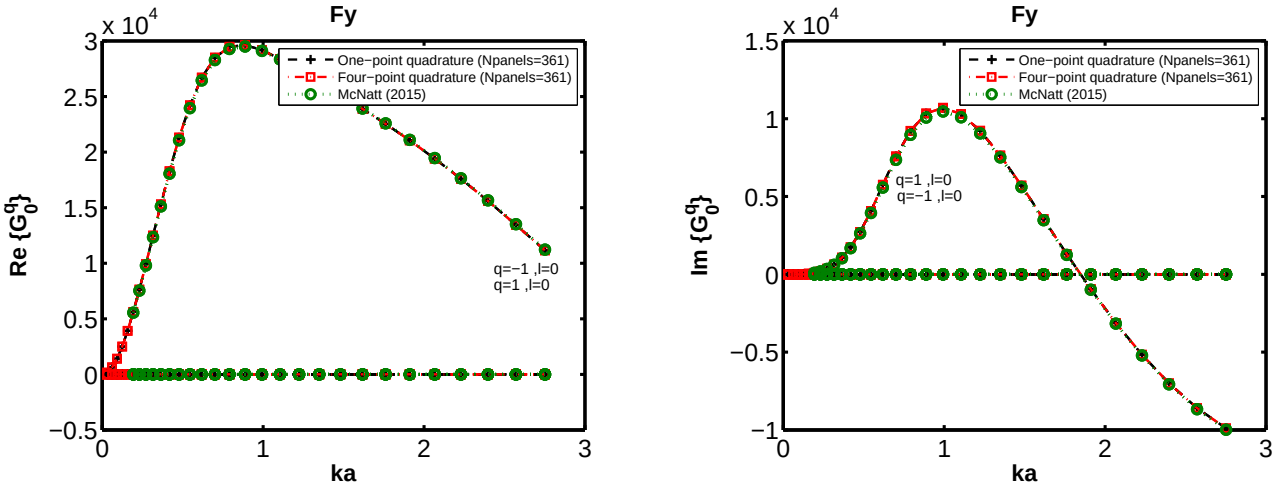

(a) (b)

Figure I.15: Real and imaginary parts of the Force Transfer Matrix progressive F_y terms for a truncated vertical cylinder of 3m radius (a), 6m draft in a 10m water depth.

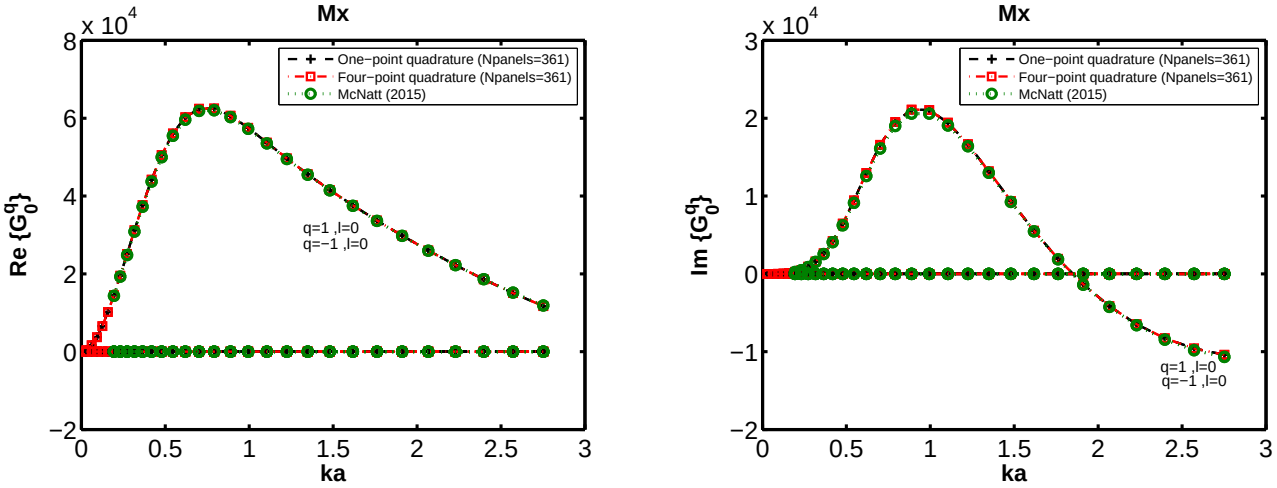

(a) (b)

Figure I.16: Real and imaginary parts of the Force Transfer Matrix progressive M_x terms for a truncated vertical cylinder of 3m radius (a), 6m draft in a 10m water depth.

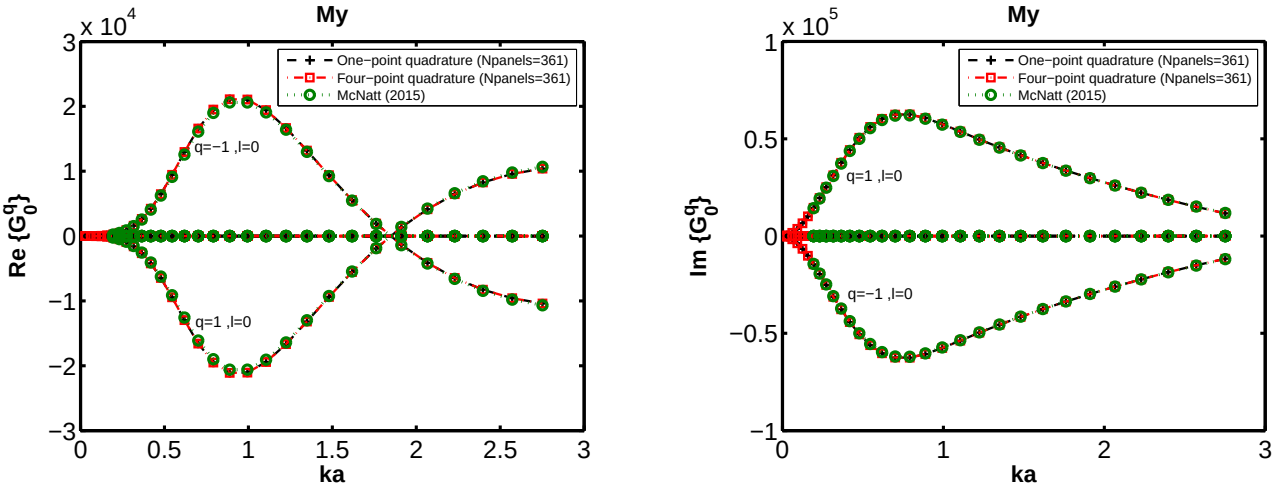

(a) (b)

Figure I.17: Real and imaginary parts of the Force Transfer Matrix progressive M_y terms for a truncated vertical cylinder of 3m radius (a), 6m draft in a 10m water depth.

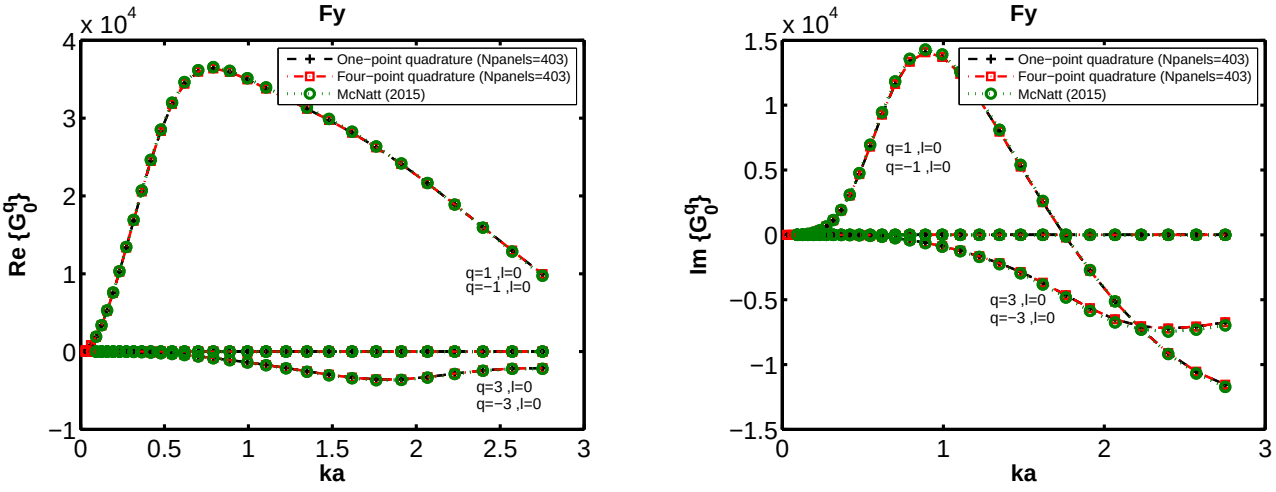

(a) (b)

Figure I.18: Real and imaginary parts of the Force Transfer Matrix progressive F_y terms for a square box of 6m side (2a), 6m draft in a 10m water depth.

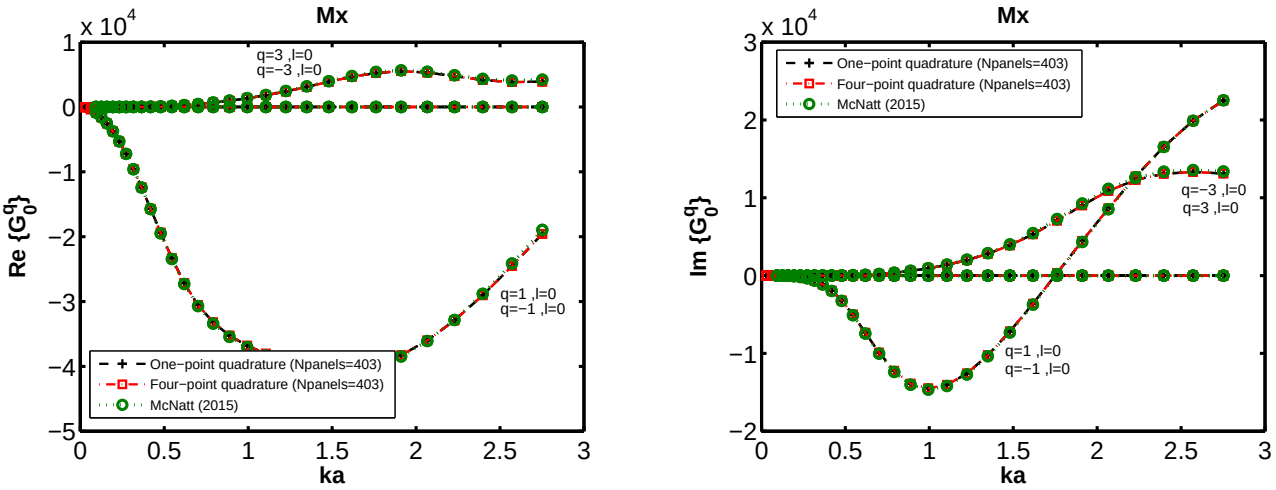

(a) (b)

Figure I.19: Real and imaginary parts of the Force Transfer Matrix progressive M_x terms for a square box of 6m side (2a), 6m draft in a 10m water depth.

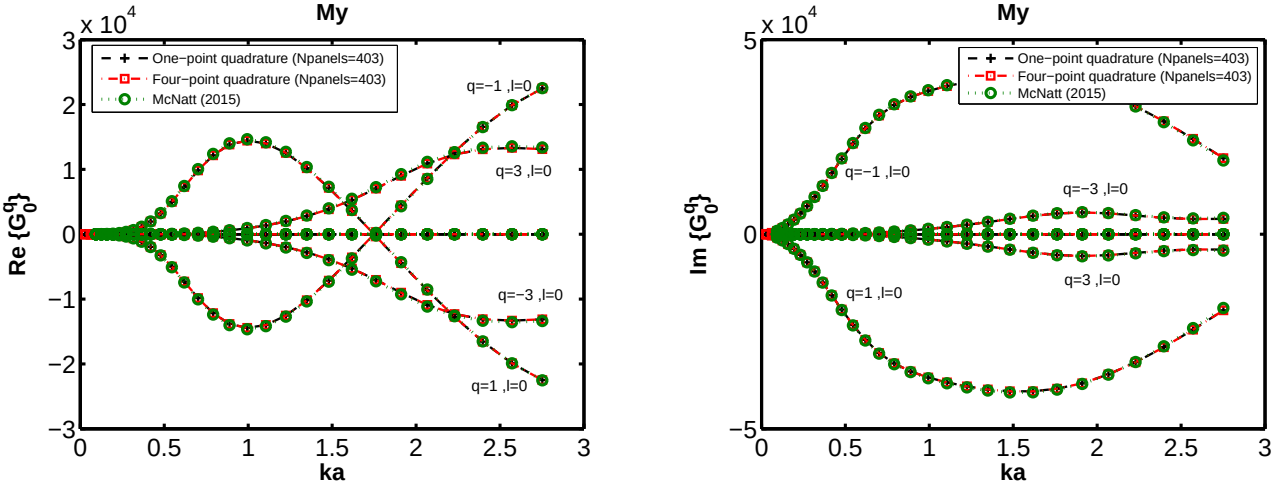

(a) (b)

Figure I.20: Real and imaginary parts of the Force Transfer Matrix progressive M_y terms for a square box of 6m side (2a), 6m draft in a 10m water depth.

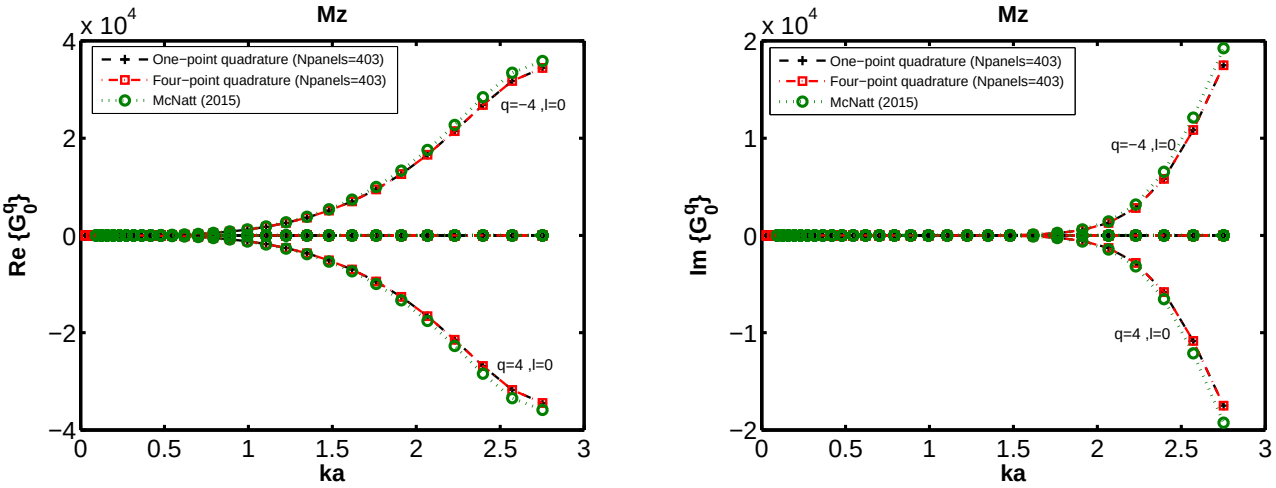

(a) (b)

Figure I.21: Real and imaginary parts of the Force Transfer Matrix progressive M_z terms for a square box of 6m side (2a), 6m draft in a 10m water depth.

Appendix J

Hydrodynamic coefficients of a small group of closely-spaced hemispheric floats

In Chapter 5, the response of an hemispheric float placed in the middle of a three unit cluster was computed with NEMOH (set as reference) and with the IT for different values of evanescent modes truncation. A comparison of the differences in percentage between both approaches was shown in Figure 5.3. Small discrepancies between results were reported even in case no evanescent modes were included in the representation of the wave fields.

At first glance, this behaviour seems rather unexpected. Indeed, in section 4.3.2 the influence of evanescent modes on the hydrodynamic coefficients, such as the added-mass, for cases where bodies are placed at close proximity (Figure 4.14) was clearly shown. As the float's response is governed by the equation of motion 5.1.3, composed of several parameters amongst which the hydrodynamic coefficients, one would predict significant errors in the evaluation of the latter to propagate through the evaluation of the float's response.

At this point, it is important to recall an important outcome of the first part of Chapter 4. The formulae (4.2.13) and (4.2.21) derived for both the excitation forces and radiation damping hydrodynamic coefficients of bodies in array relate those quantities with progressive terms only. From that it follows that both the excitation forces and the radiation damping coefficients can be evaluated dispensing with the evanescent modes or, in other words, using a wide-spacing approximation. This is shown in Figures J.2 and J.3, which depict a comparison of the output from a direct NEMOH evaluation and from the use of the IT with the evanescent modes truncation set to

zero. A perfect match of results can be observed. Contrarily, the same comparison for the added-mass coefficients is shown in Figure J.1 and significant discrepancies (on the order of 50% at some frequencies) between the output of both approaches are identified, in particular for the coupling (off-diagonal) terms. We note that deviations from the reference are more significant at the "low-frequency" range ($< 1.5 rad/s$) rather than at higher frequencies where convergence of both outputs is obtained. Lower frequencies are associated with longer wavelengths and, intuitively, it is at this region of frequencies where the wide-spacing approximation will be more difficult to comply with.

While only one of the three main hydrodynamic parameters is affected by the modeling of the near-field, the impact of spurious added-mass coefficients on motion output will strongly depend on their magnitude relative to the rest of parameters in the equation of motion.

Contrarily to other floating offshore structures, the dynamics of WECs are strongly influenced by the damping forces introduced by the Power Take-Off (PTO) system. This can be clearly deduced from a comparison of Figures 5.3 and J.4 which display the differences in percentage between the float-2 response computed using NEMOH and the IT for different evanescent modes truncation with and without including the effect of the PTO damping respectively. Contrarily to Figure 5.3, in J.4 the differences between the NEMOH output (set as reference) and the IT when a wide-spacing approximation is used are very significant in a wide-range of frequencies.

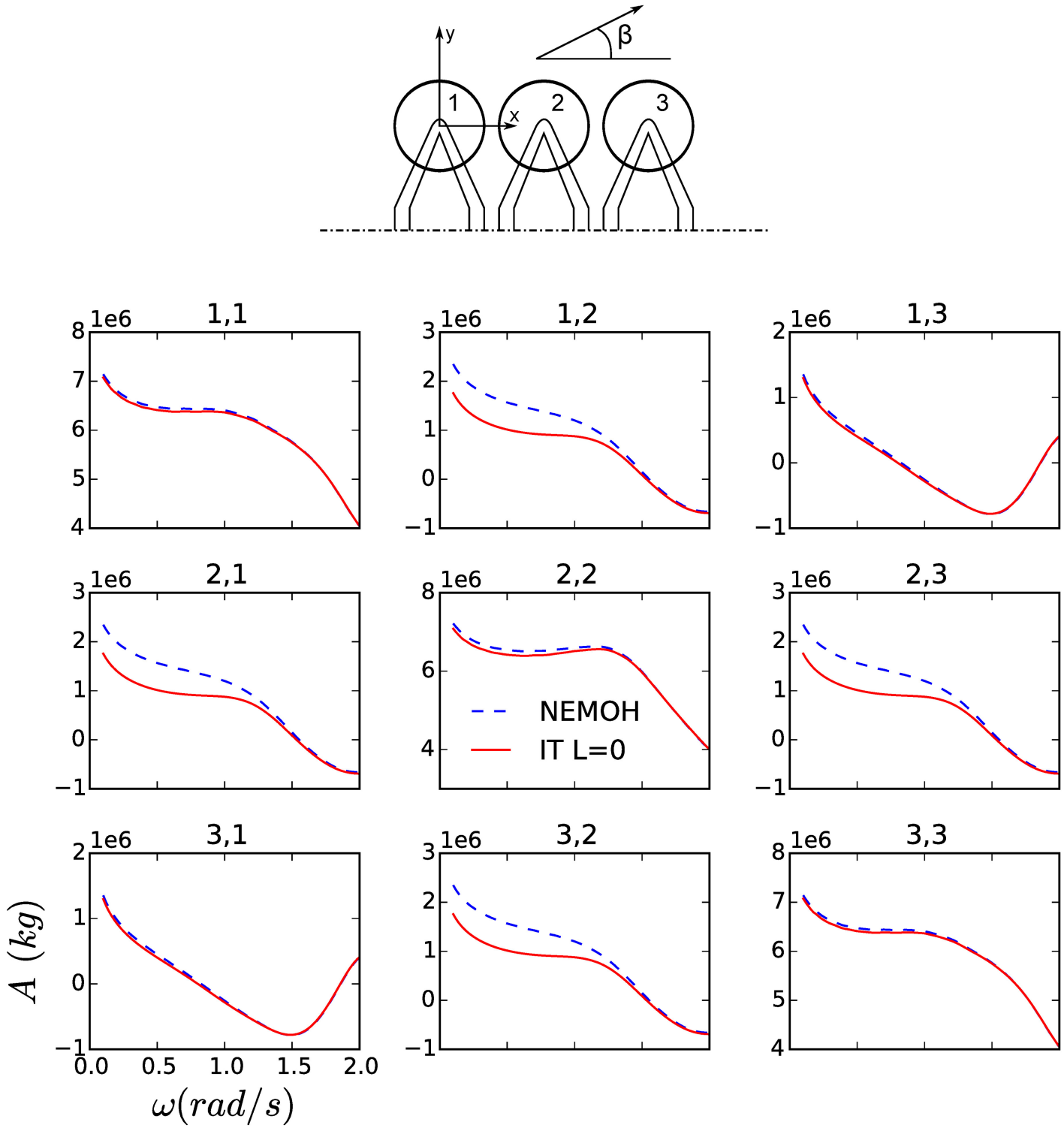

Figure J.1: Diagonal and off-diagonal terms of the added-mass coefficient matrix **A**(equation 5.1.3) of the three-float system representing part of the generic bottom-fixed heave-buoy array WEC studied in Chapter 5.

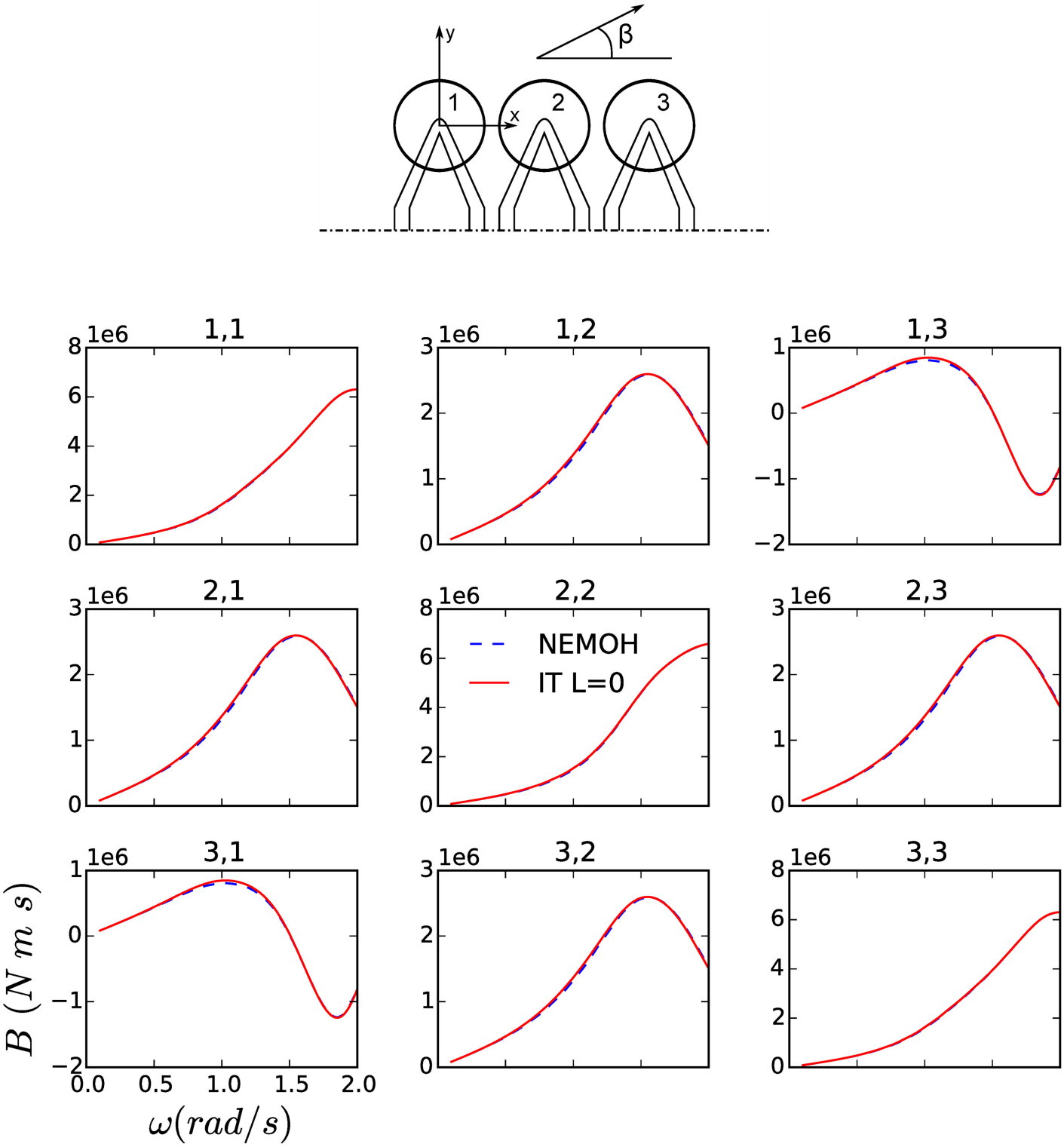

Figure J.2: Diagonal and off-diagonal terms of the hydrodynamic damping coefficient matrix **B** (equation 5.1.3) of the three-float system representing part of the generic bottom-fixed heave-buoy array WEC studied in Chapter 5.

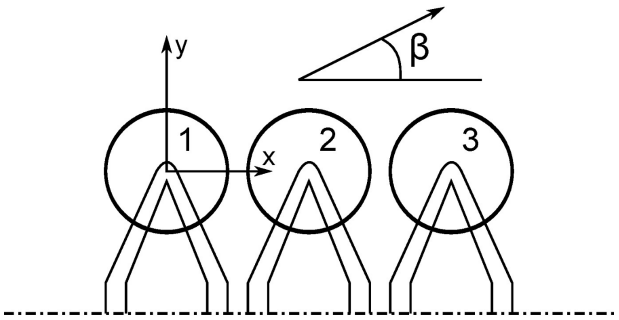

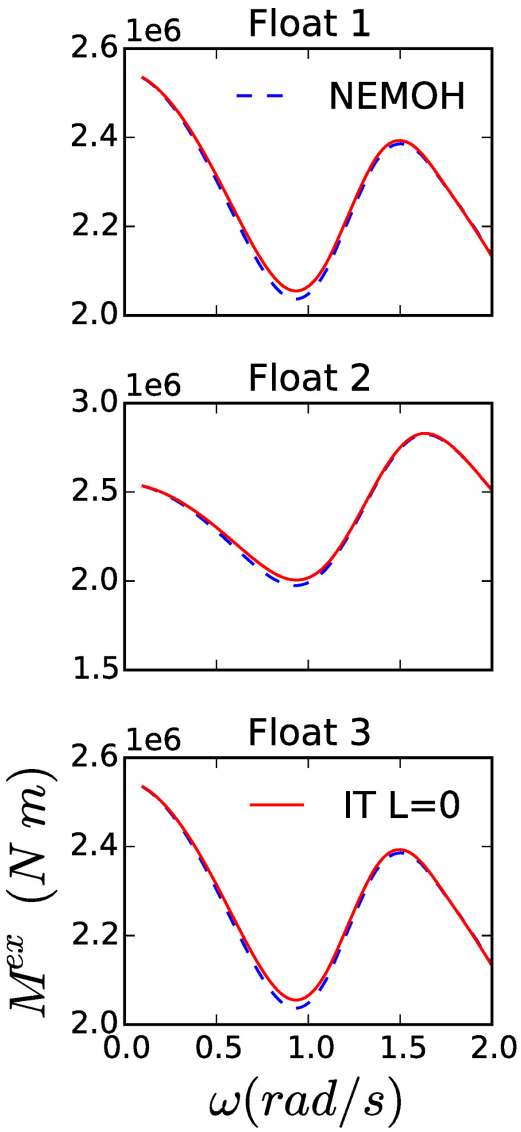

Figure J.3: Terms of the excitation moment vector $\mathbf{M^{ex}}$ (equation 5.1.3) of the three-float system representing part of the generic bottom-fixed heave-buoy array WEC studied in Chapter 5 for a wave incidence of $\beta = 90°$.

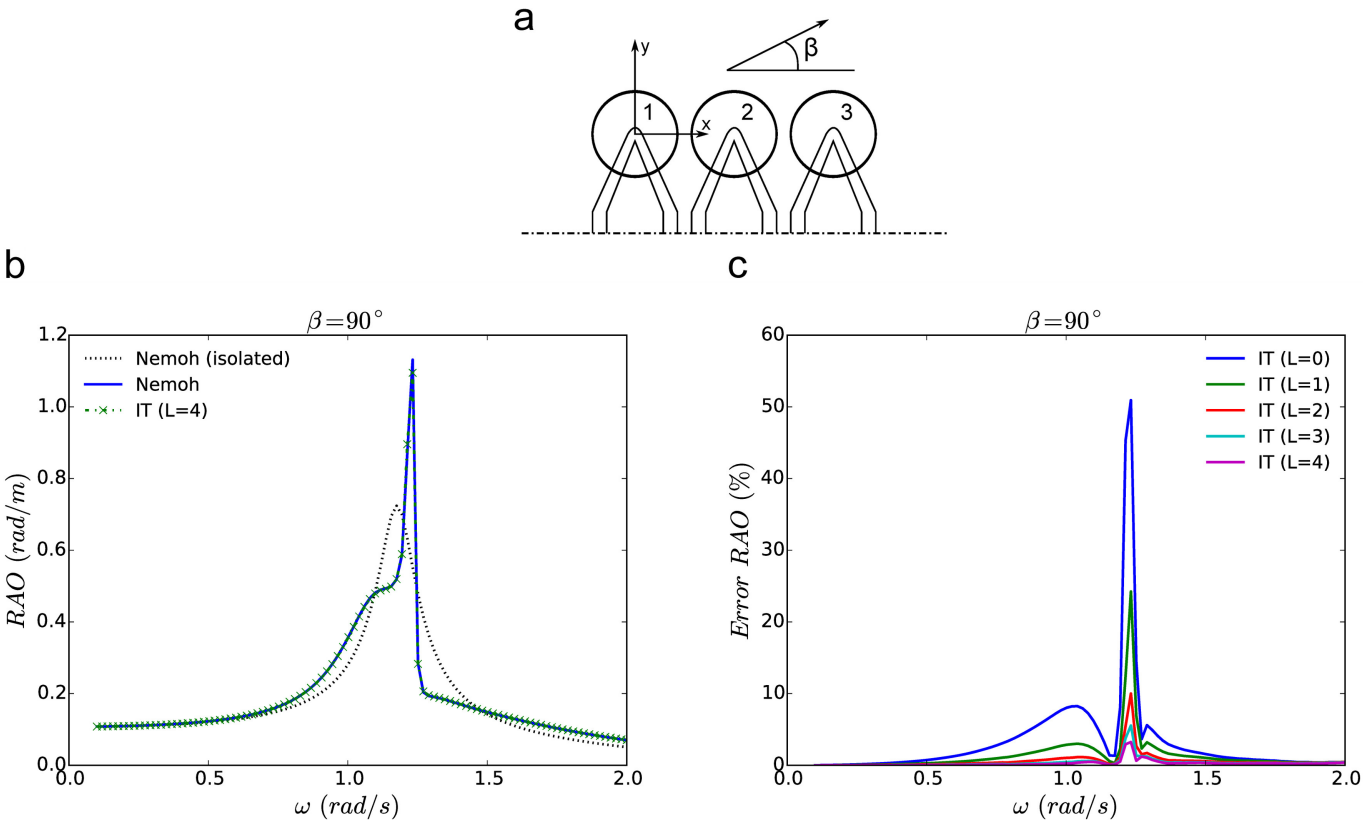

Figure J.4: (a) Top view of a section of a three-float WEC with **no Power Take-Off (PTO)**; (b) Comparison of the Response Amplitude Operator (RAO) of float 2 computed using both a direct BEM calculation (both when isolated and in array) and with the Direct Matrix Method interaction theory (IT) using 4 evanescent modes (L) and a $\beta = 90°$ wave incidence; (c) relative difference between the (RAO) of float 2 computed using both a direct BEM calculation and with the Direct Matrix Method interaction theory (IT) for different values of the evanescent modes truncation (L) and a wave incidence of $\beta = 90°$.

UNIVERSITE BRETAGNE LOIRE

CENTRALE NANTES

Thèse de Doctorat

Francesc Fàbregas Flavià

Développement d'un modèle numérique pour la simulation des grandes fermes de houlomoteurs

A numerical tool for the frequency domain simulation of large clusters of wave energy converters

Résumé

Plusieurs convertisseurs d'énergie houlomotrice composés d'un grand réseau compact O(100) de petits flotteurs ont été proposés comme étant des systèmes avantageux pour l'extraction de l'énergie des vagues et représentent une alternative aux technologies basées sur un seul flotteur de plus grande taille. Leur capacité d'extraction d'énergie ayant été prouvé, l'accent est désormais mis sur l'optimisation pour adapter le coût de l'électricité produite aux tarifs du marché.

L'un des défis les plus importants auxquels la modélisation numérique de ces systèmes houlomoteurs fait face est le calcul des interactions hydrodynamiques entre le grand nombre de sous-unités de production d'énergie qu'ils contiennent. En effet, les capacités des logiciels standards basés sur l'approche Boundary Element Method pour le calcul de l'interaction houle/structure sont largement dépassées quand un nombre de flotteurs O(100) est atteint. L'implémentation d'une méthode basée sur une théorie d'interaction plus adapté au problème de diffraction multiple s'avère donc indispensable. Cette nouvelle approche, connue sous le nom de Direct Matrix Method, permet de réduire le nombre d'inconnues du problème d'interaction traditionnel en se basant sur la connaissance de la manière dont un convertisseur d'énergie houlomotrice diffracte et génère des vagues.

L'accélération apportée par l'outil mis en place a permis de modéliser et optimiser un houlomoteur composé d'une soixantaine d'unités de type flotteur pilonnant. On a montré qu'il existe un nombre optimal de flotteurs pour une empreinte du dispositif donnée. Dépasser l'optimum entraîne une perte de performance nuisible à sa viabilité économique.

Mots clés
Interaction multiple, Méthode des éléments frontière, Direct Matrix Method, Optimisation, Houlomoteur, énergie des vagues, NEMOH, Relations d'Haskind.

Abstract

Compact arrays of small wave absorbers constitute an example of the multiple existing categories of wave energy converters (WECs) and have been identified as being an advantageous solution for the extraction of wave energy when compared to a big isolated point absorber.

Among the numerous challenges associated with the numerical modeling of such devices, one of the most relevant one is the evaluation of the hydrodynamic interactions amid the large number of floats O(100) they are composed of. Direct computations with standard Boundary Element Method (BEM) solvers, used extensively in wave/structure interaction problems, become prohibitive when the number of bodies increases. Thus, there is a need to employ an alternative approach more suitable for the study of the multiple-scattering in large arrays.

In this work, the Direct Matrix Method interaction theory has been implemented. Based on characterizing the way a WEC scatters and radiates waves, this methodology enables one to significantly reduce the number of unknowns of the classical boundary value problem dealt with by standard BEM solvers and, therefore, the computational time.

The acceleration provided by the numerical tool developed has allowed examining the power capture of a generic bottom-reference heave-buoy array WEC and optimizing its layout. We have shown that there exist an optimum number of floats for a given device footprint. Exceeding this number results in a "saturation" of the power increase which is undesirable for the economic viability of the device.

Key Words
Multiple-scattering, Boundary Element Method, Direct Matrix Method, Optimization, Wave Energy converter, Wave Energy, NEMOH, Haskind Relations.